British Columbia Geological Survey
Ministry of Energy and Mines
www.em.gov.bc.ca/geology

BRITISH COLUMBIA | Ministry of Energy and Mines

Geological Fieldwork 2013

A Summary of Field Activities and Current Research

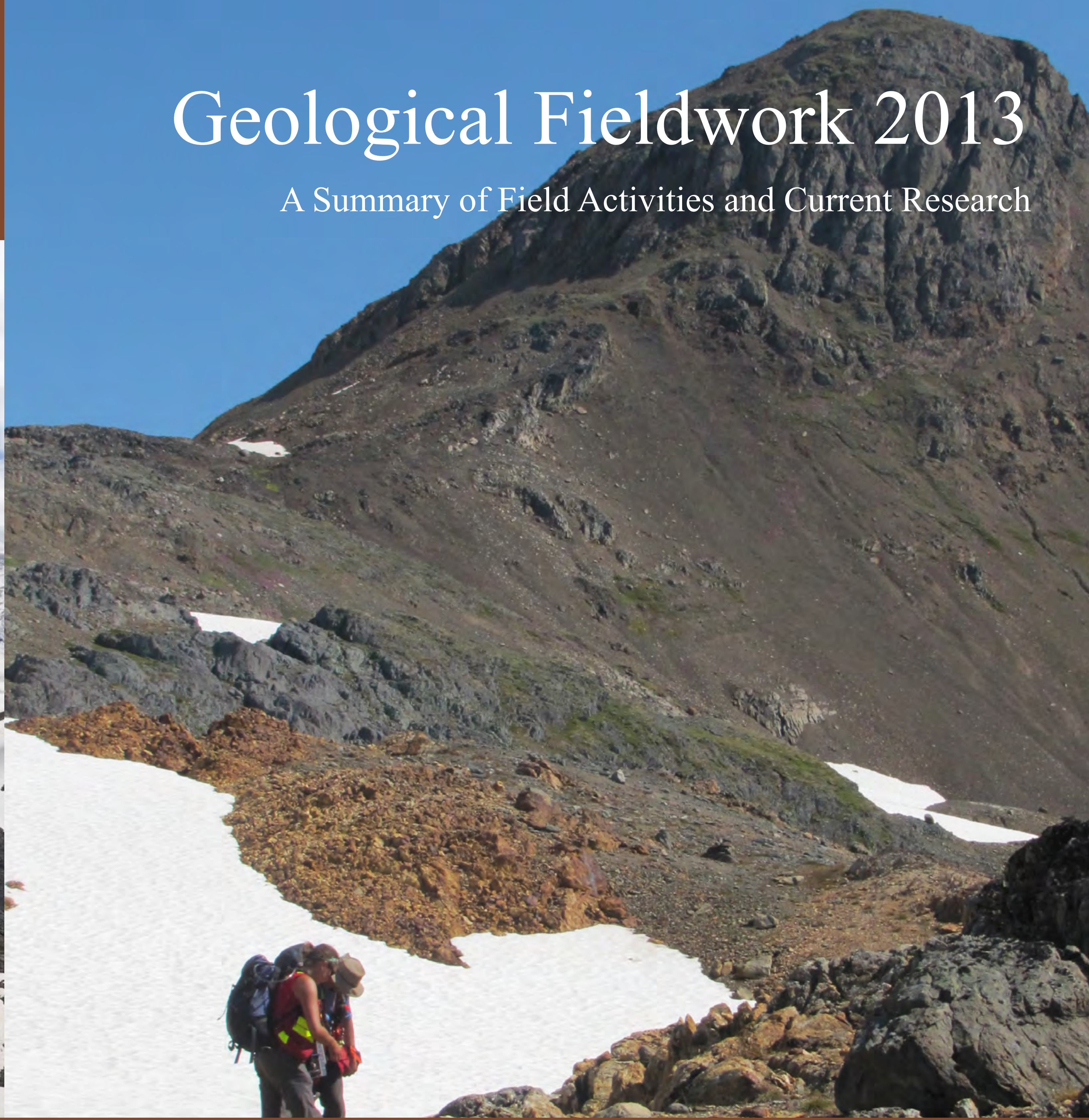

B.C. Ministry of Energy and Mines, British Columbia Geological Survey Paper 2014-1

Geological Fieldwork 2013

A Summary of Field Activities and Current Research

Ministry of Energy and Mines
British Columbia Geological Survey

Paper 2014-1

Ministry of Energy and Mines
Mines and Mineral Resources Division
British Columbia Geological Survey

Recommended citation format for individual papers:

Logan, J.M. and Schiarizza, P., 2014. The Rayfield River pluton, south-central British Columbia (NTS 92P/6): Geologic setting and copper mineralization. In: Geological Fieldwork 2013, British Columbia Ministry of Energy and Mines, British Columbia Geological Survey Paper 2014-1, pp. 15-27.

Front Cover: View to the north of the Iron Cap zone, on the east side of the McTagg anticlinorium. In the foreground, the potassic-altered core of the Iron Cap zone is being examined. In the background, rocks of the Hazelton and Bowser Lake groups are thrust imbricated east of the near-vertical Brucejack fault, which traces from upper left to lower right, extending from the notch in the skyline southward along the partly snow-covered valley. See Nelson, J., and Kyba, J., 2014. Structural and stratigraphic control of porphyry and related mineralization in the Treaty Glacier-KSM-Brucejack-Stewart trend of western Stikinia, this volume. **Photo by JoAnne Nelson**.

Back Cover: View to the south of the upper part of Treaty Glacier on the northeast side of the McTagg anticlinorium. The Konkin and Copper Belle showings are on the ridge in the foreground. Ridge on the middle right is the southward view of the prominent ridge on the front cover. See Nelson, J., and Kyba, J., 2014. Structural and stratigraphic control of porphyry and related mineralization in the Treaty Glacier-KSM-Brucejack-Stewart trend of western Stikinia, this volume. **Photo by Lauren Wilson.**

British Columbia Cataloguing in Publication Data

Main entry under title:

Geological Fieldwork: - 1974 -

Annual.

Issuing body varies

Vols. for 1978-1996 issued in series: Paper / British Columbia. Ministry of Energy, Mines and Petroleum Resources; vols. for 1997 - 1998, Paper / British Columbia. Ministry of Employment and Investment; vols. for 1999-2004, Paper / British Columbia. Ministry of Energy and Mines; vols. for 2005-2009, Paper / British Columbia. Ministry of Energy, Mines and Petroleum Resources; vols. for 2010, Paper / British Columbia. Ministry of Forests, Mines and Lands; vols. for 2011, Paper / British Columbia. Ministry of Energy and Mines; vols. for 2012- , Paper / British Columbia. Ministry of Energy, Mines and Natural Gas; vols. for 2014- , Paper / British Columbia. Ministry of Energy and Mines.

Includes Bibliographical references.

ISSN 0381-243X=Geological Fieldwork

1. Geology - British Columbia - Periodicals. 2. Mines and mineral resources - British Columbia - Periodicals. 3. Geology - Fieldwork - Periodicals. 4. Geology, Economic - British Columbia - Periodicals. 5. British Columbia. Geological Survey Branch - Periodicals. I. British Columbia. Geological Division. II. British Columbia. Geological Survey Branch. III. British Columbia. Geological Survey Branch. IV. British Columbia. Dept. of Mines and Petroleum Resources. V. British Columbia. Ministry of Energy, Mines and Petroleum Resources. VI. British Columbia. Ministry of Employment and Investment. VII. British Columbia Ministry of Energy and Mines. VIII. Series: Paper (British Columbia. Ministry of Energy, Mines and Petroleum Resources). IX. Series: Paper (British Columbia. Ministry of Employment and Investment). X. Series: Paper (British Columbia Ministry of Energy and Mines). XI. Series: Paper (British Columbia Ministry of Energy, Mines and Petroleum Resources). XII. Series: Paper (British Columbia Ministry of Forests, Mines and Lands). XIII. Series: Paper (British Columbia Ministry of Energy and Mines). XIV. Series: Paper (British Columbia Ministry of Energy, Mines and Natural Gas). XV. Series: Paper (British Columbia Ministry of Energy and Mines).

QE187.46   622.1’09711   C76-083084-3 (Rev.)

Victoria
British Columbia
Canada

January 2014

Foreword

Geological Fieldwork 2013

This is the thirty-ninth edition of **Geological Fieldwork**, a volume of peer-reviewed papers that present the results of geological research conducted by the **British Columbia Geological Survey** (BCGS) and its partners in 2013. The papers address different aspects of British Columbia's geology, with many highlighting the enormous mineral wealth of the Province. The annual Geological Fieldwork publication is one way that the BCGS helps to unlock this mineral wealth by providing comprehensive, objective, and up-to-date geoscience information, advice, and knowledge to the minerals industry.

Following the spring election in 2013, the new government of British Columbia reorganized the natural resource sector ministries. The Ministry of Energy, Mines and Natural Gas (MEMNG) was split into two separate ministries: the Ministry of Energy and Mines (MEM) and the Ministry of Natural Gas Development (MNGD). The BCGS remained with MEM as did the five geologists that deliver the Regional Geologists Program.

British Columbia Geological Survey activity highlights

Research

- Fieldwork continued on four projects that are part of the GSC's Targeted Geoscience Initiative program (TGI-4).
- New initiatives with various partners on porphyry deposits in the Nicola arc and the Stewart-Treaty Glacier corridor.
- New geochemical initiative on indicator minerals with a joint team of five researchers from the School of Earth and Ocean Sciences (University of Victoria) and the BCGS.
- BCGS geologists published nine Open Files, five GeoFiles, three Information Circulars, twenty one interagency publications, and thirteen external papers. BCGS alumni continued to publish their research, including a GeoFile by Roger Paulen and Ray Lett that presents geochemical results from gossans in the Kootenay, Slide Mountain, and Quesnel terranes, and an encyclopedic review of skarns in the Canadian Cordillera by Gerald Ray, about which one client remarked "… without question a landmark work... will be the "go-to" source for those wanting to know what skarns are all about … will serve as "the" reference for skarns for a long, long time."
- Publication of a fieldtrip volume that included papers on porphyry deposits of central and southern BC as part of the Society of Economic Geologists (SEG) annual meeting in Whistler.

Outreach at conferences and workshops

- Survey geologists presented at conferences and workshops including Roundup, PDAC, SEG, KEG, GACMAC, NWMA, GSA, Goldschmidt, International Applied Geochemistry Symposium, Minerals South, Minerals North, and the Smither's Rock Talk.
- The BCGS co-hosted the annual Canadian Tectonics Group meeting in Victoria as part of the BCGS Open House. This three-day meeting attracted over 150 geoscientists who delivered 22 oral presentations and 24 posters. It wrapped up with a field trip of the boundary between the Leech River gneiss (Pacific Rim terrane) and the Metchosin Igneous complex (Crescent terrane) near Victoria.
- Staff of the BC Mineral Development Office in Vancouver hosted various investor delegations and participated in the Asia Investment Mission, which included the China Mining Conference in Tianjin, China.

Data archiving and access

- Users can now access over 33,470 company mineral assessment reports using the online ARIS database.
- The Property File database now features more than 50,200 documents online.
- MINFILE continues to expand: 4300 occurrences were updated and 1366 were added.

Renewal

- Refurbishment of the Survey's in-house geochemical laboratory was completed with the construction of the mineral separation line by the addition of a Bico disc pulverizer and a Wilfley shaking table.

Awards

- JoAnne Nelson (BCGS Northern Manager) was included in the 2013 list of the "Top 100 Inspirational Women in Mining" by the organization Women in Mining (UK).
- The 2012-2013 Fraser Institute's global ranking of geological databases ranked MapPlace third. Since 2005, MapPlace has consistently been listed in the top ten, including two first place rankings.

Stephen M. Rowins
Chief Geologist & Executive Director
British Columbia Geological Survey

Table of Contents

British Columbia Geological Survey annual program review 2013

Adrian S. Hickin[1, a], Stephen M. Rowins[1], Larry, D. Jones[1], and Bruce Madu[2]

[1] British Columbia Geological Survey, Ministry of Energy and Mines, Victoria, BC, V8W 9N3
[2] British Columbia Geological Survey, Ministry of Energy and Mines, Vancouver, BC, V6Z 2G3
[a] corresponding author: Adrian.Hickin@gov.bc.ca

Recommended citation: Hickin, A.S., Rowins, S.M, Jones, L.D., and Madu, B., 2013. British Columbia Geological Survey annual program review 2013. In: Geological Fieldwork 2013, British Columbia Ministry of Energy and Mines, British Columbia Geological Survey Paper 2014-1, pp. 1-14.

Chief Geologist's Message

Why support public geoscience? In short, public geoscience reduces exploration costs and risk, thereby improving returns on private investment and increasing revenues accruing to governments as royalties and taxes.

> *"Most mineral resources in Canada are public assets and governments have determined that the responsible development of these resources is in the public interest. Moreover, because much of the geoscience information that underpins exploration has the economic characteristics of a public good, the provision of public geoscience to stimulate exploration is a key element of federal, provincial and territorial mining strategies".*
>
> *J.M. Duke 2010 (former Director General of the Geological Survey of Canada)*

Public geoscience is undertaken on behalf of the public through open and transparent processes, and its results are freely available to all. It traditionally consists of geological mapping, data custodianship and delivery, mineral deposit studies, geochemical and geophysical surveys, and resource studies. Duke (2010) points out that it is important to subsurface resource exploration and development because: it attracts exploration investment by allowing industry to identify areas of favourable mineral and oil and gas potential; increases exploration efficiency by making it unnecessary for individual companies to spend money on non-prospective ground or to duplicate common information; and increases exploration effectiveness by providing key information for risk-based decisions.

Geological surveys in Canada cooperate under the terms and conditions formally set out in the Intergovernmental Geoscience Accord (IGA). The agreement was first signed by Energy and Mines Ministers in 1996 and has been renewed three times, most recently in Charlottetown, 2012. The roles and responsibilities as defined by the IGA are as follows:

2.1. The Geological Survey of Canada (GSC) carries out national geoscience programs to define the geology and resources of Canada. These programs are typically thematically based, and national or broadly regional in scope and significance. They are implemented across Canada, and include aspects of fundamental research, technology development, and information transfer not contained in the programs of all of the provincial and territorial survey organizations.

2.2. The provincial and territorial geological surveys carry out programs specific to the economic development and resource management of their own jurisdictions. These programs are carried out at a scale appropriate to addressing provincial or territorial responsibilities, and are geographically limited to the jurisdiction over resources, environment, and land of the province or territory. They contribute to a systematic description of the geology of the provinces and territories, including their mineral and energy endowment. Provincial and territorial programs are largely directed toward sustainable economic development and are closely linked to the needs of clients. They are also related to provincial and territorial land use and social issues.

The IGA also sets out principles and mechanisms of cooperation. It establishes a framework for jointly setting priorities and planning programs. Although precipitated by a federal policy decision, the IGA has gained broad acceptance, indicating the appetite for collaboration among the geological surveys. The BCGS and the GSC share an especially close professional relationship due to commitments made in the British North America (BNA) Act, 1867, and the Terms of Union, 1871. Specifically, Canada agreed to assume and defray the charges for a Geological Survey in British Columbia. In response, the GSC maintains two national geoscience offices in British Columbia, the Pacific Geoscience Centre (PGC) in Sidney, and the Cordilleran Geoscience Office in Vancouver.

This spirit of cooperation extends well beyond the geological surveys to other public geoscience groups. Since 2003, a geoscience partnership agreement between the University of Victoria, the Ministry of Energy and Mines, and the Ministry of Natural Gas Development has provided over $2.6 million in funding for 33 applied geoscience projects to teams of researchers at the University of Victoria and the Ministry. The Survey has participated in numerous collaborative projects with Geoscience BC, a non-profit society established in 2005 to generate new applied geoscience information that will attract global investment to the BC mining and energy sector. Geoscience BC has no in-house capacity to undertake geoscience projects, but awards grants to consultants, contractors, and other geoscience providers to do the work. The Province has supported Geoscience BC through a series of unrestricted grants totaling $48.7 million since 2005. The strength of Geoscience BC has been successful completion of large, multi-million dollar regional geophysical and geochemical surveys in relatively short periods of time. These high-profile projects were selected to have an immediate impact, and they complement the longer term applied geoscience activities of the British Columbia Geological Survey and the Tenure and Geoscience Branch in the Ministry of Natural Gas Development.

The Mineral Deposit Research Unit (MDRU) in the Department of Earth, Ocean and Atmospheric Sciences (EOAS) at the University of British Columbia has been another long-term research partner. Geological surveys play a central role in training and mentoring the next generation of geoscientists in regional geological mapping, mineral deposit studies, database management and development, and the use of analytical instruments in modern research laboratories. Hence, particularly rewarding projects have included working with energetic students and post-doctoral fellows.

The Survey also collaborates with the minerals industry. British Columbia's mineral exploration community provides critical logistical and financial support (both in-kind and direct) for many of our geoscience projects. These professional interactions keep the Survey in touch with the needs of the minerals industry and facilitate the transfer of knowledge generated by government geoscientists to the exploration community. It is said that you are judged by the company that you keep. The British Columbia Geological Survey is fortunate to be in the company of the British Columbia mineral exploration and mining community, the members of which we are proud to call friends.

---

1. British Columbia Geological Survey overview

The BCGS was established in 1895 and is the oldest science agency in the British Columbia government. The BCGS links government, the minerals industry, and British Columbians to the province's geology and mineral resources. The key roles of the Survey are to

- create, maintain, and deliver geoscience knowledge to lead informed decision making
- attract companies and individuals to explore British Columbia for new mineral and coal resources
- act as the public steward of mineral and coal resources for current and future generations
- guide public policy by providing assessments on the nature and economic health of mineral exploration and mining activities

The BCGS is a branch in the Mines and Mineral Resources Division of the Ministry of Energy and Mines (Fig. 1). It is headquartered in Victoria, the capital city of British Columbia, on south Vancouver Island. The Survey is lead by Stephen Rowins, the Chief Geologist and Executive Director, and consists of three sections, each lead by a Director. These sections include: 1) Cordilleran Geoscience; 2) Resource Information; and 3) the Mineral Development Office (MDO). The Cordilleran Geoscience Section, lead by Adrian Hickin, is responsible for generating new geoscience knowledge largely through field-based studies and surveys. Larry Jones directs the Resource Information Section, which is responsible for maintaining and developing the provincial geoscience databases and disseminating geoscience data online. The Resource Information Section is the statutory authority for evaluating, accepting, and archiving mineral exploration assessment reports filed by the exploration and mining industry since 1947. These reports provide information on geological, geophysical, geochemical, drilling, and other exploration-related activities in BC. Most are available online from the ARIS (Assessment Report Indexing System) website. The Mineral Development Office (MDO), in Vancouver, is lead by Bruce Madu. It serves as the government's point of contact for the mineral exploration and mining industry. The MDO provides mineral and coal resources information and technical marketing to industry, governments, and the investment community. In addition, the MDO coordinates British Columbia's Regional Geologists Program.

Fig. 1. Staff of the British Columbia Geological Survey in 2013.

Publications are the primary means by which the BCGS delivers on its mission to attract exploration to British Columbia. In 2013, the Survey produced 68 publications (Fig. 2) the results of which were also presented at regional, national, and international scientific meetings. Industry is the main client of the BCGS and our efforts are largely directed at providing new geoscience products to the minerals industry. All publications, data releases, conference presentations, web

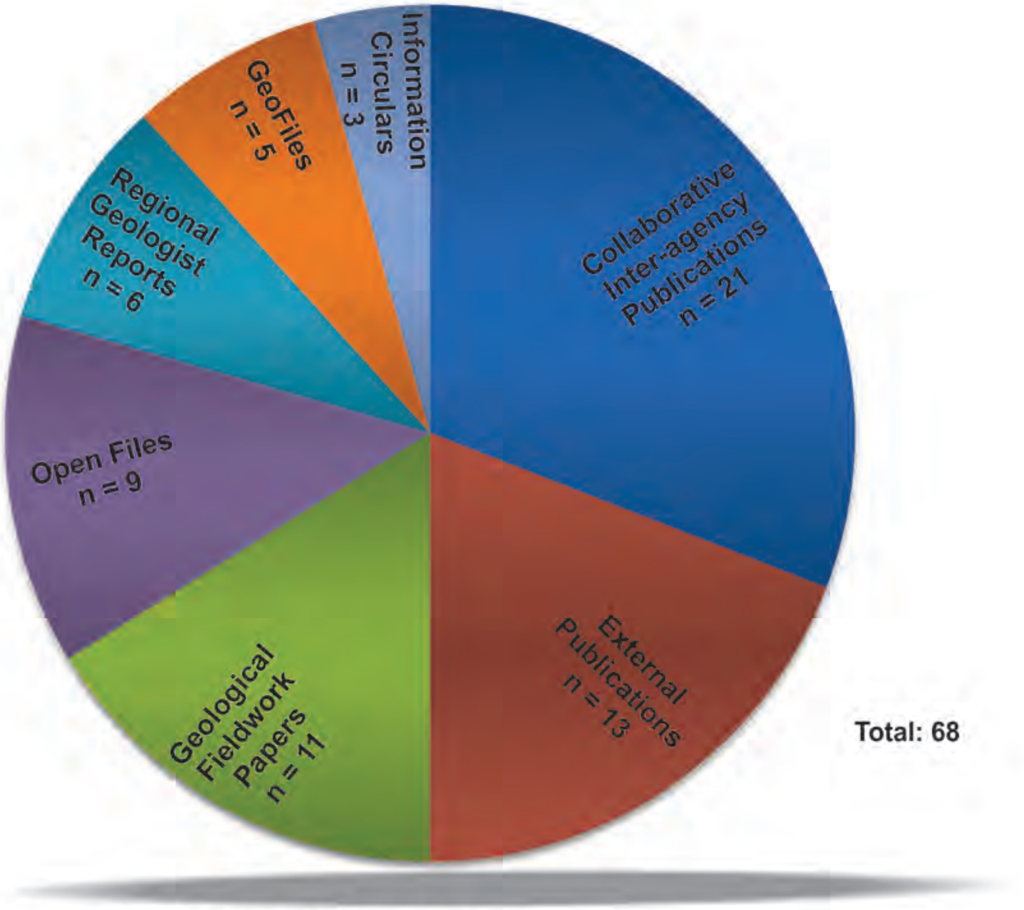

Types of Publications by the British Columbia Geological Survey

Collaborative Inter-agency publications include reports, maps, and other products published jointly by the British Columbia Geological Survey and another agency such as the Geological Survey of Canada or Geoscience BC.

External publications are contributions to the peer reviewed literature and published in a recognized national or international scientific journal.

Geological Fieldwork papers are published in British Columbia Geological Survey's annual Geological Fieldwork volume. Papers typically report the preliminary results of field activities.

Open Files include geoscience reports, maps, and databases that receive internal review and usually represent the interim products of ongoing research.

Regional Geologists reports include overviews of exploration and mining activities. The contributing articles are prepared by the Regional Geologists and provide an annual report of activities in each jurisdiction.

GeoFiles are designed for rapid information release over the internet. They are not subject to the same editorial standards as other publications.

Information circulars provide government, industry, and the general public with non-technical geoscience information.

Fig. 2. British Columbia Geological Survey and Regional Geologists publications in 2013.

updates and new databases on MapPlace (MINFILE, ARIS, Coalfile, Property File) are profiled annually at the Association for Mineral Exploration in BC (AMEBC) Mineral Exploration Roundup in Vancouver, Canada.

In recent years the Survey has expended considerable time and resources on developing new mineral exploration methodologies and technologies. Development of these practical products is now possible with the refurbishment of the

Survey's geochemical laboratory and the renewal (in 2011) of the Ministry of Energy and Mines - University of Victoria (MEM-UVic) Geoscience Partnership Agreement. New exploration methodologies and technologies under development include: 1) using Pb isotopes to establish an inexpensive technique for targeting volcanogenic massive sulphide (VMS) deposits in till-covered terranes; 2) a new MEM-UVic project using the laser ablation inductively coupled plasma mass spectrometry (LA-ICPMS) laboratory at the University of Victoria to study resistate indicator minerals (RIMs) in glacial tills to fingerprint major mineral deposit types in BC and around the world; 3) new till-potential maps, using proprietary government airphotos, that will allow industry to reduce unnecessary till sampling by up to 75% in selected areas (joint BCGS-Geoscience BC project); and 4) use of portable bench-top or hand-held X-ray fluorescence (XRF) instruments to rapidly measure rare earth element (REE) abundances in field samples as a mapping aid during property evaluation.

Given the fiscal realities facing government today, virtually all of the BCGS projects are collaborative. Limited operational dollars means that we seek out partners to maximize research effectiveness. In the past 3 years, the BCGS has partnered directly with four companies (Imperial Metals Corp., Pacific Northwest Capital Corp., Kutcho Copper Corporation, and SEGO! Resources); undertaken seven joint research projects with the Geological Survey of Canada, including three Geo-Mapping for Energy and Minerals (GEM1) and four Targeted Geoscience Initiative 4 (TGI-4) projects; collaborated on seven MEM-UVic geoscience partnership projects; and partnered with Geoscience BC on large projects such as QUEST, QUEST-NW, Nechako, and TREK in addition to many smaller collaborations. Current university partners include the University of British Columbia, the University of Alberta, Simon Fraser University, and the University of Victoria.

As a government agency the BCGS doesn't lobby government, but will advocate for the industry and its needs. The MDO actively promotes British Columbia's mineral and coal resource opportunities to private investors and the general public. The new "Communities, Mineral and Coal Exploration Investment" map (see below), which summarizes exploration investment from 2010-2012 in relation to communities across the Province, is an example of how the BCGS and the Regional Geologists demonstrate the value of the exploration industry to local municipalities and First Nation communities.

2. Cordilleran Geoscience Section

The Cordilleran Geoscience Section is responsible for generating new geoscience knowledge through regional field-based geological mapping programs and targeted geoscience projects. Projects provide the regional tectonic and geological framework to enhance mineral exploration, develop mineral deposit models, and design and evaluate new exploration methods. These activities give the Section a key role in promoting mineral and coal exploration potential in British Columbia.

In addition to regional mapping, Cordilleran Section geologists activities include: bedrock stratigraphic and lithogeochemical studies; mineral deposit studies; evaluating the tectonic evolution of the North American Cordillera; developing methods for mineral exploration; documenting the Quaternary history and surficial geology of the Province; drift prospecting, till geochemistry, and indicator mineral studies. Projects conducted in 2013 fall into four general themes: regional synthesis and map compilation; the BC Porphyry Deposits Initiative; targeted mineral deposit studies; and exploration methods (Table 1; Fig. 3).

2.1. New initiatives

2.1.1. BC porphyry deposits

Porphyry Cu-Mo-Au deposits comprise a significant component of British Columbia's mineral wealth. Calc-alkaline and alkalic porphyry deposits are associated with plutonism in island arcs formed outboard of ancestral North America during Late Triassic to Early Jurassic (pre-accretionary), and in intracontinental arcs during the Late Mesozoic to Cenozoic, following accretion and assembly of the Cordilleran terranes (post-accretionary). Projects in the BC Porphyry Deposit Initiative are designed to: 1) determine the ages and structural controls on arc magmatism and porphyry pluton emplacement; 2) establish the geological framework for major porphyry trends; and 3) develop new exploration techniques to aid in the discovery of buried or blind deposits. This ongoing multi-year initiative includes six independent projects (Table 1; Figs. 3, 4). The first of these projects to be completed is a geological review of major porphyry mines in British Columbia's south-central Intermontane Belt. This project was undertaken as part of the Society of Economic Geologists (SEG) annual meeting, which was held in Canada for the first time. The resulting fieldtrip guidebook (Logan and Schroeter, 2013) is a valuable update for the exploration community. Four other ongoing studies in the Quesnel terrane of south-central British Columbia are collectively referred to as the Nicola Arc Project (Fig. 4). A new study in northwestern British Columbia is examining the geological controls on Stikinia arc magmatism and related porphyry mineralization (Fig. 3).

2.1.1.1. Porphyry systems of central and southern British Columbia

A guidebook (Logan and Schroeter, 2013) to accompany a fieldtrip was delivered as part of the Society of Economic Geologists meeting held in Whistler, British Columbia in September. In addition to the itinerary, road log, and an overview article on porphyry systems, the volume included six review papers describing the geology of Endako (Thompson Creek Mining Limited), Gibraltar (Taseko Mines Limited), Mount Polley (Imperial Metals Corporation), Highland Valley (Teck Resources Limited), New Afton (New Gold Incorporated), and Copper Mountain (Copper Mountain Mining Corporation) mines.

2.1.1.2. Nicola Arc project

The Nicola Arc project examined parts of three temporally distinct, north-trending plutonic belts that may represent the eastward migration of Mesozoic arc magmatism in southern Quesnellia (Fig. 4). These belts host important past and producing mines. The Nicola Arc project includes four studies that are divided geographically (north, central, and south; Fig. 4).

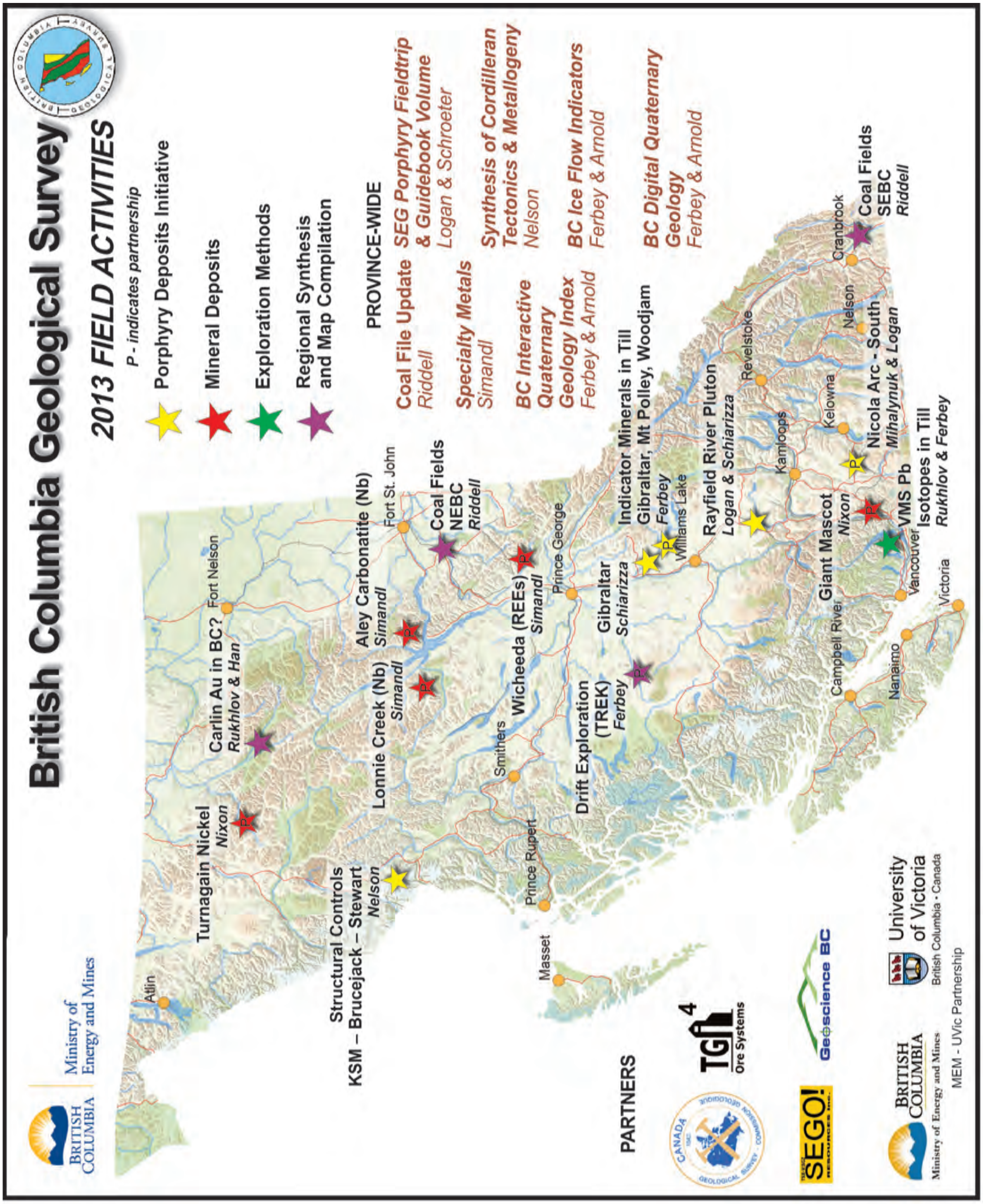

Fig. 3. British Columbia Geological Survey activities in 2013.

Table 1. British Columbia Geological Survey field projects in 2013.

Project	Theme	Lead Geologist
Porphyry systems of central and southern BC: Prince George to Princeton	BC Porphyry Deposits	Jim Logan
Geological setting of the Granite Mountain batholith, host to the Gibraltar porphyry Cu-Mo deposit, south-central British Columbia (Nicola Arc - North)		Paul Schiarizza
The Rayfield River pluton, south-central British Columbia (NTS 92P/6): Geologic setting and copper mineralization		Jim Logan
Regional Mapping and Cu-Au porphyry deposits between Princeton and Merritt (Nicola Arc - South)		Mitch Mihalynuk
Porphyry indicator minerals in till from the British Columbia Interior Plateau (Nicola Arc - North/TGI-4)		Travis Ferbey
Structural and stratigraphic control of porphyry and related mineralization in the Treaty Glacier – KSM – Brucejack – Stewart trend of western Stikinia		JoAnne Nelson
Carlin-type Au in North-Central British Columbia?	Exploration Methods	Alexei Rukhlov
Trace element systematics in apatite and other resistate minerals (MEM-UVic Partnership)		Alexei Rukhlov
Lead isotopes and trace element geochemistry of till at select Volcanogenic massive sulphide deposits west of Harrison Lake		Alexei Rukhlov
Specialty metal studies in British Columbia (TGI-4)	Mineral Deposits	George Simandl
Orogenic Ni-Cu-PGE at Giant Mascot and Turnagain (TGI-4)		Graham Nixon
The Cordillera of British Columbia, Yukon, and Alaska: tectonics and metallogeny	Regional Synthesis and Map Compilation	JoAnne Nelson
British Columbia Quaternary geology interactive map index		Travis Ferbey
Ice-flow indicators of British Columbia		Travis Ferbey
Towards a British Columbia digital Quaternary geology map		Travis Ferbey
Basal till potential maps for the TREK Project area		Travis Ferbey
British Columbia Coal Field Map Compilation		Janet Riddell

2.1.1.2.1. Nicola Arc – North

Two projects are included in the Nicola Arc – North region (Fig. 4). First, bedrock mapping surrounding the Gibraltar Cu-Mo mine was initiated to establish if the host intrusions are part of the Late Paleozoic to Early Mesozoic Cache Creek terrane or part of the Late Triassic Quesnel terrane, which hosts the Highland Valley Cu-Mo mine. Second, a program is tracking the glacial dispersion of trace elements and porphyry indicator minerals (PIMs) in till from mineralization near the Mount Polley and Gibraltar mines and the Woodjam porphyry prospect. Outcomes include developing methods that use till matrix geochemistry and PIMs to discover buried porphyry deposits. This project is a partnership with the Geological Survey of Canada and is funded through the Intrusion Related Ore Systems Targeted Geoscience Initiative (TGI-4), which concludes in 2015.

2.1.1.2.2. Nicola Arc – Central

The northern part of the Nicola Arc – Central region is challenging to explore because prospective rocks are hidden by a thick cover of Cenozoic volcanic rocks and unconsolidated Quaternary sediments. However, the potential for discovering buried deposits is significant, if the axes of the migrating magmatic arcs can be traced beneath this cover (Fig. 4). The Rayfield River intrusion is a Late Triassic syenite pluton that is being investigated to determine if a link can be established with alkalic plutons to the north and south, thus defining the trace of the magmatic arc axis of the alkaline plutonic belt (Copper Mountain suite) throughout the Nicola arc.

2.1.1.2.3. Nicola Arc – South

The Southern Nicola Arc Project (SNAP) is the main project in the Nicola Arc – South region (Fig. 4). SNAP aims to refine the stratigraphic, structural, and mineral deposit evolution of the Nicola arc between Princeton and Merritt, through 1:20 000 scale geological mapping, geochronology and paleogeographic reconstructions (Fig. 5). The resultant geological framework should aid exploration programs in a region that has produced copper and gold for the past 50 years. The work is partly supported through an industry partnership agreement with Sego! Resources.

2.1.1.3. Structural and stratigraphic control of porphyry Cu-Au and related mineralization in the Treaty Glacier – KSM – Brucejack – Stewart trend of northwestern Stikinia

One of the most important mineral trends of northwestern

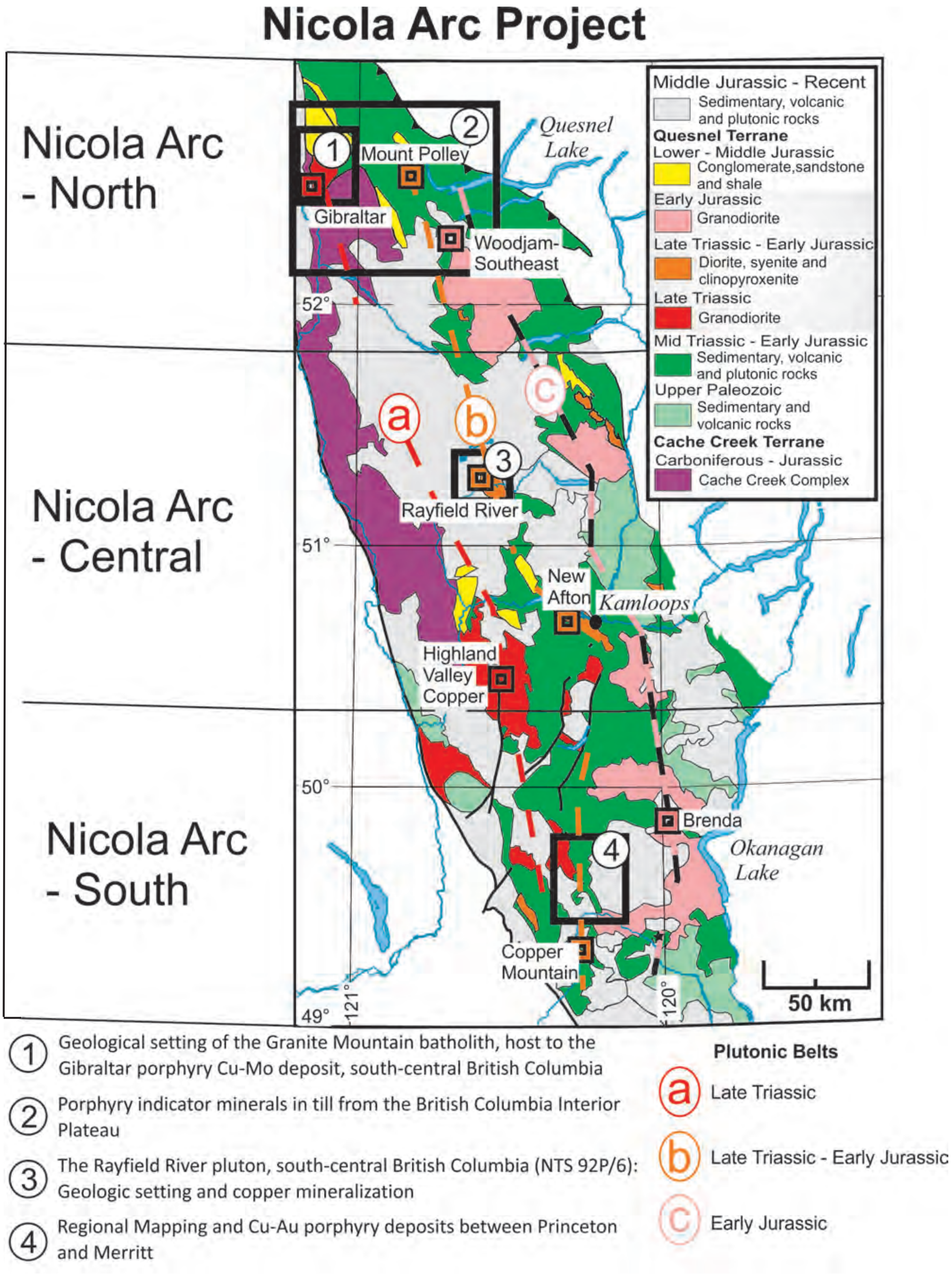

Fig. 4. Nicola Arc projects. Generalized geology of southern Quesnellia modified after Logan and Mihalynuk (2013).

British Columbia extends from immediately north of Stewart to the Treaty Glacier, in the western part of the Stikine arc (Figs. 3, 6). Major deposits along this trend include Kerr-Sulphurets-Mitchell (KSM), Brucejack, Silbak-Premier, Big Missouri, Scottie Gold and Red Mountain. All are hosted by volcanic and sedimentary rocks of the Hazelton Group (Lower Jurassic) and its subvolcanic feeder intrusions. Cordilleran section geologists and Regional Geologist Jeff Kyba are collaborating on this project, which is assessing the role of basement structures on localizing Cu-Au mineralization. Development of this geological model will provide a predictive tool for targeting new Cu-Au occurrences in this area.

Fig. 5. Drilling an oriented core for paleomagnetic study at Miner Mountain in the Nicola Arc-South project area.

Fig. 6. Examining a Mitchell intrusion breccia and mineralization near Pretium Resources Incorporated's Snowfield property.

2.2. 2012-2013 Projects

2.2.1. Exploration methods

2.2.1.1. Carlin-type gold in British Columbia?

Structurally controlled Carlin-type Au showings have recently been discovered in Proterozoic-Paleozoic Selwyn basin strata of the Rackla belt in east-central Yukon. These discoveries raise the possibility of similar occurrences in equivalent settings in British Columbia. This reconnaissance project uses the British Columbia Geological Survey's regional geochemical and MINFILE databases, in conjunction with digital geology and geophysics, to test for As ± Au ± Hg ± Sb anomalies and minerals such as realgar and orpiment. These data may show spatial associations with long-lived regional structures, and to platform to deep-water transitions in the Kechika trough (the southward extension of Selwyn basin) of north-central British Columbia (Fig. 3). This project is an example of how the Provincial geochemical archive may be used to explore for a new type of deposit using existing survey databases.

2.2.1.2. Trace-element systematics in apatite: Applications to metallogeny, petrogenesis, geochronology, and mineral exploration

Regional geochemical surveys that collect resistate indicator minerals (RIMs) in surficial materials have proven successful in diamond exploration and are now being applied to other types of mineral deposits. Porphyry indicator minerals (PIMs) including apatite, rutile, titanite, and magnetite are related to the distinctive types of alteration that characterize porphyry Cu-Mo-Au mineralization. This project focuses on developing a new exploration tool for identifying source deposit types from RIMs in till in a variety of tectonic settings. The tool uses relatively inexpensive and rapid laser ablation inductively-coupled plasma mass spectrometry (LA-ICPMS) to measure trace element abundances in apatite and other resistate minerals to "fingerprint" apatite from specific deposits. The technique also can establish U-Pb, Th-Pb, and Pb-Pb ages of apatite. This project supports a post-doctoral fellow and is a collaboration with the School of Earth and Ocean Sciences at the University of Victoria, under the Ministry of Energy and Mines – University of Victoria Partnership Program.

2.2.1.3. Lead isotopes and trace element geochemistry of till at selected volcanogenic massive sulphide deposits west of Harrison Lake

Lead isotope analysis of silt and clay fractions in tills can aid mineral exploration in glaciated terrains. In situ weathering or destruction of sulphide minerals during till formation can mask elemental signals of buried mineralization, but such signals may be retained by Pb isotopic compositions. This project is an orientation study that examines the Pb isotopic ratios of tills above and down ice-flow direction of known volcanogenic massive sulphide occurrences in the Jurassic Harrison Lake

Formation west of Harrison Lake in southwestern British Columbia (Fig. 3). Because of large differences in Pb isotopic ratios between anomalous and background samples, high-precision analytical techniques are not required, and commercial ICP-MS methods are suitable. Consequently, the method is readily accessible to the exploration community and may be an effective prospecting tool in glaciated terrains.

2.2.2. Mineral deposits

2.2.2.1. Specialty metals (TGI-4)

The British Columbia Geological Survey and the Geological Survey of Canada continued to collaborate on a five- year (2010-2015) province-wide study of specialty metals and rare earth elements. Specialty metals are uncommon, nonferrous metals used in small quantities (typically < 150 000 tonnes/year or derived from geographically restricted areas). The Specialty Metals Program is part of the Targeted Geoscience Initiatives program (TGI-4) and has two major components: 1) reviewing ore deposits and their mineral economics in Canada; and 2) developing techniques to guide exploration toward ore-grade zones in host deposits. This project is supporting three M.Sc. theses (at McGill University, Simon Fraser University, and the University of Victoria). The 2013 field programs focused on the Lonnie Creek niobium prospect and the Aley carbonatite (Figs. 3, 7). The results of the Specialty Metals project will aid exploration and development of these strategic metal resources.

2.2.2.2. Orogenic Ni-Cu-PGE (TGI-4)

The Ni-Cu-PGE-Cr Ore Systems project is another national Targeted Geoscience Initiative (TGI-4) of the Geological Survey of Canada, under the Intrusion Related Ore Systems program. The British Columbia component is a collaboration between the British Columbia Geological Survey, the Geological Survey of Canada, and the University of British Columbia. The project is examining the potential for orogenic Ni-Cu-PGE-Cr deposits associated with supra-subduction zone ultramafic-mafic intrusions exclusive of ophiolites and accreted large igneous provinces (e.g., Wrangellia). The goal is to establish mineral deposit models and exploration criteria for two poorly understood magmatic sulphide deposits in BC: 1) Giant Mascot, British Columbia's only past-producing nickel mine (1958-74); and 2) the Turnagain Alaskan-type intrusion, which has a substantial resource of low-grade Ni and Co (Fig. 3). The project supports two graduate students at the University of British Columbia.

2.2.3. Regional synthesis and map compilation

2.2.3.1. The Cordillera of British Columbia, Yukon, and Alaska: Tectonics and metallogeny

Success in mineral exploration can be greatly enhanced by understanding the regional geology and metallogeny of a prospective area. In 2013, the British Columbia Geological Survey and the Yukon Geological Survey released an update of the 2007 synthesis on the tectonics and metallogeny of the northern Cordillera (Nelson and Colpron, 2007) as part of the Society of Economic Geologist annual meeting at Whistler, British Columbia. The new publication (Nelson et al., 2013) integrates the origin of major metallic mineral deposits and mineral belts in the northern Cordillera with its protracted tectonic evolution.

2.2.3.2. British Columbia Quaternary geology interactive map index

The British Columbia Geological Survey has updated and enhanced the British Columbia surficial geology map index. This index is now interactive and available on MapPlace and through Google Earth. The index consists of all surficial and Quaternary geology maps produced by the British Columbia Geological Survey, the Geological Survey of Canada, and Geoscience BC. All maps are available for digital download free of charge. Each footprint in the index provides an accurate representation of the areal extent of surficial geology mapping for British Columbia.

2.2.3.3. British Columbia ice-flow indicator compilation

British Columbia was last glaciated in the Late Wisconsinan (~ 22-10 ka). As a result, much of the province is blanketed by thick accumulations of unconsolidated sediments that obscure the underlying bedrock. Traditional soil geochemical surveys commonly sample glacially transported material or derivative products that have been displaced from their initial bedrock source along a path determined by the transporting agent (i.e., water, ice, or wind). In the case of till, the sediment has been relocated by the flow of ice. Therefore, in order to locate the bedrock source of a geochemical anomaly, it is critical to know

Fig. 7. Stream-sediment sampling at the Aley carbonatite.

the direction of ice-flow. To address this, the British Columbia Geological Survey compiled and digitally captured over 119,000 ice-flow indicators from published and unpublished surficial geology, terrain, glacial features, and bedrock geology maps in British Columbia. Ice-flow indicators include outcrop-scale features such as striations and grooves, and landform-scale features such as drumlins and flutes. These data illustrate ice-flow directions for the Cordilleran ice sheet during the Late Pleistocene.

2.2.3.4. Towards a British Columbia digital Quaternary geology map

Like bedrock geology, knowledge of the distribution and origin of surficial materials is fundamental for many applications in mineral exploration, geotechnical engineering, and public health and safety. Currently this information exists in a variety of maps and formats. In an effort to develop a universal provincial-scale Quaternary geology map, the British Columbia Geological Survey launched a pilot project to produce a continuous 1:50,000-scale digital surficial geology layer for the entire Interior Plateau. A framework-based data model will be developed and expanded to a province-wide digital surficial geology layer. This digital surficial geology layer will complement the current BC Digital Geology Map[1] and will be a source of information on surficial materials used in resource development projects and research on the Cordilleran ice sheet during the Late Pleistocene.

2.2.3.5. Basal till potential maps for the TREK project

As a contribution to the BC Geological Survey – Geoscience BC's Targeting Resources for Exploration and Knowledge (TREK) partnership, the British Columbia Geological Survey is supervising the development and publication of "Basal Till Potential Maps" for the TREK study area in the Interior Plateau (Fig. 3). These maps are designed to assist in locating basal till, the variety of till ideally used for geochemical and mineralogical surveys. The maps identify areas where basal till is likely to occur and locations suitable for sampling. These maps will assist in the design of exploration programs by focusing expensive field based sampling to areas where the potential for collecting basal tills is high.

2.2.3.6. Coalfield compilation maps

Coal production in British Columbia accounts for most of the Province's mine production revenues. Coal license applications have reached record levels in recent years. The approval of these applications must meet with the integrated resource development goals of the government, which has resulted in a growing need for information and maps explaining coal geology and its spatial relationship with other land values. In 2013, the British Columbia Geological Survey began compiling coalfield infographics on a coalfield-by-coalfield basis. These posters help both professionals and members of the general public understand the distribution of British Columbia's coal resources in a readily understandable format. The Peace River Coal field in northeast British Columbia will be the first of these compilations (Fig. 3).

2.2.4. Geochemical laboratories

The British Columbia Geological Survey operates a geochemical laboratory that supports the Survey's field programs, targeted mineral deposit studies, and development of mineral exploration methodologies. Increasingly, indicator minerals (e.g., garnet, apatite, and magnetite) in bedrock and derivative sediments, such as till or streams, are being used as an exploration tool. To aid the development of this powerful new exploration technique, the British Columbia Geological Survey's geochemical laboratory underwent major upgrades in 2012-2013. Improvements included construction of a new rock storage facility and geochemical archive to accommodate over 600,000 geochemical pulps and rock and soil samples. New equipment included rock saws, a Linkam THMSG 600 heating-freezing stage for fluid inclusion microthermometry, an ultrapure water system, and a portable bench-top Thermo Scientific Niton X-Ray fluorescence (XRF) analyzer. The chemical fume hoods were refurbished and the addition of a Bico disk pulverizer and a Wilfley shaking table completes the laboratory's full functionality for mineral separation and processing.

3. Resource Information Section

A critical role of the British Columbia Geological Survey is to archive and disseminate geological information. The Survey is the data custodian of over 118 years of geoscience publications and geological databases created through field surveys, research, and document donations. Resource Information Section staff manage, disseminate, and guide the use of this information to support government decision making and enhance the success of the mineral exploration community. Free access to British Columbia's geological information increases exploration effectiveness by enabling the efficient gathering of regional information useful for property scale evaluation. Archived exploration results and activities help explorers advance projects without unnecessary duplication of previous work. The MapPlace[2] is the Survey's web service that has been providing visualization and query capacity to this extensive array of information since 1995.

3.1. MapPlace and database activities

3.1.1. MapPlace

Since 1995, the MapPlace web service has provided industry and government agencies with comprehensive tools and open geoscience data to aid in the discovery of mineral potential in British Columbia. MapPlace's unique and interactive applications and tools assist in investment decision making. MapPlace continues to provide clients with efficiencies in research time, data costs, and analysis. Data themes and applications available on MapPlace include mineral potential, bedrock and surficial geology, publications, mineral and petroleum tenure, MINFILE, assessment reports, geochemistry, and geophysical surveys.

As of 2013, MapPlace will continue to operate and be maintained using Autodesk MapGuide 6.5 while the next generation of software is being developed. Recent new additions to MapPlace include geochemistry data (described

---

[1] BC Digital Geology Map: http://www.empr.gov.bc.ca/mining/geoscience/bedrockmapping/pages/bcgeomap.aspx

[2] MapPlace: http://www.empr.gov.bc.ca/Mining/Geoscience/Mapplace/pages/default.aspx

below) and QUEST-Northwest aeromagnetic survey data from Geoscience BC Reports 2012-02, 2012-03 and 2013-03. The main BCGS Geoscience Map displays data from Open File 2013-06, a compilation consisting of over 119,000 ice-flow indicators digitally captured from published and unpublished surficial geology, terrain, glacial features, and bedrock geology maps in British Columbia. A new Surficial Geology Index (Open File 2013-09), which includes over 200 maps available for download, was added to MapPlace.

The British Columbia Geological Survey is prototyping web services based on MapGuide Open Source. The goal is to determine if MapGuide Open Source is a suitable replacement platform for developing web applications and delivering public geoscience, as required by the current MapPlace web services. MapGuide Open Source can use third party topographic basemaps and imagery such as Google maps, Yahoo maps, Bing maps and Open Street Map. Users can switch between these basemap layers to serve their specific needs. It is essential to MapPlace web services to support complex spatial operations and query (e.g., select MINFILE records within the buffer of a given bedrock unit), visualization, and reporting. Currently, 152 geoscience data layers in 28 layer groups have been developed, representing 70% of the data layers in the current MapPlace. The important layer groups directly related to geosciences are mineral inventory, regional geochemistry, topographic basemaps, bedrock geology, and mineral resource assessment.

MapGuide Open Source has demonstrated impressive preliminary performance. It is capable of displaying province-wide bedrock geology with over 32,000 polygons in less than two seconds, and over 61,000 RGS sample locations in less than 3 seconds. Time to display large raster layers is also acceptable, and zoom-in and zoom-out functionality is smooth and fast. The utility of MapGuide Open Source will continue to be tested to ensure that service is maintained if a decision to migrate from Autodesk MapGuide 6.5 is made.

3.1.2. Property File, MINFILE, ARIS and geochemical data

Property File[3] is a collection of over 60,000 documents, most of which were collected by British Columbia Geological Survey staff or donated by industry. These documents span the last 150 years and include hand-drawn maps, drill core records, correspondence, thin sections, reports, and prospectuses, and other items. Given the change in commodity prices and the expansion of infrastructure over time, past fieldwork that was not followed up could now be a viable exploration target. The Property File project is managed by Purple Rock Inc. Recent additions include 3300 documents from the Chevron file, over 1600 from the Placer Dome file, and 2300 from the R.V. Kirkham file. These documents complement the 1640 documents from collections donated by the estates of Dennis Gorc, W.G. Hainsworth, and W.M. Sharp; and over 9400 documents from former geological survey staff geologists (Tom Schroeter, Bill McMillan and Andre Panteleyev). Other company collections include 2800 Cyprus-Anvil, 400 Falconbridge, and 7600 Rimfire documents. In 2007, University of British Columbia donated 680 undergraduate theses and reports. Over 2760 mine plans are in Property File. The Library file and other collections number over 18,000 documents and maps. Over 50,200 documents are online and are available for free download.

MINFILE[4] contains geological, location, and economic information on more than 13,364 metallic, industrial mineral, and coal mines, deposits and occurrences in BC. From January 2012 to March 2014, additional funding was allocated to update MINFILE and to add new discoveries by reviewing mineral assessment reports, recent publications, press releases, Property File, and company websites (Fig. 8). Contractors Total Earth Science Services and Purple Rock Inc. updated over 4300 occurrences, including the addition of 1366 new occurrences to the MINFILE database.

In compliance with the Mineral Tenure Act (MTA) Regulations, results of mineral exploration programs on mineral claims in British Columbia are submitted to the Ministry of Energy and Mines. These assessment reports contain information on geology, geophysics, geochemistry, drilling, prospecting and physical work. After a one-year confidentiality period, the reports become an open resource for planning mineral exploration investment, research, land-use planning and resource management. Users can now access more than 33,470 company mineral assessment reports using the online ARIS database. More than $2 billion of exploration expenditures have been recorded in assessment reports since 1947. The value of expenditures on 2012 exploration programs reported in 804 assessment reports, moved to off-confidential status in 2013, was $196 million. The mining industry is encouraged to submit assessment reports in digital form (PDF by email, CD-ROM, DVD, or USB drive) to the Mineral Titles Branch. Benefits include higher quality digital reports; faster approval; and lower costs for printing, mailing, storage, scanning and processing. During 2013, 789 reports were approved. Four criteria improve approval rates: adequate detail in the cost statements; plot geochemical values; submit full-scale geophysical maps; and cross sections and proper scales for drillhole data. The ARIS website sees about 1.4 million hits in a month.

Ongoing efforts by government-funded agencies to update and maintain the geochemical database established by the British Columbia Regional Geochemical Survey (RGS) and the National Geochemical Reconnaissance programs have produced one of the most comprehensive collections of field information and multi-element analytical data in Canada. The database has benefitted from a series of large-scale reanalysis initiatives, which have been sponsored by Geoscience BC since 2007. To compliment the RGS 2011 data displayed on MapPlace, the following Geoscience BC Reports have been added as separate layers to display the locations for stream-sediment sample reanalysis: 2013-04 Lardeau (082K) 1297 samples by ICP-MS; 2013-06: McLeod Lake (093J) 1152 samples by INAA; 2013-09 Nelson (082F) 1394 samples by ICP-MS; and 2012-5 and 6 QUEST-Northwest (104K) 932 samples by ICP-MS and (NTS 104F & G) 1414 samples by INAA. Reports 2013-11 and 12 Northern Vancouver Island (092L, 092K and 102I) represent new data for 721 new moss mat and water from 681 stream sites, and new ICP-MS results

---

[3] Property File: http://www.empr.gov.bc.ca/mining/geoscience/propertyFile/Pages/default.aspx

[4] MINFILE: http://www.empr.gov.bc.ca/mining/geoscience/minfile/Pages/default.aspx

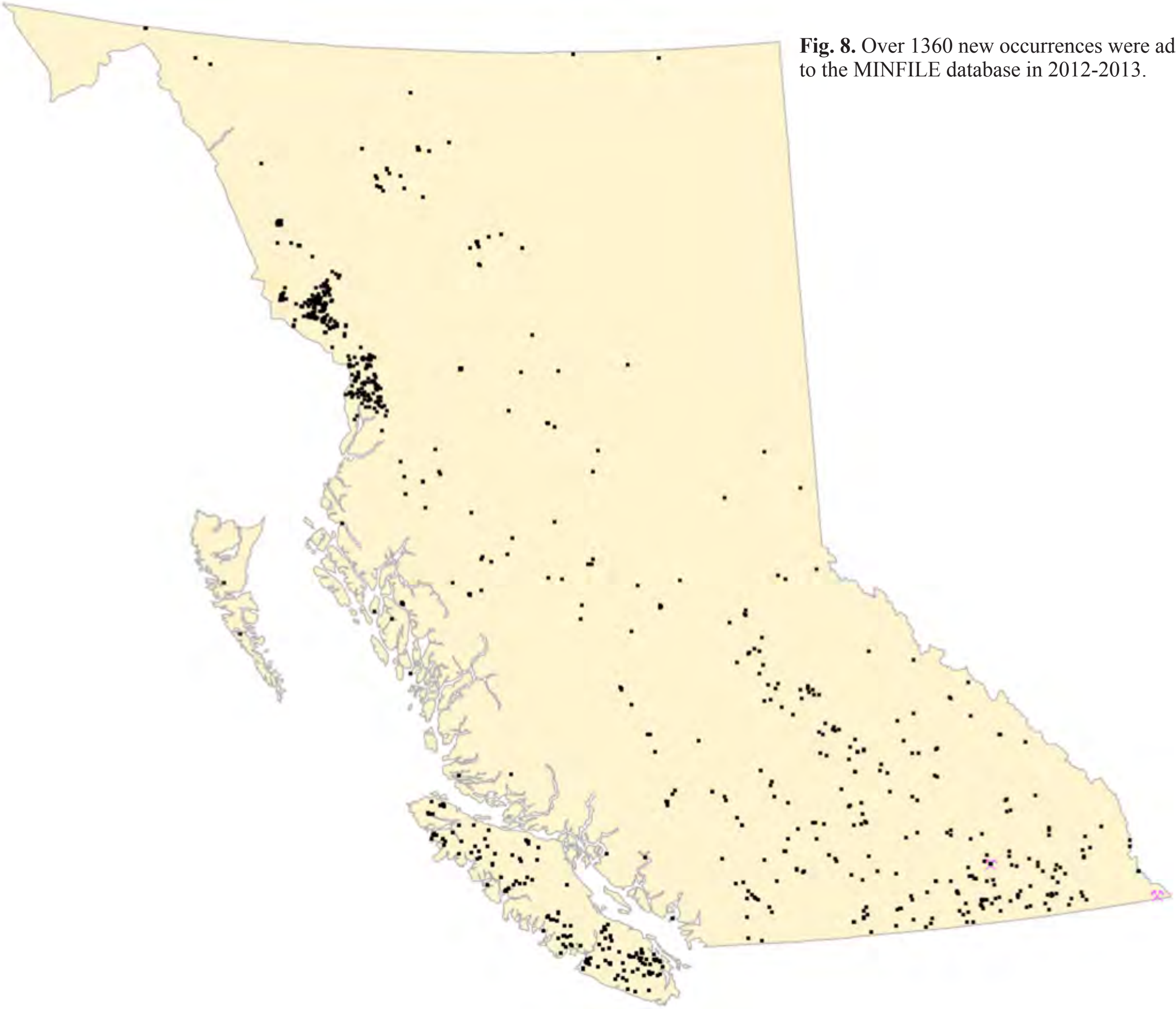

Fig. 8. Over 1360 new occurrences were added to the MINFILE database in 2012-2013.

for 433 till samples. BCGS GeoFile 2013-07 represents rock geochemistry data, collected in 1998, for 60 samples in 082L, 082M and 092P.

3.2. British Columbia's digital bedrock geology map: BCGeology Map

The BCGS has developed techniques to deliver to the exploration industry a continuously updated geological map of the province. The "geologic framework data" (GFD) model enables rapid integration of new mapping (Fig. 9). Traditionally, polygons, to define map units, are used as the base to update and integrate digital geology. However, using polygons as the base can lead to errors in editing and take excessive time to reconcile shared boundaries between adjacent map units and coincident planar geological features such as faults. To avoid these issues, the BCGS dispensed with polygons for integrating updated maps and developed the GFD model. This model consists of centroids describing map units and lines defining geological boundaries, as the source and the base to carry out data quality assurance, revision, and map integration. Bedrock polygons are not part of the GFD but are generated from GFD in the finished map.

Applying the GFD model allows a 'checking-out' and 'anchoring' mechanism to address map boundary issues that commonly arise when new maps are integrated with historical work (Fig. 9). Checking-out extracts the GFD data for the geologists working in a given project area, but with an extended regional context, to include any map units and boundaries, contained by or intersected with the project boundary. The outermost boundaries of this extended project map are tagged as 'anchor lines', with nodes on the anchor lines as 'hooks' that connect to 'rode lines' in the project map. When the mapping project is complete, the updated GFD for the project area, with its extended regional context, are returned to the provincial GFD base. The rode lines in the project map are snapped to the hooks in the provincial base in lieu of edge matching. The

Fig. 9. Geological framework data showing checking-out an extended regional context, to include any map units and boundaries contained by or intersected with the project bounding area.

GFD in the project area, its extended regional context, and the anchor lines from the provincial base are used to update the provincial map.

The BCGS GFD model builds on the 2005 edition of the provincial bedrock map and operates in a spatial database. The spatial database makes it possible to handle large volumes of data, and permits multiple users to perform concurrent operations on the same GFD base. Applications developed to automate checking-out, anchoring, and integration, not only simplify the integration process, but also streamline rules-driven data quality assurance and content standardization, and automate auditing changes, populating bedrock attributes, generating map unit colour schemes, and creating customized maps for delivery via web services. The GDF model and the spatial database applications were used in integrating new mapping, and the current version of the BC Digital Geology database includes the latest work in the QUEST, North Coast, Terrace, and Kutcho project areas.

4. Mineral Development Office

The role of the BC Mineral Development Office (MDO) in Vancouver is to provide mineral and coal resource information, promote the province's minerals and coal investment opportunities and form a point of contact on issues impacting the exploration and mining industries.

A primary output is the delivery of a technical marketing campaign that highlights the province's mineral and coal potential, geoscience resources, global expertise, and attractive business climate. This includes developing publications aimed at audiences from large foreign investors through to independent domestic entrepreneurs. These publications are distributed widely at conferences, business meetings, over the counter, and online.

In 2014, we will release an updated version of "Opportunities to Explore", a non-technical publication geared to new investors wanting to learn more about the province. Previous financial and content input for this document from the Association for Mineral Exploration British Columbia, Mining Association of British Columbia, Geoscience BC, and partner agencies have allowed large print runs in two languages. The document forms a key sector-specific document for the Ministry of International Trade, who support its reproduction for use by trade and investment staff in their international offices.

A second annual version of "Coal Industry Overview" was created by the Survey's coal geologist. Interest in the province's coal sector is steady. The previous map "Communities that Benefit from Mining" was released this year as "Communities, Mineral and Coal Exploration Investment" (Fig. 10). The non-technical publication summarizes exploration investment from 2010-2012 by watersheds and in relation to communities across the province. The use of GIS software allowed the incorporation of tenure maintenance financial data alongside the Regional Geologist's estimations of investment, giving a more comprehensive perspective to the final map. A three-year summary was adopted to smooth the annual data and allow the map to be updated less frequently.

After a decade long hiatus, the inventory of gold in the province has been updated and will be released in early 2014. "Gold Resources and Production in British Columbia (1890-

Fig. 10. The map "Communities, Mineral and Coal Exploration Investment" summarizes exploration investment from 2010-2012 relative to communities across the province.

2013)" will include a 2,000,000-scale map, spreadsheet, and infographic, and will be showcased on a new provincial basemap. The map will show occurrences by deposit type and grade category, using symbols for resources remaining verses extracted. The project has highlighted a significant increase in gold inventories in the province.

The MDO oversees the creation of provincial and regional level exploration and mining summary documents from the Regional Geologist program. These publications maintain a legacy that dates back to 1874 with the Annual Reports of the Minister of Mines.

The MDO actively promote the province's minerals and coal industry domestically and abroad. This occurs at a variety of formal and informal locations including conferences, business meetings, investment missions, and over the counter contacts. This year included numerous events such as the: Asia Investment Mission to China and Japan alongside five partner provinces and territories; meetings with delegations from China, India, Japan, Chile, Australia, Germany; Mineral Exploration Roundup, Prospectors and Developers Association of Canada Convention; Northwest Mining Association Conference, China Mining Conference; Sparwood Coal Symposium and the KEG annual conference (Fig. 11).

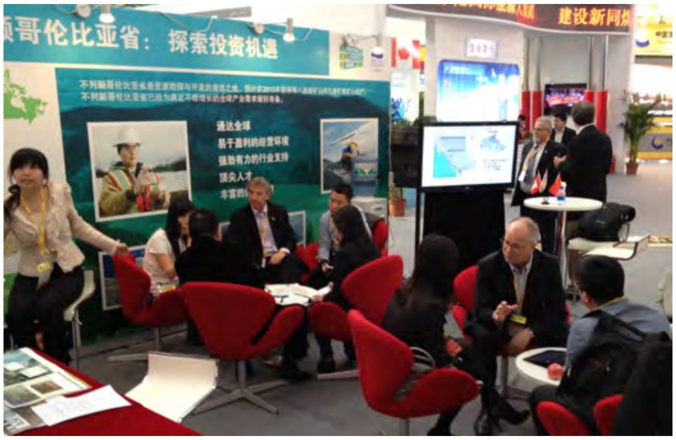

Fig. 11. The MDO works closely with the Ministry of International Trade to promote the province's minerals and coal opportunities domestically and abroad. British Columbia was joined by provincial representatives and a dozen industry partners for the Asian Investment Mission, which included the China Mining Conference in Tianjin, China.

5. Regional Geologists

The British Columbia Regional Geologists are government's experts on geological matters at a regional level and capture information on industry activity in their respective jurisdictions. Within their communities, they are recognized professionals on matters of exploration trends, support investment attraction, land use processes, First Nation capacity building, public outreach and other key deliverables of government.

Regional Geologist	Office	Region
Jeff Kyba	Smithers	Skeena
Paul Jago	Prince George	Omineca and NE
Jim Britton	Kamloops	Thompson/Okanagan/ Cariboo
Fiona Katay	Cranbrook	Kootenay/Boundary
Bruce Northcote	Vancouver	South/West Coast

References

Duke, J.M., 2010. Government geoscience to support mineral exploration: Public policy rationale and impact. Prospector's and Developer's Association of Canada Association Report, 33 p.

Logan, J. and Schroeter, T., 2013. Porphyry systems of central and southern BC: Tour of central BC porphyry deposits from Prince George to Princeton; Society of Economic Geologists Field Trip Guidebook 44, pp. 67-98.

Nelson, J.L., and Colpron, M., 2007. Tectonic and metallogeny of the Canadian and Alaskan Cordillera, 1.8 Ga to present. In: Goodfellow, W.D. (ed) Mineral Deposits of Canada, A synthesis of major deposit types, district metallogeny, the evolution of geological provinces and exploration methods, Geological Association of Canada, Mineral Division, Special Publication 5, pp. 755-791.

Nelson, J.L., Colpron, M., Israel, S., 2013. The Cordillera of British Columbia, Yukon, and Alaska: Tectonics and metallogeny. In: Colpron, M., Bissig, T., Rusk, B.G., and Thompson, J.F.H. (eds), Society of Economic Geologists, Special Publication 7, pp. 53-109.

The Rayfield River pluton, south-central British Columbia (NTS 92P/6): Geologic setting and copper mineralization

James M. Logan[1, a] and Paul Schiarizza[1]

[1] British Columbia Geological Survey, Ministry of Energy and Mines, Victoria, BC, V8W 9N3
[a] corresponding author: Jim.Logan@gov.bc.ca

Recommended citation: Logan, J.M. and Schiarizza, P., 2014. The Rayfield River pluton, south-central British Columbia (NTS 92P/6): Geologic setting and copper mineralization. In: Geological Fieldwork 2013, British Columbia Ministry of Energy, and Mines, British Columbia Geological Survey Paper 2014-1, pp. 15-27.

Abstract
The Rayfield River syenite pluton (Late Triassic, > 201 Ma) is exposed along the lower reaches of the Rayfield River, 20 km east of 70 Mile House. On its southern margin, the pluton intrudes volcaniclastic rocks of the Nicola Group (Upper Triassic). On its southeastern flank, it is apparently cut by granites of the Thuya batholith, and is otherwise overlapped by Neogene and younger basalts. The pluton consists primarily of nepheline-normative hornblende syenite, but also includes a leucosyenite phase, and dikes of quartz-normative monzonite, pegmatite, and quartz-feldspar porphyry. Copper mineralization is widespread but low grade, and is accompanied by weak potassic, albitic and sericite alteration. The composition, age, and location of the Rayfield River pluton suggest that it is part of the highly prospective Late Triassic (205-200 Ma) Copper Mountain magmatic belt.

Keywords: Alkalic, nepheline syenite, Copper Mountain suite, bornite, chalcopyrite, potassic, albitic, sericite alteration and copper-gold mineralization

1. Introduction

British Columbia porphyry copper-gold-molybdenum deposits formed by calc-alkaline and alkaline arc magmatism in two subduction episodes during which the paleo-Pacific ocean plate slid beneath ancestral North America (McMillan et al., 1995). Each episode lasted ~ 50 m.y.; the first was in the Late Triassic to Early Jurassic (beginning ~ 220 Ma), the second in the Late Cretaceous to Eocene. Early Mesozoic, pre-accretionary zoned alkalic intrusions are well documented in Quesnel and Stikine terranes (Fig. 1; Barr et al., 1976; Lueck and Russell, 1994; Lang et al., 1995; Logan and Mihalynuk, in press). Some are highly mineralized (Fig. 1; Galore Creek, Mount Polley, New Afton and Copper Mountain) with Cu-Au-Ag ± Pd-Pt deposits, whereas others are barren (Zippa Mountain, Rugged Mountain, Kamloops syenite).

A syenite pluton, with low-grade copper mineralization, was identified along the lower reaches of the Rayfield River in the 1960s, and has since received intermittent attention from exploration geologists. Although commonly considered an example of a Quesnel terrane alkaline porphyry Cu-Au system, little information about the pluton is available. This report summarizes a two-week field investigation directed at establishing the composition and distribution of intrusive phases, the nature and distribution of mineralization and alteration assemblages, and the external contact relationships of the pluton. U-Pb dates of ~ 202 Ma or as young as 198 Ma (Anderson et al., 2010) suggest a Late Triassic to early Jurassic age for the pluton, which places it at the young end of the highly mineralized 205-200 Ma Copper Mountain suite (Breitsprecher, 2010; Logan et al., 2007). Preliminary results from our geochronological studies confirm the > 200 Ma age.

Fig. 1. Location of the Rayfield River area straddling the boundary between 92P/2, 3, 6 and 7 map sheets (black), near the eastern edge of Quesnel terrane (transparent green overlay). Mineralized alkalic centres (crossed picks) = CM, Copper Mountain; NA, New Afton; MP, Mount Polley; GC, Galore Creek; unmineralized alkalic centres (K) = Ksy, Kamloops syenite; Zmt, Zippa Mountain; Rmt, Rugged Mountain.

2. Location and previous work

The Rayfield River pluton is approximately 20 km east of 70 Mile House, B.C., in map sheet 92P/6, at about 51° 18' N and 121° 06' W (Fig. 1). It straddles both sides of Rayfield River

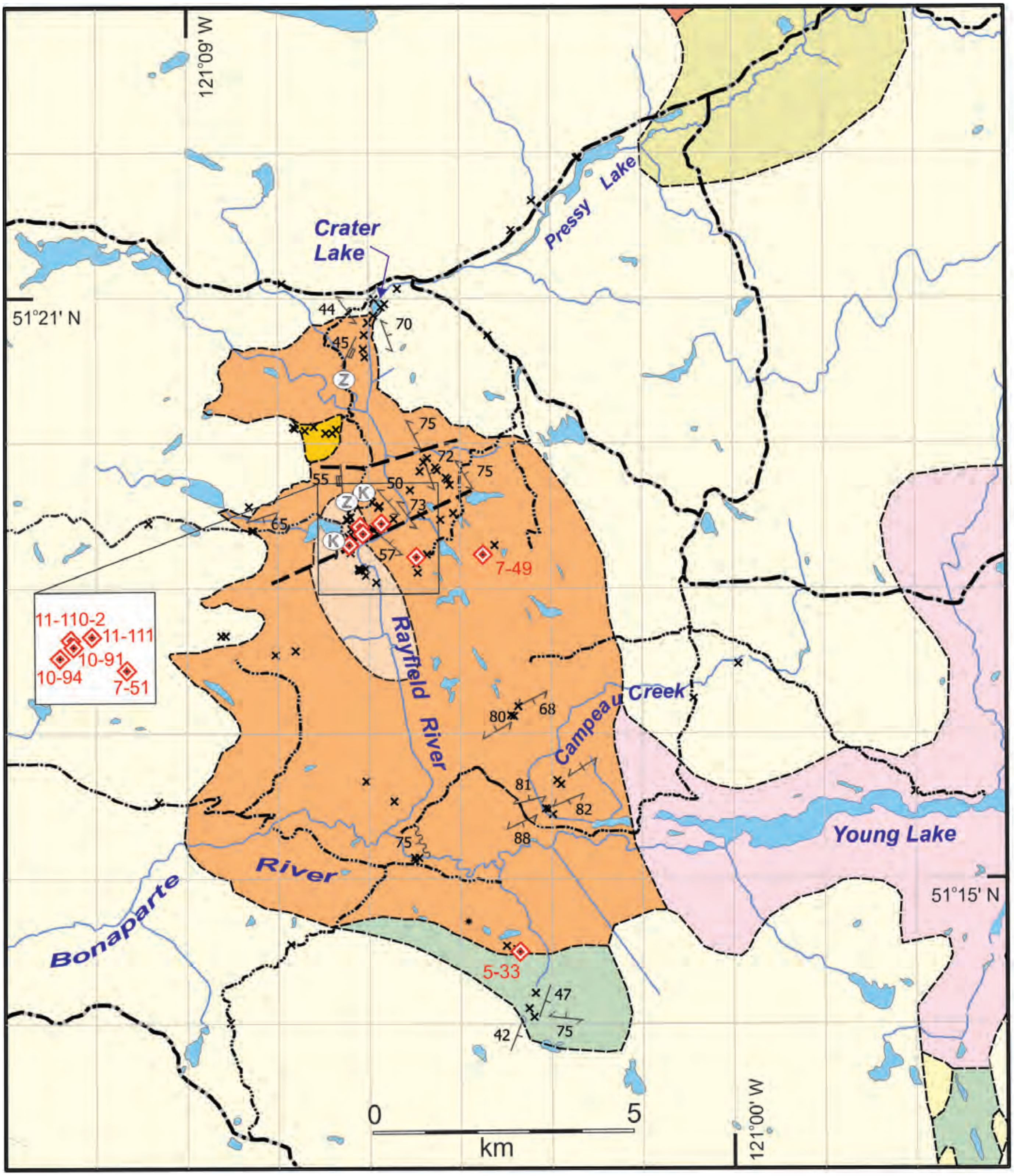

Fig. 2. Geology of the Rayfield River pluton. Geology northeast of Pressy Lake and south of Young Lake from Massey et al. (2005). Outcrops = x; geochronology samples, K = K-Ar and Z = zircon; geochemistry samples = diamonds. Inset map: geochemistry samples (Table 1).

and extends from Crater Lake in the north to the Bonaparte River in the south. Physiographically the area occupies the Cariboo Plateau (Mathews, 1989).

Campbell and Tipper (1971) included plutonic rocks along the Rayfield River as a leuco-quartz monzonite phase of the Thuya batholith, although they noted that syenite had been identified

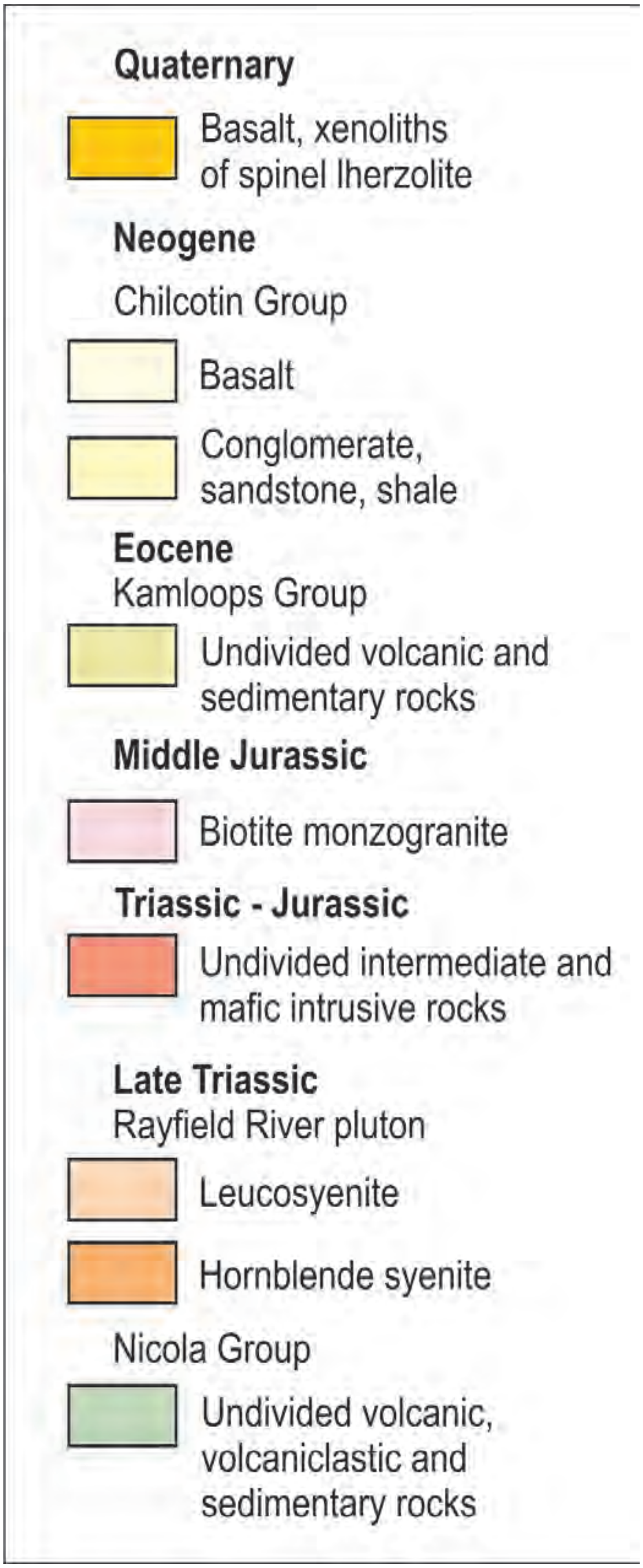

in the area after their mapping. The syenite unit (Rayfield River pluton) was outlined by exploration geologists in the mid- to late-1960s (e.g. Hodgson et al., 1969), and briefly described by Preto (1970). The TGI-3 program of the Geological Survey of Canada included work on Thuya batholith and adjacent plutonic suites, including geochronologic studies of Rayfield River pluton (Anderson et al., 2010). A high-definition airborne gamma-ray spectrometric and magnetic survey was completed over the Bonaparte-west map area (Coyle et al., 2007a, b). It was flown at an average 400-metre line spacing (reduced to 200-metres over the Rayfield River pluton) oriented N52°E at 125-metre terrain clearance. Exploration targets generated from the survey were tested by soil and rock geochemical surveys (Koffyberg, 2007a) and diamond drilling (Koffyberg, 2007b).

3. Regional setting

The Rayfield River map area is in Quesnellia, a volcanic arc terrane that developed in response to east-dipping subduction of the Cache Creek ocean beneath the western margin of ancestral North America beginning in the Late Devonian and continuing sporadically until the Middle Jurassic. Cache Creek terrane rocks are preserved ~ 30 km southwest of the map area, near Clinton, but the contact with Quesnellia is masked by Eocene volcanic and sedimentary rocks of the Kamloops Group and flat-lying Neogene basalts of the Chilcotin Group.

Calc-alkaline to alkaline arc magmatism in Quesnellia included emplacement of three Cordilleran-wide plutonic suites: the Late Triassic Guichon batholith (212-208 Ma), latest Triassic Copper Mountain (206-201 Ma) and Early Jurassic Takomkane/Wildhorse (197-193 Ma) suites (Fig. 2 in Friedman et al., this volume; Woodsworth et al. 1991; Breitsprecher et al. 2010; Logan and Mihalynuk, in press). Three porphyry copper mineralization events are directly linked to each of these calc-alkaline/alkaline magmatic episodes. The latest Triassic, central belt of alkalic plutons (Copper Mountain suite) defines a 400 km long arcuate belt that is prospective for Cu-Au mineralization (Fox, 1975; Lang et al. 1995) and hosts porphyry copper-gold deposits such as the currently producing Copper Mountain, New Afton and Mount Polley Cu-Au mines, and Cu-Au skarn and porphyry mineralization near Peach Lake. The Rayfield River pluton is projected to lie in the central part of this belt, between the New Afton and Mount Polley deposits (Fig. 2 in Friedman et al., this volume).

The Rayfield River pluton forms the western and oldest exposures of the composite Thuya batholith (Campbell and Tipper, 1971; Anderson et al., 2010), which includes Late Triassic (~ 202-200 Ma; Rayfield River pluton), Early Jurassic (195-193 Ma; Eakin Creek suite) and Middle Jurassic (164-161 Ma; Bonaparte Lake) phases. The Rayfield River pluton intrudes hornfelsed volcaniclastic rocks of the Nicola Group to the south, and is in contact with Middle Jurassic granite of the Bonaparte Lake phase to the southeast, at Young Lake (Fig. 2). The latter contact was not observed but the younger granite (Anderson et al., 2010; this study) is inferred to intrude the syenite.

4. Geology of the Rayfield River area

The Rayfield River area is underlain by (from oldest to youngest), the Nicola Group, the Rayfield River pluton, the Bonaparte Lake granite, and Neogene basalts (Fig. 2).

4.1. Nicola Group

Volcaniclastic rocks of the Nicola Group, hosts to the Rayfield River pluton, outcrop south of the Bonaparte River (Fig. 2).

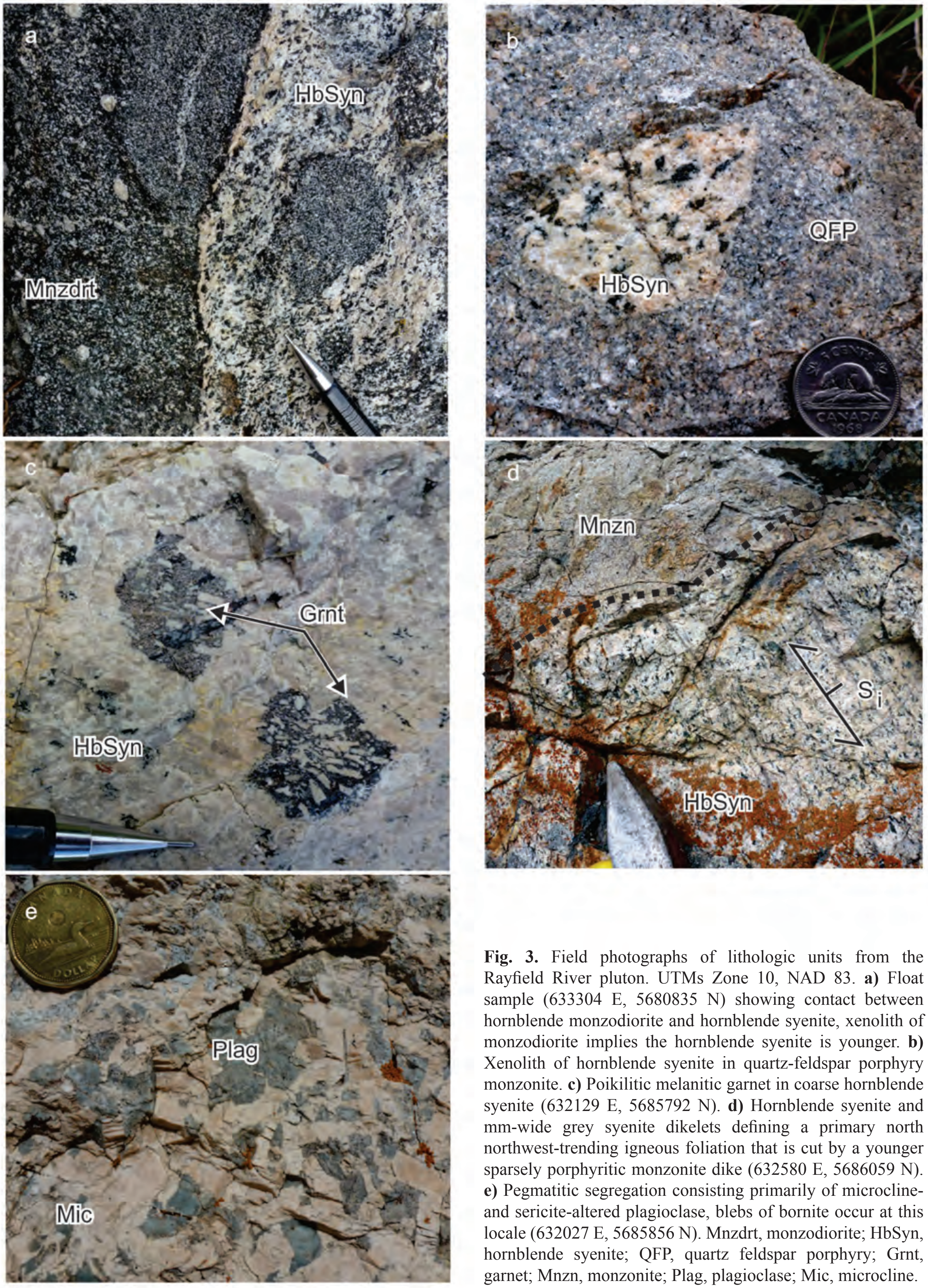

Fig. 3. Field photographs of lithologic units from the Rayfield River pluton. UTMs Zone 10, NAD 83. **a)** Float sample (633304 E, 5680835 N) showing contact between hornblende monzodiorite and hornblende syenite, xenolith of monzodiorite implies the hornblende syenite is younger. **b)** Xenolith of hornblende syenite in quartz-feldspar porphyry monzonite. **c)** Poikilitic melanitic garnet in coarse hornblende syenite (632129 E, 5685792 N). **d)** Hornblende syenite and mm-wide grey syenite dikelets defining a primary north northwest-trending igneous foliation that is cut by a younger sparsely porphyritic monzonite dike (632580 E, 5686059 N). **e)** Pegmatitic segregation consisting primarily of microcline- and sericite-altered plagioclase, blebs of bornite occur at this locale (632027 E, 5685856 N). Mnzdrt, monzodiorite; HbSyn, hornblende syenite; QFP, quartz feldspar porphyry; Grnt, garnet; Mnzn, monzonite; Plag, plagioclase; Mic, microcline.

They include: thickly bedded tuffite; cm-scale sandstone (with grains of pyroxene and plagioclase) and siltstone interlayers, and granulestone with aphyric mafic volcanic clasts. Adjacent to, and up to 1 km south of, the contact with the pluton, Nicola Group rocks are cut by irregular dikes and veinlets of hornblende diorite and, in a wide zone of contact metamorphism, contain oval clots of epidote, garnet, hematite, calcite, and pyrite. Local graded sandstone beds indicate that the east-southeast-dipping succession is right-way-up (Fig. 2). Campbell and Tipper (1971) also show Nicola Group rocks in an area west of the confluence of Rayfield and Bonaparte rivers that coincide with an isolated magnetic high (Coyle et al., 2007a, b), but the three outcrops in this area comprise hornblende syenites of the Rayfield River pluton.

4.2. Rayfield River pluton

The Rayfield River pluton occupies a 65 km^2 erosional window bounded on three sides by Neogene basalts (Fig. 2). We recognize two subunits, a hornblende syenite phase and a leucocratic syenite phase. Both phases are cut by late-stage comagmatic pegmatite, syenite, monzonite, and quartz-feldspar porphyry dikes, and by mafic dikes that are probably related to the Neogene basalt. Most of the pluton is hornblende syenite; leucosyenite comprises less than 20% and is confined to the centre of the pluton (Fig. 2). The hornblende syenite and leucosyenite phases display gradational and locally crosscutting contacts (Preto, 1970). Minor components of the pluton include a monzonite to monzodiorite phase; diorite to quartz diorite was reported from drilling near the southern margin of the pluton (Koffyberg, 2008).

Early work considered that the pluton is concentrically zoned, grading inwards from mafic to more felsic compositions (Hodgson et al., 1969). This interpretation hinged largely on outcrops of diorite to monzonite mapped by Preto (1970) at the northern (Crater Lake) and southern (close to the confluence of Rayfield and Bonaparte rivers) limits of the pluton. However, rocks at Crater Lake are coarse-grained syenite to monzonite, with 40-50% alkali feldspar, 20-30% plagioclase, 10-12% hornblende and 5-8% biotite. Cliff exposures west of Young Lake, near the confluence of Campeau Creek and Bonaparte River, contain marginally more mafic minerals and plagioclase, but normative plots indicate that they are nepheline-bearing monzonites (Fig. 3; see below). Furthermore, the southern margin of the pluton, south of the Bonaparte River, comprises holocrystalline hornblende syenite. Hence our mapping failed to confirm a concentric zonation.

4.2.1. Hornblende syenite

Hornblende syenite is the predominant component of the Rayfield River pluton. It forms cliffs along the length of the river and extends several kilometres east and west before it is lost beneath the Neogene basalt cover. The rock is light grey, generally massive to well jointed, and holocrystalline, with mainly 5-10 mm laths of microcline microperthite (65%) and interstitial stubby sodic plagioclase, hornblende, and biotite (25-30% ± corroded pyroxene, poikilitic melanite garnet, titanite, magnetite, and apatite; Figs. 3 a-d).

The hornblende syenite contains a well to weakly developed igneous foliation defined by alignment of feldspar phenocrysts and/or hornblende and biotite. Grey to pink, millimetre to metre wide fine-grained syenite dikes commonly parallel this foliation (Fig. 3d).

4.2.2. Leucosyenite

Leucosyenite is restricted to a narrow (1250 m wide) north-northwest-trending zone in the centre of the pluton. It varies from coarse to medium grained, displays a primary igneous foliation parallel to that found in the hornblende syenite, and is characteristically sericite-altered. It consists mainly of coarse laths of orthoclase > microcline microperthite, together with ~ 10-20% sodic plagioclase and less than 5% mafic minerals (green hornblende and green biotite). It also contains trace garnet, titanite, and magnetite. Hornblende crystals are mantled by biotite, which is commonly altered to chlorite. In places orthoclase rims the larger (~ 3 x 6 mm) perthitic microcline or is intimately intergrown with plagioclase. The feldspars are turbid, and plagioclase is dusted by fine sericite or entirely replaced by fine sericite and patchy mm-sized muscovite grains. Low-magnetic and low-resistivity signatures of the leucosyenite are useful for distinguishing it from the hornblende syenite (Hodgson et al., 1969).

4.2.3. Dikes

The hornblende syenite and leucosyenite units are cut by north-northwest-trending dikes that include, in decreasing order of abundance, pegmatite, syenite, orthoclase porphyritic quartz monzonite, and quartz-feldspar porphyry (Figs. 3b, d, e). Pegmatite is common as irregular pods and dike-like masses concentrated around the leucosyenite, but is also in the hornblende syenite throughout the pluton. The mineralogy is identical to the host, and contacts are gradational, suggesting these coarser grained segregations evolved from pockets of similar magmas. Pegmatites in the hornblende syenite contain coarse (up to 5 cm) tabular microcline (65-80%), interstitial (1-2 cm) equant plagioclase (15-30%), and minor nepheline, cancrinite, corroded pyroxene and/or hornblende, biotite, titanite, calcite and sericite. Pegmatites in the leucosyenite are similarly coarse grained, comprising interlocking tabular pinkish white microcline (55-70%), interstitial waxey green sericite-altered plagioclase (25-40%), and minor muscovite (Fig. 3e). Isolated mm-blebs of bornite were recognized in trench outcrops west of the river.

Lavender to grey, fine-grained, equigranular and porphyritic syenite is the most abundant phase crosscutting the hornblende syenite. It occupies centimetre to metre-wide dikes, and sheeted millimetre-wide veins, which often parallel the primary northwesterly trending foliation, and stockwork zones. The syenite consists of interlocking perthitic microcline>>sodic plagioclase, and green hornblende, biotite, garnet, titanite and apatite.

A distinctive dike of K-feldspar “rhomb” porphyry monzonite to quartz monzonite outcrops north of the dogleg in Rayfield River. About 4 m wide, the dike (321°/39°), cuts the predominant magmatic foliation of the hornblende syenite (310°/57°). The rhomb porphyry consists of 10-20 mm stubby euhedral microcline phenocrysts (10-20%) and 1-2 mm tabular oscillatory zoned sodic plagioclase phenocrysts (20-30%) in a groundmass of 0.1-0.2 mm orthoclase>>plagioclase, green hornblende, biotite, titanite, magnetite, and apatite. Weak copper mineralization is evident.

A northwest-trending dike of quartz - feldspar - hornblende porphyry monzogranite crosscuts the north end of leucosyenite (Fig. 3b) and similar monzogranite is reported at the centre of the rhomb porphyry dike north of the dogleg in Rayfield River (Hodgson et al., 1969). Hodgson et al. (1969) correlated these quartz-bearing intrusions with granite of the Thuya batholith, but the common orientation, mineralogy, and evolved composition suggests that they are probably quartz saturated end members of the Rayfield River alkaline suite. Preliminary U-Pb zircon age determinations (see below) are consistent with this hypothesis.

4.2.4. Geochronology

K-Ar cooling ages for hornblende from the hornblende syenite (193 ± 14 Ma) and biotite from the leucosyenite (186 ± 12 Ma) provide minimum ages for the Rayfield River pluton (Breitsprecher and Mortensen, 2004). Anderson et al. (2010) reported a U-Pb zircon age of ~ 202 Ma for the syenite, allowing that it could be as young as 198 Ma. We collected two samples for U-Pb zircon geochronologic work at the Pacific Centre for Isotopic and Geochemical Research of the Department of Earth, Ocean and Atmospheric Sciences, The University of British Columbia. The first is from unaltered and unmineralized hornblende syenite (13-JLO-12-129), collected 1.5 km southwest of Crater Lake (Zone 10, NAD83; 631885 E, 5688894 N). Preliminary results indicate the zircons have high uranium contents, and only 2 of 5 grains analysed generated data. The two analyses are concordant but do not overlap. The ^{206}Pb/^{208}U ages are: 198.6 ± 0.4 Ma and 200 ± 0.4 Ma. Given the high uranium contents we assume some Pb loss and therefore the latter to be a minimum age (R. Friedman, pers. comm. 2013).The second sample is from a weakly altered quartz-feldspar porphyry monzogranite dike (13-JLO-13-133) collected ~ 1 km north of the dogleg in Rayfield River (631992 E, 5686557 N). Preliminary results indicate an age of 199.7-199.9 Ma (R. Friedman, pers. comm., 2013). Because the dike intrudes the hornblende syenite, this age demonstrates that the syenite is older than 200 Ma. It also demonstrates that these quartz-bearing dikes are late, quartz-saturated phases of the Rayfield River syenite complex and unrelated to the adjacent Bonaparte Lake granite (164-161 Ma; Anderson et al., 2010).

4.3. Bonaparte Lake granite

Monzogranite of the Bonaparte Lake phase of the Tuya Batholith underlies the eastern portion of the area. It is a medium-grained, equigranular to weakly K-feldspar porphyritic biotite-hornblende granite, comprising pinkish-white orthoclase (35%), greyish-white plagioclase (30%), vitreous subhedral quartz (25%), and chloritized hornblende and biotite (10%), with minor disseminated magnetite. In thin section quartz and orthoclase exhibit 120° annealed crystal boundaries, titanite is fractured, and myrmekitic intergrowths of quartz and K-feldspar replace rims of plagioclase (Fig. 4) suggesting recrystallization, brittle strain, and K-metasomatism. Anderson et al. (2010) reported a Middle Jurassic U-Pb crystallization age of 161.2 ± 0.1 Ma for monzogranite samples collected ~ 2 km northwest of the west end of Bonaparte Lake. The granite is inferred to intrude the Rayfield River pluton, but contacts are not exposed.

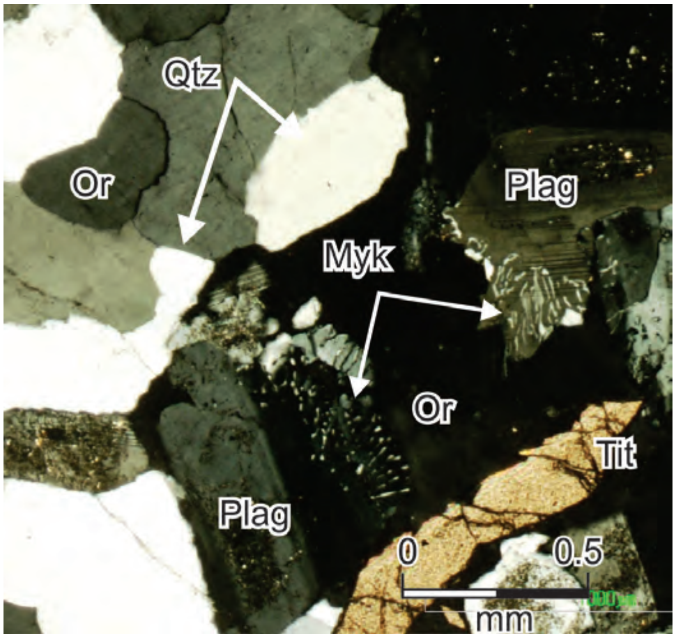

Fig. 4. Photomicrograph of Bonaparte Lake hornblende-biotite monzogranite (Middle Jurassic) in crossed-polarized light. Note the 120° annealed crystal boundaries (Or and Qtz) and the myrmekitic (myk) intergrowths of quartz and K-feldspar replacing the rims of plagioclase. Qtz, quartz; Or, orthoclase; Plag, plagioclase; Tit, titanite.

4.4. Chilcotin Group

Flat-lying basaltic flows and pyroclastic rocks of the Chilcotin Group (Early Miocene to Early Pleistocene) cover much of the Interior Plateau of south-central British Columbia (Mathews, 1989). Recent studies indicate that unit is not as continuous as was previously thought, and that regional compilations overestimate its areal extent by up to 50% (Dohaney, 2009). Furthermore, the thickness of the unit is controlled by paleotopography; thick (> 30 m) accumulations in paleochannels thin to less than 10 m in paleointerfleuve uplands (Andrews and Russell, 2010). Hence geologically and economically important Mesozoic rocks, such as Rayfield River commonly appear as windows through the basalt.

In the Rayfield River map area, the Chilcotin Group includes aphyric basalt, basalt with sparse olivine and pyroxene phenocrysts, and local subophitic gabbro. The basalt forms 5 to 12 metre thick, flat-lying benches (Fig. 5). It is black, brown weathering and massive to locally scoriaceous and red weathering. Vesicles, locally filled with calcite and/or zeolite minerals, are near the tops and bottoms of the flows, which are locally separated by breccias and interflow red and orange paleosols. The Chilcotin Group is best exposed at Crater Lake, where the Rayfield River has eroded through more than 50 metres of basalt. At this locale it consists of at least 3 coherent massive flow units that lie directly on hornblende syenite of the Rayfield River pluton (Fig. 5).

4.5. Quaternary basalt

Mantle xenoliths, mainly spinel lherzolite, have long been known from the Rayfield River area, but the host basalt, of hawaiite (Canil et al., 1987) or basanitic (Greenfield et al., 2013) composition, had been included in the Chilcotin Group. Here, we map the xenolith-bearing basalt separately, and assign

Fig. 5. Brown-weathering, 50 metre-high benched Miocene basalt flows comprise the northern shore of Crater Lake. Hornblende syenite and leucosyenite are exposed along the heavily wooded shore below the basalt (viewed easterly). MCv, Miocene Chilcotin volcanic rocks; TRRs, Triassic Rayfield River syenite.

it a Quaternary age based on correlation with similar xenolith-bearing basalt outliers above Quesnel terrane in the Thuya Creek – Woodjam Creek area to the north (Schiarizza et al., 2013).

The Quaternary basalt occurs in two areas, approximately 2.4 km southwest of Crater Lake and 3.6 km due south of Crater Lake. The best exposure is southwest of Crater Lake, where flat-lying aphyric xenolith-rich basalt and welded basalt flow breccia cover a 0.4 km^2 area. The basalt is light grey, fine grained and includes abundant (up to 20%) angular to rounded peridotite xenoliths that range from a few mm to more than 10 cm (Fig. 6). Xenoliths as large as 15 x 9 cm occur over the entire exposed thickness of about 60 m. The xenoliths contain yellowish green olivine (75%), bright green clinopyroxene (10%), orthopyroxene (10%) and lesser dark spinel.

A xenolith-bearing basalt unit on Takomkane Mountain (approximately 100 km north of Rayfield River) rests on a glaciated surface (Sutherland Brown, 1958) and has yielded a K-Ar whole rock date of 0.40 ± 0.04 Ma (Sun et al., 1991). Another, from Mount Timothy (approximately 70 km north), has yielded an Ar-Ar whole rock date of 0.465 ± 0.023 Ma (Schiarizza et al., 2013). We assume that similar basalts at Rayfield River are also Pleistocene.

5. Structure

The Rayfield River pluton contains a primary igneous foliation that is defined by the planar alignment of tabular K-feldspar and hornblende ± biotite crystals. The foliation is variably developed throughout the intrusion and generally strikes northwest and dips between 50 and 75° northeast. In the southeast part of the intrusion however, foliation strikes northeast and dips steeply to either the northwest or southeast (Fig. 2). Sheeted veins, several mm to several cm wide, follow the northeast dipping foliation in many parts of the pluton.

Fig. 6. Basalt with lherzolite xenoliths, comprising olivine (75%), bright green clinopyroxene (10%), orthopyroxene (10%) and lesser dark spinel, ~ 2.4 km southwest of Crater Lake.

Brittle fault zones occur throughout the pluton, with two main orientations. One set strikes northwest (335°) with variable steep dips, and a later set strikes northeast (055°) with moderate northwest dips. The fault zones are characterised by anastamosing slip planes coated with chlorite, epidote, hematite and/or calcite, and commonly minor malachite. Bleached, weak argillic alteration assemblages overprint the brittle structures and are probably related to surface weathering.

North of the Rayfield River dogleg, a north-northwest trending lineament marks the contact between pervasively sericite-altered leucosyenite and hornblende syenite that displays weak fracture-controlled pink K-spar alteration. Cataclastic fault rocks can be traced for more than 1 km along the course of the river. Samples of altered leucosyenite(?) from this fault zone (13JLO10-91-2, and R07-34538 from Le Couteur in Koffyberg, 2007b) have strong cataclastic textures that include brecciated orthoclase and plagioclase crystals, kinked and broken plagioclase twin planes, and biotite crystals (Fig. 7). In detail the breccias are cut by late calcite veinlets that have albite selvages.

Two east-northeast-striking faults, one coinciding with the dogleg bend in the Rayfield River, are shown on the geologic map (Fig. 2). These structures are traceable by resistivity surveys (Hodgson et al., 1969), and appear to post date mineralization. Mineral fibers on the northeast-striking fault planes plunge gently and indicate a sinistral sense for latest motion. Hodgson et al. (1969) reported that a north-trending rhomb porphyry dike extends across one of the structures with no apparent displacement.

6. Chemistry

Major oxide, trace, and rare earth element chemistry was determined for hornblende syenite, leucosyenite, a pegmatite dike, and a late stage quartz-feldspar porphyry dike from the Rayfield River pluton, and for granite from the Bonaparte phase of the Thuya batholith (Fig. 8). Complete analytical

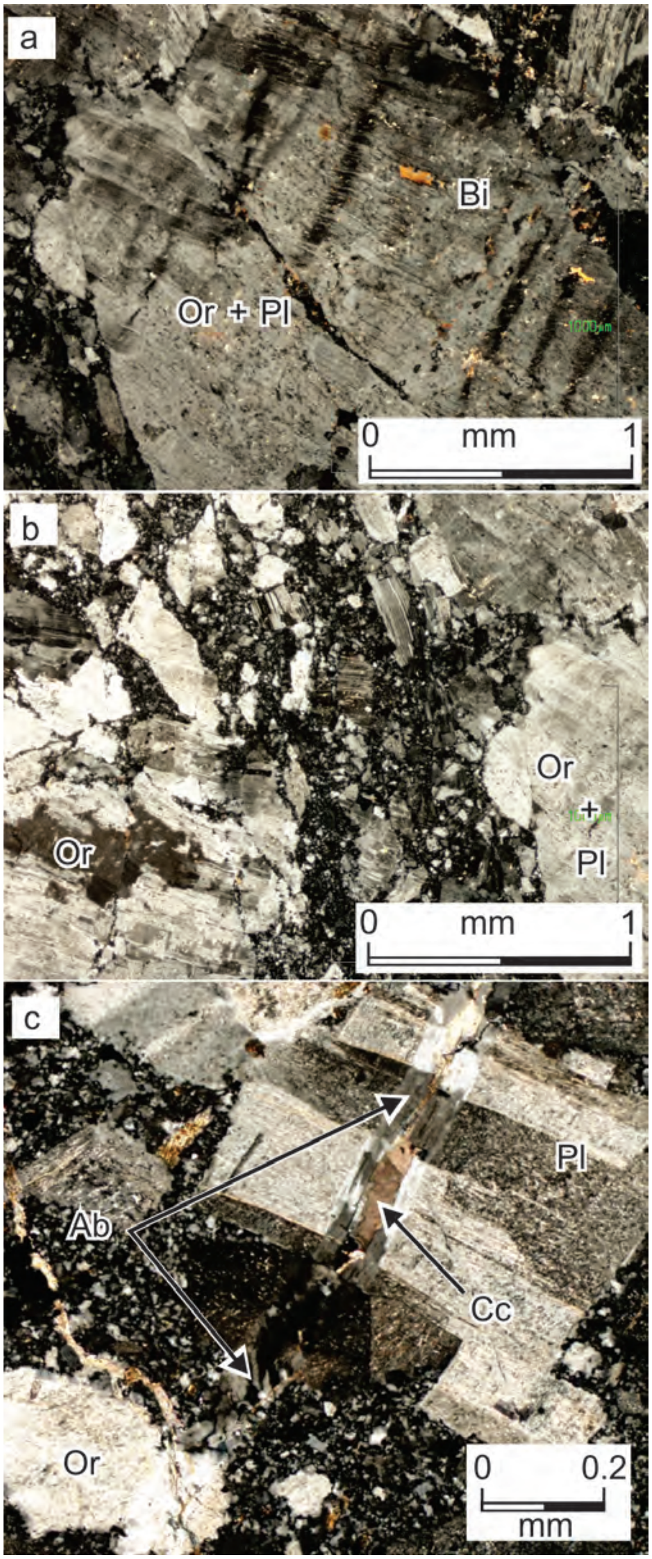

Fig. 7. Cross-polarized light photomicrograph of cataclastic leucosyenite (Zone 10, NAD 83, 632219 E, 5685884 N). **a, b)** Plagioclase/perthite crystals show kinked, broken, and sheared twin planes, and finely milled fragments of feldspar, plagioclase, and biotite. **c)** The cataclasite is cut by late calcite veinlets that have albite selvages. Abbreviations: Pl, plagioclase; Ab, albite; Bi, biotite; Cc, calcite; Ser, sericite.

data tables, classifications, tectonic discrimination diagrams, and regional comparisons with selected Late Triassic alkalic intrusions from south-central British Columbia (Mount Polley stock, Shiko Lake and Bootjack Lake stock) are in Logan and Schiarizza (2014).

Hornblende syenite samples contain 55 to 59 wt% SiO_2 and occupy the intermediate, alkaline field on the total alkali versus SiO_2 (TAS) plot of Cox et al. (1979) where they are classified as nepheline syenite to syenite (Fig. 8a). The leucosyenite sample (65 wt% SiO_2) and a pegmatite dike, (64 wt% SiO_2,) are classified as syenites, in the acid, alkaline field. A quartz-feldspar porphyry dike (67 wt% SiO_2) and a sample of the Middle Jurassic Bonaparte granite (70 wt% SiO_2) plot in the acid, subalkaline granite classification field (Fig. 8a).

CIPW normative calculations were determined and plotted on a Streckeisen diagram (Fig. 8b). The hornblende syenite is nepheline normative and occupies the transition between foid-monzosyenite to foid-bearing syenite fields, with one sample from the southern margin of the body plotting in the foid-bearing monzonite field (Fig. 8b). The pegmatite and leucosyenite are silica saturated and plot in the syenite field. The Late Triassic quartz-feldspar porphyry dike that crosscuts the leucosyenite in the core of the pluton plots with the Bonaparte intrusion in the granite field (Fig. 8b). The intrusions are metaluminous (magnetite series), plot in the volcanic arc granite field (Pearce et al., 1984) on trace element tectonic discrimination diagrams (Logan and Schiarizza, 2014) and lack Eu anomalies on chondrite-normalized REE plots (not shown).

High grain counts of thorianite (ThO_2) are reported in till samples collected from the Raft batholith and the western margin of the Thuya over the Rayfield River pluton (Plouffe et al., 2010). In addition, the airborne gamma-ray Th (ppm) equivalent measurement plots (Coyle et al., 2007a, b) show elevated Th values (between 5.00 and 8.35) extending from Crater Lake south to the dog-leg bend and within a 3.5 x 1km northwest-trending area extending west of the confluence of Rayfield and Bonaparte rivers. The pattern of thorianite grain distribution was attributed to southwestward glacial transport, which led Plouffe et al. (2010) to suggest derivation from the Rayfield River syenite. To test this hypothesis, we examined the trace geochemistry of Rayfield River complex samples. Hornblende syenite (n=10) and late stage pegmatite and quartz feldspar porphyry monzonite dike rocks (n=4) analysed by inductively coupled plasma mass spectrometry (ICP-MS) after a lithium metaborate/tetraborate fusion at Activation Laboratories Ltd., or by ICP-MS following a 4-acid digestion at ACME Labs. The detection limit for thorium is 0.05 ppm using the fusion technique and 0.1 ppm with the acid digestion. The complete geochemical data set is in Logan and Schiarizza (2014); here we focus on thorium concentrations, which range from 1.4 - 5.9 ppm with an arithmetic mean value of 3.2 ppm. Th and U-enriched syenite bodies in the literature typically have concentrations at least an order of magnitude higher than 3.2 ppm (Labhart and Rybach, 1971; Van Gosen et al., 2009; Martins et al., 2011), thus we consider that if the Rayfield River pluton is the source of the thorianite grains found by Plouffe et al. (2010) the grains must be very localized or contained in a phase not sampled during our study.

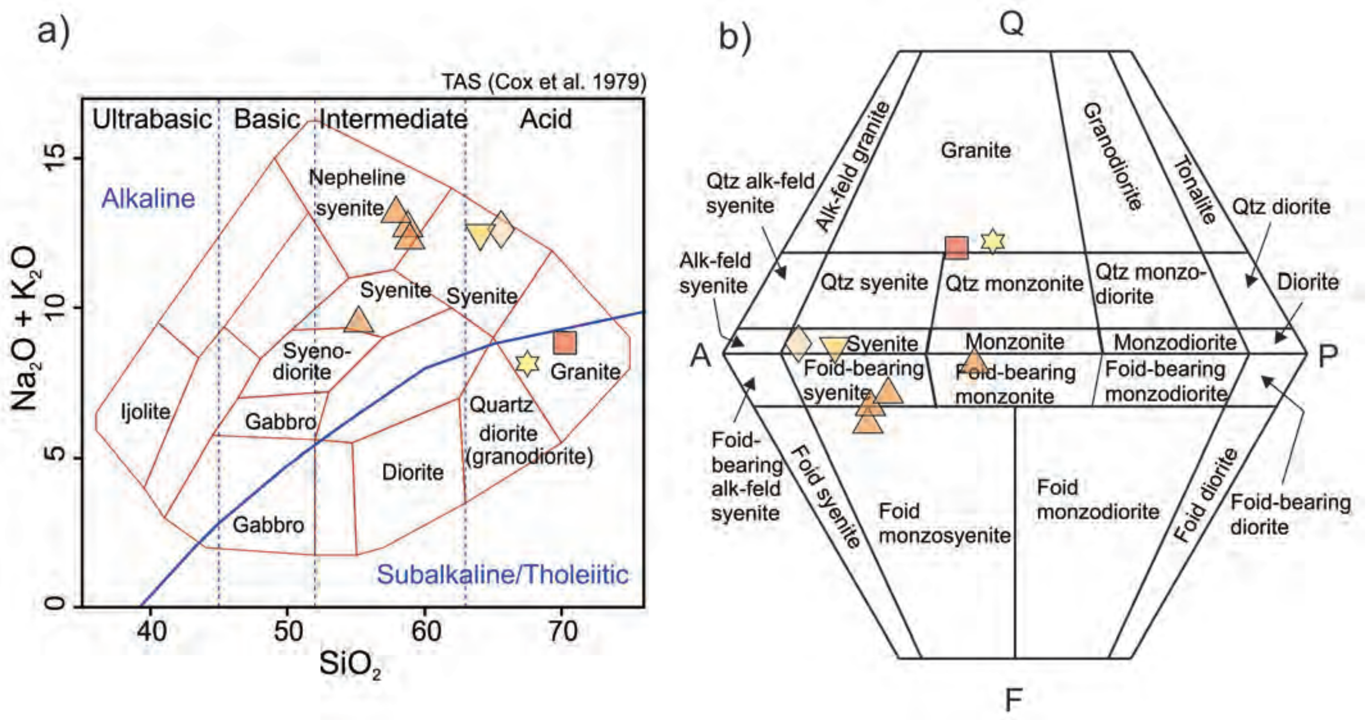

Fig. 8. Hornblende syenite (orange triangles), leucosyenite (pink diamond), pegmatite (gold inverted triangle) and quartz feldspar porphyry (yellow star) units from the Rayfield River complex and Bonaparte Lake monzogranite (red square) of the Thuya batholith plotted on **a)** total alkali versus silica (TAS) diagram (Cox et al., 1979) and **b)** an IUGS classification diagram using CIPW normative values (after Streckeisen, 1976).

7. Alteration and mineralization

Historically, exploration at Rayfield has focused on disseminated copper associated with the Rayfield River pluton. Geological, geochemical, and geophysical programs were conducted by Kennco Exploration Ltd., Cominco Ltd. and Amax Exploration Inc. between 1960 and 1970. Percussion drilling in 1970 by Amax Exploration Inc. totalled 1748 m in 31 holes and delineated a north-trending area 450 m by 2130 m of copper mineralization grading between 0.05% and 0.1% Cu on the west side of the Rayfield River (Wynne, 1990). The best copper intersection was 0.42% over 6.1 m at the north end of the zone. In 1989, Discovery Consultants carried out geological mapping, an I.P. geophysical survey and 1140.9 m of diamond drilling in eight holes (Wynne, 1990). Three of these holes ended in > 0.1% Cu at depths of < 150 m below surface. More recently, exploration targets generated from a high-definition airborne gamma-ray spectrometric and magnetic survey were tested by soil and rock geochemical surveys (Koffyberg, 2007a) and diamond drilling to depths of between 250 and 300 metres (Koffyberg, 2007b). The results confirmed low-grade porphyry Cu-Au mineralization in the upper 150 metres that did not extend to greater depths.

Our observations during 2013 fieldwork suggest that alteration of the Rayfield River pluton is relatively minor. The northern portion of the pluton is cut by abundant veins of syenite, but mineralized veins are sparse. They are generally sheeted structures, but stockworks of grey to lavender syenite veins are also common (Fig. 9). Along fractures and margins of grey syenite dikelets, alteration assemblages include: patchy intergrowths of biotite, magnetite, and hematite; epidote; and locally, chlorite or sericite. Alteration does not extend beyond the immediate contact zone. K-feldspar "pinking" and chalcopyrite are common but restricted to narrow (mm-scale) zones.

In thin section alteration is limited to weak epidote and sericite replacement of plagioclase, local orthoclase overgrowths on perthitic microcline, and replacement of primary hornblende by biotite and later chlorite. Late stage mm-thick veinlets of albite and calcite crosscut leucosyenite and feldspar porphyry dikes in the core of the pluton.

Most alteration is restricted to narrow late northerly- and northeast-trending structures that appear to postdate mineralization. Bleached, sericite - clay alteration zones are confined to these structures. Pale buff to yellow bleaching accompanies sericite and late albite-carbonate alteration of leucosyenite west of the dogleg bend in the river. K-spar pinking and pervasive sericite alteration overprinted the primary north northwest-trending magmatic foliation in leucosyenite, with the development of disseminated mm-scale muscovite crystals. A sample with secondary muscovite has been submitted for $^{40}Ar/^{39}Ar$ isotopic analysis to determine its cooling age.

Hypogene copper minerals include chalcopyrite and bornite as interstitial blebs in the syenite and pegmatite or localized along the margins of narrow (mm- to cm-wide) grey syenite dikelets, veins and tight fractures. Secondary supergene chalcocite, malachite, and rare native copper are associated with altered fault zones and surface weathering. Hematite occurs throughout the syenite, and pyrite is conspicuous by its

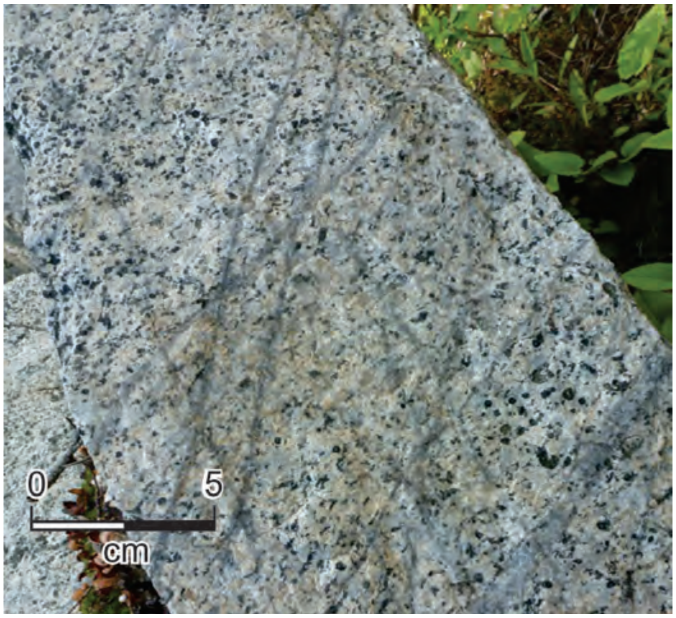

Fig. 9. Massive, coarse-grained and little altered hornblende biotite syenite intruded by at least two sets of sheeted fine-grained grey syenite dikelets. Minor malachite colours weathering fractures and attests to trace amounts of copper mineralization (Zone 10, NAD 83, 633552 E, 5685580 N). Copper mineralization is widespread and low grade.

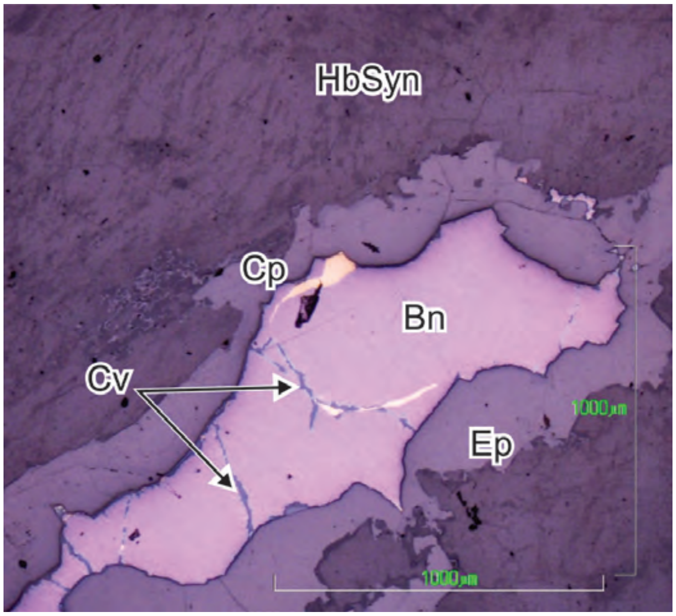

Fig. 10. Plane polarized reflected light photomicrograph of mineralized vein cutting hornblende syenite at 13JLO7-49 (Zone 10, NAD 83, 634620 E, 5685605 N). Bornite vein is enveloped by pale green epidote and contains chalcopyrite exsolution lamella. It is replaced along curved fractures by chalcopyrite and covellite. Abbreviations: HbSyn, hornblende syenite; Ep, epidote; Bn, bornite; Cp, chalcopyrite; cv, covellite.

absence. Copper grades reported from historical work (surface trenching and diamond drilling programs) average between 0.05 - 0.1% Cu and < 50 ppb Au (Selmer et al., 1968; Hodgson et al., 1969; Preto, 1970; Wynne, 1990; Koffyberg, 2008). Gold values are typically less than 10 ppb, and although elevated gold values accompany higher grades of copper, the Cu:Au ratios are several orders of magnitude below the 1:1 (1 g/t Au to 1% Cu) suggested for gold-rich porphyries (Kirkham and Sinclair, 1995) and the ranges for British Columbia alkaline deposits (Panteleyev, 1995).

Lithogeochemical analyses of mineralized samples collected during 2013 fieldwork are presented in Table 1. Sample 13JLO5-33 is from the pyritic hornfelsed southern contact zone between hornblende syenite and Nicola Group volcaniclastic rocks. The sample returned low copper, gold, and silver values and relatively elevated iron, magnesium, nickel, and vanadium. Hornblende syenite samples 13JLO7-49 and 7-51 were collected from outcrops east of Rayfield River in the central area of the pluton. The highest copper, gold and silver values came from a 5 mm-wide veinlet of bornite, malachite ± chalcopyrite and magnetite (Fig. 10) hosted in relatively unaltered hornblende syenite. The syenite here was also intruded by numerous malachite – stained pegmatites and fine-grained grey syenite dikes, as well as unmineralized quartz veins. Sample 13JLO7-51 was collected farther west from a road exposure of hornblende syenite cut by grey syenite dikes. At this location chalcopyrite and malachite mineralization and chlorite alteration are localized adjacent to dike and syenite contacts. The remaining four samples (13JLO10-91, 10-94, 11-110-2 and 11-111) originate from the cliffs north of the dog-leg bend in Rayfield River. Sample 13JLO10-94 is a sericite-altered, garnet-bearing pegmatitic leucosyenite that contains small blebs of bornite. The other three are grab samples of typically malachite-coated, weakly-altered grey syenite-veined leucosyenite or hornblende syenite, rarely with blebs of chalcopyrite replacing primary mafic mineral clots.

8. Summary and conclusions

The alkalic chemistry, crystallization age, and metal assemblages at Rayfield River are shared by porphyry deposits of the Late Triassic Copper Mountain magmatic belt (e.g. Copper Mountain porphyry Cu-Au, New Afton porphyry Cu-Au and the Mount Polley porphyry Cu-Au), inviting speculation that this intrusion is part of this highly prospective magmatic belt within Quesnellia. This hypothesis is being addressed through ongoing U-Pb zircon and Ar/Ar white mica isotopic age determinations aimed at testing the Late Triassic age of the Rayfield River intrusions and synchronicity of copper-gold mineralization.

Our preliminary study leads to the following conclusions.

1) The Rayfield River pluton consists primarily of silica-undersaturated nepheline syenite, with a minor component including late-stage silica-saturated leucosyenite, pegmatite, and quartz monzonite dikes.

2) The Rayfield River pluton is probably Late Triassic (> 201 Ma) and part of the Copper Mountain suite of alkaline intrusions.

3) The syenite contains amphibole and biotite (hydrous), poikilitic metablastic melanite garnet, coarse crystals of sphene, apatite, and magnetite, and rare blebs of bornite or chalcopyrite. Abundant hornblende and magnetite and accessory igneous melanite is a distinguishing feature of many of the alkaline plutons in Stikine and Quesnel terrane and is an important

Table 1. Selected geochemical results of mineralized samples collected during the 2013 property visit.

		Analyte	Ag	As	Au	Bi	Cd	Co	Cr	Cu	Fe	Mo	Ni	Pb	S	Sb	Sn	Th	U	W	Zn
		Unit	PPM	PPM	PPB	PPM	PPM	PPM	PPM	PPM	%	PPM	PPM	PPM	%	PPM	PPM	PPM	PPM	PPM	PPM
		MDL	2	0.1	0.2	0.02	0.01	0.1	0.5	0.01	0.01	0.01	0.1	0.01	0.02	0.02	0.1	0.1	0.1	0.1	0.1
Station Number	Easting	Northing																			
13JLO 5-33	635515	5678018	<0.1	33	8	0.3	<0.1	24.5	67	64.9	5.8	1.1	28.3	0.8	0.2	0.7	0.5	1.5	0.90	1.5	36
13JLO 7-49	634621	5685606	15.5	<1	352	3.8	0.9	6.7	9	>10000.0	2.52	0.7	1.5	23.4	0.3	0.1	0.6	3.2	1.70	0.4	85
13JLO 7-51	633347	5685526	2.2	1	50	0.7	<0.1	3.4	10	4166.2	2.1	0.2	0.8	8.9	<0.1	0.2	0.5	2.1	1.50	0.2	71
13JLO 10-91	632220	5685884	1.7	2	20	0.2	0.2	1.7	10	3926.6	1.25	2.6	0.9	11.7	0.3	1.3	0.2	3.5	1.6	1	10
13JLO 10-94	632130	5685793	1.4	3	17	0.9	0.2	1.8	9	1132.9	1.44	0.4	0.7	17	<0.1	0.3	0.4	3.4	2.3	0.3	31
13JLO 11-110-2	632624	5686092	1.9	2	37	0.2	<0.1	5.1	10	1010.5	2.31	0.3	0.6	15.5	<0.1	0.3	0.5	4.3	1.9	0.2	89
13JLO 11-111	632662	5686149	2.9	2	83	0.7	0.9	5.5	8	5646.5	2.16	0.2	1.2	13.1	<0.1	0.2	0.6	3.7	2	0.2	110
Pulp Duplicates																					
13JLO 11-111	632662	5686149	2.9	2	83	0.7	0.9	5.5	8	5646.5	2.16	0.2	1.2	13.1	<0.1	0.2	0.6	3.7	2	0.2	110
13JLO 11-111	632662	5686149	2.9	3	-	0.7	0.9	5.9	9	5866.4	2.29	0.2	1.1	13.3	<0.1	0.2	0.6	3.4	1.7	0.2	115

criteria for distinguishing mineralized from barren intrusions (Lueck and Russell, 1994).

4) Alteration and mineralization are limited to narrow (0.5-1.0 mm) envelopes of tight sheeted and stockwork grey syenite veins that crosscut the hornblende syenite and leucosyenite.

5) The complex contains low-grade Cu-Au mineralization on the order of 0.1% Cu and < 50 ppb Au.

6) Geochemistry did not indicate elevated thorium values, so the pluton is an unlikely source for anomalously abundant thorianite grains identified in nearby till samples (Plouffe et al., 2010).

References cited

Anderson, R.G., Schiarizza, P., Andrews, G., Breitsprecher, K., Davis, W., Dunne, C.E., Plouffe, A. and Thomas, M.D., 2010. Bedrock, surficial, geophysical and geochemical mapping reveals exploration targets in the Thuya batholith, southern Nicola arc. In: Geological Association of Canada, Targeted Geoscience Initiative 3 Workshop, March 2010, Vancouver, pp. 52-57. URL accessed November, 2012, http://www.gac-cs.ca/workshops/TGI3/abstracts/GAC_TGI3_workshop_abstracts.pdf

Andrews, G.D.M. and Russell, J.K., 2010. Distribution and thickness of Volcanic and glacial cover on the Interior Plateau: in Geological Association of Canada, Targeted Geoscience Initiative 3 Workshop, Vancouver, pp. 49-51. URL accessed November, 2012.

Barr, D.A., Fox, P.E., Northcote, K.E. and Preto, V.A., 1976. The Alkaline Suite Porphyry Deposits: a summary; in Porphyry Deposits of the Canadian Cordillera, Sutherland Brown, A., Editor, Canadian Institute of Mining and Metallurgy, Special Volume 15, pp. 359-367.

Bath, A.B. and Logan, J.M., 2006. Petrography and geochemistry of the Late Triassic Bootjack stock (NTS 093A/12), south-central British Columbia; in Geological Fieldwork 2005, BC Ministry of Energy, Mines and Petroleum Resources, Paper 2006-1 and Geoscience BC, Report 2006-1.

Breitsprecher, K., Mortensen, J.K., 2004. B.C. Age 2004A-1 (release 3, October 2004) - A database of isotopic age determinations for rock units from British Columbia: BC Ministry of Energy, Mines, and Petroleum Resources, British Columbia Geological Survey Open File 2004-03.

Breitsprecher, K., Weis, D., Scoates, J.S. and Anderson, R.G., 2010. Targeting mineralized Late Triassic to Early Jurassic plutons in the Nicola arc, southern Quesnel terrane, Canadian Cordillera. In: Geological Association of Canada, Targeted Geoscience Initiative 3 Workshop, Vancouver, pp. 49-51. URL accessed November, 2012, http://www.gac-cs.ca/workshops/TGI3/abstracts/GAC_TGI3_workshop_abstracts.pdf

Campbell, R.B. and Tipper, H.W., 1971. Bonaparte Lake map area, British Columba: Geological Survey of Canada, Memoir 363, pp. 100.

Canil, D., Brearley, M., and Scarfe, C.M., 1987. Petrology of ultramafic xenoliths from Rayfield River, south-central British Columbia: Canadian Journal of Earth Sciences, V. 24, 1679-1687.

Coyle, M., Dumont, R., Potvin, J., Carson, J.M., Buckle, J.L., Shives, R.B.K. and Harvey, B.J.A., 2007a. Geophysical Series – Green Lake 92P/6, British Columbia, Bonaparte Lake West geophysical survey, British Columbia: Geological Survey of Canada, Open File 5502, scale 1:50,000, 10 sheets.

Coyle, M., Dumont, R., Potvin, J., Carson, J.M., Buckle, J.L., Shives, R.B.K. and Harvey, B.J.A., 2007b. Geophysical Series – Loon Lake 92P/3, British Columbia, Bonaparte Lake West geophysical survey, British Columbia: Geological Survey of Canada, Open File 5502, scale 1:50,000, 10 sheets.

Cox, K.G., Bell, J.D. and Pankhurst, R.J., 1979. The interpretation of igneous rocks; George Allen & Unwin, London, 450 p.

Currie, K.L. (1976): The alkaline rocks of Canada: Geological Survey of Canada, Bulletin 239, 278 p.

Dohaney, J.A.M., 2009, Distribution of Chilcotin Group basalt, British Columbia: Unpublished M.Sc. thesis, Vancouver, Canada, The University of British Columbia, 123 p.

Fox, P.E. (1975): Alkaline rocks and related mineral deposits of the Quesnel Trough, British Columbia (abstract); Geological Association of Canada, Cordilleran Section, Symposium on Intrusive Rocks and Related Mineralization of the Canadian Cordillera, Program and Abstracts, 12.

Greenfield, A.M. R., Ghent, E.D., and Russell, J.K., 2013. Geothermobarometry of spinel peridotites from southern British Columbia: implications for the thermal conditions in the upper mantle. Canadian Journal of Earth Sciences, 50, 1019-1032.

Hodgson, C.J., McKnight, B.K., Horsnail, R.F., and Mustard, D.K., 1969. Geological, geochemical, geophysical report on the Dansey Rayfield River copper property. In: BC Ministry of Energy, Mines, and Petroleum Resources, Assessment report #2,135, 72 p.

International Commission on Stratigraphy, 2013, International stratigraphic chart (http://www.stratigraphy.org/)

Kirkham, R.V., and Sinclair, W.D., 1995. Porphyry copper, gold, molybdenum, tungsten, tin, silver, In Eckstrand, O.R., Sinclair, W.D., and Thorpe, R.I., eds., Geology of Canadian Mineral Deposit Types: Geological Survey of Canada, Geology of Canada, no. 8, 421-446.

Koffyberg, A., 2007a. Assessment report on the airborne gamma-ray spectrometric and magnetic surveys - Rayfield River property. In: BC Ministry of Energy, Mines, and Petroleum Resources, Assessment report #29,110, 121 p.

Koffyberg, A., 2007b. Assessment report on the geochemical soil survey and prospecting - rock sampling program - Rayfield River property. In: BC Ministry of Energy, Mines, and Petroleum Resources, Assessment report #29,538, 143 p.

Koffyberg, A., 2008. Assessment report on a diamond drill program - Rayfield River property. In: BC Ministry of Energy, Mines, and Petroleum Resources, Assessment report #30,271, 161 p.

Labhart, T.P., and Rybach, L., 1971. Abundance and distribution of uranium and thorium in the syenite of Piz Giuv (Aar-Massif, Switzerland): Chemical Geology 01 DOI:10.1016/0009-2541(71)90010-6

Lang, J.R., Lueck, B., Mortensen, J.K., Russell, J.K., Stanley, C.R. and Thompson, J.F.H., 1995. Triassic–Jurassic silica undersaturated and silica-saturated alkalic intrusions in the Cordillera of British Columbia: implications for arc magmatism; Geology, V. 23, 451–454.

Logan, J.M., and Mihalynuk, M.G., in press, Tectonic controls on Early Mesozoic paired alkaline porphyry deposit belts (Cu-Au ± Ag-Pt-Pd-Mo) within the Canadian Cordillera, in alkalic Special Volume, Economic Geology.

Logan, J.M., and Schiarizza, P., 2014. Rayfield River major oxide, trace and rare earth element geochemical data: British Columbia Ministry of Energy and Mines, GeoFile 2014-X.

Logan, J.M., Mihalynuk, M.G., Ullrich, T., and Friedman, R.M., 2007. U-Pb Ages of intrusive rocks and ^{40}Ar/^{39}Ar plateau ages of copper-gold-silver mineralization associated with alkaline intrusive centres at Mount Polley and the Iron Mask Batholith, southern and central British Columbia: British Columbia Ministry of Energy, Mines and Petroleum Resources, Geological Fieldwork 2006, Paper 2007-1, pp. 93-116.

Lueck, B.A. and Russell, J.K., 1994. Silica-undersaturated, zoned, alkaline intrusions within the British Columbia Cordillera: British Columbia Ministry of Energy, Mines, and Natural Resources, Geological Fieldwork 1993, Paper 1994-1, pp. 311-315.

Martins, T., Couëslan, C.G. and Böhm, C.O., 2011. The Burntwood Lake alkali-feldspar syenite revisited, west-central Manitoba (part of NTS 63N8); in Report of Activities 2011, Manitoba Innovation, Energy and Mines, Manitoba Geological Survey, 79–85.

Massey, N.W.D., MacIntyre, D.G., Desjardins, P.J. and Cooney, R.T., 2005. Digital geology map of British Columbia: whole Province; BC Ministry of Energy, Mines and Petroleum Resources, GeoFile 2005-1.

Mathews, W.H., 1989. Neogene Chilcotin basalts in south-central British Columbia: geology, ages, and geomorphic history; Canadian Journal of Earth Sciences, V. 26, 969–982.

McMillan, W.J., Thompson, J.F.H., Hart, C.J.R., and Johnston, S.T., 1995. Regional geological and tectonic setting of porphyry deposits in British Columbia and Yukon Territory, in Schroeter, T. G., ed., Porphyry Deposits of the north western Cordillera of North America: Canadian Institute of Mining, Metallurgy and Petroleum Special Volume 46, p. 40-76.

Miles, W.F., Shives, R.B.K., Carson, J., Buckle, J., Dumont, R. and Coyle, M., 2007. Airborne Gamma-Ray Spectrometric and Magnetic Surveys over the Bonaparte Lake Area (NTS 092P), South-Central British Columbia: In Geological Fieldwork 2006, British Columbia Ministry of Energy and Mines, pp. 375-376.

Panteleyev, A., 1995. Porphyry Cu-Au: Alkalic, in Selected British Columbia Mineral Deposit Profiles, Volume 1 - Metallics and Coal, Lefebure, D.V. and Ray, G.E., Editors, British Columbia Ministry of Employment and Investment, Open File 1995-20, 83-86.

Pearce, J.A., Harris, N.B.W. and Tindle, A.G., 1984. Trace element discrimination diagrams for the tectonic interpretation of granitic rocks: Journal of Petrology, V. 25, 956-983.

Plouffe, A., Bednarrski, J.M., Huscroft, C.A., Anderson, R.G. and McCuaig, S.J., 2010. Geochemistry of glacial sediments of the Bonaparte Lake map area (NTS 92P), south central British Columbia: Geological Survey of Canada, Open File 6440, CD-ROM.

Preto, V.A., 1970. BD, VB, WIN (Dansey-Rayfield River): British Columbia Department of Mines & Petroleum Resources, Geology, Exploration and Mining, 1970, pp. 218-221.

Rees, C., Gillstrom, G., Ferreira, L., Bjornson, L. and Taylor, C., 2013. Geology of the Mount Polley Intrusive Complex (Draft Version): Geoscience BC, Report 2013-21.

Schiarizza, P., Israel, S., Heffernan, S., Boulton, A., Bligh, J., Bell, K., Bayliss, S., Macauley, J., Bluemel, B., Zuber, J., Friedman, R.M., Orchard, M.J., and Poulton, T.P., 2013. Bedrock geology between Thuya and Woodjam creeks, south-central British Columbia, NTS 92P/7, 8, 9, 10, 14, 15, 16; 93A/2, 3, 6. British Columbia Ministry of Energy, Mines and Natural Gas, British Columbia Geological Survey Open File 2013-05; 4 sheets, 1:100 000 scale.

Schiarizza, P., Bell, K. and Bayliss, S., 2009. Geology of the Murphy Lake area, south-central British Columbia (93A/03); In Geological Fieldwork 2008, BC Ministry of Energy, Mines and Petroleum Resources, British Columbia Geological Survey Paper 2009-1, pp. 169-188.

Souther, J.G., 1970. Volcanism and its relationship to recent crustal movements in the Canadian Cordillera: Canadian Journal of Earth Sciences, V. 7, 553-568.

Sellmer, H.W., McKnight, B.K., Horsnail, R.F., and Allan, J.F., 1968. Dansey Rayfield River copper property. In: BC Ministry of Energy, Mines, and Petroleum Resources, Assessment report #1,723, 64.

Streckeisen, A., 1976. To each plutonic rock its proper name, Earth Science Reviews, 12: 1-33.

Sun, S.S., and McDonough, W.F., 1989. Chemical and isotopic systematics of oceanic basalts: implications for mantle composition and processes. In: Saunders, A.D., and Norry, M.J., (eds.) Magmatism in ocean basins. Geological Society of London Special Publication, 42: 313-345.

Sun, M., Armstrong, R.L., and Maxwell, R.J., 1991. Proterozoic mantle under Quesnellia: variably reset Rb-Sr mineral isochrons in ultramafic nodules carried up in Cenozoic volcanic vents in the southern Omineca Belt. Canadian Journal of Earth Sciences, 28, 1239-1253.

Sutherland Brown, A., 1958. Boss Mountain; In Annual Report of the Minister of Mines for 1957, BC Ministry of Energy, Mines and Petroleum Resources, 18–22.

Thomas, M.D. and Pilkington, M., 2008. New high resolution magnetic data: A new perspective on geology of the Bonaparte Lake map area, British Columbia. Geological Survey of Canada, Open File 5743.

Van Gosen, B.S., Gillerman, V.S., and Armbrustmacher, T.J., 2009. Thorium deposits of the United States—Energy resources for the future?: U.S. Geological Survey Circular 1336, 21 p. [http://pubs.usgs.gov/circ/1336].

Woodsworth, G.J., Anderson, R.G., and Armstrong, R.L., 1991. Plutonic Regimes, in Gabrielse, H., and Yorath, C. J., eds., Geology of the Cordilleran Orogen in Canada: Geological Survey of Canada, Geology of Canada, no.4, pp. 491-531.

Wynne, F.L., 1990. Assessment report on exploration on the Rayfield 1 and 3 claims, In: BC Ministry of Energy, Mines, and Petroleum Resources, Assessment report #19, 927, 118 p.

Southern Nicola Arc Project (SNAP): Preliminary results

Mitchell G. Mihalynuk[1, a], James M. Logan[1], Larry J. Diakow[1], Richard M. Friedman[2], and Janet Gabites[2]

[1] British Columbia Geological Survey, Ministry of Energy and Mines, Victoria, BC, V8W 9N3
[2] Pacific Centre for Isotopic and Geochemical Research, Department of Earth, Ocean and Atmospheric Sciences, University of British Columbia, Vancouver, BC, V6T 1Z4
[a] corresponding author: Mitch.Mihalynuk@gov.bc.ca

Recommended citation: Mihalynuk, M.G., Logan, J.M., Diakow, L.J., Friedman, R.M., and Gabites, J., 2014. Southern Nicola Arc Project (SNAP): Preliminary results. In: Geological Fieldwork 2013, British Columbia Ministry of Energy and Mines, British Columbia Geological Survey Paper 2014-1, pp. 29-57.

Abstract

Geological field studies in 2013 took advantage of new access and exposures from extensive clear-cut timber harvesting between Princeton and Tulameen. Revision mapping and laboratory investigation reveal new facets of the prolifically mineralized Nicola arc. ^{40}Ar/^{39}Ar cooling and U-Pb crystallization ages show that volcanism, long considered restricted to the Late Triassic, extends into the Early Jurassic. Volcanism changes near the Triassic-Jurassic boundary from feldspar-pyroxene ± olivine-phyric, to hornblende as an accessory or even principal phenocryst phase, perhaps indicating a change to more hydrated magma sources. Felsic volcanic rocks interpreted as part of the Nicola arc occur north of Princeton and near Tulameen, where a bimodal submarine succession contains previously unreported, possible exhalite horizons with copper mineralization. A northerly trending high-strain zone can be traced intermittently for ~ 20 km. It bisects the study area, with strain focused in calcareous strata. Extensive uplift and erosion of the Nicola arc, including its plutonic roots, preceded deposition of the Spences Bridge Group (middle Cretaceous). This volcanosedimentary succession, less than 500 m thick, includes ignimbrite and rhyolite flows not found elsewhere. In the early Eocene, down-to-the-west extension faulting is associated with syn-deformational silicic volcanism. One of these faults, the Boundary Fault, marks the western limit of copper-gold porphyry mineralization at both Copper Mountain and Miner Mountain. Deformation caused brecciation of the basin strata and offset alkali olivine basalt dikes interpreted as feeders to Miocene plateau lavas. Accurate reconstruction of geological events since the Late Triassic is a critical aid to finding offset portions of known porphyry deposits as well as successful exploration for undiscovered deposits.

Keywords: Geology, porphyry copper gold, volcanogenic massive sulphide, Miner Mountain, Axe, Princeton, Tulameen, Nicola Group, Spences Bridge Group, paleogeography

---

1. Introduction

The southern Nicola arc, (Quesnel terrane; Fig. 1) has been a mainstay for copper-gold production in British Columbia for 50 years. Taking advantage of new access and exposures from extensive clear-cut timber harvesting, the Southern Nicola Arc Project (SNAP) builds on pioneering studies by Preto (1979) and Monger (1989) and is designed to illuminate new opportunities in this prolific mining camp. The project focuses on areas where new information is most likely to expand the existing geological foundation and links to the most recent systematic mapping in the southernmost Nicola Group by Massey and Oliver (2010). SNAP aims to fine tune the stratigraphic, structural, and mineral deposit evolution of the Nicola arc between Princeton and Merritt (Figs. 1, 2), through 1:20 000-scale geological mapping and application of modern geochronologic and paleogeographic reconstruction methods.

Following a scoping study in 2012 (Fig. 3; Mihalynuk and Logan, 2013a, 2013b), we initiated systematic mapping in NTS 92H/9W and 10E, extending into 7W as far south as the Similkameen River (see Massey and Oliver, 2010, and Mihalynuk and Logan, 2013a for summaries of previous geologic investigations). This paper presents the preliminary stratigraphic, geochronologic and major structural elements as the first steps toward reconstructing the Late Triassic mineralizing landscape.

2. Geography and geological setting

Rocks of the southern Nicola arc are sparsely exposed on the dissected plateau between the Coast-Cascade ranges and orographic desert of the Interior Plateau (Fig. 1). Local extensive exposures are along ridges and steep valley walls. Mainly dry open pine forests, minor grasslands, and many small lakes make for ideal cattle rangeland and easy foot travel.

The southern Nicola arc and underlying basement rocks belong to the Quesnel terrane, a composite island arc that initiated at the western margin of ancestral North America in Devonian time (Monger et al., 1972; Monger, 1977; Mihalynuk et al., 1994; Ferri, 1997), on rocks at least as old as Late Silurian; (Read and Okulitch, 1977). Like modern Japan, a back-arc basin formed as Quesnel arc rifted farther from its continental margin homeland (Davis et al., 1978; Tempelman-Kluit, 1979; Ferri, 1997). As the back arc basin grew to oceanic proportions, Quesnellia became isolated enough from North America to permit the colonization of endemic organisms, the fossil remains of which are lacking in now adjacent parts of cratonic North America, but are found to the west in Stikine terrane (Ross and Ross, 1983 and 1985). Both Quesnel and Stikine terranes were repatriated with North America by Early to Middle Jurassic (Ricketts et al., 1992; Nixon et al., 1993; Mihalynuk et al., 2004;) as they buckled against the margin, capturing exotic oceanic rocks of the Cache Creek terrane between them (Monger and Ross, 1971; Mihalynuk et al.,

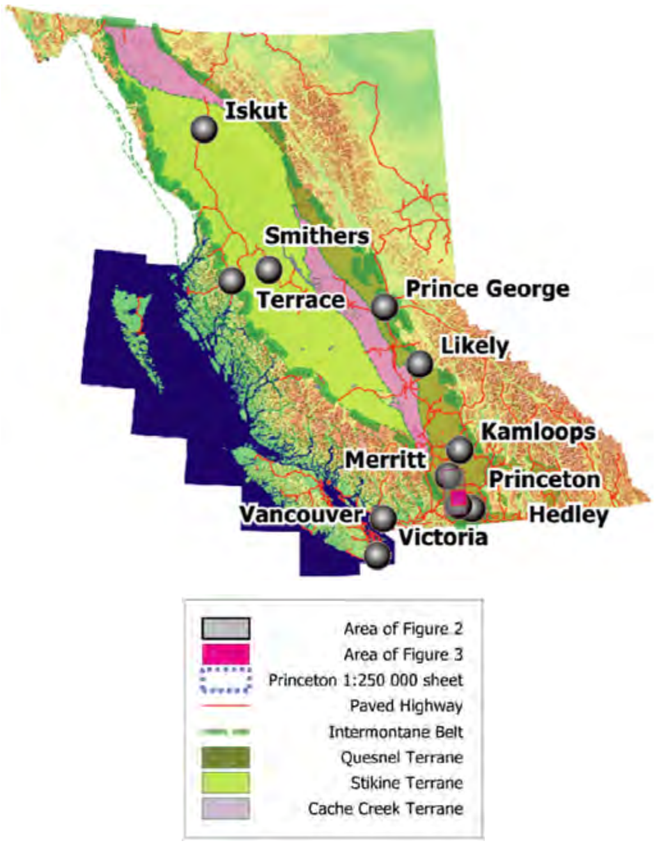

Fig. 1. Physiographic and tectonic setting of the Southern Nicola Arc Project (SNAP) study area between Princeton and Merritt.

1994). Since Middle Jurassic time, rocks of the Quesnel arc were deformed during collisions that shuffled rocks along the ancestral continental margin southward and then northward, coming to rest in the Eocene (Enkin, 2006; Sigloch and Mihalynuk, 2013).

Eocene extension in the southern Cordillera (Brown and Journeay, 1987) gave rise to the landscape from which the modern topography was inherited, with relatively minor modification by Quaternary glaciation (Tribe, 2005). Accurate reconstruction of the prolifically mineralized Late Triassic arc cannot be achieved without restoring the effects of Jurassic to Eocene (and younger?) deformation.

3. Stratigraphy

Four main volcanosedimentary assemblages, each with comagmatic intrusions, are exposed in the SNAP study area (Figs. 2, 3): the Nicola Group; the Spences Bridge Group (middle Cretaceous); the Princeton Group (Eocene); and Miocene-Pliocene plateau basalts (Monger, 1989; Preto, 1979). New geochronologic data presented herein (see below) demonstrate that parts of the Nicola Group, hitherto considered Late Triassic, extend into the Early Jurassic.

3.1. Nicola Group

The southeastern and northeastern extents of the Nicola Group in the current study area are part of the “Eastern Belt” of Preto (1979). Summarizing after Mihalynuk and Logan (2013a, 2013b): in the north, a lower succession of volcaniclastic strata derived from coarse augite porphyry breccia is overlain by coarse augite-hornblende porphyry. They are intruded by mineralized synvolcanic intrusions. All magmatic rocks show geochemical characteristics typical of arc parentage (Fig. 4, see also below). Polymictic conglomerate derived from these rocks overlies, and is intercalated with the youngest augite-hornblende-phyric volcanic rocks. In the south, at Miner Mountain, the lower coarse augite porphyry units are not well represented. Instead, tuffaceous carbonate at the lowest structural levels (found mainly in drill core), pass upward into medium- and fine-grained feldspar-and pyroxene- ± olivine-phyric flows and pyroclastic rocks, and finally into coarse hornblende-pyroxene-feldspar porphyry breccia. As in the north, thick polymictic epiclastic strata apparently cap the succession. They consist of angular pyroxene- or pyroxene-hornblende fragments in massive layers tens of metres thick. This suggests that volcanism was synchronous with sedimentation. Because clasts in the conglomerate can reach almost a metre in diameter and match those in the underlying arc, they are interpreted as arc-proximal. Mafic rocks invariably display an authigenic epidote-chlorite-actinolite ± prehnite assemblage typical of low-grade regional depth-controlled hydrothermal metamorphism in Cordilleran volcanic terranes (Cho and Liou, 1987; Mihalynuk and Ghent, 1996). However, intercalations of sedimentary strata are common, and it is likely that crosscutting intrusions maintained a geothermal gradient to generate greenschist mineral assemblages, and that distal or shallow strata of very low grade have been eroded or structurally removed.

Below we describe units of regional importance not described in (Mihalynuk and Logan, 2013a, 2013b).

3.1.1. Tabular feldspar porphyry clast-bearing heterolithic breccia

One of the most widespread units in this part of the Nicola arc consists of heterolithic breccia that contains clasts of tabular feldspar porphyry, and intercalations of lahar and tuffite derived from coeval arc strata. In the relatively well-exposed highland north of Missezula Mountain (Fig. 3), this unit is probably at least 300 m thick. Because of abrupt volcanic and sedimentary facies changes we have grouped several different lithologies into the one unit.

Outcrops weather light to dark green-grey; greenschist alteration produces fresh surfaces that are usually bright green. Coarse breccia is the most common lithology; in lesser lapilli tuff, tabular feldspar is typically the most abundant phenocryst, but either pyroxene or hornblende and pyroxene (hornblende:pyroxene about 1:1 to 5:1) is also present.

Reworked equivalents of fragmental deposits produce boulder to granule conglomerate with indistinct to well-developed bedding. Grading and dewatering structures are common. Clasts derived from outside the local volcanic environment include limestone, diorite, and hornblende-feldspar porphyry. Carbonate is a common matrix constituent. Local, decimetre-thick, discontinuous beds of poorly fossiliferous limestone suggest deposition of part of the succession in a marine environment.

3.1.2. Rusty rhyolite lapilli tuff

Pyritiferous lapilli tuff forms a kilometre-wide belt north of

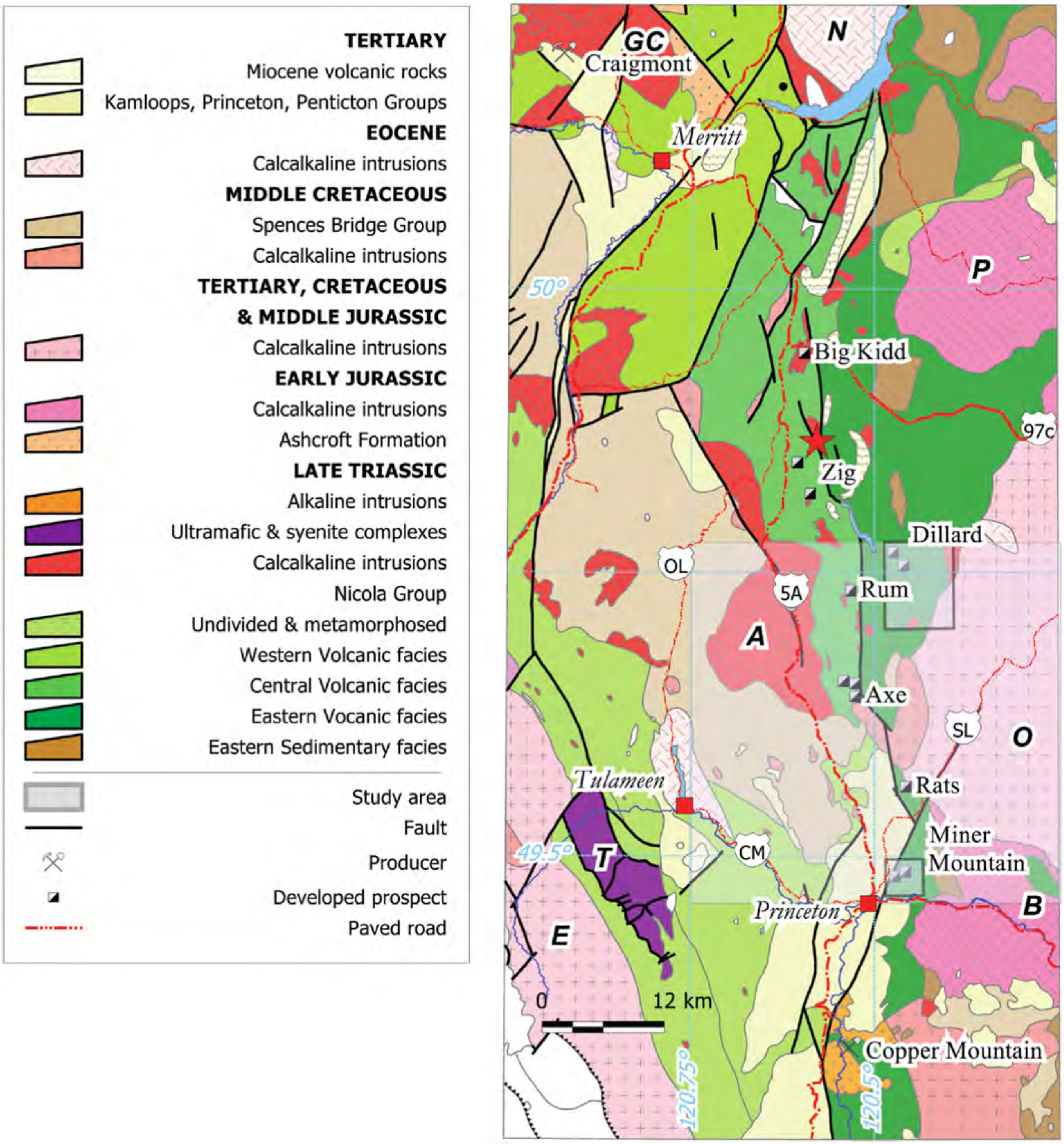

Fig. 2. Geological setting of 2013 field mapping, Southern Nicola Arc Project (SNAP), between Princeton and Merritt. Extents of Preto's Western belt (mafic submarine volcanic and sedimentary rocks), Central belt (arc axis, mafic volcanic and coeval intrusive rocks) and Eastern belt (intermediate to felsic volcanic and sedimentary rocks) are shown for reference, as adapted from Massey et al. (2005). Abbreviations denote major plutons: A = Allison Lake, B = Bromley, BI = Boulder intrusion, E = Eagle, GC = Guichon Creek, N = Nicola, O = Osprey Lake, P = Pennask, S = Summers Creek, T = Tulameen Complex. See Figure 1 for context.

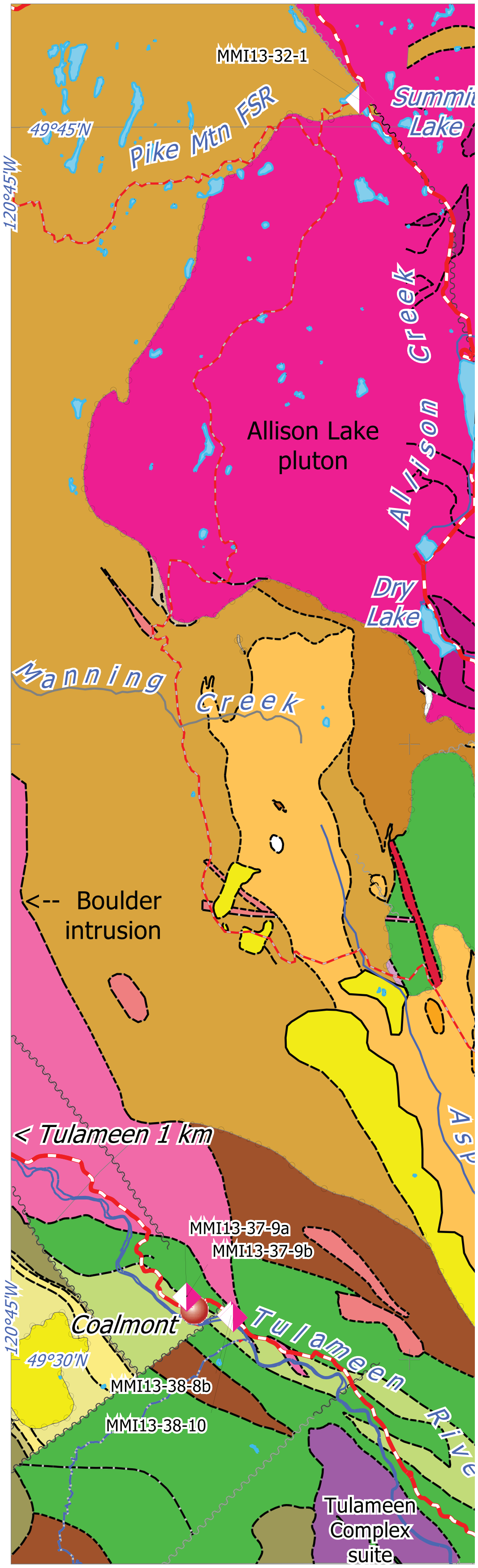

Fig. 3. Simplified geology of the Summers Creek area (NTS mapsheets 92H/9W and 10E and adjacent parts of sheets to the north and south). Compilation includes geological information from Monger (1989, regional framework), Preto (1979, mainly including areas adjacent and between Highway 5A and Summers-Rampart creeks), Massy and Oliver (2010, southwest of Tulameen River), McMechan (1983, margins of the Princeton basin), Massey (2000, Princeton basin interior), and Sego! Resources Inc. (unpublished data from within 5 kilometres of Miner Mountain). More detailed geology of the boxed areas can be found in Mihalynuk and Logan (2013a) for the southern boxed area around Miner Mountain, and Mihalynuk and Logan (2013b) for the northern boxed area around Dillard Lake and Primer prospects. See Figure 2 for context.

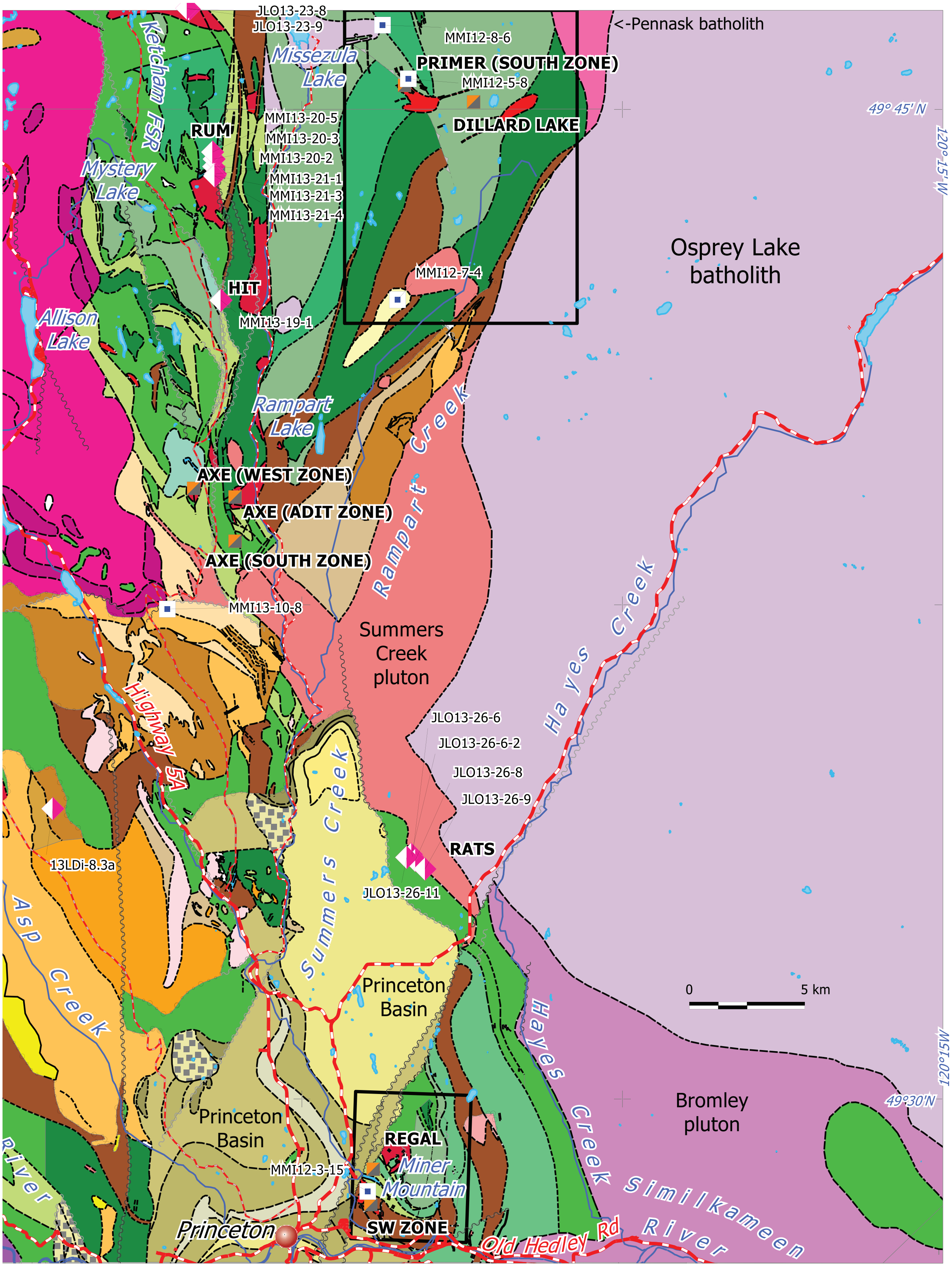
JLO13-23-8
JLO13-23-9
MMI12-8-6
<-Pennask batholith
Ketcham FSR
Missezula Lake
PRIMER (SOUTH ZONE)
MMI12-5-8
49° 45' N
DILLARD LAKE
RUM
MMI13-20-5
MMI13-20-3
MMI13-20-2
MMI13-21-1
MMI13-21-3
MMI13-21-4
Mystery Lake
120° 15' W
Osprey Lake batholith
MMI12-7-4
HIT
MMI13-19-1
Allison Lake
Rampart Lake
Rampart Creek
AXE (WEST ZONE)
AXE (ADIT ZONE)
AXE (SOUTH ZONE)
MMI13-10-8
Summers Creek pluton
Hayes Creek
Highway 5A
JLO13-26-6
JLO13-26-6-2
JLO13-26-8
JLO13-26-9
RATS
13LDi-8.3a
JLO13-26-11
Asp Creek
Summers Creek
Princeton Basin
0
5 km
120°15'W
49°30'N
Bromley pluton
Princeton Basin
REGAL
Miner Mountain
MMI12-3-15
River
Princeton
SW ZONE
Old Hedley Rd
Similkameen River

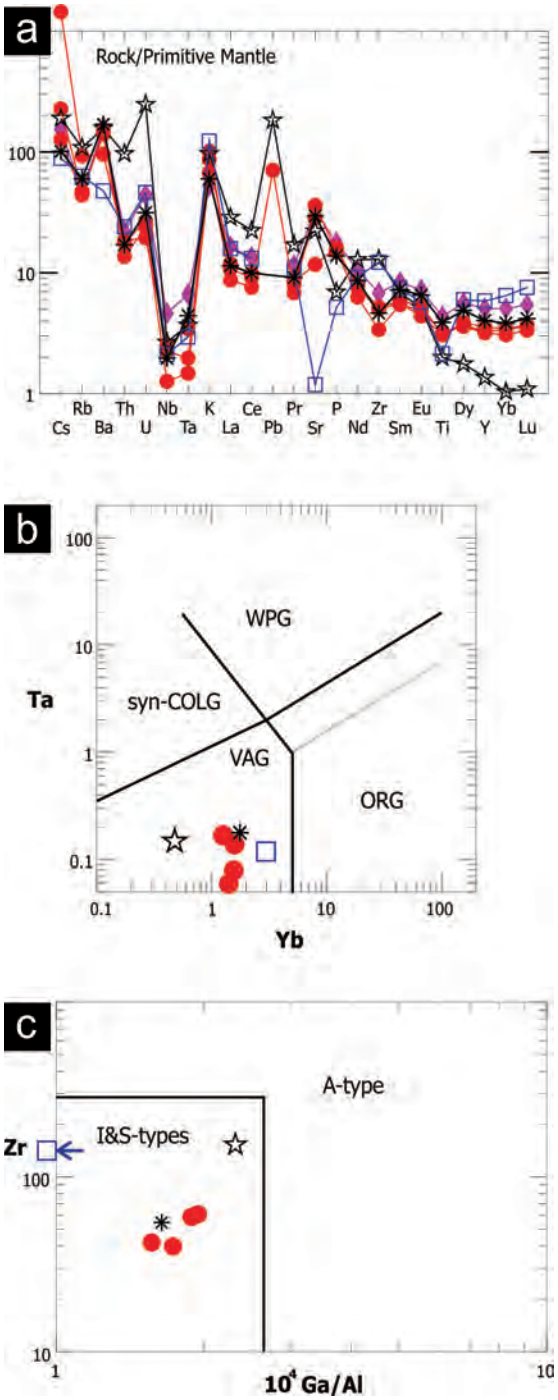

Fig. 4. Geochemical characteristics of felsic members of the Nicola arc and younger strata. **a)** Primitive mantle normalized extended trace element plot (Sun and McDonough, 1989), solid red circles are dioritic intrusions of mainly Early Jurassic age, asterisk is mineralized granodiorite at the Axe deposit, solid purple diamond is mafic volcanic breccia with diorite fragments, open blue square is the foliated Axe ignimbrite, open black star is Eocene Princeton Group rhyolite. **b)** Ta-Yb plot with fields after Pearce et al. (1984). **c)** Zr vs 10^4 Ga/Al fields discriminate anorogenic granitoids (A-type) from orogenic granitoids generated from igneous or sedimentary source rocks (I and S types) after Whalen et al. (1987).

the Axe deposit (Fig. 3), where orange and cream-weathering quartz-sericite schist contains flattened lapilli-sized white-mica-rich patches, interpreted to be collapsed pumice fragments. This lithology passes northward abruptly into weakly to unfoliated, rusty-weathering, pyritic, felsic lapilli tuff. Phenocrysts are limited to ghost feldspars (originally sanidine?), that are now altered to clay minerals. A possible equivalent is exposed south of the Axe deposit, where quartz-eye tuffs are adjacent to a several-metre-thick fossiliferous carbonate unit.

Between Princeton and Tulameen, rhyolitic (± mafic) rocks that may correlate with those near the Axe deposit, form a belt > 10 km long and < 2 km wide. East of Coalmont (Fig. 3), a belt of pyritic, sparsely quartz-phyric, white mica and clay-altered rhyolite lacks definitive extrusive textures. This unit could be a hypabyssal sill related to the Boulder intrusion, which displays border phases that are lithologically identical (see below). A similar unit, speculated to be at approximately the same stratigraphic level, outcrops farther northwest, between Coalmont and Tulameen. Where best exposed in roadcuts, it includes rhyolite blocks nearly a metre across, floating in an altered, dark grey ash matrix, that locally grades into felsic lapilli tuff. Some cherty fragments containing polycrystalline quartz grains the size of radiolaria are interpreted as biogenic. Beds of granulestone with mainly embayed quartz clasts (Fig. 5a) are in a part of the section containing finely laminated cherty layers with pyrite and chalcopyrite that are interpreted as exhalite (Fig. 5b). This succession is bimodal; basaltic pillow breccias (Fig. 5c) point to a submarine depositional setting.

Like other intrusive and volcanic samples of the Nicola Group, a sample of rhyolite (MMI12-11-15, north of the Axe deposit, Fig. 3) displays geochemical characteristics of arc parentage (Fig. 4a). It is metaluminous, with elevated Large Ion Lithophile elements (LIL) and depleted in Ta, Nb and Ti, and shows minor enrichment of Heavy Rare Earth Elements (HREE) (Mihalynuk and Logan, 2013c). Strong depletion of the relatively mobile element Sr (25 ppm), and to a lesser extent, Ba and P (333 ppm and 0.11% P_2O_5), is attributed to alteration. Typical unaltered rhyolite displays Sr that is an order of magnitude more abundant at similar Rb concentrations (40 ppm) (Halliday et al., 1991). Using trace element discrimination criteria, the rhyolite shows characteristics of arc-related (Fig. 4b) orogenic (Fig. 4c) granitoids. The rusty ignimbritic tuff is distinguished from Princeton Group rhyolites, which have strong HREE depletions.

The rusty tuff and rhyolite lapilli tuff units are significant in that they show that felsic volcanic rocks extend from the Western facies belt, where rhyolitic rocks are a hallmark, to the eastern facies belt, where they are not well known. However, attempts to extract zircons for U-Pb geochronology from the foliated "ignimbrite" that would verify correlation, have been unsuccessful.

Regardless of age, the submarine volcanic rocks are important because they represent an environment where volcanogenic massive sulphides can accumulate. Positive indicators are: quartz-sericite alteration such as displayed by foliated lapilli flattened into a strong phyllitic fabric west of the Tulameen River at Coalmont (Fig. 6c) and traces of copper mineralization east of the river (as noted above) in which felsic volcanic strata containing reworked quartz eyes (Fig. 5a) are intercalated with laminated cherty layers containing pyrite, chalcopyrite (stained

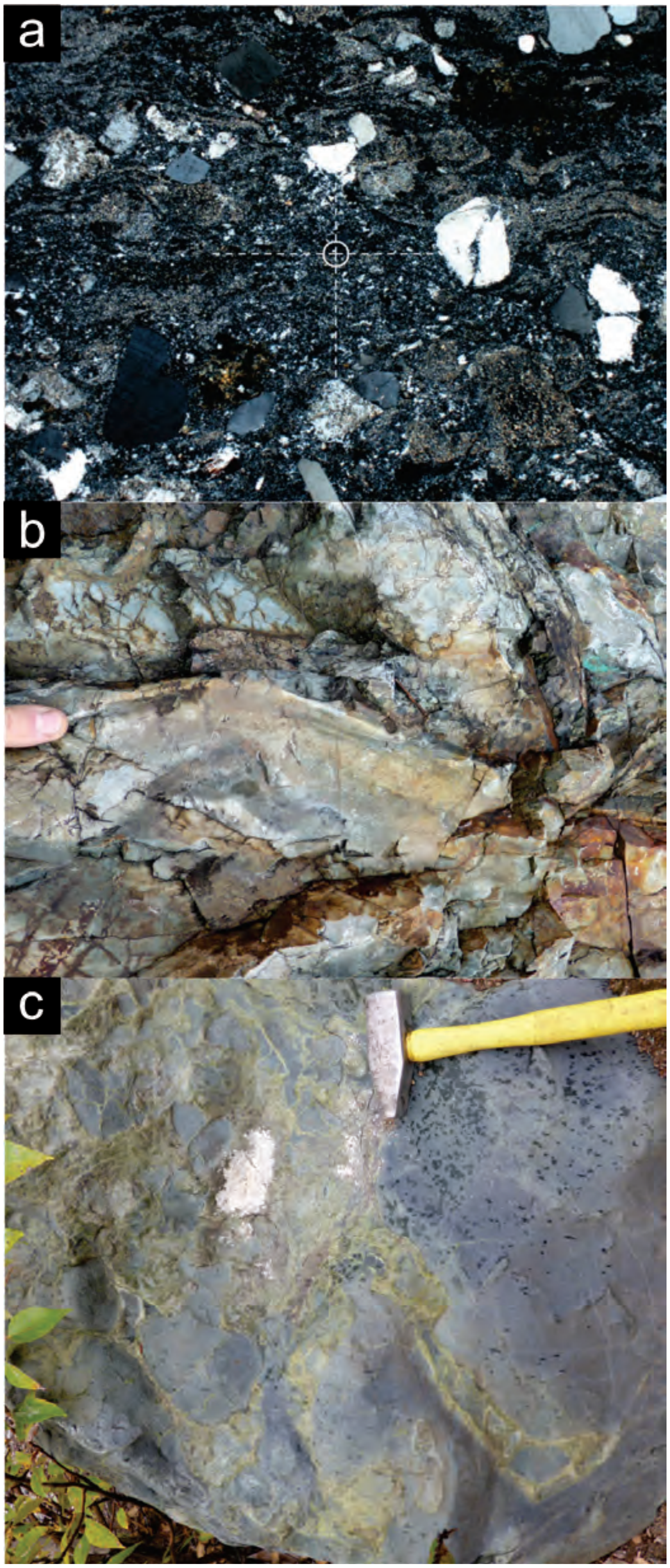

Fig. 5. Examples of Nicola Group units from a submarine bimodal succession near Coalmont. Top = epiclastic. Middle = cherty tuff. Bottom = pillows. **a)** Photomicrograph of an epiclastic layer showing rounded and embayed quartz grains (circle at cross hairs has a radius of 100 µm). **b)** Laminated light green and rust-weathering cherty tuff is mineralized with pyrite and minor chalcopyrite. **c)** Strongly epidote-altered pillow breccia.

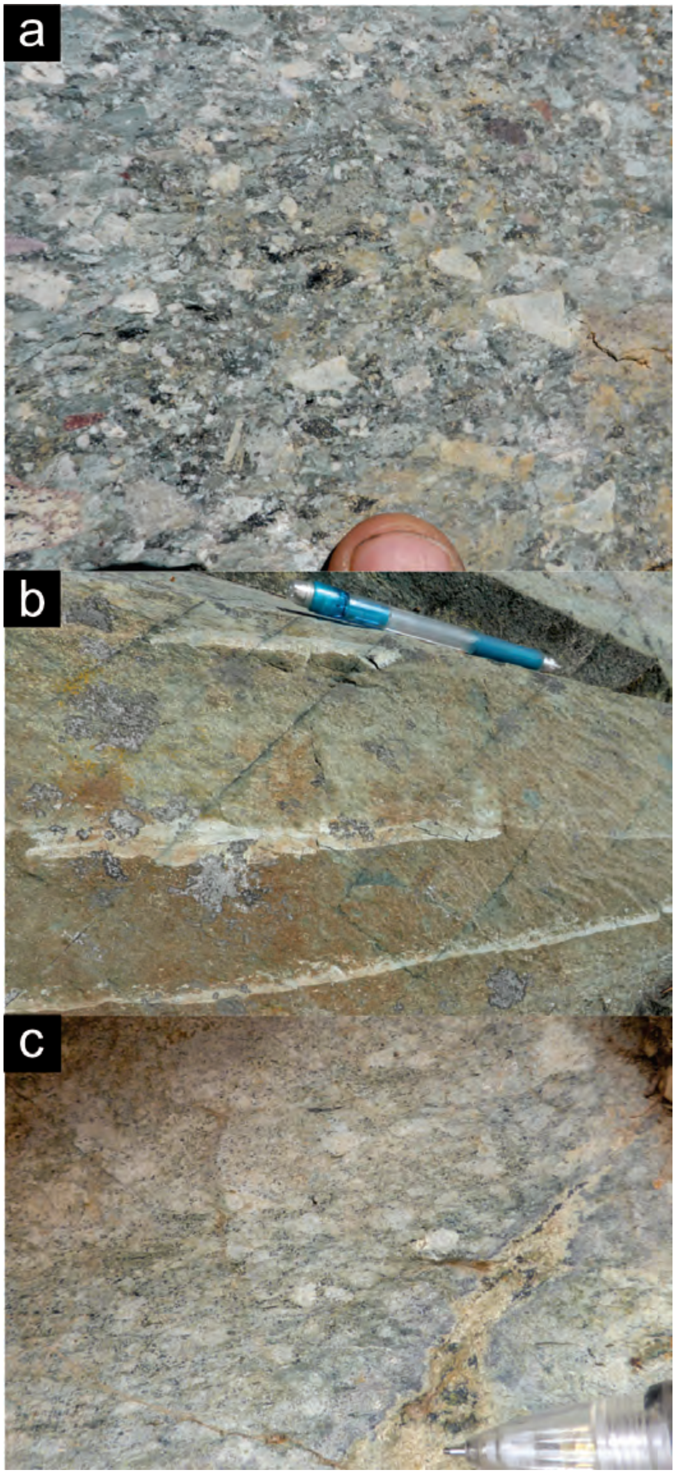

Fig. 6. Tuffite correlated with the Nicola Group. **a)** Lapilli tuff with angular sparsely quartz-phyric felsic fragments. **b)** Well-bedded and calcareous crystal ash tuffite. **c)** Felsic tuff near Coalmont is similar to a) but is altered by white mica and is foliated.

by malachite-azurite bloom in Fig. 5b) that may have formed near an exhalative vent.

3.1.3. Carbonate tectonite

Tectonized carbonate rocks outcrop in a linear belt along the western rim of the Summers Creek valley. The belt is generally less than 20 m wide, as exposed or estimated from regional dips and map patterns. In most places, limestone is well foliated and folded, but it can be massive and recrystallized, especially near the middle of the unit. South of the Axe, it crops out between volcanogenic quartz-bearing sandstone and mafic tuffaceous rocks. North of the Axe, near Mystery Lake, it is flanked to the east by a foliated limestone-boulder conglomerate with a matrix of feldspar, pyroxene, and olivine-phyric tuff. Along strike, the unit grades into well cleaved, maroon, calcaereous volcanic sandstone. The western contact of the tectonite unit is covered, but must lie within 10 m of phyllitic tuffaceous siltstone, which contains auriferous quartz veins at the Hit prospect (see below). At one locality near Mystery Lake (Fig. 3) its upper (eastern) contact is an erosional unconformity beveled beneath conglomerates containing boulders and cobbles of limestone (see below).

3.1.4. Limestone and picrite clast-bearing conglomerate

Immediately east of the Ketchan Road, near Mystery Lake, an approximately 30 m-thick conglomerate unit containing cobbles and boulders of limestone rests unconformably on the tectonized limestone unit. Cobbles and small boulders of coarse augite and augite-olivine porphyry (loosely referred to as picrite) are of secondary abundance. Some olivine-bearing clasts also contain sparse rounded pink phenocrysts < 5mm in diameter that may be altered analcime or leucite. A scattering of well-rounded cherty red tuff cobbles are notable, as they are unaffected by the foliation into which the carbonate, and to a lesser degree, the picritic clasts are flattened. Foliation is most strongly developed in the matrix, which is composed of mixtures of carbonate and picritic detritus, possibly tuff.

Overlying the basal conglomerates are very well bedded polymictic conglomerate and sandstone beds displaying water escape structures and clastic dikes. Pyroxene ± analcime-porphyritic hyaloclastite layers several metres thick point to synvolcanic deposition. Traces of copper mineralization are ubiquitous, with one sample returning 0.34% Cu, 1.7 ppm Ag and 20 ppb Pd (MMI13-17-11, Table 1).

This conglomerate unit is only locally developed, suggesting deposition on an irregular paleosurface. Across Summers Creek valley to the southeast, pyroxene and olivine-rich sandstone beds centimetres-thick occur in a conglomerate-rich sedimentary succession at least 500m thick. Coarse, magnetite-rich gabbro clasts suggest that both the deepest (gabbroic roots) and shallowest (olivine-bearing extrusive units) arc levels were exposed to erosion at this time.

3.1.5. Acicular hornblende porphyry

About 40 m of coarse trachytic hornblende porphyry lies above the conglomeratic unit, but its lower contact is covered. Hornblende comprises ~ 20% of the unit and can reach 1.5 cm long, although it is typically < 0.5 cm and aligned in a pervasively chlorite-epidote altered, green-grey matrix. Generally the hornblende phenocrysts are less altered, and are locally vitreous.

Cobbles of hornblende porphyry in an overlying conglomerate suggest that sedimentary reworking was coeval with volcanism. The conglomerate passes eastward and probably upsection, into medium-grained feldspar and pyroxene > hornblende-phyric breccia.

3.1.6. Felsic tuffite

Well-bedded and moderately to unfoliated ash and lesser lapilli tuff underlies low, glacially sculpted ridges in a clear cut between Missezula and Mystery lakes. Contact relationships with layered strata of the Nicola Group could not be established; however, the lowest level of the section is apparently a nonconformity with altered diorite. Tight, near vertical folds repeat the section, which appears to have been originally ~ 200 m thick. The most characteristic units are coarse felsic ash tuffite, and green ash and crystal tuffite. Other minor beds include polymictic conglomerate with mainly limestone pebbles in a matrix of tuffaceous wacke with conspicuous coarse quartz grains.

Massive beds of felsite tuffite consist of angular, white to dark green, coarse ash to lapilli-sized clasts (Fig. 6a) and grade into thinner beds with sand-sized grains of similar composition. Most fragments are aphanitic or very fine-grained, but some contain up to 30% feldspar, interpreted from simple twinning to be sanidine, and sparse medium-grained quartz.

Of similar thickness is an adjacent unit of green ash and crystal tuffite that is very well bedded (Fig. 6b), with beds typically centimetres to decimetres thick. Flame structures, graded bedding, scours, and soft-sediment gravity slides are common. Lithic fragment and feldspar crystal-bearing sandstone and siltstone have a calcareous cement.

Although the felsite tuffite unit is similar to the Skwel Pecken Formation (Early to Middle Jurassic) defined near Hedley (Ray and Dawson, 1994), we provisionally include it in the Nicola Group, following Preto (1979). The unit resembles distal facies of the rusty tuff and rhyolite lapilli tuff unit described above (compare Figs. 6a and b).

3.2. Spences Bridge Group

Spences Bridge Group units define a continuous, narrow belt that extends 180 kilometres northwest from Princeton (Fig. 2). During regional mapping near Princeton, Rice (1960) recognized two Lower Cretaceous volcanic sequences, the Spences Bridge Group and the overlying Kingsvale Group. The term 'Kingsvale' was later abandoned (Monger, 1989) and the Spences Bridge Group was formally divided into the Pimainus Formation and the overlying Spius Formation from detailed work near Gillis Lake south of Merritt (Thorkelson and Rouse, 1989). In 2001 and 2002, soil sampling and prospecting by Strongbow Exploration near Lytton and Merritt led to discovery of the first known epithermal vein-style mineralization in the Spences Bridge Group. Diakow and Barrios (2008, 2009) refined the geology at the type area near Gillis Lake, and expanded it to adjacent areas near notable epithermal gold occurrences.

In the study area, the Spences Bridge Group unconformably overlies the Nicola Group and related plutons adjacent to Allison Creek and Highway 5A. The unconformity, generally concealed by vegetation, is represented by a basal conglomerate containing Triassic granite clasts. We recognize three volcanic facies above the basal conglomerate, based on a near-continuous section that extends from Dry Lake, along Highway 5A, then westward onto the plateau (Fig. 3). The lowest facies consists of compositionally uniform feldspar ± pyroxene andesite

Table 1. Selected elements from the suite analyzed by Inductively Coupled Plasma – Mass Spectroscopy (ICP-MS). A complete array of elements analyzed, plus determinations by Instrumental Neutron Activation Analysis are reported in Mihalynuk et al. (2014). UTMs are Zone 10, NAD 83.

Lab No.	Station No.	UTME	UTMN	Ag ppb	As ppm	Au ppb	Cd ppm	Co ppm	Cu ppm	Fe %	Hg ppb	Mn ppm	Mo ppm	Ni ppm	Pb ppm	Pd ppb	Pt ppb	S %	Zn ppm
62353	JLO13-1-9	684666	5486546	333	10.4	4.2	0.13	19.6	128.65	5.56	2138	697	0.63	7.4	12.23	15	6	3.00	51.7
62354	JLO13-6-6	685374	5512460	6	1.5	<0.2	0.15	8.8	2.85	1.42	7	669	0.07	3.8	2.50	<10	<2	<0.02	46.4
62355	JLO13-6-10	685323	5513423	164	1.4	3.2	0.05	17.3	255.07	3.74	8	486	0.30	6.8	0.31	<10	3	0.02	45.4
62356	JLO13-6-11	685552	5513493	276	1.8	3.9	0.08	21.5	381.44	1.54	30	454	0.22	8.6	0.95	16	4	0.25	21.9
62357	JLO13-8-2	681596	5513260	45	3.4	0.9	0.33	22.5	187.51	4.26	29	1249	0.10	16.9	4.56	<10	<2	<0.02	70.5
62358	JLO13-10-7	679167	5495695	113	1.4	<0.2	0.02	16.6	61.50	3.20	<5	517	0.27	8.1	3.43	<10	2	1.20	42.7
62359	JLO13-11-10	676088	5500643	177	3.6	6.8	0.03	3.2	2.88	3.99	36	990	4.09	1.0	1.15	<10	<2	1.23	103.9
62360	JLO13-11-11	676113	5500372	77	5.0	0.7	0.04	10.8	52.24	4.08	22	141	7.57	1.9	1.75	<10	<2	2.36	16.9
62361	JLO13-12-9	675096	5506753	51	5.3	1.8	0.01	56.5	26.28	10.94	<5	2993	0.65	18.3	0.68	<10	5	4.16	138.5
62362	JLO13-12-21	674985	5502908	3540	1.0	7.1	1.61	46.0	5870.03	2.95	1017	825	1.69	31.2	1.23	<10	3	0.19	35.7
62363	JLO13-10-16-2	678534	5491973	15310	29.0	7.1	16.36	33.5	>10000.00	16.88	55	978	11.23	109.1	33.32	<10	5	0.06	2291.6
Log prospect																			
62364	JLO13-23-8	676833	5516535	19074	<0.1	975.2	1.14	27.1	>10000.00	6.61	312	1183	0.33	9.3	60.95	58	35	0.20	141.3
62365	JLO13-23-9	676763	5516564	148	5.0	59.9	0.12	16.0	2140.69	4.22	38	747	0.97	1.3	4.72	323	22	0.13	71.5
RATS prospect																			
62366	JLO13-26-6	683900	5492971	729	16.1	6.9	5.96	26.4	983.46	4.30	21	1767	1.25	64.8	19.40	<10	<2	<0.02	582.5
62367	JLO13-26-6-2	683868	5493033	17278	2.7	41.1	663.19	38.8	>10000.00	18.13	<5	1539	28.86	59.5	36.15	<10	3	0.04	>10000.0
62368	JLO13-26-8	683984	5492864	11134	6.9	6.4	1.44	44.5	7591.77	4.92	148	1798	123.21	70.7	25.81	11	<2	0.31	135.6
62369	JLO13-26-9	684266	5492632	5599	8.5	30.7	0.56	33.1	6370.60	4.82	71	1061	19.70	4.6	38.59	17	5	<0.02	274.4
62370	JLO13-26-11	683738	5492942	2244	9.4	3.0	0.58	40.3	4869.99	4.38	29	969	90.55	7.9	11.32	<10	3	0.12	79.5
62371	STD till1#1750	-	-	265	16.5	19.0	0.21	14.4	45.53	3.31	108	1183	0.70	19.7	16.50	<10	<2	<0.02	68.4
62372	13LDi-7.5	672627	5497504	24	1.3	0.3	0.08	1.5	3.39	1.21	<5	647	0.53	0.7	13.40	<10	<2	<0.02	51.1
Epithermal vein																			
62373	13LDi-8.3a	673718	5493984	122	0.2	<0.2	1.17	4.8	55.48	0.99	<5	694	3.87	31.2	24.99	<10	<2	<0.02	164.2
62374	13LDi-8.3b	673718	5493984	170	0.7	<0.2	1.19	5.3	151.18	0.91	<5	585	10.30	37.1	19.57	<10	<2	<0.02	126.8
62375	13LDi-8.3c	673718	5493984	205	0.2	<0.2	0.99	1.8	55.94	0.37	<5	384	1.78	5.7	61.00	<10	<2	<0.02	69.6
62376	MHE13-18-6	677040	5511769	179	0.8	2.0	0.02	7.0	137.86	2.09	<5	276	0.39	10.5	3.15	<10	<2	0.10	17.3
62377	MHE13-19-10	679209	5507702	79	4.6	1.5	0.05	33.4	101.77	4.76	12	747	0.97	12.6	1.23	<10	7	0.61	40.3
62378	MHE13-24-2	669125	5488241	54	0.7	0.3	0.03	30.0	105.86	4.29	<5	804	0.41	7.0	0.31	<10	<2	0.11	56.6
62379	MHE13-6-2	685516	5567552	62	4.7	<0.2	0.11	5.2	2.24	2.34	7	679	0.17	2.3	4.43	<10	<2	<0.02	59.0
62380	MMI13-2-1	686381	5492520	189	2.0	4.7	0.20	8.2	57.81	2.39	<5	369	0.90	4.7	9.12	<10	<2	0.92	28.5

Table 1. Cont'd.

Lab No.	Station No.	UTME	UTMN	**Ag** ppb	**As** ppm	**Au** ppb	**Cd** ppm	**Co** ppm	**Cu** ppm	**Fe** %	**Hg** ppb	**Mn** ppm	**Mo** ppm	**Ni** ppm	**Pb** ppm	**Pd** ppb	**Pt** ppb	**S** %	**Zn** ppm
62381	MMI13-2-2a	686465	5492864	291	<0.1	5.2	0.03	1.0	13.80	0.61	10	12	19.49	1.6	22.47	<10	<2	0.36	4.4
62382	MMI13-2-2b	686465	5492864	238	1.3	21.6	0.18	1.6	30.59	0.91	7	278	8.25	2.0	8.71	<10	<2	0.18	34.7
62383	MMI13-2-3	685875	5491013	189	0.3	2.5	0.09	27.1	263.92	4.33	<5	796	0.38	16.6	1.76	<10	5	0.11	55.0
62384	MMI13-2-6	685726	5490996	1801	5.1	257.0	0.47	21.8	5074.04	2.81	9	940	26.52	7.0	5.35	<10	<2	2.17	112.4
62385	MMI13-2-7	685562	5490715	1001	1.8	83.3	0.22	17.4	3287.11	2.98	18	538	4.50	10.0	3.83	<10	5	2.56	47.8
62386	MMI13-2-12	686042	5491343	458	6.3	58.2	0.03	3.8	126.68	3.78	96	494	7.00	5.7	3.44	13	4	0.62	42.8
62387	MMI13-4-5	683564	5505376	229	1.8	10.6	0.12	5.0	209.96	2.09	<5	505	6.03	2.1	9.92	<10	2	0.20	48.6
62388	MMI13-4-7	683659	5505377	92	0.4	3.4	0.01	1.1	6.83	0.95	9	8	7.54	1.1	3.52	<10	<2	0.41	2.0
62389	MMI13-7-6b	686742	5511482	6	2.0	<0.2	0.10	2.7	2.10	1.80	<5	1413	4.16	2.5	1.29	<10	<2	<0.02	17.9
62390	MMI13-8-4	678061	5498946	35	32.5	0.5	0.08	5.5	4.81	2.56	25	477	1.41	1.3	8.33	<10	<2	<0.02	76.0
62391	MMI13-9-11	677006	5498406	40	3.0	0.3	0.08	16.6	32.76	4.37	31	1244	0.26	10.4	5.16	<10	<2	1.25	77.2
62392	MMI13-9-12	676945	5498377	59	8.1	1.1	0.10	15.5	30.27	4.72	44	1082	1.33	7.6	5.34	<10	<2	3.27	91.2
62393	MMI13-9-13	676755	5498740	122	5.4	1.1	0.17	21.6	73.26	5.51	40	1216	0.94	9.9	6.67	<10	<2	2.62	92.8
62394	STD till1#1657	-	-	246	15.8	21.6	0.24	12.7	45.94	2.98	89	1097	0.61	16.5	13.96	<10	<2	<0.02	60.5
62395	MMI13-12-2	677618	5500676	52	4.3	5.2	0.04	10.7	53.69	2.18	6	375	0.11	17.9	1.94	<10	<2	<0.02	30.1
62396	MMI13-12-4	677434	5501164	62	3.0	1.2	0.04	32.9	104.93	6.34	<5	711	0.14	32.8	0.48	19	5	<0.02	76.2
62397	MMI13-17-2	671970	5512050	3	1.0	1.9	3.28	27.1	1.82	3.96	11	1454	0.36	44.2	21.54	<10	9	<0.02	203.8
62398	MMI13-17-11	676559	5510905	1718	2.2	5.7	0.53	20.6	3413.78	4.23	67	1221	0.04	5.9	3.05	20	4	0.04	122.4
Hit prospect																			
62399	MMI13-19-1	677986	5508413	21659	<0.1	1790.2	144.28	0.8	4.24	0.67	2023	209	4.05	3.4	5176.07	<10	<2	0.62	2848.1
62400	MMI13-19-10	677274	5512008	307	13.8	3.1	0.84	11.7	86.71	3.49	363	419	0.36	5.9	37.34	<10	9	1.15	187.2
Rum prospect																			
62401	MMI13-19-11	677360	5511985	175	5.2	3.3	0.06	29.0	553.84	6.06	27	318	2.78	16.6	2.66	<10	6	0.74	30.7
62402	MMI13-19-12	677456	5511961	45	47.8	7.0	0.08	32.3	199.80	5.42	39	326	1.33	10.8	2.95	<10	7	2.07	13.9
62403	MMI13-20-1	677641	5512150	66	28.5	4.2	0.07	10.7	8.38	3.14	38	86	1.69	4.7	9.61	<10	3	0.79	27.0
62404	MMI13-20-2	677660	5512154	403	3.4	21.0	0.07	19.1	2681.02	1.76	25	300	3.77	5.8	1.24	<10	6	0.87	15.1
62405	MMI13-20-3	677664	5512364	95	1.7	9.7	0.35	6.5	572.59	4.74	11	867	3.64	6.0	1.96	<10	<2	0.06	23.5
62406	MMI13-20-5	677616	5512559	1150	11.3	2.1	0.22	26.2	132.78	4.11	53	433	0.66	11.3	24.96	<10	4	3.15	31.8
62407	MMI13-21-1	677718	5511951	12580	<0.1	83.8	0.20	7.7	8574.74	4.34	120	835	28.63	5.5	6.60	<10	<2	0.04	149.7
62408	MMI13-21-3	677705	5511898	340	5.9	52.4	0.52	23.3	1096.58	3.81	15	966	0.75	52.2	4.47	<10	4	0.50	108.9
62409	MMI13-21-4	677693	5511894	792	1.4	388.9	0.15	17.8	1674.74	3.31	17	750	0.81	6.7	2.58	<10	<2	0.14	94.8
62410	MMI13-21-7	678003	5511483	572	19.9	8.3	0.35	109.6	266.93	10.79	12	1531	0.48	106.6	5.98	<10	<2	5.23	77.8

Table 1. Cont'd.

Lab No.	Station No.	UTME	UTMN	Ag ppb	As ppm	Au ppb	Cd ppm	Co ppm	Cu ppm	Fe %	Hg ppb	Mn ppm	Mo ppm	Ni ppm	Pb ppm	Pd ppb	Pt ppb	S %	Zn ppm
62411	MMI13-25-4	686620	5488916	603	0.8	7.5	0.09	32.3	872.69	4.85	6	1326	0.13	5.9	2.14	13	3	<0.02	104.4
62412	MMI13-25-6	687116	5489375	202	2.6	2.4	0.09	17.4	343.93	3.65	14	1189	0.64	13.1	2.37	39	4	0.04	70.1
62413	MMI13-25-7	687045	5488938	2266	<0.1	2.0	0.26	25.0	8441.80	6.02	<5	1150	0.35	7.6	1.72	<10	<2	0.19	95.7
62414	MMI13-26-8	670147	5488585	95	4.3	1.7	0.03	18.3	81.65	4.91	<5	632	0.25	6.8	1.79	<10	4	<0.02	54.8
62415	STD till1#1657	-	-	211	16.0	5.7	0.22	12.0	45.46	3.03	69	1079	0.59	15.7	14.75	<10	<2	0.02	55.7
62416	MMI13-27-6	669169	5487812	78	1.3	<0.2	0.02	5.9	48.07	2.88	<5	1070	0.13	3.8	1.67	<10	3	0.41	56.7
62417	MMI13-27-7	669298	5487861	99	2.0	1.0	0.04	19.7	42.29	3.14	<5	306	0.83	49.5	0.58	<10	4	<0.02	32.7
62418	MMI13-27-7b	669298	5487861	264	26.9	0.8	0.71	16.9	31.82	3.67	22	964	1.56	6.0	4.92	<10	<2	0.41	118.3
62419	MMI13-27-8	668787	5485336	111	8.4	<0.2	0.10	22.7	193.54	4.38	6	801	0.46	18.1	3.49	17	3	0.65	36.0
62420	MMI13-27-10	669339	5485477	32	2.4	0.5	0.04	5.9	7.13	2.49	11	450	0.69	3.4	2.92	<10	<2	0.09	20.9
62421	MMI13-27-11	669795	5483651	32	5.0	<0.2	0.02	26.4	59.34	3.30	18	686	0.27	16.9	0.75	<10	3	0.16	39.0
62422	MMI13-28-2	683667	5488693	413	1.5	<0.2	0.24	22.2	432.50	2.15	8	952	0.14	13.4	2.29	17	5	0.02	81.7
62423	MMI13-29-4	672572	5483280	146	2.3	<0.2	0.30	0.9	24.55	2.39	73	264	1.22	1.2	10.75	<10	<2	0.29	96.1
62424	MMI13-31-5	669264	5503003	116	1.4	14.6	0.08	6.9	54.84	3.18	9	140	1.65	2.6	1.63	<10	<2	1.06	23.4
Epithermal vein																			
62425	MMI13-32-1	669943	5514124	6309	246.4	116.6	0.06	24.3	52.72	5.20	80	4368	3.14	47.9	12.51	<10	<2	3.02	30.8
62426	MMI13-37-8	666620	5487206	893	0.5	8.2	0.09	11.0	6636.65	1.06	75	71	5.90	5.8	0.70	<10	<2	0.29	5.1
Possible exhalative mineralization																			
62427	MMI13-37-9a	666872	5487010	564	0.3	4.0	0.27	10.7	2932.69	1.31	<5	382	3.82	58.7	0.16	13	<2	0.04	23.9
62428	MMI13-37-9b	666872	5487010	124	0.6	6.4	0.02	49.3	81.42	5.39	12	362	2.37	106.5	0.81	<10	7	2.51	38.6
62429	MMI13-38-8b	667894	5486628	871	<0.1	4.3	0.07	5.3	3376.03	0.82	39	49	5.37	5.6	0.50	<10	<2	0.16	5.8
62430	MMI13-38-10	667945	5486574	100	0.5	1.8	0.07	59.0	362.35	14.52	<5	876	20.38	120.4	0.20	<10	2	0.62	39.0
62431	MMI13-39-4	669304	5485670	42	<0.1	1.5	<0.01	4.1	55.70	3.05	<5	137	3.96	5.4	1.03	<10	<2	0.48	11.7
62432	MMI13-39-11	670701	5485123	4949	<0.1	34.1	0.42	22.5	>10000.00	8.87	77	1421	5.88	36.3	7.20	<10	<2	1.50	38.1
62433	MMI13-40-9	675337	5481491	70	1.3	0.2	0.16	15.9	38.68	4.08	24	996	3.46	3.8	4.90	<10	<2	0.67	70.9

porphyry. It is overlain by a felsic succession consisting of tuffs that are conformably overlain by rhyolite flows. Locally, the andesite unit pinches out and the felsic succession rests directly on basal conglomerate. East of Allison Creek the same general stratigraphy is recognized, however, the Spences Bridge Group rocks are locally strongly chlorite-epidote altered and can be difficult to distinguish from feldspar-phyric parts of the Nicola Group.

3.2.1. Conglomerate

Locally, the conglomerate consists of rounded granitic clasts, suggesting derivation mainly from the nearby Allison pluton. About 6 km west of Dry Lake, sparse granitic pebbles float in a grus-like matrix consisting of disaggregated crystals resembling those in the subjacent intrusion (Fig. 7a). Elsewhere, more diverse clast suites are exposed. For example, along the Allison Lake pluton margin southwest of Dry Lake on Highway 5A (Preto, 1979), and in the headwaters of Manning Creek, where conglomerate beds contain mainly volcanic and sedimentary clasts, with a large proportion derived from nearby Nicola Group (Fig. 7b). Intraformational conglomerate beds higher in the Spences Bridge Group section contain clasts from nearby Cretaceous and underlying Triassic strata and are indistinguishable from polymictic conglomerate beds at the base of the unit. Locally, well-bedded sandstone and siltstone interbeds form intervals up to a few metres thick. Rare exposures display cross stratification (Fig. 7c) and water escape structures. Tuff layers are common, with some composed exclusively of flattened dark green, chloritized pumice lapilli and coarse ash. A coarse sandstone to granulestone layer containing a few percent chloritized pumice lapilli was sampled for geochronological determination (sample MMI13-10-8, see Geochronology results, below). Near this locality, tongues of breccia along a rhyolite flow margin extend into conglomerate, demonstrating that felsic volcanism was coeval with coarse siliciclastic sedimentation.

3.2.2. Feldspar ± pyroxene andesite porphyry

Dark grey, feldspar-pyroxene-phyric andesites, interlayered with rhyolite breccia, occupy the lowest stratigraphic level east of Highway 5A. The andesite consists of fine to medium-grained plagioclase porphyry, with or without sparse pyroxene phenocrysts, in a dark green groundmass. It is mainly breccia, but also occurs as sparsely amygdaloidal flows. Epiclastic beds include several thin intervals of sandstone and intraformational volcanic conglomerate containing rounded clasts of fine-plagiophyric andesite, some as large as 40 cm in diameter.

The andesite porphyry unit generally lacks significant secondary alteration; this relatively fresh appearance distinguishes it from similar units in the Nicola Group in which epidote-chlorite-calcite extensively replaces groundmass and phenocrysts, and coats fractures.

3.2.3. Felsic tuff

The felsic tuff unit interfingers with, and ultimately overlies, the andesite unit. It contains a variety of light green and cream-colored, subangular and angular lithic pyroclasts typically smaller than a few centimetres diameter, but rarely attaining block size (Fig. 8a). In order of abundance, clasts include aphanitic and laminated rhyolite, fine-grained porphyritic andesite, dark green chlorite-altered ash, and rare holocrystalline granitic lapilli. Plagioclase comprises up to 30 % of the matrix together with scattered quartz eyes. In several areas, fiamme define eutaxitic texture caused by welding (Fig. 8b), suggesting

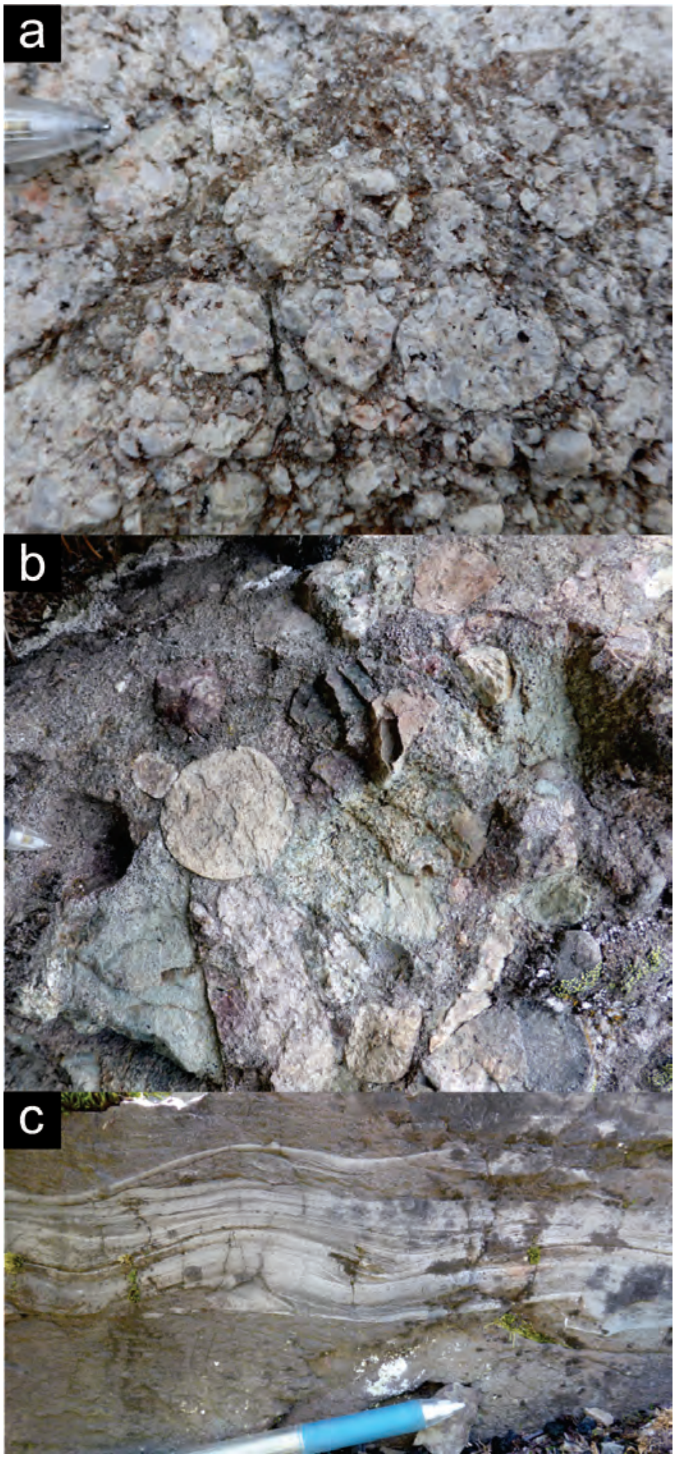

Fig. 7. Variation in Spences Bridge Group basal conglomerate ~6 km west of Dry Lake from **a)** gruss-like granulestone with granitic fragments to **b)** polymictic containing clasts representing most units in the Nicola arc: augite porphyry (foliated and non-foliated), limestone, feldspar porphyry, Allison Lake granitoids, and diorite. **c)** Cross stratification in sandstone.

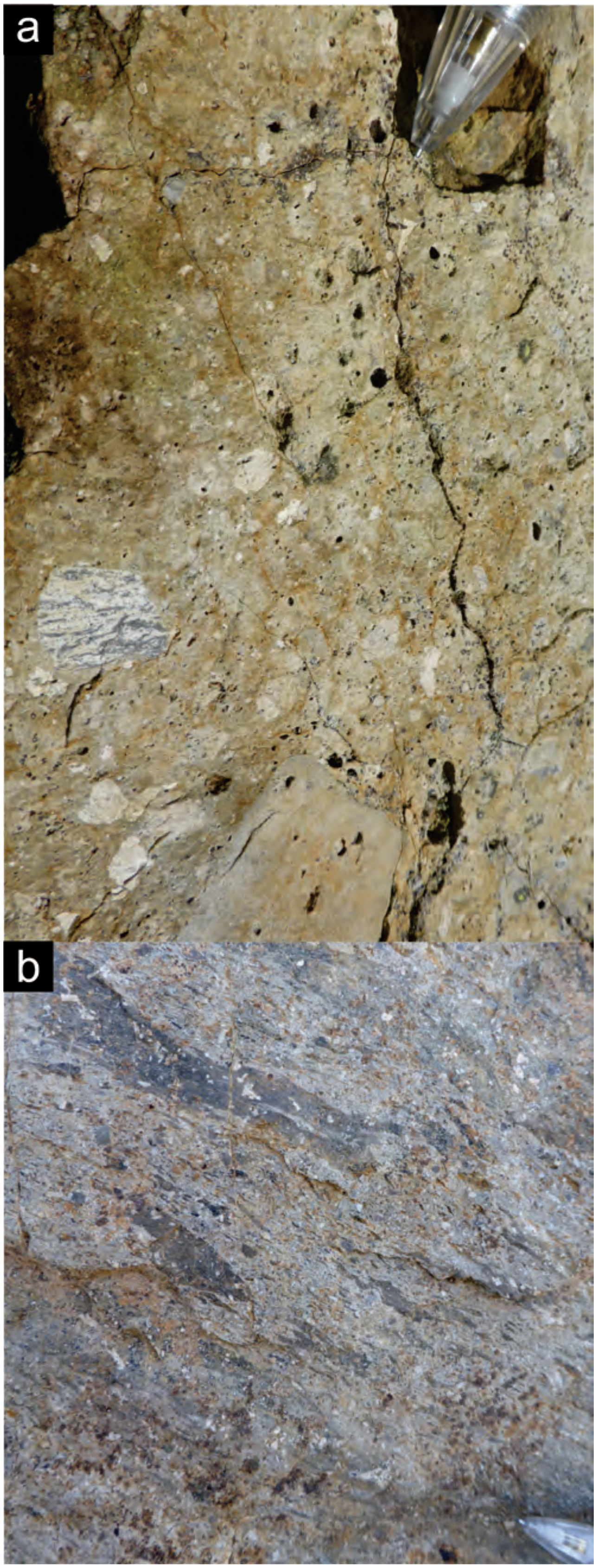

Fig. 8. Spences Bridge Group, Pimainus Formation. **a)** Felsic tuff showing characteristic aphanitic and flow-laminated rhyolitic fragments. **b)** Welded ignimbrite texture is locally developed.

that parts are ash-flow tuff deposits.

3.2.4. Rhyolite flows

More than ~ 150 m of rhyolitic lava flows sharply overly the felsic tuff unit. West of Highway 5A (Allison Creek), they form resistant hummocks across an area greater than 13 km^2. The flows appear homogeneous, showing only faint internal flow laminations. On fresh surfaces, they contain 15 to 20 percent medium-grained feldspar phenocrysts in a grey-green aphanitic groundmass. These formerly glassy rocks have devitrified to spherulites, and less commonly, small lithophysae, and alter to a chalky white, fine-grained assemblage composed mainly of clay minerals and quartz with hematite staining.

East of Highway 5A, rhyolite flows have a similar character but are more intimately interdigitated with other rock types, especially feldspar ± pyroxene porphyritic breccias and flows. In addition, the thickest, most massive rhyolite flows are cream to rusty white (like west of Allison Creek), but varicoloured, grey with white and pink flow-banded units are more numerous. Well-developed flow banding is characteristic, in addition to coarse flow breccia. Some individual flows are over 10 m thick.

The rhyolite deposits are probably flow domes and collapsed domes. However, coherent flows have been traced at least 500 m.

3.2.5. Correlation

The provisional tripartite volcanic subdivision of the Spences Bridge Group in the study area broadly resembles the stratigraphy of the Pimainus Formation in the Shovelnose Mountain area, about 30 kilometres to the northwest as described by Diakow and Barrios (2009). Although lithofacies are similar at the Shovelnose section (> 2 km thick), they are thicker and recur at multiple levels. U-Pb zircon ages from samples taken near the base and the top of the Shovelnose Mountain constrain subaerial eruptions of the entire section to ~ 104 Ma (Thorkelson and Rouse, 1989; Diakow and Barrios, 2009). A U-Pb age determination from a rhyolite in the study area is pending; however, detrital zircons from a coarse sandstone immediately adjacent to flow-banded rhyolite, yielded a cluster of ages around 103 Ma, suggesting derivation from the rhyolite and coeval tuff (see Geochronology below).

3.3. Princeton Group

Eocene rocks of the Princeton Group have long been a target for coal exploration, hence Princeton Basin has been relatively well mapped (see synthesis by McMechan, 1983). We mapped a ~ 3 km^2 area of Princeton Group along the eastern margin of Princeton Basin, near the Boundary fault north of Miner Mountain, and a ~ 1 km^2 area near Rampart Lake (Fig. 3).

3.3.1. Rhyolite breccia

Mauve to tan, flow-banded rhyolite breccia discontinuously in a clearcut ~ 4 km north-northeast of Rampart Lake (Mihalynuk and Logan, 2013b). Athough the basal contact is not exposed, we infer that the breccia was deposited unconformably above Late Triassic Nicola Group augite porphyry volcanic rocks and an outlier of the Summers Creek pluton.

Mihalynuk and Logan (2013b) included these rocks with the Spences Bridge Group (Early Cretaceous), the closest previously mapped felsic volcanic rocks (Monger, 1989).

However, the rocks are similar to volcanic units in the Princeton Group as described by (Church, 1973). To resolve this ambiguity we collected a sample for geochronological study. Based on lithology and an ^{40}Ar/^{39}Ar plateau age of 50.2 ± 0.6 Ma (see Geochronology below), we now correlate the breccia with volcanic rocks of the Princeton Group described by McMechan (1983).

3.3.2. Rhyolite ash tuffite and arkose

Recessive weathering, white arkosic wacke to granulestone (Fig. 9a) contain coal partings and uniform ash layers up to several centimetres thick. Ash layers are distinguished by their low density and black vitric shards that stand out in sharp contrast to the white, clay-rich matrix. Cuspate margins on the shards (Fig. 9b) distinguish them from coal fragments. The partings and fragments of coal in the sandstones and granulestones suggest sedimentation in a fluvial setting that was intermittently blanketed by pyroclastic material.

This unit correlates with Allenby Formation unit 7e of McMechan (1983). The Allenby Formation was assigned a middle Eocene age based on fossil teeth from *Trogosus*, a bear-like rodent (Russell, 1935). However, a U-Pb age of 52.08 ± 0.12 Ma (Mortensen and Archibald, in Moss et al., 2005) from tuff layers at an Allenby fossil flora site indicate that part of the unit is no younger than early Eocene. Ickert et al. (2009) collated available isotopic ages to show that Princeton Group magmatism lasted from 53 to 47 Ma (early part of Eocene, Cohen et al., 2013 timescale).

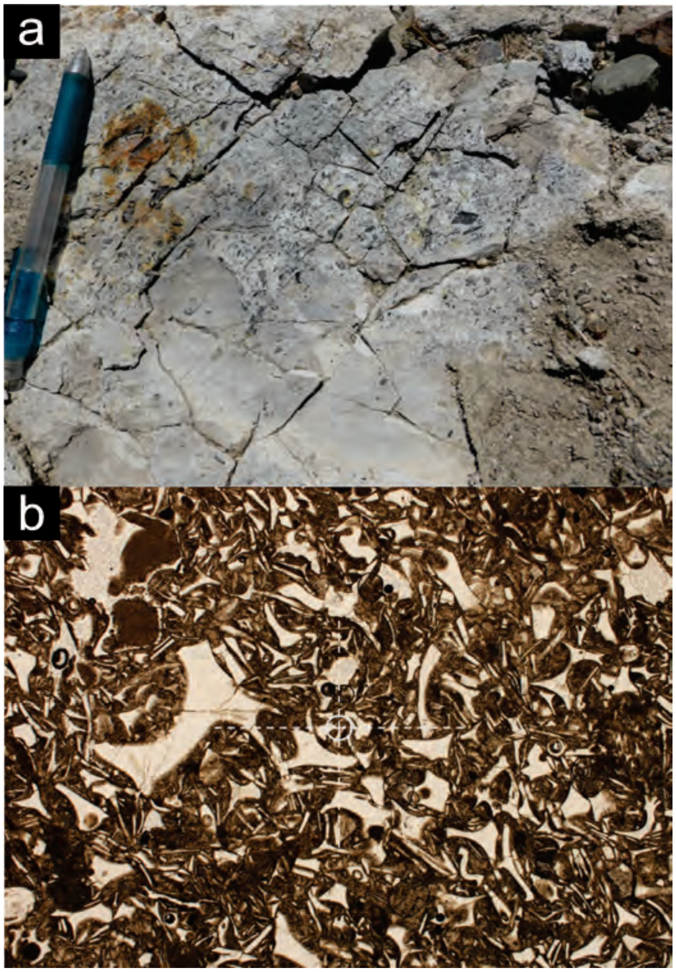

Fig. 9. Princeton Group rhyolite ash tuffite and arkose unit. **a)** Tuffaceous sandstone and granulestone with some layers containing abundant black coaly material. **b)** Photomicrograph of tuff layer with angular, concavo-convex shards (plane polarized light, field of view is ~ 4 mm).

3.3.3. Osprey pebble-bearing conglomerate

Exposures of Princeton Group strata north of Miner Mountain are predominantly granule to cobble conglomerate and immature sandstone. Most conglomerate beds contain mainly K-feldspar crystal and granite clasts (Fig. 10a) almost certainly derived from the Osprey batholith, 7 km to the northeast (McMechan, 1983; Hills, 1965), consistent with southwest paleocurrents (McMechan, 1983).

A curious feature of the Osprey pebble conglomerate near Miner Mountain is that many clasts are broken, as seen upon microscopic examination (Fig. 10b). Clast fragments have been

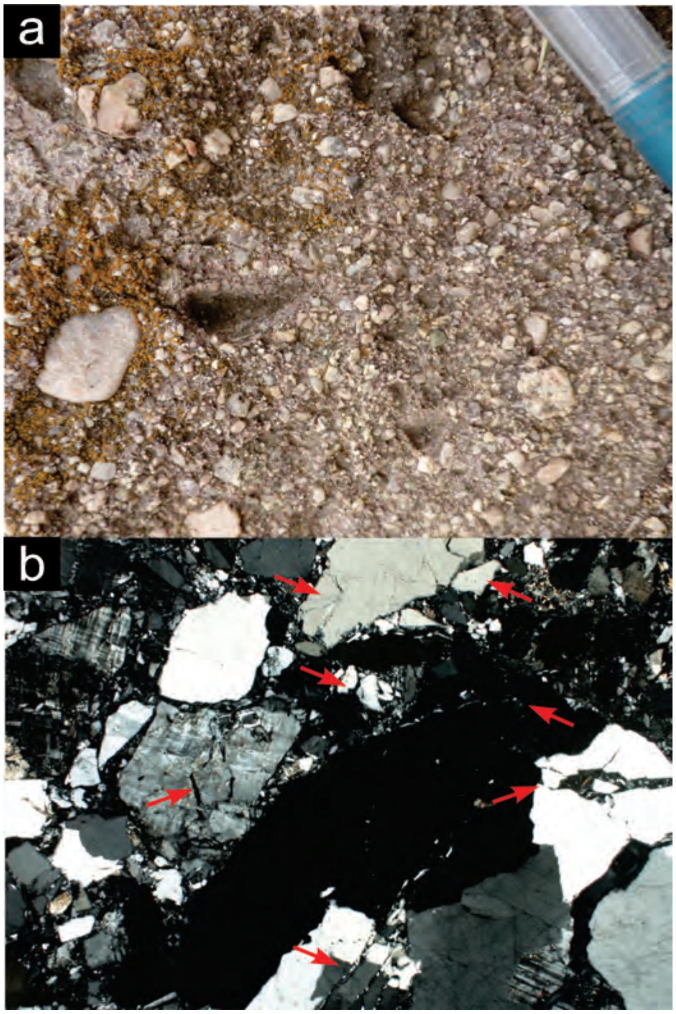

Fig. 10. Princeton Group, Osprey pebble-bearing conglomerate unit. **a)** Pebble and granule conglomerate derived primarily from the Osprey Lake batholith. **b)** Photomicrograph of conglomerate shows quartz and feldspar grains have been broken (arrows), fragments translated and rotated, and fractures infilled with matrix material (crossed polarized light, field of view is ~ 4 mm).

variably rotated and the spaces between infilled with matrix material. The process responsible for grain fragmentation is speculative, but it may be related to extensional faulting. If so, it is of importance to ongoing porphyry copper exploration at Miner Mountain.

3.4. Chilcotin Group

Outliers of Cenozoic olivine basalt of the Chilcotin Group (Mathews, 1989), crop out sporadically at elevations between 1240 and 1620 asl. The basalts unconformably overlie the Spences Bridge rhyolite flow unit. Dry exposures are dun to orange weathering with darker brown spots identifying small, less than 2 millimetre diameter, olivine grains. Fresh surfaces are jet-black and shimmer in sunlight due to the fresh, fine-crystalline aggregate of plagioclase microlites and 15 to 20 percent yellowish olivine grains (Fig. 11). Deeply-weathered exposures display bulbous, onion skin exfoliation concentrated along fractures, and dark green-grey or brown fresh surfaces. Brownish soil results from weathering of the basalt and is a telltale indicator where it is concealed by thin overburden. Massive, locally columnar jointed flows can form uninterrupted cliff faces more than 8 m high. At one locality, olivine basalt sharply overlies oxidized deep red to purple scoria and amygdaloidal basalt, with the amygdales infilled by oxidized, chalky zeolite (?) and white chalcedony. A suite of weathered dikes exposed along the Tulameen River are interpreted as correlative. They are cut and offset by shallowly dipping faults.

Fig. 11. Contrasting dun-weathering and jet black fresh surfaces of Miocene Chilcotin Group plateau basalt.

Flows overlying the Eocene coal measures near Coalmont have K-Ar ages of 9 and 9.2 ±1.8Ma (Mathews, 1989; Breitsprecher and Mortensen, 2004; Late Miocene, Cohen et al., 2013 timescale).

4. Intrusive units

Plutonic rocks in the study area range from Late Triassic to Eocene (Fig. 3) and dikes are as young as those interpreted to feed the Chilcotin Group. The eastern parts of the study area are underlain by the southern limits of the Pennask batholith (194 ±1 Ma; Early Jurassic) and western parts of the Bromley pluton (193 Ma), both of which are cut by the Osprey Lake K-feldspar megacrystic granite batholith (166 ±1 Ma; U-Pb zircon, Parrish and Monger, 1992). In the central belt, as defined by Preto (1979), Late Triassic intrusions mark the axis of the Nicola arc and include the Allison Pluton (204 ±10 to 207 ±10 Ma, K-Ar hornblende and muscovite cooling ages in Preto, 1979; recalculated by Breitsprecher and Mortensen, 2004) and numerous undated dioritic bodies interpreted as part of the ~ 205 Ma Copper Mountain suite. Also along the arc axis is the Summers Creek stock (middle Cretaceous, 99.1 ± 1 to 101 ± 5.2 Ma, K-Ar biotite, Preto, 1979; recalculated by Breitsprecher and Mortensen, 2004), which may be comagmatic with the Spences Bridge Group. Along the western margin of the study area is the Boulder intrusion. Although undated, it is presumed to be Jurassic because it intrudes Nicola Group, and is in turn cut by the Otter Lake stock (Cretaceous; Massey and Oliver, 2010). Outcrops of the Pennask batholith were not encountered in the map area. For descriptions of the Osprey and Copper Mountain intrusions see Mihalynuk and Logan (2013a, b). Probable Copper Mountain suite equivalents are described in Mineralization section below. Possible hypabyssal equivalents to the Summers Creek pluton are the Mine dikes (also known as Candy Stripe dikes), are also described in Mihalynuk and Logan (2013a). Similar north-trending dikes are common in the study area.

4.1. Allison Lake pluton

The Allison Lake pluton underlies an area of ~ 160 km^2 in the northern part of the study area. It cuts Late Triassic Nicola Group in the east, and is nonconformably overlain by basal strata of the Spences Bridge Group. The Allison fault has an inferred sinistral offset within the pluton; it continues outside, trending farther northwest where the fault juxtaposes an elongate plutonic body against Cretaceous and Eocene strata (Monger, 1989; note that a colouring error on this map shows Nicola Group breccia east of Allison Lake, where it is meant to show pluton).

Preto (1979) subdivided the pluton into main granite to monzonite phases and subordinate granodiorite to gabbro phases. Outcrops at valley level, southwest of Dry Lake along Highway 5A, expose reddish, medium-grained, equigranular granite or quartz monzonite containing 25 percent (combined) hornblende and biotite. The pluton contains irregular sheared, rusty aphanitic mafic volcanic xenoliths, similar to rocks considered to be Nicola Group bordering the pluton. Rocks in the contact zone are locally malachite stained. Farther west on the plateau, variegated tonalitic and granodioritic phases occur near the margin of the pluton. At two localities along the margin, the intrusion consists of > 2 m wide zones of frothy quartz and matted tourmaline in veinlets.

4.2. Bromley pluton

Bromley pluton is a typical white to pink-weathering granodiorite. In the study area, its contact follows Hayes Creek where it has intruded and thermally metamorphosed the Nicola Group, upgrading adjacent rocks to biotite grade within about 500 metres of the contact, and biotite-garnet within a few tens of metres of the contact. The pluton contains conspicuous books of euhedral biotite 0.5 cm across and 1 cm thick that comprise ~ 5% of the rock. Hornblende comprises ~ 10%, and together with biotite, is variably chloritized.

Subparallel with the contact is an extensive set of dikes, typically containing phenocrysts of K-feldspar, plagioclase, quartz, and chloritized hornblende in varying combinations. Some dikes attain widths of 10 m or more. They are interpreted to be co-genetic with the Bromley pluton; however, a preliminary U-Pb zircon determination suggests that one of the widest dikes is middle Cretaceous, correlative with the "Mine dikes" and Spences Bridge Group.

4.3. Boulder intrusion

The Boulder intrusion is compositionally variable, with major phases of quartz diorite to granodiorite. Outcrops are invariably cut by parallel sets of epidote-chlorite ±pyrite-quartz-calcite veinlets (Fig. 12). Many of these veinlets have a white or pinkish halo interpreted as secondary alkali feldspar that extends a centimetre or more from the vein wall. Some intrusive phases display conspicuous miarolitic cavities up to 0.5 cm across; these phases tend to be more quartz-rich.

Near its western contact, a strongly cataclastic fabric is locally developed. Near its southern termination, it is very pyritic with overlying metres-thick gossanous zones of Fe-oxide/hydroxide-cemented colluvium.

4.4. Summers Creek pluton

Many outcrops of the Summers Creek pluton are granodioritic and display characteristic crowded medium- to coarse-grained, blocky plagioclase crystals and prismatic hornblende. Interstices between large grains are filled by late K-feldspar-quartz, fine-grained biotite-hornblende and ~ 1% magnetite. Mafic xenoliths are common (~ 0.5%) and only partly digested, suggesting high-level stoping. A sample was collected for U-Pb age determination to confirm three middle Cretaceous K-Ar age determinations (Preto, 1979); results are pending.

5. Structure

Folding and faulting have both played a role in the distribution and orientation of rock packages across the study area, but the contribution of each throughout time is difficult to assess, especially in the central and eastern belts. Part of the difficulty arises from the superposition of different faulting events. In general, earliest syndepositional basin-forming faults have been overprinted by strike-slip faults, and further modified during episodes of late extensional faulting. Extensive dissection of folds by later faulting obscures the original cause of bedding orientation changes. Folds that are most susceptible to such overprinting are intermediate in scale: regional fold patterns will persist despite local faults, and outcrop-scale folds will persist between fault strands, but folds with wavelengths of hundreds of metres are most likely to lose coherence through fault dissection. Thus, we recognize a gentle regional synform east of northern Summers Creek (Mihalynuk and Logan, 2013b), and can point to outcrop-scale folds (Fig. 13a) with half wavelengths of up to ~ 100 m, but well-documented intermediate-scale folds are lacking. Existence of such folds and repetition by thrust faults can be verified in areas with excellent exposure and easily traced marker units, such as at Hedley to the immediate east (Ray and Dawson, 1994) and along the Coquihalla Highway to the northwest (Diakow and Barrios, 2008).

Fig. 12. Boulder intrusion displays intergrown fresh grey plagioclase that becomes turbid and weathers white to pink- where altered along epidote-lined fractures. An incipient fracture is located at the 0.5mm pencil tip and an epidote-lined fracture is along the left side of the photo.

Systematic changes in bedding-phyllitic cleavage relationships in western Nicola Group sedimentary rocks document intermediate-scale folding. Intensity of folding increases westward into the Eagle Metamorphic complex (Massey and Oliver, 2010), which was deformed in the Late Jurassic and Middle Cretaceous (Greig et al., 1992).

6. Faults

Regional, possibly long-lived, steep faults were recognized by Preto (1979) and Monger (1989) along Summers and Allison creeks, the Tulameen River west of Coalmont, and bounding the Princeton Basin.

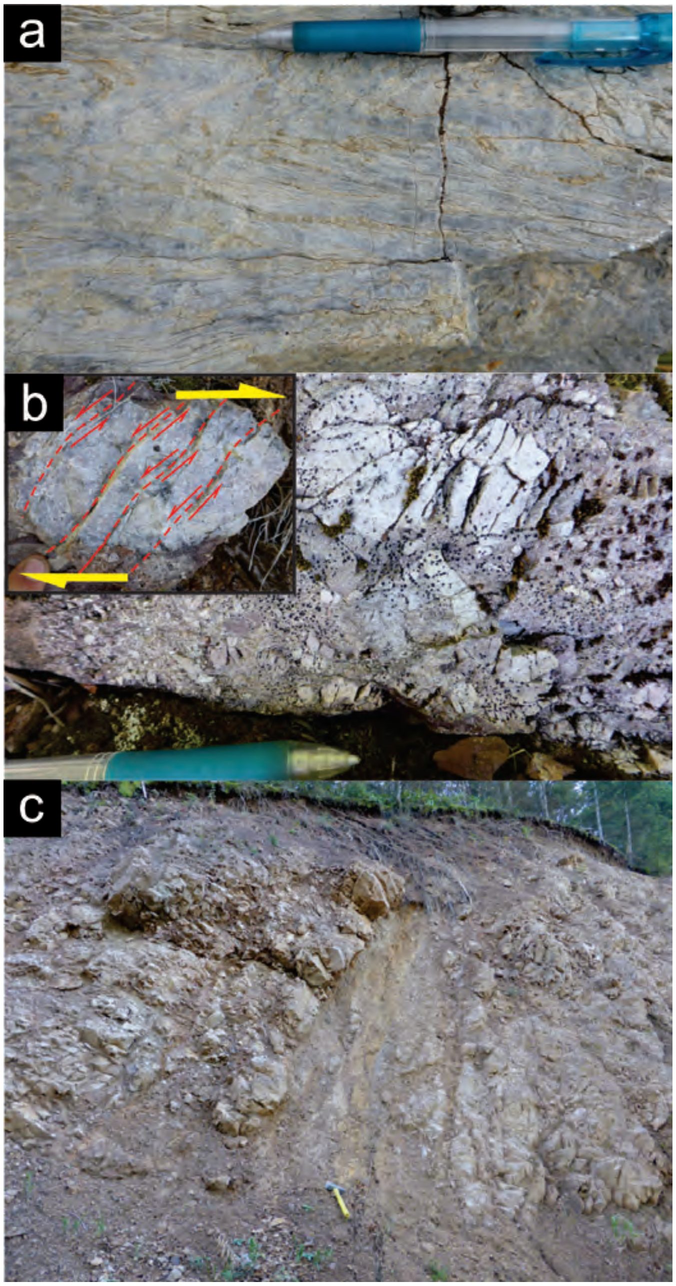

Fig. 13. a) Carbonate tectonite displays intrafolial isoclines. **b)** Calcareous volcanic sandstone deforms in a ductile fashion around brittle blocks with antithetic sinistral faults, consistent with an overall dextral sense of shear. **c)** One of a set of brittle fault gouge zones parallel to the main trace of the Allison Creek fault in the upper Allison Creek valley; here the faults cut volcanic rocks interpreted as Spences Bridge Group.

6.1. Summers Creek and Allison Creek faults

Summers Creek and Allison Creek faults are part of a north-northwest-trending system that extends for at least 160 km and is suspected to have focused emplacement of mineralized Late Triassic plutons (Preto, 1979). On its western boundary, the Summers Creek fault system passes into a zone of ductile strain. Cored drill intercepts of this zone at the Axe deposit reveal carbonate clasts with elongation ratios between 10 to 20 (extend beyond core diameter). North of the Axe, the zone is at least 300m wide and involves quartz-sericite-altered felsic tuff and carbonate. Foliation developed in the carbonate is locally strongly folded; axial surfaces dip from steeply southeast to nearly horizontal (Fig. 13 a) and hinges plunge 35-45° northeast. Late stages of motion generated voids along minor fabric-parallel faults and perpendicular carbonate-filled extensional veins. A dextral sense of shear is indicated by semi-rigid blocks that are cut by antithetic brittle faults in a more ductile, finer-grained, carbonate-rich matrix (Fig. 13b). A sample of rhyolite from the strain zone was collected to establish the maximum age of deformation.

Near Summit Lake, the Allison Creek fault appears to have juxtaposed Spences Bridge Group against the Allison pluton. Within ~ 0.5 km west of Allison Creek, numerous discrete faults that cut the adjacent Spences Bridge Group mainly dip moderately to steeply east (Fig. 13c).

6.2. Extensional faults

Down-to-the-west extensional faults (as indicated by fault corrugations, steps, and slickensides) are well exposed along the Old Hedley Road where they offset a pegmatitic sill (Fig. 14a) cutting Nicola Group volcano-sedimentary strata that are thermally metamorphosed to biotite grade. In most places the faults clearly cut the pegmatitic sill, but at one locality the sill is cut by, and then cross-cuts a shallow fault plate (Fig. 14b). We interpret this as evidence of syn-extensional intrusion. A sample of the pegmatite was collected to establish the age of deformation.

Low-angle faults also offset dikes along the Coalmont Road between Coalmont and Princeton. Based on the rotation of hangingwall and footwall fabrics, the apparent sense of offset is top-to-the west, but the fault zone is shattered and the dikes are friable (Fig. 14c), so a reliable fault lineation could not be evaluated. Nevertheless, the offset dikes are interpreted as feeders to overlying Chilcotin plateau basalt. If correct, extensional deformation may range to at least as young as Miocene.

7. Geochronology

Geochronological results for all but one of the 16 samples collected in 2013 are pending. Presented here are completed analyses from samples collected during 2012 fieldwork, which focused on areas around the Miner Mountain deposit and the Primer South prospect.

7.1. Methods

7.1.1. Hornblende and biotite $^{40}Ar/^{39}Ar$: Laser step heating

Samples were crushed in a ring mill, washed in distilled water and ethanol, and sieved when dry to - 40 + 60 mesh. Biotite or hornblende were then picked out of the bulk fraction, wrapped in aluminum foil and stacked in an irradiation capsule into which samples of similar ages and neutron flux monitors (Fish Canyon Tuff sanidine (FCs), 28.201 ± 0.046 Ma, Kuiper et al., 2008) were added. Sample irradiation at the McMaster Nuclear Reactor in Hamilton, Ontario, occured for 180 MWH in the medium flux site 8E. Analyses (n=65) of 17 neutron flux monitor positions produced errors of < 0.5% in the J value.

Sample analyses were conducted at the Noble Gas Laboratory, Pacific Centre for Isotopic and Geochemical Research (PCGIR), University of British Columbia, Vancouver, BC, Canada. The

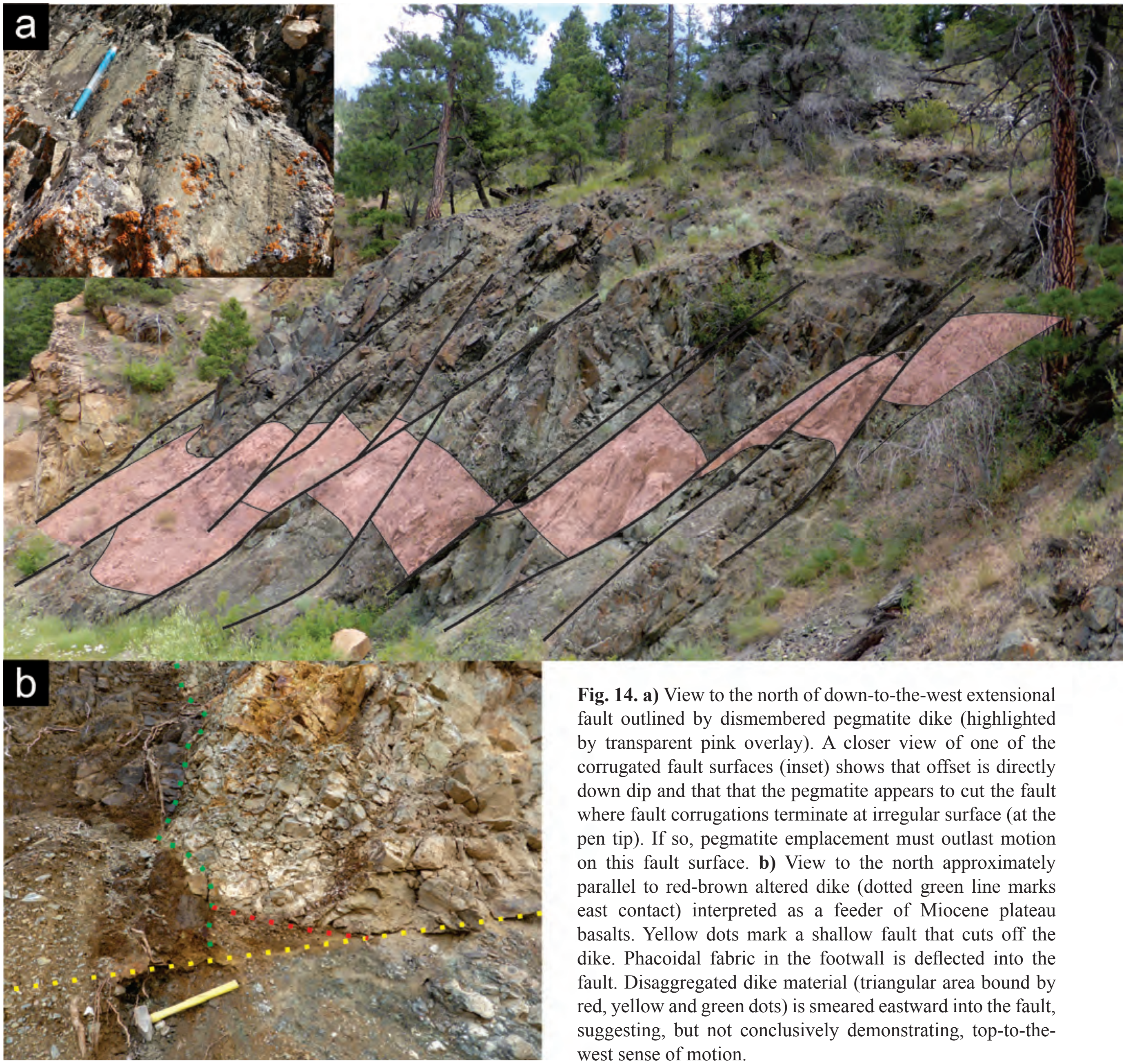

Fig. 14. a) View to the north of down-to-the-west extensional fault outlined by dismembered pegmatite dike (highlighted by transparent pink overlay). A closer view of one of the corrugated fault surfaces (inset) shows that offset is directly down dip and that that the pegmatite appears to cut the fault where fault corrugations terminate at irregular surface (at the pen tip). If so, pegmatite emplacement must outlast motion on this fault surface. **b)** View to the north approximately parallel to red-brown altered dike (dotted green line marks east contact) interpreted as a feeder of Miocene plateau basalts. Yellow dots mark a shallow fault that cuts off the dike. Phacoidal fabric in the footwall is deflected into the fault. Disaggregated dike material (triangular area bound by red, yellow and green dots) is smeared eastward into the fault, suggesting, but not conclusively demonstrating, top-to-the-west sense of motion.

mineral separates were step-heated at incrementally higher powers in the defocused beam of a 10W CO_2 laser (New Wave Research MIR10) until fused. Gas evolved from each step were analyzed by a VG5400 mass spectrometer equipped with an ion-counting electron multiplier. All measurements were corrected for total system blank, mass spectrometer sensitivity, mass discrimination, and radioactive decay during and subsequent to irradiation, and interfering Ar from atmospheric contamination and the irradiation of Ca, Cl, and K using isotope production ratios of: $(^{40}Ar/^{39}Ar)K = 0.0302 \pm 0.00006$, $(^{37}Ar/^{39}Ar)Ca = 1416.4 \pm 0.5$, $(^{36}Ar/^{39}Ar)Ca = 0.3952 \pm 0.0004$, $Ca/K = 1.83 \pm 0.01(^{37}ArCa/^{39}ArK)$.

Initial data entry and calculations were performed using ArArCalc algorithms (Koppers, 2002). Plateau and correlation ages were calculated using Isoplot ver.3.09 (Ludwig, 2003). Errors were propagated from all sources except mass spectrometer sensitivity and age of the flux monitor at the 2σ (95% confidence) level. A plateau age was calculated from the statistical best fit where: 1) more than 60% of the ^{39}Ar comprised three or more contiguous steps; 2) the probability of fit of the weighted mean age was greater than 5%; 3) the slope of the error-weighted line through the plateau ages equaled zero at 5% confidence; 4) the ages of the two outermost steps on a plateau were not significantly different from the weighted-mean plateau age (at 1.8σ, six or more steps only); the outermost two steps on either side of a plateau did not have nonzero slopes with the same sign (at 1.8σ, nine or more steps only).

7.1.2. Zircon: Chemical Abrasion - Thermal Ionization Mass Spectroscopy (CA–TIMS)

CA-TIMS procedures described here are modified from Mundil et al. (2004), Mattinson, (2005) and Scoates and Friedman (2008). Rock samples underwent standard mineral separation procedures; zircons separates were handpicked in alcohol. The clearest, crack- and inclusion-free grains were selected, photographed and then annealed at 900˚C for 60 hours. Annealed grains were chemically abraded and then spiked with a $^{233-23}$5U-^{205}Pb tracer solution (EARTHTIME ET535), and then dissolved. Resulting solutions were dried and loaded onto Re filaments (Gerstenberger and Haase, 1997).

Isotopic ratios were measured by a modified single collector VG-54R or 354S thermal ionization mass spectrometer equipped with analogue Daly photomultipliers. Analytical blanks are 0.2 pg for U and 1.0 pg for Pb. U fractionation was determined directly on individual runs using the ET535 mixed $^{233-235}$U-^{205}Pb isotopic tracer. Pb isotopic ratios were corrected for fractionation of 0.23%/amu, based on replicate analyses of NBS-982 reference material and the values recommended by Thirlwall (2000). Data reduction employed the Excel™-based program of Schmitz and Schoene (2007). Standard concordia diagrams were constructed and regression intercepts, weighted averages calculated with Isoplot (Ludwig, 2003). All errors are quoted at the 2σ or 95% level of confidence, unless otherwise noted. Isotopic dates are calculated with the decay constants λ^{238}=1.55125E-10 and λ^{235}=9.8485E-10 (Jaffe et al, 1971). EARTHTIME U-Pb synthetic solutions were analysed on an on-going basis to monitor the accuracy of results.

7.1.3. Zircon: Laser Ablation (LA) ICP-MS

Zircons analyzed using laser ablation (LA) ICP-MS employ techniques as described by Tafti et al. (2009). Instrumentation at the PCIGR comprises a New Wave UP-213 laser ablation system and a ThermoFinnigan Element2 single collector, double-focusing, magnetic sector ICP-MS. All zircons greater than about 50 microns in diameter were picked from the mineral separates and mounted in an epoxy puck along with several grains of the Plešovice (337.13 ± 0.13 Ma, Sláma et al., 2007), and Temora2 (416.78 ± 0.33 Ma) zircon standards and brought to a very high polish. Prior to analysis, the surface of the mount was washed for 10 minutes with dilute nitric acid and rinsed in ultraclean water. The highest quality portions of each grain selected for analysis were free of alteration, inclusions, or possible inherited cores. Line scans rather than spot analyses were employed to minimize elemental fractionation during the analyses. A laser power level of 40% and a 25 μm spot size were used. Backgrounds were measured with the laser shutter closed for ten seconds, followed by data collection with the laser firing for approximately 35 seconds. The time-integrated signals were analysed using Iolite software (Patton et al., 2011), which automatically subtracted background measurements, propagated all analytical errors, and calculated isotopic ratios and ages. Corrections for mass and elemental fractionation were made by bracketing analyses of unknown grains with replicate analyses of the Plešovice zircon standard. A typical analytical session at the PCIGR consists of four analyses of the Plešovice standard zircon, followed by two analyses of the Temora2 zircon standard five analyses of unknown zircons, two standard analyses, five unknown analyses, etc., and finally twoTemora2 zircon standards and four Plešovice standard analyses. The Temora2 zircon standard was analysed as an unknown to monitor the reproducibility of the age determinations on a run-to-run basis. Final interpretation and plotting of the analytical results employed the ISOPLOT software of Ludwig (2003).

7.2. Geochronology results

Complete raw data tables, cathode luminescence imagery of zircons analyzed, and ancillary plots such as inverse ^{40}Ar/^{39}Ar isochrons and Ca/K can be found in Mihalynuk et al. (2014b).

7.2.1. Hornblende and biotite ^{40}Ar/^{39}Ar

Release spectra and interpreted ages for three samples are presented in Figure 15 (a, b, c) and the data are presented in Table 2.

Sample MMI12-5-8 (Fig. 15a) was collected from a mineralized hornblende diorite at the Primer South prospect (see Mihalynuk and Logan 2013b, c for description and major and minor element geochemistry). A good plateau, formed by six steps, includes 98.7% of the ^{39}Ar released. There is no obvious sign of thermal disturbance and the sample analyzed is relatively fresh and unlikely to have been completely reset. Thus, the plateau age, 188.2 ± 2.5 Ma is interpreted as recording the post eruptive crystallization age.

Mihalynuk and Logan (2013b) and previous workers assumed that the intrusion was part of the Copper Mountain suite (~ 205-200 Ma, Late Triassic). However, the new age, if interpreted correctly, requires emplacement in the Early Jurassic. Intrusions of this age are known elsewhere in the Nicola arc. For example, to the north, young, mainly mafic phases of the Takomkane batholith have ages of 187.7 ±1.1 Ma (^{40}Ar/^{39}Ar hornblende (Schiarizza et al., 2009), and in southern BC, the Bromley batholith has a K/Ar hornblende cooling age of 186 ± 3 Ma (Hunt and Roddick, 1988), and the Skwel Peken Formation age is ~ 187 ± 9 Ma based on 3 discordant zircon fractions (Ray and Dawson, 1994).

Sample MMI12-8-6 (Fig. 15b) was collected from a hornblende-pyroxene porphyritic volcanic breccia that interrupts a thick epiclastic succession (Mihalynuk and Logan, 2013b) upsection from augite porphyry breccias and flows that are the defining rock types of the Nicola arc. Fresh euhedral hornblende from this unit yields a stable plateau with 94.3% of ^{39}Ar released in 9 of 11 steps from which an age of 182.1 ± 2.3Ma is calculated (first and last steps omitted from age calculation).

The hornblende lacks a fabric and is unaltered (see Fig. 6 of Mihalynuk and Logan, 2013b) suggesting that the sample has not been completely reset. Therefore, we interpret that the age records crystallization at the time of eruption. In addition, intercalation of this unit with epiclastic strata, which contain clasts lithologically identical to dated pluton sample MMI12-5-8, is consistent with an age younger than ~ 188 Ma. Early Jurassic magmatic ages such as these are important in southern Quesnellia as they show that Nicola arc volcanism extended into the Early Jurassic, and is not limited to the Late Triassic as has been widely assumed.

Sample MMI12-7-4 (Fig. 15c) was collected near the northern boundary of the 2013 study area, from an oxyhornblende-phyric rhyolite breccia (see section 3.3.1 above) interpreted as part of a series of coalescing flow domes (Mihalynuk and

Logan, 2013b). A release spectrum with a strong plateau comprising 78.6% of the ^{39}Ar yields a calculated age of 50.2 ± 0.6 Ma. Previously considered part of the Spences Bridge Group (Mihalynuk and Logan, 2013b), this new age indicates that it is part of the Princeton Group. The Early Eocene, 50 Ma age is typical of the late stage of Eocene magmatism that swept across southern British Columbia (Bordet et al., 2013).

7.2.2. U-Pb CA-TIMS and LA-ICPMS

Concordia plots for two samples are presented in Figures 16a and 16a and corresponding data are presented in Tables 3 and 4. Age distribution of individual zircons analyzed by LA-ICPMS is presented in Figure 17b.

Sample MMI12-3-15 was collected in the Southwest zone at Miner Mountain from a rusty diorite dike that contains chalcopyrite as disseminations and veins. Descriptions of the dike, its major and trace element geochemistry, and mineralization are presented in Mihalynuk and Logan (2013a). Five single zircon grains were analyzed: three whole crystals, which were anhedral, oblate, pitted, and up to ~ 200 µm long; and two crystal fragments about ~ 100 µm and ~ 70 µm in

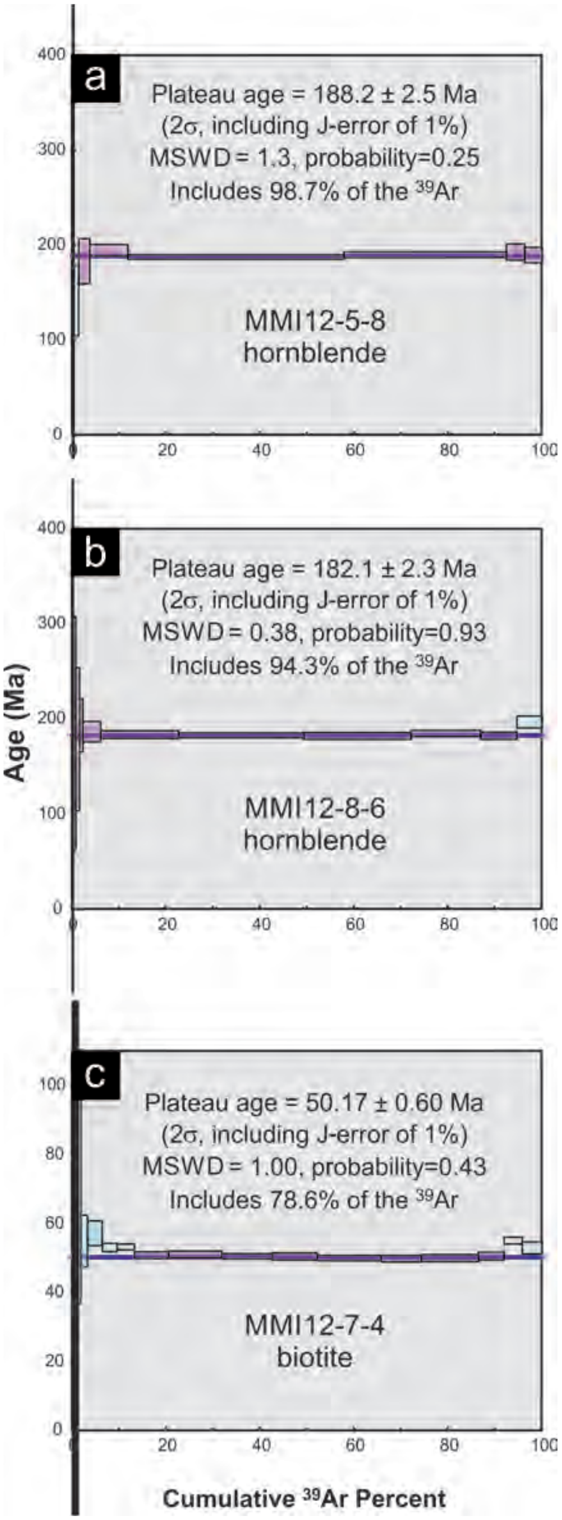

Fig. 15. Argon release spectra yield ^{40}Ar/^{39}Ar cooling ages from the Dillard Creek area. **a)** Sample MMI12-5-8 is from mineralized diorite at the Primer deposit. **b)** MMI12-8-6 is from hornblende-pyroxene porphyry lapilli tuff and breccia that presumably caps the Primer section. **c)** MMI12-7-4 is from a section of rhyolite flows, breccia and tuff south of the Primer, originally suspected to correlate with the Early Cretaceous Spences Bridge Group, but based on its age, fits well with the Princeton Group. Plateau steps are shown in magenta, rejected steps are cyan. Box heights are 2σ.

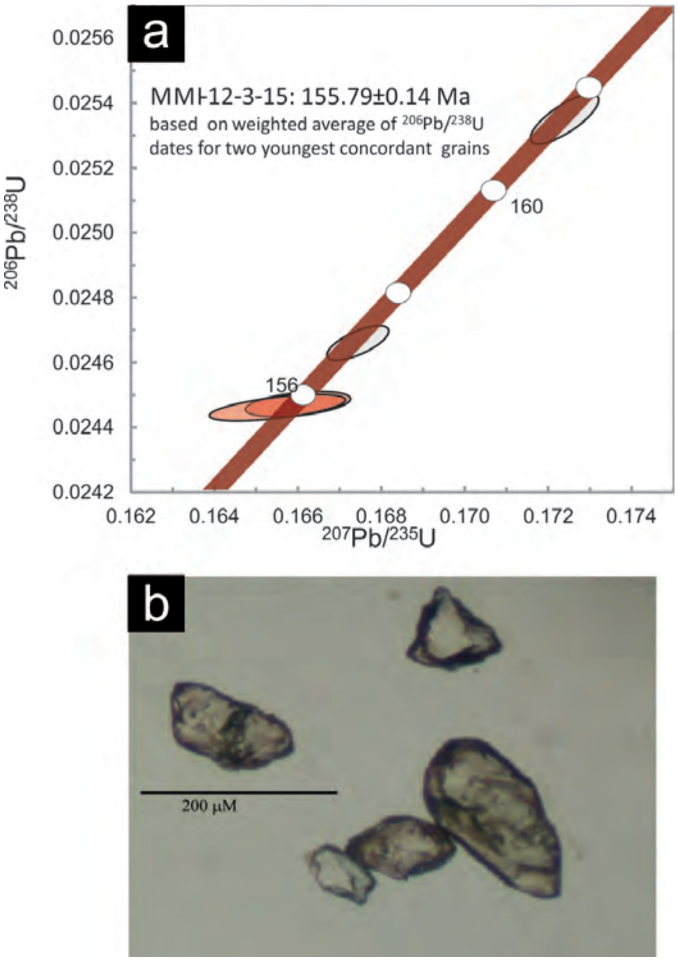

Fig. 16. a) Thermal Ionization Mass Spectrometric (TIMS) analysis of zircon U-Pb from a sample of mineralized dyke at the Southwest zone on Miner Mountain. Best estimate of the age is 155.8 ±0.14 Ma based on two overlapping fractions on concordia. Slightly discordant older grains may include an inherited older zircon component. Data point error ellipses are 2σ. **b)** Photomicrograph of zircons analyzed.

Table 2. Results of ^{40}Ar/^{39}Ar release during laser step heating of three samples from the SNAP study area.

12MMI2-5-8
hornblende

Laser Power(%)	^{40}Ar/^{39}Ar	1σ	^{37}Ar/^{39}Ar	1σ	^{36}Ar/^{39}Ar	1σ	Ca/K	%^{40}Ar atm	f ^{39}Ar	^{40}Ar*/^{39}ArK	Age	2σ
2.30	486.26	9.28	3.66	0.21	1.457	0.071	6.71	88.49	0.35	56.124	387.95	± 241.57
2.60	71.76	1.68	1.76	0.09	0.179	0.010	3.23	73.54	0.99	19.008	140.91	± 37.47
3.00	69.25	0.72	1.60	0.08	0.151	0.006	2.94	64.12	2.38	24.875	182.27	± 23.83
3.40	31.91	0.23	4.73	0.10	0.020	0.001	8.70	17.18	8.06	26.519	193.70	± 6.01
3.70	27.42	0.17	5.91	0.10	0.009	0.000	10.88	7.47	45.98	25.481	186.50	± 2.42
4.00	26.90	0.21	5.50	0.10	0.005	0.000	10.12	4.28	34.59	25.851	189.07	± 2.97
4.40	28.99	0.27	4.69	0.09	0.011	0.002	8.61	9.72	3.93	26.260	191.90	± 8.68
5.50	28.71	0.41	4.03	0.11	0.011	0.002	7.40	10.37	3.71	25.807	188.76	± 8.13
Total/Average	29.453	0.100	3.822	0.036	0.0072	0.0002			100.00	25.715	0.123	

J = 0.0042635 ± 0.0000213 Volume ^{39}ArK = 0.074 Integrated Date = 188.13 ± 1.71 Ma
Plateau age = 188.2 ± 2.5 Ma (*2σ*, including J-error of 1%) MSWD = 1.3, probability = 0.25 Includes 98.7% of the ^{39}Ar steps 3 through 8
Inverse isochron (correlation age) results, plateau steps: Model 1 Solution (± 95%-conf.) on 86 points Age = 187.7 ± 3.9 Ma
Initial ^{40}Ar/^{36}Ar = 296 ± 30 MSWD = 2.6 Probability = 0.017

MMI12-8-6
hornblende

Laser Power(%)	^{40}Ar/^{39}Ar	1σ	^{37}Ar/^{39}Ar	1σ	^{36}Ar/^{39}Ar	1σ	Ca/K	%^{40}Ar atm	f ^{39}Ar	^{40}Ar*/^{39}ArK	Age	2σ
2.30	1608.50	49.91	2.51	0.26	4.772	0.210	4.60	87.66	0.26	198.909	1108.30	± 372.06
2.70	130.10	2.62	1.52	0.14	0.355	0.031	2.79	80.67	0.47	25.177	183.91	± 122.82
3.10	94.99	1.05	1.04	0.07	0.239	0.018	1.90	74.42	0.80	24.314	177.91	± 75.15
3.50	81.40	0.82	1.22	0.08	0.186	0.007	2.23	67.60	0.69	26.396	192.36	± 28.34
3.90	39.92	0.42	3.42	0.08	0.050	0.002	6.27	36.53	3.80	25.397	185.43	± 10.69
4.20	26.92	0.30	3.71	0.22	0.008	0.000	6.82	7.51	16.60	24.960	182.40	± 4.28
4.50	25.82	0.17	3.90	0.08	0.005	0.000	7.16	4.15	26.66	24.823	181.44	± 2.54
4.80	25.79	0.26	3.83	0.07	0.005	0.000	7.03	4.24	22.79	24.765	181.05	± 3.70
5.10	26.48	0.21	3.47	0.13	0.006	0.000	6.38	5.16	14.82	25.177	183.91	± 3.15
5.50	28.12	0.20	3.58	0.08	0.012	0.001	6.57	12.06	7.68	24.794	181.25	± 3.90
6.20	30.88	0.44	3.62	0.09	0.015	0.001	6.64	13.21	5.43	26.871	195.64	± 6.23
Total/Average	28.708	0.091	2.811	0.028	0.0062	0.0001			100.00	25.021	0.103	

J = 0.0042520 ± 0.0000213 Volume ^{39}ArK = 0.157 Integrated Date = 182.84 ± 1.44 Ma
Plateau age = 182.1 ± 2.3 Ma (*2σ*, including J-error of 1%) MSWD = 0.38, probability=0.93 Includes 94.3% of the ^{39}Ar steps 2 through 10
Inverse isochron (correlation age) results, plateau steps: Model 1 Solution (± 95%-conf.) on 9 points Age = 181.4 ± 1.9 Ma
Initial ^{40}Ar/^{36}Ar = 302 ± 16 MSWD = 0.35 Probability = 0.007

Table 2. Cont'd.

MMI12-7-4
biotite

Laser Power(%)	^{40}Ar/^{39}Ar	1σ	^{37}Ar/^{39}Ar	1σ	^{36}Ar/^{39}Ar	1σ	Ca/K	%^{40}Ar atm	f ^{39}Ar	^{40}Ar*/^{39}ArK	Age	2σ
2.30	431.97	3.59	0.11	0.03	1.353	0.141	0.21	92.55	0.44	32.179	232.83	± 565.72
2.60	307.24	2.35	0.10	0.03	0.961	0.050	0.18	92.41	0.39	23.318	171.65	± 203.63
2.90	133.23	1.07	0.11	0.03	0.421	0.024	0.20	93.47	0.40	8.705	66.00	± 103.68
3.20	49.96	0.41	0.07	0.02	0.137	0.008	0.12	81.16	0.63	9.413	71.27	± 34.57
3.50	17.13	0.12	0.04	0.01	0.034	0.002	0.07	58.03	1.39	7.190	54.69	± 7.47
3.80	11.04	0.09	0.02	0.00	0.012	0.001	0.03	32.10	3.09	7.497	56.99	± 3.58
4.00	8.91	0.07	0.02	0.00	0.007	0.000	0.04	22.03	3.18	6.944	52.84	± 1.20
4.20	8.17	0.05	0.01	0.00	0.004	0.000	0.03	14.64	3.74	6.972	53.05	± 0.86
4.50	7.83	0.05	0.01	0.00	0.004	0.000	0.01	14.99	7.23	6.657	50.69	± 0.99
4.80	7.44	0.04	0.01	0.00	0.002	0.000	0.01	10.13	11.30	6.686	50.90	± 1.01
5.10	7.33	0.05	0.00	0.00	0.002	0.000	0.01	9.78	10.76	6.612	50.35	± 0.77
5.40	7.45	0.06	0.01	0.00	0.003	0.000	0.02	11.37	9.60	6.604	50.29	± 1.07
5.70	6.85	0.05	0.00	0.00	0.001	0.000	0.01	4.58	13.55	6.533	49.76	± 0.75
6.00	7.04	0.05	0.00	0.00	0.002	0.000	0.00	7.45	8.53	6.513	49.61	± 0.94
6.50	6.96	0.04	0.00	0.00	0.001	0.000	0.01	6.15	12.20	6.532	49.75	± 0.98
7.00	7.44	0.05	0.00	0.00	0.003	0.000	0.01	11.00	5.40	6.618	50.40	± 1.14
7.50	8.06	0.06	0.00	0.00	0.003	0.000	0.00	10.53	3.96	7.207	54.81	± 0.97
8.00	8.00	0.07	0.00	0.00	0.004	0.000	0.00	13.38	4.20	6.929	52.73	± 1.72
Total/Average	7.873	0.014	0.006	0.000	0.0020	0.0000			100.00	6.715	0.019	

J = 0.0042703 ± 0.0000214 Volume ^{39}ArK = 0.635 Integrated Date = 51.12 ± 0.28 Ma
Plateau age = 50.17 ± 0.60 Ma (*2σ*, including J-error of 1%) MSWD = 1.00, probability = 0.43 Includes 78.6% of the ^{39}Ar steps 9 through 16
Inverse isochron (correlation age) results, plateau steps: Model 1 Solution (± 95%-conf.) on 15 points Age = 49.61 ± 0.49 Ma
Initial ^{40}Ar/^{36}Ar = 331 ± 15 MSWD = 1.4 Probability = 0.002

long dimension (Fig. 16b). All but the smallest grain provided adequate material for analysis, resulting in the four data points on Figure 16a. Two grains give concordant and overlapping results with a weighted ^{206}Pb/^{238}U age of 155.8 ±0.14 Ma, considered as the best estimate for the age of the rock. The other two grains lie along concordia, give older, non-overlapping results and are interpreted to have older inherited cores or to be older xenocrysts.

Mineralization at Miner Mountain has long been considered a product of the Late Triassic Nicola arc magmatism, but based on the ^{40}Ar/^{39}Ar ages above, now may extend into the Early Jurassic (~ 188 Ma). Nevertheless, a ~ 156 Ma magmatic age for mineralization is much younger than any known or suspected Nicola Group. This anomalously young age may signify: 1) that the sulphide mineralization is remobilized from a deeper, probable Late Triassic source; 2) that the new age is in error, which will be tested by further work on a sample of drill core that intersected the mineralized intrusion; or 3) there exists a ~ 156 magmatic suite with previously unappreciated copper endowment.

Intrusions emplaced around 156 Ma occur in great volumes across southern British Columbia, including the Tulameen, Similkameen and Okanagan complexes. The huge Osprey Lake batholith occupies much of the eastern third of the study area and has returned K-Ar cooling ages from biotite of 149 ± 2 Ma , and from hornblende of 154 ± 3 Ma (Hunt and Roddick, 1988), but a U-Pb crystallization age of 166 ±1Ma (Parrish and Monger, 1992).

Sample MMI13-10-8 was collected from a tuffaceous polymictic conglomerate section that sits on, and interfingers with, flow-banded rhyolite (see Spences Bridge Group, section 3.2.1 above). Clasts include limestone, granitoid intrusives, altered mafic volcanic, and those resembling immediately underlying volcanic rock types. Of the twenty-seven grains selected from the zircon separate for analysis, all but two were inspected for evidence of growth zoning and xenocrystic cores (see Mihalynuk et al., 2014b for imagery) before analysis. All LA-ICPMS analyses fall into two ^{206}Pb/^{238}U age clusters (Table 4, Fig. 17a) that have age distribution peaks at ~ 103 and ~ 220 Ma. Subsidiary peaks in the older cluster are at ~ 190 and ~

Table 3. Results of U-Pb isotopic analysis of zircons by Thermal Ionization Mass Spectroscopy (TIMS) of mineralized quartz monzonite from the Southwest zone at Miner Mountain.

	Compositional Parameters								Radiogenic Isotope Ratios									Isotopic Ages					
Sample (a)	Wt. mg (b)	U ppm (c)	Th/U (d)	Pb ppm (c)	^{206}Pb* x10^{-13} mol (e)	mol % ^{206}Pb* (e)	Pb*/Pb$_c$ (e)	Pb$_c$ (pg) (e)	^{206}Pb/^{204}Pb (f)	^{208}Pb/^{206}Pb (g)	^{207}Pb/^{206}Pb (g)	% err (h)	^{207}Pb/^{235}U (g)	% err (h)	^{206}Pb/^{238}U (g)	% err (h)	corr. coef.	^{207}Pb/^{206}Pb (i)	± (h)	^{207}Pb/^{235}U (i)	± (h)	^{206}Pb/^{238}U (i)	± (h)
MMI-12-3-15																							
A	0.0108	373	0.472	9.8	4.2594	99.92%	364	0.29	22249	0.151	0.04932	0.25	0.1724	0.39	0.02535	0.25	0.767	163.02	5.92	161.49	0.58	161.39	0.40
B	0.0014	1240	0.490	31.9	1.7840	99.80%	148	0.30	9037	0.156	0.04924	0.27	0.1674	0.36	0.02466	0.18	0.690	159.13	6.40	157.15	0.53	157.02	0.28
C	0.0016	659	0.441	16.9	1.0754	99.24%	39	0.67	2420	0.141	0.04919	0.58	0.1659	0.62	0.02447	0.13	0.423	156.91	13.62	155.89	0.90	155.82	0.20
D	0.0008	830	0.463	22.2	0.6767	98.19%	16	1.02	1024	0.147	0.04907	0.74	0.1654	0.81	0.02446	0.14	0.599	151.01	17.31	155.46	1.17	155.75	0.21

(a) A, B etc. are labels for fractions composed of single zircon grains or fragments; all fractions annealed and chemically abraded after Mattinson (2005) and Scoates and Friedman (2008).

(b) Nominal fraction weights estimated from photomicrographic grain dimensions, adjusted for partial dissolution during chemical abrasion.

(c) Nominal U and total Pb concentrations subject to uncertainty in photomicrographic estimation of weight and partial dissolution during chemical abrasion.

(d) Model Th/U ratio calculated from radiogenic ^{208}Pb/^{206}Pb ratio and ^{207}Pb/^{235}U age.

(e) Pb* and Pbc represent radiogenic and common Pb, respectively; mol % ^{206}Pb* with respect to radiogenic, blank and initial common Pb.

(f) Measured ratio corrected for spike and fractionation only. Mass discrimination of 0.23%/amu based on analysis of NBS-982; all Daly analyses.

(g) Corrected for fractionation, spike, and common Pb; up to 1.0 pg of common Pb was assumed to be procedural blank: ^{206}Pb/^{204}Pb = 18.50 ± 1.0%; ^{207}Pb/^{204}Pb = 15.50 ± 1.0%; ^{208}Pb/^{204}Pb = 38.40 ± 1.0% (all uncertainties 1-sigma). Excess over blank was assigned to initial common Pb with S-K model Pb composition at 155 Ma.

(h) Errors are 2-sigma, propagated using the algorithms of Schmitz and Schoene (2007) and Crowley et al. (2007).

(i) Calculations are based on the decay constants of Jaffey et al. (1971). ^{206}Pb/^{238}U and ^{207}Pb/^{206}Pb ages corrected for initial disequilibrium in ^{230}Th/^{238}U using Th/U [magma] = 3. Isotopic dates are calculated the decay constants l238=1.55125E-10 and l235=9.8485E-10 (Jaffey et al. 1971).

Table 4. Analytical results from zircons of sample MMI13-10-8 by laser ablation (LA) ICP-MS.
±2σ; I = integrated error, P = propagated error from all sources. $^{238}/_{206}\sigma/^{207}/_{206}\sigma$ = isotopic ratio correlated error

Sample -grain	U ppm	±2σ	Th ppm	±2σ	Pb ppm	±2σ	U/Th	±2σ	$^{207}Pb/^{235}U$	±2σ I	±2σ P	$^{206}Pb/^{238}U$	±2σ I	±2σ P	$^{206}/_{238}\sigma/^{207}/_{235}\sigma$	$^{206}Pb/^{238}U$ Ma	±2σ	±2σ P	$^{207}Pb/^{206}Pb$	±2σ I	±2σ P	$^{238}/_{206}/^{207}/_{206}$	$^{207}Pb/^{235}U$ Ma	±2σ I	±2σ P
MMI13-10-8-1	189	4.8	53	1.4	25.2	2	3.196	0.069	0.2300	0.0170	0.020	0.035	0.0010	0.0014	0.02225	223.2	6.4	8.9	0.0496	0.0040	0.0047	0.43117	206	14	17
MMI13-10-8-2	300.1	9	71.7	3.4	35.5	2.6	3.76	0.12	0.2620	0.0140	0.019	0.035	0.0010	0.0014	0.12221	219.8	6.0	8.5	0.0547	0.0033	0.0043	0.48831	233	11	15
MMI13-10-8-3	203.8	5.7	48.7	1.7	20.1	1.8	3.656	0.098	0.2070	0.0160	0.019	0.030	0.0010	0.0013	0.14620	193.1	5.9	7.8	0.0506	0.0042	0.0049	0.37341	184	14	16
MMI13-10-8-4	262.9	8.7	38.5	2.2	10.9	1.9	5.85	0.26	0.0960	0.0130	0.010	0.017	0.0008	0.0008	0.05267	108.3	5.2	5.0	0.0453	0.0066	0.0039	0.46334	93	12	8.8
MMI13-10-8-5	467	13	153.8	3.8	77.8	4.1	2.637	0.049	0.2430	0.0110	0.016	0.034	0.0008	0.0013	0.14006	215.4	5.0	7.9	0.0512	0.0025	0.0037	0.35645	218.4	9.4	14
MMI13-10-8-6	835	21	479	20	272	12	1.58	0.049	0.2599	0.0095	0.016	0.036	0.0008	0.0013	0.28987	228.1	4.7	7.8	0.0509	0.0018	0.0032	0.29251	232.6	7.6	13
MMI13-10-8-7	4650	120	6270	160	3099	91	0.6209	0.0092	0.2298	0.0046	0.012	0.032	0.0005	0.0011	0.57544	205.9	3.4	6.6	0.0505	0.0009	0.0028	0.3304	209.5	3.8	10
MMI13-10-8-8	269.2	8.9	50.9	3.3	15.4	1.8	4.97	0.27	0.1320	0.0120	0.012	0.017	0.0007	0.0007	0.15794	109.5	4.2	4.7	0.0583	0.0055	0.0056	0.42447	125	11	11
MMI13-10-8-9	159.2	4.3	67.5	2.4	12	1.4	2.07	0.049	0.1130	0.0130	0.014	0.016	0.0008	0.0009	0.08085	103.9	5.1	5.6	0.0670	0.0100	0.011	1	105	11	12
MMI13-10-8-10	401	15	154.7	6.7	58.7	4.1	2.285	0.054	0.2670	0.0120	0.018	0.035	0.0009	0.0013	0.09691	218.9	5.6	8.2	0.0561	0.0029	0.0041	0.43364	237.6	9.9	14
MMI13-10-8-11	544	23	690	44	188	13	0.86	0.031	0.2220	0.0110	0.015	0.032	0.0008	0.0012	0.25919	200.5	5.0	7.3	0.0500	0.0024	0.0034	0.23948	203.7	8.9	12
MMI13-10-8-12	283.3	9.6	146.9	5.7	45.5	3.1	1.977	0.038	0.2490	0.0170	0.021	0.035	0.0009	0.0013	0.16182	219.8	5.6	8.1	0.0508	0.0036	0.0045	0.311	220	14	17
MMI13-10-8-13	916	46	675	42	94.1	6.9	1.487	0.035	0.1063	0.0055	0.008	0.016	0.0004	0.0006	0.18375	100.8	2.7	3.9	0.0498	0.0028	0.0038	0.34982	102.4	5.1	7.2
MMI13-10-8-14	302.8	8.6	1527	58	488	22	0.215	0.0043	0.2950	0.0160	0.022	0.035	0.0009	0.0013	0.10397	223.3	5.8	8.4	0.0613	0.0037	0.0047	0.30504	259	13	17
MMI13-10-8-15	349	31	339	37	90	10	2.28	0.22	0.2500	0.0180	0.022	0.034	0.0011	0.0014	0.05648	214.7	6.7	8.9	0.0544	0.0043	0.0051	0.47547	219	15	18
MMI13-10-8-16	453.9	9.7	234.4	8.3	38.5	3	2.181	0.068	0.1175	0.0080	0.010	0.016	0.0005	0.0007	0.02016	103.2	3.2	4.3	0.0535	0.0039	0.0047	0.34333	111	7.2	8.8
MMI13-10-8-17	145	4.4	98.5	3	30.4	2.6	1.615	0.043	0.2470	0.0240	0.024	0.037	0.0017	0.0017	0.14168	234.0	10.0	10.0	0.0509	0.0051	0.0051	0.41179	217	19	19
MMI13-10-8-18	294.8	6.1	147.2	3	45.8	2.8	2.087	0.04	0.2620	0.0150	0.020	0.035	0.0009	0.0013	0.14539	221.8	5.7	8.3	0.0551	0.0034	0.0044	0.42291	236	12	16
MMI13-10-8-19	644	20	457	21	121	7.6	1.499	0.037	0.2161	0.0094	0.014	0.030	0.0006	0.0011	0.08504	188.7	4.0	6.6	0.0521	0.0024	0.0036	0.37345	198.1	7.9	12
MMI13-10-8-20	397	14	207.1	9	75.8	5.2	1.863	0.047	0.2470	0.0150	0.019	0.035	0.0009	0.0013	0.13043	220.6	5.8	8.2	0.0509	0.0031	0.004	0.29094	224	12	15
MMI13-10-8-21	161	10	101.2	7.9	32.7	4.7	1.587	0.07	0.2300	0.0300	0.120	0.036	0.0023	0.0025	0.23972	229.0	14.0	15.0	0.0473	0.0064	0.018	0.1361	203	25	56
MMI13-10-8-22	181.7	9.3	109.7	7.9	19.8	3	1.608	0.076	0.1000	0.0190	0.017	0.018	0.0012	0.0012	0.06835	117.0	7.6	7.3	0.0450	0.0088	0.012	0.49225	97	18	15
MMI13-10-8-23	1521	59	938	44	151.5	9.9	1.513	0.031	0.1067	0.0053	0.007	0.016	0.0004	0.0006	0.24527	103.7	2.7	3.9	0.0467	0.0024	0.0034	0.31919	102.7	4.9	6.7
MMI13-10-8-24	710	130	570	100	137	26	1.899	0.06	0.2710	0.0230	0.025	0.036	0.0012	0.0015	0.15448	225.9	7.4	9.3	0.0559	0.0048	0.0052	0.22966	236	18	20
MMI13-10-8-25	388	48	124	5.1	32.4	2.9	3.74	0.31	0.2300	0.0160	0.019	0.036	0.0010	0.0014	0.04161	228.6	6.4	9.0	0.0490	0.0037	0.0044	0.40856	209	13	16
MMI13-10-8-26	456	36	275	28	31.8	4.3	2.34	0.1	0.1200	0.0120	0.013	0.016	0.0008	0.0009	0.15848	104.0	5.0	5.6	0.0567	0.0058	0.0066	0.55626	114	11	12
MMI13-10-8-27	373.4	9	200.3	7.2	23.5	2.9	2.337	0.074	0.1270	0.0130	0.014	0.017	0.0006	0.0008	0.03596	107.7	4.1	5.0	0.0600	0.0064	0.0068	0.40293	119	11	12

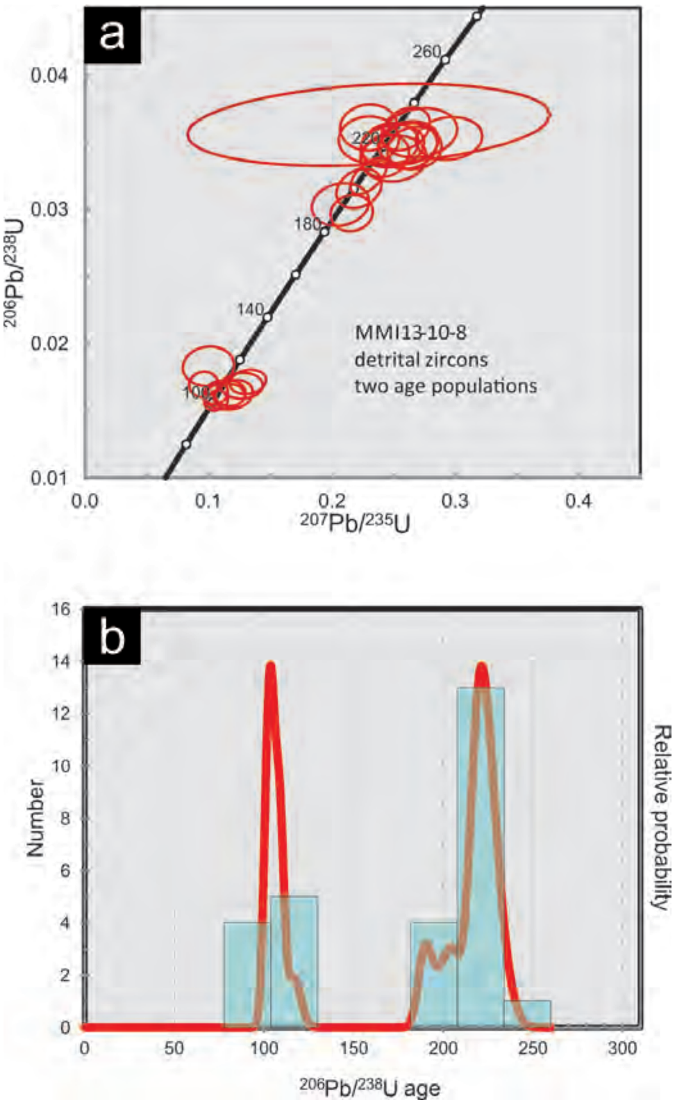

Fig. 17. Laser Ablation (LA-ICPMS) U-Pb isotopic determination of ages of detrital zircons separated from a sample of conglomerate, MMI13-10-8. **a)** Isochron plot of individual zircons analyzed with clustering of data into two populations. Data point error ellipses are 2 σ. **b)** Age distribution and "relative probability" plot showing two main populations, 103 and ~220 Ma, but also a ~190 Ma population, supporting the Early Jurassic cooling ages (see Fig. 14) and extension of the Nicola arc volcanism into the Jurassic. Provenance for the 103 Ma zircons is the Spences Bridge Group (103 Ma, Diakow and Barrios, 2008) which interfingers with, and overlies the Nicola Group formerly considered to be of Late Triassic age (229-201Ma , timescale of Cohen et al., 2013).

205 Ma.

All age distribution peaks can be easily linked to probable sources. A lack of grains younger than 103Ma and a dense cluster at 103 Ma, which is the age of the Spences Bridge Group (Diakow and Barrios, 2008), confirm our geological observations that point to synvolcanic (tuffaceous) sedimentation coeval with Spences Bridge Group felsic volcanism. All older grains were likely derived from the underlying Allison Lake pluton or nearby Nicola Group volcanic arc rocks. From a similar polymictic conglomerate near Dry Lake, Preto (1979) sampled a clast lithologically identical to the Allison Lake pluton. This clast yielded a K/Ar (muscovite) age of 207 ±10 Ma (recalculated from 203 ±5 Ma, using new decay constants and error estimates, Breitsprecher and Mortensen, 2004), confirming derivation from the plutonic roots of the underlying arc. Importantly, the ~ 190 Ma sub-peak supports our interpretation of 188 Ma cooling age of sample MMI12-5-8 (see Hornblende and biotite $^{40}Ar/^{39}Ar$, above) as a crystallization age, and indicates exposure of this or a coeval magmatic unit to erosional levels during Spences Bridge deposition.

8. Mineralization

In 2013, the most intensive mineral exploration project conducted in the study area was by Sego! Resources Inc. at their Miner Mountain deposit. The most significant assayed interval from percussion drilling of 34 holes was: 30m of 0.31% Cu and 0.15 g/t Au from 32 m to the end of hole at 62m in PDH-13-109 (Stevenson, 2013). For an overview of the geology and mineralization at Miner Mountain see Mihalynuk and Logan (2013a) and the Sego! Resources Inc. website: http://www.segoresources.com/. Here we present new observations from known and previously unreported mineral occurrences. Results from mineralized samples submitted for analysis by ICP-MS are presented in Table 1 and a complete array of elements analyzed, plus determinations by Instrumental Neutron Activation Analysis are reported in Mihalynuk et al. (2014a).

8.1. Rats prospect (MINFILE 092HNE176)

The Rats porphyry Cu-Au prospect is 12 km northeast of Princeton in a panel of Nicola volcanic and intrusive rocks that are intruded on the east by Early Cretaceous granodiorite of the Summers Creek pluton. Within one kilometre to the west, they are in fault contact with Eocene volcanic and sedimentary rocks of the Princeton Group (Fig. 3). Cu-Au-Ag ± Mo mineralization is hosted in northwest-trending brittle shear zones, sheeted veins, and breccia zones in massive plagioclase > pyroxene phyric basalt and mafic fragmental rocks that are hornfelsed within ~ 100 m of the fine-grained monzodiorite border phase of the Summers Creek pluton. A post-mineral feldspar-hornblende-quartz porphyry dike intrudes the mineralized zone.

Two styles of alteration and mineralization are recognized at the Rats, one with the assemblage K-feldspar, magnetite, actinolite and epidote with chalcopyrite (JLO13-26-6, 26-80), the other with albite bleaching, epidote, magnetite, pyrite, and chalcopyrite in quartz and calcite veins/stockworks (JLO13-26-6-2, 26-9 and 26-11). Higher gold and silver values appear to be linked to higher copper values. Analyses of Rats mineralization reveals some of the highest Mo values obtained in the study area (Table 1).

8.2. Hit prospect (MINFILE 092HNE053)

Southeast of Mystery Lake, overburden has been scraped from a north-northwest-elongate area, ~ 400 m by 75 m, down to bedrock (Fig. 18a). Exposed are a series of en echelon quartz veins (Fig. 18 inset) in scaly calcareous phyllite containing abundant irregular quartz veinlets and possibly sparse quartz eyes. Trenches further expose white and rusty quartz veins. Individual quartz veins are up to ~ 1.25 m thick (thicker

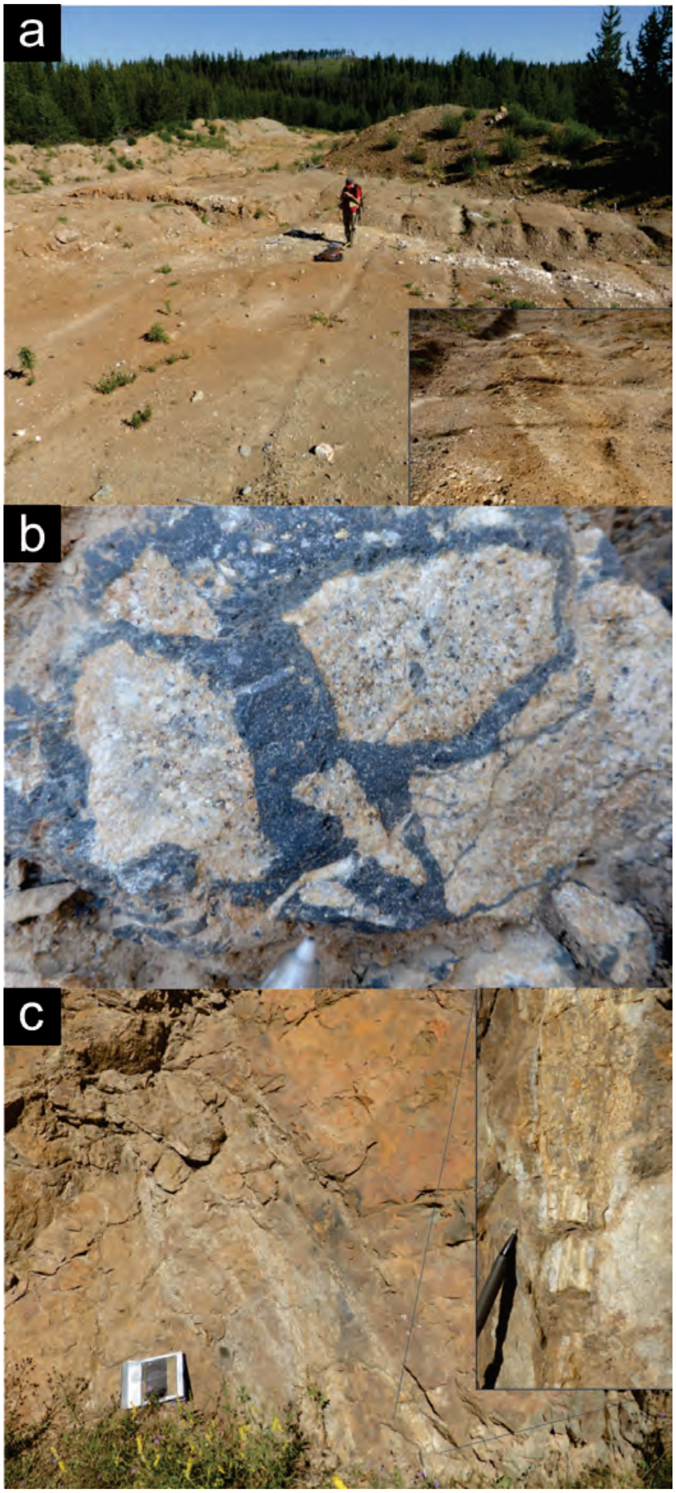

Fig 18. a) View to the north of the cleared area and exposed white precious and base metal-bearing quartz vein material at the Hit prospect. Inset is a view to the south showing the en-echelon nature of intermediate-sized veins. **b)** Tourmaline-cemented breccia at the Rum porphyry copper occurrence. **c)** Set of sheeted quartz-carbonate precious metal epithermal veins in the basal Spences Bridge Group. Inset shows vein detail.

where they intersect) and contain patchy base metal sulphides (visually estimated in most places as < 2%), mainly as galena, pyrite, sphalerite and chalcopyrite. A sample collected from one of the large mineralized veins returned 1.8 ppm Au, 21.6 ppm Ag, 0.5 % Pb, and 0.3% Zn (MMI13-19-1, Table 1).

8.3. Rum prospect (MINFILE 092HNE099)

The Rum prospect is ~ five km south of Missezula Lake and one kilometre west of Summers Creek fault. It comprises a broad zone of tourmaline-pyrite alteration extending from quartz diorite with spotty but ubiquitous copper staining at least 400 m into Nicola Group country rocks. Contrasting alteration in the country rocks is epidote-chlorite-actinolite±prehnite, a mineral assemblage typical of the low-grade regional metamorphism in the Late Triassic section. Within the white and rusty orange-weathering intrusion, tourmaline forms rosettes, aphanitic matrix flood, or cement between secondary breccia fragments (Fig. 18b).

Medium-grained holocrystalline plagioclase and chloritized mafic minerals comprise most of the rocks, with granular magnetite 5-10% (variably oxidized to hematite) and intercrystalline quartz (~ 5-10%). Plagioclase is replaced by calcite and white mica. Zones of chalcopyrite and rare bornite are disseminated or less commonly in veins up to a centimetre thick visible in outcrop and freshly broken surfaces. K-feldspar flooding is locally intense and magnetite breccia is developed in metre-wide zones. Samples collected from adjacent altered country rocks and mineralized portions of the altered intrusion contain up to 0.85% Cu, 12.5 ppm Ag, and 0.39 ppm Au (MMI13-19-11, 19-12, 20-1, 20-2, 20-3, 21-1, 21-2, 21-3, 21-4 in Table 1) with highest values coming from the intrusions.

8.4. Exhalative mineralization

In the Nicola Group near Coalmont, bimodal, submarine volcanism, and possible exhalite (Fig. 5b) containing minor iron and copper sulphides are indicators of an environment in which volcanogenic massive sulphides (VMS) could accumulate (for lithologic descriptions see “Felsic tuffite” above). Toward the east, an extensive area underlain by rhyolite (Fig. 3) is pyritic, and weathers to locally broad gossans. About a kilometre southeast of Coalmont this rhyolite belt passes along strike into a section of mafic tuffite containing thin layers of magnetite and disseminated chalcopyrite that could be exhalative. Samples collected from this unit range from 1 to 14.5 % Fe and contain up to 0.33% Cu and 0.56 ppm Ag (MMI13-37-9a, 9b, MMI13-38-8b, 10, Table 1). Whether or not the magnetite-chalcopyrite layers are of exhalative origin has not been conclusively determined. They could be related to the sub-surface extent of the Boulder intrusion, the surface expression of which terminates in this same area. Because this weakly mineralized prospect lacks elevated Ba, Se, and Co (see Mihalynuk et al., 2014a), which are common VMS pathfinder elements, an intrusive association for the magnetite-chalcopyrite layers should be considered. However, evidence of a bimodal submarine environment with possible cherty exhalite supports a VMS-related origin. Further investigation is anticipated in 2014, including sampling of the rhyolite for age determination. Detrital zircon geochronology of the quartz-bearing clastic unit interbedded with cherty “exhalite” is in progress.

8.5. Cretaceous (?) epithermal veins

Potential for epithermal precious metal mineralization has been demonstrated elsewhere in the Spences Bridge Group (Diakow and Barrios, 2009) and mapping as part of this project has revealed similar quartz vein systems.

Near the junction of Highway 5A and Pike Mountain Forest Service Road (at Summit Lake, Fig. 3), a set of sheeted, 0.1 – 15cm thick, banded quartz and quartz-carbonate veins (Fig. 18c and inset) cuts pyritic, coarse basal breccia of the Spences Bridge Group adjacent to a faulted unconformity with the Allison Lake pluton. Rounded to angular boulders and blocks of pink Allison Lake intrusion are admixed with aphanitic green volcanic blocks and sparse pyrite clasts (< 5 cm in long dimension) that have a foliated fabric, possibly originating as entrained fragments of foliated basement that was replaced by pyrite. Orange-weathering, green matrix is probably predominantly ash. Weak carbonate alteration and a crisscrossing network of carbonate veinlets affect the local outcrops. A ~ one metre chip sample collected across the most intensely veined part of the outcrop (center of Fig. 18c) returned 6.3 ppm Ag and 0.1 ppm Au with elevated Te (3.8 ppm), As (246 ppm), and Hg (80 ppb, MMI13-32-1, Table 1).

Impressive epithermal textures, albeit without significant precious metal content, are displayed by the vein system at LDI13-8.3 (UTM 673718E, 549398N, Fig. 3) at an isolated knoll of aphanitic andesite, considered to be part of the lower Spences Bridge volcanic unit. Andesite crosscut by spaced quartz veinlets resembles a black, fine-grained clastic rock. The quartz is translucent with various forms including: dismembered veinlets with ductile deformation fabrics alternating with narrow black ribbons of silicified country rock (Fig. 19a); narrow gash veinlets in fractured black silicified country rock; and angular fragments with diffuse outlines in quartz breccia (Fig. 19b). Silica replacing former bladed calcite (Fig. 19c) occupies vugs in all quartz varieties. Sericite (?)-altered fragments in the dismembered example, and host rock domains attendant to quartz apparently have undergone moderate silicification.

9. Conclusions

Principal observations arising from the orientation survey in 2012 and mapping in 2013, lead to the following conclusions.

1). Nicola arc volcanism is not restricted to the Late Triassic, but extends into the Lower Jurassic with the addition of hornblende phenocrysts in mafic extrusive rocks.

2). Felsic volcanism, previously thought to be characteristic of the western Nicola belt, apparently extends into the eastern belt. However, we have yet to verify the age of the eastern rhyolite.

3). Near the community of Coalmont, evidence for exhalative mineralization warrants further evaluation for VMS settings in probable Late Triassic bimodal volcanogenic strata.

4). Mineralized intrusive systems, such as at Dillard Creek, are Early Jurassic, significantly expanding the age range of arc rocks prospective for porphyry copper mineralization.

5). Discovery of epithermal-style quartz veins hosted by mid-Cretaceous Spences Bridge strata emphasizes the regional significance of this sequence for precious metal vein exploration.

6). In addition to block faulting, ductile deformation, including thrust faulting and folding, was important in redistributing Nicola arc facies.

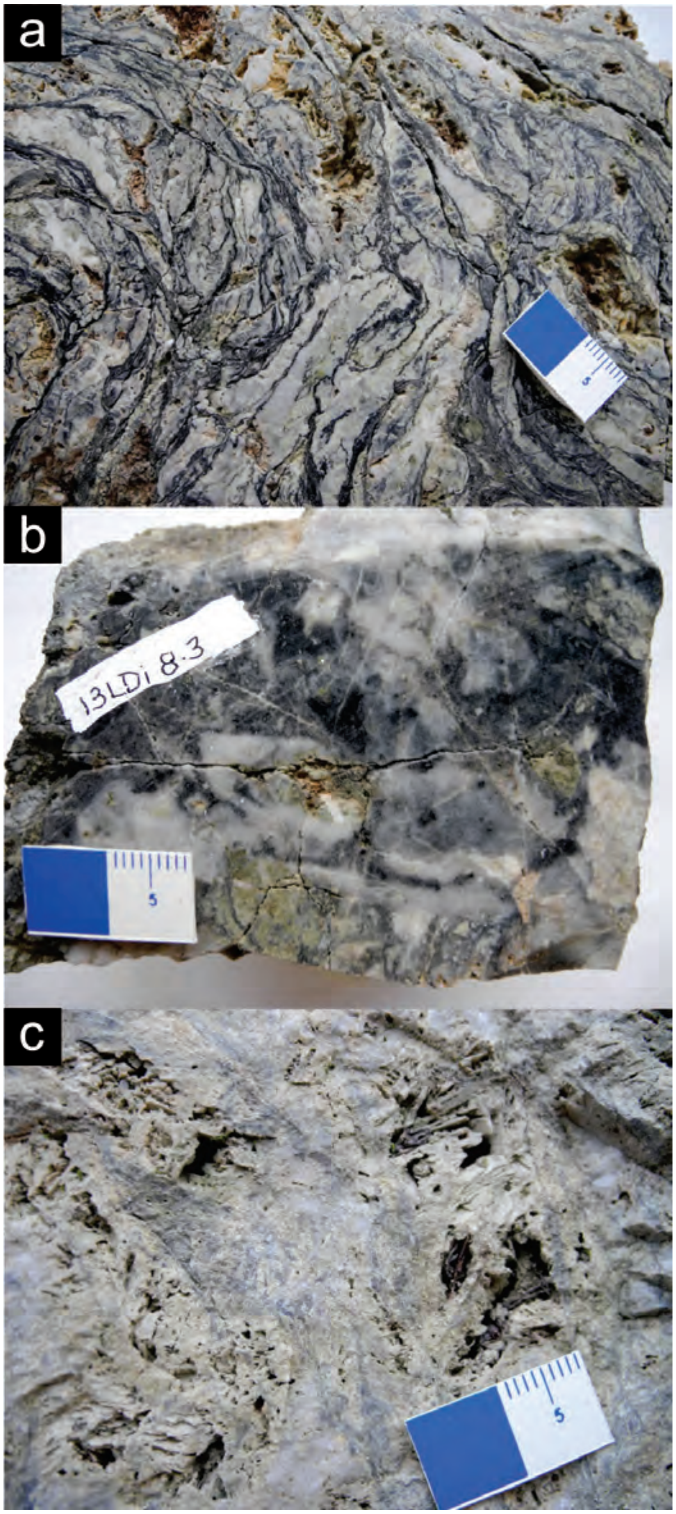

Fig. 19. Epithermal-style vein quartz, hosted by early Cretaceous volcanic rocks of the Spences Bridge Group, 15 km northeast of Princeton (UTM location 673718E, 5493984N). **a)** Dismembered and folded vein quartz containing vugs infilled with bladed quartz after calcite. **b)** Diffuse quartz fragments comprising breccia in a siliceous black, fine clastic matrix. **c)** Close-up of vuggy texture with bladed calcite crystals now replaced by silica.

7). Extensional deformation of Eocene age (and perhaps as young as Miocene) affects the entire width of the arc so far investigated. Unravelling this deformation will be an important step in reconstructing the Late Triassic mineralizing landscape of the Nicola arc.

Acknowledgments

We are indebted to past workers in the southern Nicola arc, especially J. Monger and V. Preto, both of whom have generously shared their time and knowledge with us in the field. Our corporate partners Sego! Resources Inc. are generous supporters of the Southern Nicola Arc Project.

References cited

Bordet, E.-J., Mihalynuk, M.G., Hart, C.J.R., Mortensen, J.K., Friedman, R.M., and Gabites, J., 2013. Chronostratigraphy of Eocene volcanism, Central British Columbia. Canadian Journal of Earth Sciences, in press. doi: 10.1139/cjes-2013-0073.

Breitsprecher, K., and Mortensen, J.K., 2004. BCAge 2004A-1-a database of isotopic age determinations for rock units from British Columbia. British Columbia Ministry of Energy and Mines, British Columbia Geological Survey, Open File, v. 3.

Brown, R., and Journeay, J., 1987. Tectonic Denudation of the Shuswap Metamorphic Terrane of Southeastern British-Columbia. Geology, 15, 142–146. doi: 10.1130/0091-7613(1987)15<142:TDOTSM>2.0.CO;2.

Cho, M., and Liou, J., 1987. Prehnite Pumpellyite to Greenschist Facies Transition in the Karmutsen Metabasites, Vancouver Island, BC. Journal of Petrology, 28, 417-443.

Church, B.N., 1973. Geology of the White Lake Basin. British Columbia Department of Mines and Petroleum Resources, Bulletin 61, 120 p.

Cohen, K.M., Finney, S.C., Gibbard, P.L., and Fan, J.X., 2013. The ICS International Chronostratigraphic Chart. Episodes, 36, 199-204.

Crowley, J.L., Schoene, B. and Bowring, S.A., 2007. U-Pb dating of zircon in the Bishop Tuff at the millennial scale. Geology, 35, 1123-1126.

Davis, G.A., Monger, J.W.H., and Burchfiel, B.C. 1978. Mesozoic construction of the Cordilleran "collage," central British Columbia to central California. In: Mesozoic paleogeography of the western United States. Edited by D.G. Howell and K.A. McDougall. Society of Economic Paleontologists and Mineralogists, Pacific Coast Paleogeography Symposium, 2, 1-32.

Diakow, L.J. and Barrios, A., 2008. Geology, Spences Bridge Group southwest of Merritt, British Columbia (parts of NTS 092H/14, 15 and 092I/2,3). BC Ministry of Energy Mines and Petroleum Resources, British Columbia Geological Survey, Open File 2008-8, 1:50 000 scale.

Diakow, L.J. and Barrios, A. 2009. Geology and Mineral Occurrences of the Mid-Cretaceous Spences Bridge Group near Merritt, Southern British Columbia (Parts of NTS 092H/14, 15; 092I/2, 3). In: Geological Fieldwork 2008, BC Ministry of Energy Mines and Petroleum Resources, British Columbia Geological Survey, Paper 2009-1, pp. 63-79.

Enkin, R.J., 2006. Paleomagnetism and the case for Baja British Columbia: Paleogeography of the North American Cordillera: Evidence For and Against Large-Scale Displacements. In: Geological Association of Canada, Special Paper, 46, 233–253.

Ferri, F., 1997. Nina Creek Group and Lay Range Assemblage, north-central British Columbia: remnants of late Paleozoic oceanic and arc terranes: Canadian Journal of Earth Sciences, 34, 854–874, doi: 10.1139/e17-070.

Gerstenberger, H., and Haase, G., 1997. A Highly effective emitter substance for mass spectrometric Pb isotopic ratio determinations. Chemical Geology, 136, 309-312.

Greig, C.J., Armstrong, R.L., Harakal, J.E., Runkle, D., and der Heyden, P. van, 1992. Geochronometry of the Eagle Plutonic Complex and the Coquihalla area, southwestern British Columbia. Canadian Journal of Earth Sciences, 29, 812-829.

Halliday, A.N., Davidson, J.P., Hildreth, W., and Holden, P., 1991. Modelling the petrogenesis of high Rb/Sr silicic magmas. Chemical Geology, 92, 107–114. doi: 10.1016/0009-2541(91)90051-R.

Hills, L.V., 1965. Source of the Allenby Formation, Princeton Coalfield, British Columbia. Bulletin of Canadian Petroleum Geology, 13, 271-279.

Hunt, P.A., and Roddick, J.C., 1988. A compilation of K–Ar ages: Radiogenic age and isotopic studies. Geological Survey of Canada, Report, 18, 127-153.

Ickert, R.B., Thorkelson, D.J., Marshall, D.D., and Ullrich, T.D., 2009. Eocene adakitic volcanism in southern British Columbia. Remelting of arc basalt above a slab window. Tectonophysics, 464, 164-185.

Jaffey, A.H., Flynn, K.F., Glendenin, L.E., Bentley, W.C., and Essling, A.M., 1971. Precision measurement of half-lives and specific activities of 235U and 238U. Physical Review, C4, 1889-1906.

Koppers, Anthony A.P., 2002. ArArCALC – software for 40Ar/39Ar age calculations. Computers and Geosciences, 28, 605-619.

Kuiper, K.F., Deino, A, Hilgen, F.J., Krijgsman, W., Renne, P.R., Wijbrans, J.R., 2008. Synchronizing rock clocks of earth history. Science, 320, 500-504.

Le Bas, M.J., 2000. IUGS Reclassification of the High-Mg and Picritic Volcanic Rocks. Journal of Petrology, 41, 1467–1470. doi: 10.1093/petrology/41.10.1467.

Ludwig, K., 2003. Isoplot/Ex, version 3: A geochronological toolkit for Microsoft Excel. University of California at Berkeley, Geochronology Center, Special Publication No. 4, kludwig@bgc.org.

Massey, N.W.D., MacIntyre, D.G., Desjardins, P.J., and Cooney, R.T., 2005. Digital geology map of British Columbia: Whole province. British Columbia Ministry of Energy, Mines and Petroleum Resources, Geofile 2005-1.

Massey, N.W.D., and Oliver, S.L., 2010. Southern Nicola Project: Granite Creek Area, southern British Columbia (Parts of NTS 092H/07, 10). In: Geological Fieldwork 2009, BC Ministry of Energy and Mines, British Columbia Geological Survey, Paper 2010-1, pp. 113-126.

Mathews, W.H., 1989. Neogene Chilcotin basalts in south-central British Columbia: geology, ages, and geomorphic history: Canadian Journal of Earth Sciences, 26, 969–982. doi: 10.1139/e89-078.

Mattinson, J.M., 2005. Zircon U-Pb chemical abrasion ("CA-TIMS") method: Combined annealing and multi-step partial dissolution analysis for improved precision and accuracy of zircon ages. Chemical Geology, 220, 47-66.

McMechan, R.D., 1983. Geology of the Princeton Basin. BC Ministry of Energy, Mines, and Petroleum Resources, British Columbia Geological Survey, Paper 1983-3, 52 p.

Mihalynuk, M.G., Nelson, J., and Diakow, L.J., 1994. Cache Creek Terrane entrapment: Oroclinal paradox within the Canadian Cordillera. Tectonics, 13, 575–595.

Mihalynuk, M.G., Mountjoy, K.J., Smith, M.T., Currie, L.D., Gabites, J.E., Tipper, H.W., Orchard, M.J., Poulton, T.P., and Cordey, F., 1999. Geology and mineral resources of the Tagish Lake area (NTS 104M/ 8,9,10E, 15 and 104N/ 12W), northwestern British Columbia. B C Ministry of Energy and Mines, 217 p.

Mihalynuk, M., Erdmer, P., Ghent, E.D., Cordey, F., Archibald, D.A., Friedman, R.M., and Johannson, G.G., 2004. Coherent French Range blueschist: Subduction to exhumation in < 2.5 m.y.?. Geological Society of America Bulletin, 116, 910-922.

Mihalynuk, M.G., Friedman, R.M., Gabites, J.E., and Logan, J.M., 2014b. Southern Nicola Arc Project 2013: Geochronological data. BC Ministry of Energy and Mines, British Columbia Geological Survey, Geofile 2014-3.

Mihalynuk, M.G., and Ghent, E.D., 1996. Regional depth-controlled hydrothermal metamorphism in the Zymoetz River area, British Columbia. Canadian Journal of Earth Sciences, 33, 1169-1184.

Mihalynuk, M.G., and Logan, J.M., 2013a. Geological setting of Late Triassic Cu-Au porphyry mineralization at Miner Mountain, Princeton. In: Geological Fieldwork 2012, BC Ministry of Energy, Mines and Natural Gas, British Columbia Geological Survey, Paper 2013-1, pp. 81-96.

Mihalynuk, M.G., and Logan, J.M., 2013b. Geological setting of Late Triassic Cu-Au porphyry mineralization at the Dillard-Primer prospects near Merritt, In: Geological Fieldwork 2012, BC Ministry of Energy, Mines and Natural Gas, British Columbia Geological Survey, Paper 2013-1, pp. 97-114.

Mihalynuk, M.G., and Logan, J.M., 2013c. Lithogeochemical data from porphyry environments between Princeton and Merritt: BC Ministry of Energy, Mines and Natural Gas, British Columbia Geological Survey, Geofile 2013-05.

Mihalynuk, M.G., Logan, J.M., and Diakow, L.D., 2014a, Southern Nicola Arc Project 2013: Geochemical data. BC Ministry of Energy and Mines, British Columbia Geological Survey, Geofile 2014-2.

Monger, J.W.H., and Ross, C.A., 1971. Distribution of fusulinaceans in the western Canadian Cordillera. Canadian Journal of Earth Sciences, 8, 259–278.

Monger, J.W.H., Souther, J.G., and Gabrielse, H., 1972. Evolution of the Canadian Cordillera: a plate-tectonic model. American Journal of Science, 272, 577–602.

Monger, J.W.H., 1977. Upper Paleozoic rocks of the western Canadian Cordillera and their bearing on Cordilleran evolution. Canadian Journal of Earth Sciences 14, 1832–1859.

Monger, J.W.H., 1989. Geology, Hope, British Columbia. Geological Survey of Canada, Map 41-1989, sheet 1, scale 1:250 000.

Moss, P.T., Greenwood, D.R., and Archibald, S.B., 2005. Regional and local vegetation community dynamics of the Eocene Okanagan Highlands (British Columbia – Washington State) from palynology. Canadian Journal of Earth Sciences, 42, 187–204. doi: 10.1139/e04-095.

Mundil, R., Ludwig, K. R., Metcalfe, I., and Renne, P. R., 2004. Age and timing of the Permian Mass Extinctions: U/Pb Dating of Closed-System Zircons. Science, 305, 1760-1763.

Nixon, G.T., Archibald, D.A., and Heaman, L.M., 1993, ^{40}Ar-^{39}Ar and U-Pb geochronometry of the Polaris alaskan-type complex, British Columbia; precise timing of Quesnellia-North America interaction. Geological Association of Canada, Mineralogical Association of Canada; Program with Abstracts 76.

Parrish, R.R., and Monger, J.W.H., 1992. New U-Pb dates from southwestern British Columbia: Radiogenic age and isotopic studies. Report 5, 87-108.

Patton, C., Hellstrom, J., Paul, B., Woodhead, J. Hergt, J., 2011. Iolite: freeware for the visualization and processing of mass spectrometry data. Journal of Analytical Atomic Spectroscopy, 26, 2508-2518.

Pearce, J.A., Harris, N.B.W., Tindle, A.G., 1984. Trace element discrimination diagrams for the tectonic interpretation of granitic rocks. J. Petrol. 25, 956–983.

Preto, V.A., 1979. Geology of the Nicola Group between Merritt and Princeton: BC Ministry of Energy, Mines and Petroleum Resources, British Columbia Geological Survey, Bulletin 69, 90 p.

Ray, G.E., and Dawson, G.L., 1994, The geology and mineral deposits of the Hedley gold skarn district, southern British Columbia: British Columbia Ministry of Energy, Mines and Petroleum Resources, British Columbia Geological Survey, Bulletin 87, 156 p.

Read, P.B., and Okulitch, A.V., 1977. The Triassic unconformity of South-central British Columbia. Canadian Journal of Earth Sciences, 14, 606-638.

Rice, H.M.A., 1960. Geology and mineral deposits of the Princeton map area, British Columbia. Geological Survey of Canada, Memoir 243, 136 p.

Ricketts, B.D., Evenchick, C.A., Anderson, R.G., and Murphy, D.C., 1992. Bowser Basin, northern British Columbia; constraints on the timing of initial subsidence and Stikinia-North America Terrane interactions. Geology, 20, 1119-1122.

Russell, L.S., 1935. A middle Eocene mammal from British Columbia. American Journal of Science, 29, 54-55.

Schiarizza, P., Bell, K., and Bayliss, S., 2009. Geology and mineral occurrences of the Murphy Lake area, south-central British Columbia (NTS 093A/03). In: Geological Fieldwork 2008, British Columbia Ministry of Energy, Mines and Petroleum Resources, British Columbia Geological Survey, Paper 2009-1, pp.169-188.

Scoates, J.S., and Friedman, R. M., 2008. Precise age of the platinuferous Merensky Reef, Bushveld Complex, South Africa, by the U-Pb ID-TIMS chemical abrasion ID-TIMS technique. Economic Geology, 103, 465-471.

Schmitz, M. D., and Schoene, B., 2007. Derivation of isotope ratios, errors, and error correlations for U-Pb geochronology using 205Pb-235U-(233U)-spiked isotope dilution thermal ionization mass spectrometric data. Geochemistry, Geophysics, Geosystems, 8, Q08006, doi:10.1029/2006GC001492.

Sigloch, K., Mihalynuk, M.G., 2013. Intra-oceanic subduction shaped the assembly of Cordilleran North America. Nature 496, 50–56.

Sláma, J., Košler, J., Condon, D.J., Crowley, J.L., Gerdes, A., Hanchar, J.M., Horstwood, M.S.A., Morris, G.A., Nasdala, L., Norberg, N., Schaltegger, U., Xchoene, B., Tubrett, M.N., and Whitehouse, M.J., 2007. Plešovice zircon — A new natural reference material for U–Pb and Hf isotopic microanalysis. Chemical Geology, 249, 1-35.

Stacey, J.S., and Kramers, J.D., 1975. Approximation of terrestrial lead isotopic evolution by a two-stage model. Earth and Planetary Science Letters, 26, 207-221.

Stevenson, J.P., 2013. Sego Resources Reports Drill Results and Presents a 3D Video Overview of Results to Date. October 11 News Release, 3 p. http://www.segoresources.com/.

Sun, S.S., McDonough, W.F., 1989. Chemical and isotopic systematics of oceanic basalts; implications for mantle composition and processes. Magmat. Ocean Basins 42, 313–345.

Tempelman-Kluit, D.J., 1979. Transported cataclasite ophiolite and granodiorite in Yukon: evidence of arc-continent collision. Geological Survey of Canada, Paper 79-14, 27 p.

Tafti, R., Mortensen, J.K., Lang, J.R., Rebagliati, M., and Oliver, J.L., 2009. Jurassic U-Pb and Re-Os ages for newly discovered Xietongmen Cu-Au porphyry district, Tibet: Implications for metallogenic epochs in the southern Gangdese Belt. Economic Geology, 104, 127-136.

Thirlwall, M. F., 2000. Inter-laboratory and other errors in Pb isotope analyses investigated using a 207Pb-204Pb double spike. Chemical Geology, 163, 299-322.

Stevenson, J.P., 2013. Sego Resources Reports Drill Results and Presents a 3D Video Overview of Results to Date. October 11 News Release, 3 p. http://www.segoresources.com/.

Thorkelson, D.J., and Rouse, G.E., 1989. Revised stratigraphic nomenclature and age determinations for mid-Cretaceous volcanic rocks in southwestern British Columbia. Canadian Journal of Earth Sciences, 26, 2016-2031.

Tribe, S., 2005. Eocene paleo-physiography and drainage directions, southern Interior Plateau, British Columbia. Canadian Journal of Earth Sciences, 42, 215–230. doi: 10.1139/e04-062.

Whalen, J.B., Currie, K.L., Chappell, B.W., 1987. A-type granites: geochemical characteristics, discrimination and petrogenesis. Contrib. Mineral. Petrol. 95, 407–419.

U-Pb and Ar/Ar ages from the Bonaparte mine, southern British Columbia: Late Middle Jurassic Au ± Cu vein mineralization

Richard M. Friedman[1], Janet E. Gabites[1], and James M. Logan[2, a]

[1] Pacific Centre for Isotopic and Geochemical Research, Department of Earth, Ocean and Atmospheric Sciences, University of British Columbia, Vancouver, BC, V6T 1Z4
[2] British Columbia Geological Survey, Ministry of Energy and Mines, Victoria, BC, V8W 9N3
[a] corresponding author: Jim.Logan@gov.bc.ca

Recommended citation: Friedman, R.M., Gabites, J.E., and Logan, J.M., 2014. U-Pb and Ar/Ar ages from the Bonaparte mine, southern British Columbia: Late Middle Jurassic Au ± Cu vein mineralization. In: Geological Fieldwork 2013, British Columbia Ministry of Energy and Mines, British Columbia Geological Survey Paper 2014-1, pp. 59-66.

Abstract
An erosional window in the Miocene Chilcotin Group basalt blanket exposes deformed Jurassic monzodiorite and porphyritic quartz diorite on the Bonaparte Plateau, 38 km north of Kamloops. These plutonic rocks host at least eight separate, metre- to cm-wide Au-Cu quartz veins at the Bonaparte mine. Intrusion and mineralization appear to have coincided temporally and spatially with motion along a greenschist-grade, north-trending reverse (east side-up) shear zone. Based on its position along the Wildhorse-Takomkane intrusive belt, we previously assumed that the Bonaparte complex was ~ 195 Ma. However, new U-Pb zircon crystallization ages demonstrate that parts are significantly younger. These data indicate at least two magmatic events: Early Jurassic (~ 189 Ma) for the monzodiorite and Middle Jurassic (~ 166 Ma) for the quartz diorite. Hydrothermal muscovite associated with late stage copper-arsenopyrite-gold mineralization yields an ^{40}Ar/^{39}Ar cooling age of 160.4 ± 2.4 Ma linking mineralization to the ~ 166 Ma episode.

Keywords: Zircon crystallization ages, ^{40}Ar/^{39}Ar cooling ages, calcalkaline diorite porphyries, gold quartz veins, chalcopyrite, quartz stockwork, potassic, synkinematic alteration and mineralization, Middle Jurassic

---

1. Introduction

The Bonaparte gold mine (WestKam Gold Corporation) is approximately 38 km north of Kamloops, B.C., straddling map sheets 92I/16W & 92P/1W, at about 51° 02’ N and 128° 28’ W (Fig. 1). Mineralization at Bonaparte includes intrusion-hosted Au-Cu quartz veins and W-Mo quartz stockworks (Figs. 1, 2; MINFILE 92I-50; Peatfield, 1986; Durfeld, 1980; Logan and Mihalynuk, 2013). Lacking geochronologic control, Logan and Mihalynuk (2013) assumed that the Bonaparte intrusive complex was Jurassic, based on its position in the Wildhorse-Takomkane magmatic belt of Breitsprecher et al. (2010) and Anderson et al. (2010; Fig. 2). To test this correlation, we collected samples of quartz diorite and monzodiorite for U-Pb zircon geochronology, and a sample of sericite-altered intrusion associated with quartz-carbonate veins and gold mineralization for Ar^{40}-Ar^{39} analysis. Results presented herein demonstrate that magmatism (~ 189 Ma monzodiorite and ~ 166 Ma quartz diorite) and mineralization (~ 160 Ma) are significantly younger than in the Wildhorse-Takomkane magmatic belt, precluding correlation. Mineralization at Bonaparte appears to be related to emplacement of ~ 166 Ma quartz diorite.

2. Regional setting

As described by Logan and Mihalynuk (2013), the oldest rocks at the Bonaparte property include a succession of rusty-weathering, graphitic, and siliceous sedimentary rocks of uncertain age. This succession has been correlated with the Carboniferous to Permian Harper Ranch Group (Massey et al., 2005) which, at this latitude, is basement to Mesozoic volcanic and sedimentary rocks of Quesnel terrane (Fig. 2). The Harper Ranch Group rocks were hornfelsed during emplacement of a composite quartz diorite to monzodiorite porphyritic intrusion

Fig. 1. Bonaparte gold property (red), straddles the boundary between 92I and 92P map sheets (black), near the eastern edge of Quesnel terrane (transparent green overlay). Selected locations of Early Jurassic magmatism: Mount Milligan, porphyry Cu-Au mine; and Cariboo Gold District, gold placer and vein deposits.

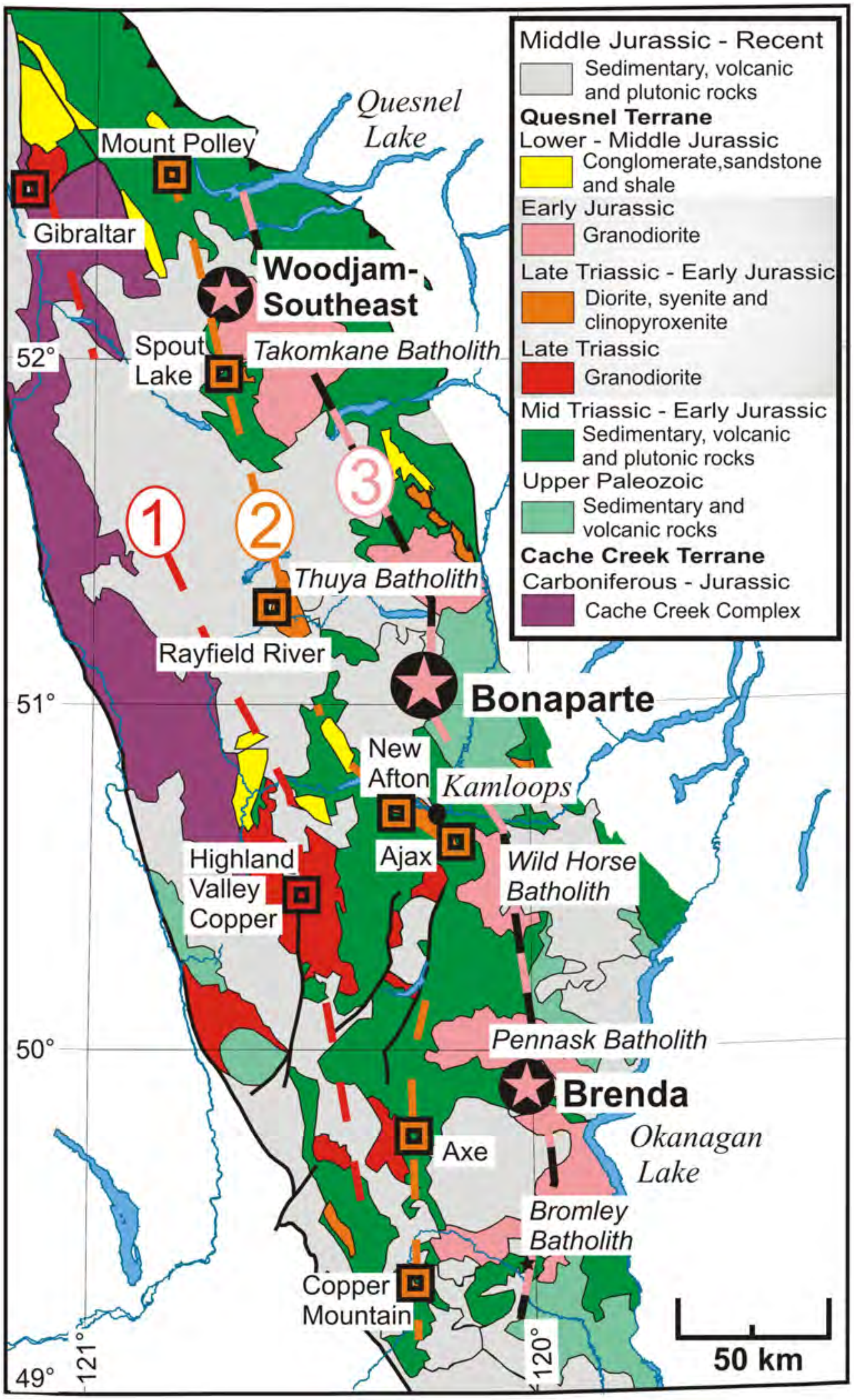

Fig. 2. Generalized geology of southern Quesnellia and Cu-Mo±Au deposits. Mesozoic arc plutons align along the length of southern Quesnellia to define three, north-trending, temporally distinct belts that get younger to the east: 1) Late Triassic; 2) Late Triassic – Early Jurassic; and 3) Early Jurassic. Discrete porphyry copper mineralizing events are directly linked to each of these magmatic episodes. The Bonaparte deposit lies in the tract of Early Jurassic plutons (Wildhorse-Takomkane plutonic suite) midway between the Brenda and Woodjam-Southeast deposits (modified after Massey et al., 2005).

and dike complex, which is mineralized. These intrusive rocks have been correlated with the Early Jurassic Eakin Creek suite of the Late Triassic to Middle Jurassic Thuya batholith (Schiarizza and Israel, 2001; Anderson et al., 2010), which is part of the regional Early Jurassic Wildhorse-Takomkane plutonic suite. Harper Ranch rocks are exposed as inliers near the southeastern margin of an extensive sheet of Chilcotin Group flood basalts (Miocene) that form much of the Bonaparte Plateau.

3. Property geology

The country rock consists of dark, rusty-weathering, polydeformed argillaceous sedimentary rocks of the Harper Ranch Group. At least three discrete intrusive phases are exposed at the "Discovery Zone": brown quartz diorite, monzodiorite and aplite. All are overprinted by late hydrothermal quartz and quartz-carbonate veins (Fig. 3 in Logan and Mihalynuk, 2013). The quartz diorite is the most intensely foliated, lineated, and altered whereas the monzodiorite is moderately foliated to unfoliated and typically moderately to weakly altered. Aplitic dykes cut both earlier phases and are unfoliated. Based on field relationships Logan and Mihalynuk (2013) interpreted that the quartz diorite is older than the monzodiorite. However, the ages reported herein indicate the reverse.

4. Sample descriptions

To better constrain the timing of the main intrusive phases, we analyzed zircons derived from weakly altered monzodiorite and pervasively biotite-altered quartz diorite porphyry. To estimate the time of mineralization, we analyzed muscovite from alteration zones enveloping mineralized quartz stockworks that cut leucocratic quartz monzonite.

4.1. Monzodiorite, sample 12JLO50-31

A 20 kg sample (12JLO50-31) was collected from a surface trench (Zone 10, UTM 679385E, 5653616N, NAD 83) on the Flicker vein (Fig. 3, Logan and Mihalynuk, 2013). The rock is a weakly propylitically altered, holocrystalline biotite-hornblende monzodiorite (Fig. 3) and is typically medium grained. Quartz comprises ~ 20% of the rock, locally as rounded quartz eyes and matrix. Hornblende and K-feldspar occur as sparse, outsized crystals up to 1 cm long. Up to 10% of the rock is biotite, both as euhedral books and replacements of hornblende. Zircon separated from the monzodiorite yielded clear, colourless, euhedral stubby zircon prisms approximately 200 μM long.

4.2. Quartz diorite, sample 12JLO50-38

A 20 kg sample of quartz diorite (12JLO50-38) was collected from the Bonaparte trench (Zone 10, UTM 679121E, 5653664N, NAD 83) at the south end of the Crow central vein (Fig. 4, Logan and Mihalynuk, 2013). At this locale, the quartz diorite porphyry ("dark matrix porphyry" of Peatfield, 1986) is pervasively biotite-altered, well foliated and lineated, and hosts disseminated chalcopyrite (Fig. 4). Typically, the diorite is coarse grained and contains white plagioclase (35%),

Fig. 3. Sample 12JLO50-31. Medium-grained equigranular hornblende monzodiorite. Quartz veined and weakly altered to propylitic mineral assemblages of albite, chlorite, epidote ± pyrite.

Fig. 4. Sample 12JLO50-38. Strongly foliated and lineated biotite-altered quartz diorite porphyry. Mylonitic fabric is defined by laminae of biotite-quartz-sericite-carbonate and opaque minerals. Equant white grains are plagioclase porphyroclasts. View is down plunge to the east, perpendicular to the northerly trend of the quartz vein.

altered hornblende (5%), distinctive, sparse blue quartz eyes in a fine-grained matrix of prismatic hornblende (20%), and intra-crystalline plagioclase-feldspar ± quartz containing biotite, apatite, titanite, magnetite and pyrite. The quartz diorite yielded a population of euhedral stubby zircons similar in size and appearance to those from 12JLO50-31.

4.3. Muscovite-quartz-carbonate veins, sample 12JLO50-30x

A muscovite sample (12JLO50-30x) for Ar-Ar step-heating comes from the ore stockpile (Zone 10, 679197E, 5653695N, NAD 83), west of the decline portal (Fig. 3 in Logan and Mihalynuk, 2013). The muscovite forms sub-mm disseminated crystals in bleached, carbonate-sericite alteration envelopes to mineralized quartz stockworks cutting leucocratic quartz monzonite (Fig. 5). Carbonate ± pyrite introduced along fractures and quartz vein margins has altered and bleached the rock. Sparry calcite fills open spaces between euhedral quartz crystals and is locally accompanied by disseminated arsenopyrite ± gold, and perhaps, bismuth tellurides (Fig. 5 in Logan and Mihalynuk, 2013).

5. U-Pb and ^{40}Ar/^{39}Ar geochronology methods

Sample preparation and analytical work was done at the Pacific Centre for Isotopic and Geochemical Research of the Department of Earth, Ocean and Atmospheric Sciences, The University of British Columbia. Details of the mineral separation and analytical techniques are presented in Logan et al. (2007) and Scoates and Friedman (2008).

Zircon was separated from the quartz diorite and quartz monzodiorite samples using standard mineral separation techniques (crushing, grinding, wet shaker Wilfley table, heavy liquids, and magnetic separation), followed by hand picking. Chemically abraded single zircon grains were analyzed by U-Pb isotope dilution thermal ionization mass spectroscopy (U-Pb ID-TIMS, or simply CA-TIMS). Muscovite and sericite were separated from a leucocratic quartz monzonite phase of the Bonaparte stock and ^{40}Ar/^{39}Ar isotopic age determinations were obtained from muscovite by laser-induced step-heating.

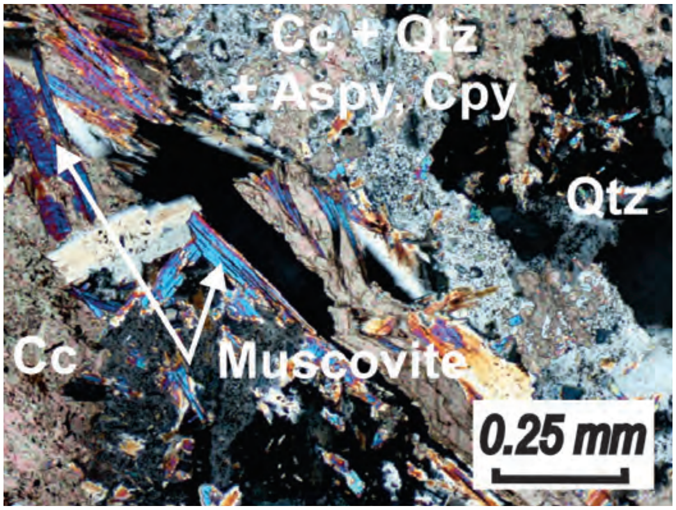

Fig. 5. Photomicrograph of mineralized quartz-carbonate-muscovite vein collected from stockpiled ore. Late-stage calcite and muscovite vein (~ 0.5 mm wide) cuts diagonally across silica- and carbonate-altered quartz diorite (cross polarized light). Disseminated fine needles of arsenopyrite and chalcopyrite are intergrown with calcite. Abbreviations: Qtz, quartz; Cc, calcite; Aspy, arsenopyrite; Cpy, chalcopyrite.

6. U-Pb geochronology results

U-Pb analyses of chemically abraded single zircon grains separated from the Bonaparte monzodiorite (n = 4) and from the quartz diorite porphyry (n = 4) are presented in Table 1 and illustrated in Figures 6 and 7.

6.1. Monzodiorite, sample 12JLO50-31

Of the four grains analyzed, two overlap concordia at the 2σ confidence level between 189 and 188 Ma, one lies between 190 and 189 Ma, and one is discordant, lying slightly off concordia at about 191 Ma (Fig. 6, Table 1). The best age estimate for the monzodiorite is from the 2 youngest grains; these give a mean ^{206}Pb/^{238}U age of 188.8 ± 0.02 Ma, which we take as the age of crystallization.

6.2. Quartz diorite, sample 12JLO50-38

All grains overlap concordia at the 2σ confidence level (Fig. 7, Table 1). Three grains lie between 166 and 165 Ma, and one is centered on 164 Ma. The best age estimate for the quartz diorite is from the three older grains; these give a mean weighted ^{206}Pb/^{238}U date of 165.9 ± 0.02 Ma, which is taken to be the age of crystallization.

7. ^{40}Ar/^{39}Ar cooling age, muscovite, sample 12JLO50-30x

Details of the analyses, including gas measurements

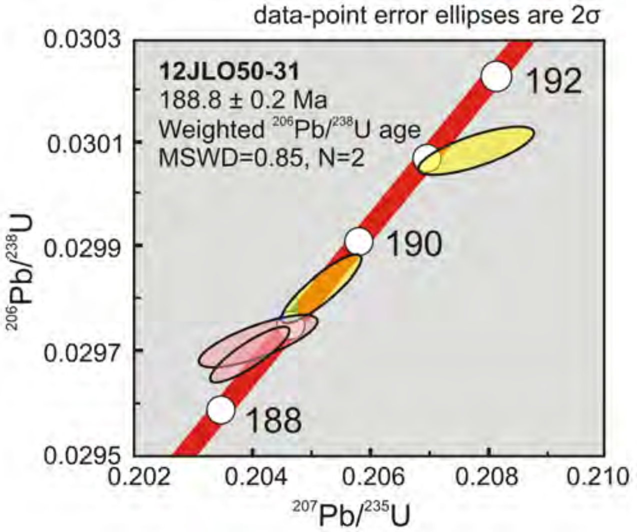

Fig. 6. Concordia plot for U-Pb TIMS data from single zircons, sample 12JLO50-31. Weighted age 188.8 ± 0.2 Ma based on ^{206}Pb/^{238}U ages of two youngest grains (pink ellipses). Concordia bands include 2 σ errors of U decay constants.

Table 1. U-Th-Pb thermal ionization mass spectrometry isotopic data for zircons from intrusive phases at the Bonaparte mine, central British Columbia.

	Compositional Parameters									Radiogenic Isotope Ratios								Isotopic Ages					
Sample	Wt. mg	U ppm	$\frac{Th}{U}$	Pb ppm	^{206}Pb* x10^{-13} mol	mol % ^{206}Pb*	$\frac{Pb^*}{Pb_c}$	Pb$_c$ (pg)	$\frac{^{206}Pb}{^{204}Pb}$	$\frac{^{208}Pb}{^{206}Pb}$	$\frac{^{207}Pb}{^{206}Pb}$	% err	$\frac{^{207}Pb}{^{235}U}$	% err	$\frac{^{206}Pb}{^{238}U}$	% err	corr. coef.	$\frac{^{207}Pb}{^{206}Pb}$	±	$\frac{^{207}Pb}{^{235}U}$	±	$\frac{^{206}Pb}{^{238}U}$	±
(a)	(b)	(c)	(d)	(c)	(e)	(e)	(e)	(e)	(f)	(g)	(g)	(h)	(g)	(h)	(g)	(h)		(i)	(h)	(i)	(h)	(i)	(h)
12JLO-50-31: monzodiorite																							
A	0.0032	316	0.217	9.1	1.2534	99.70%	94	0.31	6186	0.069	0.049788	0.185	0.203872	0.277	0.029698	0.141	0.796	185.10	4.32	188.40	0.48	188.66	0.26
B	0.0024	238	0.167	6.9	0.7149	99.35%	42	0.38	2859	0.053	0.050100	0.310	0.207813	0.380	0.030084	0.130	0.664	199.65	7.19	191.72	0.66	191.07	0.24
C	0.0037	312	0.131	8.8	1.4362	99.76%	114	0.28	7557	0.041	0.049875	0.179	0.205035	0.287	0.029816	0.171	0.812	189.18	4.16	189.38	0.50	189.39	0.32
D	0.0052	141	0.180	4.1	0.9091	99.44%	51	0.41	3326	0.057	0.049799	0.346	0.204105	0.415	0.029726	0.140	0.621	185.63	8.05	188.59	0.71	188.83	0.26
12JLO-50-38: quartz diorite																							
A	0.0041	256	0.152	6.5	1.1381	99.04%	28	0.91	1928	0.048	0.049312	0.373	0.177145	0.442	0.026054	0.172	0.562	162.71	8.72	165.60	0.67	165.80	0.28
B	0.0036	760	0.142	18.5	2.9364	99.79%	128	0.52	8619	0.045	0.049373	0.109	0.175204	0.192	0.025737	0.127	0.842	165.56	2.55	163.93	0.29	163.81	0.20
C	0.0032	198	0.088	4.9	0.6904	99.38%	43	0.36	2972	0.028	0.049327	0.570	0.177374	0.626	0.026080	0.138	0.501	163.39	13.31	165.80	0.96	165.97	0.23
D	0.0039	245	0.171	6.2	1.0359	99.38%	44	0.53	2978	0.054	0.049357	0.276	0.177189	0.403	0.026037	0.271	0.731	164.81	6.44	165.64	0.62	165.70	0.44

(a) A, B etc. are labels for fractions composed of single zircon grains or fragments; all fractions annealed and chemically abraded after Mattinson (2005) and Scoates and Friedman (2008).

(b) Nominal fraction weights estimated from photomicrographic grain dimensions, adjusted for partial dissolution during chemical abrasion.

(c) Nominal U and total Pb concentrations subject to uncertainty in photomicrographic estimation of weight and partial dissolution during chemical abrasion.

(d) Model Th/U ratio calculated from radiogenic ^{208}Pb/^{206}Pb ratio and ^{207}Pb/^{235}U age.

(e) Pb* and Pbc represent radiogenic and common Pb, respectively; mol %^{206}Pb* with respect to radiogenic, blank and initial common Pb.

(f) Measured ratio corrected for spike and fractionation only. Mass discrimination of 0.25%/ ± 0.03 per amu based on analysis of NBS-982; all Daly analyses.

(g) Corrected for fractionation, spike, and common Pb; up to 0.9 pg of common Pb was assumed to be procedural blank: ^{206}Pb/^{204}Pb = 18.50 ± 1.0%; ^{207}Pb/^{204}Pb = 15.50 ± 1.0%; ^{208}Pb/^{204}Pb = 38.40 ± 1.0% (all uncertainties 1-sigma). Excess over blank was assigned to initial common Pb with Stacey and Kramers (1975) model Pb composition at the interpreted age of the rock.

(h) Errors are 2-sigma, propagated using the algorithms of Schmitz and Schoene (2007) and Crowley et al. (2007).

(i) Calculations are based on the decay constants of Jaffey et al. (1971). ^{206}Pb/^{238}U and ^{207}Pb/^{206}Pb ages corrected for initial disequilibrium in ^{230}Th/^{238}U using Th/U [magma] = 3.

(j) Corrected for fractionation, spike, and blank Pb only.

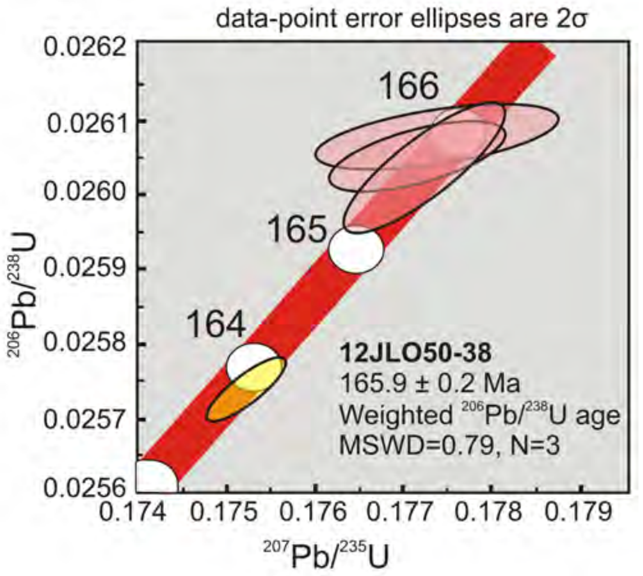

Fig. 7. Concordia plot for U-Pb TIMS data from single zircons, sample 12JLO50-38. Weighted age 165.9 ± 0.2 Ma based on ^{206}Pb/^{238}U ages of three grains (pink ellipses). Concordia bands include 2 σ errors of U decay constants.

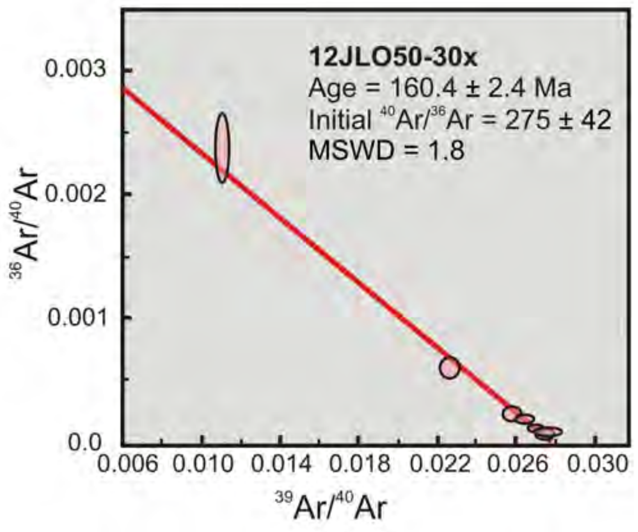

Fig. 8. Inverse isochron plot of step-heating ^{40}Ar/^{39}Ar analyses for muscovite sample 12JLO50-30x. 2 σ error ellipses for individual analytical fractions are pink. Age is 160.4 ± 2.4 Ma with an initial ^{40}Ar/^{36}Ar of 275 ± 42 Ma.

obtained during each of the heating steps are presented in Table 2. Initial data entry and calculations were carried out using the software ArArCalc (Koppers, 2002). The plateau and correlation ages were calculated using Isoplot 3.09 (Ludwig, 2003). Errors are quoted at the 2-sigma (95% confidence) level and are propagated from all sources except mass spectrometer sensitivity and age of the flux monitor. Muscovite separated from altered and mineralized leucocratic quartz monzonite yielded a complicated argon release spectra that fails to provide a good plateau cooling age. An inverse isochron plot using seven points yields a correlation age of 160.4 ± 2.4 Ma, an initial ^{40}Ar/^{39}Ar ratio of 275 ± 42 Ma and a MSWD of 1.18 (Fig. 8, Table 2).

8. Discussion

U-Pb zircon crystallization ages of the Bonaparte intrusions indicate at least two intrusive events, Early Jurassic (~ 189 Ma) and Middle Jurassic (~ 166 Ma). Both are too young to permit correlation with the ~ 195 Ma Wildhorse-Takomkane intrusive suites of Breitsprecher et al. (2010). The biotite-hornblende quartz monzodiorite (sample 12JLO50-31) is ~ 30 m.y. older than the Middle Jurassic porphyritic hornblende quartz diorite (sample 12JLO50-38), which was initially considered the oldest phase in the surface working (Logan and Mihalynuk, 2013).

Early Jurassic intrusive ages similar to the quartz monzonite are known from northern Quesnel terrane at the Mount Milligan porphyry Cu-Au deposit (Jago et al., in press). At Mount Milligan, mineralization is associated with feldspar-pyroxene porphyritic monzonite stocks such as Southern Star (182.6 + 4.3/- 0.6 Ma), Heidi Lake (183.0 ± 3 Ma) and North Slope (189.0 + 3.3/- 1.0 Ma) and late syn-mineral plagioclase + hornblende porphyritic monzonite dikes (Ghosh, 1992; Mortensen et al., 2005). At Bonaparte however, the biotite-hornblende monzodiorite (~ 189 Ma) is unlikely the cause of mineralization, but rather a host to the younger Middle Jurassic magmatism and associated hydrothermal gold-copper mineralization (~ 160 Ma).

Approximately 200 km north of Bonaparte, Rhys et al. (2009) and Mortensen et al. (2011) reported Jurassic ages for magmatism and mineralization in the Cariboo gold district (Fig. 1), an area that produced 80-97 tonnes of placer gold (Levson and Giles, 1993), roughly half of the total historical gold production in British Columbia. In the Cariboo gold district, at least two stages of quartz veins are known; an early, poorly mineralized and deformed set are cut by later Au-bearing quartz-carbonate-pyritic veins. Laser ablation ICP-MS, zircon crystallization ages from plagioclase ± quartz ± hornblende porphyritic sills and dikes at the Spanish Mountain gold deposit yielded ages of 185.6 ± 1.5 to 187 ± 0.8 Ma. The intrusions are deformed and overprinted by late carbonate-fuchsite alteration that is associated with the main mineralization (Rhys et al., 2009). ^{40}Ar/^{39}Ar geochronology from the Spanish Mountain veins (161-150 Ma) indicates that the mineralization is at least 25 m.y. younger than the intrusions, precluding a direct genetic relationship between the intrusions and mineralization (Mortensen et al., 2011). Similarly, the ^{40}Ar/^{39}Ar cooling age (~ 160 Ma) of hydrothermal muscovite in the alteration assemblage to vein mineralization at Bonaparte is too young to relate mineralization to intrusion of the ~ 189 Ma quartz monazite. However ages from the quartz diorite porphyry (~ 166 Ma) imply a link between Au-Cu mineralization and Middle Jurassic intrusion at Bonaparte.

Post-accretion Middle Jurassic plutons in central Quesnellia include the Quesnel River leucogranite (165-158 Ma), Gavin

Table 2. ^{40}Ar/^{39}Ar step heating gas release data from sample 12JLO50-30x, a muscovite separate from sericite alteration selvage.

12JLO50-30x Laser Power (%)	Muscovite Isotope Ratios ^{40}Ar/^{39}Ar	1σ	^{37}Ar/^{39}Ar	1σ	^{36}Ar/^{39}Ar	1σ	R.I.	%^{40}Ar atm	f ^{39}Ar	^{40}Ar*/^{39}ArK	Age	2σ
2.30	90.19	± 1.18	0.031	± 0.45	0.214	± 0.010	0.0332	70.04	0.58	27.023	122.10	± 26.58
2.60	38.71	± 0.27	0.004	± 0.06	0.008	± 0.001	0.0041	6.54	8.96	36.178	161.67	± 3.16
2.90	32.74	± 0.21	0.002	± 0.03	0.002	± 0.000	0.0109	1.80	39.71	32.153	144.38	± 1.87
3.10	36.35	± 0.24	0.004	± 0.05	0.002	± 0.001	0.0014	1.60	13.56	35.772	159.93	± 2.58
3.40	36.16	± 0.37	0.007	± 0.09	0.003	± 0.001	0.0026	2.17	13.51	35.373	158.22	± 3.39
3.80	36.98	± 0.21	0.012	± 0.17	0.004	± 0.000	0.0042	3.06	8.24	35.854	160.28	± 2.07
4.80	37.74	± 0.25	0.001	± 0.01	0.007	± 0.001	0.0103	5.19	9.90	35.783	159.98	± 2.50
5.80	44.10	± 0.40	0.003	± 0.04	0.026	± 0.002	0.0051	17.53	5.52	36.371	162.49	± 4.72
Total/Average	36.99	±0.098	0.002	±0.011	0.003	± 0.002			100.00	34.826		

J = 0.0025850 ± 0.0000129

Volume ^{39}ArK = 0.083

Integrated Date = 155.92 ± 0.97 Ma

Plateau age = no plateau

Inverse isochron (correlation age) results, plateau steps: Model 1 Solution (±95%-conf.) on 7 points

Age = 160.4 ± 2.4 Ma, Initial ^{40}Ar/^{36}Ar =275 ± 42

MSWD = 1.8, Probability = 0.11

Lake porphyritic quartz monzonite (162-160 Ma), Bonaparte Lake granite (164-161 Ma) and in the south, the Osprey Lake batholith (~ 166 Ma). These plutons are locally associated with minor Cu-Au-Mo mineralization (Logan et al., 2007; Logan and Moynihan, 2009) but are generally assumed to be poorly mineralized relative to the Late Triassic and Early Jurassic plutons of Quesnel terrane (Anderson et al., 2010). Geochronologic data presented herein indicate that intrusion-related Au-Cu vein mineralization did form at ~ 160 Ma in this part of Quesnel terrane.

9. Summary and conclusions

Shear-hosted gold-chalcopyrite quartz veins at Bonaparte have produced ~ 103 kg of gold or 25.58 g/t Au from the total 4,064 tonnes shipped (Beaton, 2011). The hypothesis that Bonaparte mineralization is Early Jurassic and analogous to the Brenda Cu-Mo and/or Woodjam Au, Cu-Mo porphyry deposits has been falsified by our geochronologic data. U-Pb zircon crystallization ages for the Bonaparte intrusions indicate at least two separate ages of intrusive activity; Early Jurassic (~ 189 Ma) and Middle Jurassic (~ 166 Ma), and that monzodiorite is the oldest plutonic phase, not quartz diorite as previously suggested (Logan and Mihalynuk, 2013). Muscovite from quartz-carbonate-sericite alteration associated with late-stage copper-arsenopyrite-gold mineralization yielded a cooling age of 160.4 ± 2.42 Ma, linking the bulk of mineralization to the younger, Middle Jurassic episode of magmatism. Both intrusions are younger than the ~ 195 Ma Wildhorse-Takomkane intrusive suite, ruling out correlation.

References cited

Anderson, R.G., Schiarizza, P., Andrews, G., Breitsprecher, K., Davis, W., Dunne, C.E., Plouffe, A., and Thomas, M.D., 2010. Bedrock, surficial, geophysical and geochemical mapping reveals exploration targets in the Thuya batholith, southern Nicola arc. In: Geological Association of Canada, Targeted Geoscience Initiative 3 Workshop, March 2010, Vancouver, 52-57. URL accessed November, 2012, http://www.gac-cs.ca/workshops/TGI3/abstracts/GAC_TGI3_workshop_abstracts.pdf.

Beaton, A.J., 2011. Bonaparte gold underground decline and surface trench bulk-sample project. British Columbia Ministry of Energy, Mines and Petroleum Resources, Assessment report #32,930, 382 p.

Breitsprecher, K., Weis, D., Scoates, J.S., and Anderson, R.G., 2010. Targeting mineralized Late Triassic to Early Jurassic plutons in the Nicola arc, southern Quesnel terrane, Canadian Cordillera. In: Geological Association of Canada, Targeted Geoscience Initiative 3 Workshop, Vancouver, 49-51. URL accessed November, 2012, http://www.gac-cs.ca/workshops/TGI3/abstracts/GAC_TGI3_workshop_abstracts.pdf.

Crowley, J.L., Schoene, B., and Bowring, S.A., 2007. U-Pb dating of zircon in the Bishop Tuff at the millennial scale. Geology, 35, 1123-1126.

Durfeld, R., 1980. Geology report on the JS mineral claim. British Columbia Ministry of Energy, Mines and Petroleum Resources, Assessment report #8,500, 11 p.

Gerstenberger, H., and Haase, G., 1997. A highly effective emitter substance for mass spectrometric Pb isotopic ratio determinations. Chemical Geology, 136, 309-312.

Ghosh, D., 1992. Uranium-lead zircon geochronometry and isotope geochemistry. In: Copper-Gold porphyry systems of British Columbia: University of British Columbia, Mineral Deposits Research Unit, Annual Technical Report, Year One, July 1991-June 1992, 12.1-12.11.

Jaffey, A.H., Flynn, K.F., Glendenin, L.E., Bentley, W.C., and Essling, A.M., 1971. Precision measurement of half-lives and specific activities of ^{235}U and ^{238}U. Physical Review, C4, 1889–1906.

Jago, C.P., Tosdal, R.M., Cooke, D.R., and Harris, A.C., in press.

Vertical and lateral variation of mineralogy and chemistry in the Early Jurassic Mt. Milligan alkalic porphyry Au-Cu deposit, British Columbia, Canada. Economic Geology, 108.

Koppers, Anthony A.P., 2002. ArArCALC – software for $^{40}Ar/^{39}Ar$ age calculations. Computers and Geosciences 28 (2002), 605-619.

Kuiper, K.F., Deino, A., Hilgen, F.J., Krijgsman, W., Renne, P.R., and Wijbrans, J.R., 2008. Synchronizing rock clocks of earth history. Science, 320, 500-504.

Leitch, C.H.B., 1988. A polished section and SEM study of Bi- and precious metal tellurides from the Discovery Zone, Bonaparte property. British Columbia Ministry of Energy, Mines and Petroleum Resources, Assessment report #17,206, 380 p.

Levson, V.M., and Giles, T.R., 1993. Geology of Tertiary and Quaternary gold-bearing placers in the Cariboo region, British Columbia (93A, B, G, H). British Columbia Ministry of Energy, Mines and Petroleum Resources, Bulletin 89, 202 p.

Logan, J.M., and Mihalynuk, M.G., 2013. Bonaparte gold: another 195 Ma Au-Cu porphyry deposit in southern British Columbia? In: Geological Fieldwork 2012, British Columbia Ministry of Energy, Mines and Natural Gas, British Columbia Geological Survey Paper 2013-1, 71-80.

Logan, J.M., and Moynihan, D.P., 2009. Geology and mineral occurrences of the Quesnel River map area, central British Columbia (NTS 093B/16). In: Geological Fieldwork 2008, British Columbia Ministry of Energy and Mines, British Columbia Geological Survey Paper 2009-1, 127-152.

Logan, J.M., Mihalynuk, M.G., Ullrich, T., and Friedman, R.M., 2007. U-Pb ages of intrusive rocks and $^{40}Ar/^{39}Ar$ plateau ages of copper-gold-silver mineralization associated with alkaline intrusive centres at Mount Polley and the Iron Mask Batholith, southern and central British Columbia. In: Geological Fieldwork 2006, British Columbia Ministry of Energy, Mines and Petroleum Resources, British Columbia Geological Survey Paper 2007-1, 93-116.

Logan, J.M., Mihalynuk, M.G., Friedman, R.M., and Creaser, R.A., 2011. Age constraints of mineralization at the Brenda and Woodjam Cu-Mo±Au porphyry deposits – an Early Jurassic calc-alkaline event, south-central British Columbia. In: Geological Fieldwork 2010, British Columbia Ministry of Forests, Mines and Lands, British Columbia Geological Survey Paper 2011-1, 129-144.

Ludwig, K.R., 2003. Isoplot 3.09: a geochronological toolkit for Microsoft Excel. Berkeley Geochronology Center Special Publication, 4, 70 p.

Massey, N.W.D., MacIntyre, D.G., Desjardins, P.J., and Cooney, R.T., 2005. Digital geology map of British Columbia: whole province. British Columbia Ministry of Energy, Mines and Petroleum Resources, GeoFile 2005-1.

Mattinson, J.M., 2005. Zircon U-Pb chemical abrasion ("CA-TIMS") method: combined annealing and multi-step partial dissolution analysis for improved precision and accuracy of zircon ages. Chemical Geology, 220, 47–66.

Mortensen, J.K., Ghosh, D.K., and Ferri, F., 1995. U-Pb geochronology of intrusive rocks associated with copper-gold porphyry deposits in the Canadian Cordillera. In: Porphyry Deposits of the northwestern Cordillera of North America, Schroeter, T.G., ed., Canadian Institute of Mining, Metallurgy and Petroleum Special Volume 46, 142–158.

Mortensen, J.K., Rhys, D.A., and Ross, K., 2011. Investigations of orogenic gold deposits in the Cariboo gold district, east-central British Columbia (parts of NTS 093A, H): final report. In: Geoscience BC Summary of Activities 2010, Geoscience BC, Report 2011-1, 97–108.

Mundil, R., Ludwig, K.R., Metcalfe, I., and Renne, P.R., 2004. Age and timing of the Permian mass extinctions: U/Pb dating of closed-system zircons. Science, 305, 1760-1763.

Peatfield, G.R., 1986. Geology, rock and soil geochemistry, geophysics and diamond drilling on the Bob 1986 group (Bonaparte property). British Columbia Ministry of Energy, Mines and Petroleum Resources, Assessment report #15,166, 308 p.

Rhys, D.A., Mortensen, J.K., and Ross, K., 2009. Investigations of orogenic gold deposits in the Cariboo gold district, east-central British Columbia (parts of NTS 093A, H): progress report. In: Geoscience BC Summary of Activities 2008, Geoscience BC, Report 2009-1, 49–74.

Schiarizza, P., and Israel, S., 2001. Geology and mineral occurrences of the Nehalliston Plateau, south-central British Columbia (92P/7, 8, 9, 10). In: Geological Fieldwork 2000, British Columbia Ministry of Energy, Mines and Petroleum Resources, British Columbia Geological Survey Paper 2001-1, 1-30.

Scoates, J.S., and Friedman, R.M., 2008. Precise age of the platinumiferous Merensky Reef, Bushveld Complex, South Africa, by the U-Pb ID-TIMS chemical abrasion ID-TIMS technique. Economic Geology, 103, 465-471.

Schmitz, M.D., and Schoene, B., 2007. Derivation of isotope ratios, errors, and error correlations for U-Pb geochronology using ^{205}Pb-^{235}U-(^{233}U)-spiked isotope dilution thermal ionization mass spectrometric data. Geochemistry, Geophysics, Geosystems, 8, Q08006, doi:10.1029/2006GC001492.

Stacey, J.S., and Kramers, J.D., 1975. Approximation of terrestrial lead isotopic evolution by a two-stage model. Earth and Planetary Science Letters, 26, 207–221.

Thirlwall, M.F., 2000. Inter-laboratory and other errors in Pb isotope analyses investigated using a ^{207}Pb-^{204}Pb double spike. Chemical Geology, 163, 299-322.

Geology and physicochemical conditions of copper-gold mineralization at the Three Firs porphyry prospect, Woodjam district, south-central British Columbia

Shawn Vandekerkhove[1, a], Stephen M. Rowins[1, 2, b], and Stephen T. Johnston[1]

[1] School of Earth and Ocean Sciences, University of Victoria, Victoria, BC, V8P 5C2
[2] British Columbia Geological Survey, Ministry of Energy and Mines, Victoria, BC, V8W 9N3
[a] Department of Earth Sciences, University of Toronto, ON, M5S 3B1
[b] corresponding author: Stephen.Rowins@gov.bc.ca

Recommended citation: Vandekerkhove, S., Rowins, S.M., and Johnston, S.T., 2014. Geology and physicochemical conditions of copper-gold mineralization at the Three Firs porphyry prospect, Woodjam district, south-central British Columbia. In: Geological Fieldwork 2013, British Columbia Ministry of Energy and Mines, British Columbia Geological Survey Paper 2014-1, pp. 67-94.

Abstract

The Three Firs prospect is one of six Cu-Au properties in the newly discovered Woodjam porphyry Cu-Au district of south-central British Columbia. It is hosted in Late Triassic volcanic and volcaniclastic rocks of the Nicola Group that form part of the southern Quesnel terrane, approximately 50 km northeast of Williams Lake. Copper-gold mineralization is spatially associated with medium-K, calc-alkaline, sub-vertical dikes ranging from monzonite to quartz monzonite in composition. Eight stages of vein formation and hydrothermal alteration are identified, with five stages directly associated with Cu-Au mineralization. Early potassic alteration occurs with stage 1 magnetite veins (“M” veins) and stage 2 hornblende ± actinolite veins. Main-stage veins include sinuous quartz-chalcopyrite-pyrite ± hornblende ± magnetite veins (stage 3 “A” veins) and straight, sharp-edged quartz-chalcopyrite-pyrite ± sercite ± hornblende ± magnetite veins with distinct medial suture lines (stage 4 “B” veins). Stages 3 and 4 veins are associated with calc-potassic and phyllic alteration, which replaces the earlier potassic alteration. Main-stage 5 sulphide stringer veins and veinlets consist of chalcopyrite-pyrite ± quartz, and are analogous to “D” veins in other calc-alkaline porphyry systems. Native gold has been found in the alteration halos of these veins. Stage 6 veins are weakly mineralized with open space crustification textures including layers of comb-textured quartz-carbonate ± sphalerite ± chalcopyrite ± pyrite ± tetrahedrite. These veins represent a minor carbonate-base metal stage of mineralization. Stage 7 veins consist of quartz ± pyrite ± carbonate ± epidote ± chlorite ± tourmaline and they are related to zones of propylitic alteration. The youngest veins recognized (stage 8) are unrelated to mineralization and consist of irregular and bifurcating calcite-ankerite veins. Fluid inclusion microthermometry indicates that the main stages of Cu-Au mineralization formed from saline (35 to 50 equiv. wt.% NaCl) aqueous fluids at temperatures between 300 and 400° C and pressures ranging from 0.6 to 1.42 kbar, which correspond to 2 to 4.6 km depth assuming lithostatic conditions. This P-T-X window is optimal for depositing Cu and Au, and exploration should continue to focus on the Three Firs area and its immediate environs. The Three Firs system is probably too deep for shallow, high-grade epithermal-style Au (Ag) zones, but there is the possibility, suggested by Au solubility studies, for slight enrichment of Au in zones immediately above the current level of Cu-Au mineralization.

Keywords: Porphyry, copper, gold, fluid inclusions, Jurassic, Triassic, Nicola arc, epithermal

1. Introduction

Copper in British Columbia is mined primarily from porphyry Cu-Au deposits, which accounted for $1.5 billion in revenues, or 19% of the Province’s mining sector, in 2012 (PriceWaterhouseCooper, 2012). Gold in these porphyry deposits is recovered as a byproduct of copper mining. In 2012 it accounted for $275 million in revenues, or 4% of the mining sector. These porphyry Cu-Au deposits are hosted mainly in magmatic arc rocks of the Intermontane and Insular superterranes of the North American Cordillera (e.g., McMillan et al., 1996; Nelson et al., 2013). The focus of this paper is the newly discovered Three Firs porphyry prospect in the Woodjam porphyry Cu-Au district, approximately 50 km northeast of Williams Lake in south-central British Columbia (Fig. 1).

Three Firs was discovered by exploration drilling of a subsurface magnetic anomaly by Gold Fields Canada in the summer of 2012. The Woodjam district is in the Quesnel terrane, which forms part of the large Intermontane superterrane that hosts numerous porphyry Cu-Mo-Au deposits, including Highland Valley Copper, Copper Mountain, Mount Polley, and Gibraltar (Fig. 2). The district hosts several other porphyry prospects including Deerhorn, Spellbound, Takom, Megabuck, and the Southeast Zone (Blackwell et al., 2012a; Sherlock et al., 2013). It is unusual because it potentially hosts both calc-alkaline and alkalic styles of porphyry Cu-Au mineralization (e.g., Blackwell et al., 2012a; del Real et al., 2013; Sherlock et al., 2013). The potential alkalic porphyry Cu-Au deposits include Deerhorn and Megabuck, whereas the Southeast Zone, Spellbound, Takom and Three Firs are considered calc-alkaline systems (del Real et al., 2013; Sherlock et al., 2013).

Herein we document the mineralogy and morphology of the veins and attendant alteration that constitute the main stages of Cu-Au mineralization at the Three Firs prospect, based on graphical logs from diamond drill core, petrographic examination, whole-rock geochemical analyses, and reflectance spectroscopy. To quantify the physicochemical

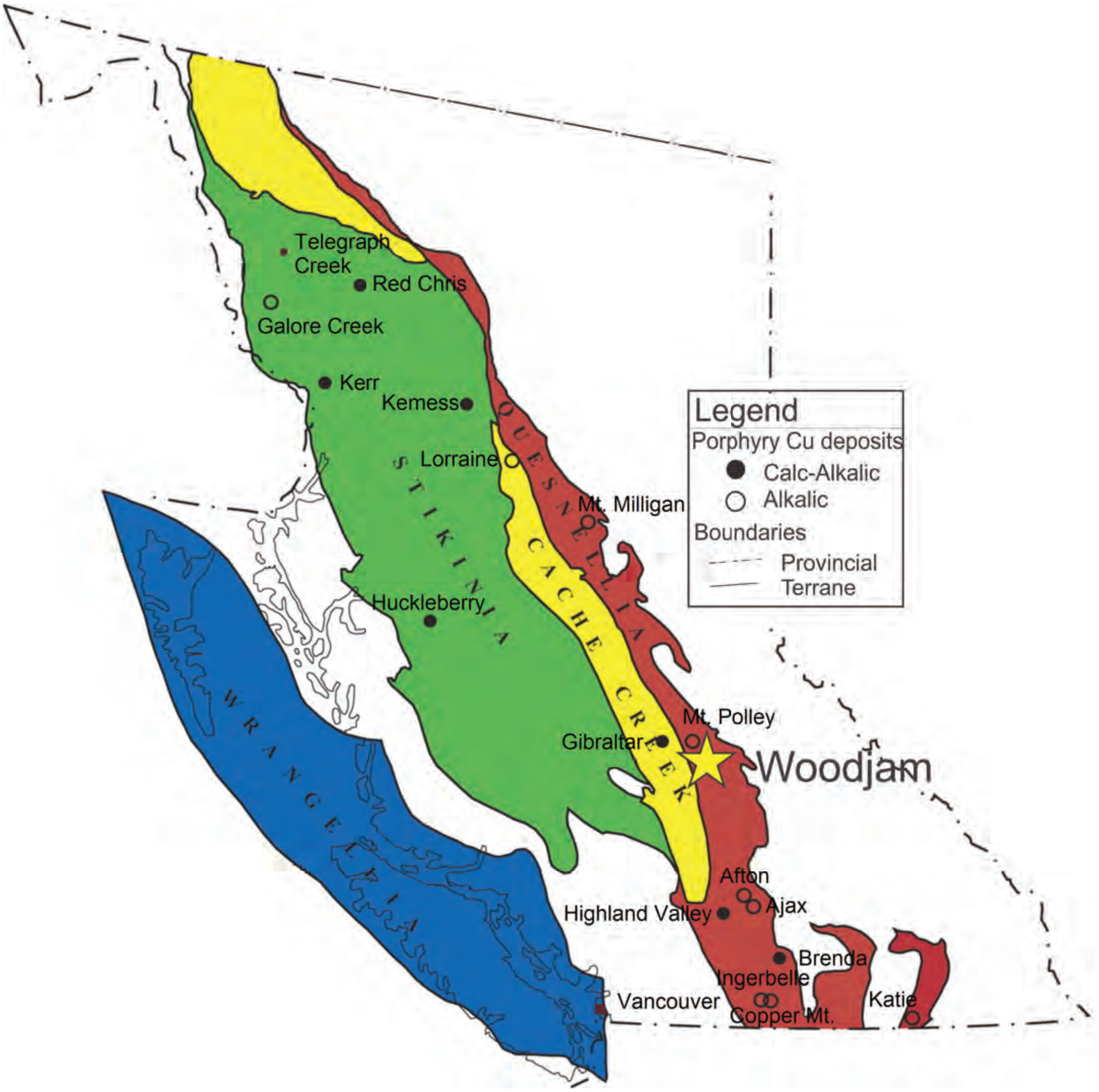

Fig. 1. Distribution of calc-alkaline and alkalic porphyry Cu±Mo±Au deposits and terranes with porphyry deposits in British Columbia.

conditions of the main Cu-Au mineralization event(s), we also present a microthermometric analysis of fluid inclusions in hydrothermal quartz from mineralized veins. Derived pressure, temperature, and fluid composition data can be useful vectors to undiscovered zones of mineralization. These data also permit a better evaluation of the ultimate ore potential (size and tonnage) of the magmatic-hydrothermal system.

We conclude that the Three Firs prospect is a Late Triassic-Early Jurassic calc-alkaline porphyry Cu-Au deposit that formed from saline (35 to 50 equivalent wt.% NaCl), aqueous brines depositing metals in quartz-chalcopyrite-bornite-pyrite veins at 300 to 400° C, and 0.6 to 1.42 kb (2 to 4.6 km depth, assuming lithostatic load). These physicochemical conditions are within the favourable pressure-temperature-compositional window for the formation of porphyry Cu-Au deposits (e.g., Hezarkhani et al., 1999).

2. Geological setting

The Canadian Cordillera consists of five major morphological belts that are aligned north to northwest, approximately parallel

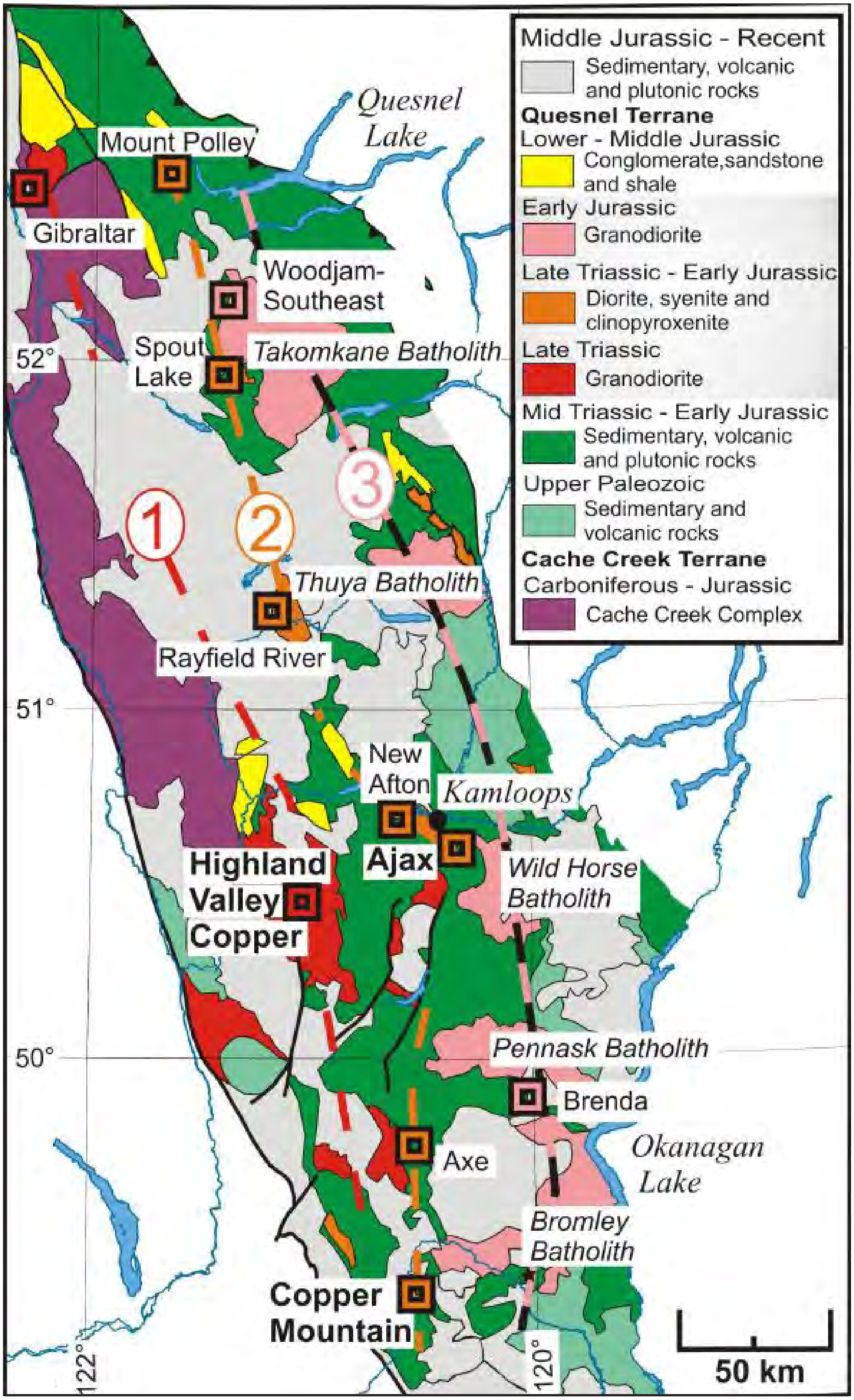

Fig. 2. Generalized geology of southern Quesnellia and porphyry Cu (Mo, Au) deposits. Mesozoic arc plutons align along the length of southern Quesnellia and define three north-trending, temporally distinct belts that young to the east: (1) Late Triassic; (2) Late Triassic – Early Jurassic; and (3) Early Jurassic. Discrete porphyry Cu (Mo, Au) mineralization events are linked directly to each of these magmatic episodes (after Logan, 2013).

to the margin of ancestral North America and the present-day coastline (Gabrielse and Yorath, 1991). From west to east they are the Insular, Coast, Intermontane, Omenica, and Foreland belts (Fig. 1). Porphyry-style mineralization in the Canadian Cordillera has a strong spatial correlation with the Intermontane and Insular superterranes, with the latter hosting most porphyry deposits (e.g., McMillan et al., 1995). Quesnel terrane, in the south-central part of the Intermontane superterrane, consists of upper Paleozoic and lower Mesozoic rocks. The Paleozoic components display oceanic and volcanic arc affinity and are unconformably overlain by Late Triassic and Early Jurassic island arc rocks of the Nicola and Takla groups (McMillan et al., 1995). Overlying the Early Jurassic volcanic arc rocks are lower to middle Jurassic siliciclastic rocks (Schiarizza et al., 2009).

Preto (1977) recognized two parallel, north-trending, magmatic belts in the southern part of Quesnellia. Plutonism in the western belt is calc-alkaline and related to porphyry Cu-Mo mineralization, whereas in the eastern belt it is alkaline and related to porphyry Cu-Au mineralization. Logan et al. (2011) expanded this model and proposed that the eastward migration of Mesozoic arc magmatism led to the growth of three temporally distinct, north-trending, plutonic belts. From west to east these are (Fig. 2): the Guichon Creek suite (212-208 Ma, Late Triassic); the Copper Mountain suite (206-200 Ma, Late Triassic-Early Jurassic); and the Takomkane suite (197-193 Ma, Early Jurassic). All three magmatic belts contain porphyry-style mineralization, with the middle Copper Mountain suite associated with alkalic porphyry Cu-Au deposits. The Woodjam porphyry, a sub-unit of the Takomkane batholith is 197 Ma, as reported in Logan et al. (2011). However, application of this model in the Woodjam district is potentially problematic if both calc-alkaline and alkalic styles of porphyry Cu-Au mineralization exist (e.g., Blackwell et al., 2012a; del Real et al., 2013; Sherlock et al., 2013) because it implies that the Late Triassic-Early Jurassic (Copper Mountain suite) and the Early Jurassic (Takomkane suite) magmatic belts overlapped in this part of the southern Nicola arc. This is inconsistent with an easterly migrating magmatic arc. Alternatively, additional work may reveal that the proposed alkalic prospects in the Woodjam camp (Deerhorn and Megabuck) are actually calc-alkaline porphyry Cu-Au systems that belong to the Early Jurassic Takomkane suite.

Regional 1: 100,000 scale geological mapping of the Three Firs area was carried out by Bailey et al. (1990) and more detailed maps were made by Panteleyev et al. (1996), Logan et al. (2007), and Blackwell et al. (2012a). The Three Firs prospect is hosted in volcaniclastic rocks of the Nicola Group (Triassic-Jurassic; Fig. 3). The Nicola Group is intruded by the Takomkane batholith (Late Triassic-Early Jurassic), which is exposed in the southeast part of the property. Volcanic units of the Nicola Group are pervasively hornfelsed adjacent to the Takomkane batholith, and commonly contain abundant metamorphic epidote and tourmaline. Late Miocene olivine-phyric basaltic flows of the Chilcotin Group overlie the Nicola Group immediately west of the Three Firs prospect (Fig. 3). Late Wisconsin glaciolacustrine and glaciofluvial sediments cover all but a small portion of the Woodjam property.

3. Recent exploration history

Copper-gold mineralization at Three Firs consists of fine-grained sulphide disseminations and quartz-sulphide veins containing mainly chalcopyrite and, locally, bornite. Native Au was observed in disseminated grains of chalcopyrite. Mineralized quartz vein stockworks are hosted primarily in volcanic and volcaniclastic units, monzonite dikes, and quartz monzonite dikes that intrude the host stratigraphy. Early (pre-mineralization) and late (syn- to post-mineralization) dikes are also recognized on the property.

A complete exploration history of the Woodjam district is given in Sherlock et al. (2013). Briefly, the Three Firs prospect is part of the Woodjam North claim, a property 49% owned by Consolidated Woodjam Copper Corporation (formerly the Woodjam Joint Venture, which is a 60:40 ownership agreement between Fjordland Exploration Inc. and Cariboo Rose Resources Ltd.) and 51% owned by Gold Fields Horsefly Exploration Corporation (Gold Fields) a member of the Gold Fields group of companies. The Woodjam district has been explored numerous times since the late 1800s by multiple companies with varying exploration objectives. The area became a true exploration play, however, with the discovery of the Southeast Zone in 2007 (Fig. 4). A ground geophysical program of IP chargeability, resistivity, and ground magnetics highlighted an anomalous IP chargeability response in a new area, now known as the Southeast Zone (Fig. 4). A drill hole to test this IP anomaly (07-79) graded 0.34% Cu, 0.05 g/t Au, and 0.014% Mo over 203.55 m, with the upper 113.8 m returning 0.40% Cu, 0.05 g/t Au and 0.014% Mo. Further drilling and geophysical surveys led to the discovery of the Deerhorn zone in 2008. In 2011 Gold Fields acquired the Three Firs area (previously called the Megalloy area) and did a soil geochemical survey in conjunction with an expanded IP chargeability and ground magnetic survey. Drilling a coincident IP chargeability and magnetic high in 2012 resulted in discovery of the Three Firs prospect. The third drill hole (MAG12-03) of the program returned 177 m grading 0.21% Cu and 0.14 g/t Au or 0.59 g/t Au equivalent (Fig. 5).

4. Geology of the Three Firs prospect

4.1. Methods

In August 2012, four diamond-drill holes, MAG12-02, MAG12-03, MAG12-04 and MAG12-05 were logged at one-metre intervals. Core logging focused on determining: 1) alteration styles; 2) vein types, orientations, and mineral assemblages; and 3) lithological units and contacts. Core logs and accompanying 43-element assay results including Au, Cu, and As, collected previously at regular sample intervals along the length of the core, were then matched. The resultant graphical core logs were used to construct a factual geological cross-section across the Three Firs prospect. We collected 37 HQ diamond drill core samples representing the types of mineralization, veins, and rock types from all four of the MAG series drill holes. We paid particular attention to samples exhibiting crosscutting relationships that could constrain hydrothermal fluid events related to metal deposition and vein paragenesis. Thin section off-cuts were stained with sodium cobalt nitrate acid to distinguish between potassium feldspar, plagioclase, and quartz. Polished thin sections were examined to identify minerals, point count modal abundances, establish

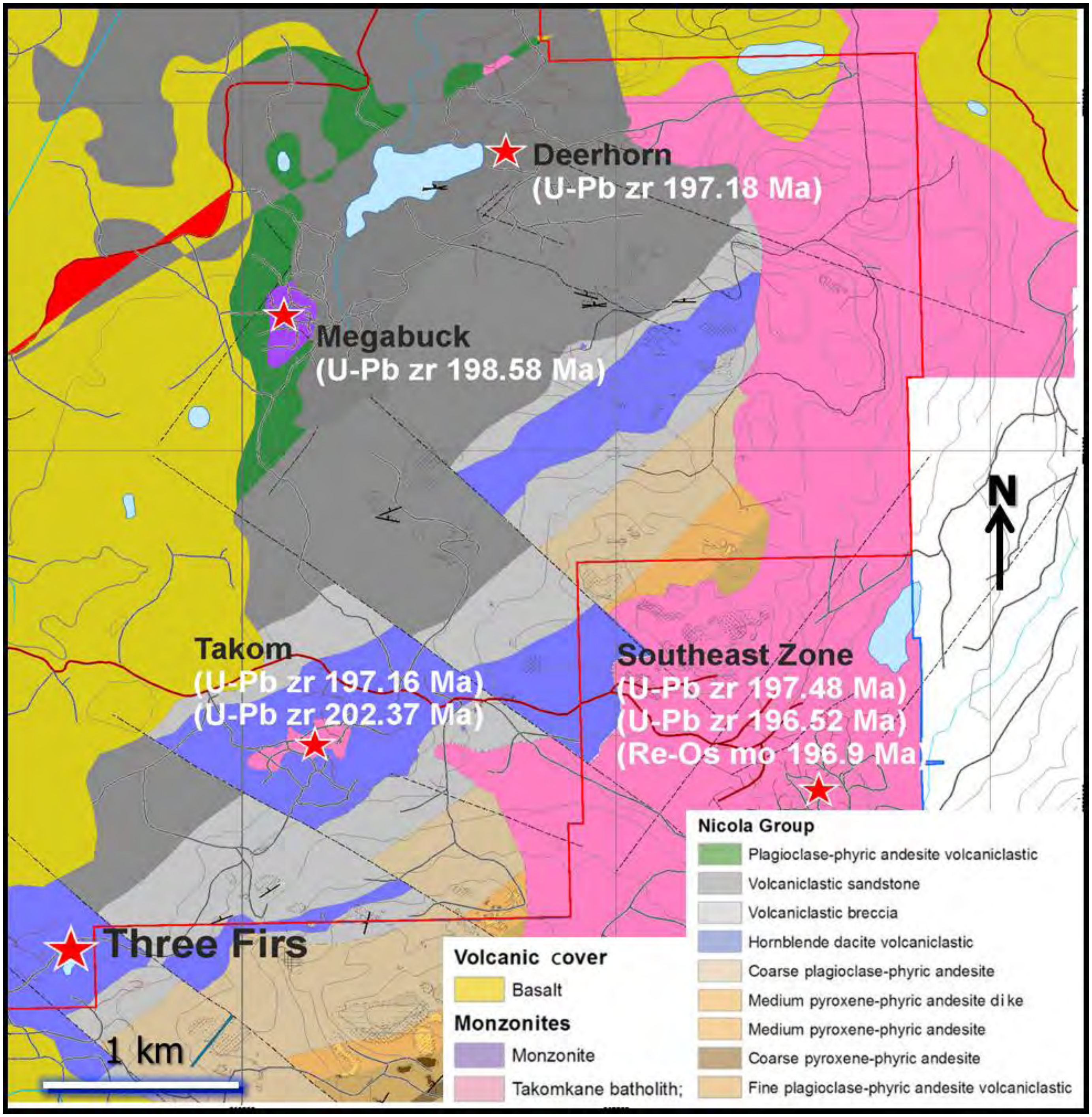

Fig. 3. Local geology of the Three Firs prospect (after Blackwell et al., 2012a; del Real et al., 2013). Geochronology from Schiarizza et al. (2009), Logan et al. (2011) and Blackwell et al. (2012a, and references therein).

textures, and document mineral paragenesis.

4.2. Overview

Volcanic and volcaniclastic rocks of the Nicola Group (~ 204 Ma; Figs. 6, 7) are oriented approximately 214° / 30° (Logan et al., 2011). The base of the Nicola section is defined by coarse-grained plagioclase-phyric andesite. At the top of this unit, a hyaloclastic bed in contact with volcanic sandstones displays pepperite structures indicating that the section is right way up, as suggested by regional mapping (Bailey et al., 1990). The Nicola Group is cut by the ~ 197 Ma Takomkane batholith (Schiarizza et al., 2009; Logan et al., 2011) that outcrops to the east (Fig. 3). Several quartz-biotite monzonite, quartz monzonite, and monzonite dikes intrude the Nicola Group and are spatially associated with the best zones of mineralization. The orientation of the dikes suggests emplacement approximately perpendicular to stratigraphy, similar to that at the Megabuck Cu-Au porphyry prospect (Sherlock et al., 2013).

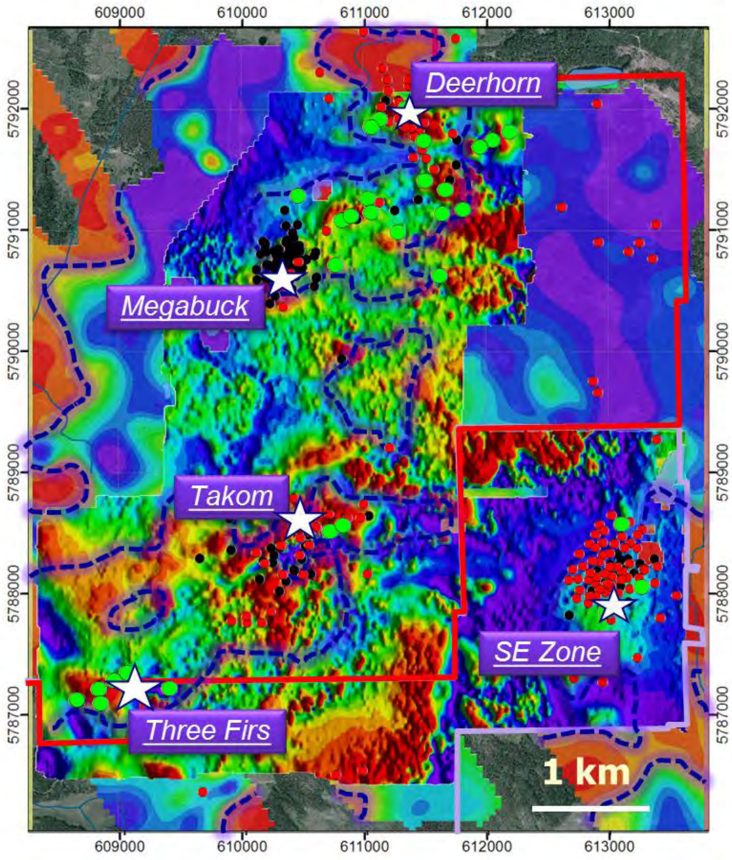

Fig. 4. Ground magnetic image of the Woodjam North property, modified from Sherlock (2013). UTM Zone 10, NAD83.

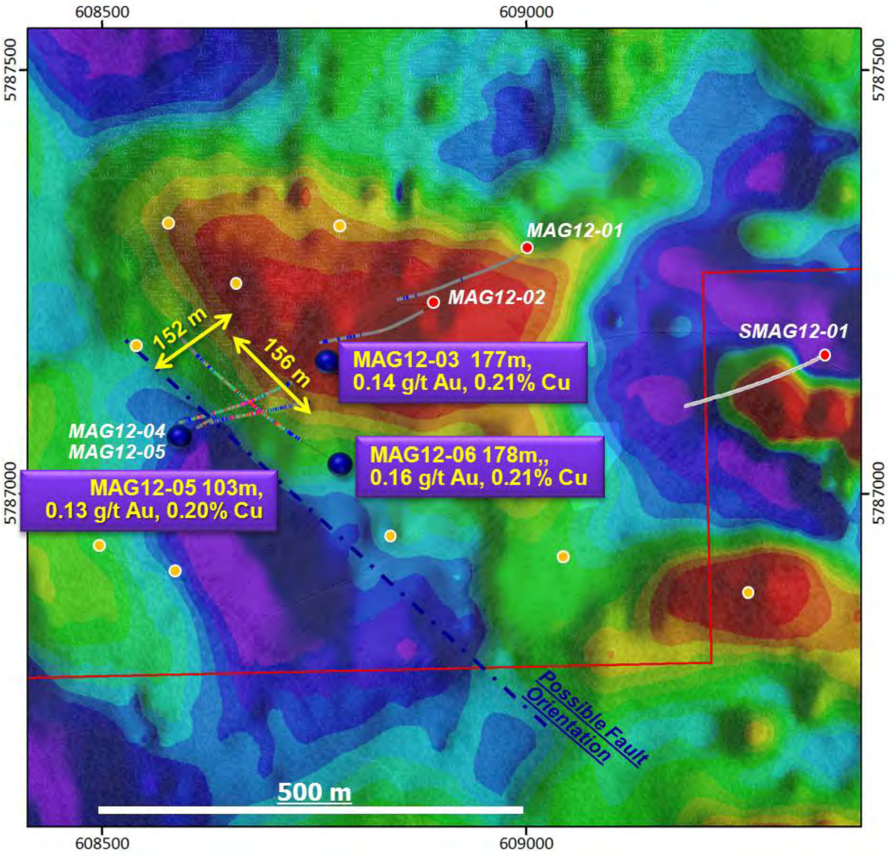

Fig. 5. Ground magnetic image of the Three Firs property, Blackwell et al. (2012a). UTM Zone 10, NAD83.

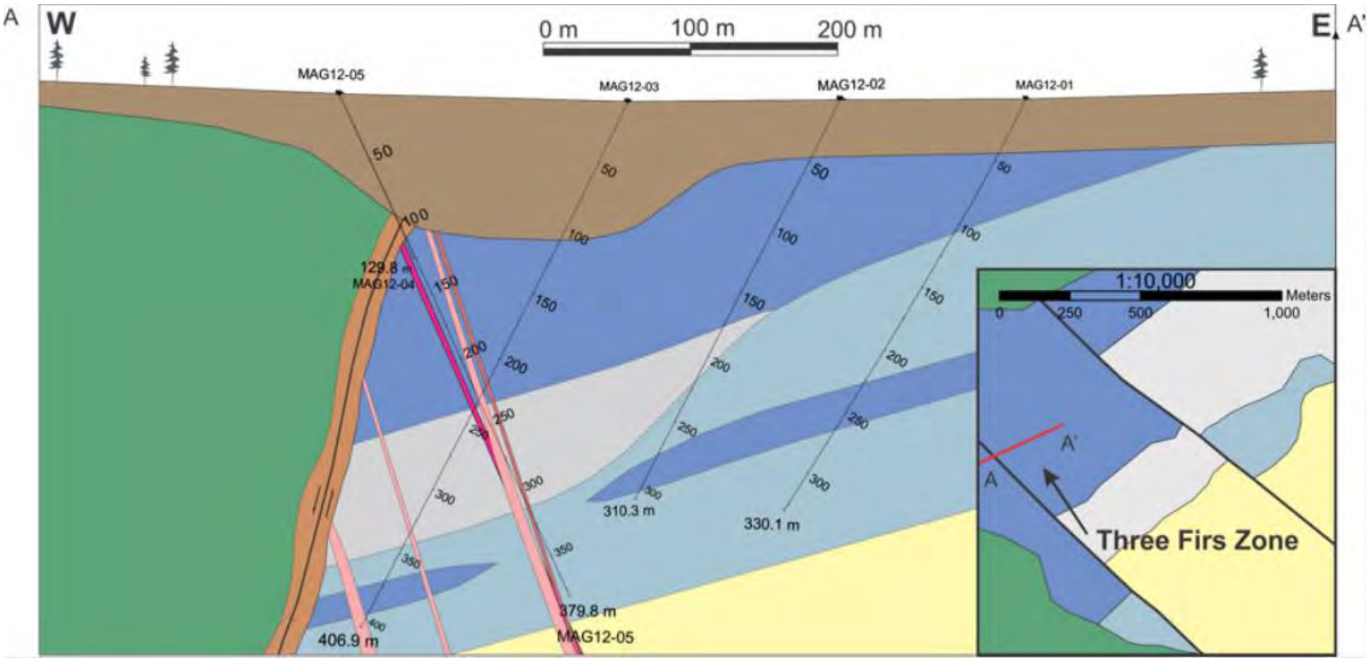

Fig. 6a. Cross-section of the Three Firs prospect (after Vandekerkhove, 2013).

■ Glacial till

// Fault

■ Shear zone
Fault gouge, broken rubble and low core recovery interpreted as broad fault zone

■ Quartz monzonite
Medium grained (<5mm), weakly porphyritic, hornblendes altered to chlorite; euhedral potassium and plagioclase feldspar phenocrysts in an aphanitic groundmass

■ Quartz-biotite monzonite
Medium grained (<5mm), weakly porphyritic, plagioclase laths 2-3 mm; biotite altered to chlorite; rare qtz phenocrysts

■ Monzonite
Medium grained (<5mm), porphyritic, shreddy biotite; zoned, euhedral plagioclase; subhedral potassium feldspar

■ Undifferentiated Nicola volcanic rocks

■ Nicola plagioclase-hornblende-phyric dacite: Medium grained (<5mm) cohesive dacite, plagioclase and hornblende phenocrysts in an aphanitic groundmass

■ Nicola plagioclase-hornblende-phyric dacite breccia: monomictic autoclastic breccia with subangular clasts ranging from 2 to 10 cm supported by sand sized, crystal rich matrix, predominated by plagioclase

■ Nicola volcanic sandstone
Medium to fine grained (1-5mm) plagioclase crystal-rich massive volcanic sandstone

■ Nicola plagioclase-phyric andesite
Coarse grained (2 cm), euhedral plagioclase laths, local trachytic textures, upper contact displays pepperitic facies

Fig. 6b. Legend of the Three Firs lithologies in cross-section.

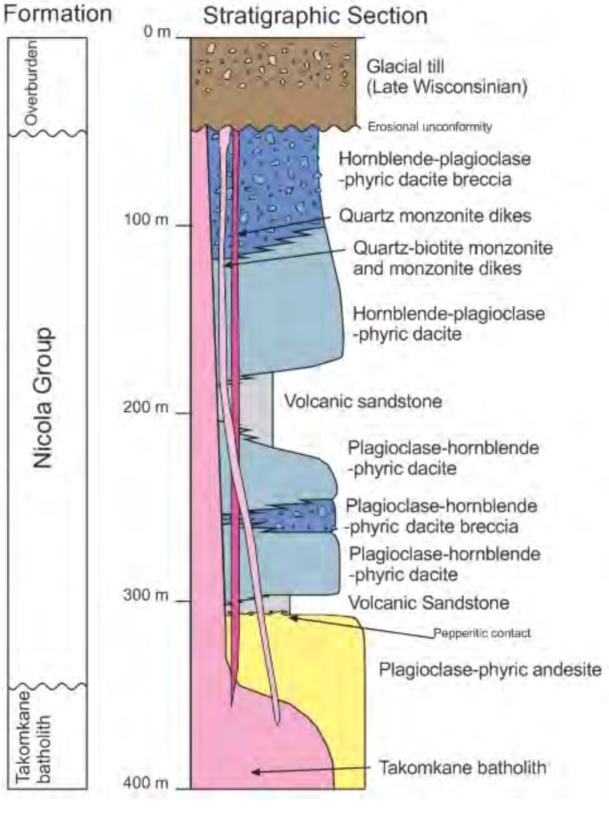

Fig. 7. Stratigraphic section of the Three Firs area.

4.3. Nicola Group host rocks

At Three Firs, the Nicola Group consists of four interfingering facies: plagioclase-phyric andesite; plagioclase-hornblende-phyric dacite; plagioclase-hornblende-phyric dacite breccia; and massive volcanic sandstone (Figs. 6, 7).

4.3.1. Plagioclase-phyric andesite

Plagioclase-phyric andesite is a visually distinctive unit with euhedral laths of greyish white plagioclase up to 2 cm long enclosed in a massive, fine-grained groundmass of dark grey plagioclase, quartz, and amphibole that is variably altered to sericite, chlorite and minor calcite. The upper contact of the unit displays pepperitic textures. A locally well developed trachytic texture defined by the alignment of plagioclase phenocrysts gives this unit the colloquial name of "Turkey Track" andesite (Blackwell et al., 2012a).

4.3.2. Plagioclase-hornblende-phyric dacite

Plagioclase-hornblende-phyric dacite has a speckled appearance and is medium to very dark grey, massive, and strongly magnetic (Fig. 8). Elongate, subhedral to euhedral, plagioclase phenocrysts (< 5 mm long), and prismatic, subhedral to euhedral, hornblende phenocrysts (< 5 mm long) are enclosed in a groundmass of fine-grained quartz, amphibole, and plagioclase. This unit exhibits gradational contacts with both plagioclase-hornblende-phyric dacite breccia and massive volcanic sandstone. Felsic dikes with sharp contacts locally intrude the dacite.

4.3.3. Plagioclase-hornblende-phyric dacite breccia

Plagioclase-hornblende phyric dacite breccia is typically strongly magnetic, medium to very dark grey, with sub-angular to angular monolithic clasts 2 to 10 cm in diameter supported in a sand-sized matrix that is rich in plagioclase crystals (Fig. 9). Clasts and matrix exhibit similar mineralogy to the plagioclase-hornblende-phyric dacite unit. Crystal fragments of plagioclase in the matrix, together with the angularity of the clasts, imply that this unit is an autoclastic breccia derived from the plagioclase-hornblende-phyric dacite. The breccia displays gradational contacts with plagioclase-hornblende-phyric dacite and massive volcanic sandstone, and is locally intruded by felsic dikes with sharp contacts.

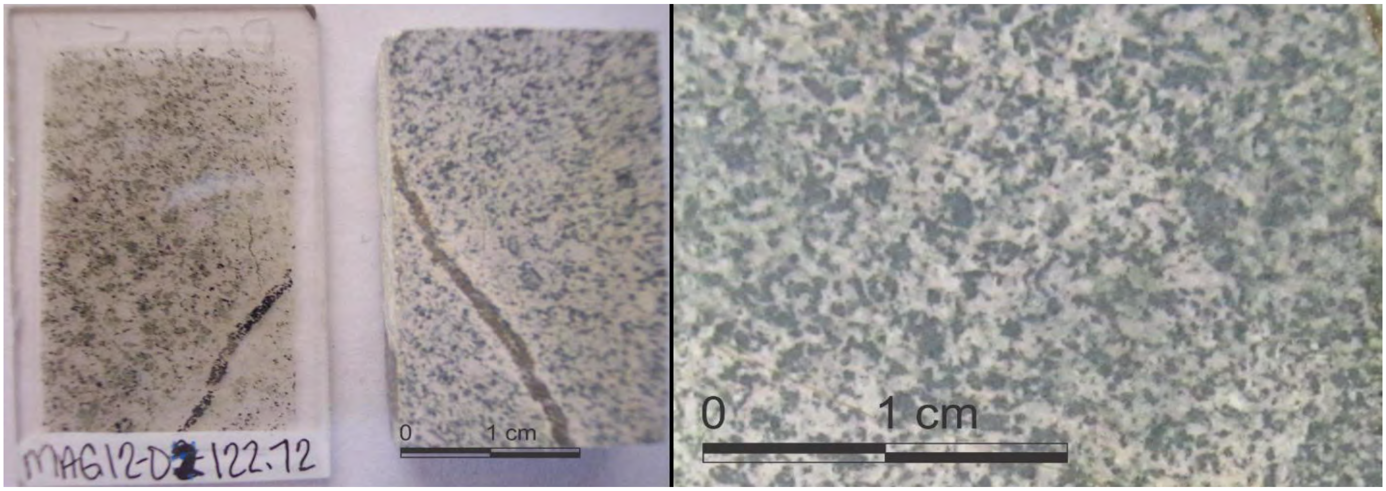

Fig. 8. Plagioclase-hornblende-phyric dacite. Thin section (left), stained off-cut (centre) and hand sample (right) taken from MAG12-02 at 122.72 m depth.

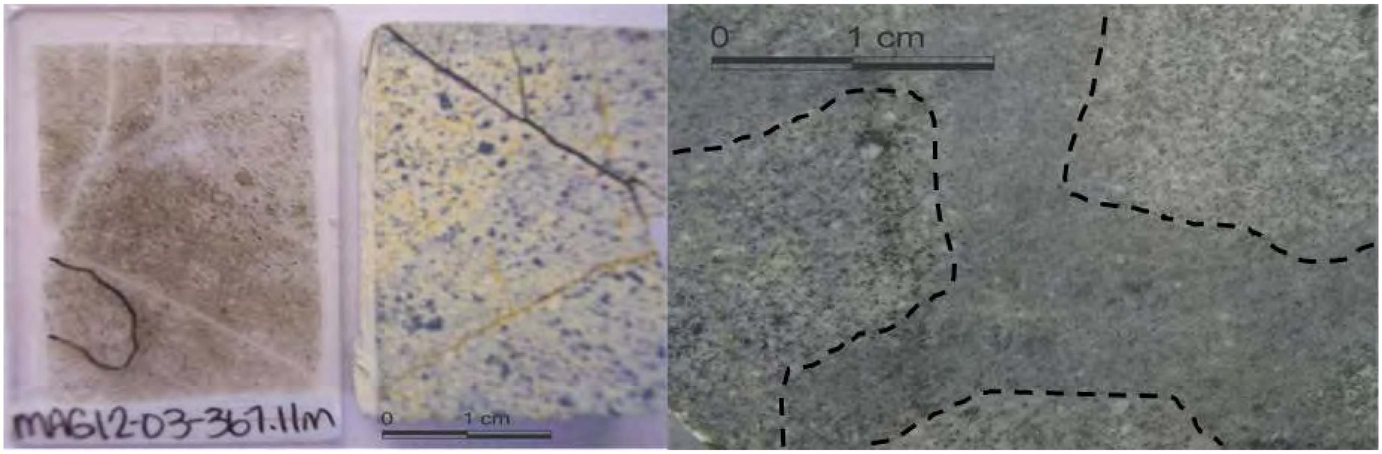

Fig. 9. Plagioclase-hornblende-phyric dacite breccia. Thin section (left) and stained off-cut (centre) taken from MAG12-03 at 367.11 m. Hand sample (right) taken from MAG12-02 at 231.50 m. Breccia fragments in hand sample outlined by dashed lines.

4.3.4. Massive volcanic sandstone

This unit is dark grey, massive, and commonly strongly magnetic. The texturally and compositionally immature plagioclase crystal-rich framework (< 5 mm) is very similar in appearance (Fig. 10) to the clast-supporting matrix in the dacite breccia (Fig. 9). Volcanic sandstones display gradational contacts with other volcanic and volcaniclastic units, and are similarly intruded by felsic dikes possessing sharp intrusive contacts.

4.4. Intrusive dikes

4.4.1. Quartz monzonite

Medium-grained quartz monzonite dikes intrude all volcanic and volcaniclastic Nicola Group units at Three Firs. Dikes display sharp, but irregular contacts that crosscut mineralized main-stage veins (below) indicating post-mineralization emplacement. Quartz monzonite dikes are weakly porphyritic, light pink, and variably mottled (Fig. 11). They contain euhedral to subhedral plagioclase phenocrysts 3 to 5 mm in diameter, subhedral K-feldspar phenocrysts < 3 mm in diameter, rare quartz crystals < 2 mm in diameter, and subhedral hornblende (nearly completely replaced by chlorite) in a fine-grained groundmass of quartz, plagioclase, and K-feldspar.

4.4.2. Quartz-biotite monzonite

Quartz-biotite monzonite dikes locally intrude the Nicola Group, displaying sharp irregular contacts. These contacts are cut by mineralized veins, indicating that emplacement was

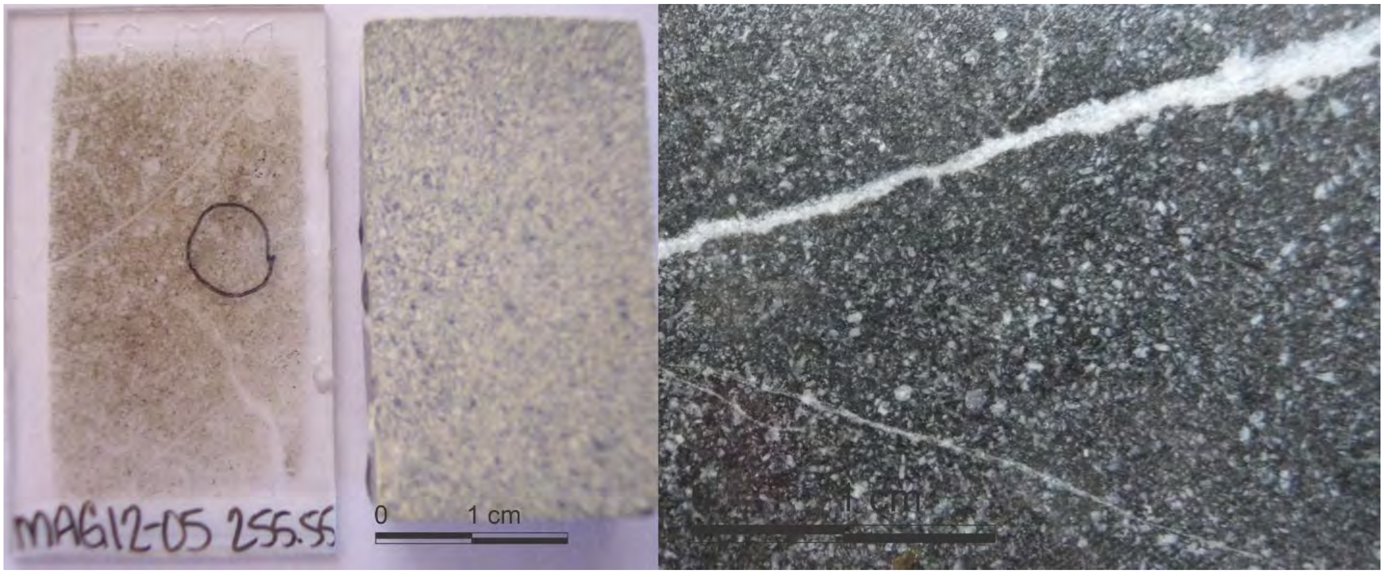

Fig. 10. Massive volcanic sandstone. Thin section (left), stained off-cut (centre) and hand sample (right) are all taken from MAG12-05 at 255.55 m depth.

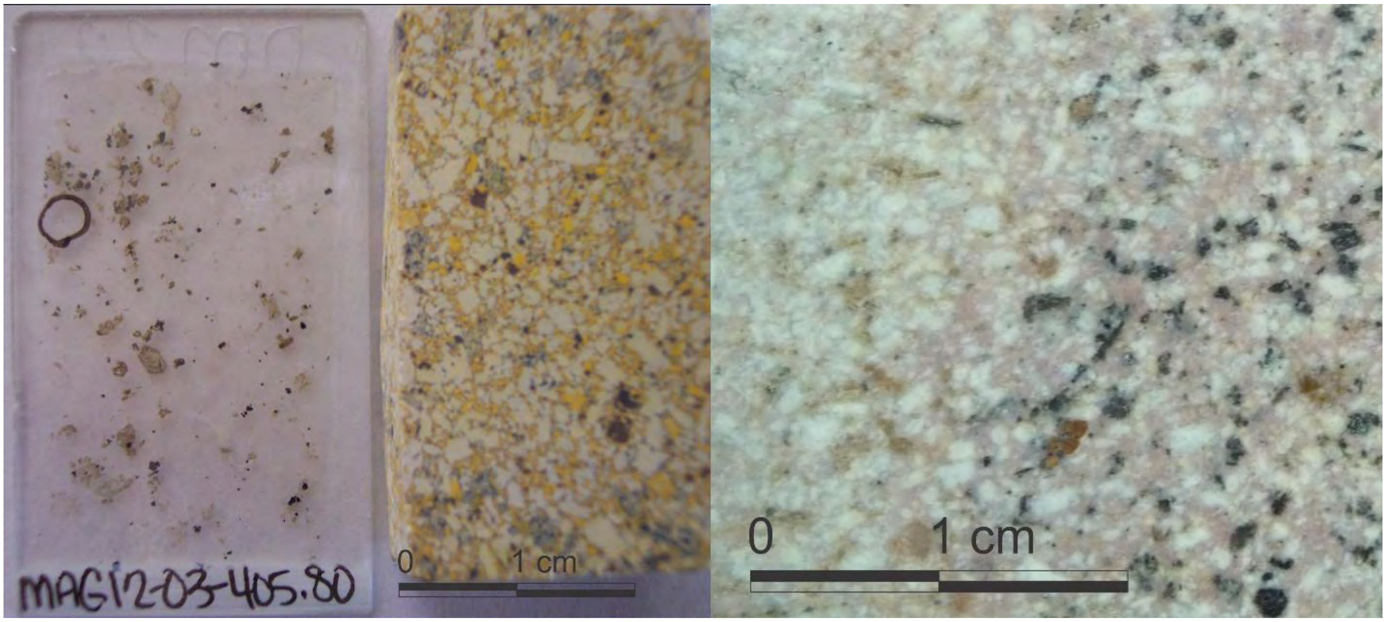

Fig. 11. Quartz monzonite dike. Thin section (left), stained off-cut (centre) and hand sample (right) are all taken from MAG12-03 at 405.80 m depth. Note the sericite and chlorite alteration of the left side of the hand sample.

pre-mineralization. The dikes are medium grained, and light greyish pink to dark grey (Fig. 12). They are weakly porphyritic and contain euhedral to subhedral plagioclase phenocrysts (3-5 mm in diameter), anhedral biotite (1-3 mm in diameter), and rare subhedral K-feldspar (1-2 mm in diameter). The fine-grained groundmass consists of plagioclase, quartz, K-feldspar, and minor biotite. Where altered, biotite phenocrysts and groundmass are replaced mainly by chlorite and clay minerals.

4.4.3. Monzonite

Monzonite dikes are medium grained and consist of weakly porphyritic hornblende, biotite, plagioclase, and lesser K-feldspar in a fine-grained groundmass of K-feldspar, plagioclase, and minor quartz. Biotite is subhedral, shreddy and largely replaced by chlorite. Elongate prismatic crystals of hornblende are similarly replaced by chlorite. Plagioclase forms both elongate euhedral laths and stubby subhedral tablets. Less abundant K-feldspar phenocrysts are equant with euhedral to subhedral habits. All phenocrysts are 2 to 5 mm long. Intrusive contacts (Fig. 13) display chilled margins with an increased abundance of fine-grained quartz and K-feldspar. Monzonite dikes both cut and are crosscut by mineralized quartz veins (Fig. 13), indicating that the monzonite was emplaced coeval with mineralization.

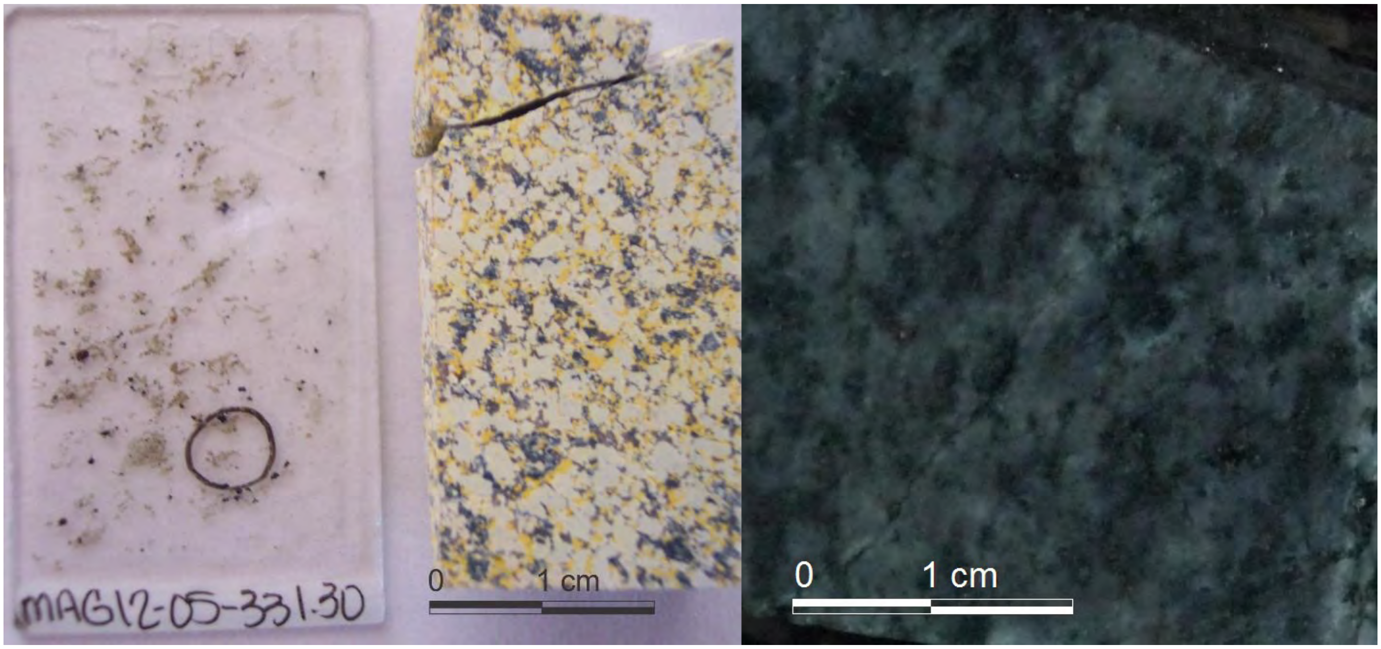

Fig. 12. Quartz-biotite monzonite dike. Thin section (left), stained off-cut (centre), and hand sample (right) are all taken from MAG12-05 at 331.30 m depth.

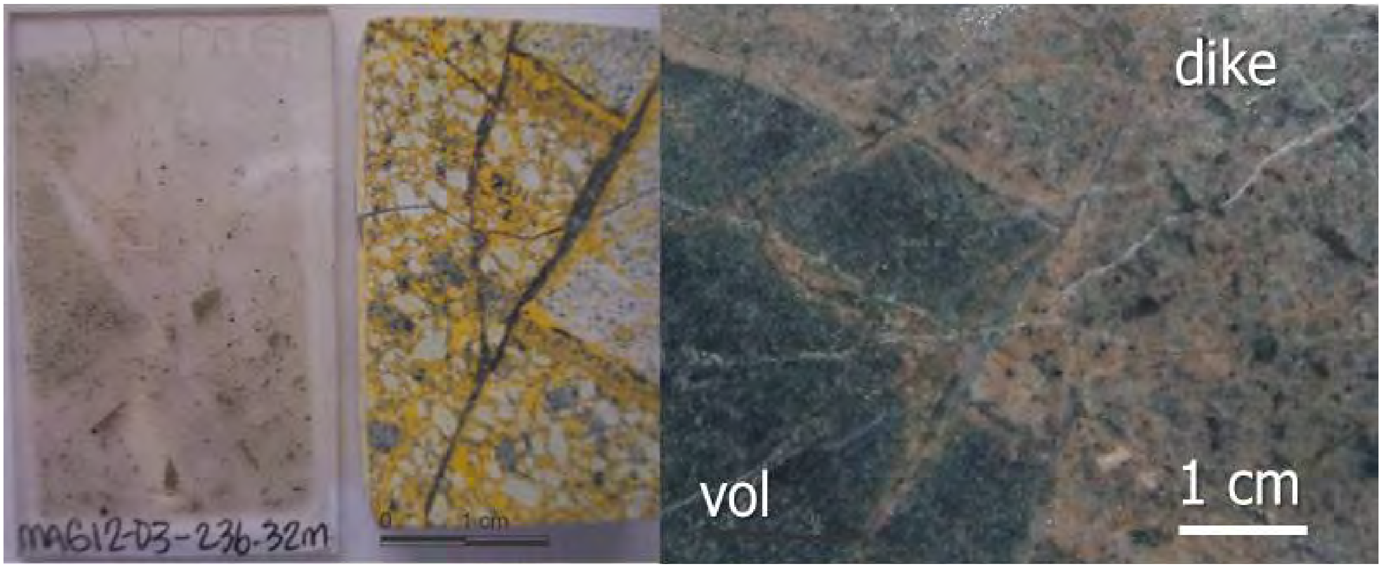

Fig. 13. Syn-mineralization monzonite dike. Thin section (left), stained off-cut (centre) and hand sample (right) are all taken from MAG12-03, at 236.32 m depth. The monzonite dike (dike) has experienced slight post-emplacement faulting and offset at the contact with volcanic host rock (vol).

4.4.4. Aplite dikes

Aplite dikes, 1 to 9 cm wide, are a late intrusive phase that crosscuts main-stage mineralization and all rock types except post-mineralization quartz monzonite. The dikes are light pink to reddish brown, fine grained, equigranular and consist of anhedral quartz and K-feldspar with rare phenocrysts of subhedral plagioclase (Fig. 14). They display moderate chloritic alteration where in contact with suitable lithologies.

4.5. Olivine-phyric basalt: Chilcotin Group (Miocene)

Several discrete basalt flows, each approximately 5 m thick, cap the Three Firs section. These flows are juxtaposed above the Nicola Group along a high-strain zone interpreted to be a fault. Lacking mineralization and significant hydrothermal alteration, this unit is likely part of the Chilcotin Group (Miocene) such as exposed west of the Three Firs prospect (Panteleyev et al., 1996). Vesicle shape, distribution, and orientation indicate that these rocks are upright (Fig. 15). The basalt contains approximately 30% olivine phenocrysts (2 to 3 mm long) and approximately 5% augite phenocrysts (1 mm maximum length) in a very fine-grained groundmass consisting of glass, plagioclase, and minor augite.

5. Three Firs veins, alteration, and mineralization

5.1. Vein paragenesis

Veins at Three Firs veins are divided into eight stages, based on mineral assemblages, textures and crosscutting relationships. We group these veins types into early, main, late and post-mineralization stages based on the presence or absence of Cu and/or Au (Fig. 16).

5.1.1. Early stage pre-mineralization veins: Stages 1 and 2

Stage 1 veins record the earliest hydrothermal fluid event. They are principally adjacent to mineralized dikes in discrete zones of strong potassic alteration. The veins or veinlets consist of magnetite, and are surrounded by very fine-grained K-feldspar alteration envelopes. These veins define the earliest stage of potassic alteration but are unmineralized (Figs. 17a-d). Magnetite veins are typically 1 to 3 mm wide, but rare examples are up to 7 mm wide. Vein margins tend to be diffuse and irregular. Magnetite veins occur singly or, more commonly, in sheeted arrays. They correspond to the early "M" veins developed in many calc-alkaline porphyry Cu-Au deposits as described by Sillitoe (2010).

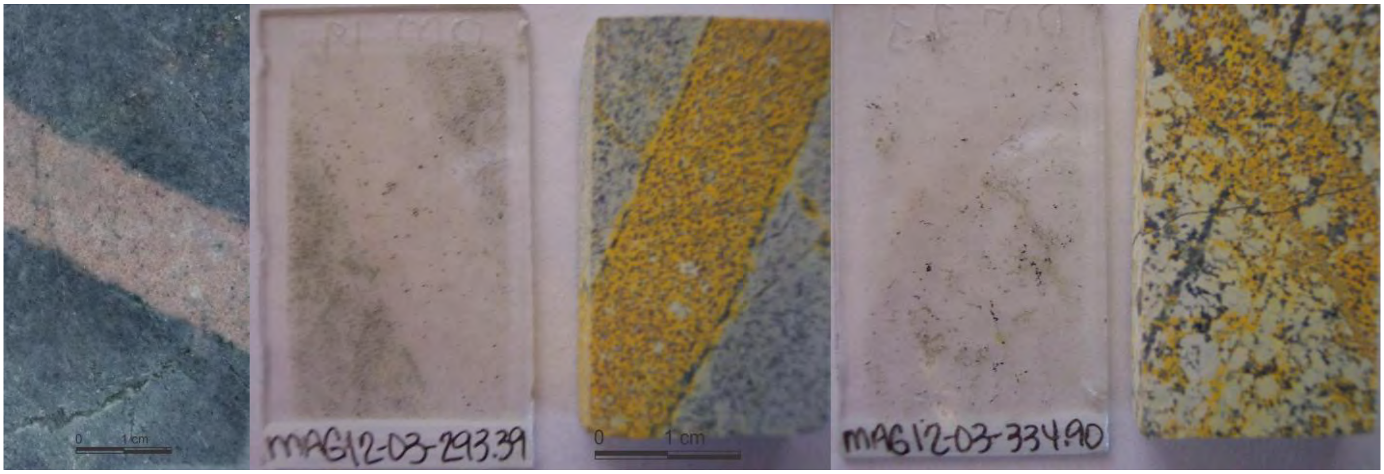

Fig. 14. Aplite dikes. Hand sample (left), thin section (left centre), and stained off-cut (centre) are from MAG12-03 at 293.39 m depth illustrate aplite intruding volcanic sandstone. Thin section (right centre) and stained off-cut (right) are from MAG12-03 at 334.90 m depth illustrate aplite intruding quartz-biotite monzonite.

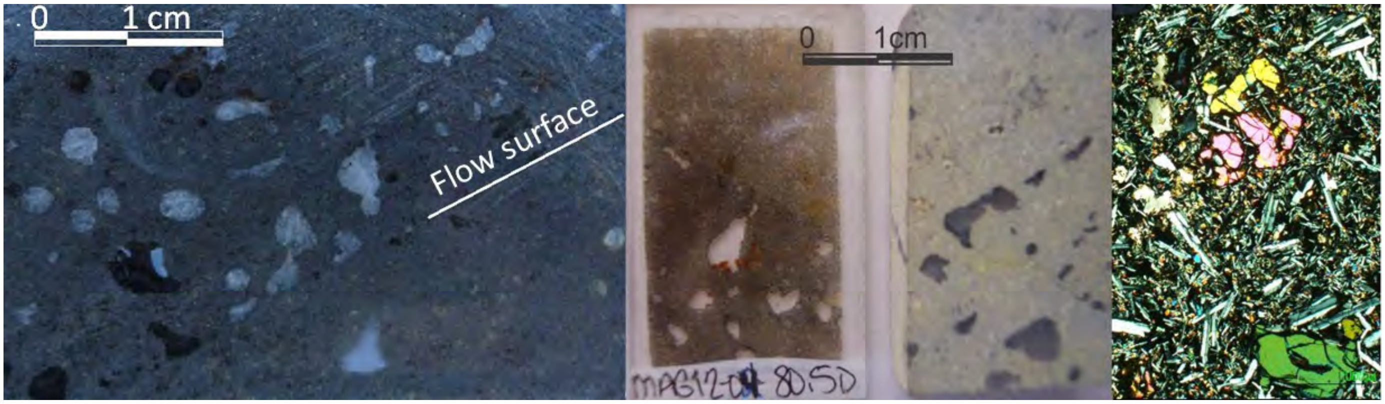

Fig. 15. Olivine-phyric basalt. Hand sample (left) indicating flow surface; thin section (left centre), stained off-cut (right centre) and photomicrograph (right) are all taken from MAG12-04 at 80.50 m depth.

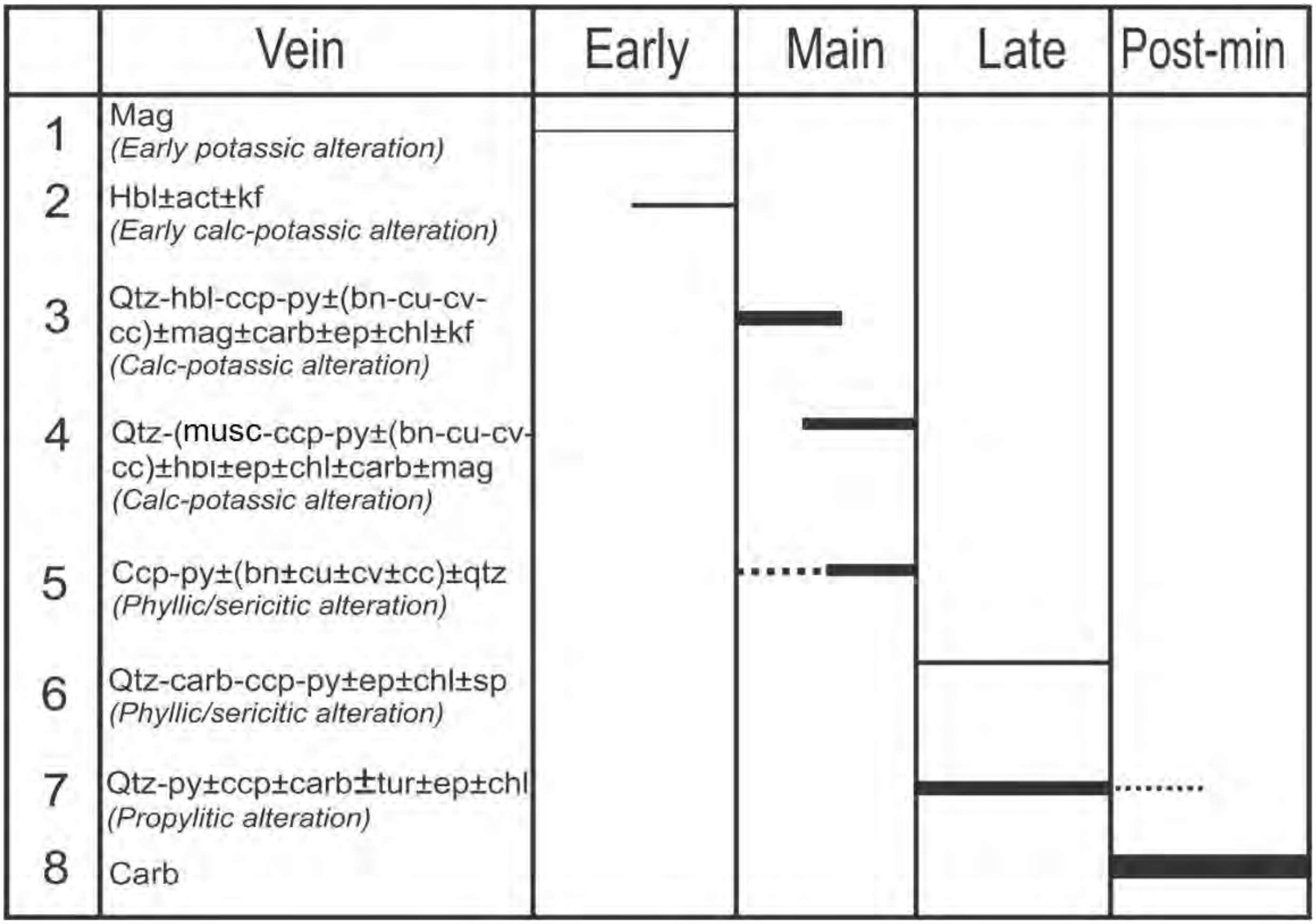

Fig. 16. Three Firs vein paragenesis. Line thickness denotes relative abundance of mineral. Only major alteration types are identified for each stage. Abbreviations: Mag-magnetite; Hbl-hornblende; Qtz-quartz; Ccp-chalcopyrite; Py-Pyrite; Bn-bornite; Cu-cubanite; Cv-covellite; Cc-chalcocite; Kf-potassium feldspar; Ep-epidote; Chl-chlorite; Carb-carbonate; Sp-sphalerite; Tur-tourmaline; Musc-muscovite.

Stage 2 veins cut stage 1 veins and consist only of hornblende. In some veins, hornblende is replaced by actinolite. Hornblende veins are present in all Nicola Group lithologies and the pre-mineralization monzonite dikes. In most cases, stage 2 veins are associated with fine-grained K-feldspar halos, which define another early stage of potassic alteration, similar to the stage 1 magnetite veins. Hornblende veins are commonly 1 to 4 mm wide and display diffuse margins. They typically occur singly, but rare sheeted arrays and multi-dimensional stockworks are recognized (Figs. 17 e-h). Epidote replacement of minerals along hornblende vein margins is widespread, but textures suggest that this epidote was not in equilibrium with hornblende. It is likely the result of a later fluid event.

5.1.2. Main stage mineralized veins: Stages 3, 4, and 5

Stage 3 veins crosscut the unmineralized early stage veins and are present in all Nicola Group rocks and pre-mineralization monzonite. Stage 3 veins have diffuse, sinuous margins with minerals only rarely displaying symmetrical distribution as wall-rock parallel bands about a medial suture line. Veins occur singly, in multi-dimensional stockworks or, rarely, as sheeted arrays. Stage 3 veins are 2 - 30 mm wide and consist mainly of quartz (25-75%), hornblende (20-50%), chalcopyrite (2-15%), pyrite (5-30%), and magnetite (5-50%), with lesser bornite (0-5%) carbonate (0-5%), epidote (0-5%), chlorite (0-5%) and K-feldspar (0-1%) (Fig. 18). Mineralogical variation correlates weakly with host rock composition. For example, veins in the Nicola Group have higher magnetite abundances than those hosted by felsic intrusive rocks.

In diamond-drill holes MAG12-03 and MAG12-05, stage 3 veins contain greater amounts of bornite than chalcopyrite from 360 to 375 m and from 249 to 265 m, respectively. The zones with predominantly bornite also contain native Au in larger grains of disseminated chalcopyrite ± bornite (Fig. 19).

Supergene sulphide minerals replacing chalcopyrite include covellite, cubanite and chalcocite. In some veins, chlorite replaces hornblende. Stage 3 veins have weak to well developed alteration envelopes that reflect, in part, the mineralogy of the host-rock. Envelopes include: 1) fine-grained K-feldspar and rare biotite (potassic alteration assemblage); and 2) sericite-quartz-pyrite with lesser epidote-chlorite (phyllic/sericitic and propylitic alteration assemblages) and rarely albite. Stage 3 veins are comparable to early “A” type veins using the terminology of Gustafson and Hunt (1975).

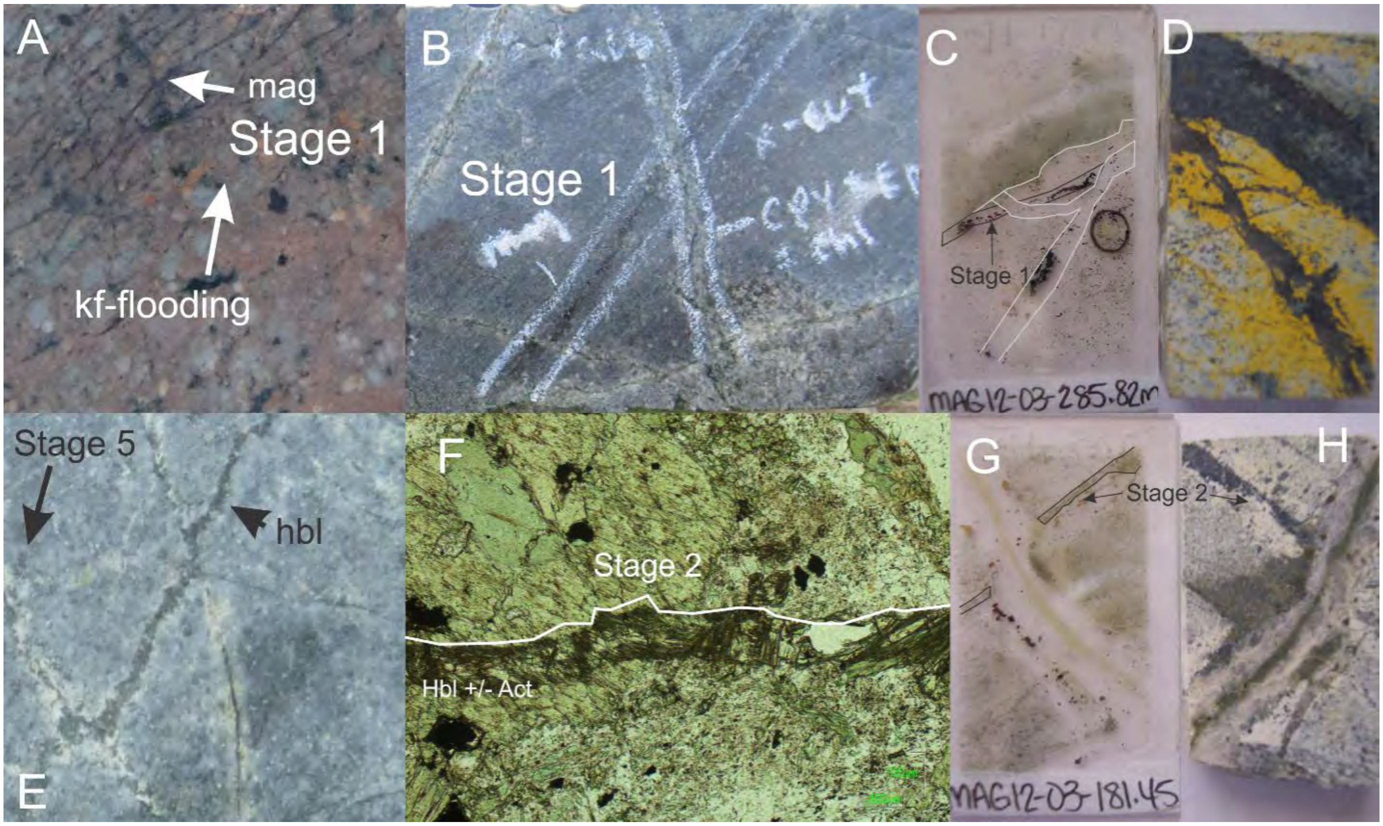

Fig. 17. Hand sample and thin section photomicrographs for Early stage veins. **a)** Hand sample of sheeted magnetite (mag) stringer veinlets. **b)** Individual magnetite vein crosscut by stage 3 vein. **c)** Thin section and **d)** stained off-cut of magnetite veinlet being cross-cut by stage 3 veins. **e)** Hand sample of hornblende (hbl) vein cross cut by stage 5 veinlet. **f)** Thin section photomicrograph of hornblende vein displaying discrete actinolite replacement. **g)** Thin section and **h)** stained off-cut of stage 2 vein crosscut by stage 3 vein.

Stage 4 veins crosscut early stage veins, stage 3 veins, and all pre-mineralization lithologies. They exhibit sharp, straight vein margins, are 3 to 35 mm wide, and have thin medial suture lines filled with chalcopyrite and epidote (Fig. 20). Stage 4 veins consist predominantly of quartz (20-80%) with lesser chalcopyrite (2-15%), pyrite (2-15%), hornblende (0-20%), epidote (0-20%), chlorite (0-10%), carbonate (0-20%) and magnetite (0-10%). These veins occur individually, in stockworks, and as sheeted arrays. Similar to stage 3 veins, bornite is more abundant than chalcopyrite from 360 to 375 m in diamond-drill hole MAG12-03 and from 249 to 265 m in MAG12-05. Supergene sulphide minerals are the same as in stage 3 veins as are the alteration envelopes. They differ from stage 3 veins principally by their sharp vein margins, medial suture lines with epidote and chalcopyrite, much less hornblende, and weaker potassic alteration. Interestingly, chalcopyrite grains display equilibrium textures with hydrothermal epidote implying a direct relation to the Cu-Au mineralization event(s). Stage 4 veins could be classified as “B” veins using the terminology of Gustafson and Hunt (1975).

Stage 5 veins crosscut early stage veins (stages 1 and 2) and, in most cases, main- stage 3 and 4 veins. Stage 5 veins occur in all pre-mineralization lithologies and may be better described as veinlets or “stringer” veins because they are typically less than 2 mm wide, although rare examples are up to 6 mm wide (Fig. 21). Veins have diffuse margins and consist primarily of chalcopyrite, bornite, pyrite, and minor quartz. Chalcopyrite is locally replaced by supergene cubanite, covellite, and chalcocite. Minor sericite or, more rarely, epidote-chlorite-calcite form alteration halos. These halos do not appear directly related to the hypogene sulphide minerals and may record late ingress of fluids into the pre-exsiting sulphide veinlets. In common with all previous stages of vein formation, bornite is more abundant than chalcopyrite from 360 to 375 m in MAG12-03 and from 249 to 265 m in MAG12-05. Stage 5 veins normally occur singly or in random stockworks; sheeted arrays are rare. Veins are locally abundant, with up to twenty veins per metre of core. High-density zones and low-density zones of veining alternate but the cause is uncertain. The alternation may be the result of pre-existing structures rather than changes in lithology. Stage 5 veins are comparable to “D” veins or stringer sulphide veins in porphyry deposits using the terminology of Gustafson and Hunt (1975).

5.1.3. Late stage mineralized veins: Stages 6 and 7

Stage 6 veins crosscut stage 5 veins and are found in all lithologies. These veins are 7 to 90 mm wide and typically display exhibit sharp, straight, margins (Fig. 22a). Stage 6 veins display open space-filling textures including comb (Fig. 22b) and rare coliform styles. The veins contain mainly quartz (30-75%), carbonate (20-80%) and, in some cases, sphalerite (0-50%). Chalcopyrite (0-5%), pyrite (0-50%), epidote (0-10%), chlorite (0-10%) and tetrahedrite/tennatite (0-5%) are minor phases. Stage 6 veins are uncommon in the Three Firs prospect

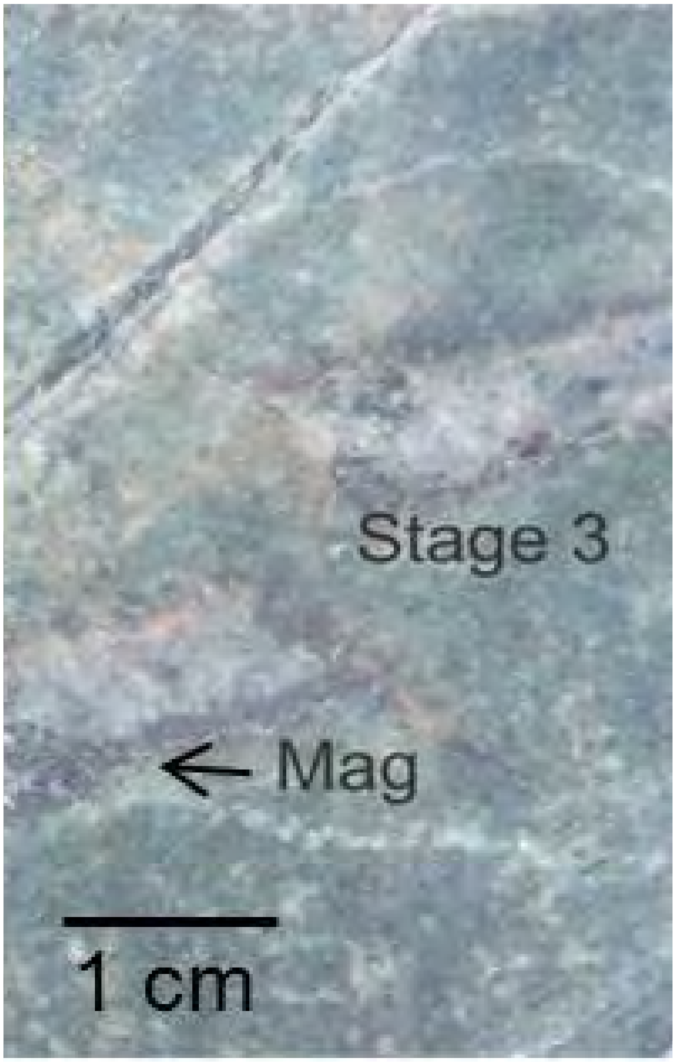

Fig. 18. Hand sample of fragmented stage 3 quartz vein with magnetite-rich margins.

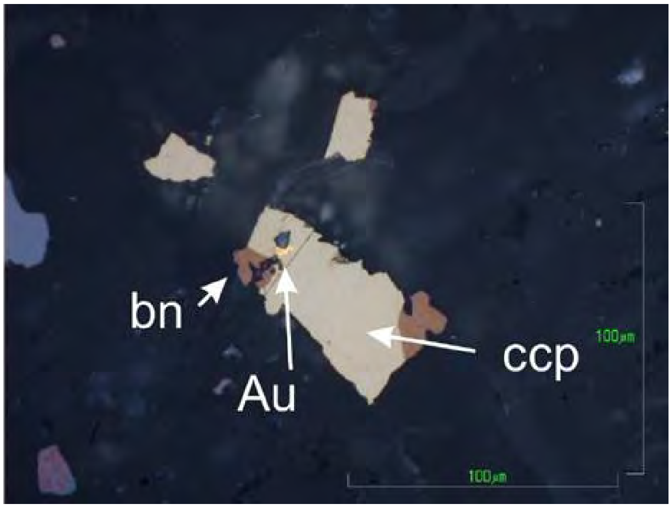

Fig. 19. Photomicrograph of native gold (Au) in chalcopyrite-bornite (ccp-bn) dissemination from MAG12-03 at 363.71 m.

but where present, correlate weakly with pre-mineralization quartz-biotite monzonite dikes. They produce strong carbonate alteration halos and weaker sericite-chlorite (phyllic) alteration. These late stage carbonate-base metal veins are common in large porphyry systems (e.g., Corbett and Leach, 1998).

Stage 7 veins crosscut those of stage 5, but have variable crosscutting relationships with those of stage 6. They exhibit a range of textures, mineral modes, and widths (Fig. 23). They consist of quartz (20-90%), pyrite (2-50%), chalcopyrite (0-5%) carbonate (0-50%), epidote (0-50%), chlorite (0-50%), and tourmaline (0-75%). Stage 7 veins occur singly or, more rarely, in discrete arrays. Vein margins range from sharp and straight to irregular and diffuse. Diffuse margins tend to correlate with higher tourmaline abundances. Adjacent to stage 7 veins are zones of propylitic alteration consisting of epidote, chlorite, and calcite; these zones do not correlate with strong Cu-Au mineralization.

5.1.4. Post-mineralization veins: Stage 8 veins

Stage 8 veins are unrelated to Cu-Au mineralization and post-date all stages of vein formation. They consist of calcite with lesser ankerite as indicated by surface staining and reflectance spectroscopy (Fig. 24a and see below). With sharp and irregular margins, the veins form singly or in swarms with multiple bifurcations (Fig. 24b). Host-rocks display minor calcite alteration adjacent to the veins.

5.2. Prospect-scale alteration

Rocks hosting the Three Firs prospect are pervasively altered and display evidence of superimposed alteration events. Common alteration assemblages include potassic, calc-potassic, phyllic (sericitic), and propylitic. The formation of these assemblages can be attributed directly to different stages of vein formation. Although we lack data to rigorously define the spatial distribution of vein types and alteration throughout the property, graphical logs and thin section petrography derived from drill holes allow us to identify the general mineralogical and textural characteristics of the alteration assemblages

5.2.1. Potassic and calc-potassic alteration

Early potassic alteration is spatially associated with stage 1, 2, and 3 veins and, to a lesser extent, with stage 4 and 5 veins. It is expressed in two styles: 1) predominantly K-feldspar (K-feldspar ± magnetite ± sericite ± biotite ± chalcopyrite-pyrite ± bornite) adjacent to vein margins as alteration envelopes; and 2) predominantly biotite-magnetite (biotite-magnetite ± sericite ± K-feldspar ± chalcopyrite-pyrite ± bornite) as dark brown patches throughout the Nicola Group. Magnetite is not a distinguishing feature of potassic alteration because it is pervasively distributed throughout Nicola Group rocks as both a primary igneous mineral and a product of secondary hydrothermal alteration.

Calc-potassic alteration is characterized by hornblende-actinolite-K-feldspar-epidote ± titanite ± chalcopyrite ± bornite. It probably represents a transitional potassic alteration assemblage resulting from variations in host-rock composition rather than a discrete calc-potassic hydrothermal fluid event.

5.2.2. Phyllic (sericitic) alteration

Phyllic alteration is characterized by both microscopic sericite and medium-grained flaky "sericite" (identified as muscovite in hand sample). In practice, the term "phyllic" is

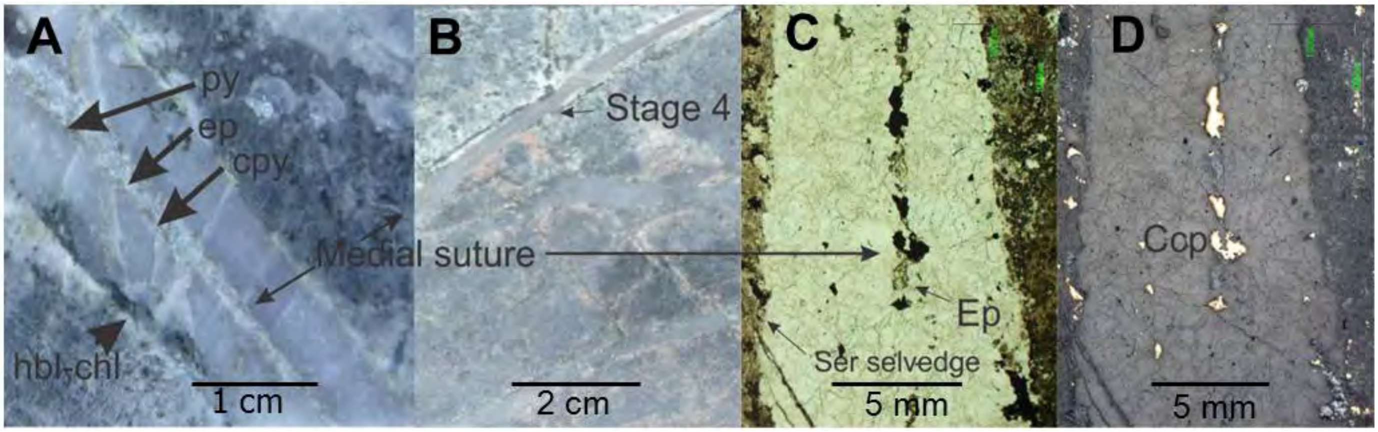

Fig. 20. Hand sample and photomicrographs of stage 4 veins with characteristic medial sutures. **a)** and **b)** are hand samples. **c)** and **d)** are transmitted and reflected light photomicrographs from thin sections of the vein in b). Abbreviations as in Figure 16.

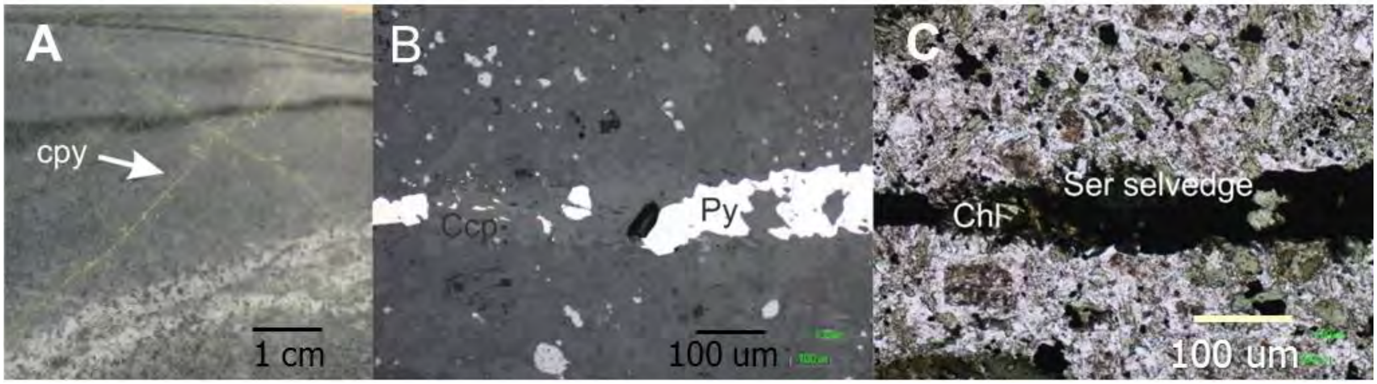

Fig. 21. a) Hand sample of stage 5 chalcopyrite-pyrite-quartz stringer vein. **b)** Reflected light and, **c)** transmitted light photomicrographs of chalcopyrite-pyrite-quartz stringer vein in thin section.

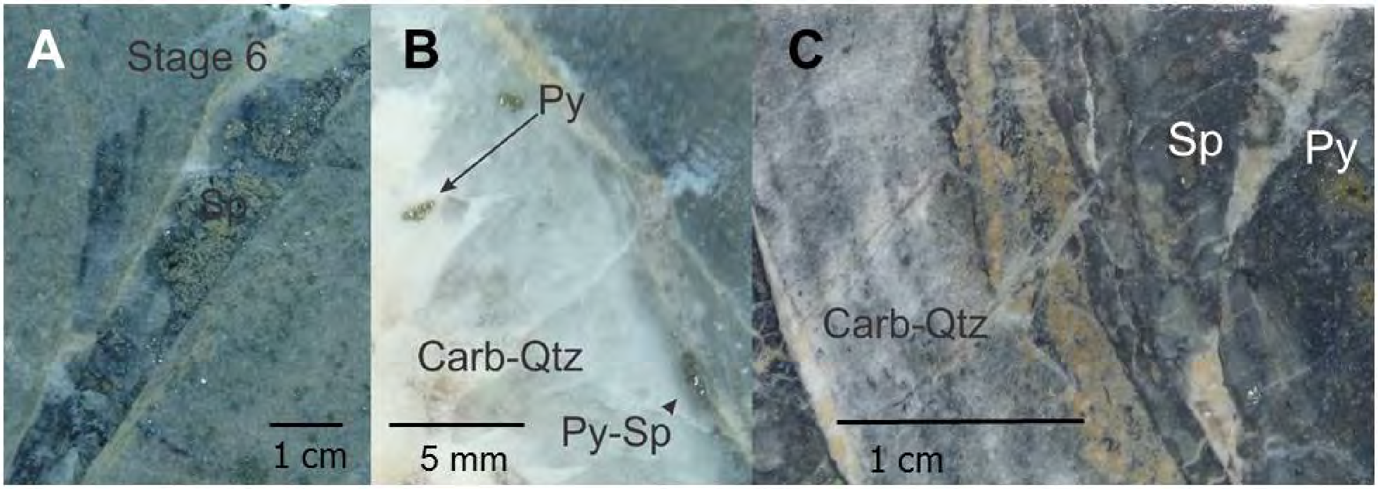

Fig. 22. Hand samples of Late stage 6 veins. **a)** Stage 6 vein with pale grey sericite and carbonate alteration. **b)** Comb-textured quartz crystals growing perpendicular to the vein wall margin. **c)** Laminated stage 6 vein with parallel mineral layers of carbonate, quartz, and grey sulphides (tetrahedrite, sphalerite, chalcopyrite and pyrite). Abbreviations as in Figure 16.

used rather than sericite or muscovite because the true variety of white mica is uncertain (e.g., Beane ands Titley, 1981). Phyllic alteration forms halos around stage 5 and 6 veins. It also pervasively alters rock in narrow faults and shear zones. These structures produce highly fragmented zones in drill core. Phyllic alteration post-dates potassic alteration throughout the Three Firs prospect, and typically consists of quartz-sericite-pyrite ± chlorite ± epidote ± calcite in various combinations. It

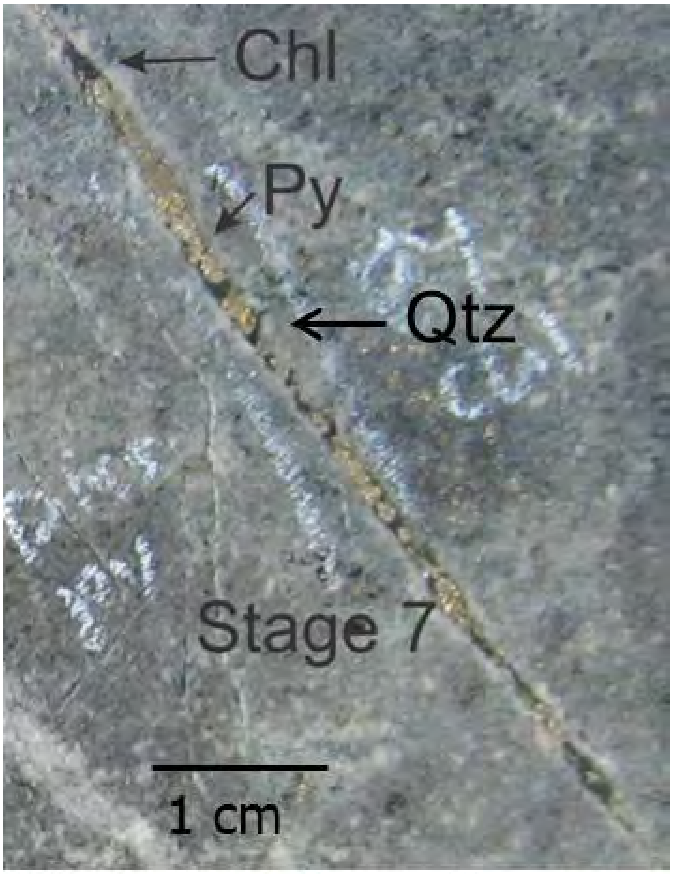

Fig. 23. a) Stage 7 vein with quartz (Qtz) and lesser pyrite (Py); propylitic alteration with predominantly chlorite (Chl) and epidote.

is associated with hypogene covellite, chalcocite, cubanite, and bornite. Reflectance spectroscopic analysis of phyllic alteration halos around stage 5 veins (see below) identified crystalline illite and hydromuscovite (Fig. 25). Phyllic alteration in the currently known Three Firs system is weak compared to other large calc-alkaline porphyry Cu deposits in British Columbia such as Kemess South (Duuring et al., 2009a) and Highland Valley (McMillan, 2005).

5.2.3. Propylitic alteration

Propylitic alteration is ubiquitous throughout the Three Firs prospect and locally replaces potassic and phyllic alteration assemblages. Mineralogy varies, but consists of epidote-calcite-chlorite ± pyrite ± minor albite. Host rock hornblende, plagioclase, and alkali feldspar are selectively replaced. Late stage 7 veins are commonly associated with propylitic alteration.

6. Three Firs whole-rock geochemistry

Twenty-one samples of the least altered rock types were selected for whole-rock geochemical analysis using existing pulps from the four MAG12 drill cores.

6.1. Geochemical methods

Samples were analyzed using ME-ICP06 (inductively coupled plasma) and OA-GRA05 methods. Major oxides were analyzed by ICP- AES (atomic emission spectroscopy) at ALS Laboratories Limited. Samples were decomposed by lithium metaborate/lithium tetraborate ($LiBO_2/Li_2B_4O_7$) fusion (FUS-LI01). The procedure for ME-ICP06 analysis used 0.2 g of sample (pulverized) mixed with 0.90 g lithium metaborate/lithium tetraborate flux that underwent fusion at 1000° C. The cooled melt was dissolved in 100 ml of 4% nitric acid and 2% hydrochloric acid, and analyzed by ICP-AES. Elemental concentrations were used to determine oxide concentration values. In the accompanying OA-GRA05 method, ICP analyte concentrations and loss-on-ignition (L.O.I.) values were used to determine the total oxide content, where percent L.O.I. was calculated from the weight difference after 0.1 g sample was placed in a 1000° C oven for one hour.

ME-MS81 is an ultra-trace level method that is used for whole rock samples. Lithium metaborate fusion (FUS-LI01) decomposed the sample and products were then analyzed by Inductively Couples Plasma Mass Spectrometry (ICP-MS). A 0.2 g sample was mixed with 0.9 g lithium metaborate and fused at 1000° C. The cooled melt was dissolved in 100 ml of 4% nitric acid and 2% hydrochloric acid and analyzed by

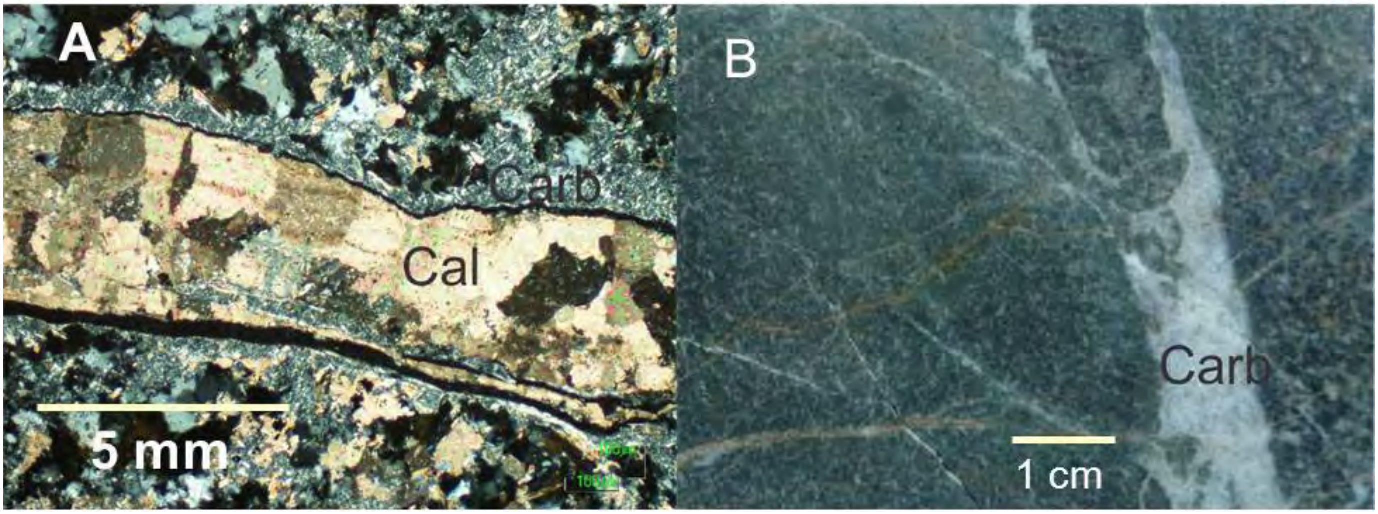

Fig. 24. Stage 8 carbonate veins. **a)** Photomicrograph (crossed-polarized light) of calcite vein and **b)** hand sample displaying irregular vein margins and multiple bifurcations.

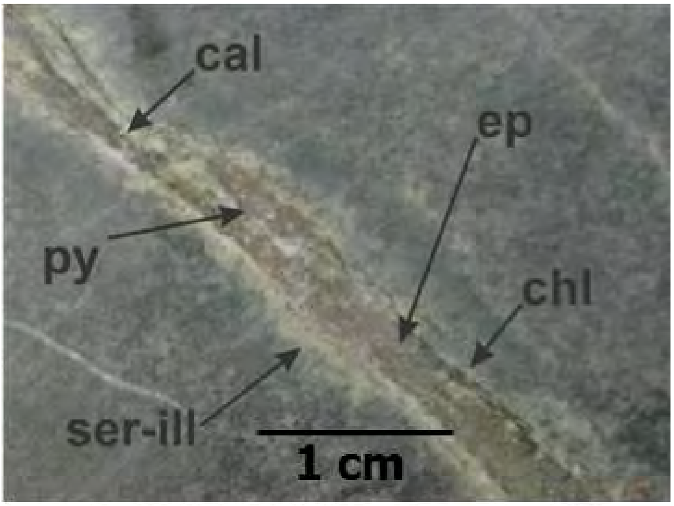

Fig. 25. Phyllic alteration halos around stage 5 veins with crystalline illite and hydromuscovite identified by reflectance spectroscopy.

ICP-MS.

Gold values were determined by AU-ICP21 with a fire assay fusion ICP-AES finish. Each sample was fused with a mixture of lead oxide, sodium carbonate, borax and silica. This combination was inquarted with 6 mg of gold-free silver and cupelled to produce a metal bead. The bead was then digested in 0.5 ml of dilute nitric acid and 15 ml of hydrochloric acid in a microwave oven. The resulting cooled solution was diluted with 4 ml of demineralized water and analyzed by ICP-AES against matrix-matched standards. Complete details on the analytical methodology and quality assurance/quality control (QA/QC) are given in Sherlock et al. (2013).

6.2. Whole-rock geochemistry results

Most drill core samples exhibit strong alteration, as expected in rocks near a large hydrothermal system. Consequently, although considerable care was taken to select sample intervals that had minimal visible alteration, geochemical analyses (Table 1) indicate that only seven samples have L.O.I. values below 3.0 wt.%, the approximate upper limit for unaltered granitic rocks (e.g., Lemaitre, 1978). All other samples have some degree of alteration. On a binary plot of K_2O (wt.%) versus SiO_2 (wt.%), most samples fall in the medium-K calc-alkaline field (Fig. 26) The few samples that plot in the high-K calc-alkaline field have been affected by secondary potassic alteration (biotite and sericite) as evidenced by relatively high L.O.I. values (Table 1). On the Rb versus Y+Nb tectonic discrimination diagram of Pearce (1984), all samples plot in the field for volcanic arc granites (Fig. 27). This origin is consistent with the generation of Three Firs magmas in the southern Nicola volcanic arc.

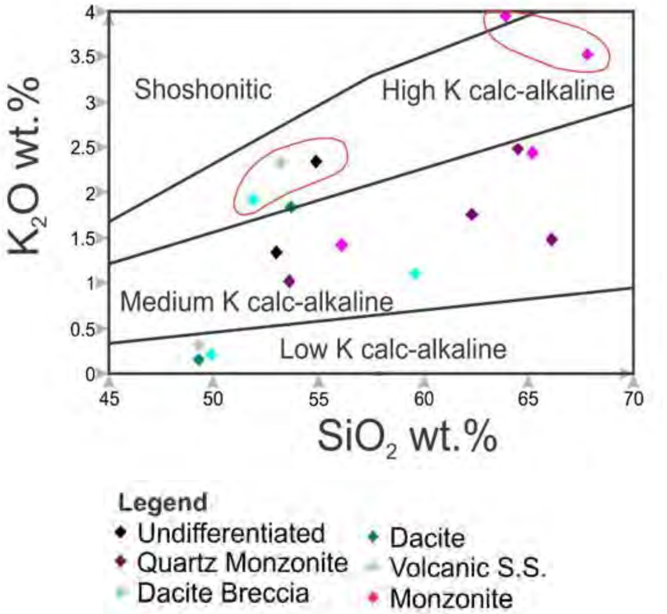

Fig. 26. K_2O vs. SiO_2 (wt.%) diagram (after Peccerillo and Taylor, 1976) for Three Firs samples. Samples circled in red in the high K calc-alkaline field have been affected by secondary potassic alteration (see text for discussion).

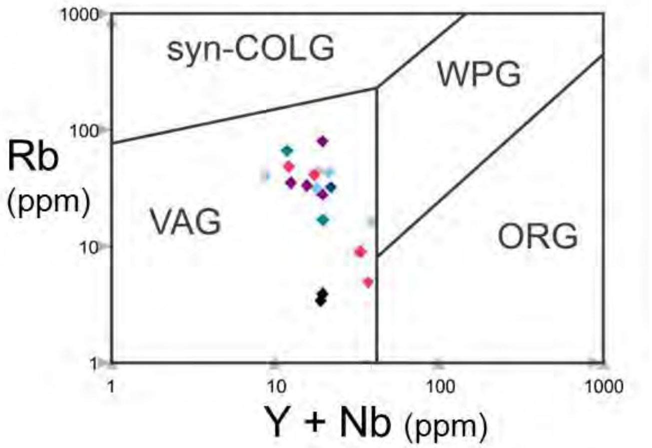

Fig. 27. Trace element tectonic discrimination diagram (after Pearce, 1984) for Three Firs samples.

7. Fluid inclusion microthermometry of main-stage hydrothermal veins

To estimate the temperature, pressure and compositional conditions of the ore fluids during metal deposition, four doubly-polished 80 µm thick sections from quartz veins were examined, two from each of stages 3 and 4 (Fig. 28). These veins were selected because they host most of the Cu-Au mineralization in the prospect and contain quartz grains that are suitable (i.e. clear and unrecrystallized) for microthermometric analysis. These veins are interpreted to be within the central region of the Three Firs porphyry Cu-Au system based on drilling and exploration activities.

Microthermometric analysis was conducted using a Linkam THMSG 600 heating-freezing stage at the British Columbia Geological Survey (BCGS). Accuracy of measurement is ± 5° C above 200° C, ± 1° C between 100° C and 200° C and ± 0.1° C below 100° C.

7.1. Types of fluid inclusions

Fluid Inclusions in hydrothermal quartz are divided into primary, pseudosecondary, and secondary inclusions using the criteria of Roedder (1984) and based on their phase proportions

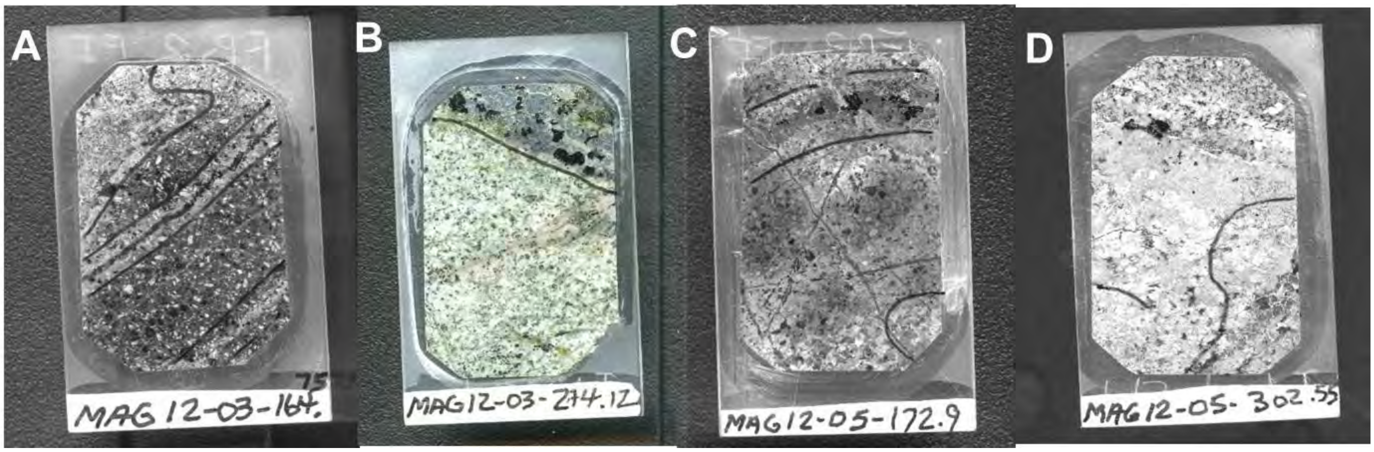

Fig. 28. Doubly polished (80-μm) thin sections of main stage veins studied for fluid inclusion microthermometry. **a)** MAG12-03 (164.75 m), stage 4. **b)** MAG12-03 (274.12 m), stage 3. **c)** MAG12-05 (172.90 m), stage 3. **d)** MAG12-05 (302.55 m), stage 4.

at room temperature (25° C) and behaviour during heating and freezing experiments. Studied fluid inclusions are further subdivided into distinct fluid inclusion assemblages (FIAs) using the criteria of Goldstein and Reynolds (1994). An individual FIA is a group of fluid inclusions that are interpreted to represent coeval inclusions that formed during a single fluid event.

Primary and pseudosecondary fluid inclusions fall into three compositional types at Three Firs (Fig. 29). Type 1 inclusions are aqueous, brine-rich, multiphase (liquid + vapour + halite ± sylvite ± carbonate ± sulphide daughter minerals) inclusions that contain less than 10 vol.% vapour. Type 2 inclusions are aqueous and typically liquid-rich (liquid + vapour ± carbonate daughter) with 10 to 35 vol.% vapour. Type 3 inclusions are two-phase (vapour + liquid), aqueous and vapour-rich, with greater than 80 vol.% vapour. Secondary fluid inclusions are common in all stages of vein formation and typically occur as two-phase (liquid ± vapour), liquid-rich inclusions in trails and arrays that crosscut quartz grain boundaries. Their timing with respect to the Cu-Au mineralization is unclear and they are not discussed further. It is assumed that the volume and composition of primary and pseudosecondary inclusions has remained constant after entrapment. In other words, they have not leaked. This assumption is based on the shape of inclusions (no "necks" or "tails") and characteristics of the host quartz grains. Specifically, grains show uniform extinction in cross-polarized light and lack deformation or recrystallization textures (Roedder, 1984; Goldstein and Reynolds, 1994).

Stage 3 quartz-hornblende ± magnetite ± chalcopyrite ± pyrite veins contain 0.25 to 2.5 mm diameter quartz grains that are unzoned, anhedral, and commonly in contact with primary sulphides. Fluid inclusion assemblages in quartz include numerous trails of secondary inclusions that crosscut grain boundaries, and trails, clusters, and arrays of primary and pseudosecondary FIAs that terminate at grain boundaries (Fig. 29b). Microthermometric measurements were made on the Type 1 brine-rich, Type 2 liquid-rich, and Type 3 vapour-rich inclusions, but only the Type 1 inclusion data are considered reliable (see below). Some Type 1 inclusions contained rare, opaque, triangular daughter minerals identified as chalcopyrite using reflected light microscopy (Fig. 29a). Measured inclusions had irregular, equant, and negative crystal shapes, and ranged from 5-20 μm in long dimension (mean 8 ± 3 μm).

Stage 4 veins contain 0.2 -3.0 mm-diameter quartz grains that are clear, unzoned, and anhedral and contain variable amounts of hornblende ± magnetite ± epidote ± chlorite ± carbonate ± K-feldspar ± sericite and sulphides. Stage 4 veins have sharp, straight margins and medial suture lines. Fluid inclusion assemblages in quartz include secondary, pseudosecondary and primary FIAs. The primary inclusions form discrete clusters and trails that terminate at quartz grain boundaries. Type 1 brine-rich, Type 2 aqueous liquid-rich, and Type 3 vapour-rich varieties are all abundant as primary and pseudosecondary inclusions. Studied inclusions displayed irregular to equant negative crystal shapes that ranged from 5 to 25 μm in long dimension (mean 9 ± 4 μm).

7.2. Microthermometric results

7.2.1. Stage 3 veins

Fluid inclusions were cooled to -110° C and reheated slowly to check for CO_2, identify major cations, and calculate fluid salinities where possible. Eutectic (T_e) and final ice melting temperatures (T_m) were not collected from Type 3 vapour-rich inclusions because of the difficulty observing the first (eutectic) and final melting of solid ice. Carbonic fluids were not detected in any of the fluid inclusions studied. The Type 1 FIAs predominately homogenized by halite dissolution (Fig. 30), which indicates that they are not the result of unmixing or "boiling" of a supercritical fluid on the H_2O-NaCl solvus into immiscible vapour and liquid phases (e.g., Bodnar and Vityk, 1994). Salinities calculated using the dissolution temperatures of halite during heating of Type 1 inclusions range from 37.8 to 47.9 equivalent weight percent NaCl (equiv. wt.% NaCl) with a mean of 41.6 equiv. wt.% NaCl (n = 9). The T_e measured during freezing of Type 1 inclusions are below the eutectic temperature for pure NaCl-H_2O (-21.2° C). This implies the presence of dissolved cations other than Na+ (e.g., Shepherd et al., 1985). This finding is consistent with the existence of sylvite (KCl) and carbonate daughter minerals (calcite, dolomite, and ankerite) in Type 1 inclusions, which indicate the presence of K^+, Ca^{2+} Mg^{2+} and $Fe^{2+,3+}$ in addition to Na^+. The presence of cations other than Na^+ is the reason that salinity is expressed as "equivalent weight percent NaCl" (e.g., Shepherd et al., 1985). Type 1 brine-rich inclusions have a homogenization

Table 1. Major (wt.%.) and trace (ppm) element data. Abbreviations as follows: Dacite BX=plagioclase-hornblende-phyric dacite breccia; Dacite=plagioclase-hornblende-phyric dacite; HBX=hydrothermal breccia; VolSS=volcanic sandstone; Undiff=undifferentiated lithology; Monz=monzonite; Qtz-bio monz=quartz-biotite monzonite; Qtz monz=quartz monzonite.

Lithology	Qtz-bio monz	Dacite BX	Qtz monz	Basalt	Basalt	Dacite BX	monz	VolSS	Qtz-bio monz	Qtz-bio monz	Qtz monz
Hole_ID	MAG12-03	MAG12-03	MAG12-03	MAG12-04	MAG12-04	MAG12-04	MAG12-05	MAG12-05	MAG12-05	MAG12-05	MAG12-05
From (m)	333.6	366	405	78	84	125	229	255	302.55	331	361
To (m)	335	368	406.91	81	86.15	127	231	257	303.27	332.1	363
Au_ppm	0.011	0.155	0.039	0.001	0.002	0.003	0.029	0.045	0.041	0.066	0.005
Cu%	0.0385	0.126	0.21	0.0051	0.0058	0.0276	0.141	0.152	0.0376	0.071	0.0197
SiO2%	67.8	51.9	65.2	49.5	46.8	59.6	66.1	53.2	64.5	62.3	53.6
Al2O3%	14.75	16.6	15.05	14.75	16.2	18.5	15.25	17.05	16.7	17.2	16.95
Fe2O3%	3.32	10.8	2.24	10.75	9.11	3.01	2.38	9.38	4.47	5	8.34
CaO%	3.95	7.45	4.67	10.5	11.2	5.01	4.13	4.36	4.43	4.27	8.61
MgO%	1.09	5.03	0.93	5.21	2.94	2.45	1.27	5.01	1.55	1.96	4.12
Na2O%	3.74	3.73	2.54	3.28	3.31	4.12	3.57	2.82	4.33	4.38	3.63
K2O%	3.53	1.92	2.44	0.61	0.45	1.11	1.48	2.33	2.48	1.76	1.02
Cr2O3%	-0.01	0.01	-0.01	0.04	0.05	-0.01	-0.01	-0.01	-0.01	-0.01	0.01
TiO2%	0.32	0.84	0.33	1.75	1.97	0.54	0.36	0.7	0.43	0.5	0.75
MnO%	0.04	0.14	0.16	0.24	0.35	0.09	0.06	0.1	0.03	0.03	0.1
P2O5%	0.12	0.25	0.12	0.3	0.38	0.27	0.14	0.29	0.19	0.21	0.24
SrO%	0.06	0.07	0.03	0.09	0.12	0.05	0.04	0.06	0.09	0.09	0.07
BaO%	0.2	0.09	0.12	0.05	0.04	0.02	0.03	0.06	0.21	0.17	0.05
LOI%	1.72	2.9	6.43	4.12	5.65	5.85	4.5	4.54	1.71	2.44	3.56
Total%	100.64	101.73	100.26	101.19	98.57	100.62	99.31	99.9	101.12	100.31	101.05
Ag_ppm	-1	-1	1	-1	-1	-1	1	-1	-1	-1	-1
Ba_ppm	1670	728	969	388	343	153	276	509	1670	1370	404
Ce_ppm	7.7	15.3	17.5	25.7	28	14.3	9.4	18.5	15.3	19.9	14.1
Co_ppm	6.4	21.7	4	49.2	43.2	18	19.4	21.5	7.4	11.1	18.1
Cr_ppm	30	80	30	340	360	20	30	20	30	30	60
Cs_ppm	0.42	1.14	5.08	0.28	0.13	2.46	2.29	2.71	0.79	1.14	1.17
Cu_ppm	327	1150	1865	51	57	264	1325	1405	359	659	220
Dy_ppm	1.13	3.55	1.7	3.95	4.38	2.57	1.5	3.2	1.72	2.19	3.05
Er_ppm	0.7	2.07	1.06	1.9	2.07	1.66	0.97	1.86	1	1.3	1.78
Eu_ppm	0.53	0.97	0.62	1.61	1.77	0.71	0.51	0.81	0.74	0.86	0.94
Ga_ppm	16.7	18.2	16.6	21.3	22.9	18.7	16.2	18.2	18.9	21	19.5
Gd_ppm	1.13	3.34	1.79	4.63	5.11	2.3	1.47	2.93	1.87	2.44	3.09
Hf_ppm	2.9	1.6	3	3.1	3.2	2	3.1	2	3.2	2.9	2
Ho_ppm	0.24	0.74	0.36	0.76	0.83	0.58	0.33	0.67	0.35	0.48	0.67
La_ppm	3.9	6.9	9.1	12.1	13.1	7.5	4.7	8.9	7.8	9.6	6.5
Lu_ppm	0.14	0.32	0.2	0.23	0.25	0.31	0.19	0.3	0.17	0.24	0.3
Mo_ppm	3	2	2	2	2	7	3	-2	2	2	6
Nb_ppm	1.7	1.5	3.1	13.8	15.3	1.9	2.5	1.7	2.4	2.8	1.6
Nd_ppm	4.5	10.7	8.6	16	17.3	8.4	5.5	11.3	8.3	10.9	9.4
Ni_ppm	8	23	6	185	127	7	10	12	9	9	20
Pb_ppm	5	5	5	-5	-5	9	-5	8	5	-5	-5
Pr_ppm	1.03	2.25	2.25	3.51	3.87	1.92	1.3	2.48	1.98	2.63	2.04
Rb_ppm	40.3	43	79.1	8.9	4.9	41.2	48.1	79.4	34.8	33.3	27.8
Sm_ppm	1.04	2.66	1.89	4.45	4.59	2.04	1.33	2.76	1.9	2.54	2.6
Sn_ppm	1	1	1	1	1	1	1	1	1	2	1
Sr_ppm	524	541	274	751	1015	369	311	453	697	701	568
Ta_ppm	0.2	0.1	0.3	0.9	1.1	0.1	0.2	0.1	0.2	0.2	0.1
Th_ppm	3.86	0.99	5.08	1.72	1.55	1.09	3.81	1.22	3.06	2.58	1.31
Tl_ppm	-0.5	-0.5	-0.5	-0.5	-0.5	-0.5	-0.5	-0.5	-0.5	-0.5	-0.5

Table 1. Cont'd.

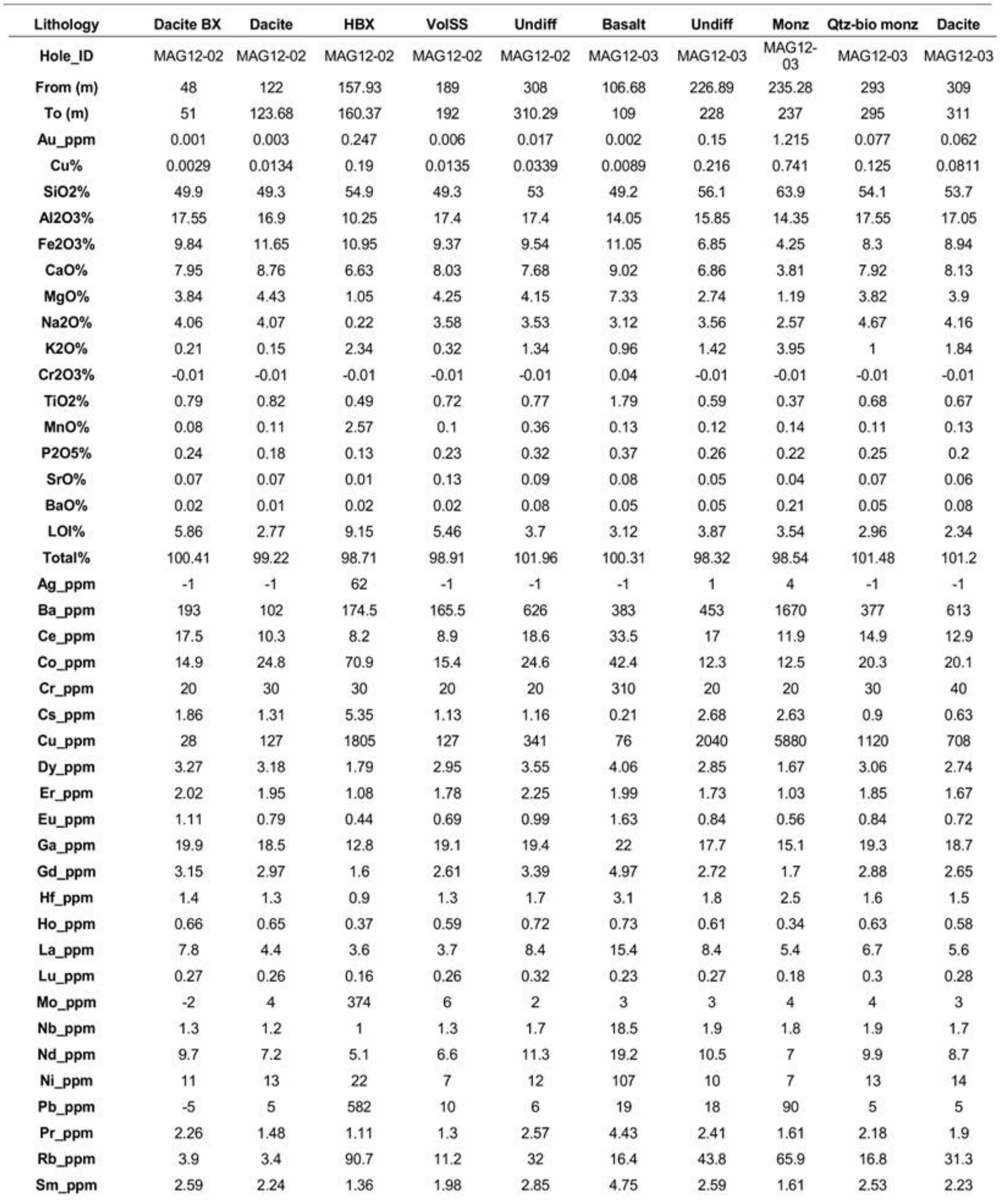

Lithology	Dacite BX	Dacite	HBX	VolSS	Undiff	Basalt	Undiff	Monz	Qtz-bio monz	Dacite
Hole_ID	MAG12-02	MAG12-02	MAG12-02	MAG12-02	MAG12-02	MAG12-03	MAG12-03	MAG12-03	MAG12-03	MAG12-03
From (m)	48	122	157.93	189	308	106.68	226.89	235.28	293	309
To (m)	51	123.68	160.37	192	310.29	109	228	237	295	311
Au_ppm	0.001	0.003	0.247	0.006	0.017	0.002	0.15	1.215	0.077	0.062
Cu%	0.0029	0.0134	0.19	0.0135	0.0339	0.0089	0.216	0.741	0.125	0.0811
SiO2%	49.9	49.3	54.9	49.3	53	49.2	56.1	63.9	54.1	53.7
Al2O3%	17.55	16.9	10.25	17.4	17.4	14.05	15.85	14.35	17.55	17.05
Fe2O3%	9.84	11.65	10.95	9.37	9.54	11.05	6.85	4.25	8.3	8.94
CaO%	7.95	8.76	6.63	8.03	7.68	9.02	6.86	3.81	7.92	8.13
MgO%	3.84	4.43	1.05	4.25	4.15	7.33	2.74	1.19	3.82	3.9
Na2O%	4.06	4.07	0.22	3.58	3.53	3.12	3.56	2.57	4.67	4.16
K2O%	0.21	0.15	2.34	0.32	1.34	0.96	1.42	3.95	1	1.84
Cr2O3%	-0.01	-0.01	-0.01	-0.01	-0.01	0.04	-0.01	-0.01	-0.01	-0.01
TiO2%	0.79	0.82	0.49	0.72	0.77	1.79	0.59	0.37	0.68	0.67
MnO%	0.08	0.11	2.57	0.1	0.36	0.13	0.12	0.14	0.11	0.13
P2O5%	0.24	0.18	0.13	0.23	0.32	0.37	0.26	0.22	0.25	0.2
SrO%	0.07	0.07	0.01	0.13	0.09	0.08	0.05	0.04	0.07	0.06
BaO%	0.02	0.01	0.02	0.02	0.08	0.05	0.05	0.21	0.05	0.08
LOI%	5.86	2.77	9.15	5.46	3.7	3.12	3.87	3.54	2.96	2.34
Total%	100.41	99.22	98.71	98.91	101.96	100.31	98.32	98.54	101.48	101.2
Ag_ppm	-1	-1	62	-1	-1	-1	1	4	-1	-1
Ba_ppm	193	102	174.5	165.5	626	383	453	1670	377	613
Ce_ppm	17.5	10.3	8.2	8.9	18.6	33.5	17	11.9	14.9	12.9
Co_ppm	14.9	24.8	70.9	15.4	24.6	42.4	12.3	12.5	20.3	20.1
Cr_ppm	20	30	30	20	20	310	20	20	30	40
Cs_ppm	1.86	1.31	5.35	1.13	1.16	0.21	2.68	2.63	0.9	0.63
Cu_ppm	28	127	1805	127	341	76	2040	5880	1120	708
Dy_ppm	3.27	3.18	1.79	2.95	3.55	4.06	2.85	1.67	3.06	2.74
Er_ppm	2.02	1.95	1.08	1.78	2.25	1.99	1.73	1.03	1.85	1.67
Eu_ppm	1.11	0.79	0.44	0.69	0.99	1.63	0.84	0.56	0.84	0.72
Ga_ppm	19.9	18.5	12.8	19.1	19.4	22	17.7	15.1	19.3	18.7
Gd_ppm	3.15	2.97	1.6	2.61	3.39	4.97	2.72	1.7	2.88	2.65
Hf_ppm	1.4	1.3	0.9	1.3	1.7	3.1	1.8	2.5	1.6	1.5
Ho_ppm	0.66	0.65	0.37	0.59	0.72	0.73	0.61	0.34	0.63	0.58
La_ppm	7.8	4.4	3.6	3.7	8.4	15.4	8.4	5.4	6.7	5.6
Lu_ppm	0.27	0.26	0.16	0.26	0.32	0.23	0.27	0.18	0.3	0.28
Mo_ppm	-2	4	374	6	2	3	3	4	4	3
Nb_ppm	1.3	1.2	1	1.3	1.7	18.5	1.9	1.8	1.9	1.7
Nd_ppm	9.7	7.2	5.1	6.6	11.3	19.2	10.5	7	9.9	8.7
Ni_ppm	11	13	22	7	12	107	10	7	13	14
Pb_ppm	-5	5	582	10	6	19	18	90	5	5
Pr_ppm	2.26	1.48	1.11	1.3	2.57	4.43	2.41	1.61	2.18	1.9
Rb_ppm	3.9	3.4	90.7	11.2	32	16.4	43.8	65.9	16.8	31.3
Sm_ppm	2.59	2.24	1.36	1.98	2.85	4.75	2.59	1.61	2.53	2.23

(to the liquid phase) temperatures (T_h) that range from 210 to 302° C. Total homogenization temperatures (T_h total) indicated by the dissolution of halite range from 295 to 404° C (Table 2). Individual FIAs show < 15° C variation between T_h.

7.2.2. Stage 4 veins

Similar to stage 3 veins, all fluid inclusions were cooled to -110° C and slowly reheated to check for CO_2, identify the major cations, and to calculate salinities where possible. Carbonic fluids were not detected in any of the fluid inclusions. Eutectic temperatures and final ice melting temperatures were not collected in Type 3 vapour-rich inclusions owing to the difficulty observing the first and final melting of solid ice. The Type 1 FIAs display predominantly halite-homogenization characteristics (Fig. 30). Salinities calculated using the dissolution temperatures of halite during heating range from 34.7 to 49.7 equiv. wt.% NaCl (mean = 41.7 equiv. wt.% NaCl, n = 7). The eutectic temperatures measured during freezing of

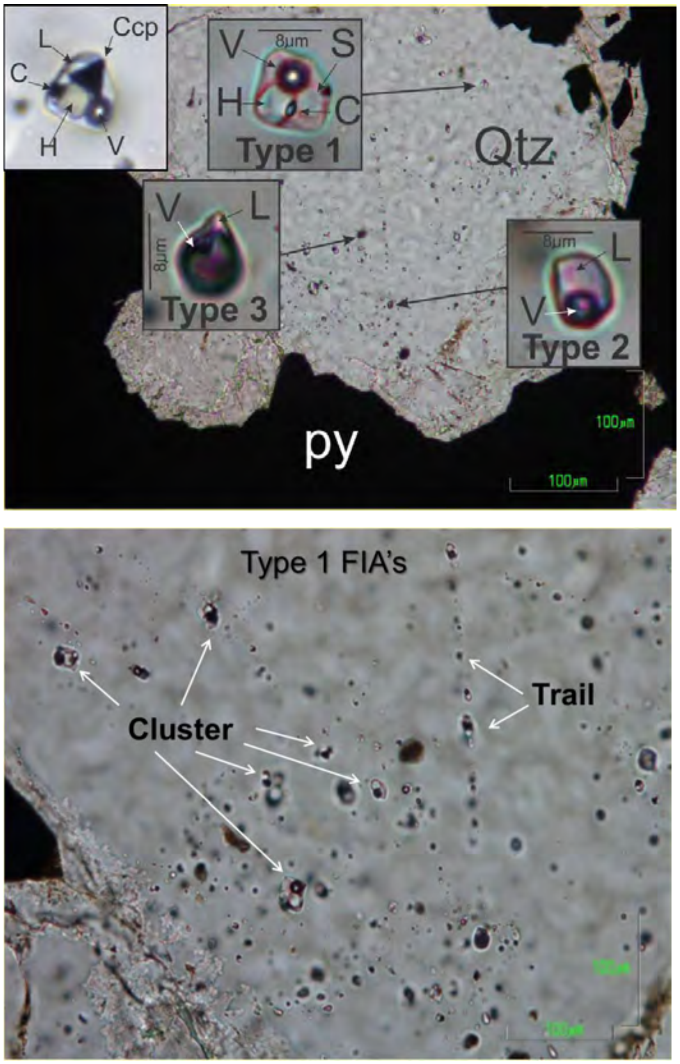

Fig. 29. Fluid inclusion classification at Three Firs. **a)** Photomicrographs of hydrothermal quartz adjacent to pyrite containing: Type 1 halite-saturated, multisoild, aqueous, liquid-rich inclusions; Type 2 "mixed" aqueous, liquid-rich inclusions; and Type 3 low salinity, aqueous, vapour-rich inclusions. Note the opaque, triangular chalcopyrite (Ccp) daughter mineral in Type 1 inclusion in top left inset figure. **b)** Type 1 FIAs occurring as primary clusters and in pseudosecondary trails in hydrothermal quartz. Abbreviations: L=liquid, V=vapour, H=halite, C=carbonate, Ccp=chalcopyrite, Py=pyrite, Qtz=quartz.

Type 1 inclusions are below the eutectic for pure NaCl-H_2O (-21.2° C), which indicate the presence of K^+, Ca^{2+} Mg^{2+} and $Fe^{2,3+}$ in addition to Na^+ (Shepherd et al. 1985). Type 1 brine-rich inclusions have T_h (to the liquid phase) that range from 237 to 430° C and (T_h total), indicated by the dissolution of the halite daughter crystal, that range from 250 to 420° C (Table 2). Individual FIAs have < 15° C variation between T_h.

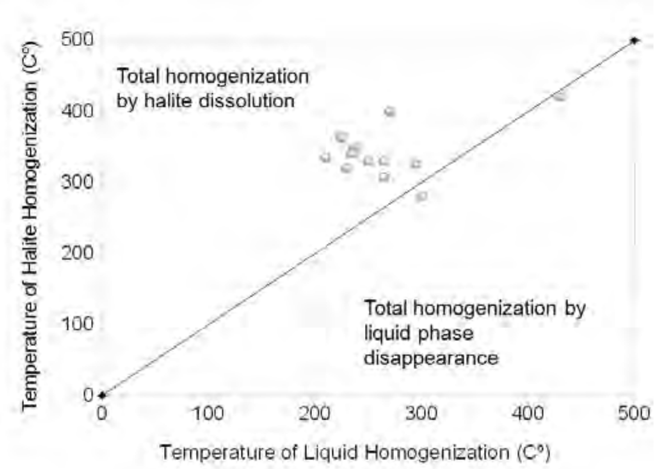

Fig. 30. Homogenization characteristics of Three Firs Type 1 fluid inclusion assemblages. Each symbol is a FIA that represents an average value of 3 to 11 individual inclusions. Symbols size is approximately equal to the error (± 10%) of the measured homogenization temperature. Note that Three Firs Type 1 inclusions are almost exclusively homogenized by halite dissolution.

7.3. Physiochemical conditions of the hydrothermal ore fluids at Three Firs

In both stage 3 and 4 veins, Type 1 inclusions homogenized by halite dissolution at temperatures higher than those recorded for the homogenization of the vapour phase to the liquid phase, i.e., "vapour bubble" disappearance (Fig. 30). Consequently, Type 1 brine-rich and Type 3 vapour-rich fluid inclusions cannot represent the immiscible endmembers of a single phase (supercritical) fluid unmixing on the H_2O-NaCl solvus as explained in Bodnar and Vityk (1994). This finding is consistent with the lack of petrographic evidence for fluid unmixing. Specifically, Type 1 brine-rich and Type 3 vapour-rich inclusions never occur together in the same trail or cluster as would be expected during fluid unmixing (Roedder, 1984). Consequently, the total homogenization temperatures measured only represent minimum estimates of the trapping temperature. The fact that Type 1 and Type 3 inclusions were trapped in the same quartz grain but are not in chemical equilibrium, suggests that aqueous brines and vapours have migrated from their original sites of fluid unmixing. This non-equlibrium trapping of immiscible vapour and brines is recognized in other porphyry systems, for example the Early Jurassic Kemess South porphyry Cu-Au deposit in the Toodoggone district (Duuring et al., 2009a) and the Bingham and Butte porphyry Cu-Mo ± Au deposits in Utah and Montana, respectively (Rusk et al., 2008 and references therein). The "mixed" Type 2 liquid-rich fluid inclusions are interpreted to be mechanical (i.e., non-equilibrium) mixtures of Type 1 brines and Type 3 vapours circulating in the Three Firs hydrothermal system. Consequently, they cannot be used to infer physicochemical conditions of ore formation and were not measured.

Total homogenization temperatures for primary and pseudosecondary fluid inclusions in stage 3 quartz-hornblende-sulphide ± K-feldspar veins range from 295 to 400° C with corresponding pressures ranging between 0.6 and 2.5 kbar (Fig. 31). These temperatures and pressures are minimum estimates because the true trapping pressure and temperature will lie somewhere higher along the projected isochores calculated for the individual FIAs. Assuming a lithostatic load of 3.3 km/kbar (Hagemann and Brown, 1996), a minimum calculated pressure of 1.1 kbar corresponds to a formational depth of 3.6 km for stage 3 veins in sample MAG12-03-172.9 (Fig. 31a). For stage 3 veins in sample MAG12-05-274.1 a minimum calculated pressure of 0.6 kbar corresponds to a minimum formational

Table 2. Summary of microthermometric data from the Three Firs veins. Microthermometric methods are described in the text. Salinities (equiv. wt.% NaCl) were calculated using the Bodnar and Vityk (1994) equations of state for the H_2O-NaCl-KCl system.

FIA	Sample Chip	Petrographic Description at STP	Type of Inclusion	Vol % (Vapor)	T_h (°C) (L-V)	T_h Halite (°C)	T_m Ice (°C)	Salinity %wt.
Stage 4 vein: ***Qtz-hbl-ccp-py ± (bo-cv-cu-cc) ± carb ± mag ± ep ± chl (medial sutures)***								
D (n=7)	MAG12-05-302.5-C4	Quartz hosts randomly arranged, equant- to negative crystal-shaped, brine-rich, pseudosecondary inclusions that contain a halite daughter crystal and a second translucent mineral (carbonate/sylvite?)	Brine rich	10-15%	295°C ± 3°C (L)	325°C ± 15°C	-38°C ± 2°C	40.1
E (n=6)	MAG12-05-302.5-C5	Quartz hosts randomly arranged, irregular- to negative crystal-shaped, brine-rich, pseudosecondary inclusions that contain a halite daughter crystal and sometimes two translucent minerals (carbonate±sylvite?)	Brine rich	10-15%	237°C ± 5°C (L)	350°C ± 5°C	-39°C ± 2°C	42.4
F (n=4)	MAG12-05-302.5-C5	Quartz hosts randomly arranged, irregular- to negative crystal-shaped, brine-rich, pseudosecondary inclusions that contain a halite daughter crystal and a second translucent sub-rounded mineral (sylvite?)	Brine rich	10-15%	430 ± 5°C (L)	420 ± 5°C	-40°C ± 5°C	49.6
Stage 4 vein: ***Qtz-hbl-ccp-py ± (bo-cv-cu-cc) ± carb ± mag ± ep ± chl (medial sutures)***								
K (n=8)	MAG12-03-164.75-C1	Quartz hosts linearly arranged, equant to negative crystal shaped, brine rich, primary inclusions with a halite daughter crystal and small translucent solid (carbonate), oriented about a growth margin proximal to chalcopyrite grain	Brine rich	10-25%	270°C ± 20°C (L)	400°C ± 20°C	-40 ± 5°C	47.4
L (n=6)	MAG12-03-164.75-C2	Quartz hosts linearly arranged, equant to negative crystal shaped, two-phase, liquid rich, several appear to have small cubic solid (halite?) pseudosecondary inclusions proximal to a chalcopyrite grain.	Brine rich	15-20%	240°C ± 5°C (L)	250 ± 10°C	-28°C ± 2°C	34.6
O (n=4)	MAG12-03-164.75-C4	Quartz hosts randomly arranged, equant- to negative crystal-shaped, brine-rich, pseudosecondary inclusions that contain a halite daughter crystal and a second translucent mineral (carbonate/sylvite?)	Brine rich	10-15%	300°C ± 5°C (L)	280°C ± 10°C	-40°C ± 6°C	36.6
R (n=7)	MAG12-03-164.75-C6	Quartz hosts randomly arranged, equant- to negative crystal-shaped, brine-rich, pseudosecondary inclusions that contain a halite daughter crystal and a second translucent mineral (carbonate/sylvite?) proximal to sulphide grain	Brine rich	10-15%	250°C ± 10°C (L)	330°C ± 15°C	-40°C ± 5°C	40.6
Stage 3 vein: ***Qtz-hbl-ccp-py ± (bo-cv-cu-cc) ± carb ± mag ± ep ± chl ± ksp***								
U (n=11)	MAG12-05-172.90-C1	Quartz hosts randomly arranged, irregular to negative crystal shaped, brine rich, psuedosecondary inclusions with a halite daughter crystal and one or two small translucent solids (carbonate and or Sylvite), proximal to chalcopyrite grain	Brine rich	10-15%	265°C ± 5°C (L)	330°C ± 15°C	-38°C ± 7°C	40.1
W (n=11)	MAG12-05-172.90-C2	Quartz hosts randomly arranged, equant- to negative crystal-shaped, brine-rich, primary inclusions that contain a halite daughter crystal and a second translucent mineral (carbonate/sylvite?) proximal to chalcopyrite grain	Brine rich	10-15%	210°C ± 10°C (L)	335°C ± 15°C	-43°C ± 5°C	41.0
Z (n=6)	MAG12-05-172.90-C5	Quartz hosts randomly arranged, irregular to negative crystal shaped, brine rich, psuedosecondary inclusions with a halite daughter crystal and one or two small translucent solids (carbonate and or Sylvite)	Brine rich	10-15%	225°C ± 5°C (L)	365°C ± 8°C	-30°C ± 5°C	43.8
AB (n=5)	MAG12-05-172.90-C6	Quartz hosts randomly arranged, irregular to negative crystal shaped, brine rich, psuedosecondary inclusions with a halite daughter crystal and one or two small translucent solids (carbonate and or Sylvite) quartz embayed by pyrite grain.	Brine rich	5-10%	265°C ± 5°C (L)	307°C ± 10°C	-37°C ± 5°C	38.7
Stage 3 vein: ***Qtz-hbl-cpy-py ± (bo-cv-cu-cc) ± carb ± mag ± ep ± chl ± ksp***								
AE (n=6)	MAG12-03-274.12-C1	Quartz hosts randomly arranged, irregular to negative crystal shaped, brine rich, psuedosecondary inclusions with a halite daughter crystal and one or two small translucent solids (carbonate and or Sylvite)	Brine rich	10-12%	225°C ± 5°C (L)	362°C ± 8°C	-42°C ± 5°C	43.5
AF (n=5)	MAG12-03-274.12-C2	Quartz hosts randomly arranged, equant, brine rich, psuedosecondary inclusions with a halite daughter crystal and small translucent solid (carbonate)	Brine rich	5-20%	235°C ± 5°C (L)	340°C ± 10°C	-34°C ± 5°C	41.4
AL (n=3)	MAG12-03-274.12-C4	Quartz hosts randomly arranged, equant to negative crystal shaped, brine rich, psuedosecondary inclusions with a halite daughter crystal, one or two small translucent solids (carbonate and or Sylvite) and daughter sulphide (triangular opaque)	Brine rich (S)	10-12%	265°C ± 5°C (L)	404°C ± 3°C	-41°C ± 4°C	47.8
AM (n=4)	MAG12-03-274.12-C4	Quartz hosts randomly arranged, equant to negative crystal shaped, brine rich, psuedosecondary inclusions with a halite daughter crystal and one or two small translucent solids (carbonate and or Sylvite)	Brine rich	5-20%	302°C ± 18°C (L)	295°C ± 15°C	-40°C ± 5°C	37.7
AQ (n=4)	MAG12-03-274.12-C7	Quartz hosts randomly arranged, equant to negative crystal shaped, brine rich, psuedosecondary inclusions with a halite daughter crystal	Brine rich	5-10%	230°C ± 5°C (L)	320°C ± 5°C	n/a	39.7

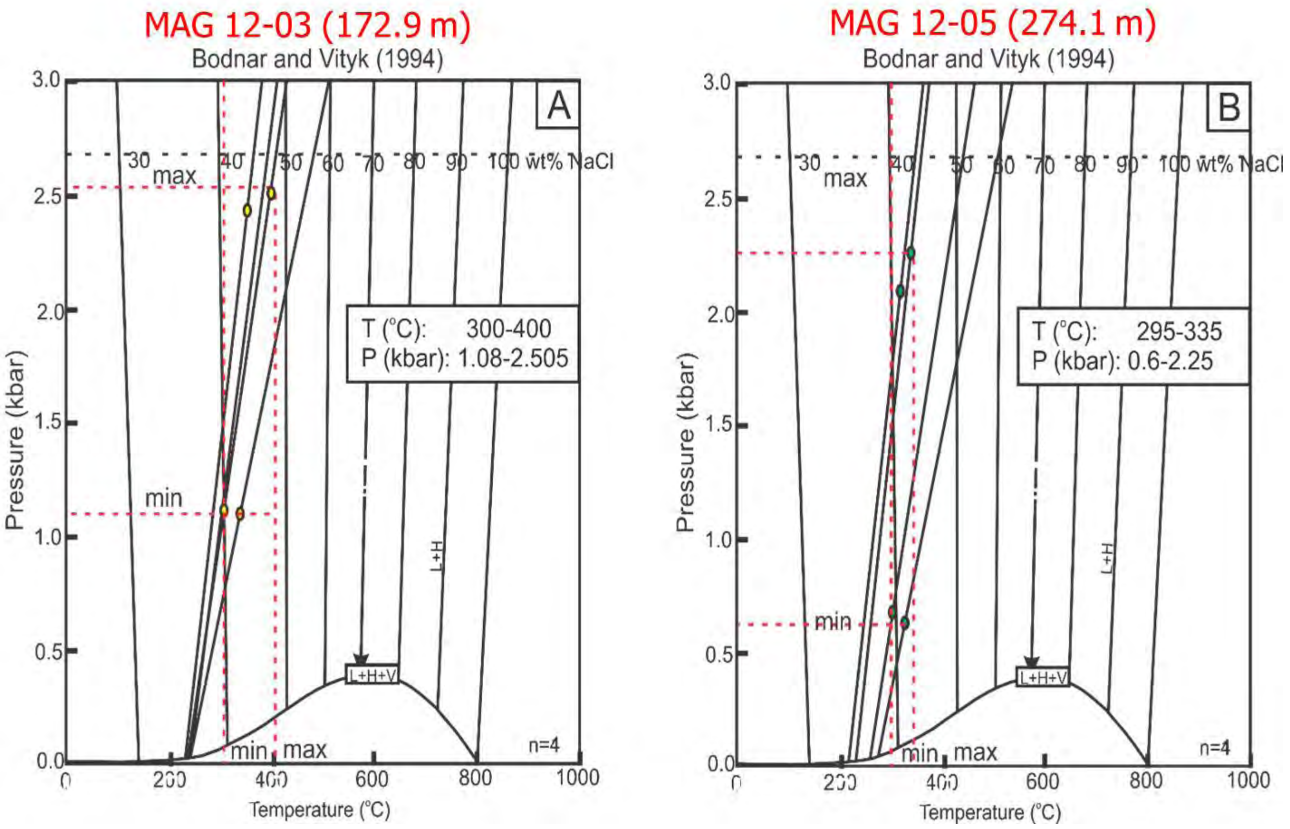

Fig. 31. Pressure-temperature diagrams showing calculated isochores for each FIA using the Bodnar and Vityk (1994) equations of state. These isochores allow estimating P-T trapping condition in stage 3 veins. **a)** Sample MAG12-03 172.9 m. **b)** Sample MAG12-05 274.1 m.

depth of 2.0 km (Fig. 31b). The higher pressures calculated for several FIA's in stage 3 veins (2.5 kbar in MAG12-03-172.9 and 2.3 kbar in MAG12-05-274.1) correspond to formational depths of 7 or 8 km, which is deeper than most porphyry deposits, although Butte porphyry Cu deposit in Montana has purportedly formed at 9 km (Rusk et al., 2008).

Stage 4 quartz-hornblende-sulphide veins host primary and pseudosecondary fluid inclusions with total homogenization temperatures that range from 250 to 420° C (Table 2) with corresponding pressures ranging between 0.6 to 2.6 kbar (Fig. 32). Similar to the stage 3 veins, these temperatures and pressures are minimum estimates. True trapping pressures and temperatures will fall somewhere higher along the projected isochores calculated for the individual FIAs. Assuming a lithostatic load of 3.3 km/1 kbar, a minimum calculated pressure of 0.6 kbar corresponds to a formational depth of 2.0 km for stage 4 veins in sample MAG12-03-164.7 (Fig. 32a). For stage 4 veins in sample MAG12-05-302.5 (Fig. 32b), a minimum calculated pressure of 1.4 kbar corresponds to a formational depth of 4.6 km. The higher pressures calculated for several FIA's in stage 4 veins (2.0 kbar in MAG12-03-164.7 and 2.6 kbar in MAG12-05-302.5) correspond to formational depths in excess of 8 km, several kilometres deeper than most porphyry deposits (e.g., Sillitoe, 2010).

In summary, the microthermometric data suggest that the main stages of Cu-Au mineralization (the stage 3 and 4 veins) occurred at depths between 2 and 4.6 km and at temperatures from ~ 300 to 400° C using minimum pressure-temperature estimates. This is the expected pressure-temperature range for the formation of porphyry Cu-Mo-Au deposits and accords well with the style of veins, types of alteration, and geological features at the Three Firs prospect. Although calculated pressures are imprecise, the steep positive slope of the isochores means that the temperatures measured are close (± 30° C) to the true trapping temperatures (Bodnar and Vityk, 1994).

The high salinities and pressures calculated for some FIAs in Main stage veins at Three Firs likely do not record the actual P-T-X conditions of mineralization for several reasons. First, the equations of state used to calculate isochores are inherently inaccurate at high salinities (> 50 wt.% NaCl) and pressures (> 2.0 kbar), resulting in potentially erroneous thermodynamic estimates of pressure and temperature (Becker et al., 2008). Second, FIAs that exhibit very high salinities (> 50 equiv. wt.% NaCl) may be the result of post-entrapment water loss along microfractures resulting in a change in volume and increased salinity, hence they do not represent original fluid compositions. Third, we may have incorporated inclusions into a FIA that are not part of a single discrete fluid event. Finally, we may have measured fluid inclusions that were opened (decrepitated) and subsequently re-sealed with little visible evidence that they were modified after entrapment.

8. Alteration reflectance spectroscopy

Spectral Evolution's (TM) SpecTERRA reflectance spectroscopy was used to identify clay alteration minerals and gain a better understanding of hydrothermal alteration at

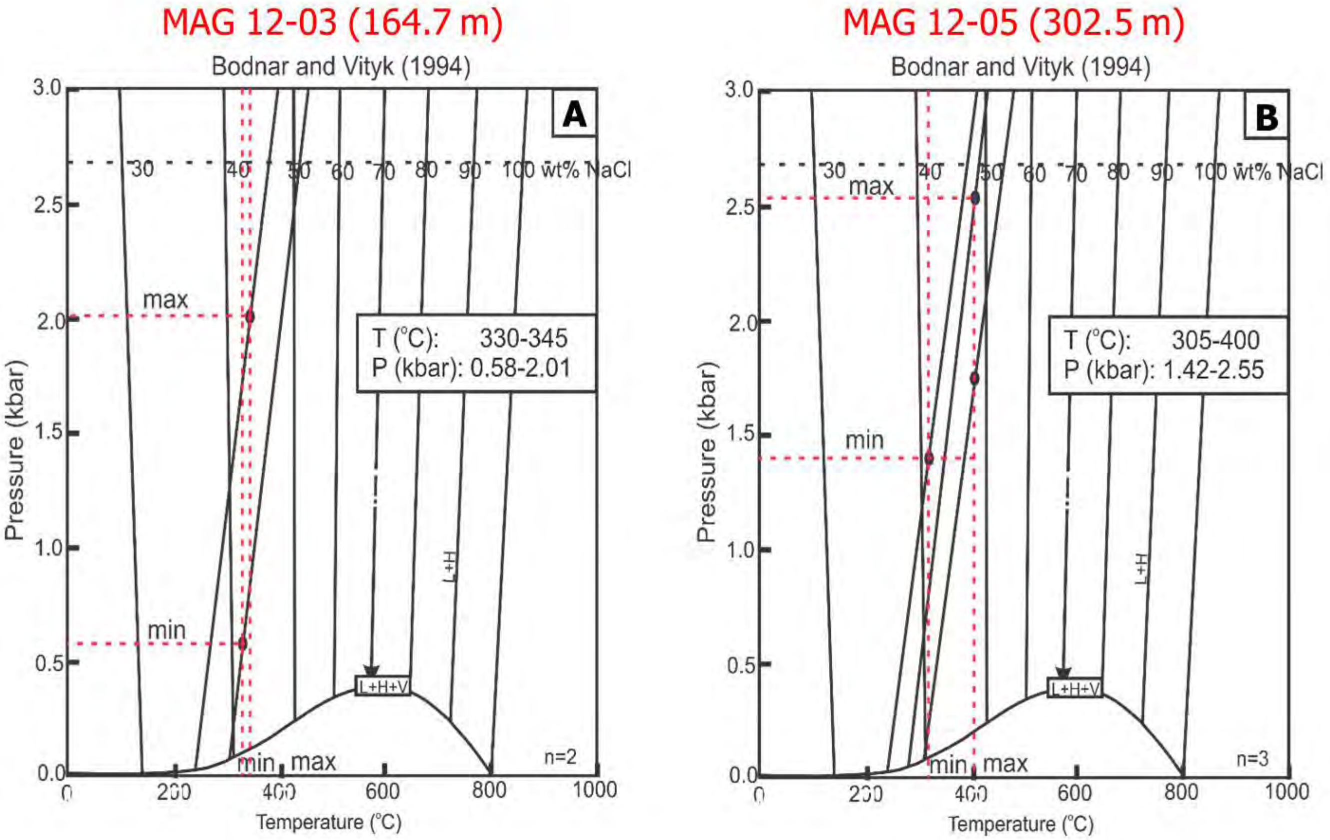

Fig. 32. Pressure-temperature diagrams showing calculated isochores for each FIA using the Bodnar and Vityk (1994) equations of state. These isochores permit estimating P-T trapping condition in stage 4 veins. **a)** Sample MAG12-03-164.7 m. **b)** Sample MAG12-05-302.5 m.

the Three Firs prospect. Clay minerals are typically too fine grained to identify in thin section, and reflectance spectra data are necessary to fully characterize mineralogy. Every mineral has its own characteristic reflectance spectra, which reflects physiochemical bonds in a mineral's crystal structure. By analyzing the position and shape of spectral features, minerals can be identified and, based on the sharpness or depth of a given spectral feature, their crystallinity established.

The reflectance data were collected on three targets in a sample interval. A comprehensive 43-element assay data for the same interval allowed for robust interpretation and comparison. Care was taken to avoid analyzing targets that were dusty or wet, which would have resulted in erroneous spectra. Where possible, targets were selected after geological interpretation and identification of minerals in hand sample. Spectra for each target were subsequently uploaded for interpretation using DarWin and SpecMin software packages.

Our reflectance spectroscopy work revealed piedmontite, clinochlore, hydromuscovite, illite-smectite interlayers, and crystalline illite (Figs. 33 a-e); crystalline kaolinite was identified by Spectral Evolution geologists (Kari Wurst, pers. comm. 2013). Crystalline illite is a white mica commonly associated with sericite and muscovite in phyllic alteration zones generated by relatively hot (> 220° C), moderately acidic hydrothermal fluids (e.g., Reyes, 1990; Ji and Brown, 2000). Crystalline kaolinite is typically associated with argillic alteration zones that form at slightly lower temperatures (> 200° C) and moderate acidities (e.g., White and Hedenquist, 1995; Seedorff et al., 2005). Both illite and kaolinite can form under near-surface conditions at very low temperatures, but with a low crystallinity. Thus, the identification of crystalline illite and kaolinite confirms that they represent hydrothermal alteration phases and are not the products of present-day surface weathering. Clinochlore is a Mg-rich chlorite associated with propylitic alteration and stage 7 (late) mineralized veins at Three Firs. It also may pre-date Cu-Au mineralization and have formed via contact and/or regional metamorphism. Consequently, a complete understanding of the origins of clinochlore at Three Firs awaits further study.

Piemontite, a Ca-rich clinozoisite (epidote group) mineral, implies Ca-rich hydrothermal alteration at temperatures > 240° C (e.g., White and Hedenquist, 1995). Consequently, hydrothermal piedmontite could belong to both the calc-potassic and propylitic alteration assemblages at Three Firs.

9. Discussion and conclusions

9.1. Prospect geology

Because the Three Firs Cu-Au prospect is a new discovery our geological understanding is still at a rudimentary stage. Nonetheless, our study indicates that the prospect displays most of the key elements found in classic northern Cordilleran calc-alkaline porphyry Cu-Au (Mo) deposits. The most intense alteration and highest metal grades are spatially and temporally associated with a series of monzonite dikes that are part of a more extensive suite of granitic dikes. The different types of veins ("M", "A", "B", and "D" varieties) and associated

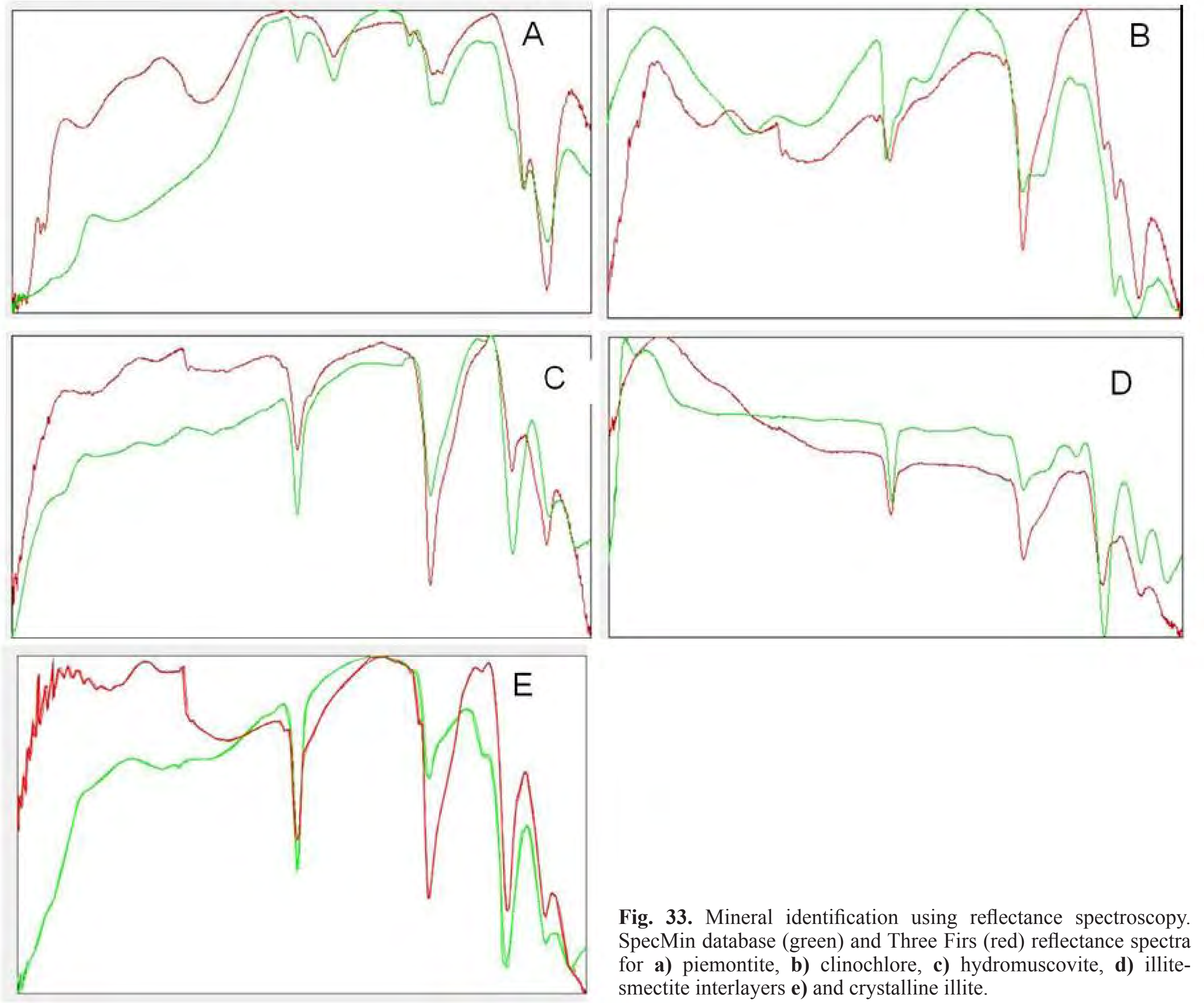

Fig. 33. Mineral identification using reflectance spectroscopy. SpecMin database (green) and Three Firs (red) reflectance spectra for **a)** piemontite, **b)** clinochlore, **c)** hydromuscovite, **d)** illite-smectite interlayers **e)** and crystalline illite.

styles of alteration (potassic, phyllic, calc-potassic, propylitic, and carbonate) are also characteristic of medium- to high-K, calc-alkaline porphyry Cu-Au-(Mo) deposits in the northern Cordillera (e.g., Seedorff et al., 2005). Eight stages of vein formation were identified, beginning with pre-mineralization, through early, main and late mineralization, ending with post-mineralization. These stages represent separate but partially overlapping fluid events with the main stages (3, 4, and 5) producing most of the Cu-Au mineralization. A suite of rocks samples collected from drill core for whole-rock geochemistry and reflectance spectrometry confirm that Three Firs is related to medium-K, calc-alkaline magmas that formed in a volcanic arc environment.

9.2. Evolution of the magmatic-hydrothermal mineral system at Three Firs

Fluid inclusion studies indicate that the main stages of Cu-Au sulphide mineralization occurred at depths between 2 and 4.6 km, and at temperatures between 300 and 400° C. This temperature range corresponds to where Cu solubility (as $CuCl_2$) drops by ~ 95% in a normal porphyry ore fluid (e.g., Hezarkhani et al., 1999). Calculations by Hezarkhani et al. (1999) indicate that Cu solubility at 400° C is approximately 1000 ppm whereas at 350° C it is only 25 ppm. Thus, the focussed deposition of Cu (Au) sulphides in “A” veins (stage 3) and “B” veins (stage 4) is to be expected, based on the dramatic decrease in Cu solubility during the formation of these main stage veins. These Cu solubility studies also provide a reason why subsequent stages of vein formation contain much less Cu: they formed from “spent” fluids that deposited virtually all their Cu at higher temperatures. Rare native Au in grains of disseminated chalcopyrite-bornite in altered wall-rock surrounding later (cooler?) stage 5 “D” veins may be attributable to the greater solubility of Au compared to Cu at lower temperatures. Gammons and Williams-Jones (1997) have shown that Au is dissolved mainly as $AuCl_2^-$ at high temperatures, and solubilities decrease steadily with cooling. At lower temperatures, the predominant complex eventually switches to $Au(HS)_2^-$, at which point Au solubility may actually increase with cooling. The specific temperature of the chloridebisulphide transition in porphyry systems depends on the pH, the H_2S/Cl ratio of the original fluid, and whether or not boiling (fluid unmixing) has occurred (Gammons and Williams-Jones, 1997).

Isochores calculated from the equations of state in Bodnar and Vityk (1994) indicate that fluid inclusions were trapped at pressures ranging form 0.6 kbar to 1.42 kbar, which correspond to 2 to 4.6 km depth, assuming a lithostatic load. The assumption of lithostatic rather than hydrostatic load is justified, given the lack of fluid inclusion evidence for boiling, which only occurs under hydrostatic conditions (e.g., Haas, Jr., 1976). As discussed above, the lack of boiling during vein formation at Three Firs is indicated by the homogenization behaviour of halite in Type 1 aqueous fluid inclusions. In addition to the pressure estimates from fluid inclusions, evidence that Three Firs is a relatively deep-seated porphyry system comes from the lack of phreatic and magmatic-hydrothermal breccias (e.g., Sillitoe, 1985), absence of bladed quartz after calcite in the veins (Simmons and Christiansen, 1984), and simple crustification textures in the main stage veins that imply only one or two episodes of open-space filling. Finally, shallow (< 2 km) Au-rich epithermal zones have not been intersected in any holes drilled into the Three Firs prospect, although we have identified rare native Au (Fig. 19) and elevated Au abundances (up to 23 g/t Au) are found in small intervals (Sherlock et al., 2013).

9.3. Comparision to other porphyry prospects in the Woodjam district and elsewhere in the Canadian Cordillera

It has been suggested that the Woodjam district hosts both calc-alkaline and alkalic styles of porphyry Cu-Au mineralization (e.g., Blackwell et al., 2012a; del Real et al., 2013; Sherlock et al., 2013). This study demonstrates that Three Firs is a calc-alkaline porphyry Cu-Au deposit with many similarities to the Southeast Zone and Takom prospects. It also shares similarities with the Deerhorn (Scott, 2012; del Real et al., 2013) and Megabuck prospects, both of which have been tentatively identified as alkalic porphyry systems. Although work on these two porphyry systems is at an early stage, published studies on the types of alteration and styles of veins reveal many more similarities than differences amongst all the prospects (del Real et al., 2013). Moreover, the monzonite dikes associated with the Deerhorn porphyry prospect have been shown to be calc-alkaline and not alkalic intrusions (Scott, 2012). The ages of felsic intrusions associated with porphyry prospects in the Woodjam camp (Fig. 3) are also consistently younger than the alkalic intrusions that comprise the Late Triassic Copper Mountain suite (206-200 Ma). With few exceptions (Takom?), the U-Pb (zircon) ages of intrusions and Re-Os (molybdenite) ages of mineralization are < 200 Ma, consistent with magmatism in the Woodjam district being exclusively related to different phases of the Late Triassic-Early Jurassic (~203-193 Ma) Takomkane batholith (Schiarizza et al., 2009; Logan et al., 2011; Blackwell et al., 2012a).

Other calc-alkaline porphyry deposits in British Columbia with similarities to the Three Firs prospect include the Late Jurassic porphyry Cu-Au±Mo deposits (Kemess South, Kemess North and Pine) in the Toodoggone district (Duuring et al., 2009a, b), the Late Triassic Schaft Creek Cu-Mo-(Au) deposit in the Stikine arch (Scott et al., 2008), and the Late Cretaceous porphyry Cu±Mo±Au deposits (Huckleberry and Seel) associated with the Bulkley Intrusive Suite in the in Skeena arch (Jackson and Illerbrun, 1995; McDowell and Giroux, 2012).

9.4. Implications for further exploration

This study demonstrates that the Three Firs prospect formed in a pressure-temperature "window" that is optimal for the deposition of Cu and Au. Consequently, future exploration should continue to focus on the current Three Firs area and its immediate environs. It is unlikely that the bulk of the deposit remains undiscovered at depth because Cu and Au would have been in solution as soluble chloride complexes at the higher temperatures found in a porphyry root zone at depths of 4-5 km. The Au solubility studies allow that a slightly Au enriched zone could lie immediately above the current level of Cu-Au mineralization, but as discussed, there is no evidence for the development of high-grade, epithermal vein-style Au (Ag) zones. The Three Firs system is probably too deep.

On a regional scale, it may be worthwhile to reconsider the proposal that the Woodjam district hosts both alkalic and calc-alkaline styles of porphyry Cu-Au deposits. The geological, geochemical, and geochronological evidence is equivocal. A simpler model that considers all porphyry prospects to be high- to medium-K, calc-alkaline systems that formed from different intrusive phases of the Takomkane batholith removes the vexing problem of explaining how both alkalic and calc-alkaline porphyry systems form at the same time in the same place (e.g., Lang et al., 1995). To our knowledge there is no other porphyry camp in the world where this situation exists. A model invoking only calc-alkaline porphyry Cu-Au±Mo deposits in the Woodjam district is also more consistent with the easterly migrating Mesozoic magmatic arc proposed for the southern Nicola (Logan et al., 2011). According to this model, any alkalic porphyry Cu-Au deposits of the Late Triassic-Early Jurassic Copper Mountain suite should lie to the west of the younger calc-alkaline porphyry Cu-Au±Mo deposits of the Early Jurassic Takomkane suite at Woodjam. There is no requirement to have these two magmatic belts somehow converge and overlap in the Woodjam district.

Acknowledgments

This study is the result of a B.Sc. Honours thesis done by S. Vandekerkhove at the University of Victoria in 2012-2013, under the supervision of Drs. S. M. Rowins and S.T. Johnston. Gold Fields Canada, the British Columbia Geological Survey and the University of Victoria are all thanked for funding various aspects of this project and providing access to laboratory facilities. Gold Fields geologists Ross Sherlock, Twila Skinner, Amelia Rainbow, Jacqueline Blackwell, Matt Eckfeldt, Irene del Real, and Julia Scott are thanked for insightful discussions on the geology of the Three Firs prospect and the Woodjam district. Larry Aspler is thanked for a thorough review of the paper, which helped to clarify content and presentation. Finally, thanks go to friends and family of S. Vandekerkhove for their unstinting support during completion of this study.

References cited

Bailey, D.G., Bloodgood, M.A., Campbell, R.B., Panteleyev, A., Hancock, K.D., and Struik, L.C.,1990. Geology of the central

Quesnel Belt British Columbia NTS 93A/5, 6, 7, 11, 12, 13; 93B/9, 16; 93G/1; 93H/4; British Columbia Geological Survey Bulletin 97, Map 1, scale 1:100 000, 1 sheet.

Beane, R.E., and Titley, S.R., 1981. Porphyry copper deposits. Part II. Hydrothermal alteration and mineralization. Economic Geology 75th Anniversary Volume, p.235-269.

Becker, S.P., Fall, A., Bodnar, R.J., 2008. Synthetic fluid inclusions. XVII. PVTX properties of high salinity H_2O-NaCl solutions (> 30 wt.% NaCl): Application to fluid inclusions that homogenize by halite disappearance from porphyry copper and other hydrothermal ore deposits. Economic Geology, 103, 539-554.

Blackwell, J., Black, E. and Skinner, T., 2012a. National Instrument 43-101 Technical Report on 2011 activities on the Woodjam North Property, Cariboo Mining Division, British Columbia, Internal report prepared for Woodjam Consolidated Copper Corp., 134 p.

Blackwell, J.L., Lesage, G., Skinner, T., Eckfeldt, M., Black, E., Hamilton, J., Hertel, J., Laird, B., Madson, J., Rainbow, A., Sherlock, R., and Sepp, M., 2012b. Geology of the Woodjam Property core area, Gold Fields Internal Document, 15 p.

Bodnar, R.J., 1994. Synthetic fluid inclusions. XII: The system H_2O-NaCl. Experimental determination of the halite liquidus and isochores for a 40 wt.% NaCl solution. Geochimica et Cosmochimica Acta, 58, 1053–1063.

Bodnar R.J., and Vityk, M.O., 1994. Interpretation of microthermometric data for NaCl–H_2O fluid inclusions. In: De Vivo B., and Frezzotti M.L. (Eds.), Fluid inclusions in minerals: methods and applications. Virginia Polytechnic Institute and State University, Blacksburg, pp. 117–131.

Corbett, G.J., and Leach, T.M., 1998. Southwest Pacific Rim gold-copper systems: Structure, alteration, and mineralization. Society of Economic Geologists Special Publication 6, 154-182.

del Real, I., Hart C.J.R., Bouzari, F., Blackwell, J.L., Rainbow, A., Sherlock, R., and Skinner, T., 2013. Paragenesis and alteration of the Southeast Zone and Deerhorn deposits, Woodjam Property, Central British Columbia (Part of 093A). In: Geoscience BC Summary of Activities 2012. Geoscience BC Report 2013-01, 79-90.

Duuring, P., Rowins, S.M., McKinley, B.S.M., Dickinson, J.M., Diakow, L.J., Young-Seog, K., and Creaser, R.A., 2009a. Magmatic and structural controls on porphyry-style Cu-Au-Mo mineralization at Kemess South, Toodoggone District of British Columbia, Canada. Mineralium Deposita, 44, 435-462.

Duuring, P., Rowins, S.M., McKinley, B.S.M., Dickinson, J.M., Diakow, L.J., Young-Seog, K., and Creaser, R.A., 2009b. Examining potential genetic links between Jurassic porphyry Cu-Au±Mo and epithermal Au±Ag mineralization in the Toodoggone District of north-central British Columbia, Canada. Mineralium Deposita, 44, 463-496.

Gabrielse, H., and Yorath, C.J., 1991. Introduction. Chapter 1. In: Gabrielse, H., and Yorath, C.J., (Eds.), Geology of the Canadian Cordilleran Orogen in Canada, Geological Survey of Canada, Geology of Canada, no. 4., pp. 3-11.

Gammons, C.H., and Williams-Jones, A.E., 1997. Chemical mobility of gold in the porphyry-epithermal environment. Economic Geology, 92, 45-59.

Goldstein R.H., and Reynolds, T.J., 1994. Systematics of Fluid Inclusions in Diagenetic Minerals. Society for Sedimentary Geology Short Course 31, 199 p.

Hagemann S.G., and Brown P.E., 1996, Geobarometry in Archean lode gold deposits. European Journal of Mineralogy, 8, 937–960.

Haas, J.L., 1976. Physical properties of the coexisting phases and the thermochemical properties of the H_2O component in boiling NaCl solutions. U.S. Geological Survey Bulletin, 1421-A, 73 p.

Hezarkhani, A., Williams-Jones, A. E., & Gammons, C. H., 1999. Factors controlling copper solubility and chalcopyrite deposition in the Sungun porphyry copper deposit, Iran. Mineralium Deposita, 34, 770-783.

Ji J., and Browne, P. R., 2000. Relationship between illite crystallinity and temperature in active geothermal systems of New Zealand. Clays and Clay Minerals, 48, 139-144.

Lang, J.R., Stanley, C.R., and Thompson, J.F.H.,1995. Porphyry copper-gold deposits related to alkalic igneous rocks in the Triassic-Jurassic arc terranes of British Columbia. In: Wahl Pierce, F., and Bolm, J.G., (Eds.), Porphyry Copper Deposits of the American Cordillera, Arizona Geological Society, Digest 20, pp. 219-236.

Lemaitre, R.W., 1978. The chemical variability of some common igneous rocks. Journal of Petrology, 17, 589-637.

Logan, J.M., 2013. Porphyry systems of central and southern BC: Overview and field trip road log. In: Logan, J.M. and Schroeter, T.G., (Eds.), Porphyry Systems of Central and Southern BC: Prince George to Princeton. Society of Economic Geologists Guidebook 44, pp. 1-45.

Logan, J.M., Mihalynuk, M., Ullrich, T., and Friedman, R.M., 2007. U-Pb ages of intrusive rocks and ^{40}Ar/^{39}Ar plateau ages of copper-gold-silver mineralization associated with alkaline intrusive centres at Mount Polley and the Iron Mask batholith, southern and central British Columbia: In: Geological Fieldwork 2006, British Columbia Ministry of Energy, Mines and Petroleum Resources, British Columbia Geological Survey Paper 2007-1, pp. 93-116.

Logan, J.M., Mihalynuk, M.G., Friedmen, R.M., and Creaser, R.A., 2011. Age constraints of mineralization at the Brenda and Woodjam Cu-Mo +/- Au porphyry deposits - an Early Jurassic calc-alkaline event, south-central British Columbia. B.C. In: Geological Fieldwork 2010, British Columbia Ministry of Forests, Mines and Land, British Columbia Geological Survey Paper 2011-1, pp. 129-143.

Lowell, J. D., & Guilbert, J. M., 1970. Lateral and vertical alteration-mineralization zoning in porphyry ore deposits. Economic Geology, 65, 373-408.

McDowell, C., and Giroux, G., 2012. Mineral resource estimate update for the Seel copper-gold porphyry deposit, 43-101 report, 136 p.

McMillan, W.J., 2005. Porphyry Cu-Mo deposits of the Highland Valley district, Guichon Creek batholith, British Columbia, Canada. In: Porter, T.M. (Ed.), Super Porphyry Copper & Gold Deposits: A Global Perspective, PGC Publishing, Adelaide, 1, pp. 259-274.

McMillan, W.J., Thompson, J.F.H., Hart, C.J.R., and Johnston, S.T., 1995. Regional geological and tectonic setting of porphyry deposits in British Columbia and Yukon Territory. In: Schroeter, T.L. (Ed.), Porphyry Deposits of the Northwestern Cordillera of North America, Canadian Institute of Mining and Metallurgy Special Volume 46, pp. 40-57.

Monger, J.W.H., Souther, J.G., and Gabrielse, H., 1972. Evolution of the Canadian Cordillera; A plate-tectonic model. American Journal of Science, 272, 577-602.

Nelson, J.L., Colpron, M., and Israel, S., 2013. The Cordillera of British Columbia, Yukon, and Alaska: Tectonics and metallogeny. In: Colpron, M., Bissig, T., Rusk, B.G., and Thompson, J.F.H. (Eds.), Tectonics, Metallogeny, and Discovery: The North American Cordillera and Similar Accretionary Settings. Society of Economic Geologists Special Publication Number 17, pp. 53-110.

Panteleyev, A., Bailey, D.G., Bloodgood, M.A., and Hancock, K.D., 1996. Geology and mineral deposits of the Quesnel River-Horsefly map area, central Quesnel Trough, British Columbia NTS map sheets 93A/5, 6, 7, 11, 12, 13; 93B/9, 16; 93G/1; 83H/4; British Columbia Geological Survey Bulletin 97, 156 p.

Pearce, J. A., Harris, N. B., and Tindle, A. G.,1984. Trace element discrimination diagrams for the tectonic interpretation of granitic rocks. Journal of Petrology, 25, 956-983.

Peccerillo, A., and Taylor, S. R., 1976. Geochemistry of Eocene calc-alkaline volcanic rocks from the Kastamonu area, northern Turkey. Contributions to Mineralogy and Petrology, 58, 63-81.

Preto, V.A., 1977. The Nicola Group: Mesozoic volcanism related to rifting in southern British Columbia. In: Baragar, W.R., Coleman, L.C., and Hall, J.M., (Eds.), Volcanic Regimes in Canada.

Geological Association of Canada Special Paper 16, pp. 39-57.

PriceWaterhouseCooper, 2012. Stay the course: The mining industry in British Columbia 2012. 28 p.

Reyes, A.G., 1990. Petrology of Philippine geothermal systems and the application of alteration mineralogy to their assessment. Journal of Volcanology and Geothermal Research, 43, 279-309.

Roedder, E. 1984. Fluid Inclusions. Reviews in Mineralogy Volume 12, 644 p.

Rusk, B.G., Reed, M.H., and Dilles, J.H., 2008. Fluid inclusion evidence for magmatic-hydrothermal fluid evolution in the porphyry copper-molybdenum deposit at Butte, Montana. Economic Geology, 103, 307-334.

Schiarizza, P., Bell, K., Bayliss, S., 2009. Geology and mineral occurrences of the Murphy Lake area, south-central British Columbia (NTS 093A/03). In: British Columbia Ministry of Mines, Energy and Petroleum Resources, Geological Fieldwork 2008, British Columbia Geological Survey Paper 2009-1, pp. 169-188.

Scott, J.E., Richards, J.P., Heaman, L.M., Creaser, R.A., and Salazar, G.S., 2008. The Schaft Creek porphyry Cu-Mo-(Au) deposit, northwestern British Columbia. Exploration and Mining Geology, 17, 163-196.

Seedorff, E., Dilles, J.H., Proffett Jr., J.M., Einaudi, M.T., Zurcher, L., Stavast, W.J.A., Johnson, D.A., and Barton, M.D., 2005. Porphyry deposits: Characteristics and origin of hypogene features. In: Hedenquist, J.W., Thompson, JF.H., Goldfarb, R.J., and Richards, J.P. (Eds.). Economic Geology 100th Anniversary Volume. Society of Economic Geologists, pp. 251-298.

Shepherd, T.J., Rankin, A.H., Alderton, D.H.M., 1985. A Practical Guide to Fluid Inclusion Studies. Blackie, Glasgow, 239 p.

Sherlock, R., Blackwell, J. and Skinner, T., 2013. National Instrument 43-101 Technical Report for 2012 Activities on the Woodjam North Property, Cariboo Mining Division, British Columbia, 275 p.

Sillitoe, 1985. Ore-related breccias in volcanoplutonic arcs. Economic Geology, 80, 1467-1514.

Sillitoe, R. H., 2010. Porphyry copper systems. Economic Geology, 105, 3-41.

Simmons, S.F., and Christenson, B.W., 1984. Origins of calcite in a boiling geothermal system. American Journal of Science, 294, 361-400.

Ulrich, T., Günther, D., & Heinrich, C. A., 2002. The evolution of a porphyry Cu-Au deposit, based on LA-ICP-MS analysis of fluid inclusions: Bajo de la Alumbrera, Argentina. Economic Geology, 97, p.1889-1920.

Vandekerkhove, S., 2013. Mineral paragenesis, fluid inclusions and geochemistry of the Three Firs porphyry Cu-Au prospect: Woodjam porphyry Cu-Au district, British Columbia, Canada. B.Sc. (Honours) thesis, University of Victoria, 64 pages plus CD.

White, N.C. and Hedenquist, J.W., 1995. Epithermal gold deposits: Styles, characteristics and exploration. Society of Economic Geologists Newsletter Number 23, p. 9-13.

Geological setting of the Granite Mountain batholith, host to the Gibraltar porphyry Cu-Mo deposit, south-central British Columbia

Paul Schiarizza[1, a]

[1] British Columbia Geological Survey, Ministry of Energy and Mines, Victoria, BC, V8W 9N3
[a] corresponding author: Paul.Schiarizza@gov.bc.ca

Recommended citation: Schiarizza, P., 2014. Geological setting of the Granite Mountain batholith, host to the Gibraltar porphyry Cu-Mo deposit, south-central British Columbia. In: Geological Fieldwork 2013, British Columbia Ministry of Energy and Mines, British Columbia Geological Survey Paper 2014-1, pp. 95-110.

Abstract
The Granite Mountain project was initiated in 2013 to clarify the contact relationships, structural history, and terrane affinity of the Granite Mountain batholith (Late Triassic), host to the Gibraltar porphyry Cu-Mo deposit. Rocks mapped along the northeast margin of the batholith include a succession of predominantly volcanogenic sandstone (locally gritty to pebbly), intercalated with conglomerate, mafic and felsic volcanic breccia, siltstone, limestone, and basalt. This succession has yielded Middle or Late Triassic conodonts from one locality. On the basis of its strong lithologic similarity, this succession is likely part the Nicola Group of Quesnel terrane. Felsic volcanic breccias, which have no counterpart in nearby Nicola exposures, suggest possible affinities with the western Nicola belt of the Merritt-Ashcroft area. In contrast to historical interpretations, the Granite Mountain batholith is inferred to be part of Quesnel terrane, on the basis of its spatial association with the Nicola Group, and a link provided by a common overlap assemblage, the Dragon Mountain succession, which is part of a Lower to Middle Jurassic intra-Quesnel clastic basin. The Granite Mountain batholith, together with adjacent Nicola Group and Dragon Mountain succession, form a panel of Quesnel rocks that is bounded to the east, south, and west by rocks of Cache Creek terrane. The eastern boundary is inferred to be a significant north-northwest striking fault, previously unrecognized, that may record more than 20 km of sinistral strike slip.

Keywords: Granite Mountain batholith, Late Triassic tonalite, Burgess Creek stock, Nicola Group, Cache Creek Complex, Dragon Mountain succession, Gibraltar Cu-Mo porphyry deposit, Quesnel terrane, Cache Creek terrane

1. Introduction

The Gibraltar Mine is a large Cu-Mo deposit hosted by the Granite Mountain batholith (Late Triassic) near McLeese Lake in south-central British Columbia (Fig. 1). It began production in 1972, reopened in 2004, and currently has a projected mine life extending to 2037 (van Straaten et al., 2013).

Geological work near the Granite Mountain batholith prior to the late 1990s included regional mapping of the Quesnel River (93B) map area by Tipper (1959, 1978), geological mapping of the Granite Mountain batholith by Panteleyev (1978), and more detailed studies of the geology and mineralization in and near the Gibraltar deposits by Sutherland Brown (1958, 1967, 1974), Eastwood (1970), Drummond et al. (1973, 1976), and Bysouth et al. (1995). These early workers considered the batholith part of Cache Creek terrane because of widespread Cache Creek rocks to the south and east (Tipper, 1959, 1978) and because skarns and schists along the southwest margin of the batholith were interpreted as Cache Creek rocks altered during batholith emplacement (Drummond et al., 1976; Panteleyev, 1978; Bysouth et al., 1995). Tipper (1978) and Bysouth et al. (1995) inferred that siliciclastic, volcaniclastic, and local volcanic rocks along the northeast and north margins of the batholith were predominantly younger (Jurassic) than the batholith. Sutherland Brown (1974) Drummond et al. (1976) and Bysouth et al. (1995) regarded Gibraltar as a porphyry Cu-Mo deposit, but noted that it had some unusual characteristics, including a spatial association of orebodies with zones of ductile deformation.

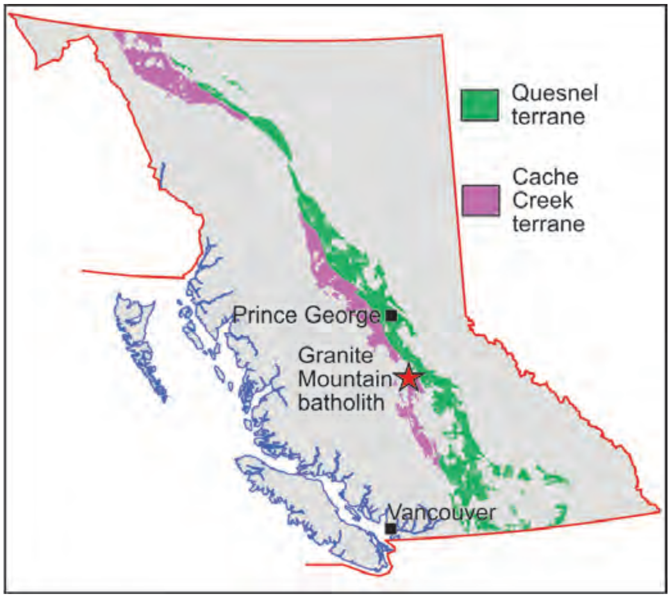

Fig. 1. Map of British Columbia showing location of the Granite Mountain batholith and distribution of Quesnel and Cache Creek terranes.

Ash et al. (1999a, b) carried out a geological mapping program of the Granite Mountain batholith and surrounding rocks in 1998. This was followed by a description of the Gibraltar deposit by Ash and Riveros (2001), based on mapping of the Gibraltar pits in 1998, 1999 and 2000, mainly during a hiatus in mining activity that lasted from 1999 to 2003. Ash et al. (1999a, b) challenged earlier interpretations by suggesting that the Granite Mountain batholith is a part of Quesnel terrane, and that volcaniclastic rocks on the northeast margin of the batholith belong to the Late Triassic Nicola Group. They suggested that the batholith was faulted against Cache Creek rocks in post-Triassic time, and that ductile shear zones within the Gibraltar deposit formed during this tectonic event. This implied that Gibraltar might not be a porphyry deposit, or at least that mineralization had been significantly remobilized during younger deformation.

Oliver et al. (2009) and van Straaten et al. (2013) presented summaries of the deposit as it is currently understood. They stressed that the styles of vein and disseminated mineralization are consistent with an origin as a calcalkaline porphyry, as also suggested by Late Triassic Re-Os ages on molybdenum that overlap the age of the host tonalite (Harding, 2012). van Straaten et al. (2013) also argued that mineralization was before or during deformation because ductile deformation zones contain abundant, folded, sheared, and transposed hydrothermal veins, but generally lack crosscutting veins.

This report summarizes preliminary results from the first field season of a two-year bedrock mapping program designed to clarify the geological setting and structural history of the Granite Mountain batholith. This initial work focuses on the package of volcaniclastic rocks on the northeast margin of the Granite Mountain batholith that were assigned to a Lower-Middle Jurassic siliciclastic assemblage by Tipper (1978), but correlated with the Nicola Group (Late Triassic) of Quesnel terrane by Ash et al. (1999a, b). The main conclusion from the 2013 fieldwork is that these rocks are part of the Nicola Group.

2. Regional setting

The Granite Mountain batholith crops out on the Fraser Plateau, seven to eighteen kilometres east of the Fraser River, within the traditional territories of the Northern Secwepemc te Qelmucw and Tsilhqot'in First Nations (Fig. 2). The community of McLeese Lake, on Highway 97, is 10 km south-southwest of the Gibraltar ore deposits, and is linked to the mine site by paved road. Access to other parts of the batholith and surrounding areas is by extensive networks of logging and Forest Service roads, although many roads have been deactivated and are no longer accessible by truck.

Quesnel terrane is an important metallogenic province that extends along most of the length of the Canadian Cordillera (Nelson et al., 2013). It is characterized by a Late Triassic to Early Jurassic magmatic arc complex that formed outboard of the western margin of ancestral North America. Quesnel terrane is flanked to the east by Proterozoic and Paleozoic siliciclastic, carbonate and volcanic rocks of pericratonic affinity, and locally by an intervening assemblage of mid to Late Paleozoic oceanic basalt and chert assigned to Slide Mountain terrane, which is commonly interpreted as the imbricated remnant of a Late Paleozoic marginal basin. Late Paleozoic through mid-Mesozoic oceanic rocks of Cache Creek terrane west of Quesnel terrane are interpreted as part of the accretion-subduction complex that was responsible for generating the Quesnel magmatic arc.

At the latitude of McLeese Lake, rocks of Quesnel terrane crop out mainly in a ~ 30 km-wide, northwest-trending belt, 20 km east of the Granite Mountain batholith (Fig. 2). The terrane is represented mainly by Middle to Upper Triassic volcanic and sedimentary rocks of the Nicola Group, together with abundant Late Triassic to Early Jurassic calcalkaline and alkaline intrusions (Logan et al., 2010). Lower to Middle Jurassic siliciclastic sedimentary rocks that outcrop along the western margin of the terrane are assigned to the Dragon Mountain succession (Logan and Moynihan, 2009). These rocks represent a basin derived from, and deposited on, Quesnel terrane (Petersen et al., 2004; Logan and Moynihan, 2009).

Cache Creek terrane, represented by the Cache Creek Complex, lies to the west of the main Quesnel belt, and is represented by abundant exposures to the east and south of the Granite Mountain batholith (Fig. 2). These exposures include chert, argillite, basalt, limestone, conglomerate, and greywacke (Tipper, 1959; Ash et al., 1999a, b). The complex is not well dated in the area represented by Fig. 2, although one limestone exposure, 10 km east of the southern part of the Granite Mountain batholith, yielded Permian fossils (Tipper, 1978). Contiguous, but better-studied parts of the Cache Creek Complex to the south and north include rocks ranging from Carboniferous to Early Jurassic (Cordey and Read, 1992; Read, 1993; Struik et al., 2001).

The youngest rocks in the region include Middle Jurassic and Early Cretaceous plutons, Eocene volcanic and local sedimentary rocks, Oligocene-Pliocene siliciclastic sequences localized along parts of the Fraser River, and widespread Miocene-Pleistocene basalt of the Chilcotin Group (Fig. 2). The Cretaceous plutonic suite includes tonalite of the Sheridan Creek stock, directly south of the Granite Mountain batholith. The Burgess Creek stock, on the northeast margin of the Granite Mountain batholith (Fig. 3), has been interpreted as a relatively young, post-batholith intrusion (Panteleyev, 1978; Bysouth et al., 1995), or a border phase of the Granite Mountain batholith (Ash et al., 1999a, b).

3. Geology of the northeastern margin of the Granite Mountain batholith

The southwestern part of the area mapped in 2013 is underlain by coarse-grained leucocratic tonalite of the Granite Mountain phase of the Granite Mountain batholith (Fig. 3). The area to the north and east of the batholith is underlain mainly by a succession of volcaniclastic and volcanic rocks that are assigned to the Nicola Group. The Nicola Group is cut by undated, predominantly tonalitic intrusive rocks of the Burgess Creek stock, and is locally overlain by a small outlier of slate and siltstone correlated with the Dragon Mountain succession. Chert, basalt, and limestone exposed in the eastern part of the area are part of the Cache Creek Complex, and are inferred

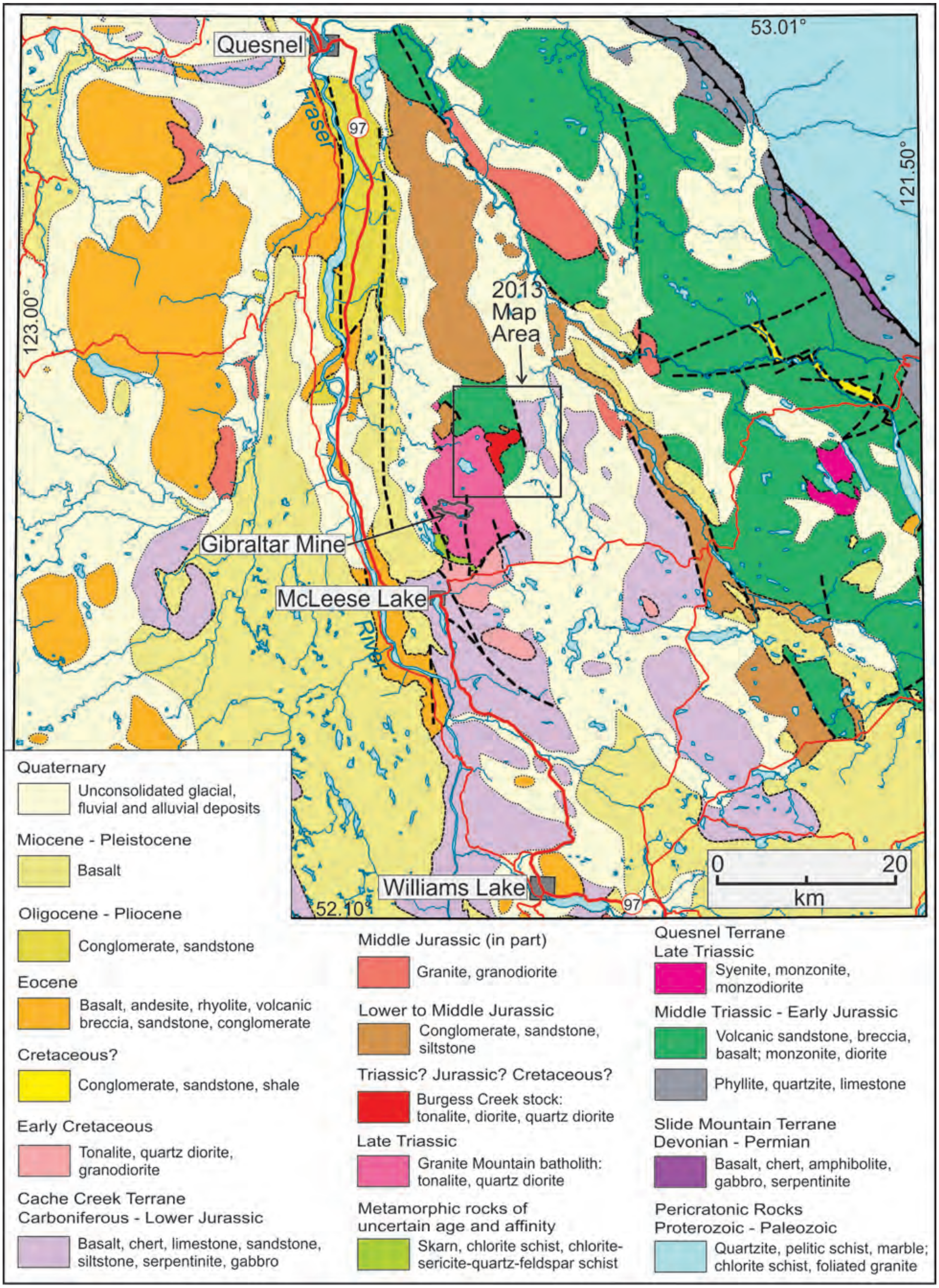

Fig. 2. Geological map of the area between Williams Lake and Quesnel, showing the location and setting of the Granite Mountain batholith.

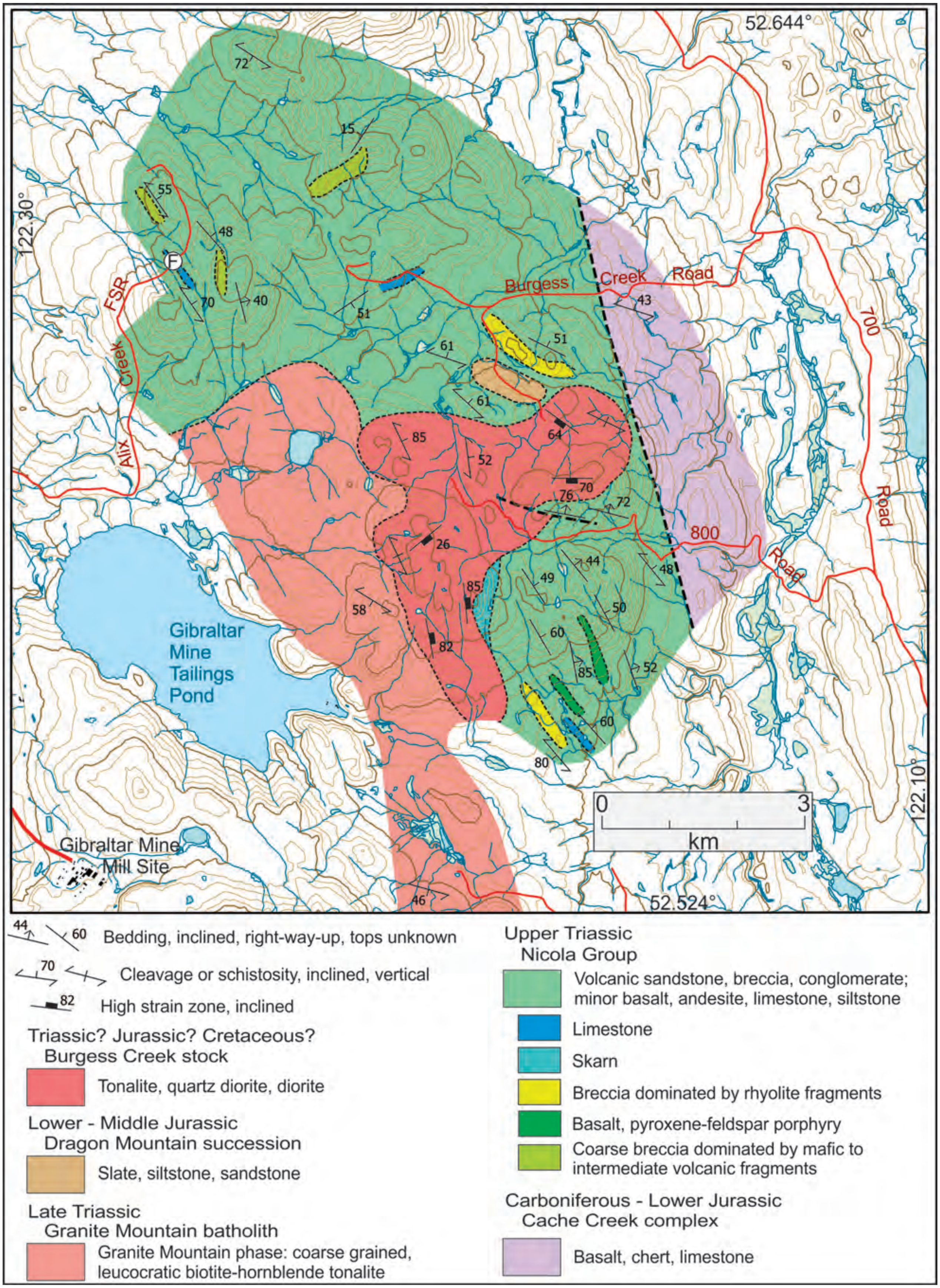

Fig. 3. Geology of the northeast margin of the Granite Mountain batholith, based on 2013 fieldwork.

to be separated from the Nicola Group by a significant north-northwest-striking fault (Fig. 3).

3.1. Nicola Group

Rocks assigned to the Nicola Group consist mainly of sandstone and gritty to pebbly sandstone, with local intercalations of conglomerate, breccia, siltstone, limestone, and basalt (Fig. 3). These rocks were included in the upper (Lower to Middle Jurassic) part of the Quesnel River Group (equivalent to the Dragon Mountain succession) by Tipper (1978), and were assigned to an unnamed unit of suspected Early Jurassic age by Panteleyev (1978). Correlation with the Nicola Group follows the interpretation of Ash et al. (1999a, b). This correlation is based mainly on lithology, but is corroborated by the only fossils, Middle or Late Triassic conodonts, known from the succession.

The Nicola Group consists mainly of medium green, locally grey to purplish-grey, fine- to coarse-grained, commonly gritty to pebbly, volcanogenic sandstone. The sandstone is well bedded in places, but elsewhere forms massive units, up to several tens of metres thick, in which bedding is not apparent. In well-bedded sections (Fig. 4), thin to medium beds of sandstone are intercalated with thin beds of green to grey siltstone, and locally display normal grading and erosive bases. The sandstones are rich in feldspar, and also contain grey to green volcanic lithic grains and altered mafic mineral or lithic grains. Gritty and pebbly sandstone intervals contain angular to subrounded fragments of mainly grey and green, locally feldspar and/or pyroxene-phyric volcanic rock (Fig. 5). Local medium- to thick-beds of sand matrix-supported pebble conglomerate in well-stratified intervals contain a similar suite. Less common clasts include fine-grained diorite, quartz diorite, hornblende porphyry, quartz-feldspar-phyric rhyolite, limestone, argillite, and siltstone.

Siltstone is uncommon, and typically forms cm-scale layers intercalated with substantially thicker beds of sandstone. However, at one isolated outcrop along the 800 road, 300 m west of the Cache Creek contact, several metres of grey-green, rusty-weathered, weakly cleaved siltstone lacking intercalations of coarser rock are exposed.

Fig. 5. Pebbly sandstone, Nicola Group, north of Burgess Creek stock.

Relatively coarse, mafic volcanic breccias outcrop at three locales in the northwestern part of the map area; although contacts are not exposed, the breccias appear to be intercalated with typical sandstones and pebbly sandstones (Fig. 3). The breccias are medium to dark green, greenish-brown to rusty-brown weathered, matrix supported, poorly sorted and apparently unstratified. Angular to subrounded fragments 1-10 cm in long dimension, float in a matrix of sand-size feldspar, pyroxene, and mafic volcanic-lithic grains (Fig. 6). The fragments are mainly pyroxene and/or plagioclase-phyric basalt, but fragments of aphyric feldspathic volcanic rock and hornblende-feldspar porphyry are also present. The easternmost mafic breccia unit contains rare subrounded clasts of pyroxenite.

Distinctive breccia units with predominantly felsic volcanic fragments outcrop north and south of the Burgess Creek stock

Fig. 4. Thinly bedded sandstone and siltstone, Nicola Group, north of Burgess Creek stock.

Fig. 6. Mafic volcanic breccia, Nicola Group, northwest part of map area.

(Fig. 3). These breccias consist of angular to subrounded fragments in a mixed matrix of fine-grained foliated chlorite and sericite, and sand-size grains and granules of quartz, feldspar, and felsic volcanic lithoclasts. They are typically medium green on fresh surfaces, and weather to pale shades of green, grey-green or brownish-green. Coarse intervals with poorly sorted, angular to subangular fragments up to 20 cm across (Fig. 7) are intercalated with beds containing pebble fragments, and well foliated granulestones with sparse pebbles (Fig. 8). The fragments consist mainly of pale green, grey or purplish-grey aphanitic felsic volcanic rocks, commonly with 1-2 mm phenocrysts of quartz ± feldspar (Fig. 9). Medium to dark green intermediate to mafic volcanic rock fragments, some with small pyroxene phenocrysts, form a small proportion of the clast population. The felsic breccia unit on the north side of the Burgess Creek stock is at least 100 m thick, and was traced for about 1 km, with possible strike extensions to both the northwest and southeast concealed by overburden. The base of the unit is not exposed; it is overlain by sandstones and pebbly sandstones in which rhyolite fragments constitute a minor component of the clast population.

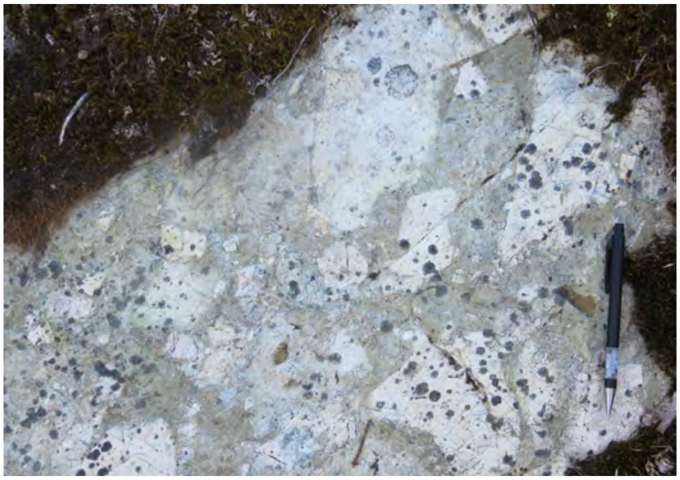

Fig. 7. Felsic volcanic breccia, Nicola Group, north of Burgess Creek stock.

Fig. 8. Well foliated granulestone, Nicola Group, felsic volcanic breccia unit, south part of map area.

Fig. 9. Quartz-feldspar-phyric rhyolite fragment from felsic breccia, Nicola Group, north of Burgess Creek stock.

Two mafic volcanic units outcrop within the Nicola Group south of the Burgess Creek stock (Fig. 3). The eastern unit is a dark green amygdaloidal basalt flow. The flow is about 10 m thick and was traced for 350 m. It features abundant ovoid to irregularly-shaped vesicles, filled with combinations of epidote, quartz, actinolite and albite, in a very-fine-grained groundmass of plagioclase laths and altered mafic grains (Fig. 10). The western unit is a pyroxene-feldspar porphyry flow or sill. It contains 1-6 mm pyroxene and feldspar phenocrysts (~ 20%) in a fine-grained groundmass of relict plagioclase and secondary epidote, actinolite, and chlorite (Fig. 11). Units of coherent plagioclase ± pyroxene porphyry, similar to this unit, occur elsewhere in the Nicola succession, but are not abundant and are typically not well-enough exposed to determine if they are flows, sills, or dikes. The Nicola Group also hosts dikes and small plugs of diorite, hornblende ± feldspar porphyry and diabase.

Narrow limestone units are intercalated with volcanic sandstones of the Nicola Group at three localities (Fig. 3). Relationships are best exposed near the southern limit of Nicola outcrops, where a unit of grey, weakly foliated limestone (Fig. 12), at least 10 m thick, was traced intermittently for 250 m. This unit is overlain by variably calcareous volcanic

Fig. 10. Amygdaloidal basalt, Nicola Group, south of Burgess Creek stock.

Fig. 11. Pyroxene-plagioclase porphyry, Nicola Group, south of Burgess Creek stock.

Fig. 12. Foliated limestone, Nicola Group, south part of map area.

sandstone that includes a few narrow limestone lenses. The interval of calcareous rocks projects north-northwestward to the southeast margin of the Burgess Creek stock, where the Nicola Group is represented by poorly exposed epidote-garnet skarn (Fig. 3). The limestone unit near the northwestern edge of the map area was sampled by Jim Logan (British Columbia Geological Survey) in 2005; this sample yielded conodonts of Middle or Late Triassic age (Orchard, 2006; GSC Loc. No. C-307484). This is currently the only age constraint available for the Nicola Group on the northeast margin of the Granite Mountain batholith. Samples collected from all limestone units encountered in 2013 have been submitted for microfossil extraction.

3.2. Granite Mountain batholith

The Granite Mountain batholith is commonly subdivided into three main units (Panteleyev, 1978; Bysouth et al., 1995; Ash et al., 1999a, b). These are, from southwest to northeast: Border phase diorite to quartz diorite; Mine phase tonalite; and Granite Mountain phase leucocratic tonalite. The rocks exposed in the 2013 map area are part of the Granite Mountain phase. They are very uniform in composition and texture, comprising light grey, light grey to white-weathered, coarse-grained, equigranular biotite-hornblende tonalite (Fig. 13). A typical rock contains approximately equal proportions of quartz and plagioclase, and 5-10% mafic minerals, with biotite slightly more abundant than hornblende. The rocks are commonly isotropic, but locally display a weak, southwest-dipping foliation defined by imperfect alignment of plagioclase and/or mafic grains. Variably oriented dikes and veins, 1-25 cm thick, are uncommon, and include aplite, quartz porphyry, and medium-grained leucotonalite.

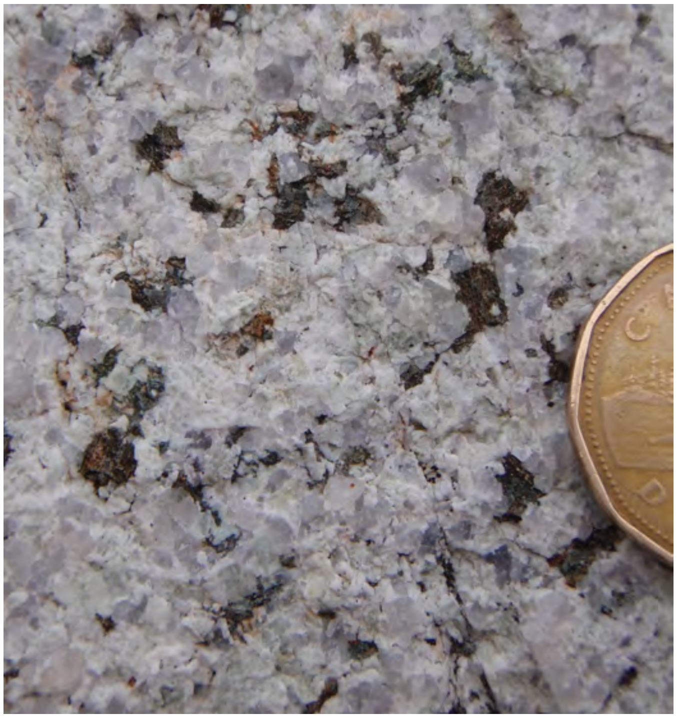

Fig. 13. Coarse-grained leucocratic tonalite, Granite Mountain phase, south part of map area.

Late Triassic U-Pb zircon magmatic ages have been reported from the Granite Mountain phase of the Granite Mountain batholith: 215 ± 0.8 Ma (Ash and Riveros, 2001; Ash et al., 199a), and 209.6 ± 6.3 Ma (Oliver et al. 2009). Geochronologic work on samples taken from the batholith and Burgess Creek stock in 2013 is ongoing.

3.3. Burgess Creek stock

The Burgess Creek stock (Panteleyev, 1978) comprises a heterogeneous assemblage of tonalites, quartz diorites, and diorites that intrude the Nicola Group (Fig. 3). Panteleyev (1978) considered the stock to be younger than the Granite Mountain batholith, but Ash et al. (1999a, b) concluded that the assemblage represents part of the batholith, and referred to them as border phase quartz diorite (unit EJGb). The present study confirms that the rocks in the stock intrude the Nicola Group, and can be mapped separately from the Granite Mountain phase of the batholith. However, age relationships between the stock and the Granite Mountain phase remain uncertain and the possibility that it is a component of the Granite Mountain batholith remains open.

The most common and widespread component of the Burgess Creek stock is light grey, light grey-weathered, medium-grained, equigranular hornblende-biotite tonalite (Fig. 14). The tonalite is typically leucocratic, with 7-10% mafic minerals (hornblende > biotite), 30-40% quartz, and 50-60% plagioclase, but darker varieties, with 15-25% mafic minerals, are also present. An older, less abundant but equally widespread phase comprises greenish-grey, light brownish-grey-weathered, medium- to coarse-grained hornblende-biotite quartz diorite. It typically contains 20-30% mafic minerals, 5-10% quartz, and 60-70% plagioclase, but quartz content is highly variable, such that some rocks are diorites and others are mafic tonalites. Locally, this phase contains irregular mafic patches several centimetres to tens of centimetres in size, consisting mainly of hornblende and magnetite, intergrown with minor amounts of quartz and plagioclase (Fig. 15). A third component of the stock comprises fine-grained diorite, consisting of hornblende (30-40%) and plagioclase. It is most common as screens and xenoliths in the predominant tonalite phase (Fig. 16), but is the main rock type in some exposures along the southeast margin of the stock. It is typically equigranular, but locally displays a porphyritic texture, with phenocrysts of hornblende and/or plagioclase scattered through a fine-grained dioritic groundmass. The youngest component of the Burgess Creek stock is leucotonalite, which forms dikes, commonly 1-30 cm thick, that occur throughout the stock and cut all other rock types (Fig. 15). The dikes consist of quartz and plagioclase with only a few per cent chloritized mafic minerals. They display a variety of textures, ranging from fine grained aplitic, to coarse

Fig. 14. Medium-grained tonalite, northeast part of Burgess Creek stock.

Fig. 15. Coarse-grained quartz diorite with hornblende-magnetite segregation, cut by leucotonalite dike, northeast part of Burgess Creek stock.

Fig. 16. Tonalite with screens of fine-grained diorite, central part of Burgess Creek stock.

grained with pegmatitic patches. Quartz porphyry, comprising phenocrysts of quartz ± plagioclase ± hornblende in a fine-grained leucotonalite groundmass, is locally developed, but contact relationships with adjacent components of the stock were not observed.

Most phases of the Burgess Creek stock display textures that vary from isotropic to weakly foliated. The foliation dips steeply to the northeast or southwest, and is defined by weakly flattened plagioclase and mafic mineral grains and/or by discontinuous narrow seams of oriented sericite. The stock is locally cut by high-strain zones, 40 cm to 30 m wide, defined by strongly foliated, locally mylonitic rock (Fig. 3). Steeply dipping shear zones in the southern and eastern parts of the stock incorporate various tonalite, quartz diorite, and diorite phases, but, where relationships are exposed, are cross-cut by younger tonalite and leucotonalite phases (Fig. 17). A well-foliated zone that dips gently to the southeast in the west-central part of the stock is localized in a quartz porphyry unit, and locally displays S-C fabrics indicating northwest-directed thrust movement.

The intrusive contact between the Burgess Creek stock and Nicola Group is exposed at one outcrop, north of the 800 road. This intrusive relationship is corroborated by observations elsewhere, including dikes of tonalite and quartz diorite cutting the Nicola Group near the contact, xenoliths of Nicola rock in the stock near the contact, and a zone of skarn-altered rocks in the Nicola Group along the southeast margin of the stock. The contact between the Burgess Creek stock and the Granite Mountain phase is locally well defined, but is not exposed. Burgess Creek rocks near the contact consist of tonalite that is distinguished from the adjacent Granite Mountain tonalite by finer grain size, lower quartz content, and higher mafic content. The contact is inferred to be intrusive, but it is unclear which unit intrudes which.

3.4. Dragon Mountain succession

Exposed in a small area along and near a branch of the Burgess Creek road, north of the Burgess Creek stock (Fig. 3), is an assemblage of dark grey slate with laminae and thin interbeds of lighter grey siltstone and less common thin beds of quartz-rich, fine- to medium-grained yellowish-brown-weathered sandstone (Fig. 18). Sandstone beds are commonly graded, and locally display scour-and-fill structures. These rocks differ from the Nicola Group, but are similar to the basal unit of the Dragon Mountain succession (Lower to Middle Jurassic; dark banded phyllite unit of Logan and Moynihan, 2009). Hence these rocks are interpreted as a small outlier of the Dragon Mountain succession, resting above the Nicola Group across an unconformity. Five km west of the present map area, is another likely Dragon Mountain succession outlier in which slate and siltstone overlap both Nicola Group and adjacent granitic rocks of the Granite Mountain batholith (Fig. 2; Ash et al., 1999b). Twenty-five km north of the map area, along the French Creek Road, the basal Dragon Mountain unit contains Early Jurassic (Late Pliensbachian) fossils (Petersen et al., 2004; Logan and Moynihan, 2009).

Fig. 17. Strongly foliated tonalite cut by unstrained leucotonalite, southwest part of Burgess Creek stock.

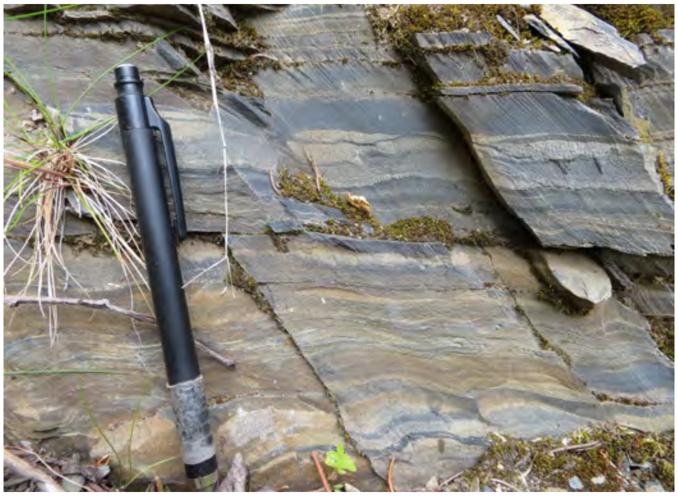

Fig. 18. Stacked, cm-scale, sharp-based, fining-upward sequences of sandstone, siltstone, and slate; slaty cleavage from upper left to lower right; Dragon Mountain succession, north of Burgess Creek stock.

3.5. Cache Creek Complex

Rocks included in the Cache Creek Complex crop out at a few scattered localities in the eastern part of the area (Fig. 3). Exposures along the 800 Road comprise grey to greenish-grey chert, which forms lenses and layers, 1-5 cm thick, separated by partings or thin interbeds of greenish-grey argillite (Fig. 19). Farther north, in cutblocks south of the Burgess Creek road, are small exposures of green, carbonate-altered, rusty-brown-weathered basalt, and basalt breccia, which locally contains fragments and lenses of grey limestone. The contact between the Cache Creek Complex and adjacent rocks of the Nicola Group is not exposed, but is inferred to be a significant north-northwest trending fault.

3.6. Structure

A weak to moderately developed cleavage, typically

Fig. 19. Chert with mudstone partings, Cache Creek Complex, 800 road.

with steep dips to the northeast or southwest, cuts siltstone, limestone, and some breccia units of the Nicola Group, and fine-grained portions of the Dragon Mountain succession (Fig. 18), but is generally not developed in the sandstones and pebbly sandstones that form most of the Nicola Group. The cleavage, typically defined by oriented chlorite and/or sericite, is accentuated by variably flattened lithic fragments in breccia units. Plutonic rocks of the Granite Mountain batholith and Burgess Creek stock locally display a weak foliation defined by discontinuous foliae of sericite and chlorite, and/or weakly flattened plagioclase grains and mafic mineral clots. This foliation dips at steep angles to the northeast or southwest in the Burgess Creek stock, congruent with cleavage in the adjacent Nicola Group, but dips at moderate angles to the south-southwest in the Granite Mountain batholith (Fig. 3). Local, narrow, high-strain zones in the Burgess Creek stock are of uncertain significance, but seem to be restricted to the stock itself, and are commonly cross-cut by the youngest phases of the stock.

Nicola rocks south of the Burgess Creek stock comprise a right-way-up homoclinal panel that dips at moderate angles to the east-northeast (Fig. 3). Mesoscopic folds of bedding were observed in uncleaved, thin to medium-bedded volcanic sandstone at one locality near the southern margin of the belt. The folds plunge at moderate angles to the north and verge to the west. Although not exposed, a west-northwest trending fault is inferred from an apparent 300 m sinistral offset of the southern contact of the Burgess Creek stock (Fig. 3). The wedge of Nicola rocks between this structure and the stock have dips that are steeper and oriented more to the north than those displayed by the main panel of Nicola rocks to the south.

The Nicola Group directly north of the Burgess Creek stock, and near the western edge of the map area farther to the northwest, displays moderate northeast dips, with rare right-way-up younging indicators, that are congruent with those to the south of the stock. Bedding observations in a poorly exposed area along, and north of, the east end of the Burgess Creek road, are more variable, indicating structural complications that have not yet been resolved. The only mesoscopic folds observed in this part of the map area are in the small outlier of Dragon Mountain succession that is inferred to overlie the Nicola Group. These folds plunge gently to the northwest, and slate beds within the folded sandstone, siltstone, slate succession display an axial planar slaty cleavage that dips at moderate angles to the north-northeast.

The most significant structure in the area is an inferred fault that separates the Nicola Group from the Cache Creek Complex to the east. The orientation of the fault is not well constrained, but exposures within and adjacent to the map area indicate a general north-northwest trend. The anomalous geometry of Nicola rocks to the west of Cache Creek rocks could be explained by at least 20 km of sinistral displacement along this structure. This fault, and potentially related structures inferred along or near the south margin of the Granite Mountain batholith, will be a major focus of the 2014 field program.

4. Discussion

4.1. Correlation of the volcaniclastic succession with the Nicola Group

The Nicola Group comprises a diverse assemblage of Middle and Upper Triassic volcanic, volcaniclastic, and sedimentary rocks that extend across a broad area in south-central British Columbia. It, and coeval to slightly younger intrusions, form the characteristic units of the Quesnel arc terrane. The Nicola Group has not been formally subdivided on a regional scale, but informal subdivisions have been applied in areas where it has been studied in reasonable detail.

The predominantly sandstone succession on the northeast margin of the Granite Mountain batholith is similar to Nicola Group units mapped elsewhere (e.g. Unit uTrNvs of Logan et al., 2010; Bosk Lake succession of Schiarizza et al., 2013) and, in particular, to those along the western part of the main Quesnel belt near Granite Mountain. These include: the green volcaniclastic succession in the Quesnel River map area to the northwest (Logan and Moynihan, 2009); the western volcaniclastic succession in the Cottonwood map area farther north (Logan, 2008); and, east of the Granite Mountain area, rocks referred to as the Gavin Lake succession by Logan and Bath (2006) and mapped as units LTrNs and LTrNvb by Logan et al. (2007). These contiguous units consist mainly of feldspathic volcanic sandstone, siltstone, and conglomerate and include mafic volcanic breccia, basalt, and limestone. Late Triassic conodonts have been extracted from limestone in the green volcaniclastic succession (Logan and Moynihan, 2009) and from limestone in the Gavin Lake succession (Logan and Bath, 2006). Correlation is further supported by the fact that, like the volcaniclastic succession in the current map area, these Upper Triassic units are overlain by Lower-Middle Jurassic rocks of the Dragon Mountain succession (Logan et al., 2007; Logan and Moynihan, 2009).

Felsic volcanic breccias in the Granite Mountain area have not been reported from otherwise remarkably similar Nicola successions in adjacent areas. Felsic volcanic rocks are uncommon in most parts of the Nicola Group, where volcanic rocks are almost exclusively feldspar-pyroxene-phyric basalts and andesites. However, rhyolites, dacites, and associated felsic breccias form a significant part of a belt along the western edge of Quensel terrane in the Merritt-Ashcroft area of southern British Columbia. These rocks, referred to as the western Nicola belt by Preto (1979) and the western volcanic facies of the Nicola Group by Monger and McMillan (1989), host the Guichon Creek batholith (Late Triassic). The felsic breccias in the current map area suggest that the Nicola rocks here have an affinity with the western Nicola belt of southern British Columbia. This is consistent with their location in the westernmost part of Quesnel terrane, and their association with the Granite Mountain batholith (same age as the Guichon Creek batholith).

4.2. Contact relationships and terrane affinity of the Granite Mountain batholith

The Granite Mountain batholith is interpreted to be part of Quesnel terrane (Fig. 20). This is based mainly on its spatial association with the Nicola Group mapped along its north and northeastern margins (Ash et al., 1999a, b; this study). Intrusive contacts were not observed between the Granite Mountain phase and adjacent Nicola rocks, but this reflects poor exposure in critical areas. The Burgess Creek stock clearly intrudes the Nicola Group, but it remains to be established if this unit is part of the Granite Mountain batholith, as proposed by Ash et al (1999a, b), or is a younger pluton, as suggested by Panteleyev (1978) and Bysouth et al. (1995). Outliers of Dragon Mountain succession overlie both the Nicola Group and the Granite Mountain batholith, and conglomerate that is part of this unit farther north contains clasts that may have been derived from the Granite Mountain batholith (Tipper, 1978). The Dragon Mountain succession provides an additional link between the Granite Mountain batholith and Quesnel terrane, as regional studies suggest that this succession represents an intra-Quesnel basin that was derived from, and deposited on, older units of Quesnel terrane (Petersen et al., 2004; Logan and Moynihan, 2009).

The Granite Mountain batholith is in contact with definitive Cache Creek rocks over a small area along its southeast margin. Contacts are not exposed, but are reasonably inferred to be north-northwest and northeast-striking faults that have similar orientations to structures that separate Cache Creek from Nicola Group to the east and northeast (Fig. 20; Ash et al., 1999a, b). Relationships between the Cache Creek Complex and Granite Mountain batholith farther west are largely obscured by the intervening Sheridan Creek stock (Early Cretaceous). A belt of metamorphic rocks along the southwest margin of the Granite Mountain batholith is bounded to the south by the Sheridan Creek stock and is overlapped to the west by Neogene basalt flows of the Chilcotin Group (Fig. 20). This belt was inferred to be contact-metamorphosed Cache Creek Complex by many previous workers (Drummond et al., 1976; Panteleyev, 1978; Bysouth et al., 1995), but was interpreted as a sheared, mafic-rich border phase of the Granite Mountain batholith by Ash et al. (1999a, b). Reconnaissance work in the present study revealed mainly garnet-epidote skarn, with subsidiary amounts of chlorite schist and sericite-chlorite-quartz-feldspar schist. A sedimentary ± volcanic ± plutonic protolith is inferred, but the rocks observed could have been derived from either the Nicola Group or the Cache Creek Complex. This belt will be studied in detail in 2014.

4.3. Structural implications of Quesnel terrane correlation

The Nicola Group mapped on the northeast margin of the Granite Mountain batholith, together with the batholith itself and overlying rocks of the Dragon Mountain succession, form a coherent panel of rocks that is part of Quesnel terrane. This panel is bounded to the east by a north-tapering wedge of Cache Creek rocks, indicating significant local shuffling of the terrane boundary because, regionally, Cache Creek terrane lies west of Quesnel terrane. The contact between the Quesnel panel and the Cache Creek wedge is inferred to be a north-northwest trending fault (Fig. 20). This fault is inferred to be Middle Jurassic or younger because it cuts the Dragon Mountain succession. It may have been the locus of more than 20 km of sinistral strike-slip displacement, as required to restore the southern end of the Quesnel block to the northern termination of the Cache Creek wedge. However, models involving predominantly vertical movement cannot be entirely ruled out, as this could result in the same map pattern if the pre-fault terrane contact had a gentle dip. The inferred fault has not previously been mapped, and no obvious strike extensions are apparent, although Logan (2008) documented local northwest-trending sinistral fault zones in Quesnel terrane along the Cottonwood River, 60 km north-northwest of Granite Mountain. Orogen-parallel sinistral faults with significant displacement are known elsewhere along or near the western margin of Quesnel terrane, including the Pasayten fault of southern British Columbia and adjacent Washington State, which records about 20 km of sinistral displacement in Early Cretaceous time (Greig, 1992; Hurlow, 1993).

A Quesnel terrane origin for the Granite Mountain batholith implies that it is separated from Cache Creek rocks to the south by one or more fault systems. These structures might include relatively old segments of the terrane boundary that have been displaced along the sinistral fault system, as well as contractional structures that are the same age as, and kinematically linked to, the sinistral fault system. Ongoing work will address four key structural questions. 1) Is the Cuisson Lake metamorphic belt part of a fault zone between the Granite Mountain batholith and Cache Creek terrane, or a zone of contact metamorphosed rocks (possibly Nicola Group) that were intruded by the Granite Mountain batholith? 2) To what extent is the Sheridan Creek stock, which locally contains south-dipping shear zones (Ash, 1999a) involved in the faulting? 3) What are the ages of faulting? 4) Are structures that deform the Gibraltar orebodies related to structures that juxtapose the batholith against Cache

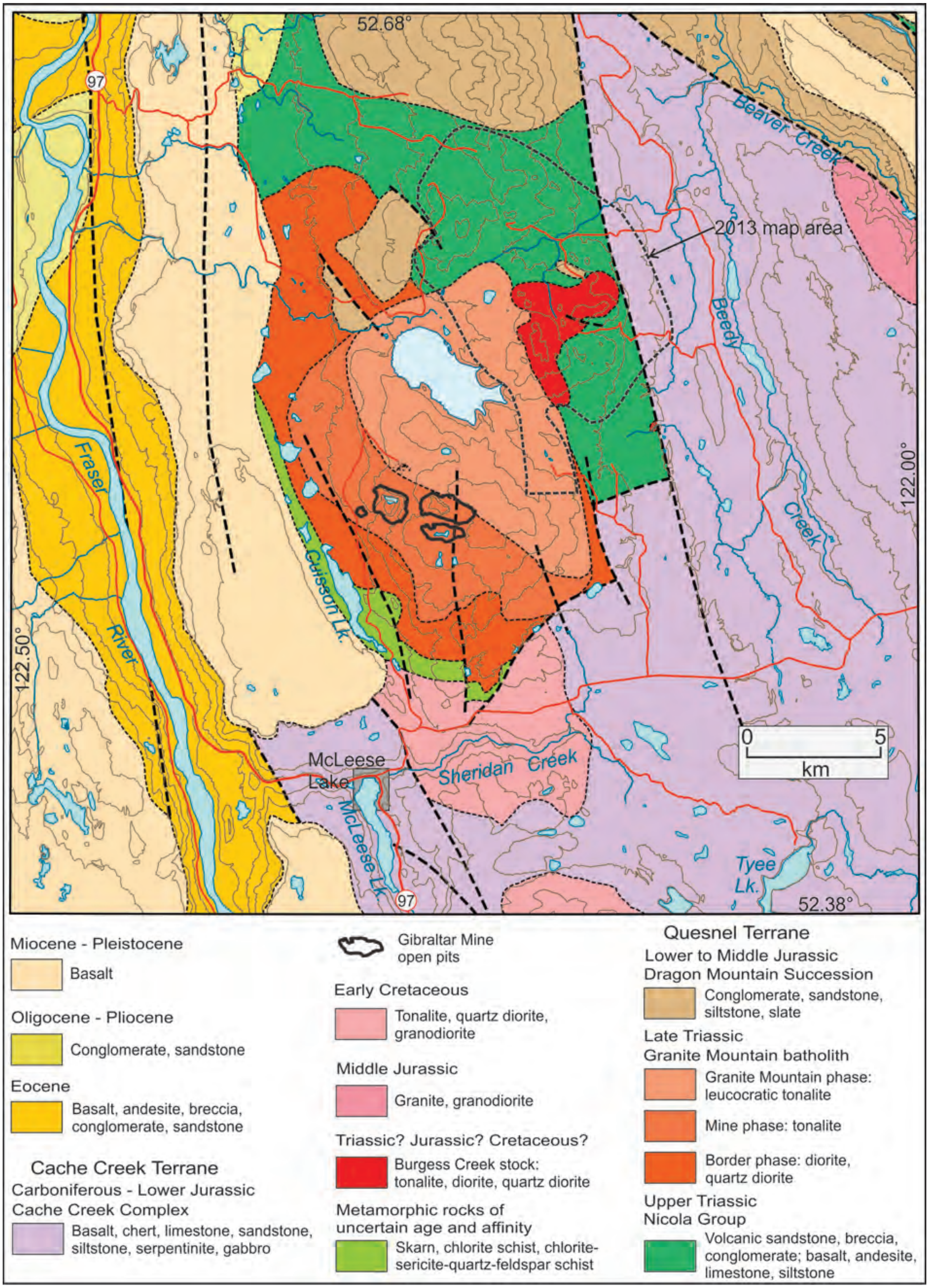

Fig. 20. Geologic map of the Granite Mountain batholith and surrounding area. Based on Tipper (1959, 1978), Panteleyev (1978), Bysouth et al. (1995), Ash et al. (1999b), and this study. Extensive areas of Quaternary overburden are not shown in order to highlight bedrock geology.

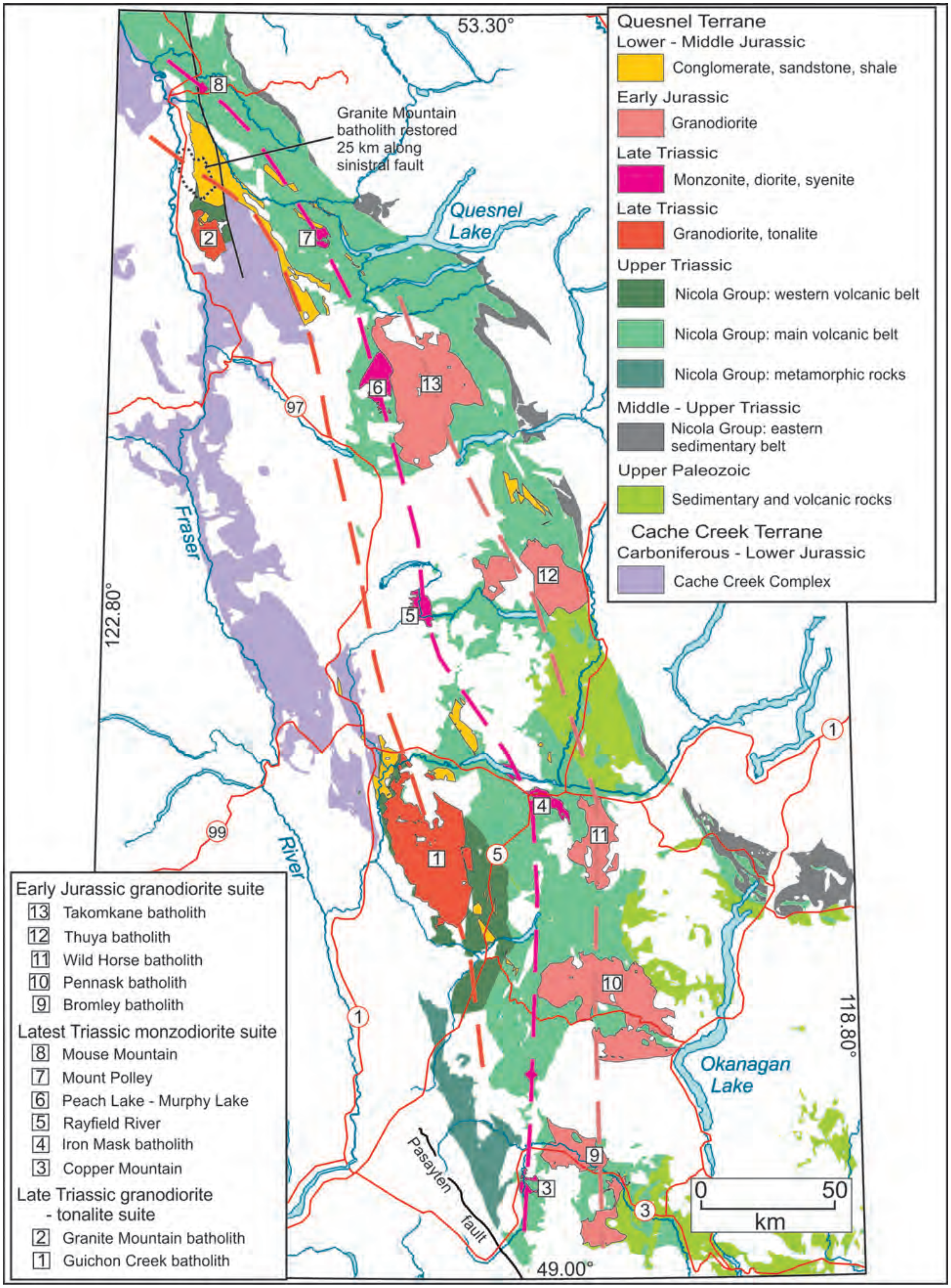

Fig. 21. Simplified geology map of southern British Columbia highlighting selected elements of Quesnel terrane. Granite Mountain batholith is shown in its present location, but a separate outline shows its position after 25 km offset along the sinistral fault inferred from this study is restored.

Creek terrane?

4.4. Plutonic patterns in southern Quesnel terrane

The Granite Mountain batholith is reasonably included in Quesnel terrane, based on its conformity to well established spatial and temporal patterns of magmatism, which are defined by parallel belts of calcalkaline or alkaline plutons that show a progressive younging from west to east (Fig. 21).

The western plutonic belt of southern Quesnel terrane includes the calcalkaline, Guichon Creek and Granite Mountain batholiths (Late Triassic). Each of these plutons hosts major calcalkaline porphyry Cu-Mo deposits. The Granite Mountain batholith is hosted in the western volcanic belt of the Nicola Group, and felsic volcanic breccias in Nicola rocks northeast of the Granite Mountain batholith suggest possible western belt affinities.

A well-defined belt to the east of the western calcalkaline belt comprises younger, latest Triassic alkaline plutons consisting of monzodiorite, monzonite, syenite, and diorite. This belt is remarkably well endowed with alkalic porphyry Cu-Au deposits, including producing mines at Copper Mountain, Afton and Mount Polley, and prospects at Rayfield River, Peach Lake and Mouse Mountain.

The eastern plutonic belt shown (Fig. 21) is defined by five large calcalkaline plutons, the Bromley, Pennask, Wild Horse, Thuya and Takomkane batholiths. These plutons consist mainly of Early Jurassic granodiorite. Locally they host calcalkaline porphyry Cu-Mo deposits, including the past-producing Brenda Mine in the Pennask batholith and the Woodjam SE zone in the Takomkane batholith.

The western Late Triassic calcalkaline plutonic belt (Fig. 21) is defined by only two plutons, the Guichon Creek and Granite Mountain batholiths. The paucity of known intrusions is because most of the belt is buried beneath Tertiary and Quaternary deposits (Fig. 21). Given the rich metal endowment of the Guichon Creek and Granite Mountain batholiths, this covered interval may be prospective for buried calcalkaline porphyry deposits.

5. Summary and conclusions

The volcaniclastic succession that crops out on the northeast margin of the Granite Mountain batholith is correlated with the Late Triassic Nicola Group of Quesnel terrane. It consists of sandstone and gritty to pebbly sandstone, with local intercalations of conglomerate, mafic and felsic volcanic breccia, siltstone, limestone, and basalt. The succession is, at least in part, Middle or Late Triassic, based on conodonts previously extracted from limestone within the succession. Correlation with the Nicola Group is based on a strong similarity to nearby Late Triassic Nicola rocks, although felsic volcanic breccias, which have no counterpart in adjacent Nicola exposures, suggest affinities with the western Nicola belt of the Merritt-Ashcroft area. The Nicola Group is intruded by undated, predominantly tonalitic intrusive rocks of the Burgess Creek stock, and overlain by slate and siltstone correlated to the Dragon Mountain succession (Lower to Middle Jurassic).

The Granite Mountain batholith (Late Triassic) was long thought to have intruded Cache Creek terrane because of its spatial association with Cache Creek rocks (Drummond et al., 1976; Tipper, 1978; Bysouth et al., 1995). The recognition that rocks on the northeast margin of the batholith are part of the Nicola Group (Ash et al., 1999a, b; this study), and are locally overlapped by the Dragon Mountain succession (part of an intra-Quesnel siliciclastic basin), indicate that it is more likely a part of Quesnel terrane, and correlative with the Late Triassic, calcalkaline Guichon Creek batholith, which hosts the Highland Valley porphyry Cu-Mo deposits 250 km to the south-southeast.

The Granite Mountain batholith, together with adjacent Nicola Group and Dragon Mountan succession, form a panel of Quesnel rocks that is bounded to the east by a north-tapering wedge of Cache Creek rocks. The boundary is inferred to be north-northwest striking fault, previously unrecognized, that may record more than 20 km of sinistral strike-slip displacement, as required to restore the southern end of the Quesnel block to the northern termination of the Cache Creek wedge.

The preliminary assessment of geological relationships presented here (Fig. 20) will be refined with ongoing paleontologic and geochronologic studies, and 2014 geological mapping, which will focus mainly on the southern part of the batholith. The Granite Mountain mapping project will compliment geological studies in and near the Gibraltar Mine that are part of the Geological Survey of Canada's TGI-4 intrusion-related ore systems program.

Acknowledgments

I thank Wes Harman, Lori Kennedy and Adrian Hickin for their cheerful and capable assistance during fieldwork. Jim Logan provided notes and data related to a few traverses he conducted in and around the area in 2005, and has shared many ideas on the geology of Quesnel terrane over the past several years. Lawrence Aspler provided a thorough review that improved the paper.

References cited

Ash, C.H., Rydman, M.O., Payne, C.W., and Panteleyev, A., 1999a. Geological setting of the Gibraltar mine, south-central British Columbia (93B/8, 9). In: Exploration and Mining in British Columbia 1998, British Columbia Ministry of Energy and Mines, pp. A1-A15.

Ash, C.H., Panteleyev, A., MacLennan, K.L., Payne, C.W., and Rydman, M.O., 1999b. Geology of the Gibraltar mine area, NTS 93B/8, 9. British Columbia Ministry of Energy and Mines, British Columbia Geological Survey Open File 1999-7; scale 1:50 000.

Ash, C.H., and Riveros, C.P., 2001. Geology of the Gibraltar copper-molybdenite deposit, east-central British Columbia (93B/9). In: Geological Fieldwork 2000, British Columbia Ministry of Energy and Mines, British Columbia Geological Survey Paper 2001-1, pp. 119-133.

Bysouth, G.D., Campbell, K.V., Barker, G.E., and Gagnier, G.K., 1995. Tonalite-trondhjemite fractionation of peraluminous magma and the formation of syntectonic porphyry copper mineralization, Gibraltar mine, central British Columbia. In: Schroeter, T.G. (Ed.), Porphyry deposits of the northwestern cordillera of North America, Canadian Institute of Mining, Metallurgy and Petroleum, Special Volume 46, pp. 201-213.

Cordey, F., and Read, P.B., 1992. Permian and Triassic radiolarian ages from the Cache Creek Complex, Dog Creek and Alkali Lake areas, southwestern British Columbia. In: Current Research, Part E, Geological Survey of Canada Paper 92-1E, pp. 41-51.

Drummond, A.D., Tennant, S.J., and Young, R.J., 1973. The interrelationship of regional metamorphism, hydrothermal alteration and mineralization at the Gibraltar Mines copper deposit in B.C. Canadian Institute of Mining and Metallurgy Bulletin, 66, 48-55.

Drummond, A.D., Sutherland Brown, A., Young, R.J., and Tennant, S.J., 1976. Gibraltar – regional metamorphism, mineralization, hydrothermal alteration and structural development. In: Sutherland Brown, A. (Ed.), Porphyry deposits of the Canadian Cordillera, Canadian Institute of Mining and Metallurgy, Special Volume 15, pp. 195-205.

Eastwood, G.E.P., 1970. McLeese Lake: Geology of the Granite Mountain stock. In: Geology, Exploration and Mining in British Columbia 1969, British Columbia Department of Mines and Petroleum Resources, pp. 162-172.

Greig, C.J., 1992. Jurassic and Cretaceous plutonic and structural styles of the Eagle Plutonic Complex, southwestern British Columbia, and their regional significance. Canadian Journal of Earth Sciences, 29, 793-811.

Harding, B., 2012. The characterization of molybdenum mineralization at the Gibraltar mines Cu-Mo porphyry, central British Columbia. B.Sc. thesis, Queen's University, 52 p.

Hurlow, H., 1993. Mid-Cretaceous strike-slip and contractional fault zones in the western Intermontane Terrane, Washington, and their relation to the North Cascades-southeastern Coast Belt orogen; Tectonics, 12, 1240-1257.

Logan, J.M., 2008. Geology and mineral occurrences of the Quesnel terrane, Cottonwood map sheet, central British Columbia (NTS 093G/01). In: Geological Fieldwork 2007, British Columbia Ministry of Energy, Mines and Petroleum Resources, British Columbia Geological Survey Paper 2008-1, pp. 69-86.

Logan, J.M., and Bath, A.B., 2006. Geochemistry of Nicola Group basalt from the central Quesnel trough at the latitude of Mount Polley (NTS 093A/5, 6, 11, 12), central British Columbia. In: Geological Fieldwork 2005, British Columbia Ministry of Energy and Mines, British Columbia Geological Survey Paper 2006-1, pp. 83-98.

Logan, J.M., and Moynihan, D.P., 2009. Geology and mineral occurrences of the Quesnel River map area, central British Columbia (NTS 093B/16). In: Geological Fieldwork 2008, British Columbia Ministry of Energy, Mines and Petroleum Resources, British Columbia Geological Survey Paper 2009-1, pp. 127-152.

Logan, J.M., Bath, A., Mihalynuk, M. G., Rees, C.J., Ullrich, T.D., and Friedman, R., 2007. Regional geology of the Mount Polley area, central British Columbia. British Columbia Ministry of Energy, Mines and Petroleum Resources, British Columbia Geological Survey Geoscience Map 2007-1; scale 1:50 000.

Logan, J.M., Schiarizza, P., Struik, L.C., Barnett, C., Nelson, J.L., Kowalczyk, P., Ferri, F., Mihalynuk, M.G., Thomas, M.D., Gammon, P., Lett, R., Jackaman, W., and Ferbey, T., 2010. Bedrock geology of the QUEST map area, central British Columbia. British Columbia Ministry of Energy, Mines and Petroleum Resources, British Columbia Geological Survey Geoscience Map 2010-1; scale 1:500 000 (also Geoscience BC, Report 2010-5; Geological Survey of Canada, Open File 6476).

Monger, J.W.H., and McMillan, W.J., 1989. Geology, Ashcroft, British Columbia (92I). Geological Survey of Canada, Map 42-1989; sheet 1, scale 1:250 000.

Nelson, J.L., Colpron, M., and Israel, S., 2013. The cordillera of British Columbia, Yukon and Alaska: tectonics and metallogeny. In: Tectonics, metallogeny and discovery: the North American cordillera and similar accretionary settings, Society of Economic Geologists, Special Publication 17, pp. 53-109.

Oliver, J., Crozier, J., Kamionko, M., and Fleming, J., 2009. The Gibraltar Mine, British Columbia. A billion tonne deep copper-molybdenum porphyry system: structural style, patterns of mineralization and rock alteration. In: Association for Mineral Exploration British Columbia, 2009 Mineral Exploration Roundup, program with abstracts, pp. 35-36.

Orchard, M.J., 2006. Report on conodonts and other microfossils, Quesnel Lake (93A); Report No. MJO-2006-1, Geological Survey of Canada, Paleontological report on samples collected by J. Logan, British Columbia Geological Survey.

Panteleyev, A., 1978. Granite Mountain project (93B/8). In: Geological Fieldwork 1977, British Columbia Ministry of Energy, Mines and Petroleum Resources, British Columbia Geological Survey Paper 1977-1, pp. 39-42.

Petersen, N.T., Smith, P.L., Mortensen, J.K., Creaser, R.A., and Tipper, H.W., 2004. Provenance of Jurassic sedimentary rocks of south-central Quesnellia, British Columbia: impications for paleogeography. Canadian Journal of Earth Sciences, 41, 103-125.

Preto, V.A., 1979. Geology of the Nicola Group between Merritt and Princeton. British Columbia Ministry of Energy, Mines and Petroleum Resources, British Columbia Geological Survey Bulletin 69, 90 p.

Read, P.B., 1993. Geology of northeast Taseko Lakes map area, southwestern British Columbia. In: Current Research, Part A, Geological Survey of Canada Paper 93-1A, pp. 159-166.

Schiarizza, P., Israel, S., Heffernan, S., Boulton, A., Bligh, J., Bell, K., Bayliss, S., Macauley, J., Bluemel, B., Zuber, J., Friedman, R.M., Orchard, M.J., and Poulton, T.P., 2013. Bedrock geology between Thuya and Woodjam creeks, south-central British Columbia, NTS 92P/7, 8, 9, 10, 14, 15, 16; 93A/2, 3, 6. British Columbia Ministry of Energy, Mines and Natural Gas, British Columbia Geological Survey Open File 2013-05; 4 sheets, scale 1:100 000.

Struik, L.C., Schiarizza, P., Orchard, M.J., Cordey, F., Sano, H., MacIntyre, D.G., Lapierre, H., and Tardy, M., 2001. Imbricate architecture of the upper Paleozoic to Jurassic oceanic Cache Creek Terrane, central British Columbia. Canadian Journal of Earth Sciences, 38, 495-514.

Sutherland Brown, A., 1958. Williams Lake: McLeese - Cuisson lakes area. In: Annual Report of the Minister of Mines for 1957, British Columbia Department of Mines, pp. 14-18.

Sutherland Brown, A., 1967. Geology of the Granite Mountain – Cuisson Lake area. In: Annual Report of the Minister of Mines and Petroleum Resources for 1966, British Columbia Ministry of Mines and Petroleum Resources, pp. 121-124.

Sutherland Brown, A., 1974. Gibraltar Mine (93B-12, 13). In: Geology, Exploration and Mining in British Columbia 1973, British Columbia Ministry of Energy, Mines and Petroleum Resources, pp. 299-318.

Tipper, H.W., 1959. Quesnel, British Columbia. Geological Survey of Canada, Map 12-1959; scale 1:253 440.

Tipper, H.W., 1978. Northeastern part of Quesnel (93B) map-area, British Columbia. In: Current Research, Part A, Geological Survey of Canada, Paper 78-1A, pp. 67-68.

van Straaten, B.I., Oliver, J., Crozier, J., and Goodhue, L., 2013. A summary of the Gibraltar porphyry copper-molybdenum deposit, south-central British Columbia, Canada. In: Logan, J. and Schroeter, T. G. (Eds.), Porphyry systems of central and southern BC: Prince George to Princeton, Society of Economic Geologists Field Trip Guidebook 43, 55-66.

Structural and stratigraphic control of porphyry and related mineralization in the Treaty Glacier – KSM – Brucejack – Stewart trend of western Stikinia

JoAnne Nelson[1, a] and Jeff Kyba[2]

[1] British Columbia Geological Survey, Ministry of Energy and Mines, Victoria, BC, V8W 9N3
[2] Ministry of Energy and Mines, Smithers, BC, V0J 2N0
[a] corresponding author: Joanne.Nelson@gov.bc.ca

Recommended citation: Nelson, J., and Kyba, J., 2014. Structural and stratigraphic control of porphyry and related mineralization in the Treaty Glacier – KSM – Brucejack – Stewart trend of western Stikinia. In: Geological Fieldwork 2013, British Columbia Ministry of Energy and Mines, British Columbia Geological Survey Paper 2014-1, pp. 111-140.

Abstract

One of the most important mineral trends of northwestern British Columbia extends from near the town of Stewart north to the Treaty Glacier, in the western part of the Stikine arc terrane. Major deposits along this trend include Kerr-Sulphurets-Mitchell (KSM), Brucejack, Silbak-Premier, Big Missouri, Scottie Gold and Red Mountain. All are hosted by volcanic and sedimentary rocks of the Hazelton Group (Lower Jurassic) and its subvolcanic feeders (193-195 Ma Premier porphyries near Stewart; Mitchell intrusions at KSM). Although the Hazelton Group is widespread throughout Stikinia, the narrow, consistently NNW-SSE trend of mineralization along a 60 km strike length suggests structure-controlled magmatic and hydrothermal systems, possibly influenced by basement anisotropies. The Jack Formation, a unique basal Hazelton unit restricted to the flanks of the McTagg anticlinorium, is characterized by quartz-rich arkoses and polymictic pebble conglomerates with high-level intrusive, felsic volcanic and quartz clasts. Stratigraphic and sedimentologic data from Jack Formation sections are consistent with depositional control by penecontemporaneous, basin-bounding faults and by volcanic centres. The McTagg anticlinorium was probably a topographic high during sedimentation. Initial sedimentation at the Treaty Glacier and Brucejack sections on the eastern side of the anticlinorium is marked by sharpstone conglomerates derived from immediately underlying Stuhini Group (Triassic) and may represent mechanical weathering fronts on a gently sloping upland, whereas at the Bruce Glacier section to the west, basal units include isolated remnants of carbonaceous mudstone that are overlain by thick (100 m +) sections of polymictic cobble-boulder conglomerate, which imply abrupt basin deepening and underfilled conditions followed by uplifting, significant relief, and a proximal but integrated drainage system. An overlying predominantly fine-grained siliciclastic section thins eastward from ~ 400 m at the Bruce Glacier section to ≤ 80 m at the Treaty Glacier section. Local cross beds in mass flow sandstones at the Bruce Glacier section indicate derivation from the east, away from the area now occupied by the McTagg anticlinorium. Sandstone megaclast-bearing olistostromes in equivalent carbonaceous mudstones at the Brucejack section attest to fault-induced uplift and cannibalization of previously deposited Jack Formation sandstones. Andesitic pyroclastic and epiclastic volcaniclastic rocks in the middle of the Jack Formation represent an episode of intense volcanism. Black mudstone intraclasts in the volcaniclastic units indicate that background deep-water sedimentation resumed during intervals of volcanic quiescence. Thick coarse volcaniclastic sections at the Bruce Glacier and Treaty glacier sections suggest proximity to discrete coeval volcanic centres. In the Iron Cap section, highly altered lower Jack Formation arkosic sandstones and polymictic pebble conglomerates occur as screens within the potassic and phyllic-altered porphyry body, which is overlain by a thin andesitic volcaniclastic blanket and unaltered Jack conglomerates, showing the coeval relationship of sedimentation, intrusion, alteration and local volcanism. At the Bruce Glacier section, the volcaniclastic facies grades back into a mudstone-rich sedimentary section and a return to deep- water sedimentation. In marked contrast, at the Treaty Glacier section to the east, rocks above the volcaniclastic facies indicate shallow-marine sedimentation (basal limestone beds with shelly fauna, sandstones with interference ripples and plant debris, polymodal paleocurrents). Apparently, as with the onset of Jack Formation sedimentation, the region on the eastern side of the McTagg anticlinorium was high standing relative to the eastern side. Integration of facies variations in the Jack Formation with first-order Cretaceous structures leads to a model in which the eastern margin of the McTagg anticlinorium was once a basin-bounding master growth fault. Accordingly, the KSM porphyries and their associated alteration haloes were channeled along this fault, and the Brucejack epithermal system to the east developed adjacent to a complex set of related north-trending and east-trending faults. The Early Jurassic structural regime may have been transtensional or purely extensional.

Keywords: Stewart, Treaty Glacier, Iskut region, KSM, Brucejack, Hazelton Group, Jack Formation, Early Jurassic, McTagg anticlinorium

1. Introduction

Although it has long been appreciated that basement structures extending west from ancestral North America influenced depositional and structural patterns in Cordilleran platformal cover rocks (Fig. 1; e.g., Aitken and Long, 1978; Cecile et al., 1997; McMechan, 2012) and focused mineralization at deposits such as Sullivan and Pine Point (Höy et al., 2002; Nelson et al., 2002), the possibility that basement to accreted arc terranes exerted a similar control has not been fully investigated. Most of British Columbia's copper and gold endowment is in latest Triassic to Early Jurassic porphyry and related deposits of the Quesnel and Stikine arcs (Fig. 1). In Quesnellia, these deposits and their igneous hosts form arc-parallel, eastward-younging belts (Logan and Mihalynuk, 2013, in press). In contrast, those

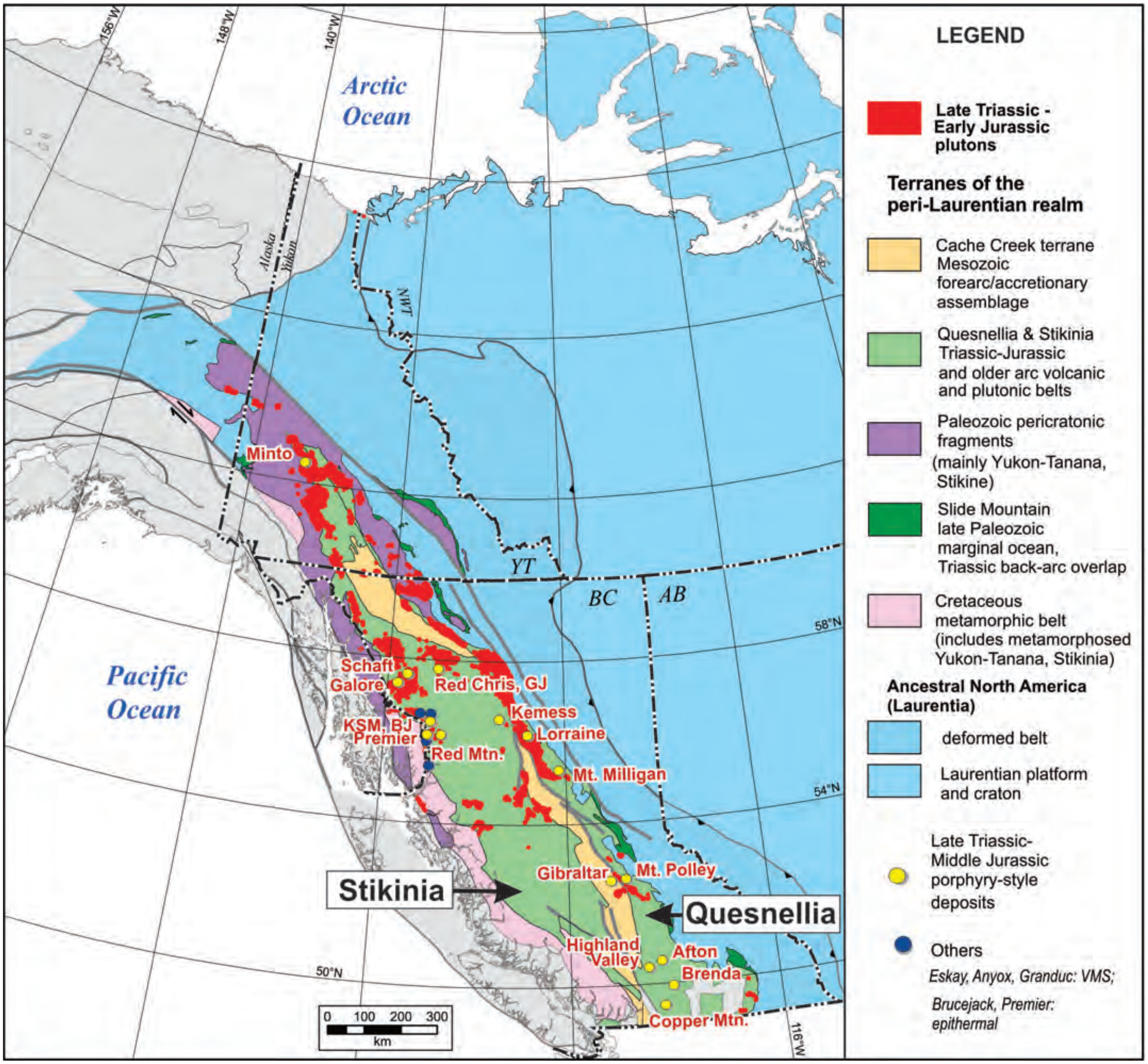

Fig. 1. Tectonic setting of Triassic-Jurassic porphyry and related deposits of Quesnellia and Stikinia in the northern Cordillera of BC and Yukon, from Nelson et al. (2013).

in Stikinia form several discrete clusters and trends of differing ages, including Kemess, Iskut (Red Chris, GJ), Schaft Creek-Galore Creek, and Treaty Glacier-KSM-Brucejack-Stewart (Fig. 1).

The Treaty Glacier-KSM-Brucejack-Stewart trend is one of the most productive and promising in northwestern British Columbia (Figs. 2, 3). Major deposits include Kerr-Sulphurets-Mitchell (KSM), Brucejack, Silbak-Premier, Big Missouri, Scottie Gold, and Red Mountain. All are hosted by, and related to, volcanosedimentary rocks of the Hazelton Group (Lower Jurassic) and its subvolcanic feeders, the ~ 195 Ma Texas Creek and Premier porphyries near Stewart (Alldrick, 1993) and Mitchell intrusions at KSM (Kirkham and Margolis, 1995). Mineralized bodies define a northerly trend, extending discontinuously for ~ 60 km, from near the town of Stewart north to Treaty Glacier (Figs. 2, 3). Although the Hazelton Group is widespread throughout Stikinia, the narrow, consistently NNW-SSE trend of mineralization along a 60 km strike length suggests structure-controlled magmatic and hydrothermal systems. Furthermore, Alldrick (1993) considered that local pre-ore structures controlled mineralization at Silbak Premier, Big Missouri and Scottie Gold, and work by Pretivm Resources (2013) at Brucejack suggests that replacements and stockworks in basal Hazelton Group strata formed adjacent to north-striking

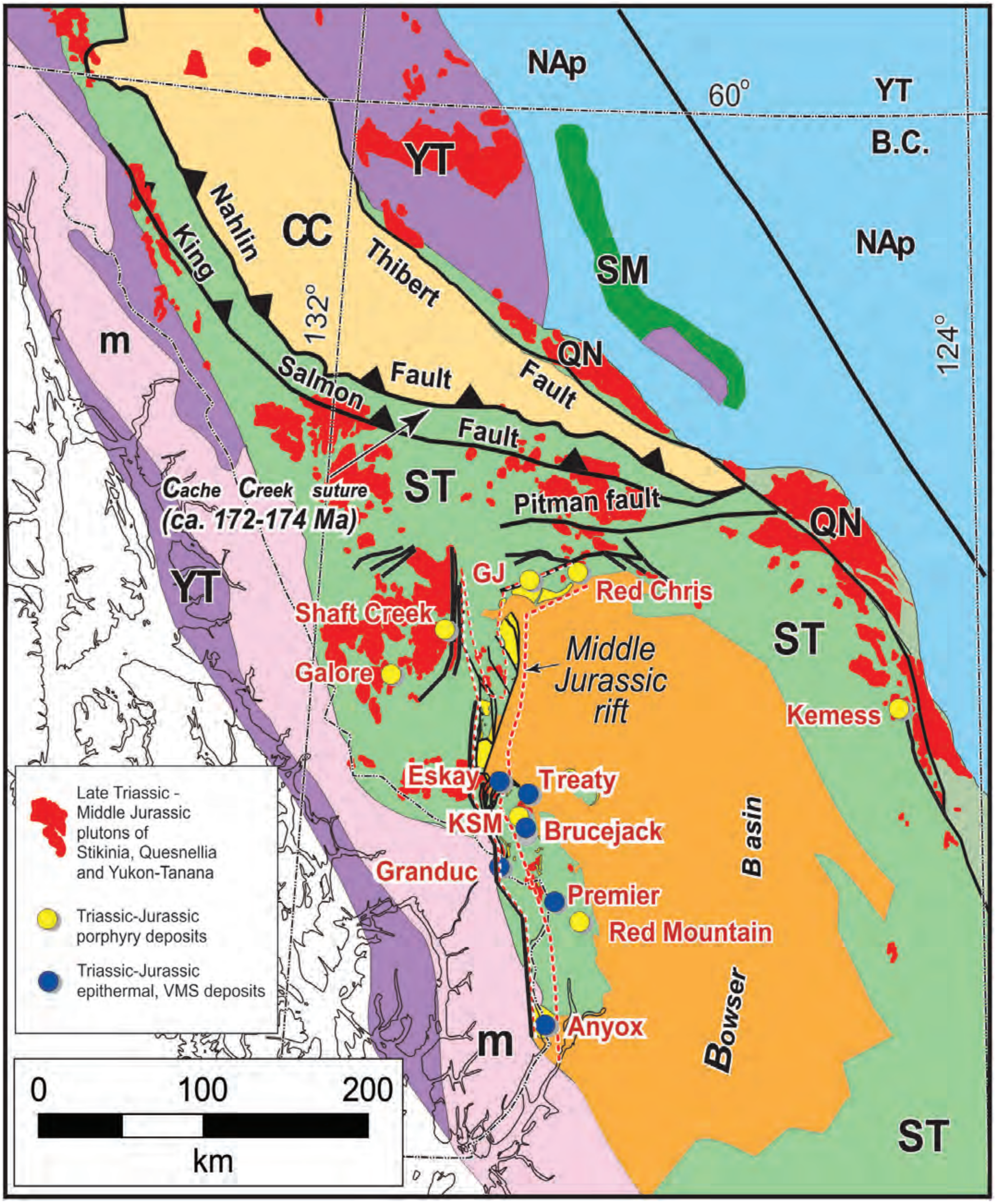

Fig. 2. Tectonic and structural setting of Triassic-Jurassic porphyry and related deposits in northern Stikinia, from Nelson et al. (2013). Terrane abbreviations: CC = Cache Creek, Na = North America (platformal), QN = Quesnellia, SM = Slide Mountain, ST = Stikinia, YT = Yukon-Tanana; m = metamorphic rocks of the Coast Plutonic complex.

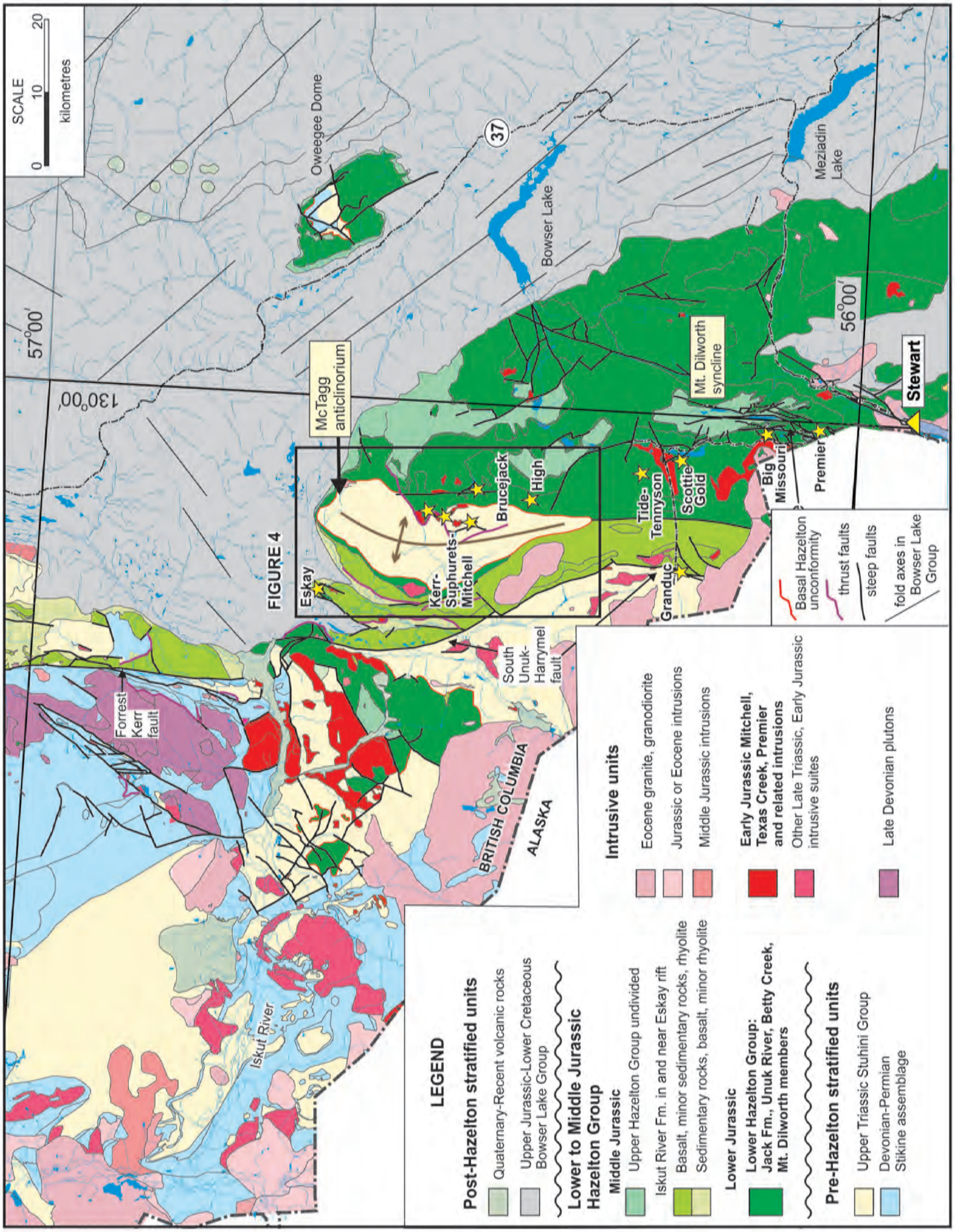

Fig. 3. Treaty-Stewart trend and western Iskut region geology and mineral deposits, generalized from the digital geological map of British Columbia 2005 from Massey et al. (2005).

growth faults. Moreover, the northerly and northeasterly structures along the trend, which formed during the Cretaceous as part of the Skeena fold and thrust belt, are highly discordant to the overall northwesterly Skeena grain, hinting at a local control by basement anisotropies.

Fault reactivation creates a structural veil that typically obscures previous events. To fully document reactivation of basement structures and penecontemporaneous faulting, integrated stratigraphic, sedimentologic, structural, geochronologic, and geophysical data are required (e.g., Holdsworth et al., 1997). Herein we present stratigraphic and sedimentologic data from basal Hazelton strata (Jack Formation), the favoured host for porphyry and epithermal deposits, exposed near the McTagg anticlinorium (Fig. 3). Together with a first-order analysis of Cretaceous structural patterns, these data provide circumstantial evidence consistent with structural control of sedimentation, magmatism, and mineralization along the Treaty Glacier-KSM-Brucejack-Stewart trend.

2. Mineralization in the Treaty Glacier-KSM-Brucejack-Stewart trend

Mineralization along the trend is diverse, even within individual deposits, indicating complex, episodic ore formation. Besides porphyries, there are gold stockworks, shear-hosted veins, hydrothermal breccias and replacements (Alldrick, 1993). Past gold producers include Silbak-Premier (1918-1968 and 1989-1997), Big Missouri (1927-1942), and Scottie Gold (1981-1984). Owing to major exploration programs in the last five years, the Kerr-Sulphurets-Mitchell (KSM) Cu-Au porphyries and high-grade gold zones at Brucejack are approaching the mine development stage. Seabridge Gold submitted its EA application for the KSM deposit in April 2013. Proven and probable reserves for the KSM porphyries are over 2.16 billion tonnes grading 0.21% Cu, 0.55 g/t Au, 2.74 g/t Ag and 44.7 ppm Mo (December 2012, pre-feasibility study). In 2013, 23,800 m of drilling on the Deep Kerr target identified a Cu-Au-rich zone with a weighted average of drill intercepts grading 0.46 g/t Au and 0.71% Cu over a width of 220 metres (Seabridge release, 23-11-13, not 43-101 compliant). At the adjoining Brucejack property, the Valley of the Kings (VOK zone) hosts a probable reserve totalling 15.1 Mt grading 13.6 g/t Au and 11 g/t Ag (June 2013 feasibility, Pretivm Resources, 2013). A 10,000 tonne underground bulk sample has been excavated and is currently being processed to further validate the deposit. Preliminary results indicate that over 4200 ounces of gold had been recovered from 8090 tonnes, with recovery from the remaining 1810 tonnes pending (Pretivm Resources, 2013). Other exploration projects in the area in 2013 (Figs. 3, 4) include the Tide-Tennyson porphyry-epithermal target south of the Frank Mackie Glacier by HDI Brigade; the High property between Brucejack and the Frank Mackie Glacier by Teuton Resources, and Premier-Big Missouri by Ascot Resources.

3. Regional setting: Stikine terrane

Stikinia is a long-lived arc terrane in the Intermontane belt of the Canadian Cordillera. At its northern end near Tulsequah and its far western extent in the Coast Mountains, it developed near the Yukon-Tanana terrane, which is partly underlain by siliciclastic basement units rifted from the edge of ancestral North America (Fig. 1; Nelson et al., 2006). The oldest rocks in Stikinia are Devonian to Mississippian arc-related volcanic and plutonic bodies and accompanying sedimentary strata of the Stikine assemblage (upper Paleozoic; Logan et al., 2000). The Stikine assemblage contains the products of multistage arc magmatism and marine sedimentation as young as Middle Permian (Gunning et al., 2006). It is unconformably overlain by Triassic arc and marine sedimentary strata of the Stuhini Group. Above a Late Triassic-Early Jurassic unconformity, the Hazelton Group and its intrusive sources (latest Triassic to Middle Jurassic) represent the final stage of island arc magmatism and its aftermath. Unconformably above the Hazelton Group, the Bowser Lake Group (Middle Jurassic to Lower Cretaceous) is a northeasterly-sourced, southwestward-younging clastic overlap sequence derived from the collision of the Intermontane terranes and the edge of ancestral North America (Evenchick et al., 2007).

The Hazelton Group is distributed throughout most of Stikinia, around the margins of the Bowser basin (Fig. 2; Tipper and Richards, 1976). The lower Hazelton Group (latest Triassic to Early Jurassic; 205-185 Ma) records successive pulses of arc volcanism. Basal units are generally coarse, immature, locally-derived conglomerates and volcanic breccias. Regionally, thick sections of coarse conglomerates and olistostromal units (Ash et al., 1997a) suggest significant relief and syndepositional uplifting of source rocks (Greig, 1992). The upper Hazelton Group (Pleinsbachian to Callovian; ~ 190-161 Ma) consists of mainly post-arc sedimentary and minor volcanic strata (Gagnon et al., 2012), except for the Iskut River Formation, the bimodal volcanosedimentary fill of the Eskay rift in western Stikinia (Alldrick et al., 2005; Gagnon et al., 2012), and felsic tuffs in the southwestern part of the terrane, which represent a reconfigured, post-accretionary arc axis.

The subduction geometry of the Hazelton arc or arcs has long been debated. Unlike the contemporary Nicola-Takla arc of Quesnellia, which is characterized by a narrow, linear arc axis that migrated sequentially eastward from Late Triassic through Early Jurassic time (Logan and Mihalynuk, 2013 in press), in Stikinia, arc volcanism is thought to have occurred continuously or at least sporadically throughout the terrane, at present over a width of about 500 km (Marsden and Thorkelsen, 1992).This extent exceeds any reasonable width of a single magmatic arc; therefore it is likely that the Hazelton Group was fed by the products of two separate, possibly opposing arcs, similar to the modern Philippines (Marsden and Thorkelsen, 1992).

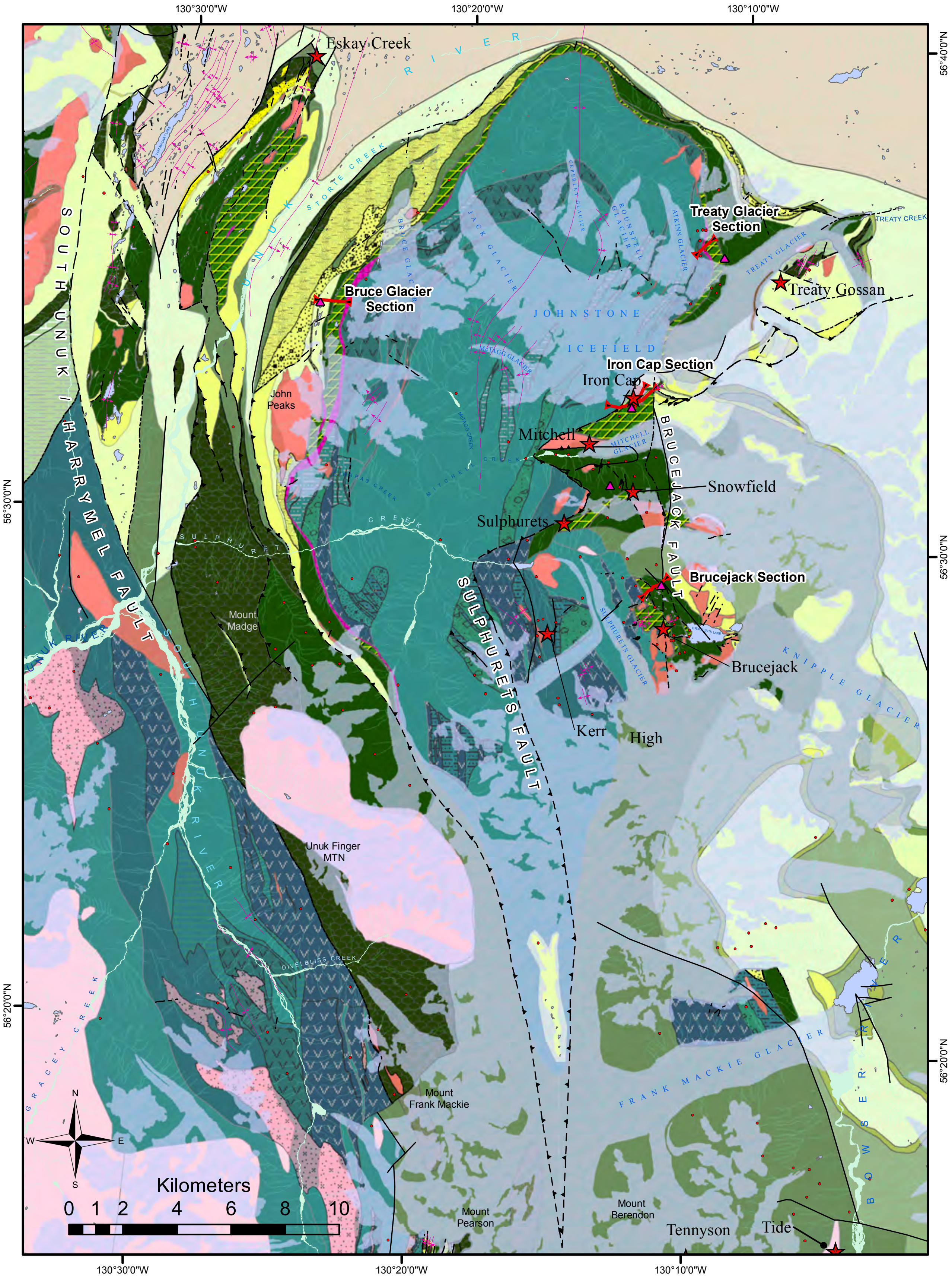

Fig. 4. Detailed geological map of KSM-Brucejack area and McTagg anticlinorium, and section locations. Compiled from Lewis (2013); additional sources MacIntyre et al. (1994), Evenchick et al. (2002).

Legend

Stratified Rocks

Quaternary

- 🟫 Edziza volcanic rocks

Cretaceous - Upper Jurassic

- 🟫 Bowser Lake Group undivided

JURASSIC

Hazelton Group

- 🟩 Volcanic and sedimentary rocks undivided

Volcanic Rocks

- 🟩 Volcanic rocks undivided
- 🟨 Felsic Volcanics undivided
- ▨ Coherent rhyolite, autoclastic breccia
- ▨ Variably welded felsic lapilli tuff
- ▨ Epiclastic felsic breccia and crystal tuff
- 🟩 Andesitic- basaltic volcanic rocks
- 🟩 Subareal calc-alkalic andesite and dacite flows, pyroclastic and epiclastics and lapilli tuff
- ▨ Pillow lavas, pillow breccias, interbedded mudstone and mafic volcanic rocks

Sedimentary rocks

- 🟩 Sedimentary rocks undivided
- ▨ Limestone
- ▨ Calcareous sandstone
- ▨ Turbiditic mudstone - siltstone
- 🟩 Intercalated sedimentary rocks
- ▨ **Jack Formation** Sandstone, siltstone, mudstone, wacke, tuff; Intermediate grey-green, beige and maroon, very fine to coarse grained, thin to thickly bedded, arkosic arenites, lesser quartz, graded in part, minor fossils.
- ▨ **Basal Jack Formation** Polymictic conglomerate with well rounded clasts of mainly (70%) felsic to intermediate intrusive rocks. Intrusive clasts are generally plagioclase-hornblende-phyric and crowded plagioclase porhyries with tonalitic to granodioritic compositions. Common intraclasts of black argillite (10%). Minor clasts of white polycrystalline quartz (10%), andesite (5%), siltstone + tuff (3%), gossanous quartz-sericite-pyrite replaced clasts (1%) and carbonate (1%). Quartz-rich arkoses and pebbly arkoses. Isolated basal carbonaceous mudrocks.

TRIASSIC

Stuhini Group

- 🟦 Undivided volcanic and sedimentary rocks

Volcanic Rocks

- ▨ Intermediate volcanic rocks
- ▨ Mafic volcanic rocks
- ▨ Andesite boulder conglomerate

Sedimentary Rocks

- 🟦 Sedimentary rocks undivided
- ▨ Limestone and Marble
- ▨ Argillite, siltstone turbidites, sandstone and wacke
- ▨ Arkosic sandstone, siltstone, mudstone
- ▨ Arkosic sandstone, tuffaceous polylithic conglomerate

Intrusive Rocks

Eocene	🟪	Coast Plutonic Suite
Early Jurassic	🟥	Texas Creek Plutonic Suite
Paleozoic	▨	Stikine Pluitonic Suite

- · MINFILE
- ★ significant deposit
- ▲ 2013 flycamp
- ▶—◀ section lines
- rivers
- 🟦 lakes
- ▨ glaciers

Faults

Type

- —— defined
- — — — approximate
- - - - - - inferred

Motion

- normal
- thrust
- strike slip

Structure Lines

- antiform, upright
- synform, overturned
- synform, upright

4. Geology of the Treaty Glacier-KSM-Brucejack trend

4.1. Local subdivisions of the Hazelton Group: history and present usage

Grove (1971; reprinted in 1986) and Alldrick (1993) mapped the area between Stewart and Frank Mackie Glacier at a 1:50,000 scale. Grove's subdivision of the Hazelton Group into the Unuk River, Betty Creek, and Salmon River formations was modified by Alldrick (1993), who recognized six subunits of the Unuk River Formation and introduced the Mt. Dilworth Formation, a dacitic unit that separates the mainly sedimentary Salmon River Formation from the underlying Betty Creek Formation near the Mt. Dilworth syncline in the vicinity of the Big Missouri and Premier deposits (Fig. 3; Table 1). This stratigraphic scheme was extended northward during mapping of the Sulphurets, Unuk River, and Snippaker areas (Alldrick and Britton, 1988, 1991; Alldrick et al. 1989; Alldrick and Britton, 1992; Alldrick et al., 1990).

Table 1. Historical and current stratigraphic nomenclature for the Hazelton Group in the Treaty-Stewart-western Iskut region.

Series	Stage	ages (U-Pb range)	Alldrick, 1993	Lewis, 2013	Gagnon et al., 2012		This study	
Middle Jurassic	Bajocian	172-178 Ma	Salmon River Formation	Salmon River Formation • Bruce Glacier member • Troy Ridge member • John Peaks member • Eskay member	in Eskay rift: Iskut River Formation	outside Eskay rift: Quock Formation	in Eskay rift: Iskut River Formation • Bruce Glacier member • John Peaks member • Eskay member	outside Eskay rift: upper Hazelton Group (includes Troy Ridge member, Treaty Ridge member)
	Aalenian							
Lower Jurassic								
	Toarcian Pleinsbachian		Mt. Dilworth Formation	Betty Creek Formation • Unuk River member • Brucejack Lake member • Treaty Ridge member	Betty Creek Formation		Betty Creek Formation • Unuk River member • Brucejack Lake member	
			Betty Creek Formation					
	Pleinsbachian Sinemurian Hettangian	Brucejack: 194-186 Ma Unuk: 194-192 Ma	Unuk River Formation		Unuk River Formation			
				Jack Formation	Jack Formation		Jack Formation	
Upper Triassic		215-225 Ma	Stuhini Group	Stuhini Group	Stuhini Group		Stuhini Group	

The richly mineralized area between Eskay Creek and the Kerr-Sulphurets-Brucejack camp has been studied in detail for the last 40 years. Notable contributions, other than Alldrick and colleagues, include Henderson et al. (1992), Kirkham and Margolis (1995), Lewis et al. (2001) and a new 1:50,000 compilation map (Lewis, 2013). Understanding of Hazelton stratigraphy in the area has been strengthened by fossil collections and U-Pb ages (compiled by Lewis et al., 2001). According to Lewis (2013; Table 1) the lower Hazelton Group includes a basal sedimentary unit of polymictic conglomerate, arkosic sandstone, and mudstone (Jack Formation) that is overlain by discontinuous volcanosedimentary units in the Betty Creek Formation (Unuk River, Brucejack Lake and Treaty Ridge members). The Salmon River Formation overlies Betty Creek Formation units and includes the Troy Ridge, Eskay, Bruce Glacier, and John Peaks members. We adhere to the nomenclature proposed by Lewis (2013) except in the case of the Salmon River Formation, which has been superseded by the Iskut River Formation in the Eskay rift and the Quock Formation elsewhere (Table 1; Gagnon et al., 2012).

4.2. Structure

To the east and south of Eskay Creek mine, including the Treaty-Stewart trend, the principal structures resulted from mid-Cretaceous sinistral transpression during development of the Skeena fold and thrust belt (Fig. 3; Kirkham and Margolis, 1995; Lewis, 2013). Farther west, the South Unuk-Harrymel and Forrest Kerr faults show evidence of earlier origins. They are steep, major, north to north-northwesterly normal, east-side-down faults that bound the Iskut River Formation to the west, and by definition, the Eskay rift (Fig. 3). They underwent sinistral motion in mid-Jurassic time (~ 172 Ma; Lewis, 2001a), roughly coeval with opening of the rift and eruption of bimodal Iskut River Formation volcanic rocks (~ 175 Ma). Exposures west of these faults are at a comparatively deep level, predominantly Paleozoic Stikine assemblage and Stuhini Group with patchy Hazelton cover (Fig. 3). North-south alignment of Devonian-Mississippian plutons immediately west of the Forrest Kerr fault (Fig. 3) may have been controlled by pre-existing structures (Logan et al., 2000).

East of the South Unuk-Harrymel fault, strata of the Stuhini, Hazelton, and Bowser Lake groups were deformed as part of the Skeena fold and thrust belt into a series of north- to northeast-trending folds with strongly curvilinear hinges that produced local culminations such as the McTagg anticlinorium and Eskay anticline (Fig. 3). The McTagg anticlinorium is a north-trending Cretaceous structural culmination that forms the western boundary of thick lower Hazelton Group exposures (Fig. 3). All Hazelton Group units thin markedly across the axis of the anticlinorium (Figs. 3, 4; see also Lewis, 2013), suggesting that it persisted as a high-standing block during the Early Jurassic. It is bounded in part by thrust faults that verge away from its hinge, particularly the east-vergent Sulphurets fault (Figs. 4, 5). The Kerr-Sulphurets-Mitchell-Iron Cap system forms a single northerly band of alteration in the immediate footwall of the Sulphurets thrust. The Mitchell thrust is a prominent footwall splay of the Sulphurets thrust that separates the Snowfield and Iron Cap zones in its hanging wall from the Mitchell zone in its footwall (Fig. 4). The Eskay anticline is cored by the Middle Jurassic host sequence of the Eskay Creek VMS deposit.

In addition to the South Unuk fault, Grove (1986, his fig. 13) outlined a north-trending zone of high strain, the Cascade Creek shear zone, along the Granduc Road in the Stewart camp east of the Salmon Glacier (Fig. 3). This fault was interpreted by later workers as a zone of north-trending mid-Cretaceous folds such as the Mt. Dilworth syncline (Alldrick, 1993) and east-vergent thrust faults (Ascot Resources, unpublished 2013), rather than a zone of mylonitization or shearing. It is probably better termed the Cascade Creek deformation zone (Fig. 3). It is expressed as a concentration of northerly faults in the vicinity of the Premier and Big Missouri mines.

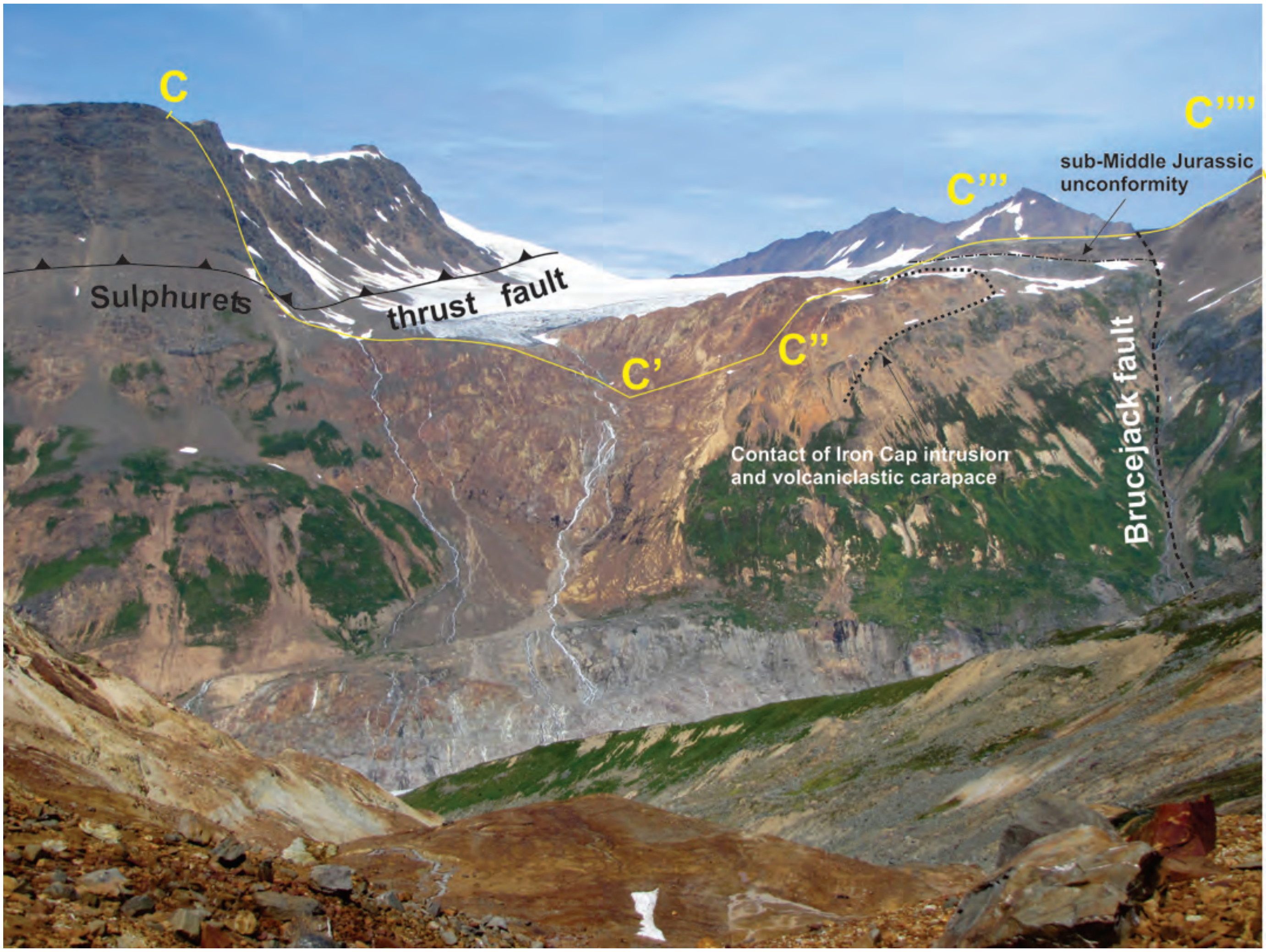

Fig. 5. Looking north from the Snowfield zone across the Mitchell Glacier to the Iron Cap zone and structurally higher Sulphurets fault. C-C'-C''-C''' refers to section presented in Figure 16.

5. Stratigraphy and sedimentology of the Jack Formation (basal Hazelton Group)

We examined the Jack Formation at four sections on the margins of the McTagg anticlinorium: Bruce Glacier, Treaty Glacier, Brucejack, and Iron Cap (Fig. 4). We also studied a fifth section of basal Hazelton Group at the Tide-Tennyson prospect south of the McTagg anticlinorium (Fig. 4).

5.1. Bruce Glacier section

The Bruce Glacier section is in a west-younging, overturned panel west of the McTagg anticlinorium (Fig. 4). It exposes rocks from beneath the unconformity between the Stuhini Group and Jack Formation, across the entire Jack Formation, and into the unconformably overlying Bruce Glacier member (Fig. 6; Lewis, 2013). The basal unconformity cuts at a low angle (< 15°) through a Stuhini Group section of polymictic conglomerate, pillow basalt and pillow breccia (Fig. 6). It truncates units within the Stuhini Group at a regional scale (Fig. 4). Weak foliation and minor shears in the uppermost Stuhini Group are truncated at the unconformity and greenschist-grade mineral assemblages in the Stuhini Group (chlorite-epidote-actinolite) are lacking in the Jack Formation. The unconformity is a smooth surface with minimal relief.

We recognize four facies in the Jack Formation at the Bruce Glacier section: basal conglomerate; lower mudstone ± sandstone and siltstone; volcaniclastic; and upper mudstone ± sandstone and siltstone.

5.1.1. Basal conglomerate facies

The base of the Jack Formation consists of an 0.8 metre-thick felsic clast-bearing granule conglomerate, which is overlain by 100 metres of polymictic conglomerate containing rounded cobbles and boulders of felsic intrusive and volcanic rocks and quartz in an arkosic matrix (Fig. 7a). The low percentage (< 2%) of clasts (Fig. 8) derived from subjacent Stuhini Group is remarkable. Clasts are well rounded, and moderately to highly spherical. Angular black mudstone intraclasts occur singly and as clusters throughout the facies (Fig. 7b). Several kilometres north of the section, between the Bruce and Jack glaciers (414251 E, 6271398 N), black carbonaceous mudstones occur at the base of the Jack Formation, below the lowest conglomerate.

The conglomerate thickens and coarsens south of the line of section: two kilometres to the south, the largest tonalite clast is 2 metres in diameter (Fig. 7c). At that locality, conglomerate matrix varies from black mudstone to arkose. To the south

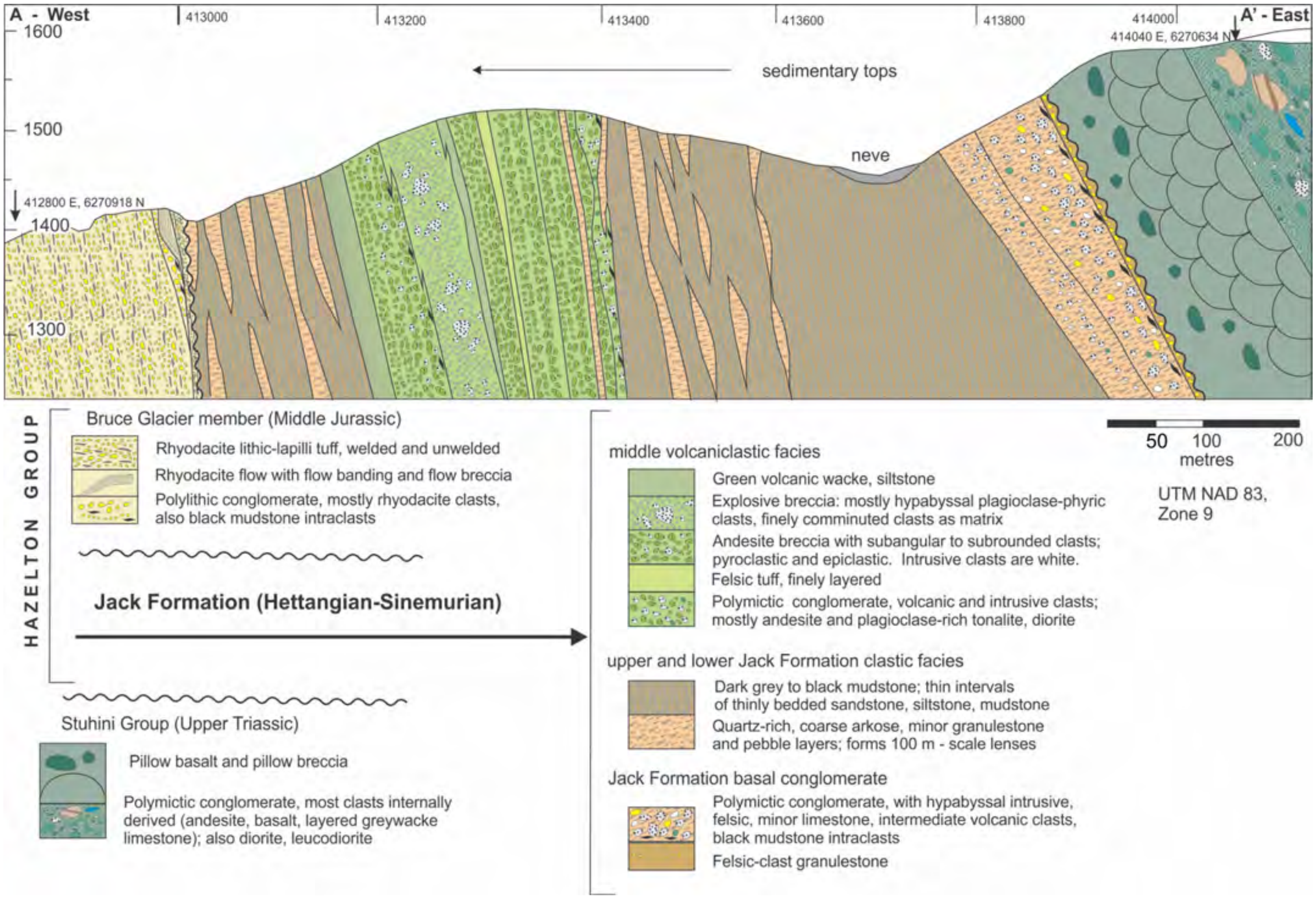

Fig. 6. Bruce Glacier section.

Fig. 7. Jack Formation siliciclastic units, Bruce Glacier section. **a)** Basal polymictic conglomerate, 413850 E, 6269040 N. **b)** Concentration of angular, tabular, black mudstone intraclasts at base of conglomerate bed, likely ripped up from underlying black mudstone layer; near base of Jack Formation, 414404 E 6271697 N. **c)** Large boulder of tonalite in basal conglomerate. Note other round intrusive cobbles (white outlines), 413875 E, 6268846 N. **d)** Thinly-bedded calcareous siltstone, fine-grained sandstone and carbonaceous mudstone, mudstone ± sandstone and siltstone facies. Cross-beds show paleocurrent to west (toward bottom of photo), 413557 E, 627708 N. **e)** Quartz-rich coarse sandstone, typical of sandstone lenses in mudstone facies, 413567 E, 6270704 N.

(413818 E, 6269809 N) beneath the lowest conglomerate, laminated to thinly bedded fine-grained volcanic sandstones rest unconformably on sheared Stuhini andesite conglomerate. These beds were probably locally derived from immediately underlying Stuhini Group.

Isolated exposures of fine-grained rocks beneath the basal conglomerate, and the ubiquitous presence of black mudstone intraclasts in coarse clastic units, suggest that basin initiation

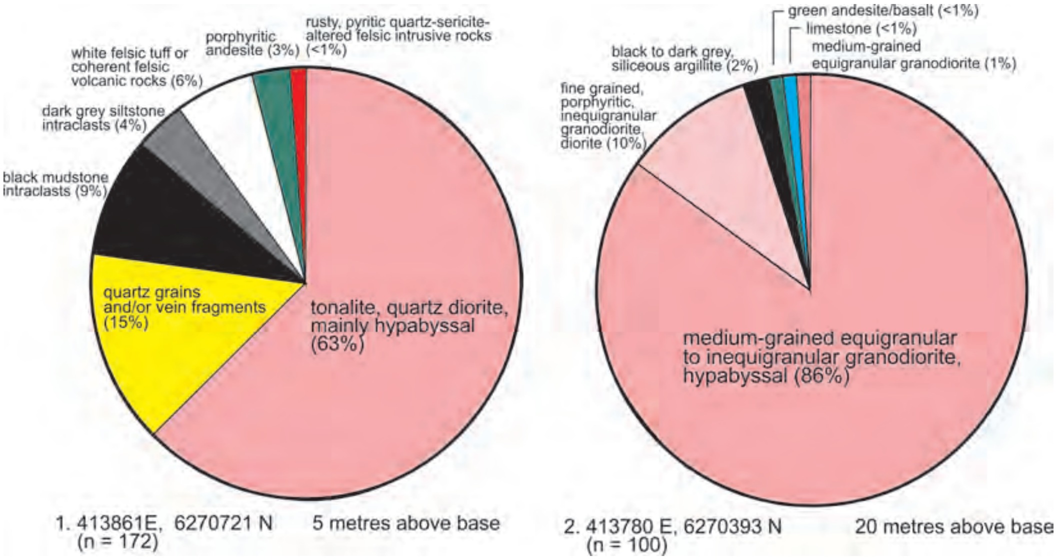

Fig. 8. Clast counts from basal Jack Formation conglomerates in the Bruce Glacier area.

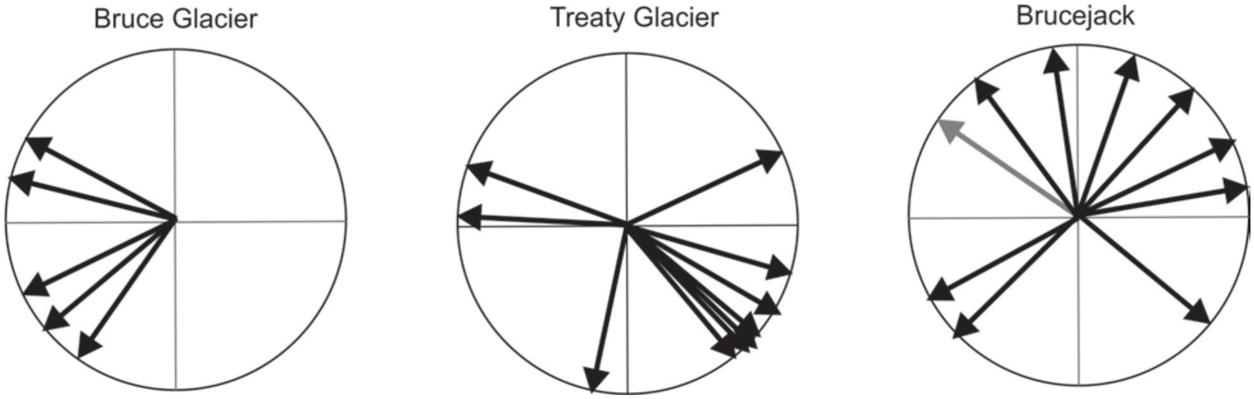

Fig. 9. Jack Formation paleocurrents; measurements corrected for tilted bedding. Grey arrow for Brucejack Lake section is from olistostromal block.

was marked not by an influx of coarse debris, but quiet water sedimentation in a standing body of water. Thick sections of cobble-boulder conglomerate imply later influx of debris from a relatively nearby area of high relief.

In its upper 40 metres, the basal conglomerate fines upwards to thick-bedded quartz-rich arkose with scattered pebbles and granules. Its top is abrupt, passing into mudstone over a few metres.

5.1.2. Lower mudstone ± sandstone and siltstone facies

Predominantly mudstone intervals are exposed both above the basal conglomerate facies and in the upper part of the Jack Formation (Fig. 6). The lower succession is about 400 m thick. The mudstones are carbonaceous, laminated to thinly bedded, and lack evidence of bioturbation. They are interrupted by cm- to dcm-scale layers of sandstone with rare cross stratification and siltstone (Fig. 7d). The sandstones are cemented by carbonate (calcite-ferrodolomite), which weathers bright orange. Lenticular beds of sharp-based, very coarse-grained quartz-rich arkose to arkosic granulestone (Fig. 7e) are scattered in the upper half of the interval. These beds are typically 10 to 20 metres thick and can be traced laterally for about 100 metres. They show sharp, erosive bases with scours, and graded tops. Other sedimentary structures are sparse, except subtle internal bedding. Black mudstone intraclasts and polymictic pebble layers are concentrated at the base of many beds, but can be scattered throughout.

The lower mudstone ± sandstone and siltstone facies grades to the volcaniclastic facies through a transition in which quartz-rich sandstone and pebbly beds interfinger with beds containing andesite and diorite clasts. Furthermore, local beds of arkose, siltstone, and mudstone, similar to those in the predominantly mudstone facies are found in the volcaniclastic facies, emphasizing a gradational boundary.

The carbonaceous mudstones likely represent quiet water sedimentation (below wave base) in an anoxic standing body of water. Coarse interbeds are likely subaqueous mass flow deposits that punctuated background fine-grained sedimentation. Five cross bedding measurements from fine-grained sandstones in the lower and upper mudstone units indicate southwesterly to west-northwesterly paleocurrents (Fig. 9), away from the area now occupied by the McTagg anticlinorium.

5.1.3. Volcaniclastic facies

Most of the volcaniclastic facies consists of matrix-supported andesitic-hypabyssal porphyry breccias (Fig. 10a). In contrast to conglomerates lower in the section, clasts are almost exclusively of andesite and porphyritic diorite. Black mudstone intraclasts occur in some beds (Fig. 10b). The breccias define thick (15-30 m) unstratified to poorly stratified depositional units; in most cases the distinction between a pyroclastic or epiclastic origin cannot be made. However, one breccia unit contains angular clasts (± jig-saw fit) of crowded plagioclase-porphyry in a fine-grained matrix that includes ~ 50% broken plagioclase crystals (Figs. 6, 10c), suggestive of an origin by phreatic explosion.

Although predominantly consisting of cobble and block breccias and conglomerates, the volcaniclastic facies contains local beds of coarse-grained quartz-rich arkose, siltstone, and mudstone, and one interval of laminated to thinly bedded felsic tuff (Figs. 6, 10d). Over an interval of 25 metres at the top of the unit, coarse andesitic breccia and conglomerate grade upward through green volcanic wacke to coarse-grained quartz-rich arkose and grey argillite. This interval is overlain by dark grey to black mudstone of the upper siliciclastic unit. Transitional upper and lower boundaries suggests that the volcaniclastic facies is an integral part of the Jack Formation (rather than Unuk River member, cf. Lewis, 2013).

The appearance of pyroclastic beds and coarse volcanic-derived detritus indicates that an episode of andesitic volcanism interrupted the background quiet-water sedimentation indicated by the underlying and overlying predominantly mudstone units.

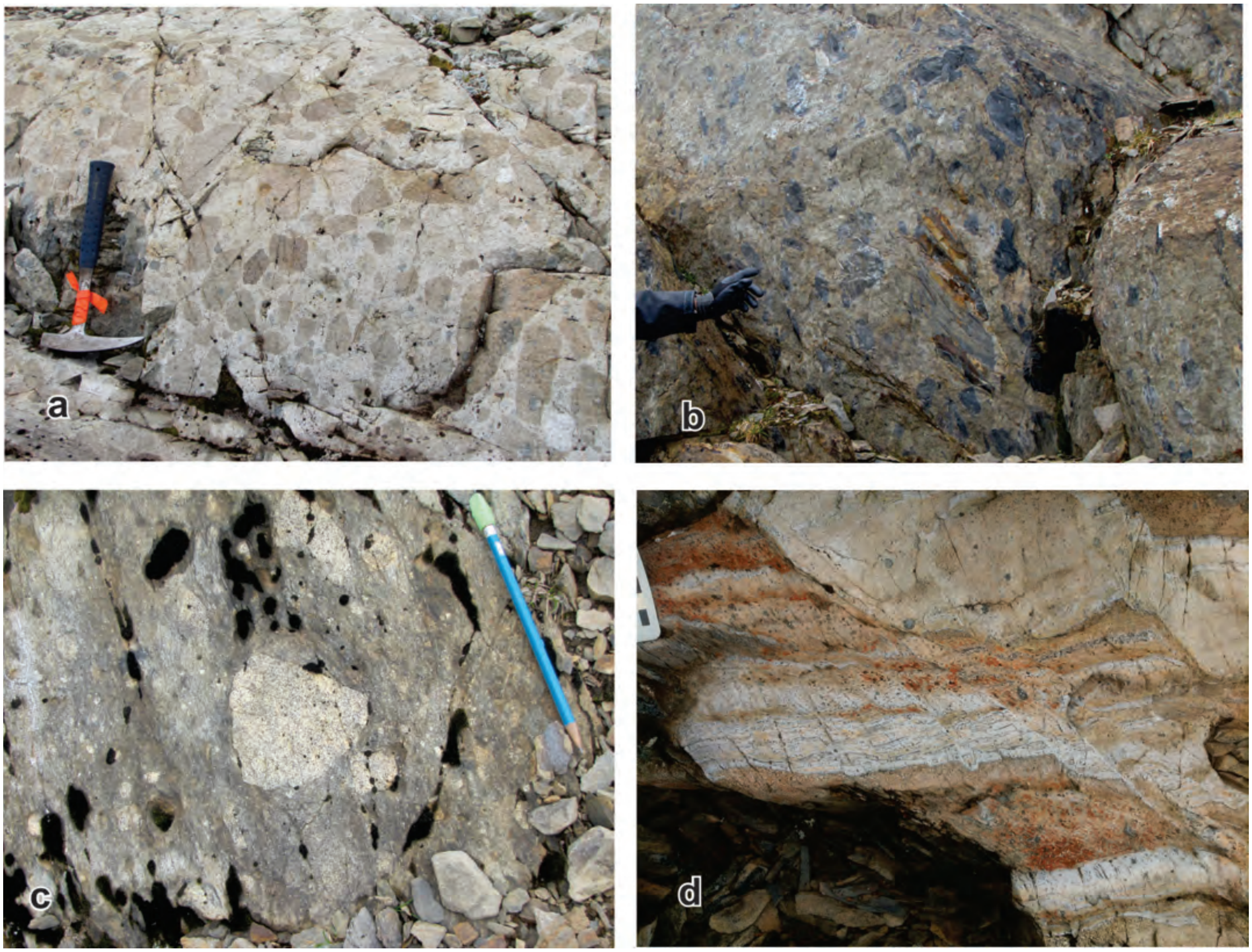

Fig. 10. Jack Formation volcaniclastic units, Bruce Glacier section. **a)** Andesite block breccia from volcaniclastic facies, 413278 E, 6270599 N. **b)** Concentration of black mudstone intraclasts near base of volcanic breccia bed. 413145 E, 6370655 N. **c)** Monolithologic crowded plagioclase porphyry-clast explosion breccia from volcaniclastic facies, 413200 E, 6270667 N. **d)** Small-scale penecontemporaneous normal faults (with overstepping relationships and sediment smeared along fault surfaces) in thinly bedded felsic tuff, 413929 E 6270547 N.

5.1.4. Upper mudstone ± sandstone and siltstone facies

This facies is identical in character and clast composition to the lower predominantly mudstone interval, except that lenticular coarse layers are scattered throughout, and conglomeratic beds in the coarse-grained lenses are sparser and finer grained. Although Lewis (2013) assigned this facies to the Betty Creek Formation, based on its stratigraphic position above the interpreted Unuk River member, we include it in the Jack Formation because of its close resemblance to the lower mudstone-sandstone-siltstone unit. It is abruptly overlain by felsic volcaniclastic rocks of the Bruce Glacier member (upper Hazelton Group, Middle Jurassic, ~ 173-176 Ma; Lewis, 2001b). Although paraconformable along the line of the section, the base of the upper Hazelton Group bevels downsection through the lower Hazelton sequence from south to north along the western side of the McTagg anticlinorium (Lewis, 2013). This upper mudstone unit represents a return to quiet water sedimentation following an episode of andesitic volcanism.

5.2. Treaty Glacier section

The Treaty Glacier section, on the northeastern nose of the McTagg anticlinorium, follows a northeast-trending ridge between the Treaty and Atkins glaciers (Fig. 4). The section extends from the Stuhini Group to the base of the paraconformably overlying Unuk River member of the lower Hazelton Group (Lewis, 2013). The base of the section is in the Stuhini Group at the "Mama Susu A" showing, where it consists of andesite block breccia, polymictic conglomerate, thinly to medium-bedded litharenite, and dark grey argillite (Fig. 11). Compared to the Jack Formation, the volcanic rocks are relatively primitive (andesites have augite rather than hornblende) and the sedimentary rocks are compositionally immature (sandstones are quartz deficient). Load casts and argillite intraclasts are present in the sandstones. As in the Stuhini Group at the Bruce Glacier section, but in contrast to mudstone rip-up clasts in the Jack Formation, sedimentary clasts in the polymictic conglomerates consist of multiple sandstone-siltstone-argillite beds, indicating reworking of a previously lithified section. The basal unconformity of the Jack

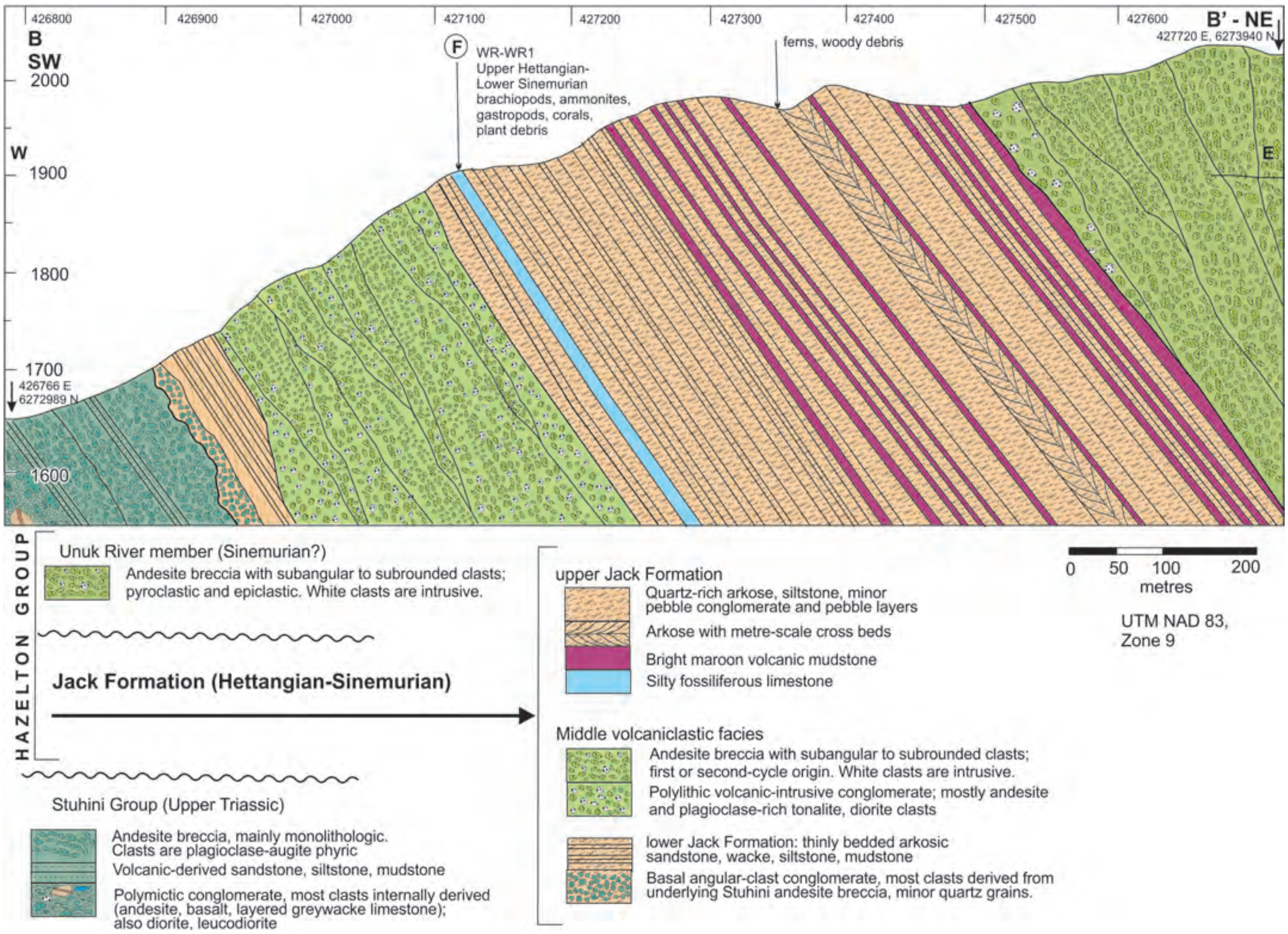

Fig. 11. Treaty Glacier section.

Formation cuts across underlying bedding at a high angle. The unconformity is a jagged, highly irregular surface at decimetre to metre scale (Fig. 12a). Four Jack Formation facies are developed at the Treaty Glacier section: basal conglomerate; arkose, siltstone, and mudstone; volcaniclastic; and arkose, tuffaceous mudstone ± limestone.

5.2.1. Basal conglomerate facies

Above the unconformity is a 20-m section of locally-derived, clast-supported (siltstone matrix) sharpstone conglomerate. Clasts are from the underlying Stuhini Group and include dark grey argillite and siltstone, dark green and maroon andesite, and crowded porphyry. The conglomerate contains a carbonate-Fe-oxide cement.

5.2.2. Arkose, siltstone, and mudstone facies

Above the basal conglomerate is a drab, olive-green unit of arkose, siltstone, and thinly bedded mudstone. Thickness of this unit varies locally from 80 metres to only a few metres, due to downcutting beneath the overlying volcaniclastic facies. The absence of black, carbonaceous mudstone in this facies is notable, compared with the Bruce Glacier section.

5.2.3. Volcaniclastic facies

The volcaniclastic unit is about 250 metres thick and, similar to rocks at the Bruce Glacier section, consists mainly of thickly bedded conglomerates and breccias that contain volcanic and intrusive clasts. Some beds contain matrix-supported angular to subangular andesite clasts with subordinate intrusive clasts. Others, particularly near the top of the unit, are polymictic clast-supported conglomerates in which intrusive clasts (plagioclase-hornblende porphyry, hornblende diorite and monzodiorite, quartz monzonite, and crowded plagioclase porphyry) are more abundant than volcanic clasts. The polymictic conglomerates also contain clasts of andesite, dark grey mudrock, and pale green tuff. As at the Bruce Glacier section, it fines upward and passes transitionally into the overlying succession, in this case a unit of arkose and volcanic mudstone with one bed of limestone.

5.2.4. Arkose, tuffaceous mudstone ± limestone facies

The upper 500 metres of the Treaty glacier section consist predominantly of interbedded arkose and maroon tuffaceous mudstone (Fig. 13). Sedimentary structures include interference ripples (~ 100 m upsection from the base of the unit, Fig. 12b;), impressions of delicate fern fronds and woody debris (~ 325 metres above the base of the unit Fig. 12c), and m-scale trough cross stratification (Fig. 12d). Bedding in some of the cross-stratified beds is highlighted by single pebble layers. Paleocurrents, mainly derived from cross-bed measurements in the upper part of the facies, are polymodal, with southeasterly directions predominant (Fig. 9). Within a few metres of the base of the facies, argillaceous limestone and silty calcareous sandstone contain a rich shelly fauna of brachiopods, gastropods and ammonites (Fig. 12e). A macrofossil collection from this locality (WR-WR1; Lewis et al. 2001) is of Upper Hettangian to Lower Sinemurian age.

Maroon and green tuffaceous mudstones appear ~ 200 metres above the base of the section, along with a 60 centimetre-thick layer of green vitric lapilli tuff. The mudstones are interbedded on decimetre to metre scale with quartz-rich arkoses that have a maroon tuffaceous matrix (Fig. 13). The arkoses contain maroon and green fine-grained volcanic pebble layers; some are cross-stratified. The absence of black carbonaceous mudstone beds and intraclasts in this mudstone-rich section is noteworthy, considering their abundance in siliciclastic facies at the Bruce Glacier section. Toward the top of the section, the number and thickness of mudstone intervals increases (Fig. 11), indicating a progressive increase in nearby volcanic activity.

A succession of bright maroon tuffaceous mudstones with thin, sparse arkose interbeds forms the uppermost 50 metres of the facies. It is overlain by the basal Unuk River member, a 10-20 metre-thick unit of matrix-supported polymictic conglomerate containing subrounded to subangular clasts of monzonite, pink syenite, maroon crystal tuff, and pink rhyodacite (Fig. 12f). The conglomerate is overlain by a thick section of andesite block breccias, bomb breccias, and heterolithic andesite-hypabyssal clast breccias. Shown as over 2 kilometres in mapped width (Lewis, 2013), and given local dips, this andesitic section is probably 1.25 to 1.5 kilometres thick.

The transition from the volcaniclastic facies to rocks of the arkose, tuffaceous mudstone ± limestone facies represents the cessation of relatively proximal andesitic volcanism and the establishment of a shallow-marine depositional environment. Initial carbonate sedimentation (with shallow-water fauna) was overwhelmed by siliciclastic input. Interference ripples, polymodal paleocurrents, and fern imprints suggest a shoreface environment.

5.3. Brucejack section

The Brucejack section is about 1.5 kilometres northwest of Brucejack Lake, east of the McTagg anticlinorium (Fig. 4). It extends northeasterly from near the top of the Stuhini Group, through a comparatively thin section of Jack Formation and into an overlying andesitic pyroclastic sequence assigned to the Unuk River member by Lewis (2013). The section forms a northeast-younging panel that is truncated by the Brucejack fault (Fig. 14). We recognize three facies: basal conglomerate; sandstone megaclast-bearing mudstone; and volcaniclastic.

The Stuhini Group in this section is similar to that at Treaty and Bruce Glaciers, in that it generally comprises interbedded, compositionally monolithologic but texturally polylithic, mainly andesite breccias, and polymictic conglomerates, arkosic sandstones and siltstones. A unique feature at this locality, however, is the presence of a thick polylithic breccia at the top of the Stuhini Group, in which fine-grained grey felsic clasts are more abundant than andesites. Such rocks in the Stuhini Group are a possible source for the grey to white felsic clasts in the Jack Formation.

Fig. 12. Treaty Glacier section photos. **a)** Stuhini Group-Jack Formation unconformity, showing small-scale rugged topography, in part controlled by fractures in underlying Stuhini Group. Jack Formation fills paleodepression; clasts mainly derived from immediately subjacent Stuhini breccia, 426997 E, 627040 N. **b)** Interference ripples marks on bedding surface, arkose, tuffaceous mudstone ± limestone facies, 427184 E, 6273417 N. **c)** Fern fronds in arkose, tuffaceous mudstone ± limestone facies. 427346 E, 6273592 N. **d)** Large-scale trough cross-beds in arkose, tuffaceous mudstone ± limestone facies, 427429 E, 6272976 N. **e)** Brachiopod from near base of arkose, tuffaceous mudstone ± limestone facies, 427114 E, 6273364 N. **f)** Basal conglomerate, Unuk River member, 427490 E, 6272920 N.

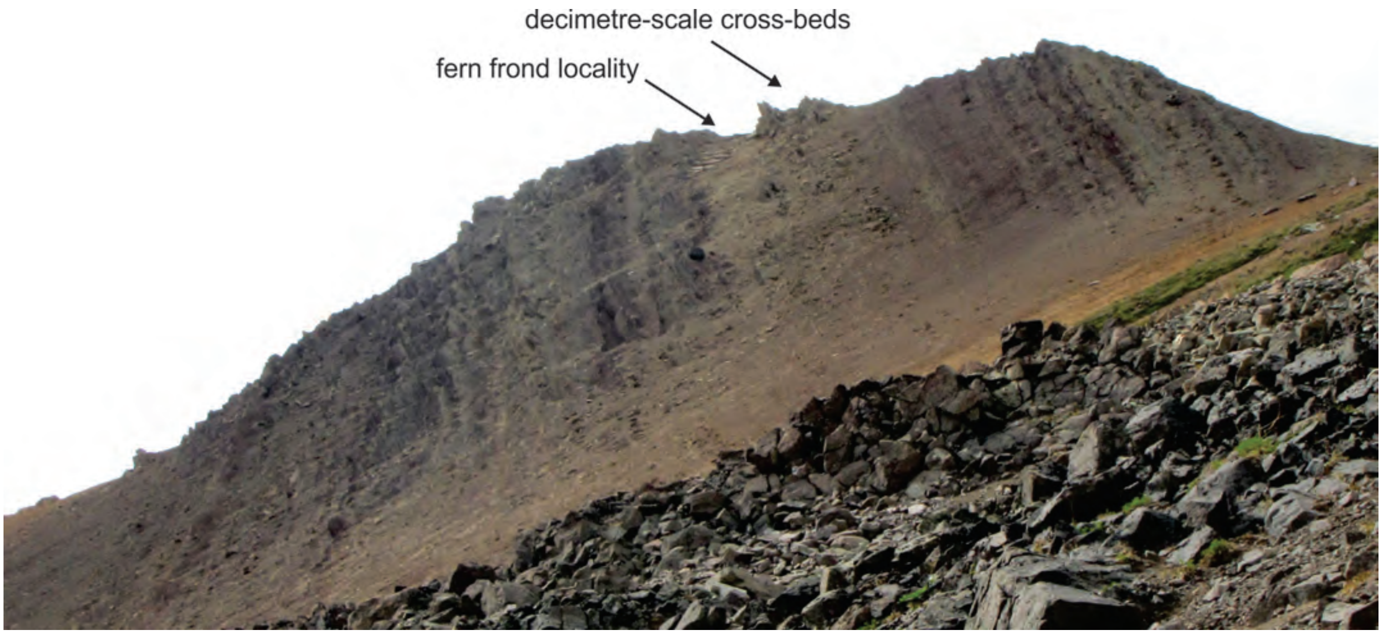

Fig. 13. View to the northwest of interbedded arkose and maroon tuffaceous mudstone in the upper part of Treaty Glacier section.

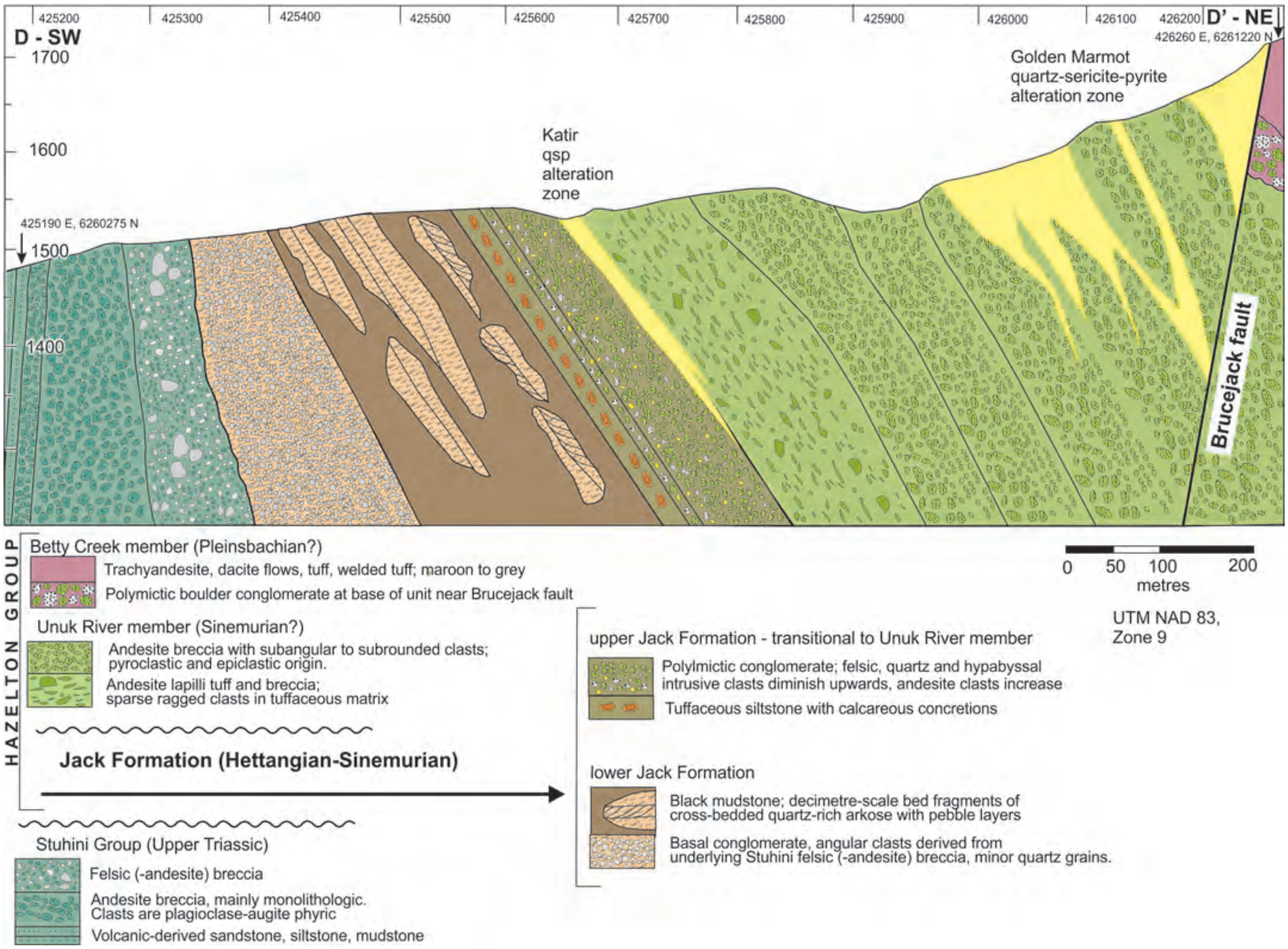

Fig. 14. Brucejack section.

5.3.1. Basal conglomerate facies

As at Treaty Glacier, the basal Jack Formation is a massive sharpstone conglomerate 80 metres thick containing mostly clasts derived from felsic and andesitic rocks in the immediately subjacent Stuhini Group. Unlike Stuhini Group conglomerates, those in the Jack Formation contain matrix quartz grains. The conglomerate is overlain abruptly by black carbonaceous mudstone.

5.3.2. Sandstone megaclast-bearing mudstone facies

Above the basal conglomerate facies is a 200 metre-thick section of carbonaceous mudstone that surrounds densely-packed, large (5-20 m scale) fragments of stratified and cross-stratified, coarse-grained (± pebbles), quartz-rich arkose and tuffaceous siltstone (Fig. 15a). Bedding attitudes in the blocks are concordant with the overall layering in the section. Mudstone penetrates block boundaries, creating marginal zones of in situ breccia (Fig. 15b), and stratification in the blocks is truncated at clast boundaries, indicating that the blocks are allochthonous and the unit an olistostrome. As elsewhere in the Jack Formation, pebbles in the blocks are of felsic high-level intrusions, fine-grained felsic volcanic rocks, and mudstone intraclasts. The nearest possible source for the blocks is an intact section of thickly-bedded and cross-bedded arkoses 500 metres to the southeast (Fig. 15c). Paleocurrents at this intact section are polymodal, with a slight tendency to northeasterly flow (Fig. 9). Along strike northwest of the section, the megaclast-bearing unit is replaced by bedded arkosic sandstone, siltstone, and mudstone. Above the megaclast-bearing unit is a transition from siliciclastic to volcaniclastic deposits. At the transition, a distinctive light green tuffaceous siltstone unit containing large (5-10 cm) concentrically coated calcareous concretions directly overlies the highest olistostrome (Fig. 15d).

The megaclast-bearing facies is significant to structural interpretations for this area. Because sands lack cohesion, preservation of large sandstone blocks indicate that previously deposited sands were deposited, buried, lithified, uplifted, and reworked as gravity slides into an environment accumulating muds, which is consistent with penecontemporaneous faulting.

5.3.3. Volcaniclastic facies

The concretionary layer is overlain by a 5-metre thick clast-supported polymictic conglomerate that contains clasts of hypabyssal crowded plagioclase-phyric intrusive rocks, and fine-grained felsic volcanic rocks in a quartz sand-rich matrix. This conglomerate also contains concretions reworked from the underlying siltstones (Fig. 15e). The conglomerate passes upward into quartz-rich coarse-grained sandstones and granulestones, and then to tuffaceous wacke with scattered concretions. Upward, juvenile andesite clasts increase in abundance over 50 metres, across the layer-parallel Katir quartz-sericite-pyrite alteration zone, which occupies a deep gully. From the northeastern side of the gully to the Brucejack fault, monolithologic andesite breccias form all of the section. Some of these contain ragged clasts with chilled margins (Fig. 15f), and are of pyroclastic origin. Other block and cobble breccias may be either pyroclastic or epiclastic deposits. The base of the Unuk River member is placed at the bottom of the andesitic breccias (Fig. 14).

5.4. Iron Cap section

The Iron Cap section is in the immediate footwall of the Sulphurets fault. It extends eastward from the centre of the Iron Cap intrusion, north of the Mitchell Glacier, to near the Brucejack fault (Figs. 4, 5). The base of the Jack Formation is not exposed; at the top of the section, a thin sequence of unaltered andesite breccia and arkosic granule-pebble conglomerate is unconformably overlain by the Treaty Ridge member (Middle Jurassic; Lewis, 2013).

The Iron Cap intrusion, part of the ~ 195 Ma Mitchell suite (Kirkham and Margolis, 1995) is the hornblende-plagioclase porphyry that hosts the Iron Cap porphyry Cu-Au deposit. Most of the section is in highly altered rocks of the intrusion (Figs. 16, 17). Our primary goal at this section was to document the relationship between the intrusion and the Jack Formation. Near the centre of the transect (west of C', Figs. 16, 17), the intrusion contains septa of quartz-bearing granule and pebble conglomerate (Fig. 18a). These septa, along with the porphyry, display silica-sericite-pyrite-alteration, demonstrating that the Iron Cap intrusion and porphyry deposit developed, at least in part, after Jack Formation deposition.

Near the eastern end of the transect, the intrusion passes into a thin, variable carapace of explosion breccia, andesite flows, pillowed flows and breccias, and very small felsic volcanic units (Figs. 5, 16, 17). The explosion breccia consists of crowded porphyritic hypabyssal monzodiorite clasts, derived from phases of the Iron Cap intrusion, along with irregularly-shaped, juvenile andesite clasts, in a finely comminuted rock matrix. Contact relationships show that the explosion breccia cuts the upper part of the intrusion, but also interfingers with extrusive andesite breccias (Figs. 16, 17). The limit of intense phyllic, texturally-destructive alteration corresponds approximately with the edge of the pluton, but extends into the explosion breccia, and to a lesser extent, into the overlying andesite unit. The andesite breccia, highly variable in thickness (from over a hundred metres south of the zone to less than ten metres along the section), passes upward into lapilli tuff and green, tuffaceous siltstone. Over less than ten metres these volcaniclastic units pass upward into dark grey mudstone and black mudstone intraclast-bearing, quartz-rich arkosic conglomerate and granulestone that are similar to siliciclastic units of the Jack Formation elsewhere (Fig. 18b). Lying above the andesitic extrusive carapace, these arkosic beds are unaltered, suggesting that they post-date development of the mineralized system.

Similar intimate relationships between Jack Formation deposition, intrusion, alteration and phreatic explosion breccias are exposed near the Snowfield zone, south of Mitchell Creek. There, a band of highly altered Jack Formation quartz-rich arkose lies in the main alteration zone (Fig. 19a), but in its

Fig. 15. Brucejack section. **a)** Arkose megaclast surrounded by black carbonaceous mudstone matrix; edge of decimetre-scale broken bed behind, sandstone megaclast-bearing mudstone facies, 425511 E, 6260571 N. **b)** Brecciated margin of arkose bed in sandstone megaclast-bearing mudstone facies, 425511 E, 6260571 N. **c)** Parallel-stratified and cross-stratified coarse-grained sandstone, on strike with sandstone megaclast-bearing mudstone facies. **d)** Tuffaceous siltstone with carbonate concretions, volcaniclastic facies, 425559 E, 6260553 N. **e)** Pebble conglomerate with well-rounded clasts of crowded plagioclase porphyry and felsic tuffs and reworked concentrically-zoned concretions, volcaniclastic facies, 425579 E, 6260573 N. **f)** Ragged-clast andesite lapilli tuff, base of Unuk River member; clasts have chilled rims, 422237 E, 6260255 N.

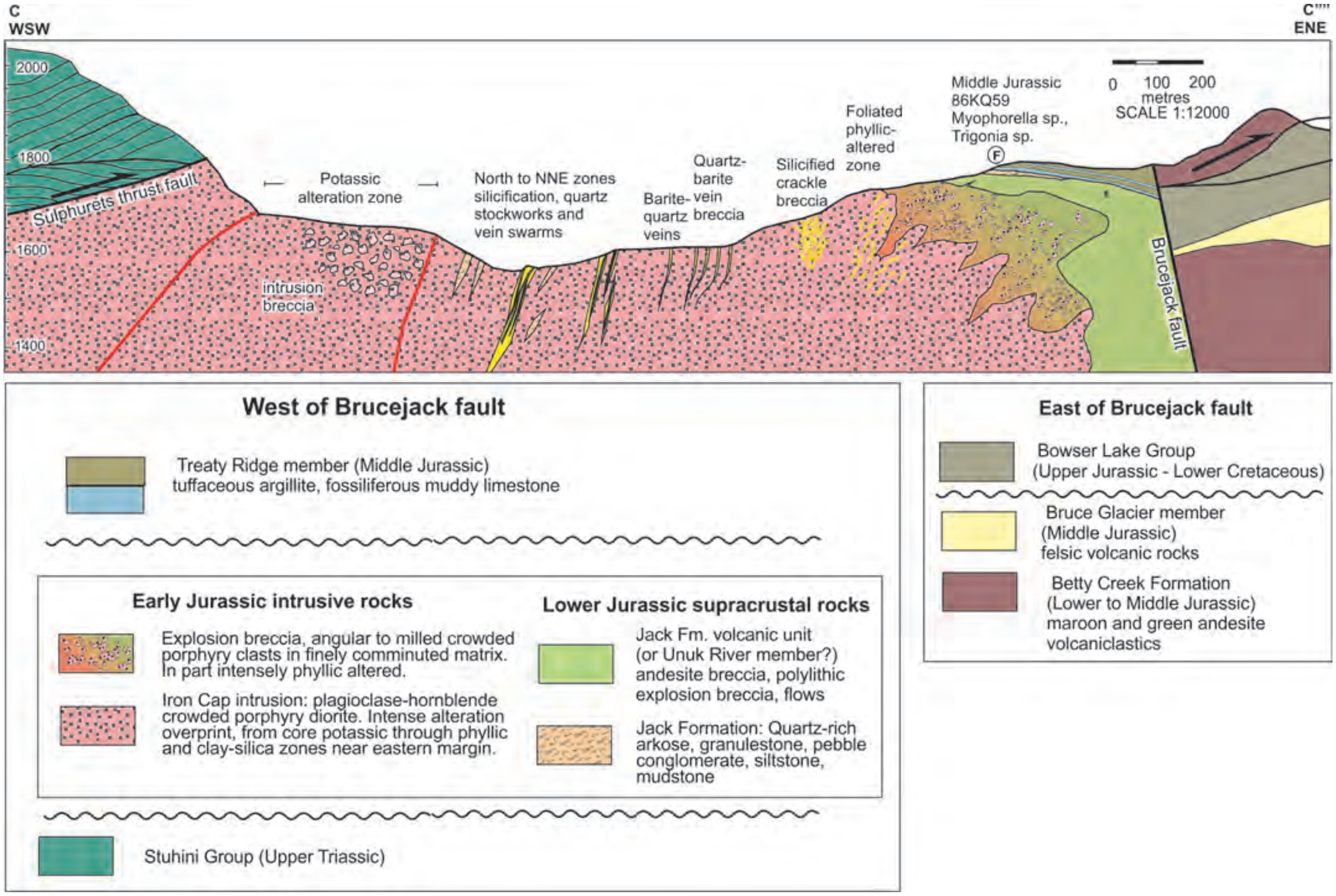

Fig. 16. Iron Cap section from Sulphurets fault to Brucejack fault; compare with panoramic photo in Figure 5.

western continuation outside the zone, unaltered Jack Formation conglomerates interfinger with plutonic-clast explosive breccias (Figs. 19b, c). Breccia dikes crowded with angular quartz clasts cut the Mitchell intrusion in the eastern part of the Mitchell zone (Fig. 20a, b). Surface eruption of breccias like these could have provided locally abundant polycrystalline quartz to the Jack Formation.

An isolated outcrop of tightly folded and strongly sheared black carbonaceous argillite and dark grey limestone is exposed 100 metres west of the section, approximately on strike with the andesite volcaniclastic to siliciclastic transition. Its relationship to the layered rocks of the section is unclear, but on the basis of rock type and deformation, it could be Stuhini Group. If so, the exposure might be the remains of a sub-Jack Formation paleohigh.

The highest Jack Formation clastic beds are overlain paraconformably by silty, fossiliferous limestone at the base of a sequence of interbedded tuffaceous siltstone and silty limestone (Figs. 5, 16, 17). A macrofossil collection from near this location (86KQ59, Lewis et al., 2001) yielded a Middle Jurassic age, which places it within the upper Hazelton Group (Table 1). The unit was assigned to the Treaty Ridge member of the Betty Creek Formation by Lewis (2013). However, it is similar in age and character to the Smithers Formation, part of the upper Hazelton Group in the Terrace-Smithers area (Gagnon et al., 2012). At this locality, either the higher pyroclastic and epiclastic units of the lower Hazelton Group were never deposited, or they were removed by erosion prior to the Middle Jurassic, and a prolonged hiatus (20 million years) separates the upper from the lowermost Hazelton Group. This unconformable relationship between the upper and lower Hazelton Group is equivalent to that seen on the west side of the McTagg anticlinorium.

5.5. Tennyson section south of Frank Mackie Glacier

Near the Tide-Tennyson prospect south of the McTagg anticlinorium (Figs. 3, 4), is a thick (> 500 m), coarse conglomerate with two 10 m interbeds of maroon pebbly mudstone (Fig. 21). The conglomerate contains clasts of andesite, basalt, black siliceous argillite, diorite, chert, quartz, limestone and silicified, cherty limestone. The clasts were derived from the Hazelton and Stuhini groups and, in the case of the limestone (Fig. 21a), possibly the Stikine assemblage (Permian Ambition Formation, Gunning et al., 2006). The clasts are angular to subrounded, have maximum diameters ranging from a few centimetres to several metres (average 20-50 cm), and are generally supported in a fine-grained matrix.

The maroon pebbly maroon mudstones have different

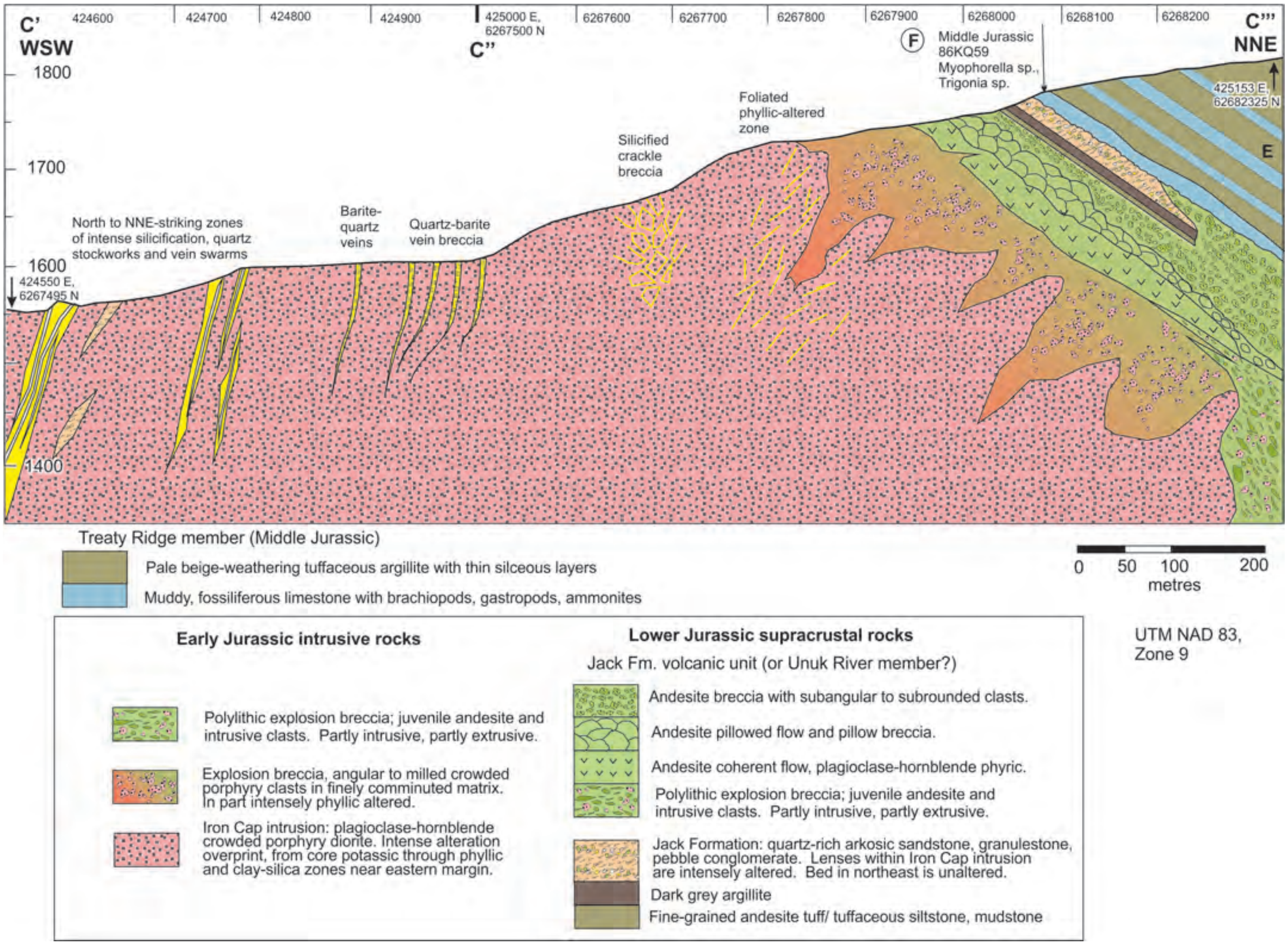

Fig. 17. Detailed eastern part of Iron Cap section.

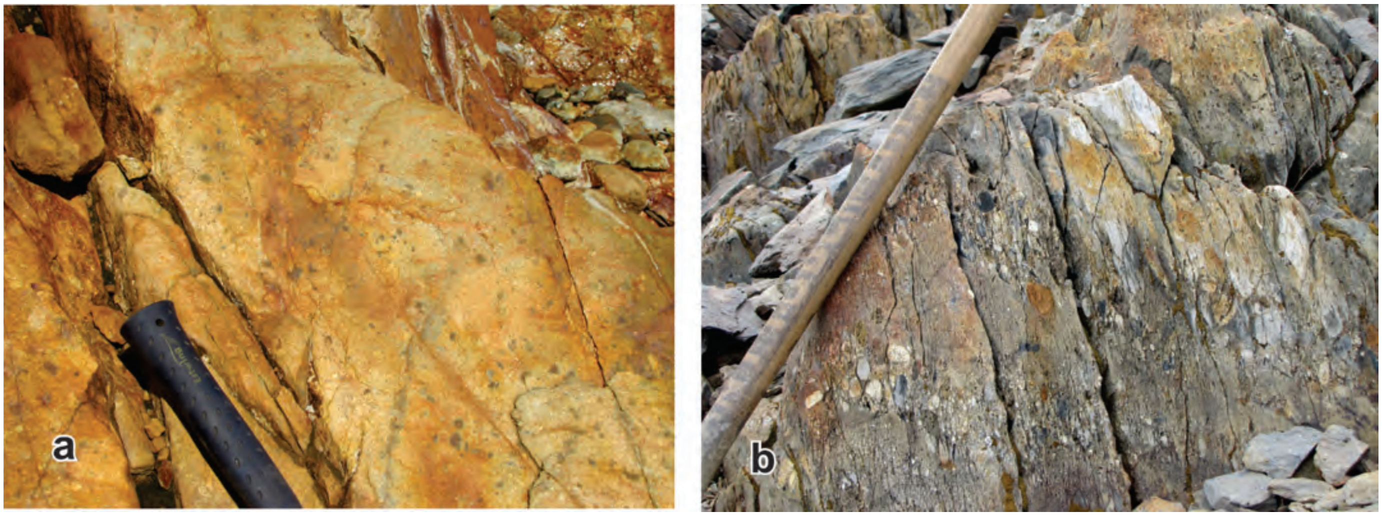

Fig. 18. Iron Cap photos. **a)** Jack Formation septa in the Iron Cap intrusion: highly altered polymictic pebble conglomerate with volcanic and quartz clasts, 424637 E, 6267358 N. **b)** Unaltered Jack Formation bed above the Iron Cap system: interbedded polymictic pebble conglomerate and pebbly sandstone with carbonaceous mudstone intraclasts, 425139 E, 6268056 N.

Fig. 19. Relationships between Jack Formation, porphyry intrusion, and phreatic explosion breccias in the Snowfield zone. **a)** Quartz-rich granulestone from inclusion within Snowfield zone intrusion (424699 E, 6264448 N; photo credit Gayle Febbo). **b)** Polymictic Jack Formation conglomerate from above western edge of Snowfield alteration zone (423837 E, 6263678 N). **c)** Unaltered explosive breccia with pink hypabyssal syenite clasts from west of the Snowfield zone. This breccia interfingers with and locally overlies Jack conglomerate of b); 423751 E, 6264170 N.

clast populations than the coarse conglomerates. In them, plagioclase porphyry, hypabyssal diorite and quartz stockwork clasts (Fig. 21b) probably reflect coeval sources related to the nearby Tennyson porphyry intrusion (~ 200 Ma, U-Pb, van Straaten, 2013) and its associated alteration zone. The quartz stockwork clasts are similar to those in breccia dikes in the Mitchell zone (see above). In the lower part of the section is a disaggregated hornblende-plagioclase phyric andesite flow with local peperitic textures, which is cut by clastic dikes. It probably was emplaced during conglomerate deposition.

The main exposure of conglomerate is separated by an east-vergent thrust fault from the Tennyson intrusion, which in turn is thrust eastward onto a sequence of monolithologic andesite conglomerates, breccias and volcaniclastic sedimentary beds (van Straaten, 2013) that probably belongs to the Unuk River member. The porphyry intrusion is affected by zones of potassic, phyllic and propylitic alteration; at one locale northerly quartz vein swarms were observed (428000 E, 6236450 N).

The thick, very coarse, poorly bedded and sorted, lithic-matrix conglomerate unit at Tennyson does not resemble the Jack Formation on the flanks of the McTagg anticlinorium. However, it is very similar to basal conglomerates of the Hazelton Group regionally, such as near the town of Iskut (Ash et al., 1997a) and in the Terrace area (Nelson et al., 2008).

6. Discussion

Because all Hazelton Group units thin markedly across the axis of the McTagg anticlinorium (Figs. 3, 4; see also Lewis, 2013) it probably was a paleohigh during the Early Jurassic. Stratigraphic and sedimentologic data presented above from the Jack Formation on the periphery of the McTagg anticlinorium are consistent with this interpretation and with syndepositional faulting during initial Hazelton Group sedimentation. Below we: 1) discuss lateral and vertical relationships of Jack Formation facies (Fig. 22) and present a first-order paleogeographic analysis; 2) evaluate the significance of detritus in the Jack Formation that is compositionally mature relative to subjacent source rocks and regional basal Hazelton Group units; 3) consider how structural and aeromagnetic data in the area contribute to the concept of syndepositional fault-controlled sedimentation, magmatism, and mineralization, and 4) present a regional model for Early and Middle Jurassic tectonism.

6.1. Variation of the Jack Formation near the McTagg anticlinorium

Although a paleosol is lacking at the Stuhini Group-Jack Formation unconformity, sharpstone conglomerates containing clasts derived from immediately subjacent Stuhini basement at the Treaty Glacier and Brucejack sections may represent mechanical weathering fronts developed on a gently sloping upland on the eastern flank of the McTagg anticlinorium. Similar basal sharpstone conglomerates are lacking west of the anticlinorium. Instead isolated remnants of carbonaceous mudstone (± fine-grained sandstone) are the lowest preserved rocks, and at the Bruce Glacier section, the basal Jack

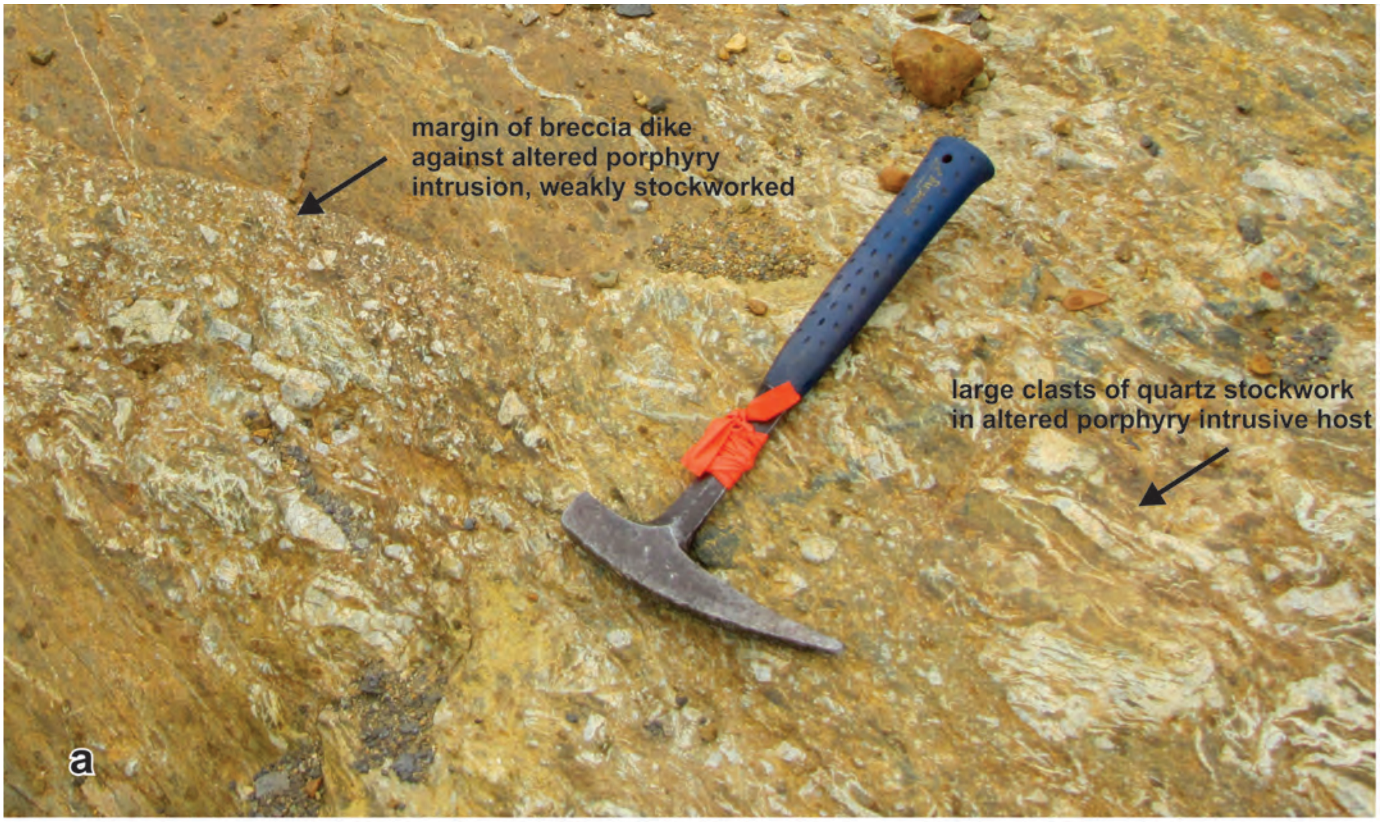

Fig. 20. Breccia dikes, Mitchell intrusion. **a)** Breccia dike of quartz stockwork clasts ("bone breccia") in the Mitchell intrusion (423467 E, 6265668 N). Stockworks cut relatively older phase of intrusion; dike emplaces fragmented stockwork into relatively younger phase. **b)** Detail of quartz stockwork clast in breccia. Note that veins lack a preferred orientation.

Formation consists of ~ 100 metres of polymictic cobble-boulder conglomerate with felsic extrusive and intrusive clasts. The mudstones at the base of the section imply abrupt basin deepening and underfilled conditions during initial

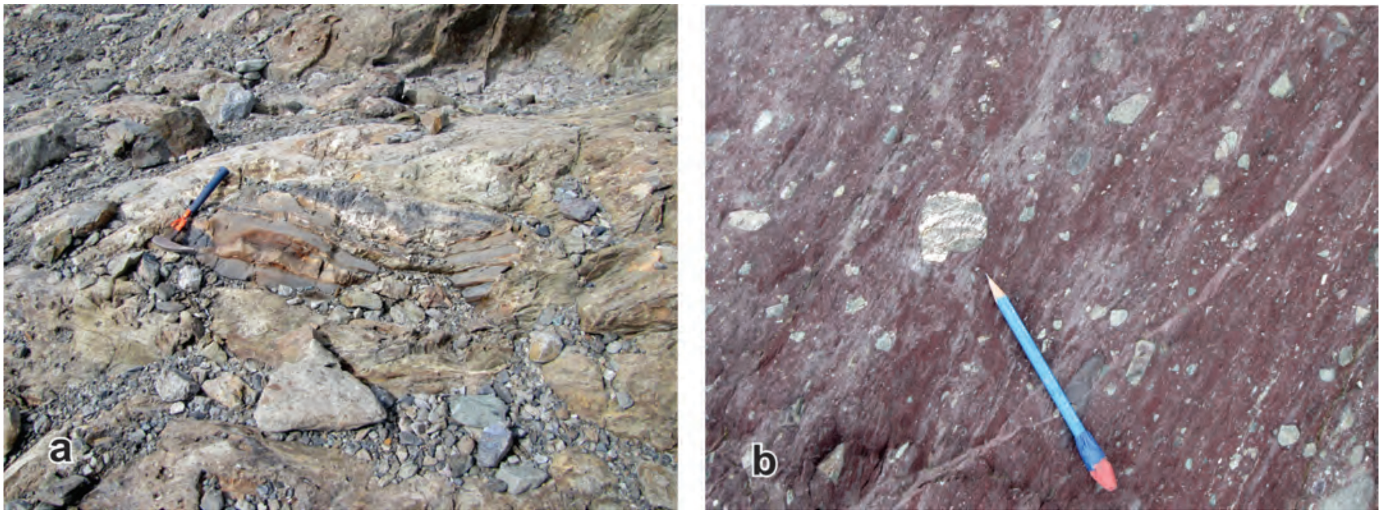

Fig. 21. Conglomerates at Tide-Tennyson. **a)** Coarse, poorly sorted conglomerate with mainly volcanic clasts. Large clast in centre of photo is limestone with bedding-parallel chert, probably derived from Permian limestone, 427213 E, 6236386 N; **b)** Pebbly mudstone with angular to subrounded hypabyssal porphyry and quartz clasts. Pencil points to quartz stockwork clast, 427193 E, 6236240 N.

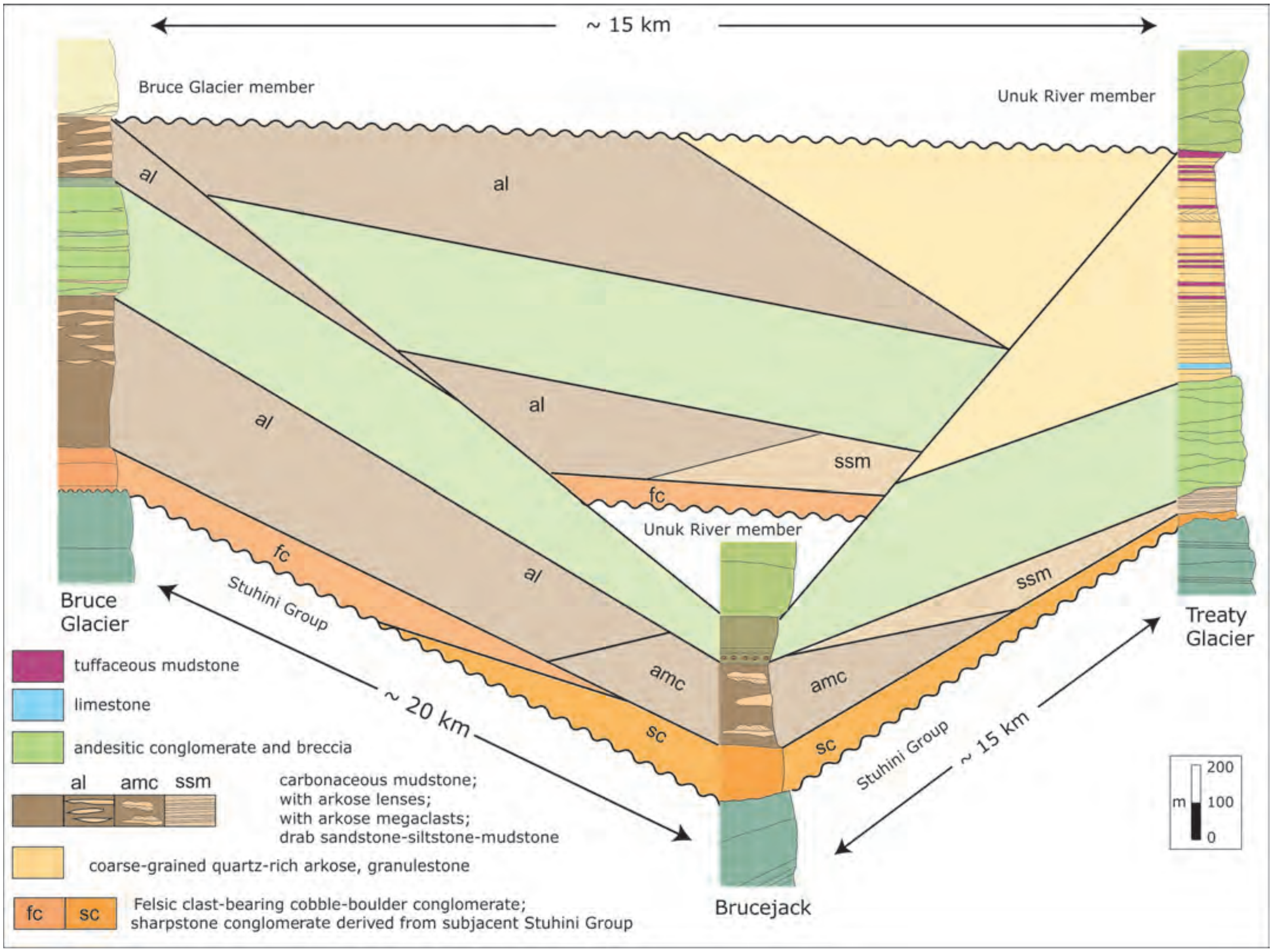

Fig. 22. Fence diagram illustrating facies relationships in the Jack Formation, McTagg anticlinorium.

sedimentation. The influx of polymictic conglomerates, which thicken and coarsen south of the Bruce Glacier section, implies uplifting, significant relief, and an integrated drainage system drawing from diverse, but proximal, sources.

At the Bruce Glacier section, the 400-m thick section of carbonaceous mudstone above the basal conglomerate represents a return to underfilled conditions and signifies abrupt, likely fault-induced, basin deepening. Sparse cross stratification in mass flow sandstone lenses indicate sediment sources to the east, from the region of now occupied by the McTagg anticlinorium. This facies thins east across the McTagg anticlinorium to 80 metres or less at the Treaty Glacier section and 200 metres at the Brucejack section (Fig. 22). Arkose megaclast-bearing olistostromes in carbonaceous mudstones at the Brucejack section attest to burial, lithification, uplift, and cannibalization of previously deposited Jack Formation, indicative of coeval faulting and fault-induced changes in basin morphology.

In the Bruce Glacier and Treaty Glacier sections, andesitic pyroclastic and epiclastic volcaniclastic rocks in the middle of the Jack Formation (Fig. 22) represent an episode of intense volcanism. Black mudstone intraclasts in the volcaniclastic units indicate that background deep-water sedimentation resumed during intervals of volcanic quiescence. The thick coarse volcaniclastic sections at the Bruce Glacier and Treaty Glacier sections suggest proximity to discrete coeval volcanic centres. The Iron Cap section and relationships at the Snowfield and Mitchell zones also record the development of Early Jurassic volcanic centres during deposition of the Jack Formation. Jack Formation siliciclastic units were host to the intrusions, as indicated by septa of likely basal Jack Formation in the intrusion, but were also deposited on their extrusive carapaces, where unaltered Jack conglomerates interfinger with plutonic clast-bearing explosive breccias (Figs. 16, 17). Surface eruption of phreatic explosive breccias composed of milled, high-level intrusive and quartz stockwork clasts could have provided hypabyssal and polycrystalline quartz detritus to the Jack Formation (see below).

At the Bruce Glacier section, the volcaniclastic facies grades back into a mudstone-rich siliciclastic section and a return to deep-water sedimentation interrupted by coarse-grained mass flow pulses. In marked contrast, at the Treaty Glacier section, rocks above the volcaniclastic facies indicate shallow-marine sedimentation (basal limestone beds with shelly fauna, sandstones with interference ripples and plant debris, polymodal paleocurrents). Apparently, as with the onset of Jack Formation sedimentation, the region on the northeastern side of the McTagg anticlinorium was high standing relative to the western side.

In summary, the Jack Formation provides important insights into events during earliest Hazelton deposition and emplacement of the Mitchell porphyries and their accompanying mineralization, including older episodes in the Brucejack system. Depositional patterns and overall thickness variations display evidence of syndepositional faulting and that the McTagg anticlinorium was probably a regional topographic high during sedimentation.

6.2. Compositional maturity of Jack Formation arenites and conglomerates

The Jack Formation is distinguished as a unit by polymictic conglomerates with felsic intrusive and extrusive clasts, and quartz-rich arkoses. Elsewhere throughout Stikinia, basal Hazelton Group units consist of mantle-derived volcanic rocks and compositionally immature sedimentary rocks, including thick, coarse basal conglomerates that in some cases contain olistostromal blocks (Greig, 1992, Ash et al., 1997a, Nelson et al., 2008). A local example is near the Tennyson prospect, where a 500 metre-thick very coarse basal conglomerate was derived from local fault block uplift of Stuhini Group and Stikine assemblage basement, as well as internally derived volcanic and explosive sources. Compared to these, and to underlying basement rocks, quartz grains and felsic volcanic and intermediate plutonic detritus are significantly over-represented in the Jack Formation. A similar mismatch between quartz-rich sedimentary rocks and subjacent greenstone belt sources has been noted in the Archean (Donaldson and Jackson, 1965; Condie, 1981). They argued that concentration of quartz from minor sources such as felsic volcanic and plutonic rocks and quartz veins requires extreme tropical weathering and/or multiple cycles of erosion and deposition. However, the paleolatitude of Early Jurassic Stikinia was ~ 32^{o} North (Kent and Irving, 2010), north of tropical latitudes, and Pleinsbachian ammonite faunas are a mixture of warm-water and cold-water species (Smith et al., 2001). Nonetheless, ferns and woody debris in the Jack Formation suggest moist, temperate conditions. Hence we suggest that the compositional maturity of the Jack Formation records both warm, wet chemical weathering and a protracted period of tectonic quiescence following the end-Stuhini deformational event. Regionally, the oldest known rocks in the Hazelton Group are ~ 203-205 Ma (Griffith Creek volcanics, Spatsizi area, Marsen and Thorkelsen 1992; basal Telkwa Formation, Terrace area, J. Nelson and R. Friedman, unpublished data 2013; basal Hazelton Group, Iskut area, Ash et al., 1997b). Fossil ages from the Jack Formation and oldest Jurassic igneous ages in the KSM area are Hettangian-Sinemurian, ~ 192-195 Ma (Table 1; Kirkham and Margolis, 1995). A protracted interval of uplift and erosion, perhaps as long as 10 million years, could have intervened in this area between the end of Stuhini deformation and the onset of Jack sedimentation. During this interval, the most mechanically durable and chemically stable minerals and rock types would have been preferentially preserved. Potential silica-rich sources include small (< 1 km^2), local intermediate intrusive bodies (see Lewis, 2013 for distribution) and Stuhini felsic volcanic rocks, such as those at Brucejack. Contributions from local coeval explosive eruptions could have enhanced the proportions of felsic and quartz vein material, as is seen from the incorporation of these clasts in near-surface breccia dikes and in phreatic explosion breccias at Iron Cap and the Bruce Glacier section.

6.3. Structural considerations

The eastern margin of the McTagg anticlinorium is a

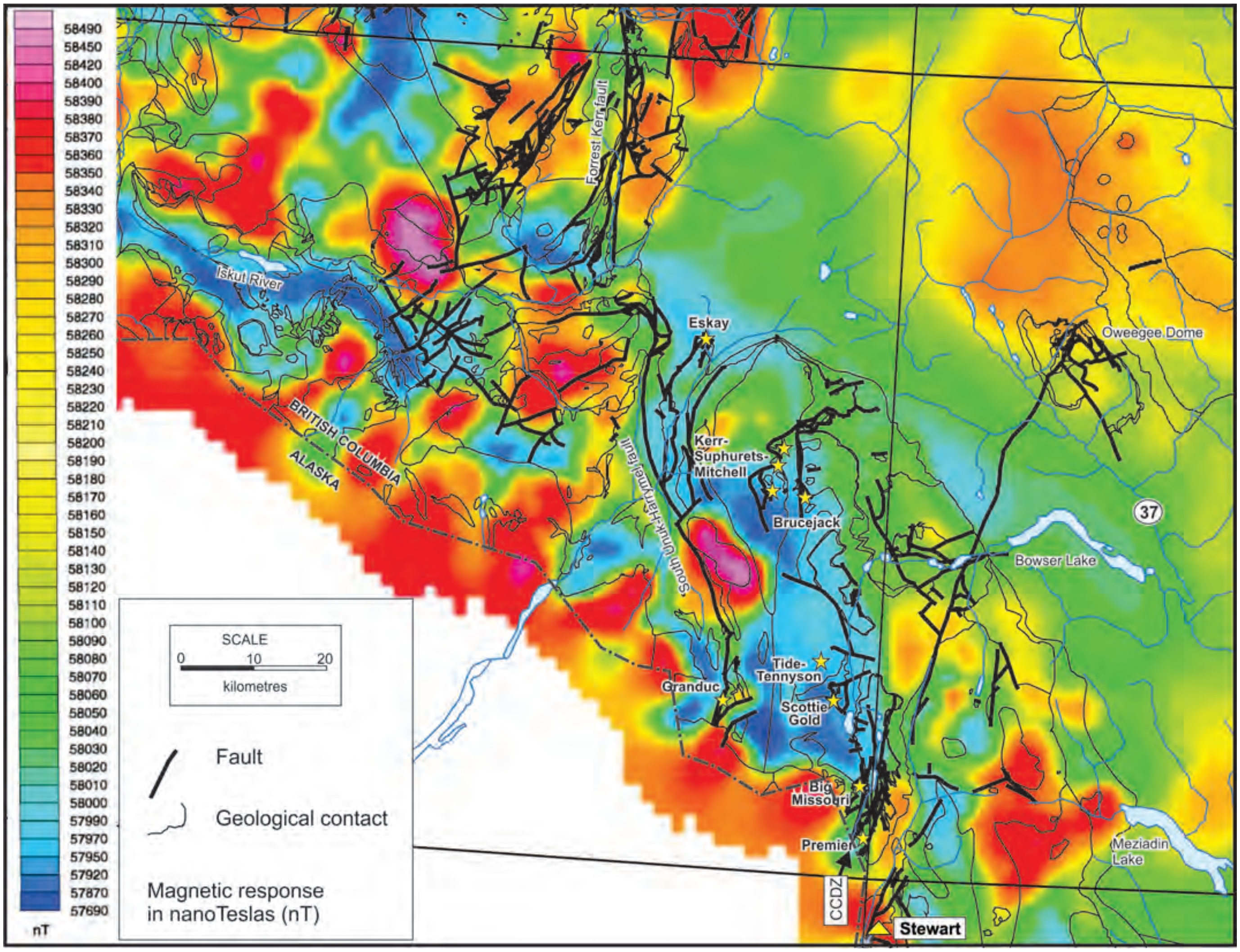

Fig. 23. Aeromagnetic map of the Treaty-Stewart trend and western Iskut region. Faults and contacts from the digital geological map of British Columbia 2005 from Massey et al. (2005).

likely location for an Early Jurassic basin-bounding fault, in that the Kerr-Sulphurets-Mitchell-Iron Cap system forms a continuous 12 kilometre-long zone of intrusion, alteration, and mineralization in the immediate footwall of the Sulphurets thrust fault at its eastern boundary. Veins and alteration zones trend either northerly parallel to the anticlinorium, or east-west at high angles to it (Kirkham and Margolis, 1995, their Fig. 2). Detailed geological mapping and extensive core logging at the Brucejack property have revealed a complex stratigraphy in the lower Hazelton Group, with rapid local facies changes probably controlled by penecontemporaneous faults (Pretivm Resources, 2012). Their model invokes a set of north-south and subsidiary east-west faults that were active during deposition, eruption, intrusion, and mineralization. The newly discovered Cleopatra vein in the Valley of the Kings zone trends north-northeast and is considered to be a feeder to the system (W. Board, personal communication, August 2013). On a broader scale, the prominent north-striking Brucejack fault (Fig. 4) trends through the Brucejack area for over 11 km between the Valley of the Kings zone on the east and the Snowfield and Golden Marmot zones on the west. It offsets upper Hazelton and Bowser Lake Group units (Lewis, 2013), and was active as late as Eocene (Kirkham and Margolis, 1995). However, its position within and parallel to the overall zone of alteration and mineralization suggest that it is a remobilized Early Jurassic structure (W. Board, personal communication, 2013).

A similar structural setting is likely for the Tennyson porphyry, adjacent to a Hazelton basin-margin fault, as shown by thick, coarse conglomerate in the fault panel immediately to the west. The intervening fault was subsequently remobilized as a Cretaceous east-vergent thrust.

On a regional scale, the northerly trends of mineralization reflect deep north-trending basement structures identified aeromagnetically (Fig. 23). A broad magnetic low is bounded to the west by the South Unuk-Harrymel fault, and to the east by the Cascade Creek deformation zone. Surface exposures in this broad, north-trending zone include the entire stratigraphic column of western Stikinia, units that range in age from Paleozoic to Eocene. Only the Eocene plutons stand out as isolated magnetic highs. The dimensions, uniformity and lack of

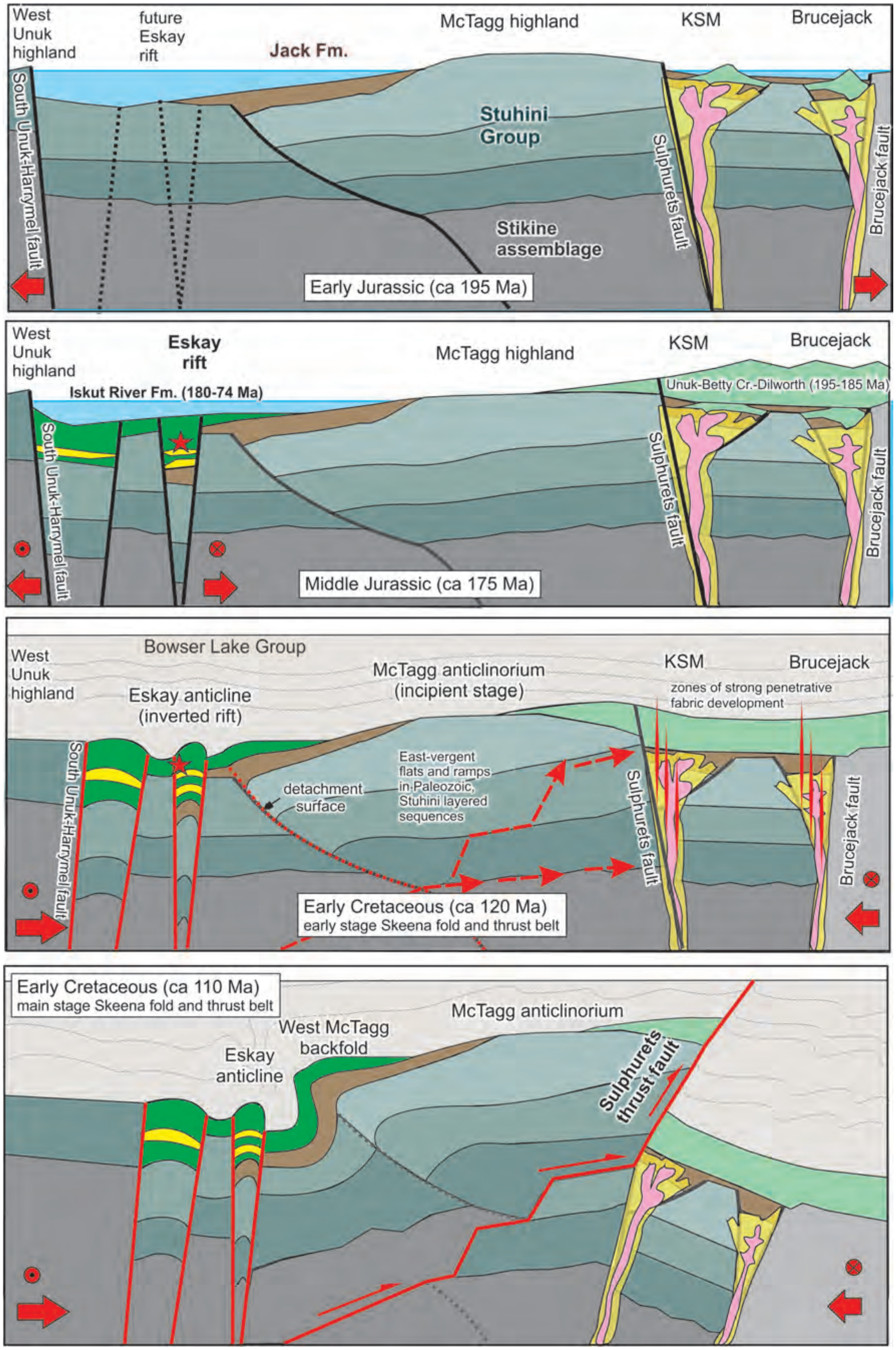

Fig. 24. Model for the structural evolution and reactivation of the McTagg half-graben and Eskay rift.

response to different supracrustal units argue for a deep crustal source, probably related to magnetite destruction by regional-scale alteration. The most likely time frame for this event would be during the Early Jurassic, as a broader expression of the fluid flow systems that produced intense local alteration around the porphyry and related deposits. The framing of this crustal-scale alteration system by the South Unuk-Harrymel fault and Cascade Creek deformation zone implicates them as block-bounding features in Early Jurassic time.

6.4. Early and Middle Jurassic tectonic reconstructions

The east-vergent Cretaceous Skeena fold and thrust belt structures that are prevalent throughout the region can be modelled as reactivated Jurassic basin-bounding faults. Figure 24 shows Early and Middle Jurassic tectonic reconstructions along a NW-SE cross section through Eskay Creek, the McTagg anticlinorium, and the KSM-Brucejack area. The Eskay Creek deposit is in a narrow, north-northeast trending sub-basin of the Middle Jurassic Eskay rift (Alldrick et al., 2005), which has since been inverted to form the Eskay anticline (Fig. 24). Pop-up structures like this are a common feature of basin inversion, as shown by McClay et al. (1989) in their analysis of Jura-Cretaceous northeast-vergent compression superimposed on rift basins of the Paleozoic Kechika trough of northeastern British Columbia. In contrast, the Sulphurets thrust fault that forms the eastern boundary of the McTagg anticlinorium is modelled as a reactivated but not inverted structure. It is comparable to the Mt. Waldemar fault in the Kechika trough; both were originally steep normal faults on the west side of graben that became ramps in subsequent east-vergent thrusting. As the proto-Mt. Waldemar fault formed the plumbing system for Devonian sedex deposits (McClay et al., 1989), so the proto-Sulphurets fault may have been the conduit for the Kerr-Sulphurets-Mitchell-Iron Cap porphyries and associated hydrothermal fluids. The precursor of the McTagg anticlinorium is the McTagg highland, a Jurassic topographic high that supplied sediments to adjacent depocentres, underlain by a west-tilted half graben. This reconstruction explains the thinning of all Hazelton units across the anticlinorium, and the contrast between the Eskay rift to the west, with its thick Iskut River Formation bimodal volcanic and sedimentary fill, and very thick lower Hazelton accumulations to the east overlain by thin, rift-shoulder Middle Jurassic units. It also accounts for the sedimentologic contrast between the deep Jack basin on its western flank, with coarse conglomerates that probably were fed by an extensive drainage system, and smaller-scale, more structurally complex depocentres to the east that hosted volcanic and porphyry centres.

The relative importance of orthogonal extension versus transtension in driving basin subsidence is unclear. The only demonstrable Jurassic sinistral motion in the region is shown by the ~ 172 Ma synkinematic dike in the south Unuk fault zone on the western margin of the Eskay rift (Lewis et al., 2001). Indicators of sinistral shear are well developed, but generally attributed to the Skeena fold and thrust belt (Kirkham and Margolis, 1995). The teardrop shape of the McTagg anticlinorium, with its highly attenuated southern “tail”, is consistent with a positive flower structure. Preliminary field observations in the tail area in 2013 indicate very strong sinistral shear sense in andesitic and felsic tuffs. Samples are being processed to determine protolith ages.

7. Conclusions and future directions

Facies analysis of the Jack Formation is in agreement with regional evidence that first-order structures of the Cretaceous Skeena fold and thrust belt, from the Eskay anticline to Stewart, are reactivated Jurassic (and possibly older) faults that controlled intrusion, alteration and mineralization. The overall northerly trend of Early Jurassic mineralization coincides with a set of original basin-bounding faults, that developed during extensional or transtensional tectonics that prevailed during development of the Hazelton arc. U-Pb analysis of detrital zircons is in progress to identify sources of the Jack Formation. Future work will focus on additional sections of the Jack Formation and structural mapping of the mineralized corridor between Brucejack and Stewart.

Acknowledgments

This project was conceived through the innovation and enthusiasm of Adrian Hickin. Larry Diakow aided greatly in project design, bringing to bear his deep knowledge of the Hazelton Group. Warwick Board and Charlie Greig of Pretivm Resources and Mike Savell and Gayle Febbo of Seabridge Resources generously shared their observations and ideas. Larry Aspler contributed key sedimentological insights and commented on an early draft of the manuscript. Tian Han and Lauren Wilson were sturdy companions in the field and made important contributions such as multispectral analysis of alteration zones (TH) and digital compilations (LW). We thank Prism Helicopters base manager Lewis Tuck and his crew for excellent, safe service in sometimes difficult flying conditions.

References cited

Aitken, J.D., and Long D.G.F., 1978. Mackenzie tectonic arc - reflection of early basin configuration? Geology, 6, 626-629.

Alldrick, D.J., 1993. Geology and metallogeny of the Stewart mining camp, northwestern B.C. British Columbia Ministry of Energy, Mines and Petroleum Resources, British Columbia Geological Survey Bulletin 85, 105 p.

Alldrick, D.J., and Britton, J.M., 1988. Geology and mineral deposits of the Sulphurets area (104A/5, 12; 104B/8, 9). British Columbia Ministry of Energy, Mines and Petroleum Resources, British Columbia Geological Survey Open File 1988-04, scale: 1:50,000.

Alldrick, D.J., and Britton, J.M., 1991. Sulphurets area geology (parts of 104A/5W, 12W; 104B/8E, 9E). British Columbia Ministry of Energy, Mines and Petroleum Resources, British Columbia Geological Survey Open File 1991-21, scale: 1:20,000.

Alldrick, D.J., and Britton, J.M., 1992. Unuk River area geology (104B/7E, 8 & 9W, 10E). British Columbia Ministry of Energy, Mines and Petroleum Resources, British Columbia Geological Survey Open File 1992-22, scale: 1:20,000.

Alldrick, D.J., Britton, J.M., Webster, I.C.L., and Russell, C.W.P.,

1989. Geology and mineral deposits of the Unuk area (104B/7E, 8W, 9W, 10E). British Columbia Ministry of Energy, Mines and Petroleum Resources, British Columbia Geological Survey Open File 1989-10, scale: 1:50,000.

Alldrick, D.J., Britton, J.M., MacLean, M.E., Hancock, K.D., Fletcher, B.A., and Hiebert S.D., 1990. Geology and mineral deposits of the Snippaker area (104B/6E, 7W, 10W, 11E). British Columbia Ministry of Energy, Mines and Petroleum Resources, British Columbia Geological Survey Open File 1990-16, scale: 1:50,000.

Alldrick, D.J., Nelson, J.L., and Barresi, T., 2005. Geology and mineral occurrences of the upper Iskut River area: tracking the Eskay rift through northern British Columbia. In: Geological Fieldwork 2004, British Columbia Ministry of Energy, Mines and Petroleum Resources, British Columbia Geological Survey Paper 2005-1, 1-30.

Anderson, R.G., and Thorkelsen, D.J., 1990. Mesozoic stratigraphy and setting for some mineral deposits in Iskut River map area, northwestern British Columbia. In: Current Research, Part E, Geological Survey of Canada Paper 90-1 E, 131-139.

Ash, C.H., MacDonald, R.J.W., and Friedman, R.M., 1997b. Stratigraphy of the Tatogga Lake area, northwestern British Columbia (NTS 104H, 12, 13; 104G/9, 16. In: Geological Fieldwork 1996, British Columbia Ministry of Energy, Mines and Petroleum Resources, British Columbia Geological Survey Paper 1997-1, 283-290.

Ash, C.H., MacDonald, R.J.W., Stinson, P.K., Fraser, T.M., Read, P.R., Psutka, J.F., Nelson, K.J., Arden, K.M., Friedman, R.M., and Lefebure, D.V., 1997a. Geology and mineral occurrences of the Tatogga Lake area, NTS 104G/9NE, 16SE and 104H/12NW, 13SW. British Columbia Ministry of Energy, Mines and Petroleum Resources, British Columbia Geological Survey Open File 1997-3, scale: 1:50,000.

Ash, C.H., MacDonald, R.J.W., and Friedman, R.M., 1997b. Stratigraphy of the Tatogga Lake area, northwestern British Columbia (NTS 104H, 12, 13; 104G/9, 16). In: Geological Fieldwork 1996, British Columbia Ministry of Energy, Mines and Petroleum Resources, British Columbia Geological Survey Paper 1997-1, 283-290.

Condie, K.C., 1981. Archean Greenstone Belts; Elsevier, Amsterdam, 434 p.

Cecile, M.P., Morrow, D.W., and Williams, G.K., 1997. Early Paleozoic (Cambrian to Early Devonian) tectonic framework, Canadian Cordillera. Canadian Society of Petroleum Geology Bulletin 45, 54-74.

Donaldson, J.A., and Jackson, G.D., 1965. Archaean sedimentary rocks of North Spirit Lake area, northwestern Ontario. Canadian Journal of Earth Sciences, 2, 622-646.

Evenchick, C.A., Hayes, M.C., Buddell, K.A., and Osadetz, K.G., 2002. Vitrinite and bitumen reflectance and preliminary organic maturity model for the northern two thirds of the Bowser and Sustut basins, north-central British Columbia. Geological Survey of Canada Open File 4343, British Columbia Ministry of Energy and Mines Open File 2002-1.

Evenchick, C.A., McMechan, M.E., McNicoll, V.J., and Carr, S.D., 2007. A synthesis of the Jurassic-Cretaceous tectonic evolution of the central and southeastern Canadian Cordillera: exploring links across the orogen. In: Sears, J.W., Harms, T.A., and Evenchick, C.A., eds., Whence the mountains? inquiries into the evolution of orogenic systems: a volume in honour of Raymond A. Price, Geological Society of America, Special Paper 433, 117-145.

Gagnon, J.F., Barresi, T., Waldron, J.W.F., Nelson, J.L., Poulton, T.P., and Cordey, F., 2012. Stratigraphy of the upper Hazelton Group and Jurassic evolution of the Stikine terrane, British Columbia. Canadian Journal of Earth Sciences, 49, 1027-1052.

Greig, C.J., 1992. Fieldwork in the Oweegee and Snowslide ranges and Kinskuch Lake area, northwestern BC. In: Current Research Part A, Geological Survey of Canada Paper 92-1A, 145-155.

Grove, E.W., 1971. Geology and mineral deposits of the Stewart area, British Columbia. British Columbia Ministry of Energy, Mines and Petroleum Resources, British Columbia Geological Survey Bulletin 58, 229 p.

Grove, E.W., 1986 (reprint). Geology and mineral deposits of the Unuk River-Salmon River-Anyox area. British Columbia Ministry of Energy, Mines and Petroleum Resources, British Columbia Geological Survey Bulletin 63, 152 p.

Gunning, M.H., Hodder, R.W.H., and Nelson, J.L., 2006. Contrasting volcanic styles within the Paleozoic Stikine assemblage, western Stikine terrane, northwestern British Columbia. In: Colpron, M., and Nelson, J.L., eds., Paleozoic evolution and metallogeny of pericratonic terranes at the Ancient Pacific Margin of North America, Canadian and Alaskan Cordillera. Geological Association of Canada, Special Paper 45, 201-227.

Henderson, J.R., Kirkham, R.V., Henderson, M.N., Payne, J.G., Wright, T.O., and Wright, R.L., 1992. Stratigraphy and structure of the Sulphurets area, British Columbia. In: Current Research, Part A, Geological Survey of Canada Paper 92-1A, 323-332.

Holdsworth, R.E., Butler, C.A. and Roberts, A.M., 1997. The recognition of reactivation during continental deformation. Journal of the Geological Society of London 154, 73-78.

Höy, T., Anderson D., Turner, R.J.W., and Leitch, C.H.B., 2000. Tectonic, magmatic and metallogenetic history of the early synrift phase of the Purcell basin, southern British Columbia. In: Lydon, J.W., Slack, J.F., and Knapp, M.A., eds., The geological environment of the Sullivan Deposit, British Columbia. Geological Association of Canada, Mineral Deposits Division, Special Publication 1, 32-60.

Kent, D.V., and Irving, E., 2010. Influence of inclination error in sedimentary rocks on the Triassic and Jurassic apparent pole wander path for North America and implications for Cordilleran tectonics. Journal of Geophysical Research, 115, B10103, doi:10.1029/2009JB007205,2010.

Kirkham, R.V., and Margolis, J., 1995. Overview of the Sulphurets area, northwestern British Columbia. In: Schroeter, T.G., editor, Porphyry deposits of Western North America. Canadian Institute of Mining and Metallurgy Special Volume 46, 473-523.

Lewis, P.D., 2001a. Structural evolution of the Iskut River area-preliminary results. In: Lewis, P.D., Toma, A., Tosdal, R.M., (eds.), Metallogenesis of the Iskut River area, northwestern British Columbia. Mineral Deposit Research Unit, Special Publication Number 1, 63-76.

Lewis, P.D., 2001b. Geological maps of the Iskut River area. In: Lewis, P.D., Toma, A., Tosdal, R.M., eds., Metallogenesis of the Iskut River area, northwestern British Columbia. Mineral Deposit Research Unit, Special Publication Number 1, 77-83.

Lewis, P.D., 2013. Iskut River area geology, northwest British Columbia (104B/08, 09, 10 & part of 104B/01, 07, 11). Geoscience British Columbia Report 2013-05, 3 1:50,000-scale maps, legend and notes, .shp files.

Lewis, P.D, Macdonald, A.J., Bartsch, R.D., 2001. Hazelton Group/Bowser Lake Group stratigraphy in the Iskut River area - progress and problems. In: Lewis, P.D., Toma, A., Tosdal, R.M., eds., Metallogenesis of the Iskut River area, northwestern British Columbia. Mineral Deposit Research Unit, Special Publication

Number 1, 9-30

Logan, J.M., and Mihalynuk, M.G., 2013. Tectonic controls on early Mesozoic paired alkaline porphyry deposit belts (Cu-Au + Ag-Pt-Pd-Mo) within the Canadian Cordillera. Economic Geology, Special Issue on Alkalic Porphyry Deposits, in press.

Logan, J.M., Drobe, J.R., and McClelland, W.C., 2000. Geology of the Forrest Kerr - Mess Creek area, northwestern British Columbia (NTS 104B/10, 15 & 104G/2 & 7W). British Columbia Ministry of Energy, Mines and Petroleum Resources, British Columbia Geological Survey Bulletin 104, 163 p.

MacIntyre, D.G., Ash, C.H., Britton, J.B., Kilby, W., Grunsky, E., 1994. Mineral potential assessment of the Skeena – Nass area, British Columbia. In: Geological Fieldwork 1994, British Columbia Ministry of Energy, Mines and Petroleum Resources, British Columbia Geological Survey Paper 1995-1, 459-468.

Marsden, H., and Thorkelsen, D.J., 1992. Geology of the Hazelton volcanic belt in British Columbia: implications for the Early to Middle Jurassic evolution of Stikinia. Tectonics, 11, 1266-1287.

Massey, N.W.D., MacIntyre, D.G., Desjardins, P.J., and Cooney, R.T., 2005. Digital geology map of British Columbia: Whole province. British Columbia Ministry of Energy, Mines and Petroleum Resources, Geofile 2005-1.

McClay, K.R., Insley, M.W., and Anderton, R., 1989. Inversion of the Kechika Trough, northeastern British Columbia. In: Cooper, M.A., and Williams, G.D., eds., Inversion tectonics, Geological Society of London, Special Publication 44, 235-257.

McMechan, M.E., 2012. Deep basement structural control of mineral systems in the southeastern Canadian Cordillera. Canadian Journal of Earth Sciences, 49, 693–708.

Nelson, J.L., Paradis. S., Christensen, J., and Gabites, J., 2002. Canadian cordilleran Mississippi Valley-type deposits: a case for Devonian-Mississippian backarc hydrothermal origin. Economic Geology, 93, 184-200.

Nelson, J.L., Colpron, M., Piercey, S.J., Dusel-Bacon, C., Murphy, D.C., and Roots, C.F., 2006. Paleozoic tectonic and metallogenetic evolution of pericratonic terranes in Yukon, northern British Columbia and eastern Alaska. In: Colpron, M., and Nelson, J.L., eds., Paleozoic evolution and metallogeny of pericratonic terranes at the Ancient Pacific Margin of North America, Canadian and Alaskan Cordillera. Geological Association of Canada, Special Paper 45, 323-360.

Nelson, J.L., Kyba, J., McKeown, M., and Angen, J., 2008. Terrace regional mapping project, year 3: contributions to stratigraphic, structural and exploration concepts, Zymoetz River to Kitimat River, east-central British Columbia. In: Geological Fieldwork 2006, British Columbia Ministry of Energy, Mines and Petroleum Resources, British Columbia Geological Survey Geological Paper 2007-1, 159-174.

Nelson, J.L., Colpron, M., and Israel, S., 2013. The Cordillera of British Columbia, Yukon and Alaska: tectonics and metallogeny. In: Colpron, M., Bissig, T., Rusk, B.G., and Thompson, J.F.H., eds., Tectonics, metallogeny and discovery: the North American cordillera and similar accretionary settings. Society of Economic Geologists Special Publication 17, Chapter 3, 53-109.

Pretivm Resources, 2012. Online presentation http://www.pretivm.com/; September, 2012.

Pretivm Resources, 2013. Brucejack Project website: http://www.pretivm.com/. Press release on Valley of the Kings preliminary results from bulk sample analysis, November 22, 2013.

Smith, P.L., Tipper, H.W., and Ham, D.M., 2001. Lower Jurassic Amaltheidae (Ammonitina) in North America: paleobiogeography and tectonic implications. Canadian Journal of Earth Sciences, 38, 1439-1449.

Tipper, H.W., and Richards, T.A., 1976. Jurassic stratigraphy and history of north-central British Columbia. Geological Survey of Canada, Bulletin 270, 73 p.

Van Straaten, B., 2013. Geological, geochemical, and geophysical work on the Tennyson property. British Columbia Ministry of Energy and Mines, Assessment Report #33,928, 220 p. (off confidential 2014-02-27).

Platinum-group mineralogy of the Giant Mascot Ni-Cu-PGE deposit, Hope, B.C.

Matthew J. Manor[1, a], James S. Scoates[1], Graham T. Nixon[2], and Doreen E. Ames[3]

[1] Pacific Centre for Isotopic and Geochemical Research, Department of Earth, Ocean and Atmospheric Sciences, University of British Columbia, Vancouver, BC, V6T 1Z4
[2] British Columbia Geological Survey, Ministry of Energy and Mines, Victoria, BC, V8W 9N3
[3] Geological Survey of Canada, Natural Resources Canada, 601 Booth St., Ottawa, ON, K1A 0E8
[a] corresponding author: mmanor@eos.ubc.ca

Recommended citation: Manor, M.J., Scoates, J.S., Nixon, G.T., and Ames, D.E., 2014. Platinum-group mineralogy of the Giant Mascot Ni-Cu-PGE deposit, Hope, B.C. In: Geological Fieldwork 2013, British Columbia Ministry of Energy and Mines, British Columbia Geological Survey Paper 2014-1, pp. 141-156.

Abstract

The Giant Mascot Ni-Cu-PGE deposit is British Columbia's only past-producing nickel mine (1958-1974), having yielded ~ 4.2 Mt of ore grading 0.77% Ni and 0.34% Cu with minor Co, Ag and Au. Intrusive ultramafic rocks (olivine-orthopyroxene ± hornblende ± clinopyroxene cumulates) host the Ni-Cu sulphide mineralization. Field mapping and petrographic study have revealed primary magmatic cumulus textures and minimal alteration of the ultramafic rocks. Platinum-group minerals (PGM) determined by microbeam techniques are predominantly bismuthotellurides, primarily moncheite [$(Pt,Pd)(Te,Bi)_2$], merenskyite [$Pd(Te,Bi)_2$], and palladian melonite [$(Ni,Pd)(Te,Bi)_2$]. Other precious-metal minerals include sperrylite ($PtAs_2$), hessite (Ag_2Te) and altaite (PbTe). Pt-, Pd- and Ni-bismuthotellurides are in or at the margins of base metal sulphides, predominantly pentlandite, or in fractures; precious-metal minerals are mostly along fractures in silicate minerals. Textures are consistent with an orthomagmatic origin for sulphides and PGM involving exsolution from base metal sulphides during cooling. Locally abundant fractures filled by chalcopyrite and platinum-rich moncheite are evidence for relatively late-stage mobilization of residual Cu-rich sulphide melts. PGE-enriched sulphides containing identifiable PGM and associated precious-metal minerals in the Giant Mascot intrusion indicate that 'orogenic' Ni-Cu mineralization in the Canadian Cordillera and elsewhere may provide significant exploration targets for economic Ni-Cu-PGE deposits.

Keywords: Giant Mascot, platinum-group minerals, Ni-Cu-PGE mineralization, ultramafic, magmatic sulphide, Coast Plutonic Complex, Spuzzum pluton

---

1. Introduction

Conventionally, subduction-zone environments are considered poor targets for nickel-copper-platinum group element (Ni-Cu-PGE) sulphide mineralization due to the paucity of ultramafic bodies with economic Ni-sulphides (Ripley, 2010). Although PGE mineralization in supra-subduction zone ('orogenic') settings is commonly associated with Ural-Alaskan-type intrusions (ultramafic bodies typically devoid of orthopyroxene), their prospectivity with respect to Ni-sulphides remains unclear (Nixon et al., 1997; Ripley, 2010). Nonetheless, Ni-Cu-PGE deposits in orogenic settings hosted by ultramafic-mafic rocks containing orthopyroxene as an essential mineral are becoming an increasingly important resource or exploration target (e.g., Aguablanca, Spain, Piña et al, 2008; Portneuf-Mauricie Domain, Québec, Sappin et al, 2012; St. Stephen, New Brunswick, Paktunc, 1989; Americano do Brasil and Limoeiro, Brazil, Mota-e-Silva et al., 2011, 2013).

To better understand these orogenic deposits, herein we present preliminary results from an ongoing study of the Giant Mascot Ni-Cu-PGE deposit in southern British Columbia (Fig. 1), where intrusive ultramafic rocks (olivine-orthopyroxene ± hornblende ± clinopyroxene cumulates) host Ni-Cu sulphide mineralization. Through field mapping, petrographic study, scanning electron microscopy, and electron microprobe analyses we provide the first systematic documentation of the occurrence and textural features of platinum-group minerals (PGM) and Ni-Cu sulphide mineralization hosted by the Giant Mascot intrusion.

2. Geological setting

The Giant Mascot deposit is east of Harrison Lake, approximately 12 kilometres north of Hope, in southwestern British Columbia. The deposit is in the Northern Cascade region near the southeastern margin of the Coast Plutonic Complex (Fig. 1; Brown and McClellan, 2000; Reiners et al., 2002). Plutons and batholiths in this area are catazonal to epizonal, tonalitic to gabbroic intrusions that were emplaced in a magmatic arc setting during the Cretaceous (107-76 Ma, Richards, 1971; Brown and McClellan, 2000; Mitrovic, 2013, and references therein).

The Spuzzum pluton (early Late Cretaceous, ca. 95 Ma, M.J. Manor, unpublished data), a 60 x 20 km granitoid batholith, hosts the Giant Mascot Ni-Cu-PGE deposit and associated ultramafic rocks (Fig. 1). It is compositionally zoned from pyroxene diorite in the core to hornblende diorite near the margins, and has an outermost rim of tonalite (Richards and McTaggart, 1976; Vining, 1977). The pluton intrudes Settler schist (Upper Triassic), a Barrovian-facies metamorphic complex consisting of pelitic and quartzofeldspathic schist and micaceous quartzite, and locally containing garnet, staurolite and kyanite (Pigage, 1973; Mitrovic, 2013).

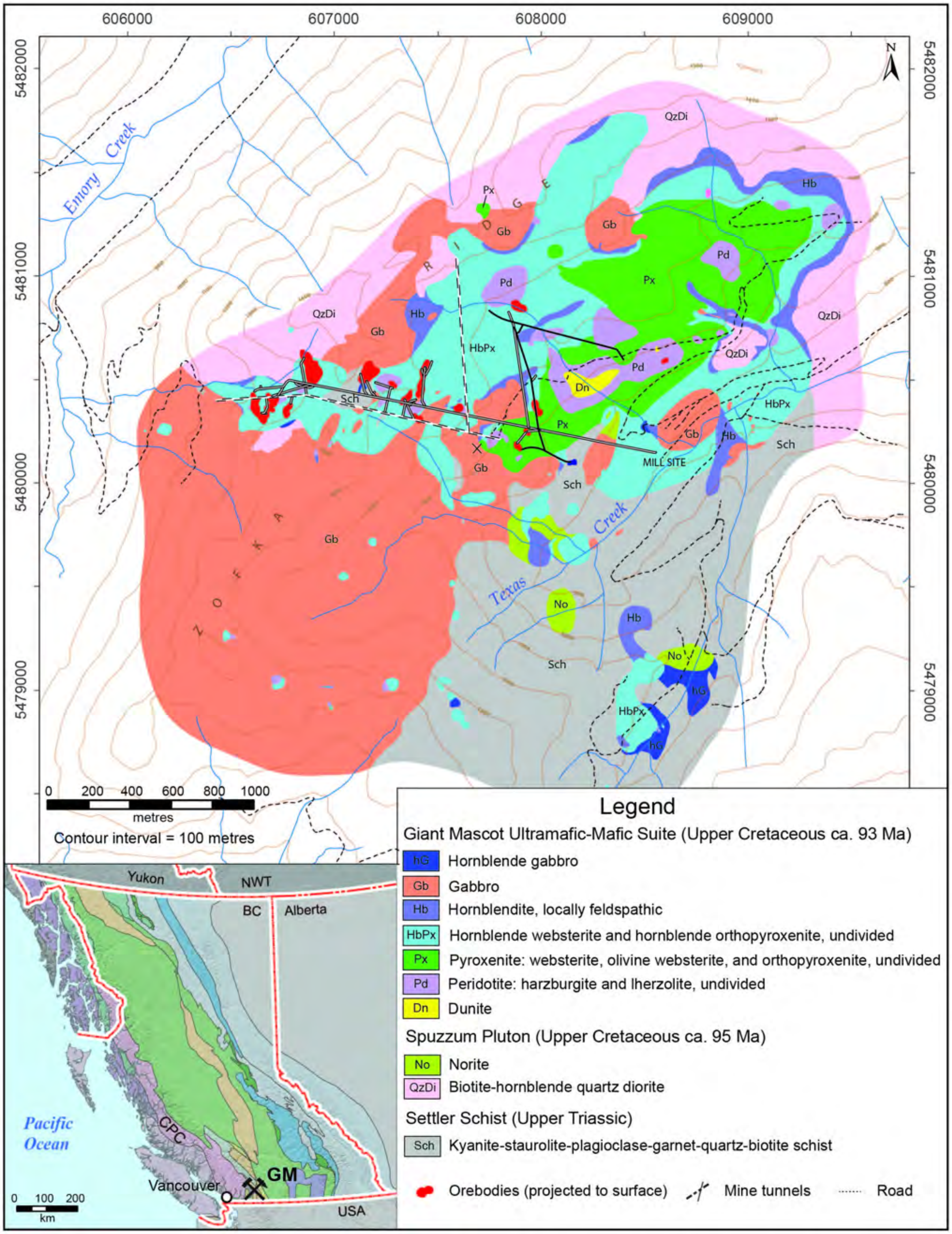

Fig. 1. Geologic map of the Giant Mascot ultramafic-mafic intrusion (modified from Aho, 1954) and inset showing its location in southwestern British Columbia (GM, Giant Mascot; CPC, Coast Plutonic Complex). The cross at map centre marks UTM coordinates of 607700 E, 5480180 N (NAD83, Zone 10).

3. Giant Mascot mine history

The Giant Mascot Ni-Cu-PGE deposit is British Columbia's only past-producing nickel mine (Pinsent, 2002). Nickel showings were first discovered in 1923, and diamond drilling defined the orebodies up until 1937. After a hiatus during and after World War II, exploration resumed in 1951, and the mine went into production in 1958 (Fig. 2). The deposit was mined for nickel and copper from 1958 to 1974 by open-stope methods, and produced approximately 4.2 Mt of ore with average grades of 0.77% Ni and 0.34% Cu along with minor Co, Ag and Au (Christopher and Robinson, 1974). Platinum-group-element abundances in the ores of the Giant Mascot deposit were uncertain or unreported (Pinsent, 2002; Nixon, 2003). Metcalfe et al. (2002) reported "platinum values in excess of 1 gram," although a specific source was not cited, and Hulbert (2001) reported six PGE analyses without any geologic or mineralogic information.

Fig. 2. Photograph from Western Miner (Stephens, 1959) showing the main mill site at Giant Mascot in the early years of production and the primary crusher (centre) and secondary crusher (left).

A total of 28 orebodies occur along a west-east mineralized corridor (orebodies projected to surface, Fig. 1). Twenty-two of these were mined, including five major contributors to production: Pride of Emory, Brunswick #2 and #5, 4600, and 1500 (Christopher and Robinson, 1974). Mine workings and major portals to the underground stopes are north of Texas Creek, on the southern slope of Zofka Ridge (Fig. 1).

4. Lithological units

The Giant Mascot intrusion, a crudely elliptical, 4 x 3 km body, comprises ultramafic and mafic rocks that are hosted by quartz diorites of the Spuzzum pluton and metapelites of the Settler schist (Fig. 1). Nine main rock units (Figs. 1, 3) include ultramafic, mafic and country-rock lithologies, where each lithology is characterized by a range of mineral compositions. Mean olivine, pyroxene, and plagioclase compositions determined by electron microprobe analysis (EMPA) are reported in Muir (1971) and McLeod (1975). In addition, plagioclase compositions (n=19) for gabbro and quartz diorite have been determined optically in this study based on the Michel-Levy method.

4.1. Ultramafic rocks

The Giant Mascot ultramafic-mafic intrusion (ca. 93 Ma; M.J. Manor, unpublished data) consists predominantly of olivine- and orthopyroxene-rich cumulates with variable amounts of clinopyroxene and hornblende. The rocks display primary igneous textures involving olivine, orthopyroxene, clinopyroxene, and hornblende, with minor biotite, plagioclase, and quartz. Minor secondary alteration occurs mostly at grain boundaries as tremolite-actinolite, chromian Mg-chlorite, talc, serpentine, and carbonate. Alteration of clinopyroxene to hornblende is common, whereas reaction of orthopyroxene to hornblende is less prevalent.

The major ultramafic units are dunite, peridotite and pyroxenite; the latter two lithologies contain variable amounts of hornblende. Dunite occurs in the core of the intrusion and, although the smallest rock unit by volume, is a major host of nickel mineralization. The rock is fine grained and contains 90-95 vol.% equigranular olivine with sparse euhedral chromite inclusions and secondary Cr-magnetite, interstitial clinopyroxene (5-10%), and minor orthopyroxene. Peridotite, the other major host of mineralization, is represented by fine- to medium-grained lherzolite and harzburgite orthocumulates with variable amounts of hornblende. Olivine (40-80%; ~Fo_{84}; Muir, 1971) occurs as cumulus crystals or grains enclosed in subpoikilitic pyroxene. Intergranular orthopyroxene (30-60%) is the predominant pyroxene (En_{84}; Muir, 1971), accompanied by variable (0-10%) clinopyroxene and interstitial hornblende. Pyroxenite typically contains no sulphide and forms medium-grained orthocumulates of websterite, olivine websterite, and orthopyroxenite. Brown subhedral orthopyroxene (En_{82}; Muir, 1971) forms sparse oikocrysts and is more abundant than black-green clinopyroxene (55-90% total pyroxene). Olivine (5-35%) forms intergranular grains or inclusions, whereas hornblende (0-10%) is interstitial. Locally, plagioclase (5-10%) occurs in clots.

Hornblende-rich units of the Giant Mascot ultramafic-mafic intrusion include hornblende pyroxenite and hornblendite. Hornblende pyroxenites are medium-grained hornblende websterite and orthopyroxenite, commonly oikocrystic and locally feldspathic. Orthopyroxene (En_{77-81}; Muir, 1971) and clinopyroxene abundances are highly variable (20-60%) and textures are predominantly cumulate. Pyroxene grains are commonly enclosed by oikocrystic hornblende (20-80%), which ranges in diameter from 4 to 50 mm. Hornblendite commonly occurs at marginal contacts with gabbro and Spuzzum quartz diorite, where it typically forms feldspathic pegmatite zones up to 40 m wide at the contact. Prismatic hornblende (90-98%) ranges in length from 0.2 to 25 cm and is commonly altered to cummingtonite-tremolite intergrowths and anthophyllite. Clinopyroxene (0-5%) is interstitial or forms euhedral inclusions in pegmatitic hornblende. Locally, plagioclase clots (An_{80-90}; McLeod, 1975) may attain 30% of the mode. Hornblende pyroxenite rarely contains sulphide; exceptions are reported in the Chinaman, Climax and 4300 orebodies, which hosted disseminated and minor massive sulphide mineralization (Christopher and Robinson, 1974).

4.2. Mafic rocks

Hornblende gabbro is a minor lithology in the Giant Mascot intrusion. It is medium to coarse grained and variably

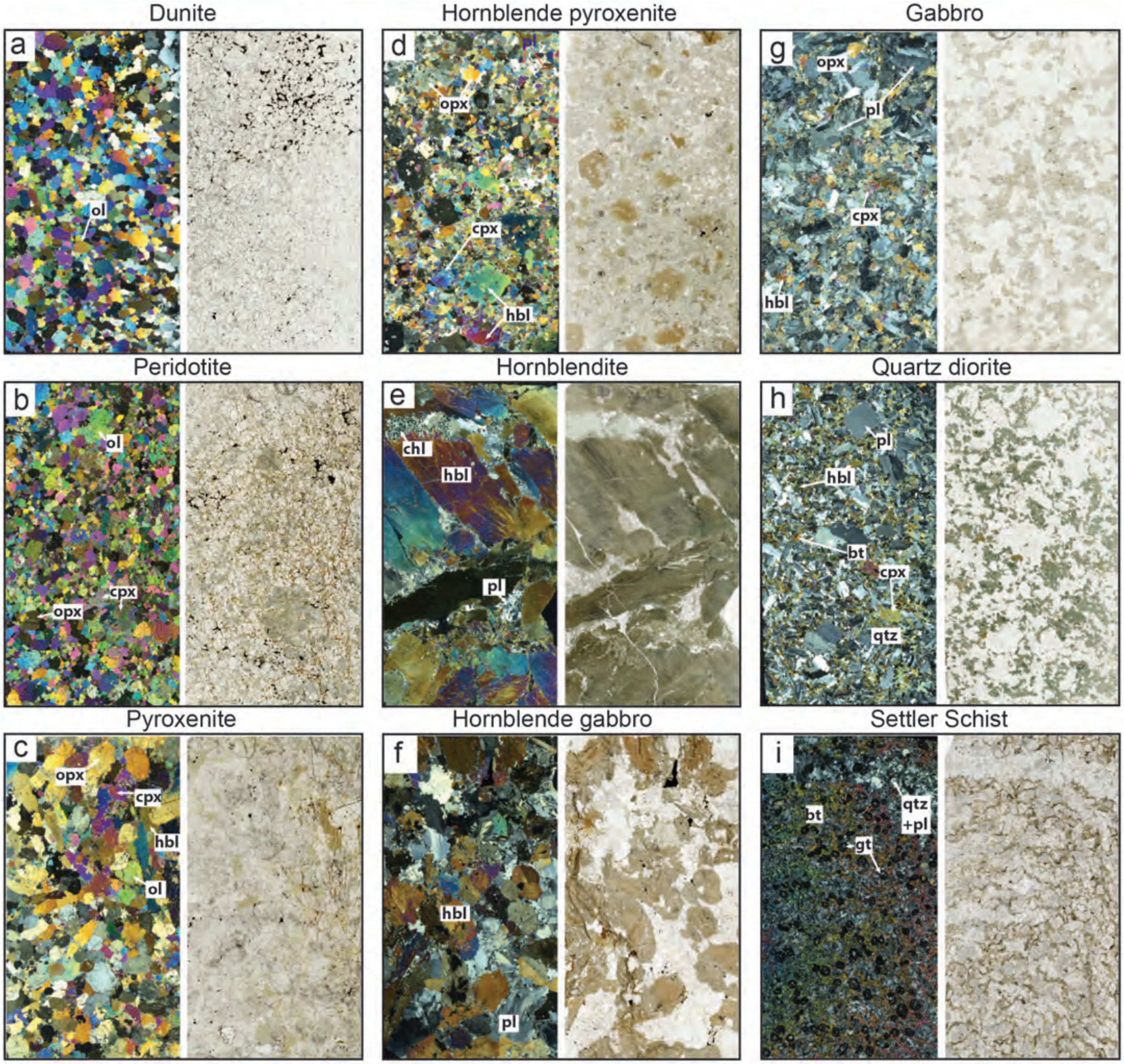

Fig. 3. Scanned images of thin sections showing lithological units at the Giant Mascot intrusion. Ultramafic units: **a)** dunite, sample 12MMA-7-8-1; **b)** peridotite, 12MMA-7-10-1; **c)** pyroxenite, 12MMA-5-4-1; **d)** hornblende pyroxenite, 12MMA-2-4-1; **e)** hornblendite, 11GNX-1-2-1. Mafic units: **f)** hornblende gabbro, 13MMA-9-9-3; **g)** gabbro, 12MMA-9-1-2. Country rocks: **h)** Spuzzum quartz diorite, 12MMA-2-1-5; **i)** Settler schist, 13MMA-5-1-1. Cross-polarized (left) and plain-polarized light (right) thin sections are 2 x 4 cm. Mineral abbreviations: ol, olivine; opx, orthopyroxene; cpx, clinopyroxene; hbl, hornblende; bt, biotite; pl, plagioclase; chl, chlorite; qtz, quartz; gt, garnet.

melanocratic, and contains subhedral, prismatic hornblende (15-55%), interstitial plagioclase (30-75%), and interstitial pyroxene (5-15%). Veins and dikes of unmineralized hornblende gabbro, one of the youngest intrusive phases, cut all mafic and ultramafic units.

Two-pyroxene gabbro is common along the margins of the intrusion, or within ultramafic rocks, and contains plagioclase (An$_{48-72}$; 45-70%), orthopyroxene and clinopyroxene (15-35%), hornblende (5-15%), biotite (0-5%), and quartz (0-15%). These gabbros share many mineralogical similarities to dioritic units in the surrounding Spuzzum pluton. Locally, gabbro intruding hornblende pyroxenite and Spuzzum quartz diorite displays chilled margins, and the gabbro contains rare lobate hornblende pyroxenite inclusions.

Norite units were mapped by Aho (1954, 1956) as orthopyroxene-plagioclase rocks (An$_{65-90}$; McLeod, 1975) that define small pods in contact with Settler schist. Our field and petrographic observations revealed significant clinopyroxene in these noritic units, which thus appear similar in composition to the gabbroic units described above.

The youngest phases of the Giant Mascot intrusion are felsic pegmatite and aplite veins and dikes (2-10 cm wide) cutting hornblendite, hornblende pyroxenite, hornblende gabbro, and gabbro.

4.3. Country rocks

The Spuzzum pluton, comprising diorite, quartz diorite, and tonalite, hosts the Giant Mascot ultramafic-mafic intrusion. Adjacent to the ultramafic rocks are white to grey, variably melanocratic, medium-grained, hornblende-biotite quartz diorite and diorite (An_{32-55}). Locally, these rocks are foliated; foliation is particularly well developed at pluton contacts. The main (15-55%) components of these diorites are orthopyroxene, clinopyroxene, hornblende, and biotite (± phlogopite). The diorites contain local lobate and elongate melanocratic inclusions rich in hornblende and biotite (> 90% mafic minerals).

The Settler schist is a series of layered metasedimentary rocks (siltstones and quartzofeldspathic arenites) that crop out on the east and southeast margins of the intrusion (Fig. 1). Schist directly in contact with the Giant Mascot intrusion contains variable proportions of kyanite, staurolite, and garnet, and strongly foliated biotite, quartz, and plagioclase. In the western part of Zofka Ridge, a large raft of Settler schist is in contact with hornblende pyroxenite to the west and gabbro on all other sides. At its northern contact, the schist locally exhibits evidence of incipient anatectic melting adjacent to a 70 x 100 m zone of garnetiferous gabbro that is cut by siliceous veins (Fig. 1).

5. Ni-Cu-PGE mineralization

Ni-Cu-PGE sulphide mineralization in the Giant Mascot intrusion is commonly hosted in the olivine-rich rocks, including dunite, peridotite, and olivine-bearing pyroxenite. Sulphide orebodies occur in 28 steeply dipping, north-northwest-trending, pipe-like structures that have diameters of 6 to 75 m and extend to depths of 30 to 360 m (Christopher and Robinson, 1974). At both outcrop and hand-sample scale, mineralization defines disseminated, net-textured, semi-massive and massive textures, and locally forms Cu-rich veins (Figs. 4a-h). Polished ore samples reveal brecciated textures in which olivine and pyroxene cumulates form inclusions in sulphide (Fig. 4e), or discontinuous intrastratal folds interpreted to record syndepositional ductile deformation during emplacement of the orebodies (Fig. 4g).

5.1. Mineralogy

The predominant sulphide minerals, present in all ores of the Giant Mascot intrusion, are pyrrhotite ($Fe_{1-x}S$), pentlandite [$(Fe,Ni)_9S_8$], chalcopyrite ($CuFeS_2$), and minor pyrite (FeS_2). Pyrrhotite is the most abundant sulphide (Fig. 4), both as magnetic, monoclinic (Fe_7S_8), and non-magnetic, hexagonal (e.g., $Fe_{11}S_{12}$), varieties (e.g., Becker et al., 2010). Pyrrhotite and pentlandite were the first sulphide minerals to crystallize from the sulphide melt, with chalcopyrite and pyrite following at somewhat lower temperatures (based on Naldrett, 2004). Minor phases include troilite (pure FeS), magnetite, argentopentlandite [$Ag(Fe,Ni)_8S_8$], mackinawite [$(Fe,Ni)_{1+x}S$], cubanite (Cu_3FeS_4), cobaltite (CoAsS), gersdorffite (NiAsS), and nickeline (NiAs). Sulphide phases associated with secondary alteration include pyrite, marcasite, violarite ($FeNi_2S_4$), and polydymite ($Ni^{2+}Ni^{3+}{}_2S_4$).

5.2. Sulphide textures

Pyrrhotite, the predominant sulphide, is commonly massive, and locally infills fractures in silicate minerals. Pentlandite may be massive and blocky (Figs. 5a, c, d, h) or form crystallographically oriented exsolution lamellae in pyrrhotite and argentopentlandite (Figs. 5b, c, g). The pyrrhotite:pentlandite ratio is approximately 2:1. Chalcopyrite is typically massive (Figs. 5a, d, f, g, i) or fills fractures in silicate minerals and pyrrhotite (Fig. 5e). Pyrite-pentlandite and pyrite-chalcopyrite symplectic intergrowths surround blocky pentlandite (Fig. 5a). Argentopentlandite is invariably found with chalcopyrite as exsolution lamellae and euhedral grains. Locally, pentlandite exsolved at crystallographic orientations in argentopentlandite (Figs. 5g; 6h). Low-temperature exsolution lamellae are common features in pentlandite, troilite, mackinawite and cubanite. Troilite is locally massive, but more commonly defines exsolution lamellae hosted by pyrrhotite (Fig. 5b). Mackinawite and cubanite form exsolution lamellae in pentlandite (Fig. 5h) and chalcopyrite (Fig. 5i), respectively.

Sulpharsenide minerals, such as gersdorffite, cobaltite and nickeline, are euhedral to subhedral grains hosting or contacting PGM or precious-metal minerals (PMM) (Figs. 6f, i). Secondary sulphides include marcasite, which occurs as veins within pyrrhotite (Fig. 5e), and pyrite, common as veins in pyrrhotite and pentlandite (Figs. 5d, e). Magnetite forms both euhedral inclusions in pyrrhotite or veins cutting pyrrhotite and chalcopyrite (Fig. 5f).

6. Microbeam techniques

6.1. Scanning electron microscopy (SEM)

Polished petrographic thin sections (n=10) were carbon coated and prepared in the Electron Microbeam/X-Ray Diffraction Facility at the University of British Columbia, Vancouver (UBC) and the SEM Facility at the Geological Survey of Canada, Ottawa (GSC). At UBC, back-scattered electron (BSE) imaging and qualitative energy-dispersive spectrometry (EDS) were carried out on a Philips XL-30 scanning electron microscope (SEM) equipped with a Bruker Quanta 200 energy-dispersion X-ray microanalysis system. An operating voltage of 15 kV was used, with a spot diameter of 6 μm and peak count time of 30 s. At the GSC, BSE imaging and EDS analyses were carried out on a Zeiss EVO 50 series SEM with extended pressure capability (up to 3000 Pascals), and equipped with a backscattered electron detector (BSD), Everhart-Thornley secondary electron detector (SE) and variable pressure secondary electron detector (VPSE). The Oxford EDS system includes the X-MAX 150 Silicon Drift Detector, INCA Energy 450 software and Aztec microanalysis software. An operating voltage (EHT) of 20 kV was used, with a probe current of 400 pA to 1 nA and peak count time of 30 s.

6.2. Electron microprobe analysis (EMPA)

Quantitative mineral analyses on PGM were carried out on carbon-coated, polished petrographic thin sections (n=9) using an automated four-spectrometer Cameca Camebax MBX electron microprobe by wavelength-dispersive X-ray analysis (WDX) at the Department of Earth Sciences, Carleton

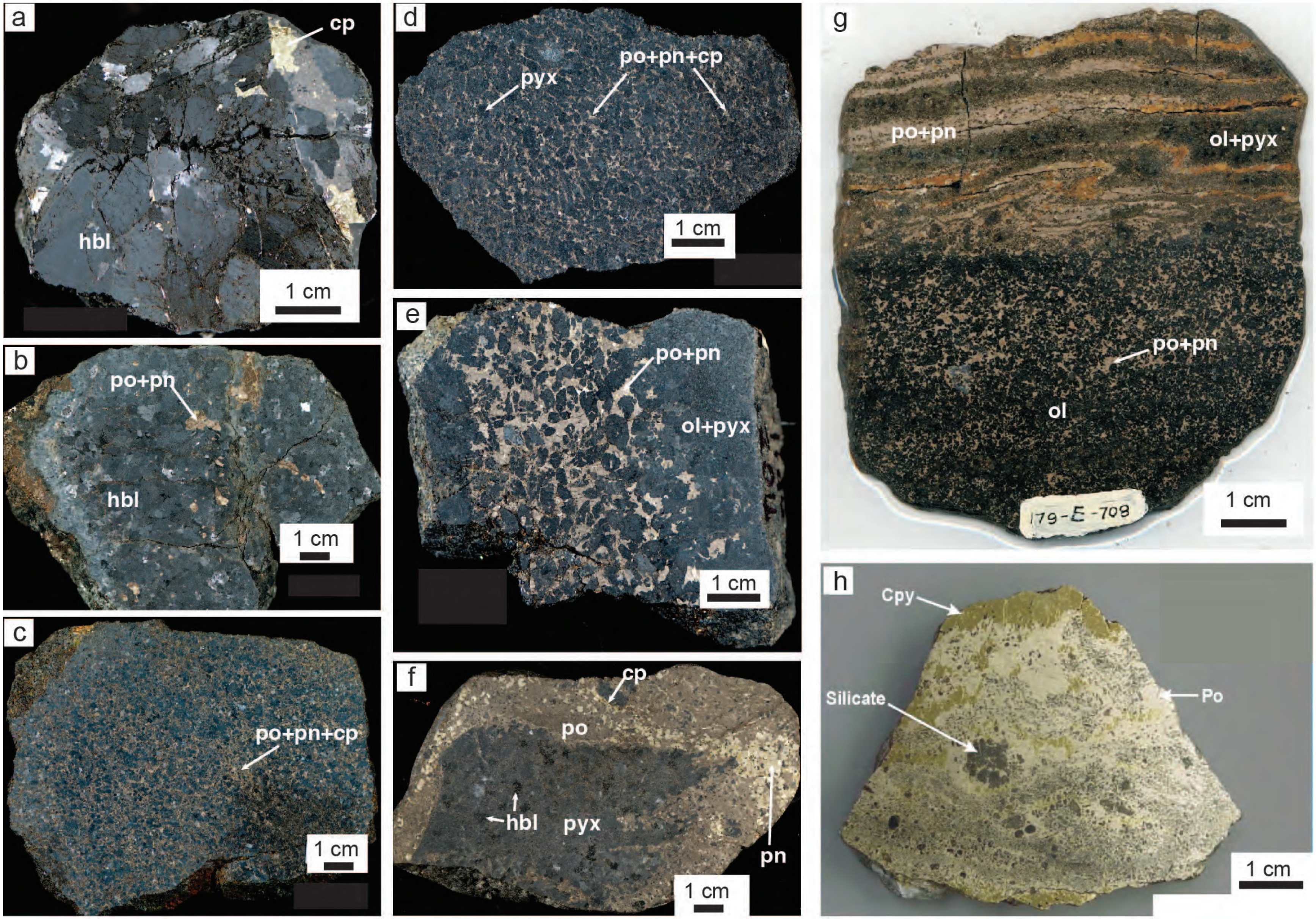

Fig. 4. Photographs of samples showing the range of mineralization types found in the Giant Mascot intrusion. **a)** 71-EI-624: hornblendite with chalcopyrite veins. **b)** 71-EI-622: disseminated pyrrhotite and pentlandite within hornblendite. **c)** 11AV-200: weakly net-textured pyrrhotite, pentlandite and chalcopyrite in pyroxenite. **d)** 11AV-201: moderately net-textured pyrrhotite, pentlandite and chalcopyrite in pyroxenite. **e)** 11AV-204: strongly net-textured pyrrhotite and pentlandite in peridotite. **f)** 71-EI-659: massive pyrrhotite, pentlandite and minor chalcopyrite in hornblende pyroxenite. **g)** 179-E-709: folded bands of disseminated pyrrhotite, pentlandite and olivine-rich peridotite at the contact with dunite. **h)** RHP01-076: massive pyrrhotite containing chalcopyrite veins and a rounded silicate inclusion. Mineral abbreviations: po, pyrrhotite; pn, pentlandite; cp/cpy, chalcopyrite; hbl, hornblende; pyx, pyroxene; ol, olivine.

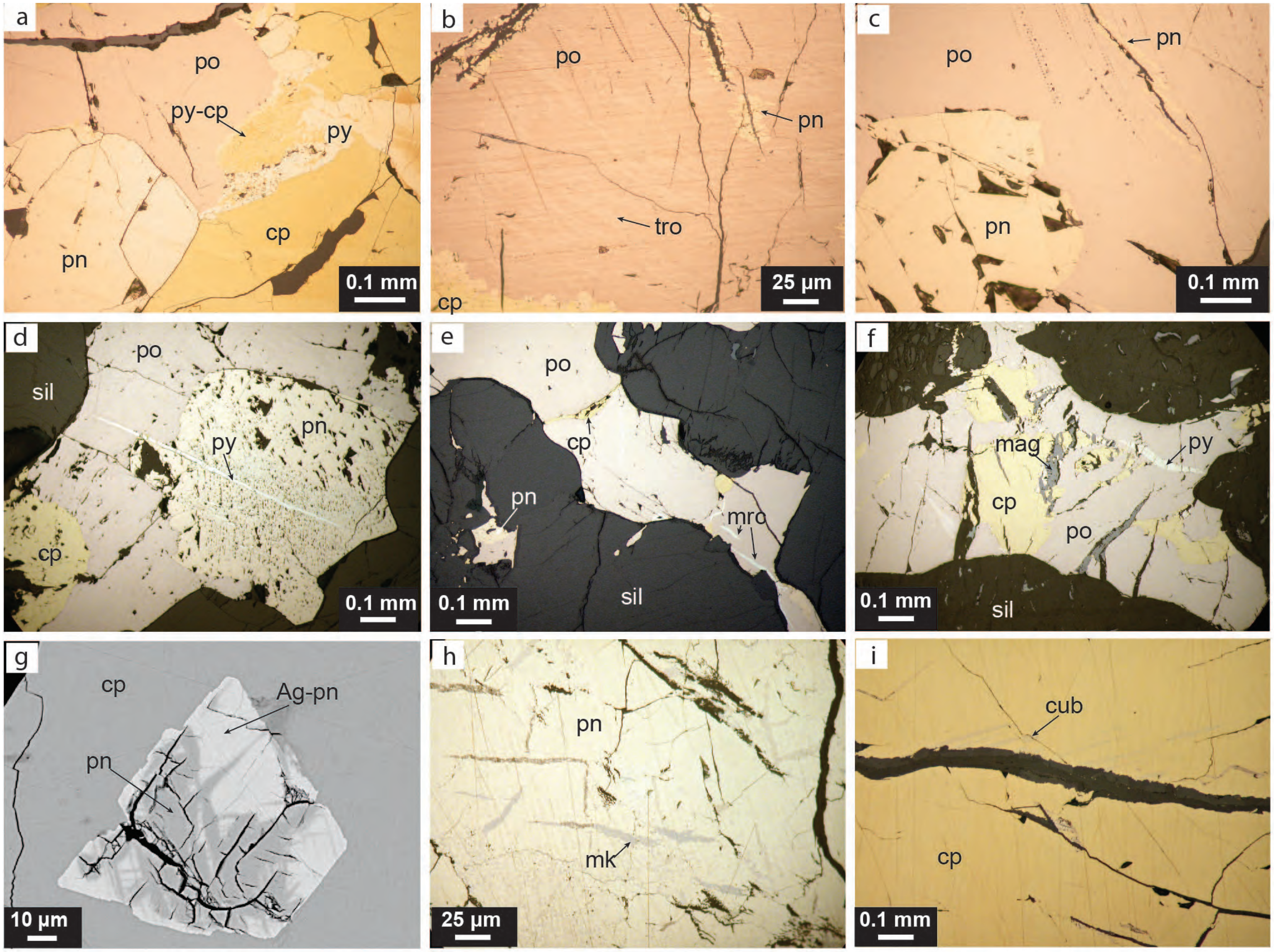

Fig. 5. Photomicrographs and backscatter electron (BSE) images of sulphide textures in the Giant Mascot intrusion. **a)** 71-EI-636: blocky pentlandite, massive chalcopyrite and pyrite, and symplectic chalcopyrite-pyrite hosted by massive pyrrhotite. **b)** 12MMA-5-8-5A: troilite exsolution lamellae, pentlandite flames and minor chalcopyrite in massive pyrrhotite. **c)** 71-EI-615C: two forms of pentlandite, blocky grains and exsolution lamellae, hosted by massive pyrrhotite. **d)** 71-EI-634: blocky pentlandite, pyrite-pentlandite intergrowths and chalcopyrite in pyrrhotite, with a pyrite vein cutting the intergrowths and pyrrhotite. **e)** 71-EI-636: net-textured pyrrhotite containing chalcopyrite veins and marcasite flames. **f)** M29-21: pyrrhotite and chalcopyrite containing veins of pyrite and magnetite. **g)** 71-EI-624A: argentopentlandite with pentlandite exsolution lamellae hosted by chalcopyrite (BSE). **h)** 12MMA-5-8-5A: massive pentlandite containing mackinawite [$(Fe,Ni)_{1+x}S$] exsolution lamellae. **i)** RHP01-078: massive chalcopyrite containing cubanite exsolution lamellae. Mineral abbreviations: po, pyrrhotite; pn, pentlandite; Ag-pn, argentopentlandite; cp, chalcopyrite; py, pyrite; tro, troilite; mrc, marcasite; mag, magnetite; mk, mackinawite; cub, cubanite; sil, silicate.

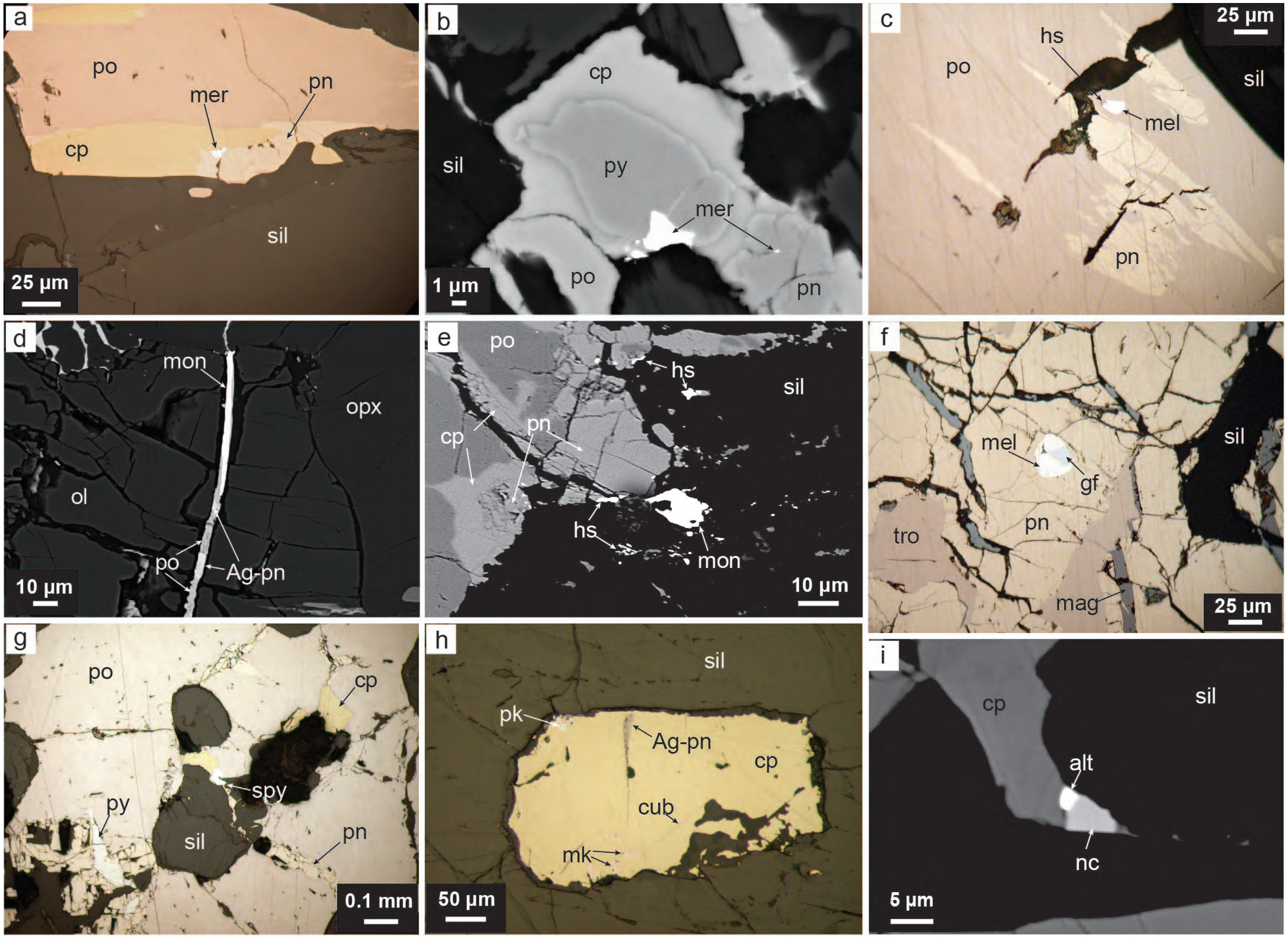

Fig. 6. Photomicrographs and backscatter electron (BSE) images of platinum-group and precious-metal minerals in Giant Mascot ores. **a)** 71-EI-615A: bright white anhedral merenskyite hosted by pentlandite at the grain boundary of chalcopyrite, both within pyrrhotite. **b)** 179-E-847: merenskyite hosted in pyrite and chalcopyrite, and associated with pyrrhotite and pentlandite (BSE); **c)** 12MMA-5-8-5A: bright white, anhedral palladian melonite tipped by hessite and fully enclosed in pyrrhotite proximal to pentlandite flames. **d)** RHP01-078: moncheite hosted by a chalcopyrite and argentopentlandite compound vein within fractured olivine (BSE). **e)** RHP01-152: moncheite fully enclosed by silicates, a smaller elongate moncheite at the boundary of pentlandite and silicate, and small satellite grains of hessite fully enclosed in silicates and along silicate-sulphide boundaries (BSE). **f)** 12MMA-5-8-5A: bright white, anhedral palladian melonite intergrown with euhedral gersdorffite, hosted by pentlandite containing magnetite veins, and surrounded by troilite. **g)** 71-EI-657: bright white sperrylite at the boundary of chalcopyrite and pyrrhotite, blocky pentlandite and pentlandite flames proximal to pyrite. **h)** RHP01-109: cream-coloured parkerite enclosed in chalcopyrite containing argentopentlandite, mackinawite and cubanite flames. **i)** RHP01-109: altaite in contact with chalcopyrite, nickeline, and silicates (BSE). Mineral abbreviations as in Figure 5 except: mer, merenskyite; mel, palladian melonite; mon, moncheite; hs, hessite; spy, sperrylite; pk, parkerite; alt, altaite; nc, nickeline; ger, gersdorffite; ol, olivine; opx, orthopyroxene.

University, Ottawa. Raw X-ray data were converted to elemental weight percent by the Cameca PAP matrix correction program. Tellurides and PMM were analyzed using a 20 keV accelerating voltage, 35 nA beam current, 2 μm diameter beam, and counting time of 10 seconds or 40,000 accumulated counts.

7. Results

7.1. PGM: Bismuthotellurides, bismuthides, and arsenides

Samples initially chosen for PGM analysis included those with high PGE abundances in whole rocks (> 1 ppm total PGE; M.J. Manor, unpublished data). Most of the PGM identified are tellurides or bismuthotellurides, predominantly merenskyite ($PdTe_2$), moncheite ($PtTe_2$) and melonite ($NiTe_2$) (Tables 1, 2). The PGM are most commonly associated with base metal sulphides (BMS), predominantly pentlandite (Figs. 6b, c; 7c). In addition, PGM may be either fully enclosed in sulphide, at sulphide-sulphide or sulphide-silicate interfaces, in sulphide veins in other sulphides or silicates, or as satellite grains in fractured silicates.

Merenskyite (3-23 μm) occurs in three compositional varieties: Pt-rich, Ni-rich, and near-stoichiometric merenskyite (28 total grains). Merenskyite grains are invariably associated with BMS (pyrrhotite, pentlandite, chalcopyrite, pyrite, troilite) and are either fully enclosed by sulphides or occur at sulphide-sulphide or sulphide-silicate interfaces (Figs. 6a, b).

Moncheite (2-56 μm) is the predominant telluride (30 total grains). Palladian moncheite has an average composition of $[(Pt_{0.35}Pd_{0.31})(Te_{1.87}Bi_{0.14})]$ (n=3). Grains are fully enclosed in pyrrhotite, pentlandite, chalcopyrite or silicate, or occur at sulphide-sulphide or sulphide-silicate interfaces. Moncheite is also common as inclusions in fracture-filling compound veins of chalcopyrite and argentopentlandite, with rare examples of < 160 μm long stringers (Figs. 6d, e).

A nickel-bearing telluride, palladian melonite (< 30 μm), has an average composition of $[(Ni_{0.84}Pd_{0.23})(Te_{1.87}Bi_{0.13})]$ (n=11). Grains of Pd-melonite invariably form inclusions in pyrrhotite, pentlandite and troilite (Figs. 6c, f).

Froodite ($PdBi_2$) is comparatively rare, and occurs as a satellite grain enclosed in silicate, but in contact with chalcopyrite. Sperrylite (< 50 μm), the only arsenide observed, has a nearly stoichiometric composition $[Pt_{0.80}As_{2.00}]$ (n=2). It is found either fully enclosed by chalcopyrite or at chalcopyrite-pyrrhotite-silicate interfaces (Fig. 6g).

7.2 Precious-metal minerals (PMM)

Hessite (Ag_2Te) is the most common PMM (> 75 grains) and occurs in cubanite, chalcopyrite, pentlandite, and silicate, at sulphide-sulphide or sulphide-silicate interfaces, or is intergrown with moncheite. It is most commonly found as satellite grains in fractures in silicate minerals (Figs. 6c, e). Hessite is typically in samples containing the highest concentrations of PGE. Rare altaite (PbTe) typically is associated with chalcopyrite (Fig. 6i). A single grain of hedleyite ($Bi_{2+x}Te_{1-x}$) was observed in silicate. Tellurobismuthite (Bi_2Te_3) is either fully enclosed by, or at the contacts between, pentlandite and pyrrhotite.

Parkerite ($Ni_3Bi_2S_2$) is a rare sulphobismuthide mineral. It is associated with chalcopyrite, locally at chalcopyrite-silicate interfaces (Fig. 6h). One grain of hollingworthite (RhAsS) as a composite grain with Ni-merenskyite was observed in a compound vein of chalcopyrite and pentlandite. Native Te and Bi grains are in pyrrhotite and pentlandite and at sulphide-silicate interfaces.

8. Discussion

Bismuthotellurides in the Giant Mascot Ni-Cu-PGE deposit exhibit a bimodal distribution between the $PtTe_2$ – $PdTe_2$ and $NiTe_2$ – $PdTe_2$ solid solution joins (Fig. 7a), forming a moncheite-merenskyite group and a merenskyite-melonite group. Analyses from the first group lie along the $PtTe_2$ – $PdTe_2$ join and most grains belong to the moncheite-merenskyite series. Tellurium contents vary substantially, such that Pt-rich merenskyite grains fall in the moncheite field, and all solid solutions are relatively Ni-poor. The second group on the $NiTe_2$ – $PdTe_2$ join contains the merenskyite-melonite series. Merenskyite is more abundant in this group compared to the $PtTe_2$ – $PdTe_2$ join, and relatively Pt-poor. The range of compositions is greater, and includes both Ni-rich merenskyite and palladian melonite. This bimodal distribution of Pt-Pd-Ni bismuthotellurides is also observed in sulphide ores from the Wellgreen Ni-Cu-PGE deposit in the northern Canadian Cordillera (Yukon) part of the Wrangellia large igneous province (Triassic; Greene et al., 2009). There, significant abundances of Sb- and As-rich PGM were reported by Barkov et al. (2002), whereas rare examples of arsenides are observed in the Giant Mascot intrusion (i.e., sperrylite). Platinum-group minerals in the Giant Mascot intrusion share features with minerals in the Aguablanca Ni-Cu-PGE deposit in Spain, notably the presence of palladian melonite-merenskyite-moncheite solid solutions. However, the Aguablanca ores contain higher abundances of Sb and Bi, allowing for the crystallization of the michnerite (PdBiTe) and the Sb-rich end-member testibiopalladite [Pd(Sb,Bi)Te] (Piña et al., 2008).

Precious-metal minerals in the Giant Mascot sulphide ores are rich in Ag, Pb, Ni, As, Bi, Te and S, but lack PGE. The presence of these elements, associated with chalcopyrite and located within fractures in primary silicates (i.e., olivine and pyroxene), is consistent with late-stage magmatic mobilization of a residual Cu- and semimetal-rich melt (Helmy, 2005). The residual melts from which the PMM crystallized were likely rich in base and precious metals relative to the original sulphide melt that crystallized Pt-, Pd- and Ni-bearing bismuthotellurides.

The textural characteristics of PGM in the Giant Mascot intrusion indicate two possible mechanisms of formation: 1) exsolution from primary BMS minerals at relatively high temperatures, either along crystallographic interfaces, at sulphide compositional boundaries, or by nucleation along fractures in sulphides (Figs. 7b, c; e.g., Cabri and Laflamme, 1976); or 2) formation of an immiscible PGE- and semimetal-rich melt for which components are incompatible in monosulphide solid solution (mss) and intermediate solid solution (iss) (650-250°C; Holwell and McDonald, 2010), the solid precursors to pyrrhotite and chalcopyrite, respectively. Locally abundant fractures filled by chalcopyrite and Pt-rich bismuthotellurides are evidence for relatively late-stage mobilization of Cu-rich residual sulphide melts. The predominance of various telluride minerals in the Giant Mascot intrusion (Fig. 7b) indicates a relatively high Te concentration in the parental magma. Tellurium may have been derived either directly from the arc mantle source or was introduced via crustal assimilation of metapelitic lithologies in the Settler schist (e.g., Afifi et al.,

Table 1. SEM energy-dispersive spectral analyses of platinum-group and precious-metal minerals from the Giant Mascot Ni-Cu-PGE deposit. SEM EDS analyses normalized to 100%.

				wt.%										
Sample name	Mineralization[1]	Host mineral[2]	Host rock[3]	Pt	Pd	Bi	Te	Ag	Ni	S	Pb	Rh	As	Mineral Name
3550 East Portal Dump														
RHP01-152-5-1	NT/HPGE	po/pn	ol websterite	21.0	9.9	10.9	58.3							merenskyite
RHP01-152-8-1	NT/HPGE	cp/sil	ol websterite	14.9	12.1	19.2	53.8							moncheite
RHP01-152-20-1	NT/HPGE	po/cp	ol websterite	30.4	8.3		61.3							Pt-merenskyite
RHP01-152-22-1	NT/HPGE	sil	ol websterite	33.0	4.4	8.8	53.8							moncheite
RHP01-152-22-2	NT/HPGE	sil	ol websterite				36.4	63.6						hessite
RHP01-152-22-3	NT/HPGE	sil	ol websterite				36.4	63.6						hessite
RHP01-152-22-4	NT/HPGE	cp/sil	ol websterite				36.4	63.6						hessite
RHP01-152-22-5	NT/HPGE	pn	ol websterite				36.4	63.6						hessite
RHP01-152-23-1	NT/HPGE	sil	ol websterite				37.4	62.6						hessite
RHP01-152-23-2	NT/HPGE	pn	ol websterite				37.4	62.6						hessite
RHP01-152-23-3	NT/HPGE	po	ol websterite	41.9			58.1							moncheite
RHP01-152-24-1	NT/HPGE	po/pn/sil	ol websterite	41.7			56.8	1.6						moncheite
RHP01-152-24-2	NT/HPGE	po/pn/sil	ol websterite	41.7			56.8	1.6						moncheite
RHP01-152-24-3	NT/HPGE	po/pn/sil	ol websterite	41.7			56.8	1.6						moncheite
RHP01-152-25-1	NT/HPGE	pn	ol websterite	10.6	16.8		72.6							merenskyite
RHP01-152-27-1	NT/HPGE	pn	ol websterite	22.8	7.1	6.4	63.8							moncheite
RHP01-152-28-1	NT/HPGE	pn/po	ol websterite	20.4	12.6		67.0							moncheite
RHP01-152-28-2	NT/HPGE	pn/po	ol websterite	20.4	12.6		67.0							moncheite
RHP01-152-28-3	NT/HPGE	pn/po	ol websterite	20.4	12.6		67.0							moncheite
12MMA-5-8-5A-1	CD	pn	lherzolite		12.5		87.5							merenskyite
12MMA-5-8-5A-2	CD	po	lherzolite		7.7	27.1	65.2							tellurobismuthite
RHP01-078-1	CD/HPGE	cp	hbl harzburgite	20.9	11.1		68.0							moncheite
RHP01-078-2	CD/HPGE	pn/po	hbl harzburgite		14.3		85.7							merenskyite
RHP01-078-3-1	CD/HPGE	cp	hbl harzburgite	29.0			71.0							moncheite
RHP01-078-4	CD/HPGE	Ag-pn/po	hbl harzburgite	28.3	9.9		61.8							moncheite
RHP01-078-5	CD/HPGE	cp	hbl harzburgite	17.1	9.4		65.9	7.6						moncheite
RHP01-078-6	CD/HPGE	pn	hbl harzburgite	19.7	12.7		67.6							moncheite
RHP01-078-7	CD/HPGE	cp	hbl harzburgite	9.8			63.7	26.6						moncheite
RHP01-078-8	CD/HPGE	cp/pn	hbl harzburgite	14.0	12.9		73.1							moncheite

Table 1. cont'd.

RHP01-078-9-1	CD/HPGE	pn/sil	hbl harzburgite				36.8	63.2				hessite
RHP01-078-9-2	CD/HPGE	pn/sil	hbl harzburgite	10.9	11.3		57.1	16.8				moncheite
RHP01-078-10	CD/HPGE	cp	hbl harzburgite		14.2		71.7	14.1				merenskyite
RHP01-078-11	CD/HPGE	pn/cp	hbl harzburgite	18.3	13.5		68.3					moncheite
RHP01-078-12	CD/HPGE	cp	hbl harzburgite	28.4	9.7		61.9					moncheite
1600 orebody												
179-E-410-1-1	CD/HPGE	pn	lherzolite		10.9	7.8	81.4					merenskyite
179-E-410-5-1	CD/HPGE	po	lherzolite		5.1	4.1	90.7					unknown
179-E-410-5-2	CD/HPGE	po	lherzolite		3.2	26.7	70.1					merenskyite
179-E-410-5-3	CD/HPGE	pn	lherzolite		4.7	8.4	86.9					unknown
179-E-410-5-4	CD/HPGE	pn	lherzolite		3.4	40.2	56.4					tellurobismuthite
179-E-410-6-1	CD/HPGE	pn	lherzolite		5.3	5.5	89.2					unknown
179-E-410-12-1	CD/HPGE	pn	lherzolite		3.3	23.3	73.4					merenskyite
179-E-410-13-1	CD/HPGE	pn/po	lherzolite		4.8	29.5	65.7					tellurobismuthite
179-E-410-14-1	CD/HPGE	po	lherzolite		1.7	40.1	58.1					tellurobismuthite
179-E-410-15-1	CD/HPGE	po	lherzolite		6.6	46.7	46.7					tellurobismuthite
4600 orebody												
M29-21-3-1	NT/SM	pn	harzburgite		2.0		98.0					tellurium
M29-21-6-1	NT/SM	pn/po	harzburgite		3.4		96.6					tellurium
M29-21-9-1	NT/SM	pn/po	harzburgite		2.8		97.2					tellurium
M29-21-12-1	NT/SM	pn	harzburgite		1.5		98.5					tellurium
Mill Site Dump												
RHP01-109-2-1	D	cp	orthopyroxenite			87.1			10.6	2.2		parkerite
RHP01-109-2-2	D	cp	orthopyroxenite			87.1			10.6	2.2		parkerite
RHP01-109-2-3	D	cp	orthopyroxenite				44.3	55.7				hessite
RHP01-109-2-4	D	cp	orthopyroxenite				44.3	55.7				hessite
RHP01-109-3-1	D	cp	orthopyroxenite				26.2				73.8	altaite
RHP01-109-6-1	D	cp	orthopyroxenite				41.7	58.3				hessite
RHP01-109-6-3	D	cp/cub	orthopyroxenite					20.0			80.0	altaite
RHP01-109-6-5	D	cub	orthopyroxenite				45.6	54.4				hessite
RHP01-109-6-6	D	cp	orthopyroxenite				26.8	6.2			67.0	altaite
RHP01-109-6-7	D	cp	orthopyroxenite				23.3				76.7	altaite
RHP01-109-7-1	D	cp/nc	orthopyroxenite				27.9				72.1	altaite
RHP01-109-8-1	D	cp/sil	orthopyroxenite		11.7	88.3						froodite
RHP01-109-8-2	D	sil	orthopyroxenite			90.1	9.9					hedleyite

Table 1. cont'd.

Climax orebody											
71-EI-615A-1	NT	pn/cp/sil	websterite	16.9		83.1					merenskyite
71-EI-615A-2	NT	pn	websterite	16.9		83.1					merenskyite
71-EI-615A-3	NT	pn/cp	websterite	23.9		76.1					merenskyite
71-EI-615A-4	NT	pn	websterite	21.1		78.9					merenskyite
71-EI-615A-5	NT	po	websterite	16.8	10.1	66.0	7.2				Ni-merenskyite
71-EI-615A-6-1	NT	pn	websterite	26.4	11.9	61.8					merenskyite
71-EI-615A-6-2	NT	cp	websterite	26.4	11.9	61.8					merenskyite
71-EI-615A-7-1	NT	pn/cp/sil	websterite	17.8	6.0	69.2	7.1				Ni-merenskyite
71-EI-615A-7-2	NT	cp	websterite	17.8	6.0	69.2	7.1				Ni-merenskyite
71-EI-615A-7-3	NT	cp/mer	websterite					22.4	36.7	40.8	hollingworthite
71-EI-615A-8	NT	pn	websterite	23.1		76.9					merenskyite
71-EI-615A-9	NT	cp/sil	websterite	22.3		77.7					merenskyite
71-EI-615A-10	NT	pn	websterite	13.4		86.6					merenskyite
71-EI-615A-11	NT	pn/sil	websterite	15.1		84.9					merenskyite

[1]NT= Net-textured sulphide, SM = semi-massive sulphide, CD = coarse disseminated sulphide, D = disseminated sulphide, HPGE = high-PGE mineralization (> 1.5 ppm total PGE). [2]po = pyrrhotite, pn = pentlandite, cp = chalcopyrite, cub = cubanite, py = pyrite, nc = nickeline, mer = merenskyite, sil = silicate mineral. [3]ol = olivine, hbl = hornblende.

Table 2. Electron-microprobe analyses of platinum-group and precious-metal minerals from the Giant Mascot Ni-Cu-PGE deposit. Raw X-ray data converted to wt.% by the Cameca PAP matrix correction program (Carlton University, Ottawa).

Sample	Mineralization[1]	Host mineral[2]	Host rock[3]	Pt	Pd	Bi	Te	Ag	Ni	S	As	Sb	Mineral Name
3550 East Portal Dump													
RHP01-152-43	NT/HPGE	po	ol websterite	14.8	7.5	8.2	62.0		5.7			0.5	Pd-moncheite
RHP01-152-47	NT/HPGE	py	ol websterite	15.0	12.5	7.8	59.5		2.7			0.5	Pt-merenskyite
RHP01-152-52	NT/HPGE	cp	ol websterite	28.6	0.5	0.1	0.2			23.5	36.2		sperrylite
RHP01-152-57	NT/HPGE	py/cp	ol websterite	22.0	10.6	5.5	60.6		1.3			0.5	Pd-moncheite
RHP01-152-58	NT/HPGE	py/cp	ol websterite	15.3	11.9	6.2	61.7		3.1			0.5	Pt-merenskyite
RHP01-152-59	NT/HPGE	pn	ol websterite	15.1	6.6	7.6	57.6	0.7	5.4	0.1		0.5	Pd-moncheite
RHP01-109-88	D	cp	orthopyroxenite			62.8			27.0	10.1		0.8	parkerite
12MMA-5-8-5A-71	CD	tr	lherzolite		11.0	12.0	64.9		10.6			0.5	Pd-melonite
12MMA-5-8-5A-75	CD	po	lherzolite		10.9	11.9	65.2		10.8			0.4	Pd-melonite
12MMA-5-8-5A-76	CD	po	lherzolite		1.7	1.3	39.3	53.8	1.6			0.5	hessite
12MMA-5-8-5A-81	CD	pn	lherzolite		4.4	11.5	67.4		15.7			0.5	Pd-melonite
12MMA-5-8-5A-83	CD	pn	lherzolite		2.6	9.1	68.4		16.8			0.5	Pd-melonite
12MMA-5-8-5A-84	CD	pn	lherzolite		10.6	12.3	64.4		11.3			0.5	Pd-melonite
12MMA-5-8-5A-91	CD	po/tr	lherzolite		9.0	8.5	65.9		11.9	4.1		0.3	Ni-merenskyite
12MMA-5-8-5A-92	CD		lherzolite		9.4	11.6	66.5		12.1			0.6	Pd-melonite
4600 orebody													
M29-21-69	NT/SM	pn	harzburgite	0.1	1.4	0.1	77.2		19.4			0.2	Pd-melonite
M29-21-71	NT/SM	pn	harzburgite	0.1	1.9		70.2		22.9	4.1		0.1	Pd-melonite
Chinaman orebody													
71-EI-632-60	CD	pn	orthopyroxenite				37.8	61.0	0.9	0.4		0.2	hessite
71-EI-632-64	CD	pn	orthopyroxenite		4.9	0.8	79.4		16.0			0.6	Pd-melonite
71-EI-632-68	CD	pn	orthopyroxenite				35.4	61.4		0.4		0.2	hessite
71-E1-657-23	NT	po/pn	hbl orthopyroxenite	55.1					0.1	0.9	43.0		sperrylite
Climax orebody													
71-EI-615A-23	NT	cp	websterite		19.5	5.7	59.6		7.0	3.3		0.2	merenskyite
71-EI-615A-31	NT	pn/cp	websterite		18.0	9.5	65.5		6.8	0.2		0.5	Ni-merenskyite
1600 orebody													
179-E-847-65	SM/HPGE	pn/po	hbl lherzolite	2.0	10.9	7.7	67.0		10.4			0.5	Pd-melonite
179-E-847-66	SM/HPGE	cp	hbl lherzolite		19.5	13.3	58.1		4.1			0.5	merenskyite
179-E-410-42	CD/HPGE	po	lherzolite		10.5	9.4	68.5		10.3			0.5	Pd-melonite
179-E-410-51	CD/HPGE	po	lherzolite	0.3	12.6	12.5	63.1		8.8	0.3		0.4	Ni-merenskyite

[1]NT= Net-textured sulphide, SM = semi-massive sulphide, CD = coarse disseminated sulphide, D = disseminated sulphide, HPGE = high-PGE mineralization (> 1.5 ppm total PGE). [2]po = pyrrhotite, pn = pentlandite, cp = chalcopyrite, py = pyrite, tr = troilite. [3]ol = olivine, hbl = hornblende.

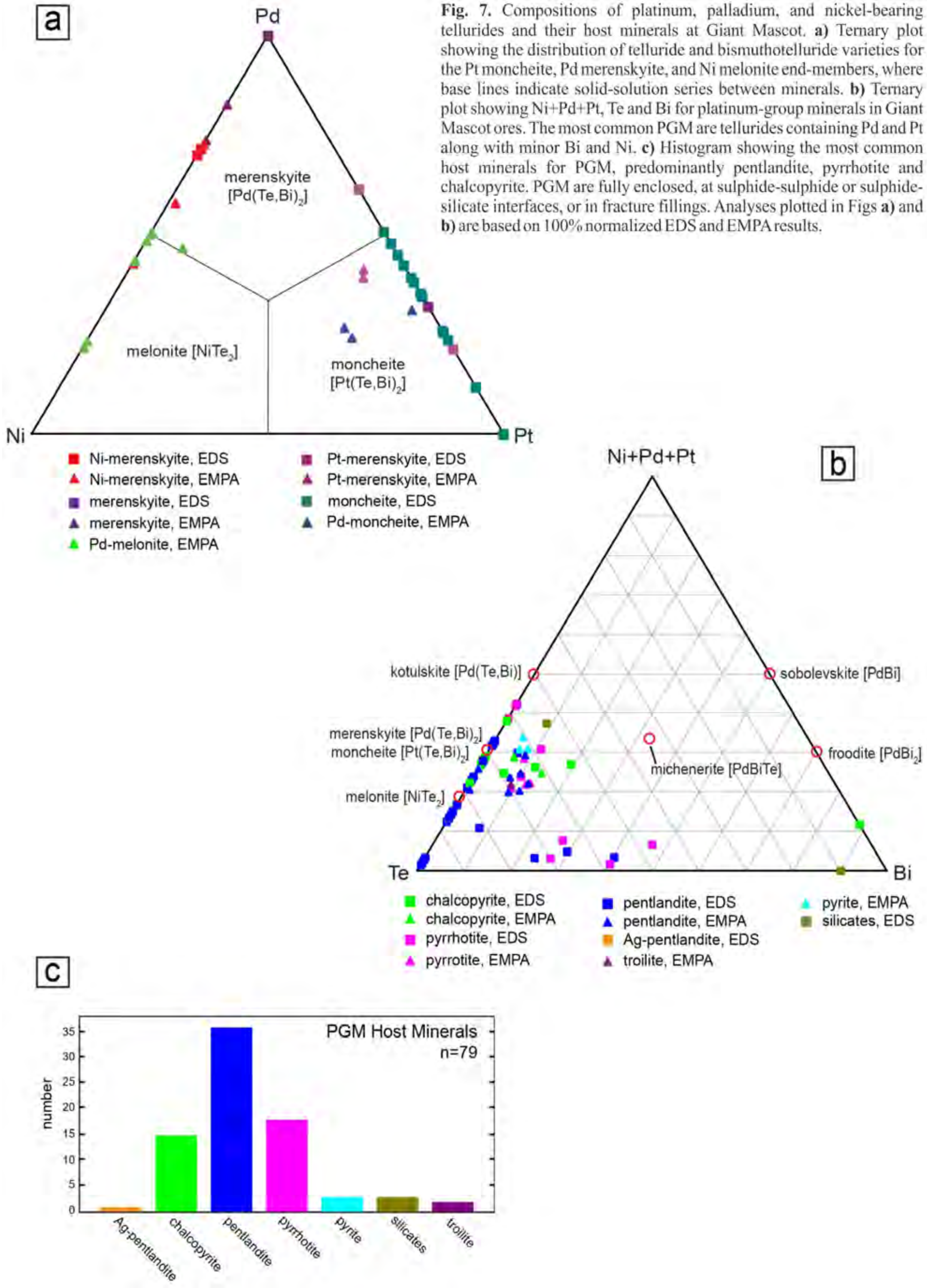

Fig. 7. Compositions of platinum, palladium, and nickel-bearing tellurides and their host minerals at Giant Mascot. **a)** Ternary plot showing the distribution of telluride and bismuthotelluride varieties for the Pt moncheite, Pd merenskyite, and Ni melonite end-members, where base lines indicate solid-solution series between minerals. **b)** Ternary plot showing Ni+Pd+Pt, Te and Bi for platinum-group minerals in Giant Mascot ores. The most common PGM are tellurides containing Pd and Pt along with minor Bi and Ni. **c)** Histogram showing the most common host minerals for PGM, predominantly pentlandite, pyrrhotite and chalcopyrite. PGM are fully enclosed, at sulphide-sulphide or sulphide-silicate interfaces, or in fracture fillings. Analyses plotted in Figs **a)** and **b)** are based on 100% normalized EDS and EMPA results.

1988a; Helmy, 2004). The limited substitution of Sb and Bi for Te in PGM is further evidence for an orthomagmatic origin (e.g., Helmy, 2005).

The textures of sulphide minerals in the Giant Mascot intrusion reveal a multistage evolution of the primary magmatic sulphide melt during cooling and subsequent crystallization. Strained and fractured sulphide and silicate minerals appear consistent with significant subsolidus compaction during the formation of the ores and cumulate sequences. Late-stage magmatic remobilization involving iss and residual semimetal-rich melts resulted in the formation of chalcopyrite veins. Low-temperature minerals, such as troilite, violarite and mackinawite, indicate significant subsolidus reequilibration of the sulphides during cooling.

9. Current and future research

Ongoing research on the Giant Mascot Ni-Cu-PGE deposit and ultramafic-mafic intrusion aims to develop a paragenetic history of the ultramafic suite and associated sulphides and PGM. Whole-rock PGE and trace element geochemistry is being used to investigate the petrogenesis of the Giant Mascot ultramafic-mafic intrusion. U-Pb and $^{40}Ar/^{39}Ar$ geochronology is being conducted to define age relationships and tectonic setting and increase our knowledge of the formation and processes for orogenic Ni-Cu-PGE ore systems. Sulphur isotope analyses of sulphide minerals in the ultramafic and mafic rocks and Settler schist, combined with electron-probe microanalysis of the nickel contents in olivine, aim to identify a mechanisms for sulphide saturation of the Giant Mascot parental magma(s) and formation of associated Ni-Cu-PGE mineralization.

10. Conclusions

This study reports the first platinum-group minerals identified in the Giant Mascot Ni-Cu-PGE deposit.

1) Platinum-group minerals commonly occur as Pd-, Pt- and Ni-bismuthotellurides hosted by base-metal sulphides, predominantly pentlandite.
2) Textures of sulphides and platinum-group minerals indicate an orthomagmatic origin involving exsolution from base-metal sulphides.
3) Textures of precious-metal minerals indicate late-stage crystallization from residual melts rich in base and precious metals.
4) The predominance of Te-bearing PGM and PMM associated with sulphides indicates a high Te concentration of the parental magma, either derived from the mantle source or assimilated during transport through mid-crustal levels.
5) PGE-enriched sulphides containing identifiable platinum-group minerals in the Giant Mascot intrusion indicate that orogenic Ni-Cu mineralization in the Canadian Cordillera and elsewhere may provide significant targets for economic Ni-Cu-PGE deposits.

Acknowledgments

We thank Dr. Mati Raudsepp, Jenny Lai, Elisabetta Pani, and Edith Czech (UBC), and Patricia Hunt (GSC-Ottawa) for SEM advice and training, and Dr. Ingrid Kjarsgaard for microprobe analytical work on PGM. A tremendous thanks to Corey Wall, Wes Harmon, Alex Colyer, and Lauren Harrison for help with fieldwork in 2012-2013. We also thank Valley Helicopters in Hope for flights to Giant Mascot, and Barrick Gold and Fraser Valley Dirt Riders Association for access to their property. Dr. Jon Scoates and Dr. Michel Houlé generously provided a thorough review of the manuscript at short notice. Editorial comments by Dr. Lawrence Aspler helped improve the manuscript. Funding for this project is provided by Natural Resources Canada through the Geological Survey of Canada's Targeted Geoscience Initiative 4 (TGI-4: 2011-2015) Magmatic-Hydrothermal Nickel-Copper-PGE-Chrome Ore System Project. Additional funding was provided by a SEG Canadian Foundation Graduate Student Research Grant awarded to Matthew Manor in 2013. This is Earth Sciences Sector contribution number 20130343.

References cited

Afifi, A.M., Kelly, C.K., Essene, E.J., 1988a. Phase relations among tellurides, sulphides, and oxides. In: Thermochemical data and calculated equilibria. Economic Geology, 83, 377-395.

Aho, A.E., 1954. Geology and ore deposits of the property of Pacific Nickel Mines near Hope, British Columbia. Unpublished Ph.D. Thesis, University of California Santa Barbara, 158 p.

Aho, A.E., 1956. Geology and genesis of ultrabasic nickel-copper-pyrrhotite deposits at the Pacific Nickel Property, southwestern British Columbia. Economic Geology, 51, 441-481.

Barkov, A.Y., Laflamme, J.H.G., Cabri, L.J., and Martin, R.F., 2002. Platinum-group minerals from the Wellgreen Ni-Cu-PGE deposit, Yukon, Canada. Canadian Mineralogist, 40, 651-669.

Becker, M., de Villiers, J., and Bradshaw, D., 2010. The mineralogy and crystallography of pyrrhotite from selected nickel and PGE ore deposits. Economic Geology, 105, 1025-1037.

Brown, E.H., and McClellan, W.C., 2000. Pluton emplacement by sheeting and vertical ballooning in part of the southeast Coast Plutonic Complex, British Columbia. Geological Society of America Bulletin, 1125, 708-719.

Cabri, L.J., and Laflamme, J.H.G., 1976. The mineralogy of the platinum-group elements from some copper–nickel deposits of the Sudbury area, Ontario. Economic Geology, 71, 1159-1195.

Christopher, P.A., and Robinson, J.W., 1974. Pride of Emory Mine 92H/SW-4. Exploration and Mining in British Columbia 1974, British Columbia Department of Mines and Petroleum Resources, 105-113.

Greene, A.R., Scoates, J.S., Weis, D., and Israel, D., 2009. Geochemistry of Triassic flood basalts from the Yukon (Canada) segment of the accreted Wrangellia oceanic plateau. Lithos, 110, 1-19.

Helmy, H.M., 2004. Cu–Ni–PGE mineralization in the Genina Gharbia mafic–ultramafic intrusion, Eastern Desert, Egypt. Canadian Mineralogist, 42, 351-370.

Helmy, H.A., 2005. Melonite group minerals and other tellurides from three Cu-Ni-PGE prospects, Eastern Desert, Egypt. Ore Geology Reviews, 26, 305-324.

Holwell, D.A., and McDonald, I., 2010. A review of the behaviour of platinum group elements within natural magmatic sulphide ore systems. Platinum Metals Review, 541, 26-36.

Hulbert, L.J., 2001. GIS maps and databases of mafic-ultramafic hosted Ni, Ni-Cu, Cr +/- PGE occurrences and mafic-ultramafic bodies in British Columbia. British Columbia Ministry of Energy and Mines, Geoscience Map 2001-2.

McLeod, J.A., 1975. The Giant Mascot ultramafite and its related ores. Unpublished M.Sc. Thesis, University of British Columbia, 136 p.

Metcalfe, P., McClaren, M., Gabites, J.E., and Houle, J., 2002. Ni-Cu-PGE deposits in the Pacific Nickel Complex, southwestern BC; a profile for magmatic Ni-Cu-PGE mineralization in a transpressional magmatic arc. Exploration and Mining in British Columbia, Ministry of Energy, Mines and Petroleum Resources, pp. 65-80.

Mitrovic, I., 2013. Evolution of the Coast Cascade orogen by tectonic thickening and magmatic loading: the Cretaceous Breakenridge Complex, southwestern British Columbia. Unpublished M.Sc. Thesis, Simon Fraser University, 133 p.

Mota-e-Silva, J., Ferreira Filho, C.F., Bühn, B., and Dantas, E.L., 2011. Geology, petrology and geochemistry of the "Americano do Brasil" layered intrusion, central Brazil, and its Ni-Cu sulphide deposits. Mineralium Deposita, 46, 57-90.

Mota-e-Silva, J., Ferreira Filho, C.F., and Della Giustina, M.E.S., 2013. The Limoeiro deposit: Ni-Cu-PGE sulphide mineralization hosted within an ultramafic tubular magma conduit in the Borborema Province, northeastern Brazil. Economic Geology, 108, 1753-1771.

Muir, J.E., 1971. A preliminary study of the petrology and ore genesis of the Giant Mascot 4600 ore body, Hope, British Columbia. Unpublished M.Sc. Thesis, University of Toronto, 125 p.

Naldrett, A.J., 2004. Magmatic sulphide deposits: geology, geochemistry and exploration. Springer, Berlin, 727 p.

Nixon, G.T., Hanmack, J.L., Ash, C.H., Cabri, L.J., Case, G., Connelly, J.N., Heanmn, L.M., LaFlamme J.H.G., Nuttall, C., Paterson, W.P.E., and Wang, R.H., 1997. Geology and platinum-group-element mineralization of Alaskan-type ultramafic-mafic complexes in British Columbia. British Columbia Ministry of Employment and Investment, British Columbia Geological Survey Bulletin 93, 142 p.

Nixon, G.T., 2003. Use of spinel in mineral exploration: the enigmatic Giant Mascot Ni-Cu-PGE deposit - possible ties to Wrangellia and metallogenic significance. In: Geological Fieldwork 2002, British Columbia Ministry of Energy, Mines and Petroleum Resources, British Columbia Geological Survey Paper 2003-1, pp. 115-128.

Paktunc, A.D., 1989. Petrology of the St. Stephen Intrusion and the genesis of related nickel-copper sulphide deposits. Economic Geology, 84, 817-840.

Pigage, L.C., 1973. Metamorphism southwest of Yale, British Columbia. Unpublished M.Sc. Thesis, University of British Columbia, 114 p.

Piña, R., Gervilla, F., Ortega, L., and Lunar, R., 2008. Mineralogy and geochemistry of platinum-group elements in the Aguablanca Ni-Cu deposit (SW Spain). Mineralogy and Petrology, 92, 259-282.

Pinsent, R.H., 2002. Ni-Cu-PGE potential of the Giant Mascot and Cogburn ultramafic-mafic bodies, Harrison-Hope area, southwestern British Columbia 092H. In: Geological Fieldwork 2001, British Columbia Ministry of Energy, Mines and Petroleum Resources, British Columbia Geological Survey Paper 2002-1, pp. 211-236.

Reiners, P.W., Ehlers, T.A., Garver, J.I., Mitchell, S-G., Montgomery, D.R., Vance, J.A., and Nicolescu, S., 2002. Late Miocene exhumation and uplift of the Washington Cascade Range. Geology, 309, 767-770.

Richards, T.A., 1971. Plutonic rocks between Hope, B.C. and the 49th Parallel. Unpublished Ph.D. Thesis, University of British Columbia, 193 p.

Richards, T.A., and McTaggart, K.C., 1976. Granitic rocks of the southern Coast Plutonic Complex and northern Cascades of British Columbia. Geological Society of America Bulletin, 87, 935-953.

Ripley, E.M., 2010. Chapter 24 - A new perspective on exploration for magmatic sulphide-rich Ni-Cu-PGE deposits. Economic Geology Special Publication, 15, 437-450.

Sappin, A.A., Constantin, M., and Clark, T., 2012. Petrology of mafic and ultramafic intrusions from the Portneuf-Mauricie Domain, Grenville Province, Canada: implications for plutonic complexes in a Proterozoic island arc. Lithos, 154, 277-295.

Stephens, F.H., 1959. New nickel production in British Columbia. Western Miner and Oil Review (August), 28-33.

Vining, M.R., 1977. The Spuzzum pluton northwest of Hope, B.C. Unpublished M.Sc. Thesis, University of British Columbia, 159 p.

Mineralogy of sulphide, arsenide, and platinum group minerals from the DJ/DB Zone of the Turnagain Alaskan-type ultramafic intrusion, north-central British Columbia

Sarah Jackson-Brown[1, a], James S. Scoates[1], Graham T. Nixon[2], and Doreen E. Ames[3]

[1] Department of Earth, Ocean and Atmospheric Sciences, 2020 - 2207 Main Mall, University of British Columbia, Vancouver, BC, V6T 1Z4
[2] British Columbia Geological Survey, Ministry of Energy and Mines, Victoria, BC, V8W 9N3
[3] Geological Survey of Canada, Central Canada Division, 750 - 601 Booth St., Ottawa, ON, K1A 0E8
[a] corresponding author: sjackson@eos.ubc.ca

Recommended citation: Jackson-Brown, S., Scoates, J.S., Nixon, G.T., and Ames, D.E., 2014. Mineralogy of sulphide, arsenide, and platinum group minerals from the DJ/DB Zone of the Turnagain Alaskan-type ultramafic intrusion, north-central British Columbia. In: Geological Fieldwork 2013, British Columbia Ministry of Energy and Mines, British Columbia Geological Survey Paper 2014-1, pp. 157-168.

Abstract

The Turnagain intrusion (ca. 190 Ma) is an Alaskan-type, ultramafic body emplaced in an orogenic setting that is host to a significant nickel-cobalt resource (865 Mt at 0.21% per tonne Ni and 0.013% per tonne Co). The 24 km^2 intrusion comprises a suite of ultramafic rocks including dunite, wehrlite, clinopyroxenite, and hornblendite with minor late-stage dioritic intrusions and inclusions of hornfelsed country rocks. Soil geochemistry and drilling led to the discovery of an area of copper and platinum group element (PGE) enrichment in a previously underexplored area of the intrusion, the DJ/DB zone, 2.5 km northwest of the nickel resource. We conducted a detailed mineralogical investigation to assess the range of compositions and textures of platinum group minerals (PGM) and associated sulphides in the DJ/DB zone. Mineralized clinopyroxenites and hornblendites, typically with less than 5 vol.% sulphide, contain mainly chalcopyrite and pyrrhotite with minor pyrite and pentlandite, and host a variety of arsenides, arsenic-antimony sulphides, and PGM. Arsenic and antimony-bearing phases are typically related to chalcopyrite and include cobaltite ($CoAsS$), nickeline ($NiAs$), gersdorffite ($NiAsS$), ullmannite ($NiSbS$) tucekite ($Ni_9Sb_2S_8$), and hauchecornite ($Ni_9Bi(Sb,Bi)S_8$). Identified PGM are predominantly sperrylite ($PtAs_2$) and sudburyite ($PdSb$), with minor Pd-melonite $[(Ni,Pd)Te_2]$, hongshiite ($PdCu$), testibiopalladite $[PdTe(Sb,Te)]$, and genkinite $[(Pt,Pd)_4Sb_3]$. Platinum- and palladium-bearing minerals commonly form equant 1 - 40 µm grains, within chalcopyrite, pyrrhotite, pentlandite, cobaltite and silicates. Sperrylite and sudburyite also occur as veinlets within and as partial rims (~ 1 - 10 µm thick) on the periphery of base metal sulphides. The textural paragenesis and mineral chemistry of PGM and associated minerals in the DJ/DB zone of the Turnagain intrusion are compared to those observed from other Alaskan-type intrusions. These findings highlight the potential for finding PGE-mineralized units in other Alaskan-type intrusions in the Canadian Cordillera and older orogenic ultramafic-mafic intrusions elsewhere in Canada.

Keywords: Platinum group elements, platinum group minerals, ultramafic intrusion, Alaskan-type, Turnagain intrusion, arsenide minerals, antimonide minerals

---

1. Introduction

Ultramafic-mafic intrusions host economic deposits of nickel, copper and platinum group element (PGE) in Canada (e.g. Sudbury, Ontario, Naldrett, 2011; Voisey's Bay, Labrador, Naldrett, 1999) and worldwide (e.g. Bushveld Complex, South Africa, Maier and Groves, 2011; Noril'sk, Russia, Naldrett, 1999; Stillwater Complex, USA, Maier and Groves, 2011). These intrusions occur in diverse geological settings, but are common in areas of continental rifting where high degrees of partial melting extract chalcophile elements from the mantle and crustal sulphur promotes sulphide saturation of the magma (Ripley, 2010; Naldrett, 2011). Historically, areas of subduction-related magmatism have been less favourable environments for exploration. However, recent examples of ultramafic-mafic-hosted Ni-Cu-PGE mineralization in supra-subduction-zone or "orogenic" settings include the Aguablanca mine in Spain (Piña et al., 2012), an Alaskan-type intrusion at Duke Island, southeastern Alaska (Irvine, 1974; Ripley, 2010), and the former Giant Mascot mine in southern British Columbia (Manor et al., this volume). Such orogenic settings may become a focus for future exploration for Ni-Cu-PGE mineralization in the Canadian Cordillera and elsewhere.

Alaskan-type ultramafic-mafic intrusions in the northern Cordillera have long been known (Taylor, 1967). In British Columbia, these intrusions are hosted by the accreted arc terranes of Quesnellia and Stikinia, and range in age from mid-Triassic (ca. 237 Ma at Lunar Creek) to Early Jurassic (ca. 186 Ma at Polaris; Nixon et al., 1997). Key petrologic traits include a general lack of orthopyroxene in ultramafic-mafic cumulates (Nixon and Hammack, 1991; Taylor, 1967) and ultramafic-hosted PGE mineralization, that is commonly related to chromitite layers and their derivative PGE-rich placer deposits (Johan, 2002; Macdonald, 1987; Nixon et al., 1990). Base metal sulphide mineralization is not a common characteristic of Alaskan-type complexes (Nixon et al., 1997). The Turnagain intrusion underlies an area of ~ 25 km^2, approximately 70 km east of Dease Lake (Fig. 1). It represents the only sulphide-bearing Alaskan-type intrusion currently known in British Columbia, with a significant Ni-Co resource: 865 Mt at 0.21% per tonne Ni and 0.013% per tonne Co (Riles et al., 2011).

Exploration of the Turnagain intrusion has mainly focussed on the large low-grade nickel resource in the southern part of the intrusion, the Horsetrail zone (Fig. 1). Geochemical soil surveys in 2004 and subsequent drilling revealed elevated concentrations of copper, platinum and palladium in the poorly exposed southwestern part of the intrusion, an area known as the DJ/DB zone (Figs. 1, 2). Relatively little information is available from this part of the intrusion. To rectify this, and to better document the Turnagain intrusion as an example of an orogenic deposit, herein we present initial observations of the textures and composition of the various sulphide, semimetal-rich and platinum group minerals (PGM) identified in drillcore samples from the DJ/DB zone.

2. Regional geology

The Turnagain intrusion lies in a 6 km wide assemblage of Late Paleozoic metasedimentary and metavolcanic rocks of the Yukon-Tanana terrane (Nixon, et al., 2012; Fig. 1). These host rocks are tectonically juxtaposed against Lower Paleozoic continental margin successions (Kechika and Boya formations) of ancestral North America (Cassiar terrane) to the east, and separated from Mesozoic granitic plutons of the Quesnel terrane to the west by the Kutcho Fault (Gabrielse, 1998; Nixon et al., 2012). The northern and eastern margins of the intrusion are in fault contact with pyritic graphitic phyllite and slate. Shear bands in the footwall of this steeply dipping (reverse) fault indicate an eastward direction of tectonic transport (Nixon, 1998; Fig. 1). At the southern and western margins, however, intrusive contacts with hornfelsed metasedimentary and metavolcanic rocks have been observed both in outcrop, at an inlier in the western extremity of the intrusion (Fig. 1), and in drillcore (Clark, 1975; Scheel, 2007).

3. Geology of the Turnagain intrusion

The Turnagain is a composite Alaskan-type intrusion that contains a suite of typical Alaskan rock types, including dunite, chromitite, wehrlite, clinopyroxenite and hornblendite (Clark, 1975, 1980; Scheel, 2007, Scheel et al., 2005).

We recognize three ultramafic stages or subintrusions, from oldest to youngest (Fig. 1): 1) wehrlites and clinopyroxenites; 2) dunite-wehrlite; and 3) clinopyroxenite-hornblendite. At the core of the intrusion, these ultramafic units are cut by a dioritic pluton (Fig. 1). Inclusions of intact and partially digested hornfelsed country rock are common in drillcore from mineralized areas, especially in dunite and wehrlite in the Horsetrail zone.

In the north, steeply dipping, cumulate layering in wehrlites and clinopyroxenites is cut by dunite along a sharp intrusive contact (Clark, 1975). Southward, the main dunite body passes into wehrlite, minor clinopyroxenite and rare hornblendite, which together form the dunite-wehrlite phase. The third and youngest phase of the ultramafic intrusion is the clinopyroxenite-hornblendite (± wehrlite) unit that comprises the DJ/DB zone. Although outcrops are scarce, the relative age of the clinopyroxenite-hornblendite unit can be established using large (up to ~ 2 m) boulders that contain angular blocks of dunite with serpentinized rims enclosed in a coarsely crystalline matrix of hornblendite and hornblende clinopyroxenite. Diorite and leucodiorite dikes cut hornblendite-clinopyroxenite indicating that the dioritic pluton represents the final intrusive event.

The sulphide content of the rocks of the Turnagain intrusion is highly variable. Most rock types carry small amounts of disseminated sulphide (up to 1 vol.%,). However, disseminated sulphides in the Horsetrail zone, the main Ni-Co resource, are generally more abundant (~ 5 vol.%), and locally become net-textured or semi-massive (up to 50% sulphide), and are mainly composed of Ni- and Co-rich pentlandite and pyrrhotite with minor chalcopyrite. The DJ/DB Cu-PGE-rich zone typically has Pt - Pd enrichment (maximum 4.9 ppm) spatially associated with areas of low sulphide content (< 5 vol.%), whereas localized areas of net-textured sulphides contain only background concentrations of platinum and palladium (< 10 ppb).

3.1. Geology of the DJ/DB zone

The DJ/DB zone is an elliptically shaped area (~ 3.5 km^2) at the southwestern margin of the Turnagain intrusion, approximately 2.5 km northwest of the well-mineralized Horsetrail zone. To date, 34 holes (60 - 413 m) have been drilled in the DJ/DB zone, both NQ (47.6 mm) and BQ (36.5 mm) drillcore. To establish lithological and mineralogical variations we examined eleven drillholes.

The rocks of the DJ/DB zone consist of interlayered units of clinopyroxenite and hornblendite with minor wehrlite. The mineralogy, modal abundances, and textures of these units vary significantly over short distances (< 50 cm) and contacts can be abrupt or gradational over 10s of metres (based on the predominant mineral, e.g. clinopyroxene or amphibole). Unit thicknesses measured in drillcore range from 50 cm to 155 m for clinopyroxenite, 15 cm to 57 m for hornblendite, and up to 26 m for wehrlite.

Pale grey clinopyroxenite (Fig. 3a) consists of fine- to coarse-grained (< 1 - 10 mm), randomly oriented clinopyroxene (> 60%) with interstitial magnetite (< 1 - 40%), hornblende (< 1 - 35%), biotite (< 1 - 20%), and serpentinized olivine (up to 15%). Primary biotite in clinopyroxenite is generally coarser grained (1 - 30 mm) than pyroxene and is randomly oriented to weakly aligned. Two types of magnetite are present: 1) > 1 to 10 mm blebs that are locally weakly to moderately banded (Fig. 3b); and 2) fine veinlets in serpentine-altered olivine. Clinopyroxenite is variably altered, ranging from nearly fresh to > 50% serpentine-chlorite ± biotite alteration along clinopyroxene grain boundaries. The clinopyroxenite is also cut by thin (1 - 50 mm) post-magmatic veins of coarse-grained to pegmatitic calcite and hornblende. The sulphide content of

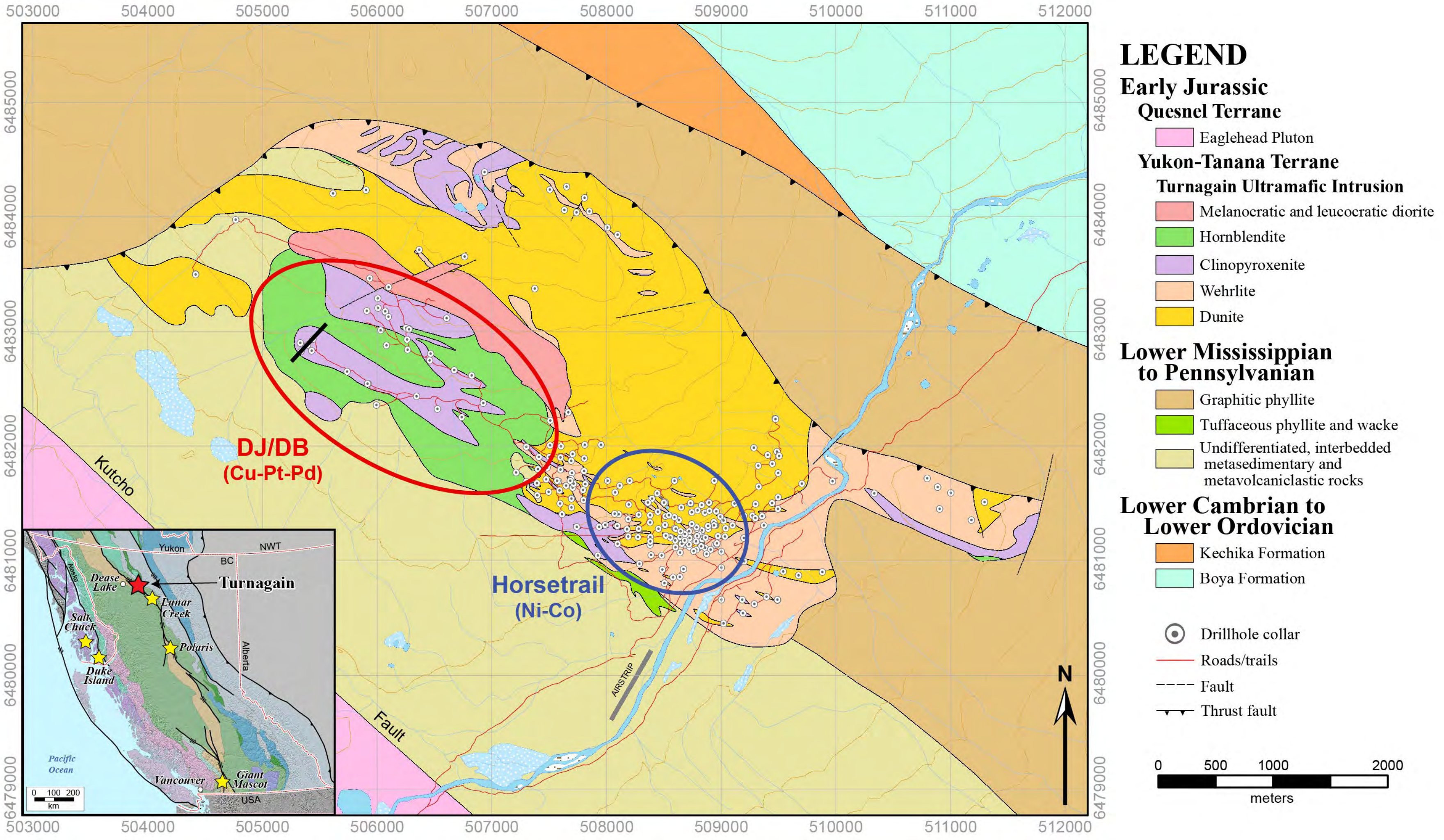

Fig. 1. Regional geological setting of the Turnagain intrusion (modified from Nixon et al., 2012) showing the DJ/DB zone (red), host to anomalous Cu-Pt-Pd concentrations and the focus of this study, and the Horsetrail zone (blue), which hosts the main Ni-Co resource. Thick black line in DJ/DB zone indicates location of cross-section in Fig. 2. Inset shows the location of the Turnagain intrusion and several other orogenic mafic-ultramafic intrusions relative to major tectonostatigraphic terranes in the northern Cordillera (modified from Colpron and Nelson, 2011). Map coordinates are in NAD 83, zone 9.

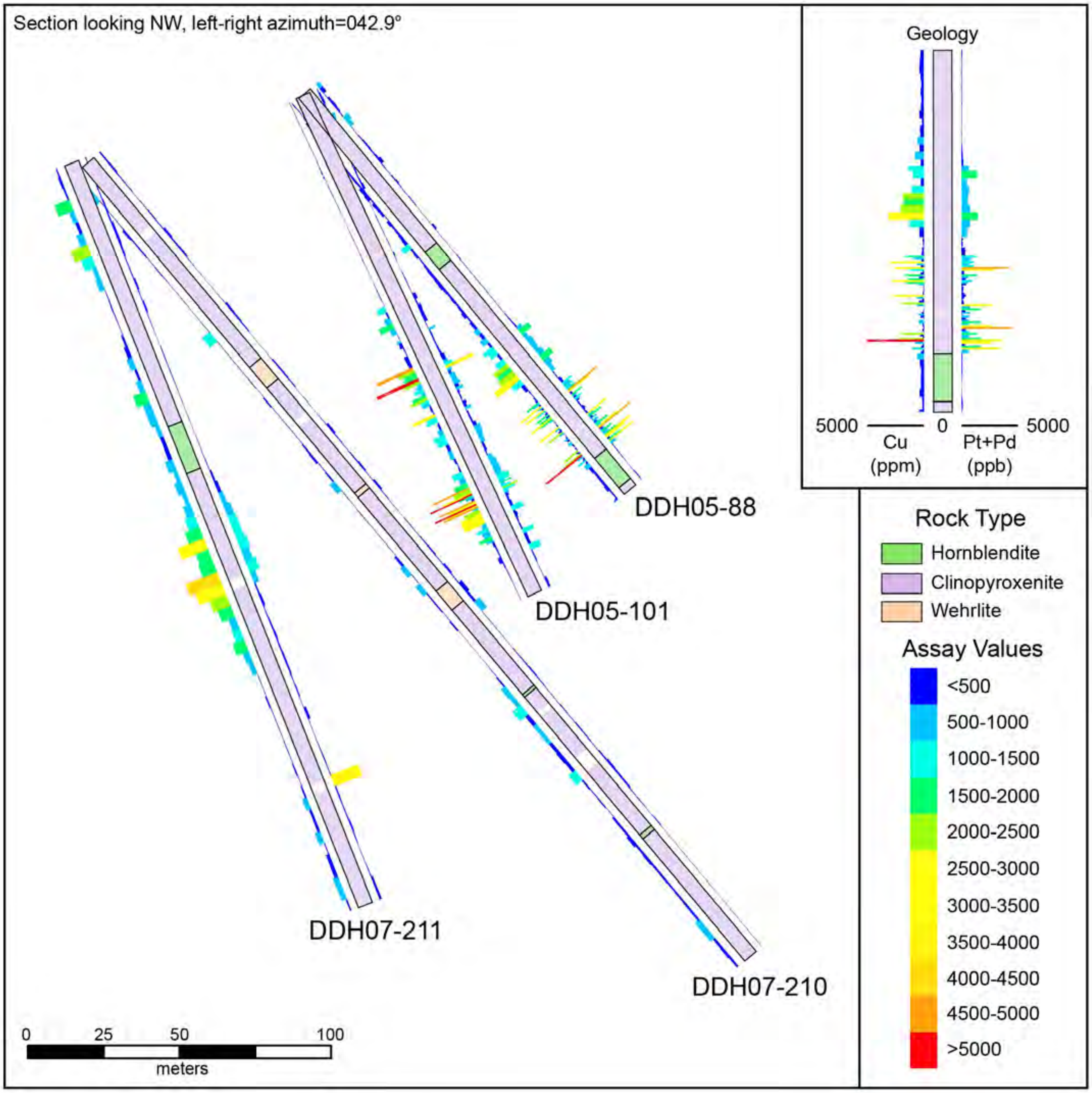

Fig. 2. Cross-section of drillhole geology and Cu, Pt and Pd concentrations through the DJ/DB zone, showing geology (centre), with Cu (left, in ppm) and PGE concentrations (right, in ppb). Maximum Cu concentration in section is 17900 ppm over 0.5 m. Maximum combined Pt+Pd concentration is 4881 ppb over 0.5 m. Note the moderate correlation between areas of high Cu and high Pt+Pd concentrations. Assay samples for all drillholes are half-core split; analytical results were obtained using 4-acid digestion ICP-ES for copper and fire assay fusion ICP-ES for Pt and Pd. Sample intervals for DDH07-210 and DDH07-211 are 4 m. Sample intervals for DDH05-88 are 2 m (3.05-105 m, 158-172.2 m EOH) and 0.5 m (105-158 m). Sample intervals for DDH05-101 are 2 m (3.7-88 m, 165-184.7 m EOH) and 1 m (88-165 m).

clinopyroxenite varies from 0 to 35% sulphide, and sulphides display disseminated, net-textured, and semi-massive textures. Areas of more intense alteration and calcite-hornblende veins also contain sulphides but these only constitute a small percentage of overall mineralization.

Dark green to black hornblendite contains fine- to coarse-grained amphibole (< 1 - 25 mm in length) with sporadic pegmatitic patches (amphibole crystal size > 45 mm). Amphiboles in the hornblendite are predominantly randomly oriented (Fig. 3c), with local zones (1 - 100 cm wide) of moderately to strongly oriented crystals (Fig. 3d). Hornblendite locally contains up to 30% clinopyroxene, with

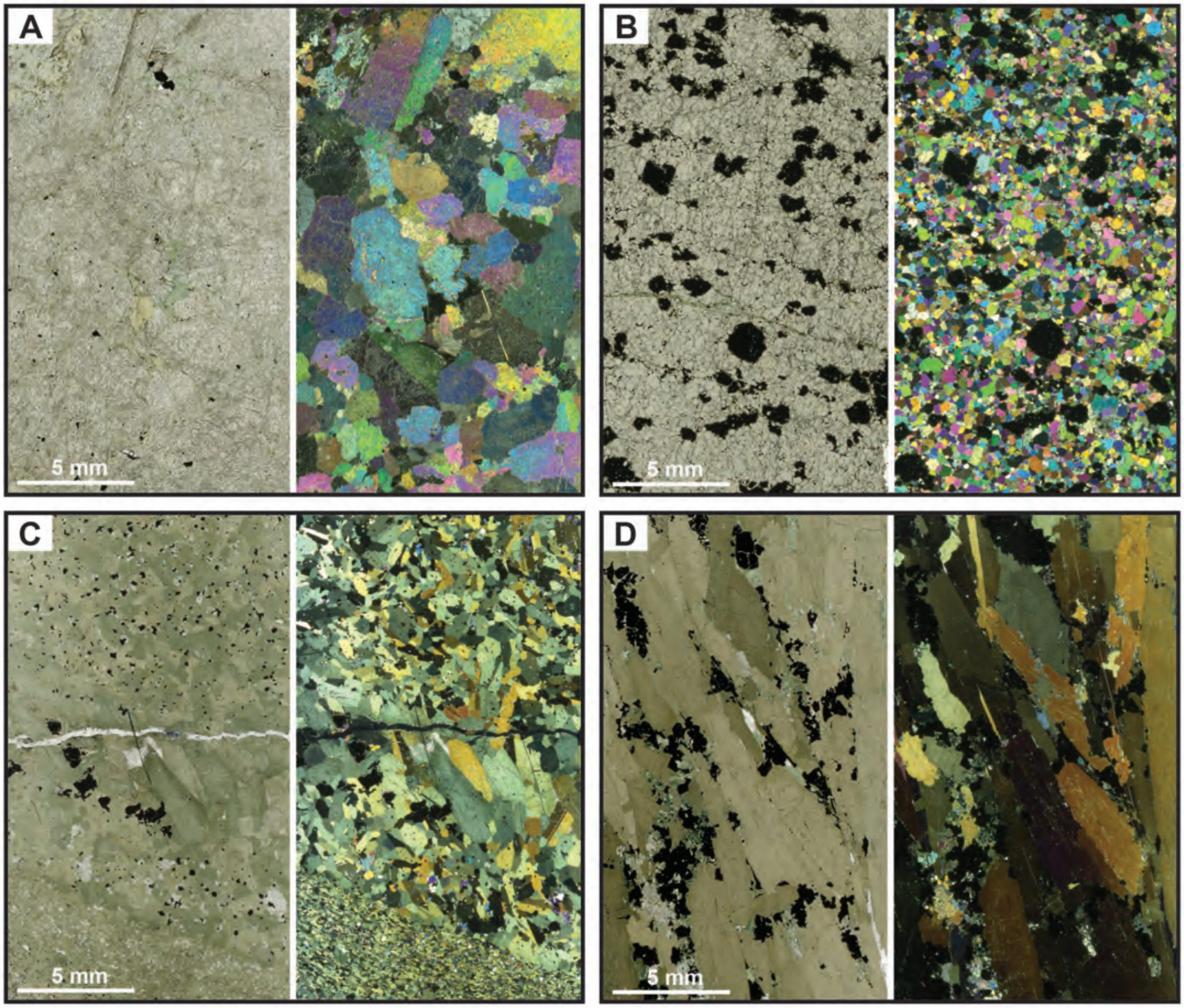

Fig. 3. Digital scans of thin sections for the major rock types from the DJ/DB zone in transmitted light (left) and cross-polarized light (right). **a)** Sample DDH05-88-1: coarse-grained clinopyroxenite with 2% sulphide and minor biotite. **b)** DDH05-89-1: fine-grained clinopyroxenite with weakly banded blebs of magnetite. **c)** DDH04-43-1: very fine-grained hornblendite in contact with fine- to medium-grained hornblendite with 5% chlorite and 3% sulphide. Coarser crystals above the contact are weakly aligned oblique to contact. **d)** DDH05-102-11: coarse-grained hornblendite with strongly oriented amphibole crystals. Sample has 5% interstitial sulphide associated with secondary chlorite.

appreciable magnetite (up to 15%) and minor biotite (up to 5%). Hornblendite contains 1 to 15% disseminated sulphide, and is mainly fresh to weakly chlorite altered. As in the clinopyroxenite, the hornblendite is cut by calcite-hornblende-sulphide veins.

Grey to pale grey, medium-grained wehrlite is typically moderately to strongly altered. Pyroxenes are largely fresh in altered wehrlite, with variable amounts of talc and chlorite along grain boundaries. Olivine typically occurs as relic grains replaced by serpentine and magnetite. The abundance of disseminated sulphide (5 - 30%) is strongly correlated to the degree of alteration, unlike those in hornblendites and clinopyroxenites.

4. Sampling and analytical methods

This study uses samples and data from surface exposures and 20 of 34 drillholes from the DJ/DB zone. Sixteen surface grab samples and 111 drillcore samples were collected during two field seasons (2011 and 2013). Surface samples were obtained from outcrop and large loose blocks close to drill sites in the DJ/DB zone. We examined core from drillholes that yielded high Cu-Pt-Pd assay values and provided even spatial distribution across the DJ/DB zone. The core was observed for variations in rock type, sulphide content and textures. Sampling was concentrated in areas with assay values greater than 500 ppb combined Pt + Pd, in addition to a suite of samples with medium (100 - 500 ppb Pt + Pd) and low (Pt + Pd > 100 ppb) concentrations, and representative lithologies from the area.

Ninety-six polished thin sections from drillcore samples were examined petrographically using plane-polarized transmitted light, cross-polarized transmitted light, and reflected light. Anomalously high Pt + Pd-bearing samples (n=14) were chosen for scanning electron microscope (SEM) analysis to identify PGM, associated sulphides, and silicates, and determine controls on the mineralization. Scanning electron microscope analyses were collected at both the Electron Microbeam/X-Ray Diffraction Facility at the University of British Columbia, Vancouver (UBC) and the SEM Facility at the Geological Survey of Canada, Ottawa (GSC). At UBC, back-scattered electron (BSE) imaging was carried out on a Philips XL-30 scanning electron microscope. An operating voltage of 15 kV was used with a spot diameter of 6 µm. At the GSC, BSE imaging was carried out on a Zeiss EVO 50 series SEM with extended pressure capability (up to 3000 Pascals), equipped with a backscattered electron detector (BSD). Results of the petrographic and SEM work obtained to date from are presented below.

5. Mineralogy

5.1. Base metal sulphides

Base metal sulphides in the DJ/DB zone of the Turnagain intrusion are mainly pyrrhotite and chalcopyrite with minor pyrite and pentlandite. Minor to trace accessory phases include millerite (NiS), sphalerite (ZnS), bornite (Cu_5FeS_4), marcasite (FeS_2), molybdenite (MoS_2), siegenite [$(Ni,Co)_3S_4$], and selenium-rich galena (PbS). Pyrrhotite is the most prevalent sulphide, commonly forming sub-millimetre to 3 mm diameter grains interstitial to silicates, with or without chalcopyrite (Fig. 4a), and locally forming net-textured layers or massive veins. Chalcopyrite is commonly intergrown with pyrrhotite, but also occupies veinlets in silicates and along silicate grain boundaries. Chalcopyrite grains may also host various arsenic- and antimony-bearing minerals (Fig. 4b). Pyrite is typically observed as aggregates of euhedral to subhedral crystals (10 - 50 µm) up to 2 mm in diameter in pyrrhotite or chalcopyrite (Figs. 4c, d). Pentlandite forms both sub-millimetre sized crystals in pyrrhotite and chalcopyrite (Fig. 4e), and exsolution flames in pyrrhotite grains (Fig. 4f).

5.2. Arsenides, sulpharsenides and sulphantimonides

Arsenides, sulpharsenides and sulphantimonides are common accessory minerals (< 1%) in the DJ/DB zone. They are only observed in clinopyroxenite and are commonly intergrown with chalcopyrite. Nickeline (NiAs) is the only true arsenide mineral present and is found exclusively as anhedral grains (2 - 30 µm) in cobaltite and gersdorffite (Fig. 5a). Sulpharsenide and sulphantimonide minerals include (in decreasing order of abundance): cobaltite (CoAsS), solid solution end-members gersdorffite (NiAsS) and ullmannite (NiSbS), tucekite ($Ni_9Sb_2S_8$), and hauchecornite ($Ni_9Bi(Sb,Bi)S_8$). Cobaltite is present in two distinct forms: 1) subhedral to anhedral grains and grain aggregates (1 - 70 µm across, Figs. 5a, 5b); and 2) single, euhedral grains (50 µm diameter, Figs. 5c, 5d). The former are only found in chalcopyrite, locally enclosing anhedral nickeline and pentlandite, whereas the latter are found enclosed by, or at the margins of, chalcopyrite or pyrrhotite blebs and in serpentine close to magnetite. Subhedral to anhedral grains of gersdorffite, up to 20 µm, are enclosed by chalcopyrite (Fig. 5e); rarely, gersdorffite encloses nickeline (Fig. 5f). The three sulphantimonide phases were only observed in one sample (DDH07-211-1), all in a single chalcopyrite bleb. Ullmannite is found as submicron to 10 µm grains, whereas tucekite is observed as 20 - 50 µm grains exhibiting 1 - 5 µm thick rims of hauchecornite (Fig. 5f).

5.3 Platinum group minerals

A variety of platinum group minerals have been identified in clinopyroxenite and hornblendite from the DJ/DB zone (Table 1). All PGM identified contain either platinum or palladium; significant concentrations of other PGE are lacking. The two main minerals observed are sperrylite ($PtAs_2$) and sudburyite [(Pd,Ni)Sb]. Minor PGM include Pd-melonite [$(Ni,Pd)Te_2$], hongshiite (PdCu), testibiopalladite [PdTe(Sb,Te)], and genkinite [$(Pt,Pd)_4Sb_3$] (Table 1). Clinopyroxenite is host to all varieties of PGM, whereas hornblendite only contains sperrylite. Sperrylite and sudburyite are present as: 1) equant grains 1 to 20 µm in diameter (Fig. 6); and 2) partial rims, 1 - 10 µm thick around sulphides (Fig. 7). Equant sperrylite and sudburyite grains are principally found in or at the margins of chalcopyrite and pyrrhotite. However, they are also in clinopyroxene and serpentine, adjacent to sulphide blebs. Sperrylite and sudburyite rims are only in clinopyroxenite, forming along the periphery of, or along fractures in, pyrrhotite and chalcopyrite. All of the minor PGM phases form equant grains, 1 to 40 µm in diameter, in chalcopyrite and pyrrhotite.

6. Discussion

The sulphide abundance and the distribution and mineralogy of platinum group minerals in the Turnagain intrusion differ from most Alaskan-type intrusions. Alaskan-type intrusions are typified by relatively low sulphur fugacities during crystallization, which results in early crystallization of Pt-Fe alloys with chromite in dunite and only minor sulphide phases (Johan, 2002). In contrast, the Turnagain intrusion is sulphide-rich (Nixon, 1998) due to significant assimilation of crustal sulphur during magma emplacement (Scheel, 2007). In addition, it is clear that the younger clinopyroxenite-hornblendite units of the DJ/DB zone and older dunite-wehrlite in the main part of the intrusion carry different metal endowments. Ni-sulphide mineralization is contained in wehrlites and dunites of the Horsetrail zone, whereas PGE mineralization in the DJ/DB zone occurs as Pt- and Pd-rich arsenides and antimonides in clinopyroxenite.

Sulphide-rich PGE mineralization is found in other orogenic intrusions in British Columbia and Alaska, including the Salt Chuck, Duke Island, and Giant Mascot intrusions. The Salt Chuck (early Paleozoic) Alaskan-type intrusion in southeastern

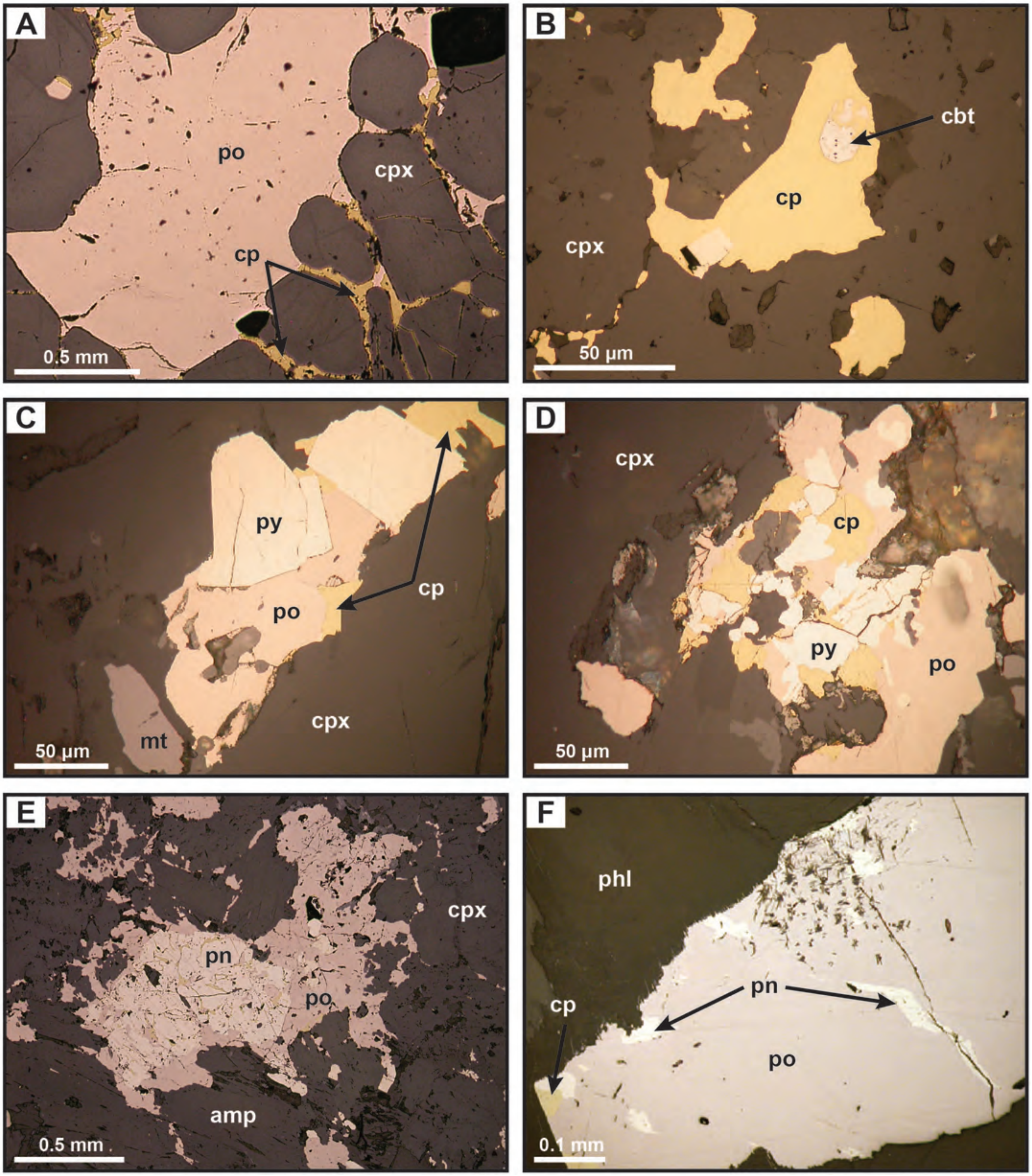

Fig. 4. Photomicrographs in reflected light of base metal sulphide minerals in clinopyroxenite from the DJ/DB zone. **a)** DDH07-211-5: coarse-grained interstitial pyrrhotite bleb with peripheral chalcopyrite along grain boundaries of surrounding clinopyroxene grains. **b)** DDH07-211-4: chalcopyrite bleb in clinopyroxenite containing a grain of subhedral cobaltite in pyroxene. **c)** DDH07-211-4: coarse-grained euhedral pyrite within a bleb of pyrrhotite and chalcopyrite. **d)** DDH07-211-4: an aggregate of subhedral pyrite in a composite bleb of pyrrhotite and chalcopyrite. **e)** DDH05-88-102: blocky pentlandite in pyrrhotite. **f)** DDH05-98-2: pentlandite exsolution lamellae (i.e., flames) in pyrrhotite. Mineral abbreviations: cpx, clinopyroxene, po, pyrrhotite; cp, chalcopyrite; cbt, cobaltite; py, pyrite; mt; magnetite; pn, pentlandite; amp, amphibole; phl, phlogopite.

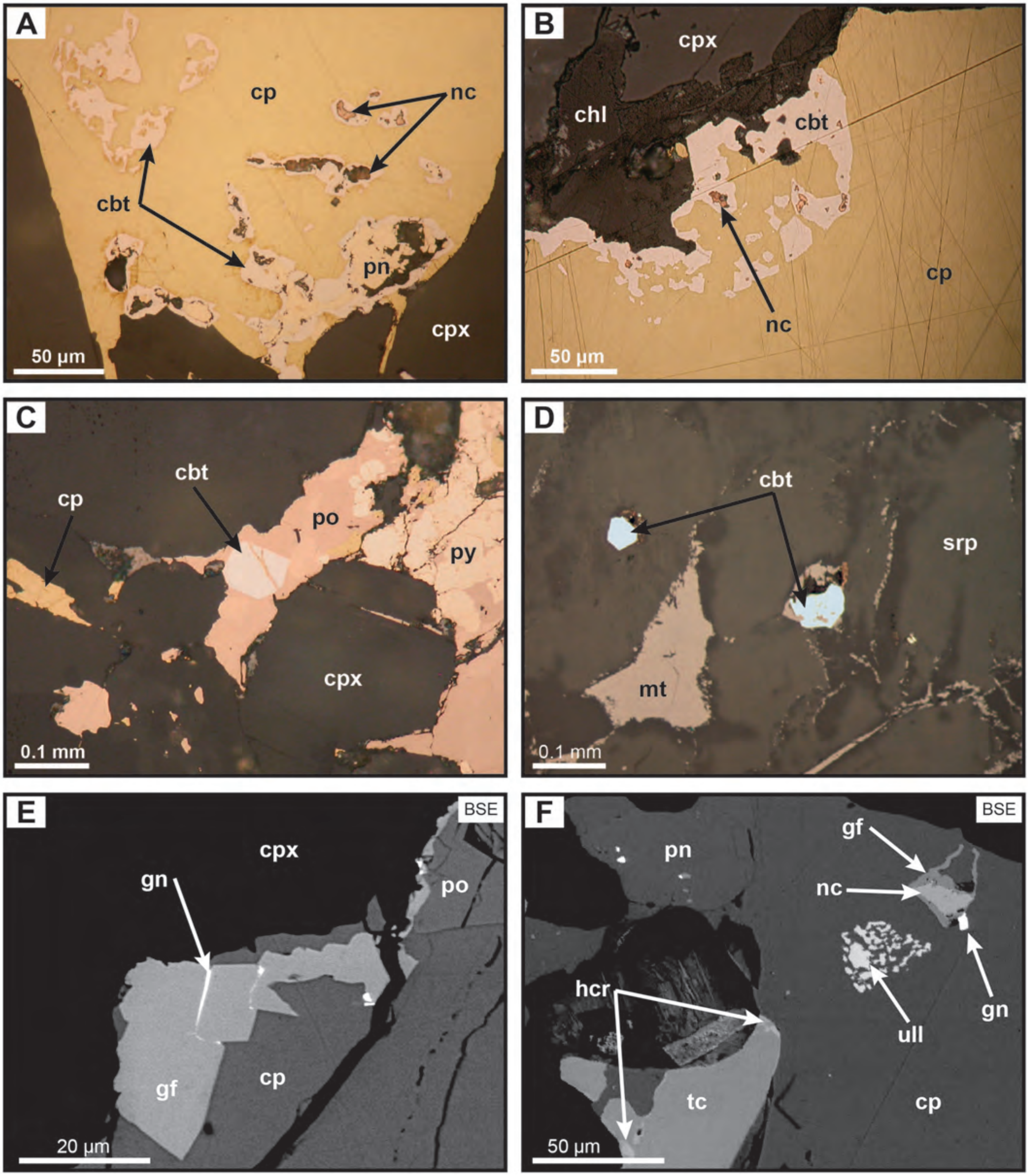

Fig. 5. Photomicrographs and electron backscatter images of arsenide, sulpharsenide and sulphantimonide minerals from the DJ/DB zone. **a)** DDH07-211-1: chalcopyrite bleb containing subhedral to anhedral cobaltite. Anhedral crystals of pentlandite and nickeline are enclosed in cobaltite. **b)** DDH07-211-1: nickeline within cobaltite at the periphery of a chalcopyrite bleb. **c)** DDH07-211-5: fractured, euhedral grain of cobaltite in pyrrhotite in clinopyroxenite. Pyrrhotite also contains pyrite and chalcopyrite. **d)** DDH05-101-1: two subhedral cobaltite crystals in serpentine near magnetite. **e)** DDH07-211-1: subhedral, cobalt-rich gersdorffite within chalcopyrite with arsenic-rich galena in fractures. **f)** DDH07-211-1: chalcopyrite bleb containing blebs of pentlandite, galena, gersdorffite, ullmannite, and tucekite. Nickeline is enclosed in gersdorffite and tucekite is partly rimmed by hauchecornite. Mineral abbreviations as in Fig. 4, except: nc, nickeline; chl, chlorite; srp, serpentine; gf, gersdorffite; gn, galena; ull, ullmannite; tc, tucekite; hcr, hauchedornite.

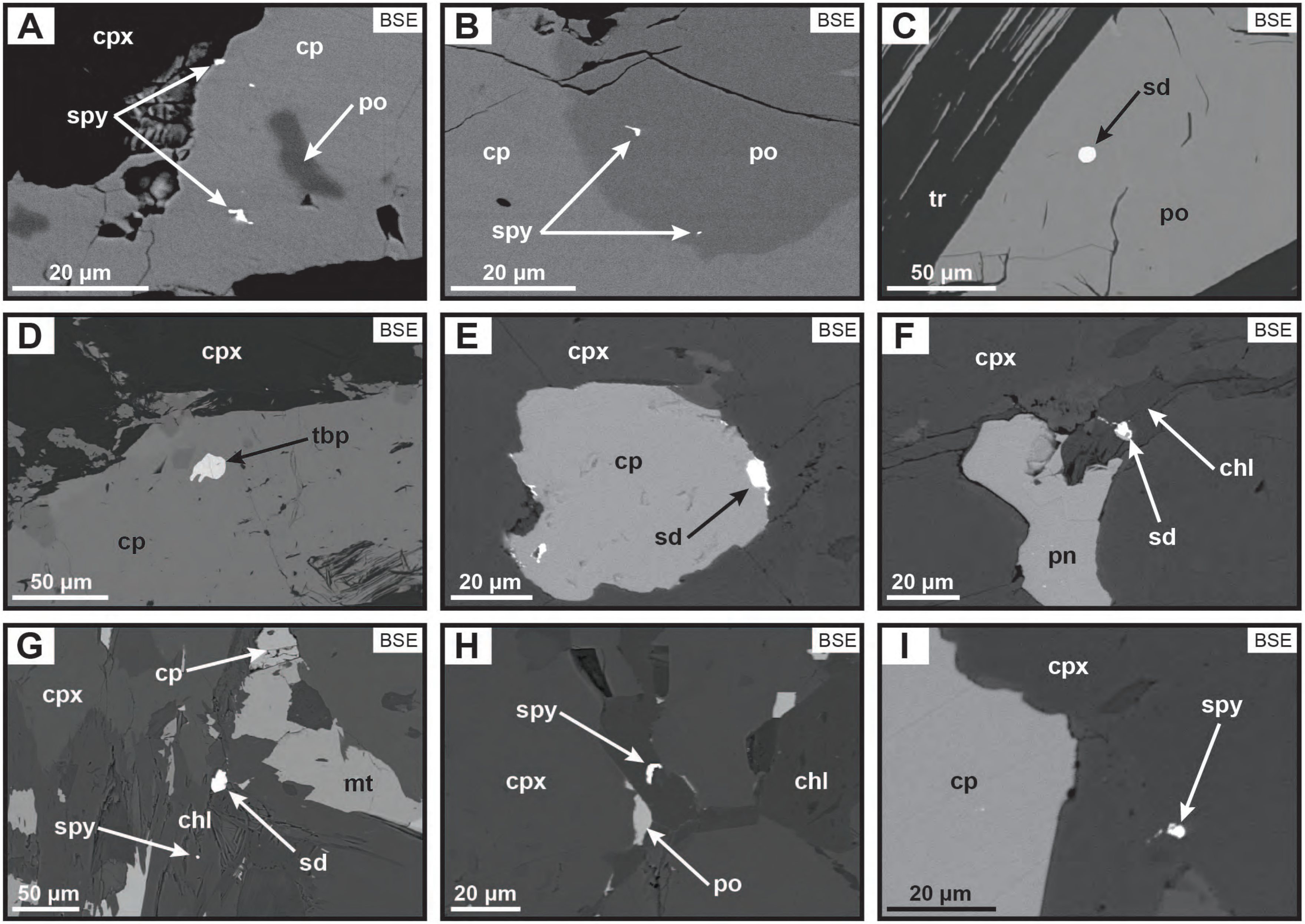

Fig. 6. Electron backscatter images of platinum group minerals from the DJ/DB zone. **a)** DDH07-211-5: sperrylite inclusions in chalcopyrite with minor pyrrhotite. **b)** DDH07-211-5: sperrylite in pyrrhotite, near a contact with chalcopyrite. **c)** DDH06-161-3: sudburyite grain enclosed in pyrrhotite. **d)** DDH06-161-3: anhedral grain of testibiopalladite in chalcopyrite. **e)** DDH05-88-1: sudburyite on the periphery of a chalcopyrite bleb in contact with clinopyroxene. **f)** DDH05-88-1: sudburyite in chlorite, adjacent to pentlandite and clinopyroxene. **g)** DDH04-59-1: sudburyite and sperrylite grains in chlorite near magnetite. **h)** DDH07-211-11: sperrylite in chlorite alteration around clinopyroxene. **i)** DDH05-88-1: satellite grain of sperrylite in clinopyroxene and adjacent to a chalcopyrite bleb. Mineral abbreviations as in Fig. 5, except: spy, sperrylite; sd, sudburyite; tr, tremolite; tbp, testibiopalladite.

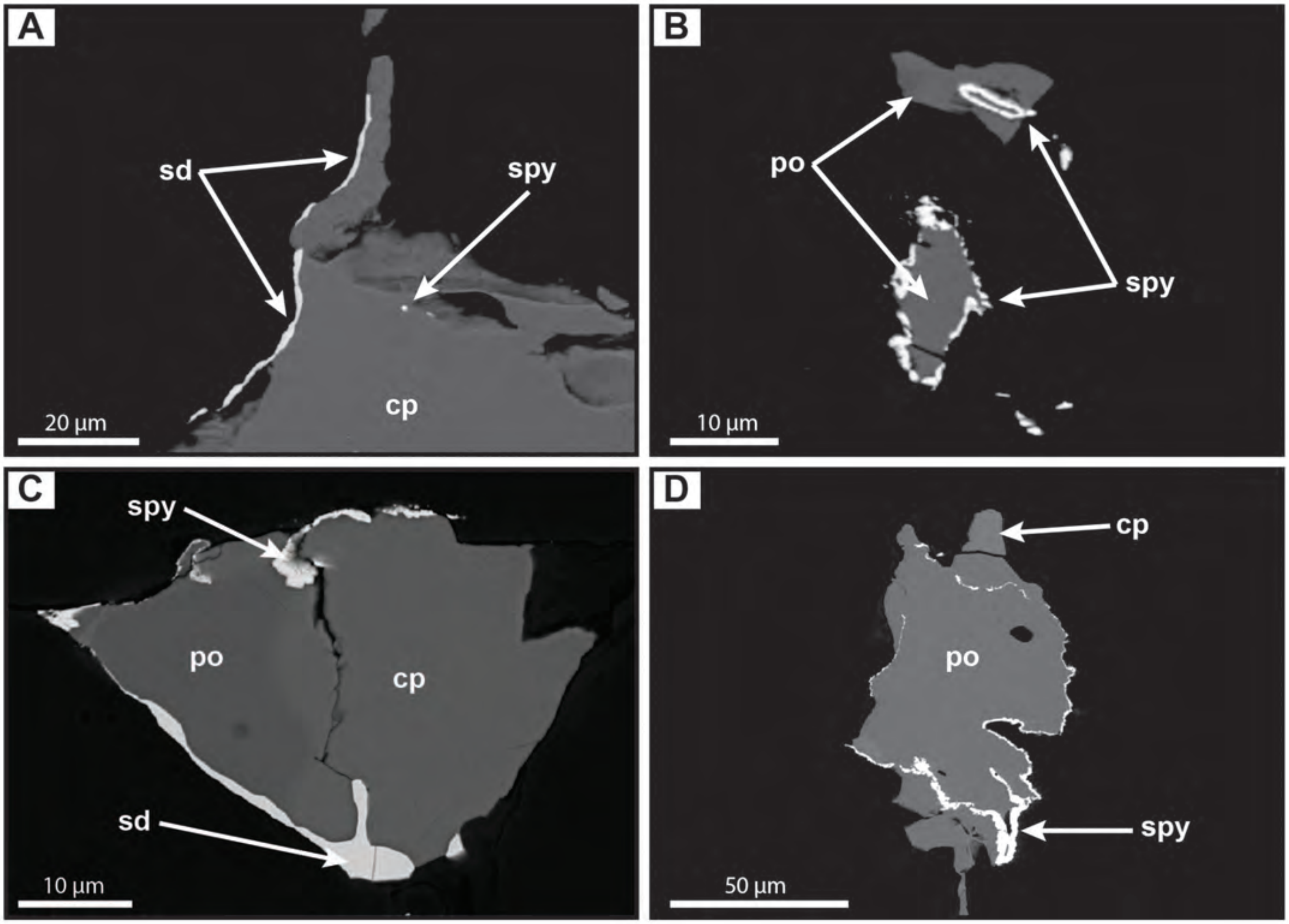

Fig. 7. Backscatter electron images of platinum group minerals forming rims around sulphides in the DJ/DB zone. **a)** DDH05-88-1: sudburyite along the periphery of a chalcopyrite grain enclosing a small grain of sperrylite. **b)** DDH05-88-1: rims and inclusions of sperrylite in pyrrhotite blebs. **c)** DDH05-102-5: sperrylite and sudburyite rims and fracture-controlled veinlets along a composite grain of chalcopyrite and pyrrhotite. **d)** DDH05-88-1: pyrrhotite bleb with a partial rim and veinlets of sperrylite. Mineral abbreviations as in Fig. 6.

Table 1. Platinum group minerals and host lithologies in the DJ/DB zone of the Turnagain intrusion (listed in decreasing order of relative abundance).

Mineral	Ideal Formula	Rock Type	Silicate/Oxide	Sulfide/Arsenide
Sperrylite (18)	$PtAs_2$	Cpxite, Hblite	cpx, chl, mt	po, cpy, cbt
Sudburyite (12)	(Pd,Ni)Sb	Cpxite	cpx, chl	po, cpy
Pd-melonite (4)	$(Ni,Pd)Te_2$	Cpxite	mt	po
Testibiopalladite (3)	PdTe(Sb,Te)	Cpxite		po, cpy
Genkinite (2)	$(Pt,Pd)_4Sb_3$	Cpxite		po
Hongshiite (1)	PtCu	Cpxite		cpy

Abbreviations: Cpxite, clinopyroxenite; Hblite, hornblendite; cpx, clinopyroxene; chl, chlorite; mt, magnetite; po, pyrrhotite; cpy, chalcopyrite; cbt, cobaltite.
Number of observed grains in brackets ( ).

Alaska (Fig. 1, inset) is an elongate body (12 km^2) that is host to significant Cu-Pd mineralization. It was mined for copper and palladium from 1916 to 1941, with average grades of 0.9% Cu, 1.4 g/t Pd, 0.57 g/t Au, and 2.8 g/t Ag, and had a total production of 2.81 million kg of Cu and 9,000 kg of Pd (Gault, 1943). The Salt Chuck intrusion is enriched in Cu and Pd (Loney and Himmelberg, 1992). However, average Cu-Pd concentrations are much higher (~ 7000 ppm Cu, ~ 1230 ppb Pd; Loney and Himmelberg, 1992) than those observed in the DJ/DB zone thus far (~ 2200 ppm Cu, ~ 174 ppb Pd; S. Jackson-Brown, unpublished data), and unlike the Turnagain intrusion, the mineralized rocks of the Salt Chuck intrusion also contain significant Au and Ag. Mineralization in the Salt Chuck intrusion, like the DJ/DB zone, is hosted by magnetite clinopyroxenite, but comprises predominantly Cu-rich sulphides (e.g., bornite, chalcopyrite) and Pd-tellurides (primarily kotulskite, PdTe; Watkinson and Melling, 1992). Metal enrichment in the Salt Chuck intrusion may record the replacement of magmatic sulphides by a Cu-rich and precious metal-rich assemblage due to the post-crystallization influx of a Cl-bearing hydrothermal fluid (Watkinson and Melling, 1992).

The Duke Island Complex, also in southeastern Alaska (Fig. 1, inset), is an Early Cretaceous Alaskan-type intrusion that has recently been found to host appreciable Ni-Cu sulphide mineralization (Ripley et al., 2005). It is an unzoned intrusion consisting of dunite, wehrlite, olivine clinopyroxenite and hornblende-magnetite clinopyroxenite (Irvine, 1974). Disseminated, and locally net-textured to massive, pyrrhotite, chalcopyrite, and pentlandite are hosted mainly in wehrlite and olivine clinopyroxenite (Thakurta et al., 2008). Elevated PGE concentrations have been reported in the Duke Island intrusion, although the mineralogy of the PGM is presently unknown. The abundance of massive sulphides in more olivine-rich rocks is similar to mineralization at the Ni-Co-mineralized Horsetrail zone of the Turnagain intrusion. PGE grades at Duke Island do not correlate with sulphide content (Freeman, 2006), similar to the DJ/DB zone (S. Jackson-Brown, unpublished data).

Mineralization in the DJ/DB zone of the Turnagain intrusion differs significantly from that of the Giant Mascot ultramafic-mafic intrusion in southern British Columbia (Fig. 1, inset), host to the province's only past-producing Ni-Cu-Co mine. The Giant Mascot deposit contains orthopyroxene-rich rock types, predominantly pyroxenite, peridotite, and minor dunite (Manor et al., this volume). Sulphide minerals include mainly pyrrhotite, pentlandite, chalcopyrite and minor pyrite, with significant PGM. Platinum and palladium commonly form bismuthotelluride and bismuthide minerals (Manor et al., this volume), distinct from the arsenic- and antimony-rich PGM identified in the Turnagain intrusion.

The Canadian Cordillera contains abundant mineral wealth, but remains underexplored for ultramafic-mafic Ni-Cu-PGE potential. This project, and others facilitated by the TGI-4 program, including work on the Giant Mascot intrusion, has confirmed that orogenic mafic-ultramafic intrusions can host significant concentrations of base and precious metals. Understanding the source(s) of, and controls on, mineralization, including mechanisms of emplacement, help derive mineralogical and geochemical methods to find similar deposits in older orogenic belts in Canada and globally.

7. Conclusions and future work

This manuscript characterizes the Cu-PGE mineralization in the DJ/DB zone of the Turnagain Alaskan-type intrusion in north-central British Columbia. The DJ/DB zone is host to a diverse population of sulphide, arsenide, sulpharsenide, sulphantimonide, and platinum group minerals that are hosted principally in clinopyroxenites and hornblendites. Field and petrographic evidence show that the clinopyroxenite-hornblendite units of the DJ/DB zone constitute a separate, later Cu-Pt-Pd-bearing intrusive phase that underwent a separate crystallization history from the earlier, Ni-Co endowed, main dunite-wehrlite units.

Investigation into the composition of the PGM and base metal sulphides in the DJ/DB zone of the Turnagain intrusion is ongoing and includes: 1) in-situ laser ablation ICP-MS analyses on PGM-bearing and non-PGM-bearing samples to determine the concentration of PGE within base metal sulphides in different textural settings; 2) whole rock PGE analyses to determine the relative metal enrichment and depletion characteristics of the late Cu-PGE enrichment in comparison to the Turnagain Ni-Co resource and other mineralization in Alaskan-type intrusions, 3) identifying hydrothermal versus orthomagmatic sources for mineralization; and 4) sulphur isotope analysis of sulphides from representative rocks types in the DJ/DB zone to evaluate the crustal sulphur source for Cu-PGE mineralization. New geoscience work on the late-stage Cu-PGE endowment of the Turnagain intrusion increases our knowledge about orogenic PGE mineralization in Alaskan-type intrusions, a style that is less common than the typical PGE-chromitite association.

Acknowledgments

We thank Tony Hitchins and Hard Creek Nickel Corperation for assistance with field work and access to Turnagain materials and data. Thanks to Dr. Mati Raudsepp, Jenny Lai, and Elisabetta Pani of the Electron Microbeam/X-ray Diffraction Facility at UBC, for their help and guidance on the SEM. Thanks to Dr. Ingrid Kjarsgaard in Ottawa for additional detailed petrographic descriptions and all EMPA analyses. Thanks also to Pat Hunt at the GSC, Ottawa, for assistance with SEM mapping of PGM using Feature. Funding for this project is provided by the Geological Survey of Canada TGI-4 program, the Government of Canada Research Affiliate Program and a SEG Canadian Foundation Graduate Student Research Grant awarded to Sarah Jackson-Brown in 2013. This is ESS contribution number 20130361.

References cited

Clark, T., 1975. Geology of an ultramafic complex on the Turnagain River, northwestern B.C. PhD thesis, Queens University, 454 p.

Clark, T., 1980. Petrology of the Turnagain ultramafic complex, northwestern British Columbia. Canadian Journal of Earth Sciences, 17, 744-757.

Colpron, M. and Nelson, J. L., 2011. A digital atlas of terranes for the northern Cordillera. British Columbia GeoFile 2011-11.

Freeman, C. J., 2006. Geologic Report DK06EXE-1: Summary report for the Duke Island Cu-Ni-PGE property, Ketchikan mining district, Alaska. Unpublished report for Quaterra Resources Incorporated, 32 p. Available online at: www.sedar.com.

Gabrielse, H., 1998. Geology of the Cry Lake and Dease Lake map areas, north central British Columbia. Geological Survey of Canada, Bulletin 504, 147 p.

Gault, H.R., 1945. The Salt Chuck Copper-Palladium Mine. Prince of Wales Island. Southeastern Alaska. United States Geological Survey, Open File Report 19, 18 p.

Irvine, T., 1974. Petrology of the Duke Island ultramafic complex, southeastern Alaska. Geological Society of America, Memoir 138, 240 p.

Johan, Z., 2002. Alaskan-type complexes and their platinum-group element mineralization. In: Cabri, L. J. (Ed.), Geology, geochemistry, mineralogy and mineral beneficiation of platinum-group elements. Canadian Institute of Mining, Metallurgy and Petroleum, Montreal, Quebec, pp. 669-719.

Loney, R.A., and Himmelberg, G.R., 1992. Petrogenesis of the Pd-rich intrusion at Salt Chuck, Prince of Wales Island: an Early Paleozoic Alaskan-type ultramafic body. Canadian Mineralogist, 30, 1005-1022.

Macdonald, A., 1987. Ore deposit models #12. The platinum group element deposits: classification and genesis. Geoscience Canada, 14, 155-166.

Maier, W.D., and Groves, D.I., 2011. Temporal and spatial controls on the formation of magmatic PGE and Ni–Cu deposits. Mineralium Deposita, 46, 841–857.

Naldrett, A.J., 1999. World-class Ni-Cu-PGE deposits: key factors in their genesis. Mineralium Deposita, 34, 227-240.

Naldrett, A.J., 2011. Fundamentals of magmatic sulfide deposits. Reviews in Economic Geology, 17, 1-50.

Nixon, G.T., 1998. Ni–Cu sulfide mineralization in the Turnagain Alaskan-type complex: a unique magmatic environment. In: Geological Fieldwork 1997, British Columbia Ministry of Energy, Mines and Petroleum Resources, British Columbia Geological Survey Paper 1998-1, 18-1 to 18-12.

Nixon, G.T., and Hammack, J., 1991. Metallogeny of ultramafic-mafic rocks in British Columbia with emphasis on the platinum-group elements. In: Ore Deposits, Tectonics and Metallogeny in the Canadian Cordillera. British Columbia Ministry of Energy, Mines and Petroleum Resources Paper 1991-4, pp. 125-161.

Nixon, G.T., Hammack, J.L., and Connelly, J.N., 1990. Geology and noble metal geochemistry of the Polaris ultramafic complex, north-central British Columbia. In: Geological Fieldwork 1989, British Columbia Ministry of Energy, Mines and Petroleum Resources, British Columbia Geological Survey Paper 1990-1, pp. 387-404.

Nixon, G. T., Hitchins, A. C., and Ross, G. P., compilers, 2012. Geology of the Turnagain ultramafic intrusion, northern British Columbia. BC Ministry of Energy and Mines, Open File 2012-05, scale: 1:10 000.

Nixon, G.T., Hammack, J.L., Ash, C.H., Cabri, L.J., Case, G., Connelly, J.N., Heaman, L.M., Laflamme, J.H.G., Nuttall, C., Paterson, W.P.E., and Wong, R.H., 1997. Geology and platinum-group-element mineralization of Alaskan-type ultramafic-mafic complexes in British Columbia. Geological Survey Branch, British Columbia Ministry of Employment and Investment, Bulletin 93. 142 p.

Piña, R., Gervilla, F., Barnes, S.-J., Ortega, L., and Lunar, R., 2012. Distribution of platinum-group and chalcophile elements in the Aguablanca Ni–Cu sulfide deposit (SW Spain): Evidence from a LA-ICP-MS study. Chemical Geology, 302-303, 61-75.

Riles, A., Molavi, M., Simpson, R., Fong, B., Reid, J., McTavish, G., and Friedman, D., 2011. Turnagain Project Hard Creek Nickel Corporation Preliminary Economic Assessment, available from the Hard Creek Nickel Corperation website: http://www.hardcreek.com, 151 p.

Ripley, E.M., 2010. Chapter 24 - A new perspective on exploration for magmatic sulphide-rich Ni-Cu-PGE deposits. Economic Geology Special Publication, 15, 437-450.

Ripley, E., Li, C., and Thakurta, J., 2005. Magmatic Cu-Ni-PGE mineralization at a convergent plate boundary: Preliminary mineralogic and isotopic studies of the Duke Island Complex, Alaska. Mineral Deposit Research: Meeting the Global Challenge, Proceedings of the Eighth Biennial SGA Meeting Beijing, China. Springer Berlin Heidelberg, Germany, 49-51.

Scheel, J.E., 2007. Age and origin of the Turnagain Alaskan-type intrusion and associated Ni-sulphide mineralization, North-central British Columbia, Canada. M.Sc. Thesis, University of British Columbia, Vancouver B.C., 201 p.

Scheel, J.E., Nixon, G.T., and Scoates, J.S., 2005. New observations on the geology of the Turnagain Alaskan-type ultramafic intrusive suite and associated Ni-Cu-PGE mineralization. In: Geological Fieldwork 2004, British Columbia Ministry of Energy, Mines and Petroleum Resources, British Columbia Geological Survey Paper 2005-1, pp. 167-176.

Taylor, H., 1967. The zoned ultramafic complexes of southeastern Alaska. In: Wyllie, P. J. (Ed.) Ultramafic and Related Rocks. Wiley, New York, 97-121.

Thakurta, J., Ripley, E.M., and Li, C., 2008. Geochemical constraints on the origin of sulfide mineralization in the Duke Island Complex, southeastern Alaska. Geochemistry, Geophysics, Geosystems, 9, 1-34.

Watkinson, D.H., and Melling, D.R., 1992. Hydrothermal origin of platinum-group mineralization in low-temperature copper sulfide-rich assemblages, Salt Chuck intrusion, Alaska. Economic Geology, 87, 175-184.

Portable X-ray fluorescence in stream sediment chemistry and indicator mineral surveys, Lonnie carbonatite complex, British Columbia

Pearce Luck[1] and George J. Simandl[1, 2, a]

[1] British Columbia Geological Survey, Ministry of Energy and Mines, Victoria, BC, V8W 9N3
[2] University of Victoria, School of Earth and Ocean Sciences, Victoria, BC, V8P 5C2
[a] corresponding author: George.Simandl@gov.bc.ca

Recommended citation: Luck, P. and Simandl, G.J., 2014. Portable X-ray fluorescence in stream sediment chemistry and indicator mineral surveys, Lonnie carbonatite complex, British Columbia. In: Geological Fieldwork 2013, British Columbia Ministry of Energy and Mines, British Columbia Geological Survey Paper 2014-1, pp. 169-182.

Abstract

The Lonnie carbonatite complex is the third most developed Nb prospect in the British Columbia alkaline province. The objective of this study was to determine the best size fraction of stream sediments for carbonatite related indicator mineral surveys. Sediments from seven sites along Granite Creek, a stream that transects the Lonnie deposit and adjacent bedrock units, were sampled for pXRF and pathfinder element studies. The results for key pathfinder elements including Nb, Ta, La, Ce, Pr, Nd, Y, P, Sr, Ba, Th, and U were precise (most having %RSD less than 5%) and prone to bias. Results for eight size fractions separated by laboratory sieves indicated a systematic distribution of key elements, with the highest abundances found in the finer size fractions. Of these, the +125µm fraction was chosen for further consideration due to its suitability for continued indicator mineral studies. With the exception of Ba, Sr, and possibly Nb samples upstream from the Lonnie deposit display higher concentrations of carbonatite pathfinder elements than samples downstream of the deposit. This indicates source(s) farther upstream, probably the Vergil carbonatite and Nb and TREE + Y soil geochemical anomalies. Indicator mineral studies are ongoing.

Keywords: Niobium, rare earth elements, carbonatite, indicator minerals, stream sediments, XRF

---

1. Introduction

Carbonatites, carbonatite-related alteration zones, and their weathered equivalents are the most important sources of Nb, and rare earth elements (Simandl et al., 2012). They contain important deposits of Ta, vermiculite, apatite (phosphate), badelleyite (zirconia), fluorite, U, and magnetite (Birket and Simandl, 1999, Mariano 1989a, 1989b). Although carbonatites are observed mainly in intracratonic rift settings, they are also present along cratonic margins (Woolley and Kjarsgaard, 2008), such as near the western flank of ancestral North America, in the British Columbia alkaline province (inset, Fig. 1).

One of the main objectives of the Specialty Metals component of the Targeted Geoscience Initiative 4 (TGI-4) is to determine if indicator minerals can guide explorationists toward carbonatite-related mineralization or at least toward carbonatites themselves. But processing heavy minerals and analysis of indicator minerals is relatively expensive and time consuming. Therefore, as an orientation survey, we measured the concentrations of Nb, Ta, REE, P, Sr, Ba, U, and Th in different grain size fractions of sediments sampled from streams draining three deposits. We used a portable X-ray fluorescence (pXRF) device to minimize the cost, improve output, and optimize the method (assuming that pyrochlore, columbite-tantalite, fersmite, apatite, REE-bearing fluorocarbonates, monazite, allanite, zircon, xenotime, and minerals of celestite-barite solid solution will be present in sediments downstream of the deposits).

Herein are results from Lonnie, a carbonatite-related Nb prospect, 7 km east of the Manson Creek settlement and 220 km northwest of Prince George (Fig. 1). Results from the Aley carbonatite, a large advanced Nb project, and the Wicheeda carbonatite plug, a medium-sized advanced rare earth element (REE) project (Fig. 1) will be presented elsewhere. We focus on grain size distributions and chemistry of samples collected near the Lonnie carbonatite; future work will concentrate on analysis of indicator minerals.

2. Geology of the Lonnie carbonatite

The Lonnie carbonatite complex belongs to a series of metacarbonatites, syenite complexes, and other alkaline rocks forming the British Columbia alkaline province (Fig. 1; Pell, 1994; Simandl et al., 2012). It is in the southern Omineca Mountains, which straddle the boundary between the Intermontane and Omineca belts. The Lonnie metacarbonatite outcrops along the projection of the Wolverine fault (Fig. 2), an extensional structure sub-parallel to the nearby dextral, 1-5 km wide Manson Creek fault system (Simandl et al., 2013a). The Wolverine fault is a probable metallotect connecting the Lonnie deposit to the Virgil carbonatite, 4.5 km to the northwest. This fault system is considered part of the Rocky Mountain Trench, separating the Quesnel terrane from the Slide Mountain and Cassiar terranes (Ferri and Melville, 1994).

Northwest of the Wolverine fault zone the Granite Creek drainage area is underlain by amphibolite-grade rocks of Ingenika Group (Neoproterozoic), and schists and quartzite of the Wolverine Metamorphic complex (Fig. 2). Bordering these

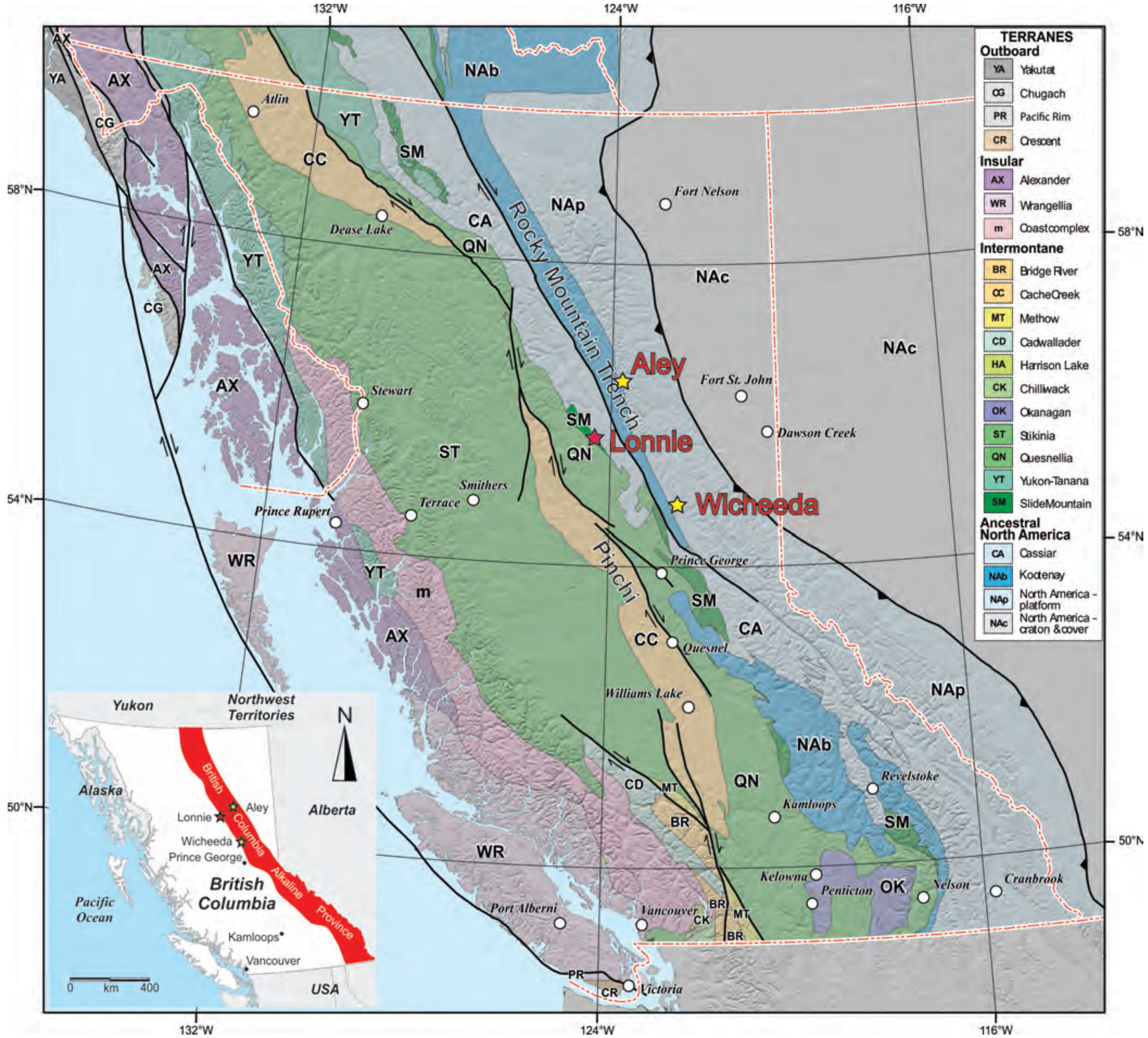

Fig. 1. Location and tectonic setting of the Lonnie carbonatite complex. Communities are indicated with white circles. Overview map modified from Colpron and Nelson (2011), inset from Pell (1994).

rocks along the hanging wall of the Wolverine fault zone is the Lonnie carbonatite complex. Farther southwest, siliciclastic and carbonate rocks of the Stelkuz Formation, limestone of the Epsee Formation, and metapelites of the Tsaydiz Formation comprise the Wolverine antiform (Ferri and Melville, 1994; Simandl et al., 2013a). Farther to the west are the Nina Creek and Big Creek groups (Fig. 2).

The Lonnie carbonatite complex has been explored episodically for sixty years (Thompson, 1955; Helmel, 2012; Simandl et al., 2013a). Traced by trenching over a length of 650 metres, it is up to 50 metres wide. Several Nb ± REE soil anomalies were identified near the deposit (Fig. 2; Helmel, 2012). The deposit consists of biotite-bearing sövite, aegerine-amphibole sövite, and a variety of quartz-free feldspathic rocks, probably produced by fenitization. Blue-green amphiboles and aegirine decrease away from the carbonatite in fenitized metasediments (Simandl et al., 2013a). A 1955 trenching program (pre- NI-43-101) reported a mineralized zone 530 metres long and approximately 17 metres wide grading 0.21% Nb_2O_5 (Rowe, 1958; Chisholm,1960). In this zone, the Na-amphibole-bearing carbonatite assayed 0.16% Nb_2O_5 over 6 metres. The feldspathic rocks averaged 0.23% Nb_2O_5 over nearly 10 metres. Furthermore, the central portion of this zone averaged 0.3% Nb_2O_5 across 8.3 metres over a length of 283 metres (Rowe, 1958). Recent analyses (Simandl et al., 2013a) failed to confirm these grades. Pyrochlore seems to be the main Nb-bearing mineral (Simandl et al., 2013a); however, columbite was also reported (Hankinson, 1958; Halleran, 1980;

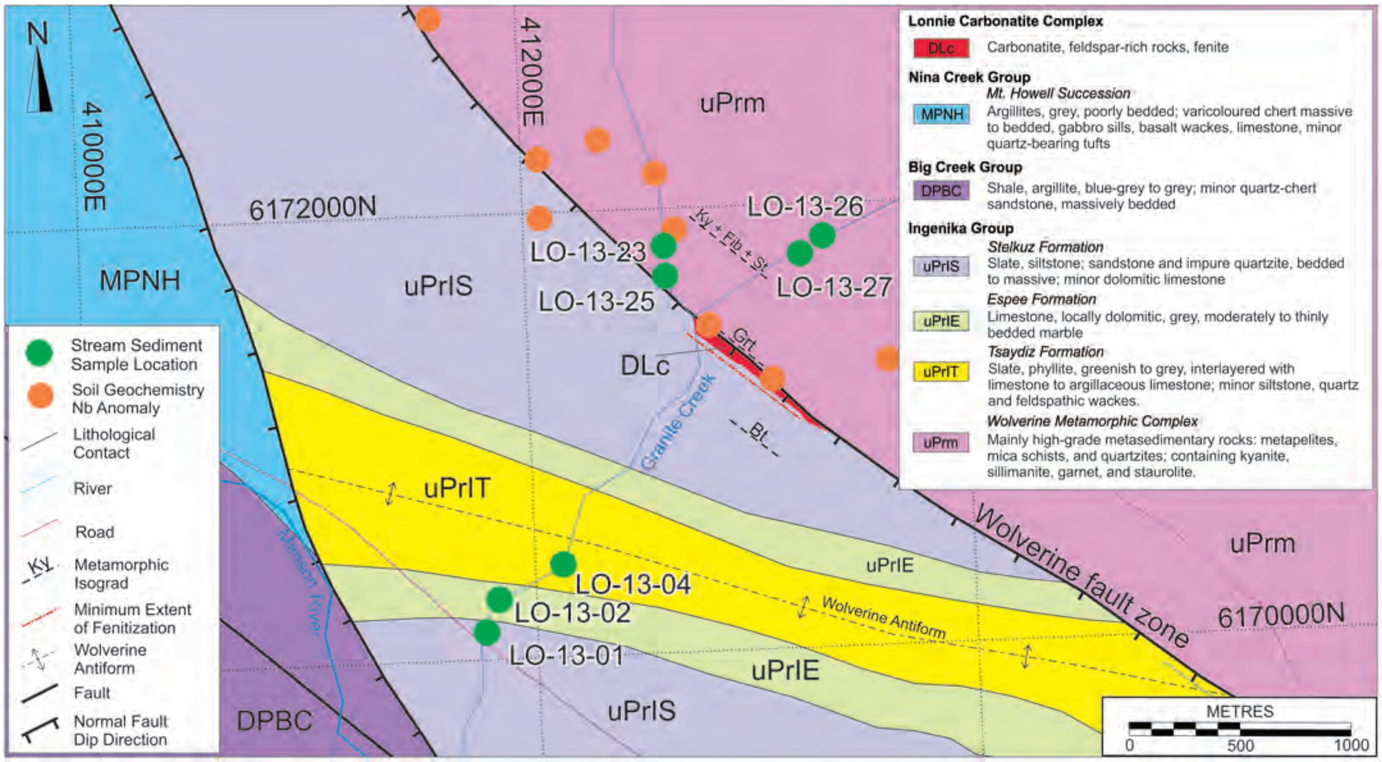

Fig. 2. Regional geologic map with sample locations. UTM coordinates are zone 10, North American Datum 1983.

Pell, 1994) and Nb-bearing rutile was reported in polished thin sections. Pell (1994) reported up to 20% apatite in the carbonatites and 3-15% zircon in associated nepheline syenite. Accessory ilmenite and ilmenorutile have also been reported (Hankinson, 1958).

3. Sampling procedure

Samples of stream sediment were collected along the drainage of Granite Creek (Fig. 2; Table 1), upstream and downstream of the Lonnie deposit. The location and spacing of samples was controlled by accessibility, as Granite Creek runs within a canyon. There is more than 180m elevation difference between sample LO-13-26 and LO-13-01. The bed of the stream consists mainly of boulders, cobbles, and pebbles. Most of the sample sites are in the lee of large boulders or logs where the material was deposited in the final stages of bedload transport. The fraction of sediments that passed through an 8 mm sieve was kept. Samples were contained in permeable canvas bags and stored in plastic pails.

4. Laboratory procedure

4.1. Sample preparation

Samples were processed at the British Columbia Geological Survey Laboratory in Victoria. Small samples were dried in a Despatch LBB Series oven (1600 Watts, 13.3A) for 24 hours at temperatures between 38 and 40°C, whereas large samples were dried for 48 hours. Separation of dry samples into eight size fractions was carried out using a Humboldt MFG. Co. laboratory sieve (serial number H4325-136). The following size fractions were separated: +4 mm, 2 mm to 4 mm, 1 mm to 2 mm, 500 µm to 1 mm, 250 µm to 500 µm, 125 µm to 250 µm, 63 µm to 125 µm, and -63 µm. For the most thorough separation of each size fraction the uppermost sieve compartment was filled no more than 3 cm from its bottom; shaking time was eight minutes. The procedure was repeated until each sample was completely sieved. Individual fractions were stored in Kraft® sample bags. Before processing a new sample, each sieve was scrubbed clean using a stiff brush and a Haver USC 200-80 ultrasonic bath.

Each size fraction passed through a riffle-type splitter. Part of the sample was kept as a witness; the remainder was further split for pXRF analyses and for magnetic separation using an isodynamic separator (Frantz). Milling was carried out with Rocklabs Limited tungsten carbide mills consisting of a ring and roller bowl for three minutes. Compressed air was used to clean the milling equipment. When required, silica sand was milled between individual samples. In all cases equipment was washed with water and dried using a combination of compressed air followed by drying in a Despatch oven at 40°C to drive off surface moisture.

Standard XRD sample cups covered by 4µm polypropylene film were filled with sediment pulp and compressed. Two filter papers (2.4 cm in diameter) were placed over the pulp, and the remainder of the sample cup was filled with gauze to ensure a snug fit when capped. To avoid contamination of the pXRF stage by pulp residue, the sides of the cup were wrapped in parafilm.

Table 1. Descriptions of stream sediment sample sites in the Granite Creek drainage (July 2013).

	Location (UTM Zone 10, NAD83)		Elevation	Stream Characteristics					
Sample	Northing	Easting	(m)	Width (m)	Depth (m)	Flow	Clast Characteristics	Weight (g)	Sample Site
LO-13-01	6170135	411788	912	5	0.5	rapid	Rounded granite gneiss boulders < 1.5 m; average 8-15 cm.	16093.3	Lee of a log. Sand (< 2 mm); quartz, feldspar, biotite, white mica, sericite schist, and trace garnet. Not sieved in the field. Upstream from bridge.
LO-13-02	6170253	411895	915	4	0.75	rapid	Rounded granite gneiss and rare angular schist boulders < 2 m, average 2-10 cm.	5369.1	Lee of 1-2 m boulders. Sand (< 2 mm); sericite schist fragments, quartz, feldspar, biotite, opaques, and white mica particles. East side of stream flanked by 50 m cliff.
LO-13-04	6170326	412085	929	6	0.5	very rapid	Rounded granite gneiss and white mica granite boulders 40 cm-1.5 m.	8540.5	Lee of a boulder. Cobbles (5-15 cm) with sand (1-2 mm) forming matrix. Upstream from major slide. Trees right to the bank.
LO-13-23	6171607	412690	1030	4	0.5	rapid	Gneiss, muscovite schist, and quartzite < 1.5 m; average 5-15 cm	8323.2	Lee of boulders adjacent to submerged outcrop 5 m below rapids. Inside of a bend. Coarse sand and granules (2-3 mm) of quartz, feldspar, and mica form matrix. Minor free garnet; approximately 0.5 mm, rounded, Cliffs flank east side of creek.
LO-13-25	6171598	412797	1032	-	-	-	Gneiss, muscovite schist, and quartzite < 1.5 m; average 5-15 cm	3711.6	Narrow levee 2 m from stream edge. Quartz sand coarsening toward the stream. Similar to LO-13-23.
LO-13-26	6171813	413331	1095	3	0.5	rapid	Gneiss and schist 5-15 cm	3833.2	Lee of boulders under a log. Sand (average 2 mm) slate fragments, rare deep red and rose garnet, apatite, pyrite. 4 m downstream from rapids, upstream from road crossing.
LO-13-27	6171813	413331	1095	3	0.5	rapid	Gneiss and schist 5-15 cm	4856.9	Lee (0.5 x 2m) of large log. Sand (2 mm average) fining upward. Similar to LO-13-26.

4.2. Portable x-ray fluorescence

Analyses were carried out using a portable Thermo Fisher Scientific Niton FXL-950 instrument (Fig. 3; manufactured on July 17, 2012). This model is equipped with an Ag anode x-ray tube (serial number 56789-00109) capable of a maximum voltage of 50 kV, current of 0.2 mA, and power of 4 W. Four beams were used to detect elements (Table 2). Analytical time of each beam was set at 60 seconds with a spot size of 8mm. The “mining Hf/Ta mode” was chosen to obtain the highest resolution measurements of fluorescent peaks for high field strength elements (HFSE), which are of interest for the investigation of Nb and REE deposits.

Detection limits for Nb, Ta, La, Ce, Pr, Nd, Y, Ba, Sr, and P are given in Table 3. The pXRF methodology in this study

Fig. 3. The pXRF Thermo Fisher Scientific Niton FXL-950 instrument used in this study.

is described in Simandl et al. (2013c). At the start of each session, the pXRF was allowed 10 minutes to achieve a stable temperature (approximately - 25°C) before running a system check. Analyses of five standard reference materials bracketed stream sediment samples. These standards included a 99.995% SiO_2 blank, Standard Reference Material NIST 2780 (May and Rumble, 2004), Certified Reference Material "TRLK" Rare Earth Ore "CGL 124" (Registration Number: USZ 42-2006; Mongolia Central Geological Laboratory, 2006), and Reference Niobium Ore OKA-1 (Steger and Bowman, 1981). Samples were subjected to three repeat analyses to measure precision and ensure homogeneity.

5. Data quality

The accuracy and precision of the pXRF data can be assessed by considering the results of repeated analyses on standard reference materials of known composition (Tables 4, 5, and 6). Accuracy is evaluated by percent difference:

$$\%\text{diff} = \frac{\text{measured value} - \text{reference value}}{\text{reference value}} \times 100\%$$

Precision was assessed as relative standard deviation expressed in percent (%RSD) and as defined by:

$$\%\text{RSD} = \frac{\text{standard deviation}}{\text{mean}} \times 100\%$$

Error bars on diagrams for results herein reflect the precision (2σ) established by multiple analyses of standards. Of the elements for which abundances are reported here, only Ce had results above the detection limit on blank analyses. For n=38 an average of 119 ± 28 (2 σ) Ce was detected. For this reason, results for Ce should be considered higher than true values.

Analyses of the standard reference material NIST 2780 (Table 4) resulted in %diff less than 10% for Ca, Sr, Th, and Zr; less than 20% diff for Fe, Ti, and Ba; and 50% diff for S. Uranium, La, and Ce were over 100% diff and Nd was over 1000% diff. Certified values for NIST 2780 to compare with elemental abundances determined in this work for Ta, Y, and Pr are unavailable. The %RSD of Fe, Ca, Ti, Ba, S, Sr, Zr, and Y were less than 5%; Ce, Nd, and Pr were less than 10%. Thorium, U, and La had %RSDs of 26.4, 29.7, and 12.5%, respectively. No measurements above detection limits were made on P, Nb, or Ta.

Repeated determinations of elemental abundances by pXRF on the Mongolian rare earth ore TRLK CGL 124 resulted in %diff of 10% or less for Sr, La, Ce, Nd, and Pr (Table 5). For the elements Fe, Ca, Th, U, Nb, Zr, and Y it was between 10 and 46%, for Ba and S it was 160 and 170%. No determination of accuracy could be made for Ta, as certified values are unavailable. The precision was better than 5 %RSD for Fe, Ca, Ba, S, Sr, Th, Y, La, Ce, Nd, and Pr and better than 10% for U. Niobium, Ta, and Zr had %RSD of 11.8, 23.9, and 13.3% respectively.

The Nb Ore OKA-1 was evaluated for accuracy with reference to the CANMET certified values. For elements where no such value was available (indicated in Table 6) the average of three Li-borate fusion ICP-MS analyses carried out by ASL Limited (Vancouver) were used instead. The %diff of Fe, Ba, Sr, Nb, and Zr were less than 10%. Those of Ca, Ti, S, Y, La, and Ce, were less than 25%. For P, Th, U, Nd, and Pr the %diff ranged from 49 to 270%. The %RSD of Fe, Ca, P, Ti, Ba, S, Sr, Nb, Y, La, Ce, Nd, and Pr were less than 5%. Thorium, U, and Zr, had %RSDs of 23.8, 16.1, and 15.4.

Table 2. Elements and analytic time interval assigned to each of the four filters used in this study. [a] Represents the balance of fluorescence not attributed to any element analyzed here.

Beam	Duration (s)	Elements Analyzed
Main	60	Sb, Sn, Cd, Ag, Bal[a], Mo, Nb, Th, Zr, Y, Sr, U, Rb, Bi, As, Se, Au, Pb, W, Zn, Cu, Re, Ta, Hf, Ni, Co, Fe, Mn
Low	60	Cr, V, Ti, Ca, K
High	60	Nd, Pr, Ce, La, Ba, Sb, Sn, Cd, Ag
Light	60	Cl, S, P, Si, Al, Mg

Table 3. Detection limits for elements pertinent to carbonatite exploration. [a] Detection limits derived from a Thermo Fisher Scientific Niton XL3t Ultra; Thermo Fisher Scientific Niton FXL-950 is expected to have lower limits.

	Matrix	
Element	SiO_2 (ppm)	Natural sample or SiO_2+Fe+Ca (ppm)
Nb	2	2
Ta	NA	NA
Y[a]	1.5	4
La[a]	34	43
Ce[a]	40	47
Pr[a]	46	57
Nd[a]	75	93
Ba	28	33
Sr	2	2
P	80	90
U	NA	NA
Th	NA	NA
S	50	60

6. Results

Three samples (LO-13-04, LO-13-23 and LO-13-26) were selected for detailed study to identify grain size fractions that have the best potential to carry carbonatite indicator minerals (Fig. 4). Sample LO-13-04, not sieved through an 8mm screen in the field, consists mainly of grains coarser than +250 µm (medium sand). Sample LO-13-23 displays a positively skewed grain-size distribution. LO-13-26 contains subequal +2 mm, +1 mm, +500 µm, and +250 µm populations.

Niobium, Y, La, Ce, U, and Th are relatively enriched in the +125 µm, +63 µm, -63 µm size fractions (Fig. 4, Table 7). Barium, Sr, Pr, Nd, and Ta show less consistent patterns, nevertheless they are always detectable. Phosphorus is consistently detectable only in the +125µm fraction. Based on this information, similar findings from Aley carbonatite and Wicheeda drainages (Mackay and Simandl 2014a; 2014b), and because of other work (McClenaghan, 2011) indicating that the +250 µm, +125 µm, +63 µm fractions can be effectively used for indicator mineral studies, the +125 µm fraction was chosen for systematic study.

The +125 µm fraction of each of the seven samples collected in the Lonnie area was analysed for major and selected trace elements using pXRF. The ranges in abundance for major oxides are: 65.1 - 71.0 wt% SiO_2, 6.8 - 7.9 wt% Al_2O_3, 2.63-5.93 Fe_2O_3, 1.06-2.47 CaO, 0.28-1.59 TiO_2, 0.3- 0.5 wt% MgO,

Table 4. Results of repeated analyses on the NIST Standard Reference Material 2780. The number of readings above the detection limit is denoted as "n", standard deviation (1σ) as Std Dev. See text for details of %diff and %RSD. [a] Non-certified values supplied by Thermo Scientific.

		Certified values		pXRF values				
		ppm	+/-	n	Average	Std Dev	%diff	%RSD
Major Elements	Fe	27800	800	38	31400	345	13	1.1
	Ca	1950	200	38	1870	82	4	4.4
	P[a]	427	40	-	-	-	-	-
	Ti[a]	6990	190	38	6200	249	11	4.0
	Ba[a]	993	71	38	840	16	15	1.9
	S	12600	420	38	18800	327	50	1.7
Trace Elements	Sr[a]	217	18	38	232	4	7	1.5
	Th	12	-	38	13	3	7	26.4
	U	4	-	26	13	4	227	29.7
Specialty Metals	Nb	18	-	-	-	-	-	-
	Ta	-	-	-	-	-	-	-
	Zr	176	-	38	193	2	9	1.1
REE	Y	-	-	38	168	3	-	1.8
	La	38	-	38	90	12	156	12.5
	Ce	64	-	38	180	15	176	8.6
	Nd	28	-	38	330	29	1064	8.9
	Pr	-	-	38	180	13	-	7.2

Table 5. Results of repeated analyses on the Certified Reference Material "TRLK" rare earth ore CGL 124. The number of readings above the detection limit is denoted as "n", standard deviation (1σ) as Std Dev. See text for details of %diff and %RSD. [a] Converted to ppm from the oxide weight percent reported by the Mongolia Central Geological Laboratory.

		Certified Values		pXRF Values				
		ppm	+/-	n	Average	Std Dev	%diff	%RSD
Major Elements	Fe[a]	39938.36	594.53	38	45400	588	14	1.3
	Ca[a]	233562.6	2858.78	38	259000	1103	11	0.4
	P[a]	688.24	15.64	-	-	-	-	-
	Ti[a]	1198.7	71.92	-	-	-	-	-
	Ba	307	10	38	800	23	160	2.9
	S[a]	560.65	-	38	1510	62	170	4.1
Trace Elements	Sr	4900	400	38	4450	40	9	0.9
	Th	946	51	38	1180	19	25	1.6
	U	51.4	-	38	75	4	46	5.6
Specialty Metals	Nb	31	4.54	38	23	3	27	11.8
	Ta	-	-	30	60	13	-	23.9
	Zr	136	-	38	80	11	40	13.3
REE	Y	167	20	38	209	2	25	1.1
	La	21100	1100	38	20700	169	2	0.8
	Ce	27600	500	38	27400	234	1	0.9
	Nd	6500	300	38	5900	150	10	2.6
	Pr	2300	300	38	2160	41	6	1.9

Table 6. Statistical assessment of repeated analyses of reference material OKA-1. The number of readings above the detection limit is denoted as "n", standard deviation (1σ) as Std Dev. See text for details of %diff and %RSD. Unless otherwise noted, values are from Steger and Bowman (1981). [a] Average of three analyses by Li borate fusion inductively coupled plasma mass spectrometry (LB-ICP-MS). The error bracket corresponds to the absolute difference of the most extreme outlier from the average.

		Certified or Laboratory Values		pXRF Values				
		ppm	+/-	n	Average	Std Dev	%diff	%RSD
Major Elements	Fe	28000	-	37	30600	494	9	1.6
	Ca	313000	-	37	354000	1592	13	0.4
	P	11000	-	37	4300	203	60	4.6
	Ti[a]	1358	40	2	1530	41	13	2.7
	Ba[a]	2887	117	37	3070	32	6	1.0
	S	6000	-	37	4900	157	18	3.2
Trace Elements	Sr[a]	13501	56	37	12400	63	8	0.5
	Th[a]	57	4	37	150	37	169	23.8
	U[a]	29	5	37	43	7	49	16.1
Specialty Metals	Nb	3700	0.01	37	3390	64	8	1.9
	Ta[a]	36	8	-	-	-	-	-
	Zr[a]	112	5	37	120	18	6	15.4
REE	Y[a]	61	1	37	74	2	20	2.4
	La[a]	1107	43	37	1360	20	23	1.4
	Ce[a]	2045	75	37	2310	32	13	1.4
	Nd[a]	535	13	37	1400	39	162	2.7
	Pr[a]	182	4	37	670	32	270	4.8

Table 7. Results of pXRF analyses in eight size fractions for LO-13-04, LO-13-23, and LO-13-26 and the +125µm size fraction for all other samples taken from the Lonnie study area. [a] Total iron is reported as Fe_2O_3.

Unit	Size Fraction	Nb ppm	Ta ppm	Y ppm	La ppm	Ce ppm	Pr ppm	Nd ppm	Ba ppm	Sr ppm	P ppm	U ppm	Th ppm	Fe_2O_3[a] wt%	CaO wt%	TiO_2 wt%	S ppm	Zr ppm
LO-13-04	+4mm	13	36	19	122	187	231	407	406	267	<90	<4	8	4.90	5.95	0.51	1616	126
	+2mm	14	48	13	81	136	145	251	425	201	<90	<4	8	3.90	2.11	0.34	<60	135
	+1mm	24	38	12	69	136	121	212	395	154	<90	<4	8	3.41	1.15	0.30	<60	129
	+500µm	18	51	11	57	102	99	177	309	134	<90	<4	6	2.59	0.91	0.24	<60	120
	+250µm	44	48	16	65	109	84	150	255	145	<90	<4	7	2.63	1.06	0.28	<60	131
	+125µm	72	38	36	134	208	131	225	294	181	155	4	22	3.38	1.51	0.50	<60	191
	+63µm	79	47	68	182	308	128	242	341	211	508	11	51	3.86	1.76	0.61	136	458
	-63µm	71	33	67	138	231	92	169	416	247	<90	12	36	5.57	1.81	0.56	<60	665
LO-13-23	+4mm	32	49	16	65	104	108	202	408	151	<90	<4	10	2.97	1.70	0.27	<60	95
	+2mm	14	51	14	43	79	61	91	297	136	<90	<4	8	2.96	1.19	0.25	<60	104
	+1mm	9	45	15	79	128	93	181	318	127	<90	<4	6	2.30	0.92	0.19	<60	87
	+500µm	29	34	27	49	88	78	150	256	112	<90	5	8	2.57	0.91	0.16	<60	105
	+250µm	54	48	57	76	133	89	168	227	121	123	6	26	3.40	1.27	0.25	<60	161
	+125µm	61	48	110	138	243	101	223	258	155	734	15	85	3.87	1.84	0.56	<60	283
	+63µm	61	50	131	246	434	125	269	339	188	<90	27	134	3.47	2.09	0.67	<60	715
	-63µm	57	37	125	188	338	64	158	409	200	<90	27	94	4.84	1.83	0.65	<60	1213
LO-13-26	+4mm	8	44	15	83	137	143	265	285	119	<90	<4	<5	3.65	1.51	0.30	<60	111
	+2mm	12	47	17	65	117	127	227	266	116	<90	<4	5	3.53	1.36	0.31	<60	101
	+1mm	8	47	21	69	114	117	221	252	113	<90	<4	7	3.18	1.10	0.24	<60	97
	+500µm	19	36	23	64	102	107	166	213	102	<90	<4	6	2.71	0.95	0.20	<60	106
	+250µm	32	48	52	95	171	177	324	210	119	<90	<4	9	3.74	1.35	0.33	<60	133
	+125µm	75	62	118	193	353	232	478	228	163	660	15	56	5.95	2.27	1.09	<60	376
	+63µm	103	49	212	436	768	228	537	277	187	<90	47	178	5.38	2.47	1.59	<60	1660
	-63µm	42	32	113	242	401	103	235	360	205	<90	27	78	5.34	1.80	0.66	<60	1224
LO-13-01	+125µm	51	47	27	103	172	122	217	280	182	141	4	14	2.68	1.57	0.46	<60	157
LO-13-02	+125µm	73	38	33	135	217	142	274	297	178	178	7	19	3.26	1.54	0.51	<60	192
LO-13-25	+125µm	39	41	67	123	216	143	240	244	156	407	8	46	2.84	1.64	0.42	<60	228
LO-13-27	+125µm	16	50	23	57	107	111	195	219	151	<90	<4	10	2.61	1.48	0.31	<60	120

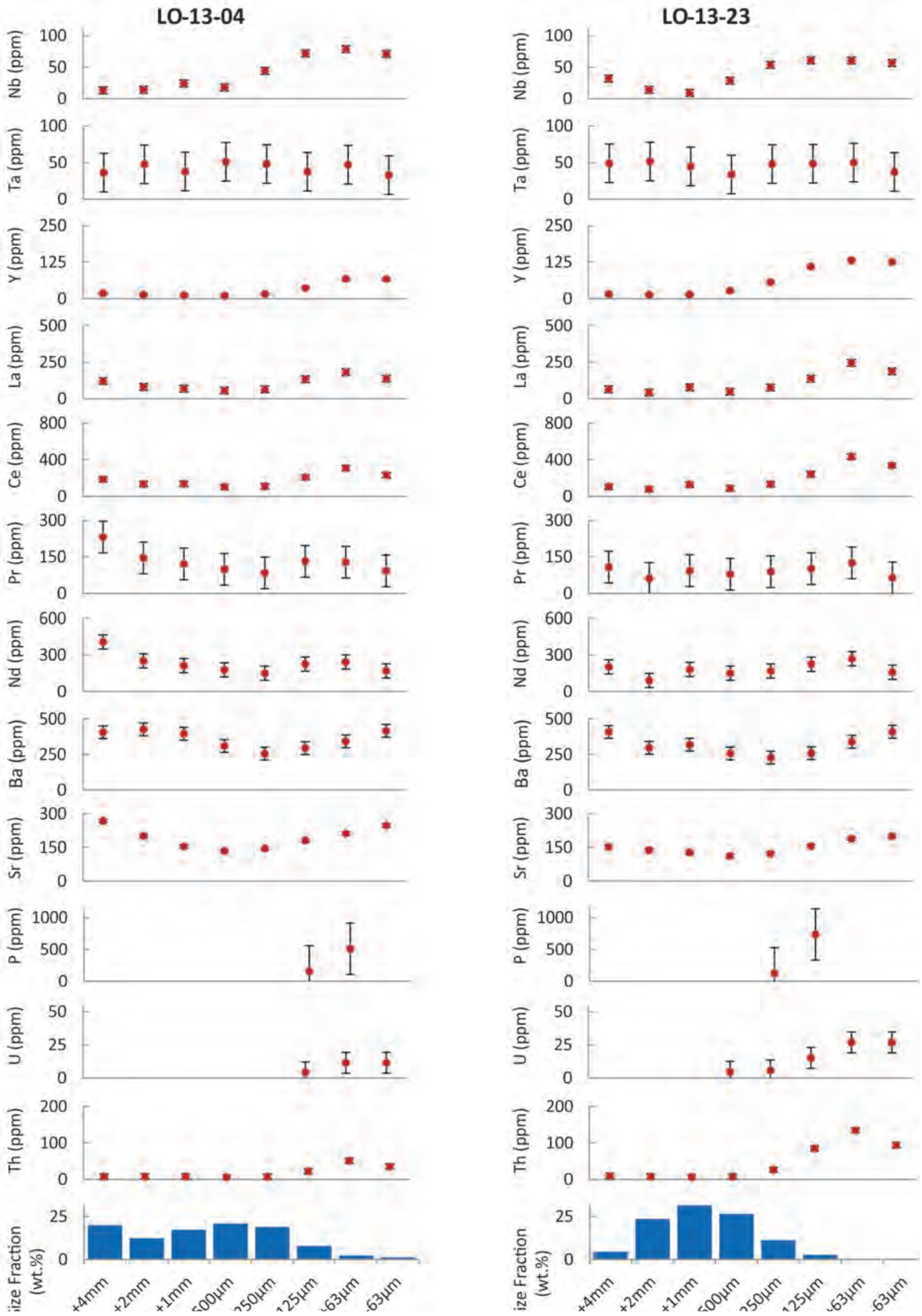

Fig. 4. Concentrations of elements, as determined by pXRF, that are expected to coincide with the greatest concentrations of indicator mineral grains for eight grain size fractions in samples LO-13-04, LO-13-23 and LO-13-26.

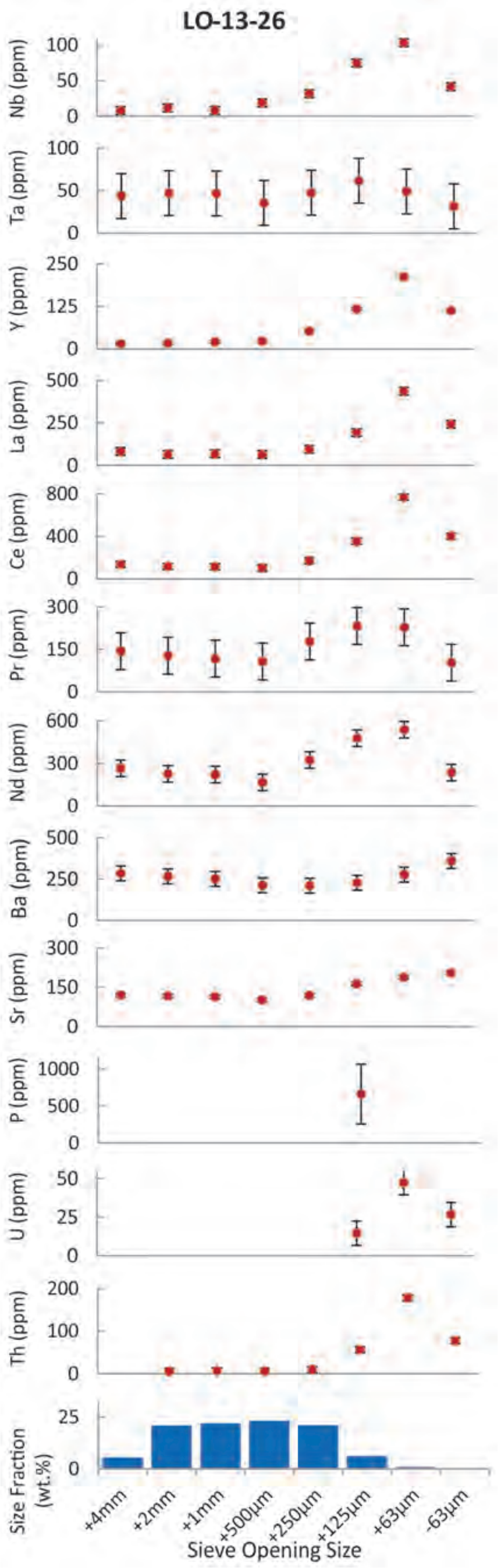

Fig. 4. Cont'd.

1.1 to 1.4 wt% K_2O and < 60-136 ppm S (Table 7).

Linear dependence between target elements and with other major and trace elements are common in sediments collected from Granite Creek (Fig. 5). There is a moderate correlation between Nb and La (R^2 = 0.72), a poor correlation between Nb and TiO_2 (R^2 = 0.41) or Fe_2O_3 (R^2 = 0.38); Nb and Ta do not correlate (R^2 = 0.002). Cerium correlates well with La (R^2 =0.96). Correlations between Ce and Nd (R^2 = 0.77), Ce and Pr (R^2 =0.64) and Ce and Y (R^2 =0.69) are weaker. For P, correlations are strongest with Y (R^2 =0.97), Th (R^2 =0.92), and U (R^2 =0.93), becoming progressively weaker with Ce (R^2 =0.53), La (R^2 =0.38), and Nd (R^2 =0.21). Zirconium correlates strongly with Ce (R^2 =0.92), Y (R^2 =0.89), and U (R^2 =0.80), and to lesser extend with Nd (R^2 =0.68) or Pr (R^2 =0.53). Significant linear dependencies also exist for Ca-Zr (R^2 =0.91), Ca-Ce (R^2 =0.81), Ca-Nd (R^2 =0.78), Ca-U (R^2 =0.70), Ca-P (R^2 =0.66), Ca-La (R^2 =0.64) and Ca-Pr (R^2 =0.60). Also of interest are the correlations of Fe_2O_3 with TiO_2 (R^2 = 0.96), Th with U (R^2 =0.82), and Sr with Ba (R^2 =0.74).

7. Discussion

Statistical assessments of pXRF results for standard reference materials (Tables 4, 5, and 6) indicate that the method is precise but prone to bias. Elements with the highest accuracy (less than 30%diff) in concentration ranges observed at Lonnie are Nb, Y, Sr, Th, Fe_2O_3, CaO, and TiO_2. Lanthanum, Ce, Nd, Ba, and U have %diff exceeding 100%. The % diff values for Ta, Pr, and P are unavailable.

Recommended values for standard reference materials are reported as a mean of results from several different techniques, making comparison with results from pXRF complicated. From a practical point of view pXRF analyses presented in this paper should be viewed as internally consistent but relative. Recalibration using results of standard laboratory analyses (as described in Simandl et al., 2013b) to correct for matrix effects and analytical biases to improve accuracy has not been performed.

Sediment size fractions commonly examined and hand picked for indicator minerals include 0.25-0.5 mm, 0.3-0.5 mm, and 0.25-0.86 mm (McClenaghan, 2011). The three finest size fractions from this study, +125 µm, +63 µm, and -63 µm, have the highest abundances of all potential pathfinder elements (Fig. 4). The +125 µm is the only size fraction that consistently returned results above the 90 ppm detection limit for P, a constituent of apatite, monazite, and xenotime, which are indicator minerals in REE exploration. The +125 µm size fraction is also the coarsest fraction of those enriched in carbonatite pathfinder elements, making it potentially the most versatile from the explorationist's point of view. However, both the +125 µm and +63 µm size fractions will be the subject of quantitative evaluation of minerals by scanning electron microscopy (QEMSCAN®)-based indicator mineral studies that we are initiating in collaboration with ACME Labs™.

Both geochemical and indicator mineral surveys relying on stream sediment sampling are based on the premise that the

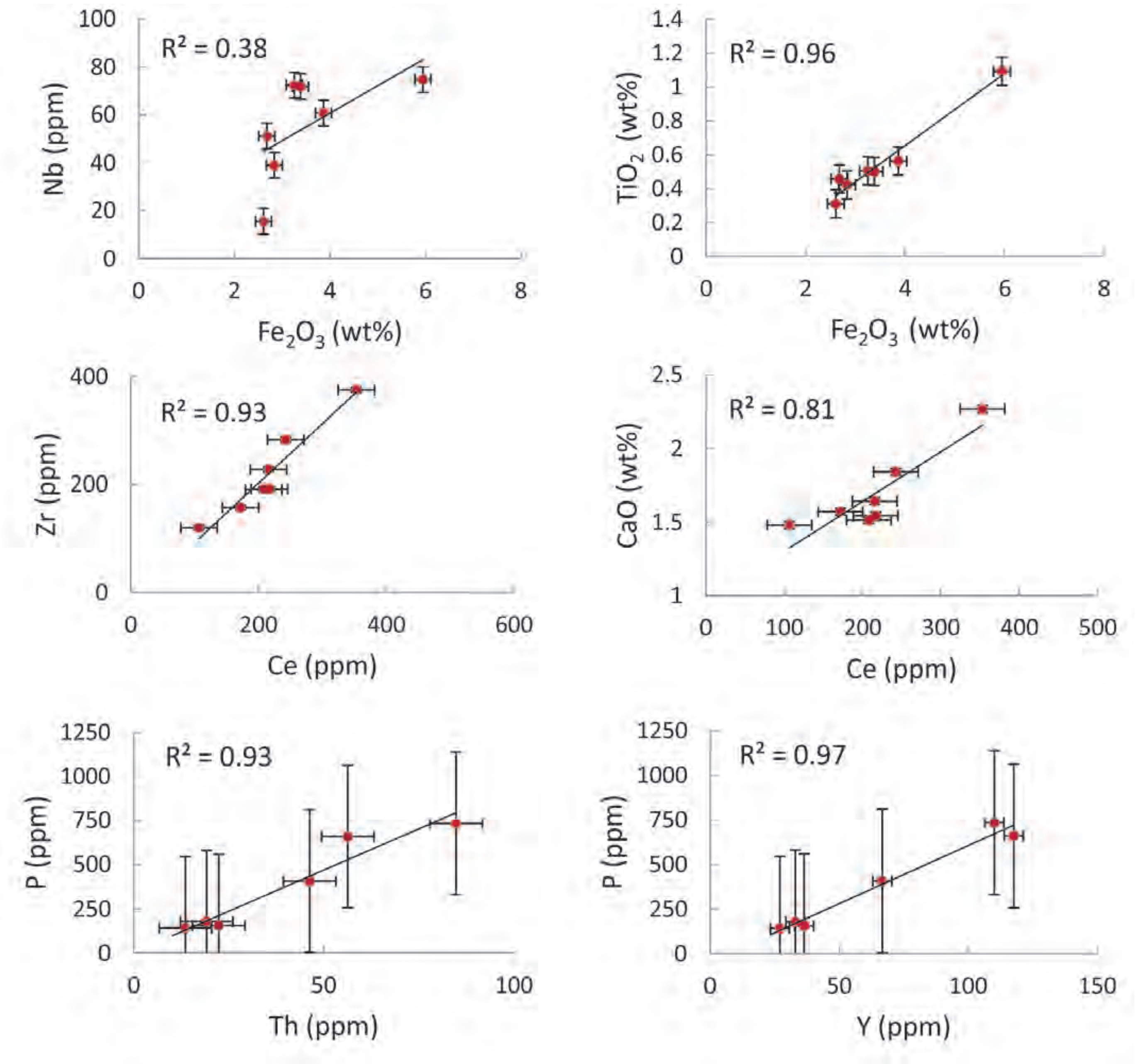

Fig. 5. Linear interpolation of elemental abundances analyzed by pXRF. The R^2 indicates strength of correlation with R^2=1 for totally dependent and R^2=0 for no relationship.

stream sediment sample is representative of the sample site. Assuming derivation of pathfinder elements and minerals from a single deposit (point source; Lonnie carbonatite), Hawkes' (1976) model should apply. Under such conditions, enrichment in carbonatite pathfinder elements (Nb, Ta, La, Ce, Pr, Nd, Y, Ba, Sr, P, U, and Th) immediately downstream of the point source relative to background abundances upstream of the point source is expected. A measurable decrease in pathfinder element abundances with increasing distance downstream of the point source is also expected until background abundances are reached.

Concentrations of pathfinder elements in stream sediments sampled in the vicinity of the Lonnie carbonatite complex are not in agreement with the ideal distribution of Hawkes' (1976) model. The upstream samples (LO-13-23, LO-13-25, LO-13-26, LO-13-27; Fig. 6) were taken to establish background concentrations of carbonatite indicator elements. No clear enrichment in Nb, Ta, La, Ce, Pr, Nd, Y, P, U, and Th in samples downstream of the Lonnie deposit (LO-13-01, LO-13-02, LO-13-04) was observed relative to those upstream of the deposit; only Ba and Sr concentrations are higher downstream of the deposit (Fig. 6; Table 7). The highest concentrations of Ta, La, Ce, Y, P, U, and Th were in samples upstream of the Lonnie carbonatite complex (LO-13-23 and LO-13-26; Fig.

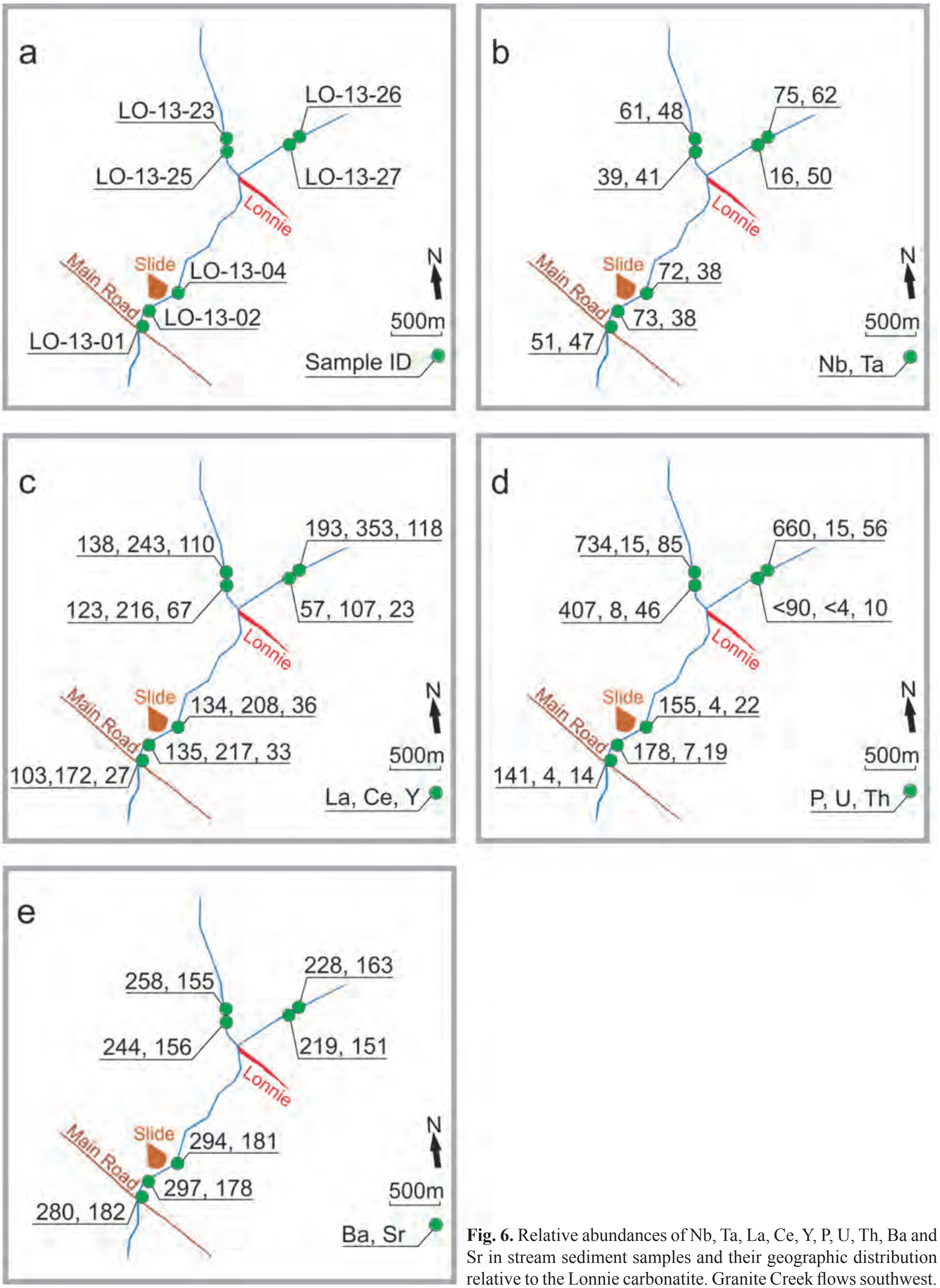

Fig. 6. Relative abundances of Nb, Ta, La, Ce, Y, P, U, Th, Ba and Sr in stream sediment samples and their geographic distribution relative to the Lonnie carbonatite. Granite Creek flows southwest.

6), suggesting that their main source is farther upstream. The most likely sources are the Vergil carbonatite (4.5 km to the northwest) and a number of Nb and TREE + Y soil geochemical anomalies (Fig. 2) identified by Rara Terra Minerals Corp. and reported by Helmel (2012).

It is unclear whether or not the Lonnie carbonatite complex is detectable by bulk stream sediment chemistry. Uncertainty is largely due to the lack of samples over a distance of more than 1300m between the Lonnie deposit and the nearest downstream sample (LO-13-04). All three of the samples downstream of the Lonnie carbonatite complex (LO-13-01, LO-13-02, and LO-13-04) are situated in a canyon. Dilution by mass wasting may have masked the influence of the Lonnie carbonatite complex on pathfinder element concentrations in these samples.

The relationships between potential indicator elements shown on X-Y plots (Fig. 5) reflect the relative proportions of indicator minerals in the sample and the chemical composition of these minerals. Frantz isodynamic separator can be used to amplify the pathfinder elements signal to noise ratio. The lack of correlation between Nb and Ta can be explained by poor pXRF precision for Ta (Table 5). Phosphorus correlations with Th and the REE may indicate the presence of monazite. Although none has been observed at Lonnie, monazite may be in the Wolverine Metamorphic complex. These elements also correlate strongly with Zr, where their relatively high abundances suggest co-occurrence of a REE-bearing mineral with zircon rather than REE being exclusively entrained within its matrix. The correlations of REE with calcium may be explained by substitution in apatite, monazite, or fluorocarbonates.

8. Conclusion

This study shows that the +125 μm size fraction is most appropriate for consideration in carbonatite indicator studies. Portable XRF is an excellent tool to assess relative abundances of elements to determine the most appropriate size fraction for indictor mineral sampling. However, a calibration procedure as described by Fajber and Simandl (2012) and Simandl et al. (2013b) should be used if increased accuracy is required. Irregular sample distribution downstream of the Lonnie deposit prevents us from concluding if the carbonatite is detectable using bulk stream sediment chemistry. Available data suggests that the main source of pathfinder elements, with the exception of Ba and Sr, is located upstream of the Lonnie carbonatite complex, possibly Vergil carbonatite or sources of Nb and TREE + Y anomalies identified by Rara Terra Minerals Corp. Much of the uncertainty in this data set will be clarified following the processing of samples by Frantz isodynamic separation and study of indicator minerals in resultant concentrates.

Acknowledgments

We thank Duncan Mackay for his assistance in the field. This project received funding and support from Targeted Geoscience Initiative 4 (2010-2015), a Natural Resources Canada program carried out under the auspices of the Geological Survey of Canada. Review and suggestions for improvement by Ray Lett and Duncan Mackay of the British Columbia Geological Survey are much appreciated.

References cited

Birkett, T.C. and Simandl, G.J., 1999. Carbonatite associated deposits. In: Simandl, G.J., Hora, Z.D., and Lefebure, D.V. (Eds.), Selected British Columbia Mineral Deposit Profiles, Vol. 3: Industrial Minerals and Gemstones. British Columbia Ministry of Energy, Mines and Petroleum Resources, British Columbia Geological Survey, Open File 1999-10.

Chisholm, E.O., 1960. Lonnie columbian deposit. British Columbia Ministry of Energy and Mines property file <http://propertyfile.gov.bc.ca/showDocument.aspx?&docid=138373> accessed October 2013.

Colpron, M. and Nelson, J.L., 2011. A digital atlas of terranes for the northern Cordillera. British Columbia Ministry of Energy and Mines, British Columbia Geological Survey, GeoFile 2011-11.

Fajber, R., and Simandl, G.J., 2012. Evaluation of Rare Earth Element-enriched Sedimentary Phosphate Deposits Using Portable X-ray Fluorescence (XRF) Instruments. In: Geological Fieldwork 2011, British Columbia Ministry of Energy, Mines and Natural Gas, British Columbia Geological Survey Paper 2012-1, pp. 199-209.

Ferri, F. and Melville, D.M., 1994. Bedrock geology of the Germansen Landing–Manson Creek area, British Columbia. British Columbia Ministry of Energy, Mines and Petroleum Resources, British Columbia Geological Survey, Bulletin 91, scale 1:100 000.

Halleran, A.A.D., 1980. Petrology, mineralogy and origin of the niobium-bearing Lonnie carbonatite complex of the Manson Creek area, British Columbia. Unpublished B.Sc. thesis, University of British Columbia, 41 p.

Hankinson, J.D., 1958. The Lonnie group columbium deposit, Unpublished B.Sc. thesis, University of British Columbia, 32 p.

Hawkes, H. E., (1976). The downstream dilution of stream sediment anomalies. Journal of Geochemical Exploration, 6, pp. 345-358.

Helmel, A., 2012. Rara Terra Minerals receives soil geochemical survey results from Lonnie Project. Press release <http://www.raraterra.com/investors/news/2012/mar27/> accessed October 2013.

Mackay, D.A.R. and Simandl, G.J., 2014a. Portable x-ray fluorescence to optimize stream sediment chemistry and indicator mineral surveys, case 1: Carbonatite-hosted Nb deposits, Aley carbonatite, British Columbia, Canada. In: Geological Fieldwork 2013, British Columbia Ministry of Energy and Mines, British Columbia Geological Survey Paper 2014-1, this volume.

Mackay, D.A.R. and Simandl, G.J., 2014b. Portable x-ray fluorescence to optimize stream sediment chemistry and indicator mineral surveys, case 2: Carbonatite-hosted REE deposits, Wicheeda Lake, British Columbia, Canada. In: Geological Fieldwork 2013, British Columbia Ministry of Energy and Mines, British Columbia Geological Survey Paper 2014-1,this volume.

Mariano, A.N. 1989a. Economic geology of rare earth minerals. In: Lipman B.R. and McKay G.A. (Eds.) Geochemistry and Mineralogy of Rare Earth Elements: Reviews in Mineralogy, Volume 21, pp. 303-337.

Mariano, A.N. 1989b. Nature of economic mineralization in carbonatites and related rocks. In: Bell, K. (Ed.) Carbonatites: Genesis and Evolution. Unwin Hyman, London, pp. 149-176.

May, W.E. and Rumble, J. Jr, 2003. Certificate of analysis - standard reference material 2780. National Institute of Standards and

Technology, Gaithersburg, USA, 4 p.

McClenaghan, M.B., 2011 Overview of processing methods for recovery of indicator minerals from sediment and bedrock samples. Workshop in the 25th International Applied Geochemistry Symposium, Vuorimiesyhdistys, Rovaniemi, Finland, pp. 1-6.

Mongolia Central Geological Laboratory, 2006. Certified Reference Material "TRLK" Rare Earth Ore "CGL 124" Certificate of Analysis. Ulaanbaatar, Mongolia, 6 p.

Pell, J., 1994. Carbonatites, nepheline syenites, kimberlites and related rocks in British Columbia. British Columbia Ministry of Energy, Mines and Petroleum Resources, British Columbia Geological Survey, Bulletin 88, 136 p.

Rowe, R.B., 1958. Niobium (columbium) deposits of Canada. Geological Survey of Canada, Economic Geology Series 18, 103p.

Simandl, G.J., Prussin, E.A., and Brown, N., 2012. Specialty metals in Canada. British Columbia Ministry of Energy and Mines, British Columbia Geological Survey, Open File 2012-7, 48 p.

Simandl, G.J., Reid, H.M., and Ferri, F., 2013a. Geological setting of the Lonnie niobium deposit, British Columbia, Canada. In: Geological Fieldwork 2012, British Columbia Ministry of Energy, Mines and Natural Gas, British Columbia Geological Survey Paper 2013-1, pp. 127-138.

Simandl, G.J., Fajber, R., Paradis, S., and Simandl, L.J., 2013b. Exploration for sedimentary phosphate (± REE) deposits using handheld XRF – An orientation survey. Geochemistry: Exploration, Environment, Analysis. Available online: http://dx.doi.org/10.1144/geochem2012-180.

Simandl, G.J., Stone, R.S., Paradis, S., Fajber, R., Reid, H.M., and Grattan, K., 2013c. An assessment of a handheld X-ray fluorescence instrument for use in exploration and development with an emphasis on REEs and related specialty metals. Mineralium Deposita. Available online: http://link.springer.com/article/10.1007/s00126-013-0493-0.

Steger, H.F. and Bowman, W.S., 1981. OKA-1: a certified niobium reference ore. CANMET Report 81-1E, Canada Centre for Mineral and Energy Technology, Ottawa, Canada, 16 p.

Thompson, R.M., 1955. Lonnie. British Columbia Department of Mines, Minister of Mines Annual Report 1954, A96-A97.

Woolley, A.R. and Kjarsgaard, B.A., 2008. Carbonatite occurrences of the world; map and database. Geological Survey of Canada, Open File 5796, scale 1:19 000 000.

Portable X-ray fluorescence to optimize stream sediment chemistry and indicator mineral surveys, case 1: Carbonatite-hosted Nb deposits, Aley carbonatite, British Columbia, Canada

Duncan A.R. Mackay[1] and George J. Simandl[1, 2, a]

[1] University of Victoria, School of Earth and Ocean Sciences, Victoria, BC, V8P 5C2
[2] British Columbia Geological Survey, Ministry of Energy and Mines, Victoria, BC, V8W 9N3
[a] corresponding author: George.Simandl@gov.bc.ca

Recommended citation: Mackay, D.A.R., and Simandl, G.J., 2014. Portable X-ray fluorescence to optimize stream sediment chemistry and indicator mineral surveys, case 1: Carbonatite-hosted Nb deposits, Aley carbonatite, British Columbia, Canada. In: Geological Fieldwork 2013, British Columbia Ministry of Energy and Mines, British Columbia Geological Survey Paper 2014-1, pp. 183-194.

Abstract
The Aley carbonatite-hosted deposit is the most important Nb resource in the British Columbia alkaline province. Portable X-ray fluorescence (pXRF) was used effectively to determine concentrations of carbonatite pathfinder elements (Nb, Ta, La, Ce, Pr, Nd, Y, Th, U, Ba, and Sr) in stream sediments. Investigation of sediments of the unnamed creek (“Al creek”) draining the Aley carbonatite area, indicates that the + 250 µm, + 125 µm, and + 63 µm size fractions contain high concentrations of carbonatite pathfinder elements (Nb, Ta, La, Ce, Pr, Nd, U, and Th) relative to other size fractions. The + 125 µm fraction was chosen for systematic evaluation of the pathfinder element distribution in Al Creek sediments because it is suitable for chemical analysis and Quantitative Evaluation of Materials by Scanning electron microscopy (QEMSCAN). This method will be used in the second part of this study, which will concentrate on indicator minerals. The same samples enriched in pathfinder elements are expected to contain minerals characteristic of carbonatites such as pyrochlore, columbite-(Fe), fersmite, monazite-(Ce), rare earth element (REE)-bearing fluorocarbonates, barite, and apatite. As expected, samples overlying the deposit and immediately downstream from the Aley carbonatite have the highest concentrations of pathfinder elements. Optical microscopy, electron microprobe (EMP), laser ablation inductively coupled plasma mass spectrometry (LA-ICP-MS), and QEMSCAN studies of these samples are required to identify the most useful carbonatite indicator minerals and quantify their relative abundances with increasing distance from the deposit.

Keywords: Niobium, tantalum, indicator minerals, pathfinder elements, stream sediment, carbonatite, portable x-ray fluorescence, pyrochlore, fersmite, columbite

1. Introduction

Carbonatites, carbonatite complexes, and their weathered equivalents are the main sources of Nb (Mariano, 1989a, b; Birkett and Simandl, 1999; Simandl et al., 2012, 2013a; Tantalum-Niobium International Study Center, 2013). They are most common along rift zones in intracratonic settings (Woolley and Kjarsgaard, 2008). The Aley carbonatite is one of a series of carbonatite complexes, syenite complexes, and other alkaline rocks that forms the British Columbia alkaline province (Fig. 1; Pell, 1994). It lies 135 kilometres north of Mackenzie, British Columbia and 20 kilometres northeast of the Ospika Arm of Williston Lake, east of the Rocky Mountain Trench (Fig. 1) and was discovered following base metal exploration (Pride, 1983). It was the subject of further study and exploration over the next 30 years (Mäder, 1986, 1987; Pride, 1987a, b; Robert et al., 2005; Nethery, 2007; Chung and Crozier, 2008). The deposit has a measured resource of 113 million tonnes at 0.41% Nb_2O_5 and an indicated resource of 173 million tonnes at 0.35% Nb_2O_5 with a cutoff grade of 0.20% Nb_2O_5 (Taseko Mines Limited, 2013).

The main objectives of this study are to: 1) determine if stream sediment geochemistry can be used effectively to explore for Aley-type deposits; 2) establish the best stream sediment size fraction for indicator minerals that might point to Nb-bearing carbonatite deposits; 3) characterize the geochemical gradient of potential pathfinder elements (Nb, Ta, REEs, P, Ba, Sr, U, and Th) in sediments downstream from the deposit; and 4) evaluate the usefulness of pXRF analyses for preliminary assessment of indicator mineral and stream sediment studies.

2. Geological setting

Rocks of the British Columbia alkaline province were emplaced during three main events: ~ 800-700 Ma (postulated breakup of Rodinia), ~ 500 Ma (extensional tectonism and attenuation of the continental margin), and ~ 360-340 Ma (renewed extensional tectonics; Pell, 1994; Millonig et al., 2012). Multiple phases of deformation and associated sub-greenschist to amphibolite grade metamorphism overprinted the carbonatites between ~ 155 and 50 Ma (Pell, 1994; Millonig et al., 2012).

The Aley carbonatite cuts Lower to Middle Paleozoic sedimentary rocks of the western Cordilleran foreland fold and thrust belt (Figs. 1, 2). The regional geology of the area was originally mapped at the scale of 1:253,440 by Irish (1970). The deposit is in the Cassiar terrane, which includes a platformal assemblage of siliciclastic and carbonate rocks

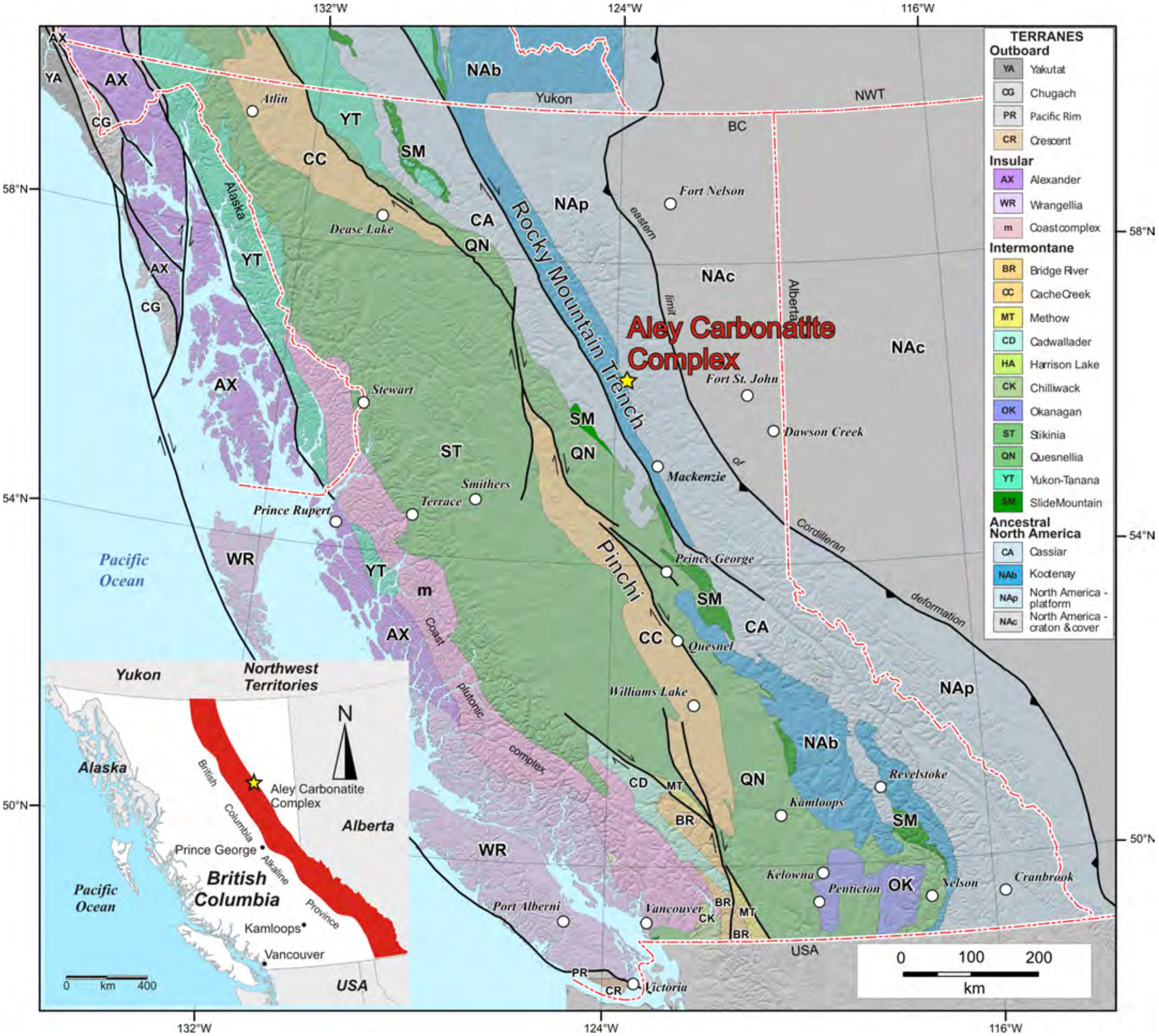

Fig. 1. Tectonic setting of the Aley carbonatite complex (yellow star). British Columbia alkaline province shown in red (inset map). Municipalities are denoted by white circles. Modified after Pell (1994).

that were deposited along the western margin of Laurentia (Mäder, 1986; Pell, 1994). The Kechika Formation (Cambrian to Early Ordovician) unconformably overlies the Rosella Formation (Lower Cambrian; Pyle and Barnes, 2001). It consists of argillaceous limestone, calcareous siltstone, and dolostone. The Skoki Formation (Lower to Middle Ordovician) is generally in fault contact with the Kechika Formation and consists of dolostone and volcanic rocks (Mäder, 1986). The Road River Group (Lower to Upper Ordovician-Silurian) caps the succession, locally unconformably overlies the Skoki Formation, and consists of cherty dolostone, shale, argillaceous limestone, and rare quartzite and quartz pebble conglomerate (Mäder, 1986; Pyle and Barnes, 2001). Regional metamorphism reached lower greenschist facies (Mäder, 1986) and coincided with convergent tectonism and orogenesis between ~ 155 and 50 Ma (Pell, 1994; Millonig et al., 2012).

The metasedimentary sequence was intruded by the Aley carbonatite, REE-bearing carbonatite dikes, the Ospika diatreme, and lamprophyre dikes (Fig. 2; Mäder, 1986; Pell, 1994; McLeish, 2013). Zircon from the dolomite carbonatite phase of the Aley carbonatite contains insufficient radiogenic Pb for U-Pb geochronology (Mäder, 1986; McLeish, 2013), but McLeish (2013) reported a U-Pb titanite age of 365.9 ± 2.1 Ma for the Ospika diatreme. The Aley carbonatite displays an early phase of deformation lacking in the Ospika diatreme indicating that it is older than ~ 366 Ma (McLeish, 2013). The Road River Group, (Lower to Upper Ordovician-Silurian, based on conodont biostratigraphy; Mäder, 1986; Pyle and

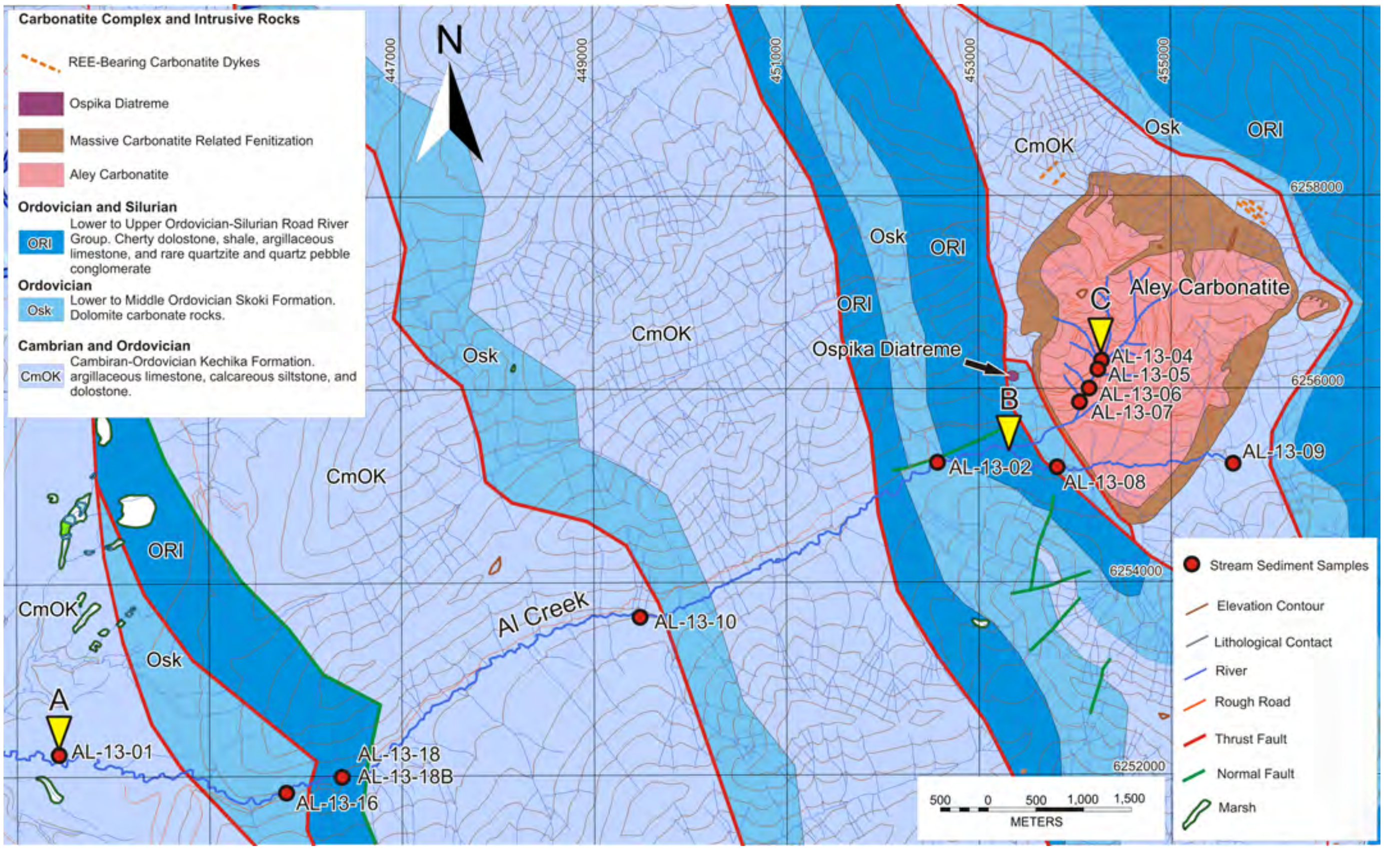

Fig. 2. Geological setting of the Aley carbonatite and locations of stream sediment samples. Yellow markers (A-B-C) denote location of profile in Figure 6. Modified after Pride (1983), Mäder (1986), Massey et al. (2005), and McLeish (2013). UTM zone 10, NAD 83.

Barnes, 2001), is the youngest unit overprinted by this early deformation that is cut by lamprophyre dikes (considered related to the Aley carbonatite and Ospika diatreme) suggesting that the Aley carbonatite is older than 366 Ma and younger than the Road River Group (McLeish, 2013).

3. Geology of the Aley carbonatite complex

The Aley carbonatite outcrops intermittently over an area 3 to 3.5 km in diameter (Fig. 2; Mäder, 1986). It intruded sedimentary host rocks as a sill and was subsequently folded within a recumbent nappe (McLeish et al., 2010; McLeish. 2013). The main phase of the carbonatite consists of layered or banded dolomite carbonatite surrounded by minor calcite carbonatite (Mäder, 1986). Kressal et al. (2010) observed that the dolomite carbonatite phase contains apatite, pyrite, calcite, and Nb-bearing minerals such as fersmite [$(Ca,Ce,Na)(Nb,Ta,Ti)_2(O,OH,F)_6$], pyrochlore [$(Na,Ca)_2Nb_2O_6(OH,F)$], columbite-(Fe) [$(Fe,Mn)Nb_2O_6$] and rare, fine-grained acicular aggregates of Nb-rich rutile [$(Ti, Nb, Fe)O_2$]. Pods or lenses of magnetite (10s of centimetres to metres in size) are found throughout the dolomite carbonatite phase and contain apatite, phlogopite, Nb-bearing minerals, zircon, and interstitial carbonates (Kressall et al., 2010). The magnetite pods likely represent deformed and distended cumulate layers (Kressall et al., 2010). Monazite commonly co-exists with fersmite in pseudomorphs after primary columbite-(Fe) or pyrochlore (Mäder, 1986; Kressall et al., 2010).

Massive fenite surrounds the carbonatite intrusion (Fig. 2). It displays a characteristic dark blue-green colour and contains abundant richterite, arfvedsonite, and aegirine (Mäder, 1986; Kressall et al., 2010). The fenite contains brecciated metasedimentary and feldspathic material. The feldspathic breccia clasts resemble altered syenite fragments; however, they are probably strongly fenitised and albitised fragments of the Kechika Formation.

Carbonatite dikes exposed on the northwest ridge above the main deposit (Fig. 2) contain significant concentrations of light rare earth elements (LREE; Mäder, 1986). The LREE mineralisation consists of REE-bearing carbonates and fluorocarbonates (Mäder, 1986). The dikes probably represent late differentiated phases of the Aley carbonatite melt (Mäder, 1986).

4. Methods

4.1. Sample collection

Twelve stream sediment samples were collected from a creek ("Al", Fig. 2) draining the Aley carbonatite during the 2013 field season (Table 1). One sample was collected upstream of the deposit to assess background geochemistry. Four samples, spaced 200 to 300 m apart, were collected along

Fig. 3. Al-13-05 sample site; dry pool below chute over fenite bedrock. Sampled material forms matrix between cobbles and boulders. Looking north up the dry stream bed valley toward the Aley Carbonatite. Shovel is 1 m long.

the dry tributary of Al Creek directly over the deposit (Fig. 3). The remaining seven samples were collected along the creek, downstream from the deposit, 1.5 to 3 km apart as access allowed (Figs. 2, 4). The bed of the creek consists mainly of boulders, cobbles, and pebbles (Fig. 4). Sample sites included dry pools (Fig. 3), and the lee areas of boulders and fallen trees, and bars (Table 1). Matrix material between cobbles and boulders, generally from an area < 1 m^2, was sampled (Fig. 4; Table 1). Organic material (conifer needles, leaves, and twigs) was scrapped from the surface of samples sites. Not all of the organic material could be avoided during sample collection, and minor amounts were retained in the coarser fractions (+ 500 µm and coarser). Material was wet sieved through a + 8 mm screen, except where noted in Table 1. Weights for dried samples range from 4.1 to 21.8 kg. Sample AL-13-18B is a pre-concentrate (washed by hand using a pan) of stream sediment close to sample AL-13-18.

Fig. 4. Al-13-08 sample site; Al creek, downstream of the Aley carbonatite. Sampled material constitutes matrix between cobbles and boulders, which form the predominant substrate. Stream is 3.5 m wide; looking east upstream.

4.2. Sample preparation and portable XRF analyses

Samples were dried in an oven at 40°C, weighed, and dry sieved into + 4 mm, 2 mm to 4 mm, 1 mm to 2 mm, 500 µm to 1 mm, 250 µm to 500 µm, 125 µm to 250 µm, 63 µm to 125 µm, and - 63 µm fractions. To shorten the text and simplify figures, the following notation was used throughout for the same grain size intervals; + 4 mm, + 2 mm, + 1 mm, + 500 µm, + 250 µm, + 125 µm, + 63 µm, and - 63 µm. Each size fraction was weighed individually. Selected size fractions were split using a riffle splitter with a portion being kept as a witness sample, a portion for magnetic separation, and a portion for XRF analyses. Samples for XRF analyses were milled using ring and roller bowl tungsten carbide mills. Standard XRF sample pulp cups were then prepared and analysed by portable XRF. Analyses were carried out using a portable Thermo Fisher Scientific Niton FXL-950 instrument. A complete description of equipment, specifications, sample preparation, and laboratory methods and information about standards, operating procedures, instrument settings, limits of detections, and data quality control are in Luck and Simandl (2014).

The factory-calibrated pXRF data are internally consistent and have acceptable precision; however, they were not recalibrated using results of standard laboratory analyses [lithium metaborate inductively couple plasma mass spectrometry (LMB ICP-MS)] as described in Simandl et al. (2013b) to improve accuracy by correcting for matrix effects and analytical bias. For example, good accuracy is expected for La and Nb. Other elements (e.g. Sr) are underestimated.

Table 1. Characteristics of stream channel and sample sites. Sample AL-13-09 was collected upstream of the deposit. Samples Al-13-04, AL-13-05, AL-13-06, and AL-13-07 were collected directly over the deposit. Remaining samples are in order of increasing distance downstream of the deposit.

	Location		Elevation	Stream Character			Clast Size (cm)		Dry wt.	Sample Site Characteristics
Sample ID	Northing	Easting	(m)	Width (m)	Depth (m)	Flow	Average	Maximum	(kg)	
AL1309	6255259	455696	1406	2.5	0.2	moderate	2 to 5	30	14.2	Lee of fallen tree; clasts predominantly white dolomite, limestone, and slate.
AL1304	6256338	454355	1520	1.5	N/A	N/A	2 to 5	50	4.9	Exposed bedrock (partly covered by boulders); dry streambed; sampled from matrix between cobbles and boulders; not sieved in the field.
AL1305	6256192	454249	1479	3	N/A	N/A	5 to 10	40	6.7	Dry pool below chute in dry streambed (Fig. 3); exposed bedrock (partly covered by boulders); not sieved in the field.
AL1306	6256016	454132	1431	2	N/A	N/A	3 to 5	150	6.8	Fine-grained material in dry pools (< 50 x 50 cm) between fenite and carbonatite cobbles and boulders; not sieved.
AL1307	6255865	454059	1400	2	N/A	N/A	2 to 5	35	6.9	Dry pool below cobbles and boulders; no exposed bedrock in dry streambed; large skree slope upstream; not sieved.
AL1308	6255181	453823	1298	3.5	0.3	rapid	5 to 15	100	9.4	Sample from matrix between cobbles and boulders (Fig. 4); predominantly slate and limestone clasts; rare fenite breccia clasts.
AL1302	6255244	452580	1246	3.5	0.3	rapid	5 to 10	150	14.7	Sample from matrix between cobbles and boulders; rare fenite boulders
AL1310	6253666	449483	1082	4.5	0.4	rapid	5 to 10	200	14.8	Near stream bank in active channel; lee of boulders; upstream of several slides; slate, limestone, and rare fenite breccia clasts are predominant.
AL1318	6251991	446312	928	4	0.8	rapid	1 to 2	200	12.2	Bar (4 x 16 m) downstream of fallen trees; sample from matrix between pebbles and cobbles; downstream of several slides; few subrounded to subangular fenite, carbonatite, and Ospika diatreme boulders a few m downstream of sample site.
AL1318B	6251991	446314	928	4	0.8	rapid	1 to 2	200	4.1	Same as above; preconcetrate (seived to 8 mm then washed in pan) sample close to AL-13-18.
AL1316	6251818	445779	891	3	0.4	rapid	2 to 5	40	14.4	5 x 10 m area in lee of fallen trees; upstream of a landslide.
AL1301	6252228	443432	793	5	0.3	rapid	1 to 3	15	21.8	Lee of fallen trees.

Remaining elements, including U and Th, are overestimated. Based on strong positive correlation between 11 U and 15 Th pXRF, and corresponding LMB-ICPMS analyses of stream sediments from Aley, Lonnie and Wicheeda (unpublished) processed in exactly the same manner as those in the present study, U and Th are overestimated of the order of 35% and 90% respectively. The pXRF is not a substitute for traditional laboratory methods where high accuracy and precision are required.

5. Results

Samples AL-13-02, AL-13-18, and AL-13-18B, were chosen for systematic study of all size fractions. The particle size distributions for samples AL-13-02 and AL-13-18 are skewed toward coarser size fractions, whereas AL-13-18B displays a nearly normal distribution (Fig. 5).

In samples Al-13-18 and Al-13-18B, Nb, Ta, Y, La, Ce, Pr, Nd, U, Th, and P are enriched in the + 125 µm, and + 63 µm size fractions relative to other sizes (Fig. 5). Similar trends exist for Al-13-02, however, the + 250 µm, and + 500 µm fractions also contain relatively high Nb, Ta, Y, La, Ce, Pr, Nd, U, and Th concentrations. Phosphorus is detectable in the + 125 µm fraction for AL-13-18 and AL-13-18B, but is below the limit of detection in the + 125 µm fraction for sample AL-13-02. High abundances of pathfinder elements (relative to other size fractions from the same samples) are also observed in the + 125 µm and + 63 µm size fractions in sediments from the nearby Lonnie (Luck and Simandl, 2014) and Wicheeda (Mackay and Simandl, 2014) carbonatite study areas. The + 125 µm fraction was chosen for systematic study because of these higher abundances and because it is a suitable size for indicator mineral studies.

The ranges in abundance of selected major oxides (Table 2) are: < 16.5 to 45.8 wt% SiO_2, < 1.8 to 7.0 wt% Al_2O_3, 1.3 to 15.2 wt% Fe_2O_3, 10.9 to 31.8 wt% CaO, < 0.1 to 0.3 wt% TiO_2, < 1.4 to 6.4 wt% MgO, and 0.2 to 2.6 wt% K_2O. Concentration ranges for trace elements (Table 2) are: 15 to 9988 ppm Nb, < 7 to 166 ppm Ta, 14 to 170 ppm Y, 70 to 2010 ppm La, 115 to 2977 ppm Ce, 147 to 1579 ppm Nd, 80 to 661 ppm Pr, 140 to 910 ppm Ba, 177 to 2018 ppm Sr, < 90 to 9412 ppm P, < 1 to 62 ppm U, and 9 to 570 ppm Th.

6. Discussion

High concentrations of Nb, Ta, La, Ce, Pr, Nd, U, and Th in the + 250 µm, + 125 µm, and + 63 µm fractions (Fig. 5) probably reflect the presence of carbonatite indicator minerals. The highest values typically coincide with the Aley carbonatite (samples AL-13-04, AL-13-05, AL-13-06; Figs. 6, 7). As expected, relative concentrations as high as 9988 ppm Nb, 133 ppm Ta, 2010 ppm La, 2977 ppm Ce, 171 ppm Y, 44 ppm U, 570 ppm Th, and 2018 ppm Sr occur over or directly downstream of the deposit and decrease with increasing distance downstream to between 3495 and 3311 ppm Nb, 79 and 73 ppm Ta, 596 and 561 ppm La, 936 and 866 ppm Ce, 72 and 71 ppm Y, 35 and 26 ppm U, 266 and 251 ppm Th, and 827 and 711 ppm Sr (Figs. 6, 7; Table 2). Barium does not follow this trend, suggesting barite input from dolostones and argillaceous limestones of the Skoki and Kechika formations.

Samples taken immediately below slides (greater than 200 m^2) and scree slopes (such as AL-13-07) show a decrease in the concentrations of Nb, Ta, La, Ce, Y, U, Th, and Sr relative to adjacent upstream (Al-13-06) and downstream samples (AL-13-02; Figs. 6, 7). This demonstrates the effect of dilution of pathfinder elements by incorporation of unmineralized material (unconsolidated overburden and slate and limestone scree). Sample AL-13-02, taken in an active stream channel, has higher concentrations of pathfinder elements relative to AL-13-07 (Fig. 6), possibly due to concentration of indicator minerals by winnowing. Sample AL-13-09, obtained upstream of the Aley carbonatite (Fig. 7), has low concentrations of carbonatite pathfinder elements relative to samples downstream of the deposit. Subrounded to subangular carbonatite, fenite, and diatreme boulders were found immediately downstream of AL-13-18 and AL-13-18B (Figs. 6, 7; Table 2). It is unclear if these boulders were derived from the Aley carbonatite or a different occurrence. Sample AL-13-16, downstream of this site, displays an increase in Nb, Ta, La, Ce, Y, U, Th, and Ba relative to Al-13-18 and AL-13-18B, which may be related to the boulders.

High coefficients of determination for pathfinder elements (Fig. 8) probably represent indicator mineral chemistry and mineral assemblages. The strong linear dependence between Nb and Fe_2O_3 ($R^2 = 0.97$; Fig. 8a) likely represents the co-occurrence of Nb-bearing minerals and magnetite in the stream sediments. Correlation between Nb and Ta ($R^2 = 0.83$; Fig. 8b) agrees with the expected presence of pyrochlore, columbite-(Fe), and/or fersmite in the stream sediments. The Nb:Ta ratio of pyrochlore and columbite-(Fe) from carbonatites is typically high and is reflected in the high (on average 50:1) Nb:Ta ratio of the sediments (Table 2). Niobium and La ($R^2 = 0.81$; Fig. 8c) display a strong relationship which is likely the result of coincidence of Nb-bearing and REE-bearing minerals in the stream sediments. It remains unclear if most of the REEs are in the crystal structure of Nb-bearing minerals rather than REE-bearing carbonates, fluorocarbonates, and/or phosphates. Poor linear dependence between Nb and TiO_2 ($R^2 = 0.20$; Fig. 8d) is likely the result of low Ti concentrations expected in pyrochlore sourced from carbonatites. It may also indicate negligible concentrations of Nb-rutile in stream sediments, mirroring the low abundances in the deposit reported by Kressal et al. (2010). Samples AL-13-04, AL-13-05, and AL-13-06 have the highest Nb contents (Fig. 7 a-d) and fail to plot directly on the best-fit line (Fig. 8a). These samples were taken from a dry tributary of Al creek; the higher Nb contents might reflect reduced levels of fluvial reworking in an intermittent stream. Alternatively, they might be the consequence of local variations in the concentration of fersmite, columbite, and pyrochlore in underlying mineralisation.

Cerium correlates strongly with La ($R^2 = 0.99$) and well with Nd ($R^2 = 0.95$), Pr ($R^2 = 0.94$), and Y ($R^2 = 0.85$). This

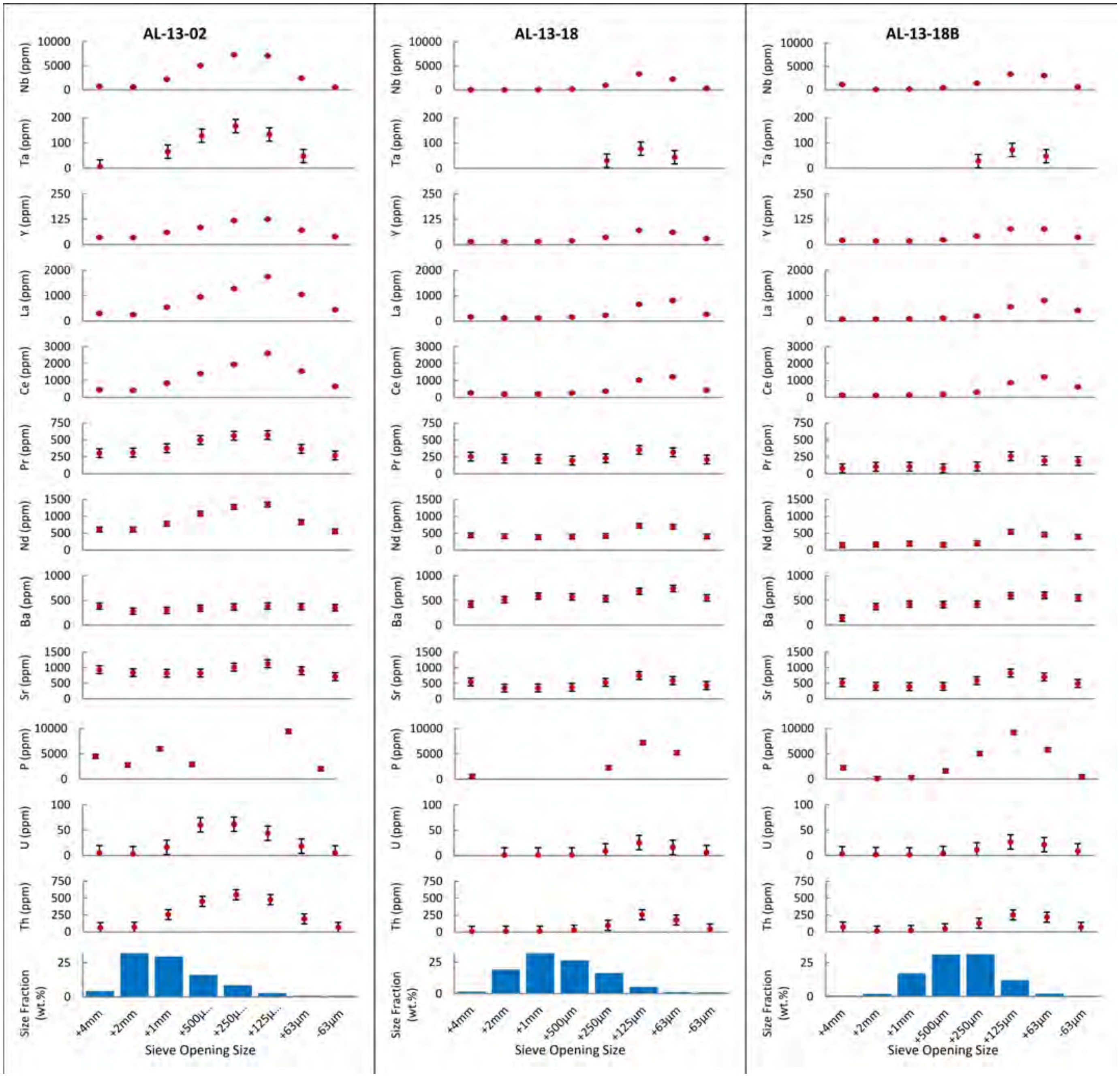

Fig. 5. Portable XRF analyses for selected trace elements and grain size fraction distributions of samples AL-13-02, AL-13-18, and AL-13-18B. The + 250 µm, + 125 µm, and + 63 µm size fractions are enriched in Nb, Ta, Y, La, Ce, Pr, Nd, P, U, and Th relative to other size fractions. Analyses below detection limits are not shown. Error bars based on average 2σ values determined from multiple analyses of standards by pXRF (Luck and Simandl, 2014).

is expected because REEs have similar physical and chemical properties and commonly substitute for each other in monazite, REE-bearing carbonates and fluorocarbonates, and Nb-bearing minerals. Strong correlation between Ce and Th ($R^2 = 0.90$) may reflect accumulations of monazite. Zirconium correlates well with Ce ($R^2 = 0.95$), Nd ($R^2 = 0.88$), and Pr ($R^2 = 0.87$), La ($R^2 = 0.86$), and Y ($R^2 = 0.82$) and may relate to concentrations of zircon and co-occurrence with REE-bearing minerals. As expected, a significant relationship exists between Th and U concentrations ($R^2 = 0.70$).

An unknown analytical error may explain < 90 ppm P values for samples collected from directly over the deposit (Figs. 6, 7), which contains local apatite (2-10%, Kressall et al. 2010). As P is a light element; it has to be present in high concentrations to be a useful pathfinder due to error induced by the matrix effects of Ca and Fe (Simandl et al., 2013b).

Lack of linear dependence between Sr and Ba ($R^2 = 0.06$) suggest that these elements are not present as a uniform barite-

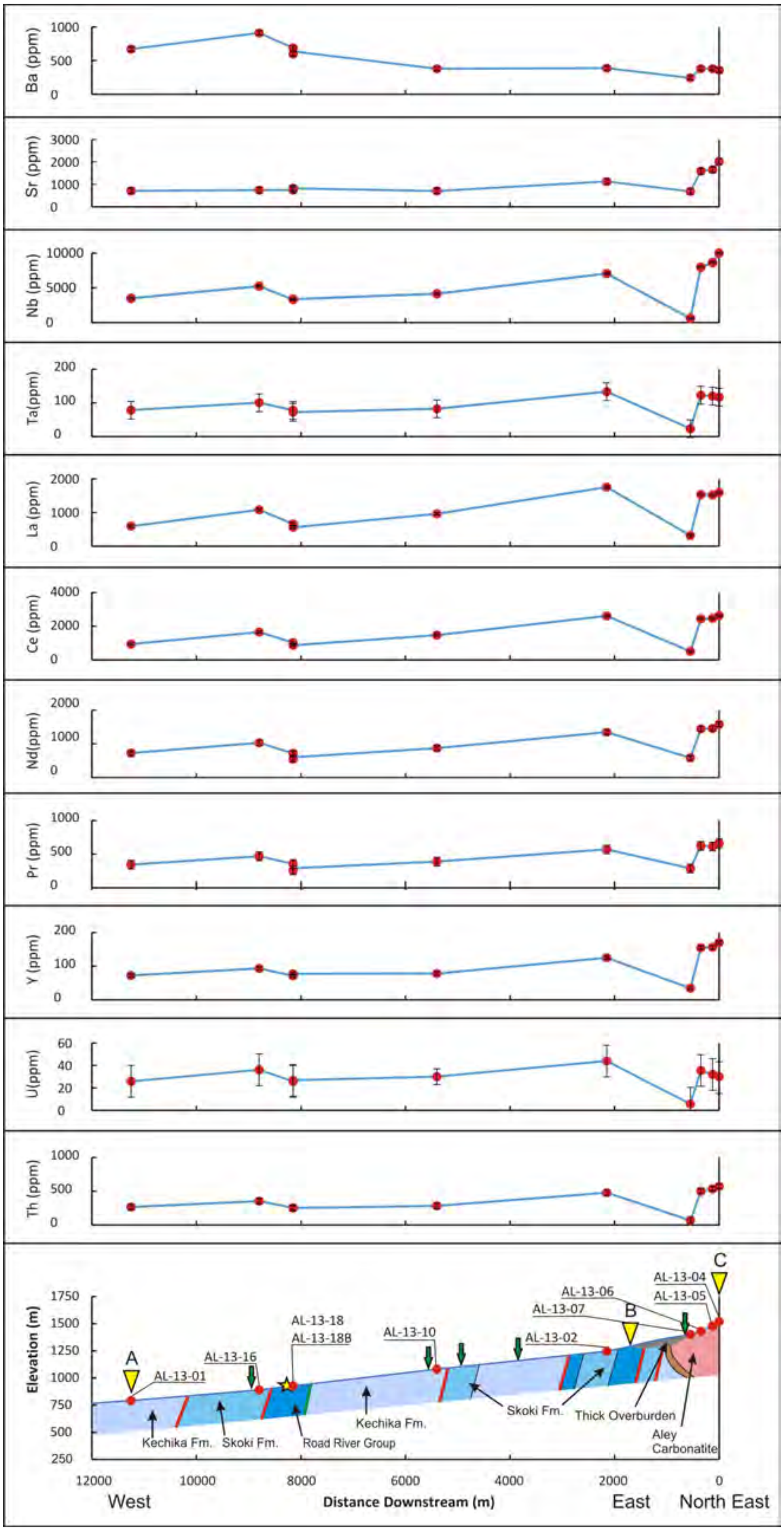

Fig. 6. Downstream variation in carbonatite pathfinder elements concentrations (+ 125 µm size fraction) with increasing distance from the Aley carbonatite. Yellow star-fenite, carbonatite, and Ospika diatreme boulders. Green arrow-landslides. A thick layer of overburden is located downhill of the Aley carbonatite. Legend for geology is the same as in Figure 2. For location see yellow markers (A-B-C) on Figure 2. Error bars based on average 2σ values determined from multiple analyses of standards by pXRF (Luck and Simandl, 2014).

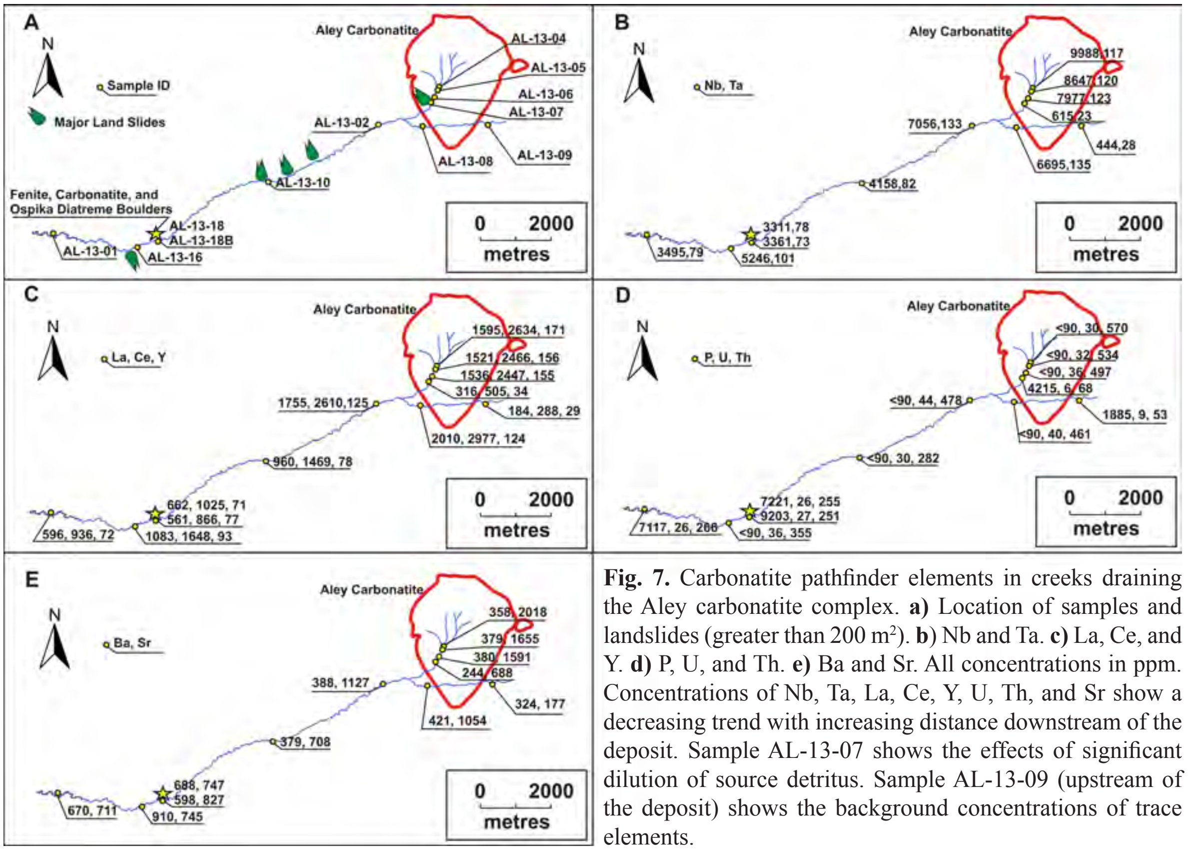

Fig. 7. Carbonatite pathfinder elements in creeks draining the Aley carbonatite complex. **a)** Location of samples and landslides (greater than 200 m^2). **b**) Nb and Ta. **c)** La, Ce, and Y. **d)** P, U, and Th. **e)** Ba and Sr. All concentrations in ppm. Concentrations of Nb, Ta, La, Ce, Y, U, Th, and Sr show a decreasing trend with increasing distance downstream of the deposit. Sample AL-13-07 shows the effects of significant dilution of source detritus. Sample AL-13-09 (upstream of the deposit) shows the background concentrations of trace elements.

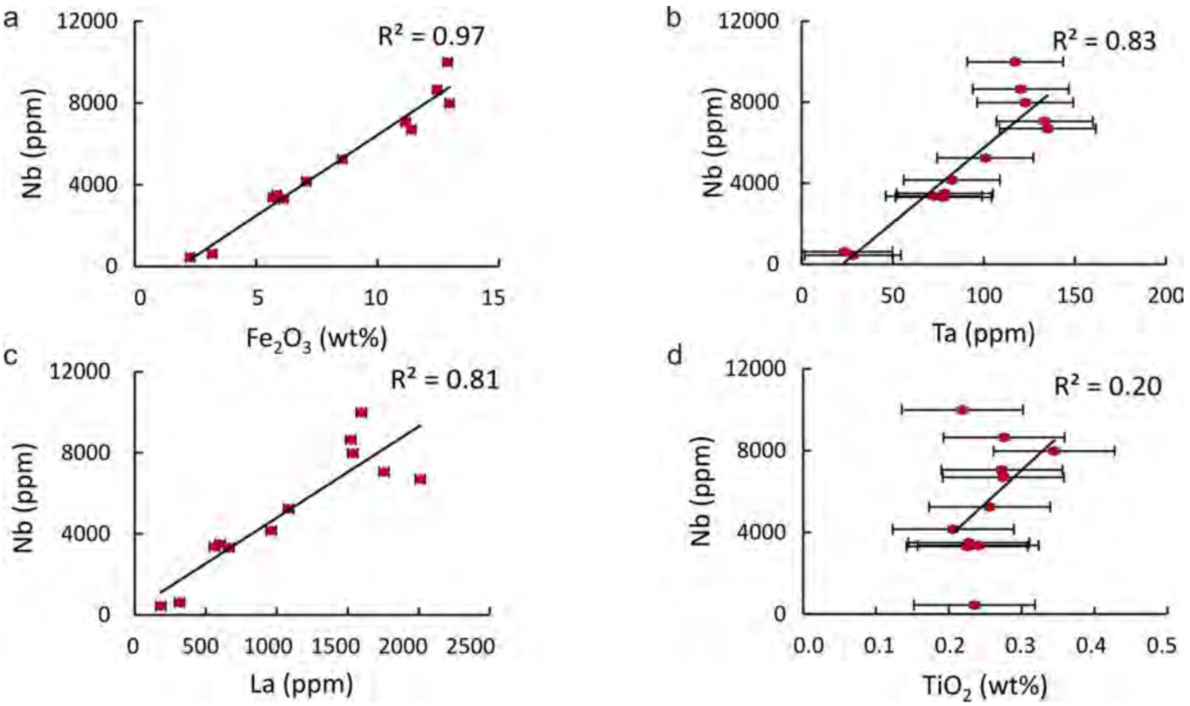

Fig. 8. Correlations between concentrations of **a)** Nb and Fe_2O_3. **b)** Nb and Ta. **c)** Nb and La. **d)** Nb and TiO_2. Error bars based on average 2σ values determined from multiple analyses of standards by pXRF (Luck and Simandl, 2014).

Table 2. Relative concentrations of major and trace element analysed by factory-calibrated pXRF. Samples are listed in order of increasing distance downstream of the deposit. Concentrations in ppm excepted were otherwise indicated. The data are internally consistent but have not been recalibrated as described in Simandl et al. (2013b) to improve accuracy by correcting for matrix effects and biases. Based on strong positive correlation between 11 U and 15 Th pXRF, and corresponding LMB-ICPMS analyses of stream sediments from Aley, Lonnie, and Wicheeda (unpublished) processed in exactly the same manner as those in the present study, systematic overestimation of U and Th, of the order of 35% and 90% respectively, is expected. [a]Total Fe as ferric oxide (Fe_2O_3).

Sample	Size Fraction (mm)	Nb	Ta	Y	La	Ce	Nd	Pr	Ba	Sr	P	U	Th	% Fe_2O_3[a]	% CaO
AL-13-09	+0.125	444	28	29	184	288	351	188	324	177	1885	9	53	2.28	10.94
AL-13-04	+0.125	9988	117	171	1595	2634	1579	661	358	2018	<90	30	570	12.88	29.34
AL-13-05	+0.125	8647	120	156	1521	2466	1453	614	379	1655	<90	32	534	12.45	27.84
AL-13-06	+0.125	7977	123	155	1536	2447	1443	623	380	1591	<90	36	497	12.96	27.06
AL-13-07	+0.125	615	23	34	316	505	580	289	244	688	4215	6	68	3.2	26.06
AL-13-08	+0.125	6695	135	124	2010	2977	1421	599	421	1054	<90	40	461	11.39	22.43
AL-13-02	+4.00	728	7	36	304	451	607	303	385	934	4475	6	63	3.32	31.84
	+2.00	585	<7	34	252	410	608	311	282	842	2788	4	70	4.03	29.99
	+1.00	2205	65	60	545	833	777	377	297	822	5983	16	255	7.75	28.55
	+0.500	5056	128	85	946	1402	1078	498	342	826	2894	60	451	15.06	25.42
	+0.250	7283	167	118	1274	1949	1276	561	370	1016	<90	62	549	15.24	24.36
	+0.125	7056	133	125	1755	2610	1347	571	388	1127	<90	44	478	11.16	23.75
	+0.063	2429	48	71	1048	1552	827	368	374	900	9412	18	192	4.63	21.83
	-0.063	530	<7	40	446	659	557	270	353	710	2042	5	67	3.34	22.48
AL-13-10	+0.125	4157	82	78	960	1469	870	390	379	708	<90	30	282	7.06	17.36
AL-13-18	+4.00	15	<7	14	166	269	442	254	427	545	560	<1	9	1.6	28.42
	+2.00	24	<7	15	122	194	414	225	516	349	<90	1	12	1.68	25.33
	+1.00	55	<7	16	128	209	387	219	588	352	<90	2	12	1.89	23.22
	+0.500	184	<7	20	159	266	403	196	574	375	<90	2	28	2.13	22.39
	+0.250	971	30	36	232	370	425	230	538	531	2292	9	99	3.34	21.6
	+0.125	3311	78	71	662	1025	721	355	688	747	7221	26	255	6.13	21.56
	+0.063	2250	44	62	813	1220	691	319	743	589	5224	16	177	4.44	19.7
	-0.063	321	<7	30	273	429	408	212	552	433	<90	6	45	3.13	20.6
AL-13-18B	+4.00	1142	<7	21	71	129	147	81	141	519	2264	3	71	1.31	30.58
	+2.00	67	<7	17	73	115	167	103	377	402	104	2	13	1.86	27.86
	+1.00	142	<7	18	87	145	191	104	427	393	260	1	22	1.91	25.69
	+0.500	431	<7	24	117	185	156	81	416	401	1636	4	47	2.46	23.57
	+0.250	1412	28	42	194	302	205	108	426	583	5036	11	129	3.75	23.16
	+0.125	3361	73	77	561	866	542	259	598	827	9203	27	251	5.69	23.24
	+0.063	3047	48	77	813	1208	458	193	604	703	5800	21	217	4.7	22.26
	-0.063	633	<7	36	416	614	396	187	552	491	453	9	68	2.82	23.8
AL-13-16	+0.125	5246	101	93	1083	1648	1028	470	910	745	<90	36	355	8.55	20.98
AL-13-01	+0.125	3495	79	72	596	936	724	346	670	711	7117	26	266	5.84	21.97

celestite solid solution. Sr is commonly a minor constituent of aragonite and calcite and is found in higher concentrations in REE-bearing carbonates, fluorocarbonates, and strontianite. Ba is also common in some REE-bearing carbonates, fluorocarbonates, and barite. All these minerals were reported by Mäder (1986) from Aley deposit and/or associated dikes; however, barite input from non-carbonatite sources such as dolostones of Kechika and Skoki Formations is an alternative explanation.

Ongoing work using a Frantz isodynamic separator and modern laboratory methods such as EMP, LA-ICP-MS, and QEMSCAN, will provide quantitative information on the indicator mineral signature of the Aley carbonatite deposit. The use of QEMSCAN is favored over grain-picking because many potential carbonatite indicator minerals are difficult to identify under binocular microscope. The pXRF chemical analyses presented here will be compared to and calibrated against laboratory chemical analysis for major and trace elements in an attempt to confirm and better quantify our data.

7. Conclusion

Stream sediment geochemistry represents a valid exploration method for Aley type carbonatite deposits. Niobium, Ta, La, Ce, Pr, Nd, Y, Th, U, and Sr in combination with each other, or alone, are good pathfinder elements in stream sediments. The Ba signature of the Aley deposit, if present, is masked by barite derived from dolostones. As P is a light element, it has to be present in higher concentrations than the above elements to be a useful pathfinder. The + 125 µm size fraction of the stream sediments is a useful geochemical sampling media and the most promising candidate for study of carbonatite related indicator minerals using QEMSCAN methods. Based on this study and the mineralogy of the Aley deposit, pyrochlore, columbite-(Fe), and fersmite are expected to be useful indicators. Monazite, REE-bearing carbonates, and fluorocarbonates, and to some extent fersmite and apatite are also possible indicator minerals based on the mineralogy of the deposit and chemical composition of stream sediments. Factory-calibrated pXRF is a cost effective method for determining relative concentrations of key pathfinder elements, such as Ni, Ta, La, Ce, Y, Th, U, and Sr in stream sediments; however, without recalibration, depending on the element, analyses can be strongly biased (e.g. Th or U). Additional mineralogical studies using modern laboratory methods such as EMP, LA-ICP-MS, and QEMSCAN, are required to establish relative concentrations of indicator minerals in stream sediments with increasing distance from the carbonatite.

Acknowledgments

This project received funding and support from Targeted Geoscience Initiative 4 (2010-2015), a Natural Resources Canada program carried out under the auspices of the Geological Survey of Canada. Logistical and helicopter support by Taseko Mines Limited is greatly appreciated. Critical review by Pearce Luck (British Columbia Ministry of Energy and Mines), John Gravel (ACME Analytical Laboratories Ltd.), and Jeremy Crozier (Hunter Dickinson Inc.) greatly improved earlier versions of this manuscript. The authors would also like to thank Pearce Luck for his assistance with sample preparation and analyses.

References cited

Chung, C.J., and Crozier, J., 2008. Assessment Report on Diamond Drilling performed on the Aley Carbonatite Property: British Columbia Ministry of Energy, Mines, and Petroleum Resources, Assessment Report 30113, 194 p.

Colpron, M., and Nelson, J.L., 2011. A digital atlas of terranes for the northern Cordillera. British Columbia Ministry of Energy and Mines, British Columbia Geological Survey, GeoFile 2011-11.

Irish, E. J.W., 1970. Geology of the Halfway River map area, British Columbia. Geological Survey of Canada, Paper 69-11, 154 p.

Kressall, R., McLeish, D.F., and Crozier, J., 2010. The Aley Carbonatite Complex – Part II Petrogenesis of a Cordilleran Niobium Deposit. In: Simandl, G.J., and Lefebure, D.V. (Eds.), International Workshop on the Geology of Rare Metals, November 9-10, 2010, Victoria, Canada. Extended Abstracts Volume. British Columbia Ministry of Energy and Mines, British Columbia Geological Survey, Open File 2010-10, pp. 25-26.

Luck, P., and Simandl, G.J., 2014. Portable X-ray fluorescence in stream sediment chemistry and indicator mineral surveys, Lonnie carbonatite complex, Canada. In: Geological Fieldwork 2013, British Columbia Ministry of Energy and Mines, British Columbia Geological Survey Paper 2014-1, this volume.

Mackay, D.A.R., and Simandl, G.J., 2014. Portable x-ray fluorescence to optimize stream sediment chemistry and indicator mineral surveys, case 2: Carbonatite-hosted REE deposits, Wicheeda Lake, British Columbia, Canada. In: Geological Fieldwork 2013, British Columbia Ministry of Energy and Mines, British Columbia Geological Survey Paper 2014-1, this volume.

Mäder, U. K., 1986. The Aley Carbonatite Complex. Master of Science thesis, University of British Columbia, 176 p.

Mäder, U. K., 1987. The Aley carbonatite complex, Northern Rocky Mountains (94B/5), British Columbia. In: Geological Fieldwork 1986, British Columbia Ministry of Energy, Mines and Petroleum Resources, British Columbia Geological Survey Paper 1987-1, pp. 283-288.

Mariano, A.N., 1989a. Economic geology of rare earth minerals. In: Lipman B.R. and McKay G.A. (Eds.), Geochemistry and Mineralogy of Rare Earth Elements. Reviews in Mineralogy, 21, 309-338.

Mariano, A.N., 1989b. Nature of economic mineralization in carbonatites and related rocks. In: Bell, K. (Ed.) Carbonatites: Genesis and Evolution. Unwin Hyman, London, pp. 149-176.

Massey, J.W.H., McIntyre, D.G., Dejardins, P.J., and Cooney, R.T., 2005. Digital geology map of British Columbia. British Columbia Ministry of Energy, Mines and Petroleum Resources, British Columbia Geological Survey Open File 2005-2, DVD.

McLeish, D.F., Kressall, R., and Crozier, J., 2010. The Aley Carbonatite Complex – Part I Structural Evolution of a Cordilleran Niobium Deposit Mine. In: Simandl, G.J., and Lefebure, D.V. (Eds.), International Workshop on the Geology of Rare Metals, November 9-10, 2010, Victoria, Canada. Extended Abstracts Volume. British Columbia Ministry of Energy and Mines, British Columbia Geological Survey, Open File 2010-10, pp. 21-24.

McLeish, D.F., 2013. Structure, stratigraphy, and U-Pb ziron-titanite geochronology of the Aley carbonatite complex, Northeast British Columbia: Evidence for Antler-aged orogenesis in the foreland belt of the Canadian cordillera. Master of Science thesis, University of Victoria, 131 p.

Millonig, L.J., Gerdes, A., and Groat, L.A., 2012. U-Th-Pb geochronology of meta-carbonatites and meta-alkaline rocks in the southern Canadian Cordillera: A geodynamic perspective. Lithos, 152, 202-217.

Nethery, B.T., 2007. Report of technical exploration and development – 2006 evaluation and exploration planning on the Aley Carbonatite property, Ospika River, BC (Omineca Mining District). British Columbia Ministry of Energy, Mines, and Petroleum Resources, Assessment Report 28733, 410 p.

Pell, J., 1994. Carbonatites, nepheline syenites, kimberlites and related rocks in British Columbia. British Columbia Ministry of Energy, Mines and Petroleum Resources, British Columbia Geological Survey, Bulletin 88, 136 p.

Pride, K.R., 1983. Geological Survey on the Aley Claims. British Columbia Ministry of Energy, Mines, and Petroleum Resources, Assessment Report 12018, 16 p.

Pride, K.R., 1987a. 1986 Year End report on the Aley Property: British Columbia Ministry of Energy, Mines, and Petroleum Resources, Assessment Report 15721, 69 p.

Pride, K.R., 1987b. 1986 Diamond Drilling Assessment Report: British Columbia Ministry of Energy, Mines, and Petroleum Resources, Assessment Report 16484, 59 p.

Pyle, L.J., and Barnes, C.R., 2001. Conodonts from the Kechika Formation and Road River Group (Lower to Upper Ordovician) of the Cassiar Terrane, northern British Columbia: Canadian Journal of Earth Sciences, 38, 1387–1401.

Robert, M., Lyons, E.M., Hardy, J.L., and Nethery, B.T., 2005. Report of technical exploration and development – trenching, sampling, metallurgical testing and evaluation on the Aley carbonatite property, Ospika River, BC (Omineca Mining District): British Columbia Ministry of Energy, Mines, and Petroleum Resources, Assessment Report 27991, 60 p.

Simandl, G.J., Prussin, E.A., and Brown, N., 2012. Specialty metals in Canada. British Columbia Ministry of Energy and Mines, British Columbia Geological Survey, Open File 2012-7, 48 p.

Simandl, G.J., Reid, H.M., and Ferri, F., 2013a. Geological setting of the Lonnie niobium deposit, British Columbia, Canada. In: Geological Fieldwork 2012, British Columbia Ministry of Energy, Mines and Natural Gas, British Columbia Geological Survey Paper 2013-1, pp. 127-138.

Simandl, G.J., Fajber, R., Paradis, S., and Simandl, L.J., 2013b. Exploration for sedimentary phosphate (±REE) deposits using handheld XRF – An orientation survey. Geochemistry: Exploration, Environment, Analysis. http://dx.doi.org/10.1144/geochem2012-180. Available online.

Tantalum-Niobium International Study Center, 2013. Niobium - Raw Materials and Processing. <http://tanb.org/niobium> Accessed July 17, 2013.

Taseko Mines Limited, 2013. Aley Niobium Project; measured and indicated resources. <http://www.tasekomines.com/aley/ID539906> Accessed Nov 5, 2013.

Woolley, A.R., and Kjarsgaard, B.A., 2008. Paragenetic Types of Carbonatite as Indicated by the Diversity and Relative Abundances of Associated Silicate Rocks: Evidence from a Global Database. The Canadian Mineralogist, 46, 741-752.

Portable X-ray fluorescence to optimize stream sediment chemistry and indicator mineral surveys, case 2: Carbonatite-hosted REE deposits, Wicheeda Lake, British Columbia, Canada

Duncan A.R. Mackay[1] and George J. Simandl[1, 2, a]

[1] University of Victoria, School of Earth and Ocean Sciences, Victoria, BC, V8P 5C2
[2] British Columbia Geological Survey, Ministry of Energy and Mines, Victoria, BC, V8W 9N3
[a] corresponding author: George.Simandl@gov.bc.ca

Recommended citation: Mackay, D.A.R. and Simandl, G.J., 2014. Portable X-ray fluorescence to optimize stream sediment chemistry and indicator mineral surveys, case 2: Carbonatite-hosted REE deposits, Wicheeda Lake, British Columbia, Canada. In: Geological Fieldwork 2013, British Columbia Ministry of Energy and Mines, British Columbia Geological Survey Paper 2014-1, pp. 195-206.

Abstract

The Wicheeda carbonatite-hosted deposit is one of the most promising rare earth element (REE) prospects within the British Columbia alkaline province. Portable X-ray fluorescence (pXRF) allows for determination of several pathfinder elements (Nb, Ta, REEs, Th, Ba, and Sr) in stream sediment samples collected downstream of this deposit. These samples are expected to contain indicator minerals derived from the main carbonatite complex such as monazite, REE-bearing carbonates and fluorocarbonates, pyrochlore, columbite-(Fe), barite-celestine, apatite, and others. Study of these samples indicates that the + 250 µm, + 125 µm, and + 63 µm size fractions contain high concentrations of Nb, La, Ce, and Th relative to other size fractions. The + 125 µm fraction was chosen for systematic chemical analyses and pathfinder element studies. Although there is no noticeable decreasing trend in pathfinder elements with increasing distance downstream, there is co-variation of Nb, Ta, La, Ce, Pr, Nd, Y, and Th. This reflects the presence of multiple mineral phases including pyrochlore, monazite-(Ce), REE-fluorocarbonates, and REE-carbonates. Mineralogical studies using optical microscopy, scanning electron microscopy (SEM), electron microprobe (EMP), and Quantitative Evaluation of Materials by Scanning electron microscopy (QEMSCAN) are required to identify and quantify minerals and their distributions downstream of the deposit.

Keywords: Indicator minerals, pathfinder elements, rare earth elements, specialty metals, portable x-ray fluorescence, carbonatite

1. Introduction

Increased use of REE in consumer and green technologies has spurred demand and made these elements a focus of economic and strategic mineral development in the past few years (Tse, 2011). With 95% of world production of REE in China, from deposits such as the carbonatite-related Bayan Obo, and recent export restrictions, western industrialised nations are faced with supply uncertainties (Tse, 2011). Hence, increased exploration for and development of REE mineral deposits is taking place outside of China.

The Wicheeda carbonatite complex and carbonatite and syenite dikes are 80 km northeast of Prince George, British Columbia (Fig. 1). The Wicheeda carbonatite complex was originally explored for its base metal potential. Between 1979 and 1987 the complex was the subject of 1:5000-scale geological mapping and trenching (Betmanis, 1987), soil sampling and stream silt sampling (Lovang and Meyer, 1987), and geophysical surveying (Bruland, 2011). Spectrum Mining Corporation (Spectrum) acquired the claims that cover the Wicheeda carbonatite complex and conducted diamond drilling in 2008 and 2009 (Graf et al., 2009; Lane, 2009).

The main objectives of this study are to determine the best size fraction in stream sediments for indicator mineral and geochemical exploration programs, and to characterize the geochemical gradients of Nb, Ta, REEs, Ba, Sr, and Th in sediments downstream of the Wicheeda carbonatite complex using pXRF. These will help assess geochemical and indicator minerals methods for Wicheeda-type carbonatite-hosted REE deposit exploration.

2. Geological setting

The Wicheeda carbonatite complex is part of a series of carbonatite, syenite, and alkaline rock complexes forming the British Columbia alkaline province, which coincides with the approximate margin of the Laurentian craton (Pell, 1994). Carbonatites in British Columbia were emplaced during three main periods of extensional tectonics ca. 800-700 Ma, 500 Ma, and 360-340 Ma (Pell, 1994; Millonig et al., 2012). Subsequent phases of deformation and sub-greenschist to amphibolite grade metamorphism between ~ 155 and 50 Ma overprint the carbonatites along this trend (Pell, 1994; Millonig et al., 2012).

The regional geology was originally mapped at a scale of 1:253,440 by Armstrong et al. (1969). The Wicheeda Lake carbonatite is immediately west of the Rocky Mountain Trench and intrudes Lower to Middle Paleozoic platformal successions deposited on the western margin of Laurentia. These rocks consist of limestone, argillite, and calcareous siltstone of the Kechika Formation (Cambrian to Early Ordovician; Fig. 2; Armstrong et al., 1969). The Kechika Formation is in fault contact with limestone, slate, siltstone, and argillite of the

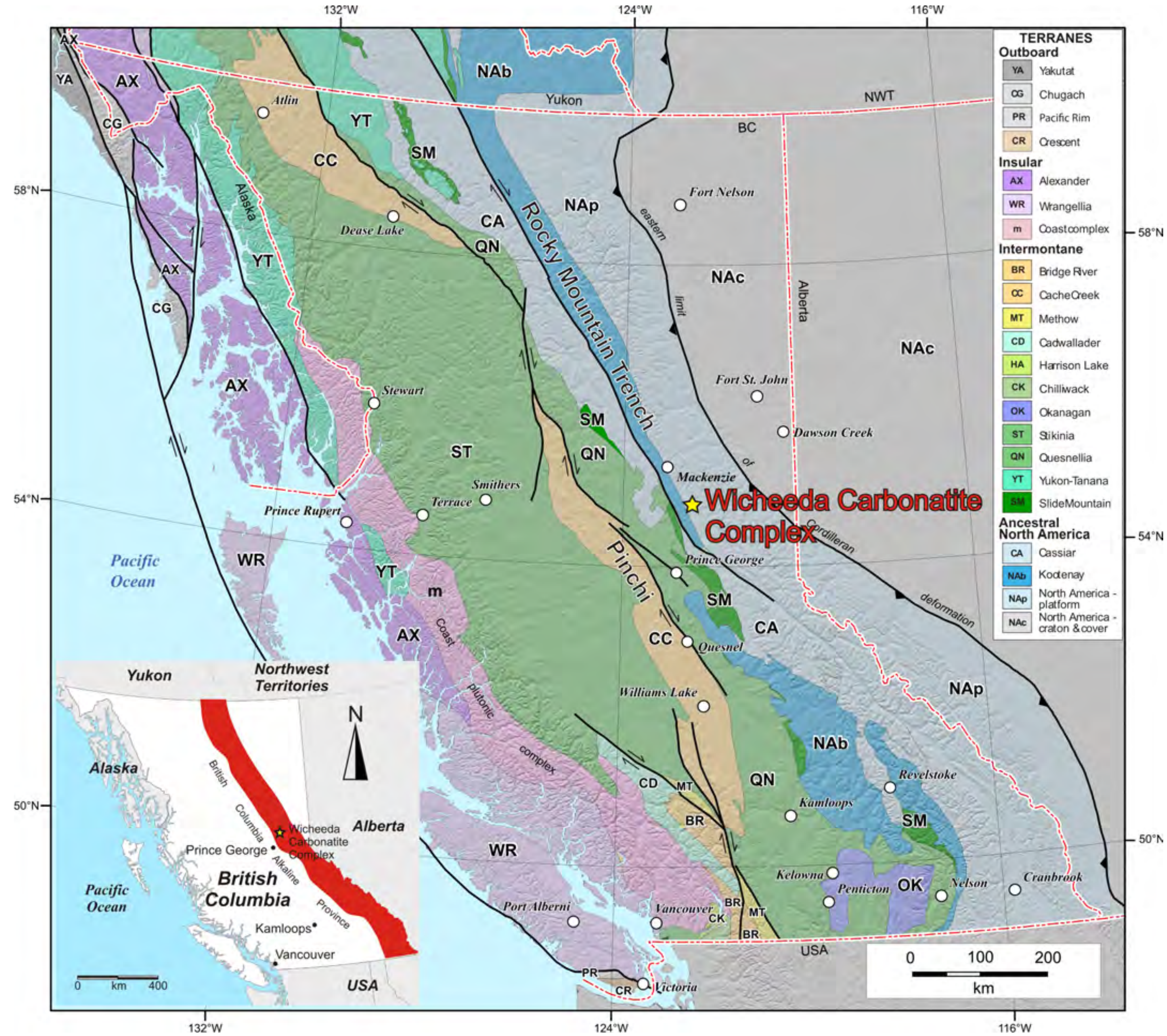

Fig. 1. Tectonic setting of the Wicheeda carbonatite complex (yellow star). British Columbia alkaline province shown in red (inset map). Municipalities are denoted by white circles. Modified after Pell (1994).

Gog Group (Neoproterozoic) and unassigned Devonian to Permian felsic volcanic rocks to the west, and unassigned Cambrian to Devonian carbonates, slates, and siltstones to the east (Armstrong et al., 1969; Lane, 2009). Lower greenschist grade regional metamorphism overprints the country rocks (Lane, 2009). Faulting in the area follows the major northwest-southeast trend of the Rocky Mountain Trench.

Dalsin (2013) reported a Sm-Nd whole rock isochron age of 316 ± 36 Ma for samples from the carbonatite dikes ~ 3 km southeast of the main Wicheeda carbonatite complex. The carbonatite and syenite dikes and the Wicheeda complex follow the same northwest-southeast structural trend and are assumed to be related.

3. Geology of the Wicheeda carbonatite complex

The shape of the Wicheeda carbonatite complex is not well defined. It is sub-circular in plan (< 500 m in diameter), based on previous mapping and a Th radiometric anomaly (Lovang and Meyer, 1988; Mäder and Greenwood, 1988; Lane, 2009; Bruland, 2011). Reconnaissance fieldwork suggests that its emplacement was controlled by the intersection of two faults (Fig. 2). Drilling in 2008 and 2009 intersected high-grade zones consisting of 3.55% total rare earth oxide (TREO) over 48.6 m, 2.2% over 144 m, and 2.9% over 72 m; other high grade intersections are near the top of drill holes in weathered dolomite carbonatite zones (Graf et al., 2009; Lane, 2009). A series of carbonatite dikes has been identified northwest of

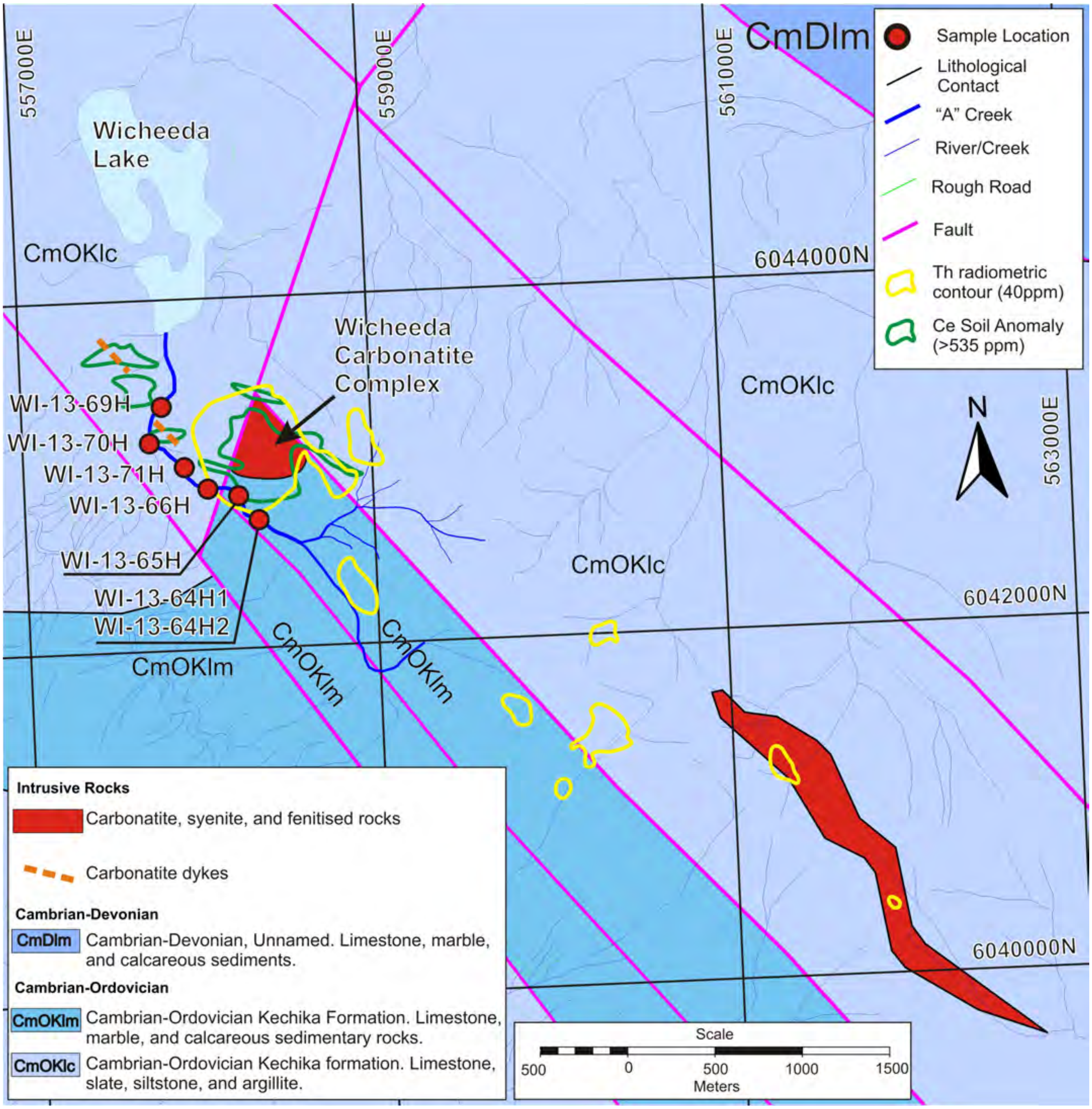

Fig. 2. Geological setting of the Wicheeda carbonatite complex, associated dikes, and locations of stream sediment samples. Base map modified after Massey et al. (2005). Thorium radiometric anomalies from Bruland (2011) shown by yellow traces. Cerium soil anomaly from Lane (2009) shown by green traces. UTM zone 10, NAD 83.

the main carbonatite complex near Wicheeda Lake; a larger syenite-carbonatite dike complex is ~ 3 km to the southeast (Fig. 2).

The main carbonatite complex consists of two main units: dolomite carbonatite; and fenitised zones formerly referred to as syenite breccias. Based on the work of Le Couteur (2008, 2009), Lane (2009), and observations from this study, the carbonatite consists mainly of dolomite (75-97%) ± ankerite. In general, calcite, plagioclase, potassium feldspar, biotite, muscovite/phlogopite, chlorite, and pyrite are minor constituents, and quartz, barite, strontianite, Fe-Ti oxides, molybdenite, galena, fluorite, apatite, and possibly powellite are present in trace amounts (Le Couteur, 2008, 2009; Lane, 2009). The main REE-bearing phases in the dolomite carbonatite are monazite [(Ce, La, Nd, Th) PO^4] and REE-bearing fluorocarbonates [such as bastnasite-(Ce), parisite-(Ce), and/or synchysite-(Ce)] and carbonates (Le Couteur, 2008, 2009; Lane, 2009); however, it is expected some REEs form minor constituents in apatite, columbite, and possibly pyrochlore. The main Nb-bearing mineral is pyrochlore [$(Na, Ca)_2 Nb_2 O_6(OH,F)$]. Columbite [$(Fe, Mn) Nb_2 O_6$] and Nb-rutile [$(Ti, Nb, Fe) O_2$] may also be present. Calcite increases in abundance with depth. Le Couteur (2008, 2009) identified zones of predominantly calcite (85%), which contains biotite, strontianite, and magnetite.

The fenitised zones (albitised and potassic altered wall rock) observed in core contain abundant feldspar-rich (90%) xenoliths in a dolomite matrix. At the surface, patchy blue-green, Na-amphibole (± pyroxene)-bearing fenite is in contact with dolomite carbonatite. By definition potassium feldspar, plagioclase, micas, amphiboles, and other silicates are more abundant in fenitised rocks than in carbonatites. The carbonatite is overlain by a characteristic red soil or regolith horizon, 5 cm to more than 50 cm thick. Mineralogical and chemical characterisation of resistate minerals in this horizon are the subject of ongoing research.

4. Methods

4.1. Sample collection

Seven stream sediment samples along "A" creek adjacent to the Wicheeda carbonatite complex were collected during the 2013 field season (Figs. 2, 3, Table 1). Sample sites are spaced 200-300 metres apart. There is more than 160m elevation difference between sample WI-13-64H1 and WI-13-69H (Table 1). The streambed consists mainly of boulders, cobbles, and pebbles. Samples were collected in the lee of boulders and logs, and from inside stream bends, typically over areas < 1 m^2. Matrix material was wet sieved in the field through a + 8 mm screen; only the < 8 mm fraction was retained. Samples were contained in permeable canvas bags and stored in plastic pails. The dried samples weighed 1.1 to 5.4 kg (Table 1). Organic material (conifer needles, leaves, and twigs) was scraped from the surface of samples sites. Not all of the organic material could be avoided during sample collection, and minor amounts were retained in the coarser fractions (+ 500 µm and coarser).

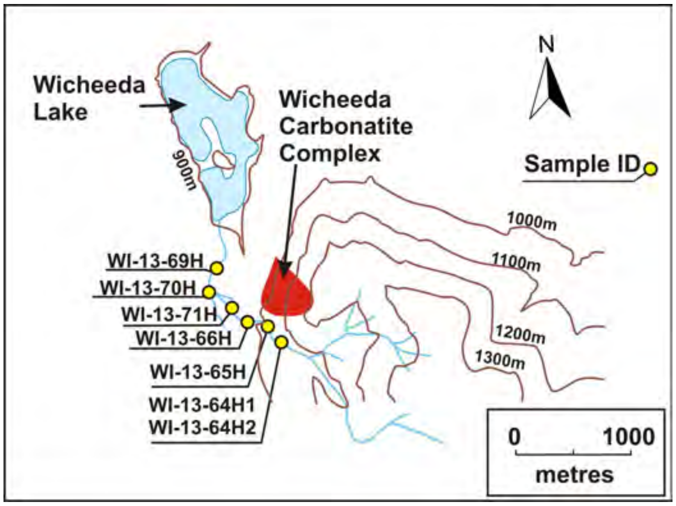

Fig. 3. Location of stream sediment samples and local topography around the Wicheeda carbonatite complex. Samples are downhill of the Wicheeda carbonatite complex. Elevation contours denoted by brown lines (100 m contour interval). Modified after Massey et al. (2005).

4.2. Sample preparation and pXRF analyses

Samples were dried in an oven at 40° C, weighed, and dry sieved into + 4 mm, 2 mm to 4 mm, 1 mm to 2 mm, 500 µm to 1 mm, 250 µm to 500 µm, 125 µm to 250 µm, 63 µm to 125 µm, and -63 µm fractions. No aggregates (clumps) were observed during the sieving process. Each size fraction was also weighed. Selected size fractions were split using a riffle splitter with portions retained for a witness sample, magnetic separation, and XRF analyses. Samples for XRF analyses were milled using ring and roller bowl tungsten carbide mills. Standard XRF sample pulp cups were then prepared and analysed by pXRF. Analyses were carried out using a portable Thermo Fisher Scientific Niton FXL-950 instrument. A complete description of equipment, sample preparation, and laboratory methods as well as information regarding the standards used, operating procedure, instrument settings, limits of detections, and data quality control are described by Luck and Simandl (2014). Relative major oxide and trace element concentrations analysed by pXRF have acceptable precision; however, pXRF data has not been recalibrated using results of standard laboratory analyses (as described in Simandl et al., 2013) to correct for analytical biases. Error bars for figures in this study are based on 2σ values for standards analysed multiple times by pXRF.

5. Results

Two samples (WI-13-66H and WI-13-71H) were chosen for detailed study. Sample WI-13-66H was collected ~ 175 metres downslope from the deposit (Fig. 3); WI-13-71H was collected 220 metres downstream of sample WI-13-66H, where "A" creek enters a cut block in an area of low topographic relief. In both samples, the + 125 µm size fraction contains higher concentrations of pathfinder elements relative to other size fractions (Fig. 4). The + 250 µm and + 63 µm fractions are the next most enriched. These results are similar to those from stream sampling near the Lonnie carbonatite (Luck and Simandl, 2014) and the Aley carbonatite (Mackay and Simandl, 2014). Based on these characteristics, the + 125 µm fractions of the remaining samples were analysed. Samples WI-13-66H and WI-13-71H show a grain-size distribution that is skewed toward coarse-grained material (Fig. 4).

Concentrations of major oxides (Table 2) range from 42.8 to 57.9 wt% SiO_2, 16.3 to 23.4 wt% Al_2O_3, 4.5 to 7.0 wt% Fe_2O_3, 2.1 to 8.2 wt% CaO, 0.4 to 0.9 wt% TiO_2, 1.8 to 2.4 wt% MgO, and 4.5 to 6.9 wt% K_2O. Trace element concentrations (Table 2) range from 57 to 283 ppm Nb, <22 to 34.7 ppm Ta, 19 to 46 ppm Y, 117 to 887 ppm La, 215 to 1301 ppm Ce, 167 to 482 ppm Nd, 97 to 225 ppm Pr, 806 to 1805 ppm Ba, 190 to 328 ppm Sr, < 5 to 7 ppm U (only 4 samples are above detection

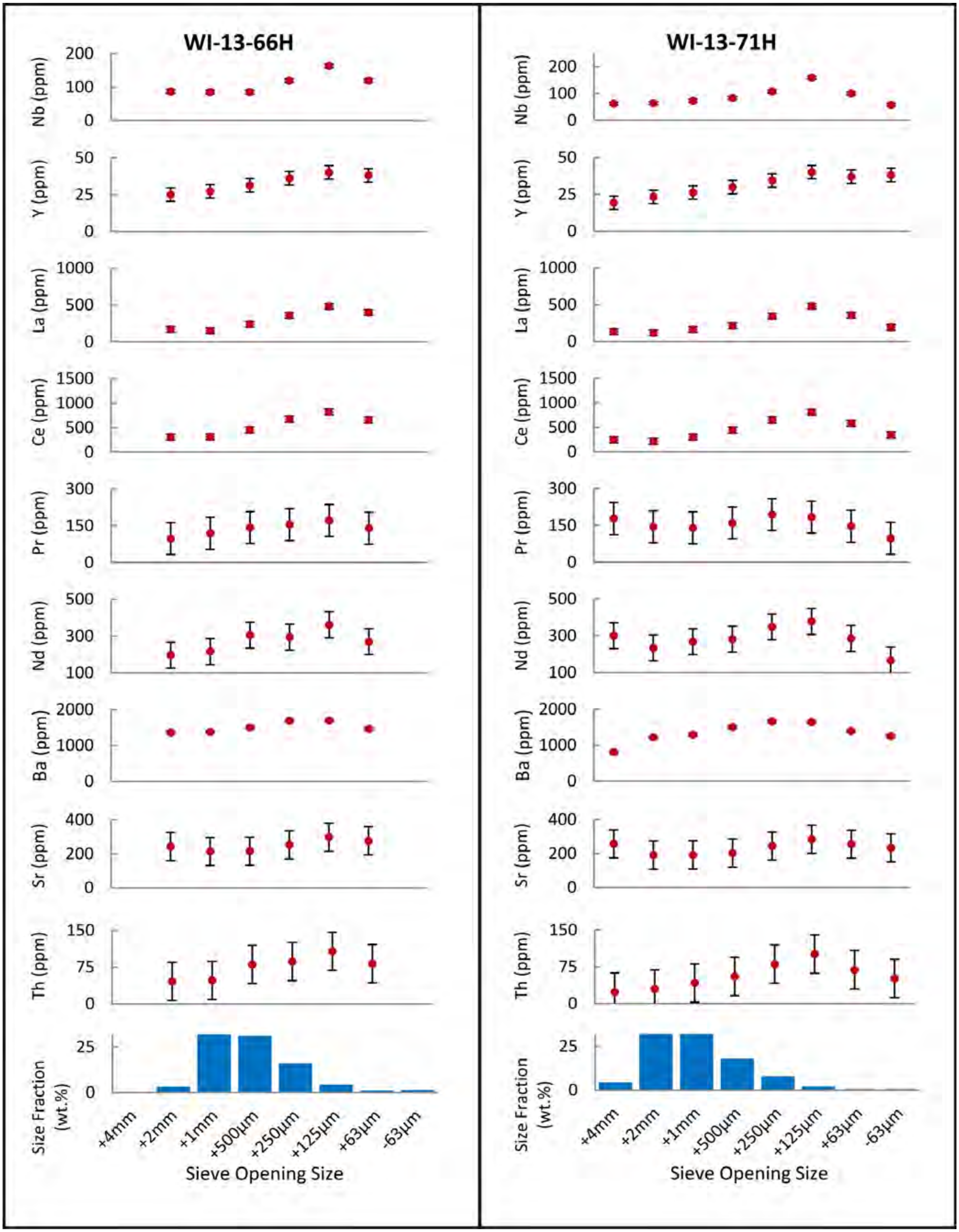

Fig. 4. Portable XRF analyses for selected trace elements and grain size fraction distributions of samples WI-13-66H and WI-13-71H. The + 250 µm, + 125 µm, and + 63 µm size fractions are enriched in Nb, La, Ce, and Th relative to other size fractions.

Table 1. Characteristics of stream channel and sample sites. Samples are in order of increasing distance downstream of the Wicheeda carbonatite complex. UTM zone 10, NAD 83.

	Location		Elevation	Channel Characteristics			Clast Size (cm)		Dry wt. (< 8 mm diameter)	Sample Site Characteristics
Sample ID	Northing	Easting	(m)	Width (m)	Depth (m)	Flow	Average	Max.	(kg)	
WI-13-64H1	6042772	558279	1077	1.5	0.10	rapid	0.5-1.5	5-7	1.7	Lee of fallen trees; steep-sided gully, upstream of trail; predominantly shale, siltstone, and carbonate clasts.
WI-13-64H2	6042772	558279	1077	1.5	0.10	rapid	0.5-1.5	5-7	1.1	2-3 m upstream of WI-13-64H1.
WI-13-65H	6042901	558198	1015	2.0	0.20	rapid	0.5-1.5	5-10	2.6	Inside of stream bend; steep-sided gully; grey slate clasts predominant.
WI-13-66H	6042929	558020	973	2.0	0.30	rapid	0.5-1.5	5-7	1.5	Pools below rapids (protected by fallen tree); steep sided gully; grey slate clasts predominant.
WI-13-71H	6043031	557916	935	1.5	0.15	slow	2-5	35	5.4	Lee of fallen tree; low relief topography; grey slate and limestone predominant.
WI-13-70H	6043178	557731	920	1.5	0.10	slow	1-2	10	2.6	Sample from matrix between cobbles; low relief topography; grey slate and limestone predominant; upstream of trail.
WI-13-69H	6043384	557792	911	1.0	0.15	moderate	0.2-0.5	5-7	2.8	Sample from matrix between cobbles; low relief topography; grey slate and limestone predominant; upstream of trail.

limits), and 24 to 141 ppm Th. All samples have P values of < 90 ppm.

6. Discussion

High concentrations of key pathfinder elements (Nb, Ta, REEs, Th, Ba, and Sr) suggest the presence of prospective indicator minerals in the +125 µm size fraction. Barium and to a lesser extent Sr concentrations decrease from southeast to northwest (Figs. 5, 6). Their source is probably upstream of the deposit. This may reflect input of material from other carbonatite-related showings in the area, or be related to sediment influx from limestones and marbles of the Kechika Formation. A slight decreasing trend in CaO with increasing distance downstream is observed, while the opposite is observed for SiO_2. This is probably due in part to a change in lithology across a fault from predominantly limestone and

Table 2. Relative major oxide and trace element concentrations analysed by pXRF. This pXRF data has acceptable precision; however, it has not been recalibrated using results of standard laboratory analyses (as described in Simandl et al., 2013) to correct for matrix effects and analytical biases to improve accuracy. Portable XRF is not a substitute for conventional laboratory analyses. Eight size fractions reported for sample WI-13-71H. Six size fractions reported for WI-13-66H. The + 125 µm fraction is reported for all other samples. Results are in ppm except where otherwise noted. Samples are in order of increasing distance downstream of the Wicheeda carbonatite complex.

Sample	Size Fraction (mm)	Nb	Ta	Y	La	Ce	Nd	Pr	Ba	Sr	P	U	Th	% SiO_2	% CaO
WI-13-64H1	+0.125	144	<22	46	455	761	319	172	1707	305	<90	<5	100	47.68	6.27
WI-13-64H2	+0.125	140	<22	41	467	771	344	148	1805	328	<90	5	101	49.42	4.80
WI-13-65H	+0.125	253	<22	45	733	1176	442	192	1802	311	<90	<5	141	52.15	4.70
WI-13-66H	+2.00	87	<22	25	171	310	196	97	1363	243	<90	7	46	50.10	4.87
WI-13-66H	+1.00	85	24	27	151	315	216	119	1379	214	<90	<5	48	50.24	3.95
WI-13-66H	+0.500	85	<22	31	239	455	305	142	1501	216	<90	7	80	52.70	3.06
WI-13-66H	+0.250	119	<22	36	358	671	294	154	1690	253	<90	<5	86	52.60	3.41
WI-13-66H	+0.125	163	<22	40	482	819	361	172	1698	298	<90	<5	107	53.69	4.77
WI-13-66H	+0.063	119	<22	38	396	655	269	139	1463	277	<90	5	82	50.09	5.01
WI-13-71H	+4.00	62	23	19	135	244	300	178	806	257	<90	<5	24	47.78	8.20
WI-13-71H	+2.00	64	22	23	117	215	234	144	1216	190	<90	<5	30	51.49	4.10
WI-13-71H	+1.00	73	25	26	164	305	268	140	1291	192	<90	<5	42	51.88	3.74
WI-13-71H	+0.500	83	<22	30	214	444	282	160	1506	203	<90	<5	55	52.20	3.32
WI-13-71H	+0.250	108	<22	34	344	648	348	194	1661	244	<90	<5	80	52.87	3.66
WI-13-71H	+0.125	159	<22	40	480	806	378	184	1644	284	<90	<5	101	53.13	4.69
WI-13-71H	+0.063	100	<22	37	358	581	286	146	1391	255	<90	<5	69	51.56	4.65
WI-13-71H	-0.063	57	<22	38	193	341	167	97	1250	233	<90	<5	51	42.76	5.09
WI-13-70H	+0.125	251	26	46	886	1301	482	225	1329	231	<90	<5	129	55.86	3.06
WI-13-69H	+0.125	283	35	43	725	1119	424	191	1295	230	<90	<5	130	57.92	2.07

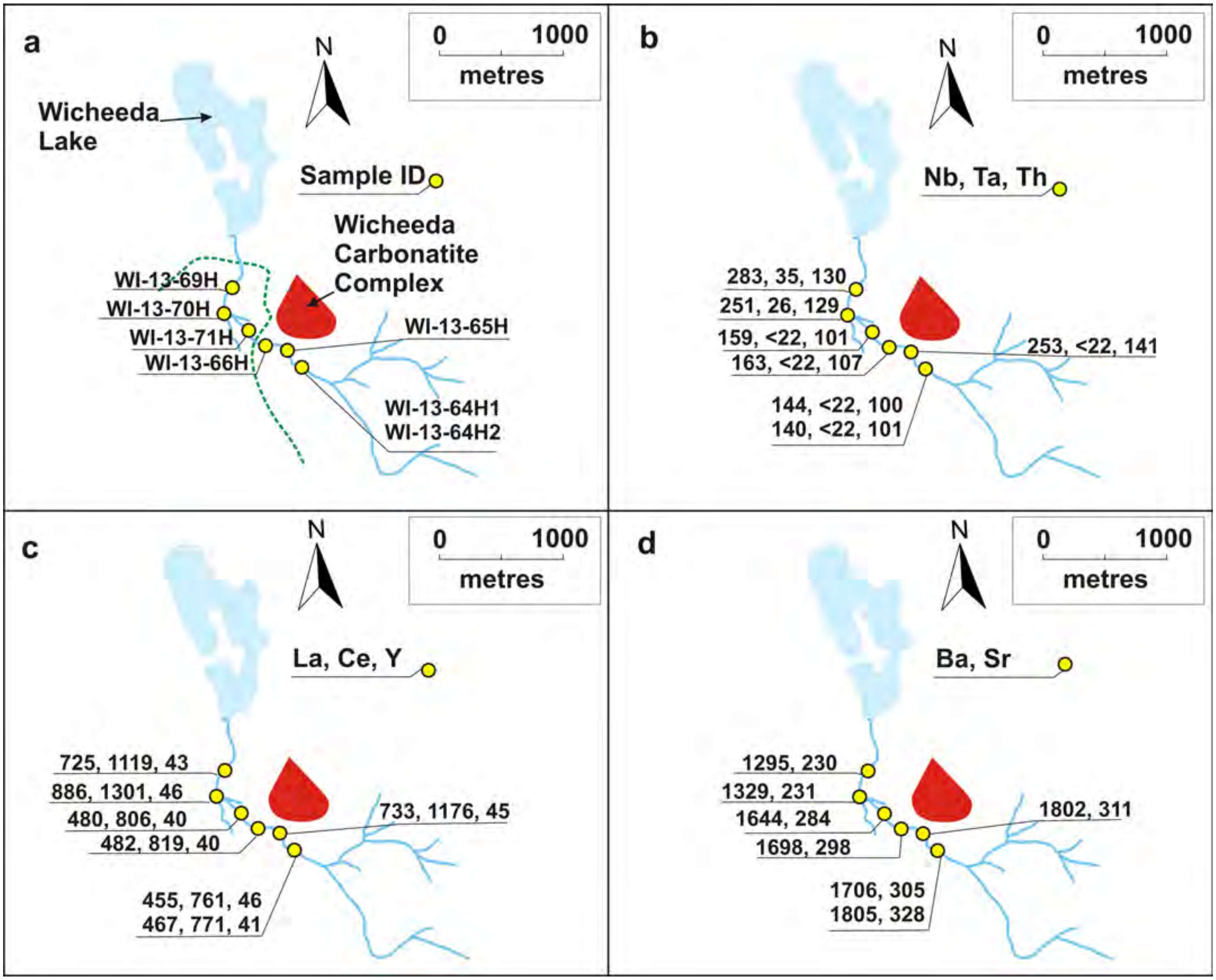

Fig. 5. Selected trace element concentrations in stream sediment samples. **a)** Sample numbers. **b)** Nb, Ta, and Th. **c)** La, Ce, and Y. **d)** Ba and Sr concentrations in ppm. The edge of the cut block and the area of low topographic relief are denoted by the green dotted line.

marble in the southeast to a predominantly pelitic assemblage in the northwest (Fig. 6).

Excluding Ba and Sr, samples WI-13-71H and WI-13-66H have consistently lower concentrations of pathfinder elements than the samples immediately upstream and downstream (WI-13-65H and WI-13-70H; Fig. 6). Calcite carbonatite dikes are reported by Lane (2009) northeast of the main carbonatite complex; during mapping in the summer of 2013, outcropping calcite carbonatite was observed near sample WI-13-70H (Fig. 2). Carbonatite boulders were also observed near the location of a dike reported by Lane (2009). Drilling in 2009 intersected one dike near sample WI-13-70H. These observations coincide with Ce soil and Th radiometric anomalies in the area (Fig. 2). Input of material from these occurrences probably contributes to increased pathfinder element concentrations in samples WI-13-69H and WI-13-70H (Fig. 7). Co-variation in pathfinder element concentrations between Nb, La, Ce, Nd, and Th (Fig. 7) is probably related to the presence of multiple indicator minerals in stream sediments. These minerals may have originated from multiple sources.

High Ta concentrations (samples WI-13-69H and WI-13-70H) coincide with two of the highest Nb values (Fig. 7) and suggest the presence of Nb-Ta-bearing minerals such as pyrochlore or columbite. Samples WI-13-69H and WI-13-70H are downstream of the inferred position of the calcite carbonatite dikes (Fig. 7). This may reflect a difference in mineralogy between the main carbonatite complex and carbonatite dikes near Wicheeda Lake. High Nb:Ta ratios are expected in carbonatites based on typical composition of Nb-bearing mineral phases.

Correlations of pathfinder elements observed in the +125 µm size fraction (Fig. 8) can be used to predict indicator minerals found in stream sediments. Strong correlations between Ce and La ($R^2 = 0.99$), Nd ($R^2 = 0.94$), and Pr ($R^2 = 0.74$) is expected due to ready substitution of these elements in the same minerals. Cerium and Th ($R^2 = 0.87$; Fig. 8a) linear dependency indicates

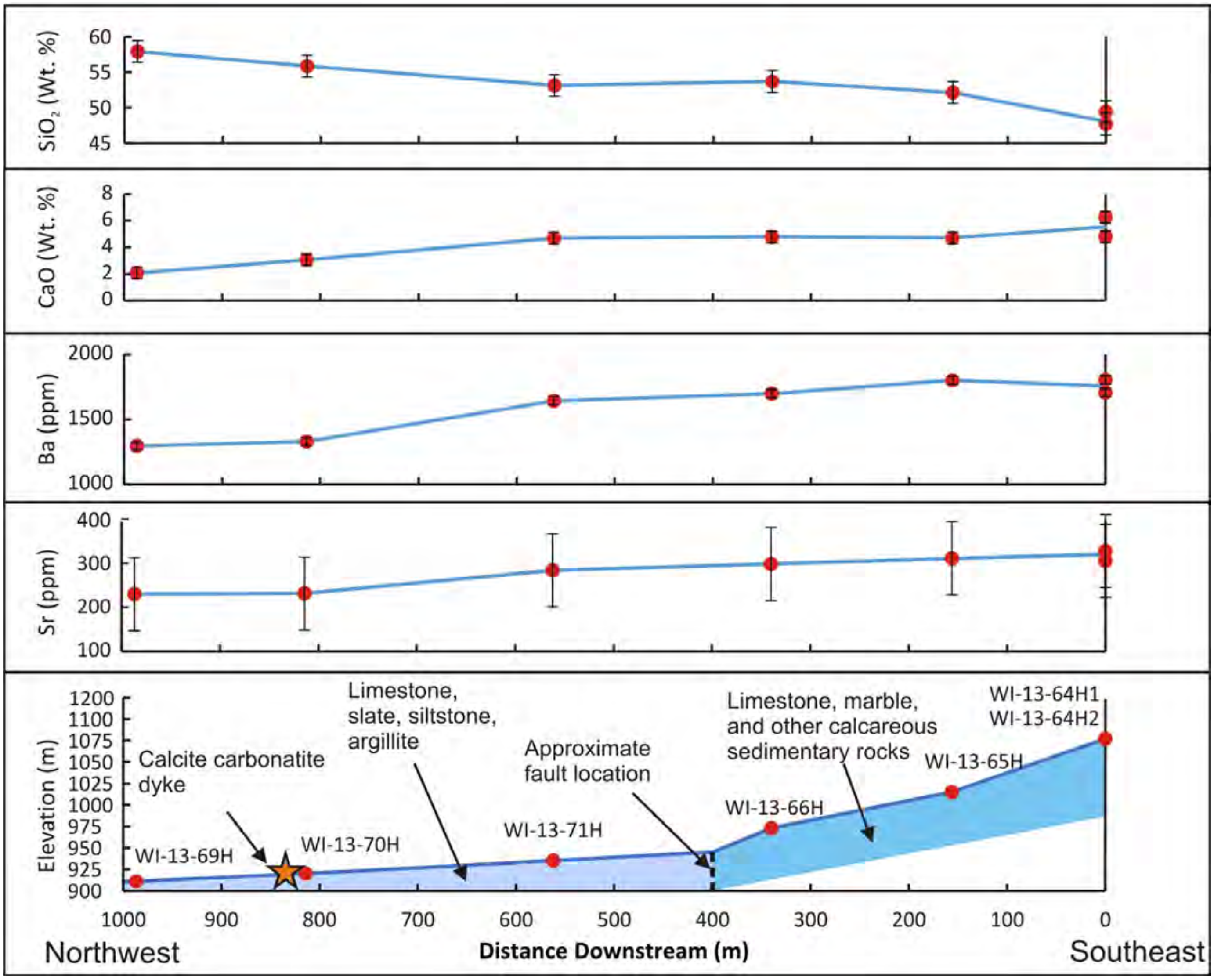

Fig. 6. Profiles of SiO_2, CaO, Ba, and Sr concentrations in the + 125 µm size fraction; elevation (m above sea level). The approximate position of the calcite carbonatite dike outcrop is projected onto the profile.

that monazite-(Ce) is also a prospective indicator mineral. The co-variation of pathfinder elements is consistent with observed mineralogy for the Wicheeda carbonatite complex (Le Couteur, 2008, 2009; Lane, 2009); REE mineralisation in the main carbonatite is predominantly in monazite-(Ce) and REE-fluorocarbonates and carbonates. All P readings are below detection limits and pXRF does not measure F, hindering identification of these minerals in sediment samples. Phosphorus, a relatively light element (atomic weight 30.97), has to be present in higher concentrations than other pathfinder elements if it is to be detectible by pXRF.

Poor correlation between Ce and Y ($R^2 = 0.34$) reflects input of indicator minerals that are strongly enriched in light REEs relative to heavy rare earth elements including Y (HREY) in the carbonatite complex. No meaningful relationship exists between Th and U.

Strong dependence between Nb-Ce ($R^2 = 0.85$; Fig. 8b) and Nb-La ($R^2 = 0.82$) probably indicates co-occurrence of Nb- and REE-bearing minerals. This is expected as REE-fluorocarbonates [such as bastnasite-(Ce), parisite-(Ce), or synchysite-(Ce)], monazite-(Ce), and pyrochlore have similar densities (4.0-5.0 g/cm^3, 4.5-5.5 g/cm^3, and 4.2-6.4 g/cm^3 respectively) and probably, settling velocities.

There is an excellent linear dependence between Nb and TiO_2 ($R^2 = 0.98$; Fig. 8c). This relationship may indicate that pyrochlore contains significant amounts of Ti, or the presence of Nb-rutile within stream sediments. The moderate correlation between Nb and Fe_2O_3 ($R^2 = 0.73$; Fig. 8d) indicates the coincidence of magnetite and Nb-bearing mineral phases such as pyrochlore and Nb-rutile. Correlation between Nb and Ta is poor (R^2= 0.61; including below detection limit data).

Linear dependence between Ba and Sr ($R^2 = 0.98$) may reflect the presence of both elements in a common mineral phase such as REE-bearing fluorocarbonates and/or a consistent composition for barite-celestine solid solution minerals in the area. Input of Sr-Ba sulphates from limestones and marbles of the Kechika

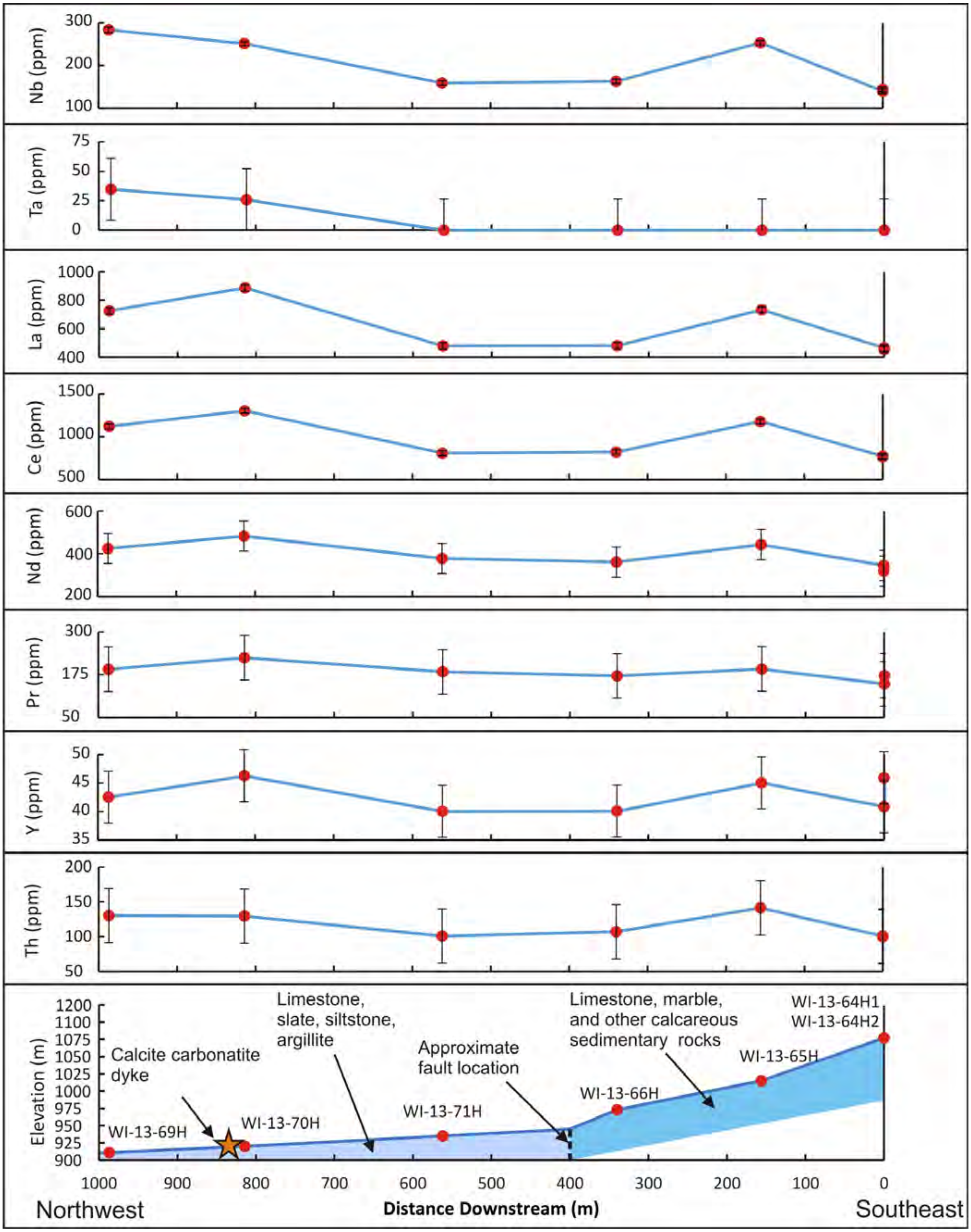

Fig. 7. Profiles of key pathfinder elements concentration in the + 125 µm size fractions; and elevation (m above sea level). The approximate position of the calcite carbonatite dike outcrop is projected onto the profile.

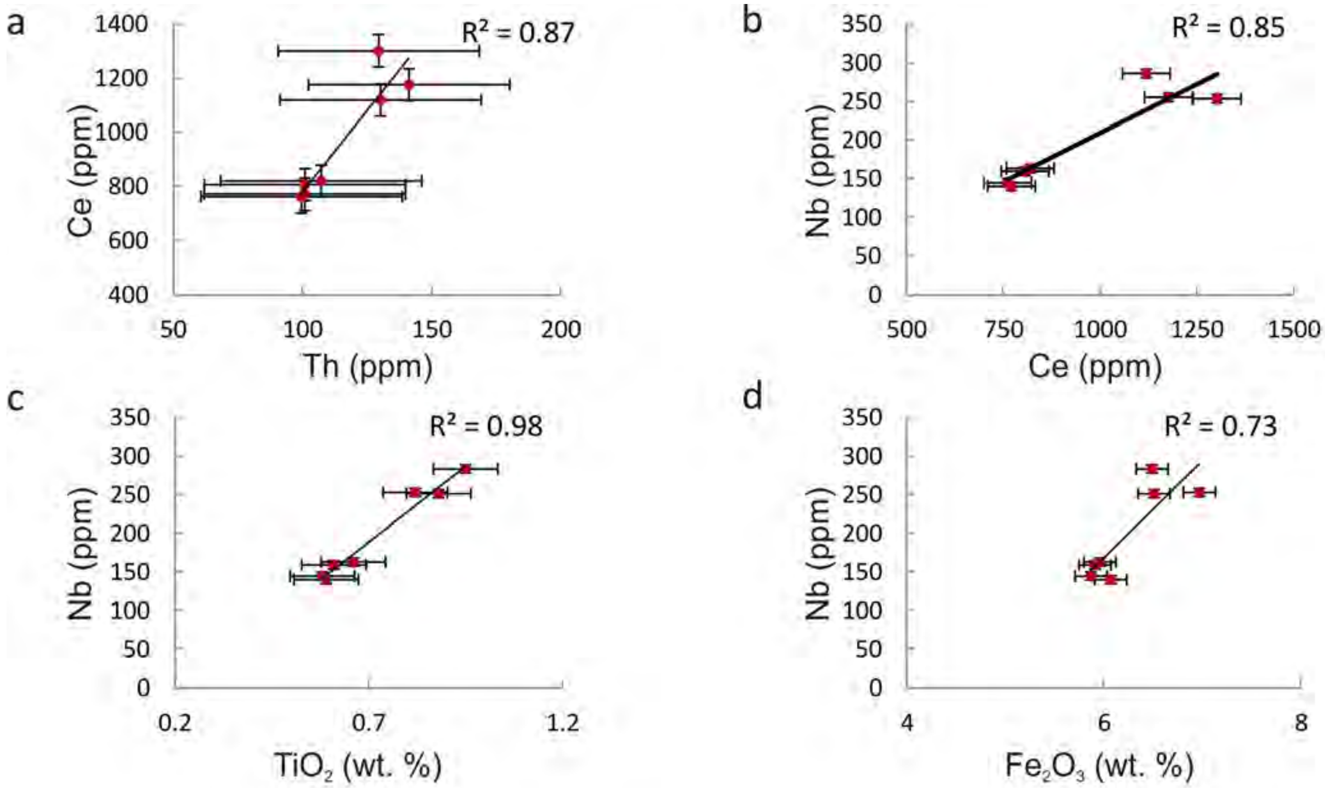

Fig. 8. Correlations between the concentrations of selected elements in the + 125 µm size fraction of samples. **a)** Ce and Th. **b)** Nb and Ce. **c)** Nb and TiO_2. **d)** Nb and Fe_2O_3.

Formation cannot be ruled out as a possible source of Ba and Sr.

Further optical microscope and electron microprobe studies, supplemented by further stream sediment and soil sampling, are required to identify and determine the chemical composition of indicator minerals. The use of QEMSCAN could reconcile stream sediment and indicator mineral chemistry and may confirm the working hypothesis of different indicator mineralogy between calcite and dolomite carbonatites. Pre-concentration of heavy minerals by Frantz isodynamic separation or Wilfley shaker table may be required. The economics and effectiveness of QEMSCAN analyses relative to traditional indicator mineral methods involving hand-picking remains to be established. In combination with EMP and SEM analyses, QEMSCAN will provide quantitative information on indicator minerals and establish mineralogical differences between calcite and dolomite carbonatites in the area. Further sampling of stream sediments downstream of other mineralisation in the area and outside the influence of the Wicheeda carbonatite complex could strengthen the findings in this study.

7. Conclusion

Portable XRF is an effective tool to measure relative concentrations of pathfinder elements (Nb, Ta, La, Ce, Pr, Nd, Y, and Th) in stream sediments collected near the Wicheeda carbonatite complex. These elements are preferentially enriched in the + 125 µm size fraction relative to other sizes. Based on the mineralogy of the Wicheeda carbonatite complex and detectable concentrations of Nb, Ta, La, Ce, Pr, Nd, and Y, monazite, REE-fluorocarbonates and carbonates, and pyrochlore (± columbite) are prospective indicator minerals for Wicheeda carbonatite-type REE deposits. Stream sediment samples collected near the Wicheeda carbonatite complex do decrease in pathfinder element and indicator mineral concentrations downstream. The economics and effectiveness of QEMSCAN analyses relative to traditional indicator mineral methods involving hand-picking, remains to be established.

Acknowledgments

This project received funding and support from Targeted Geoscience Initiative 4 (2010-2015), a Natural Resources Canada program carried out under the auspices of the Geological Survey of Canada. Spectrum Mining Corporation provided access to core and drill results. Critical review by Pearce Luck (British Columbia Ministry of Energy and Mines) and Bob Lane (Plateau Minerals Corp**.**) greatly improved earlier versions of this manuscript. Discussion with Chris Graf regarding previously identified soil and radiometric anomalies helped focus the perspective of this study. The authors would also like to thank Pearce Luck for his assistance with sample preparation and analyses and Joel Trofanenko for his assistance in the field.

References Cited

Armstrong, J.D., Tipper, H.W., and Hoadley, J.W., 1969. Geology of McLeod Lake, British Columbia. Geological Survey of Canada, Map 1204A; scale: 1:253 440.

Betmanis, A.I., 1987. Report on Geological, Geochemical, and Magnetometer Surveys on the Prince and George Groups, Cariboo Mining Division, B.C. British Columbia Ministry of Energy, Mines, and Petroleum Resources, Assessment Report 15944, 86 p.

Bruland, T., 2011. 2010 Helicopter-borne AreoTEM System Electromagnetic, Magnetic Survey and Radiometric Survey. British Columbia Ministry of Energy, Mines, and Petroleum Resources, Assessment Report 32439, 57 p.

Dalsin, M. L., 2013. The Mineralogy, Geochemistry and Geochronology of the Wicheeda carbonatite complex, British Columbia. MSc, University of British Columbia, 265 p.

Graf, C., Lane, B., and Morrison, M., 2009. The Wicheeda Carbonatite-Syenite Breccia Intrusive Complex Hosted Rare Earth Deposit. Conference Abstract, 5th Annual Minerals South Conference & Trade Show, Cranbrook, Canada. <http://www.slideshare.net/RareMetalBelt/abstract-on-the-wicheeda-rare-earth-property#> Accessed December 13, 2013.

Lane, B., 2009. Diamond Drilling Report on the Wicheeda Property, Cariboo Mining Division. British Columbia Ministry of Energy, Mines, and Petroleum Resources, Assessment Report 30873, 196 p.

Le Couteur, P.C., 2008. Petrographic Report on Four samples from the Wicheeda Property; unpublished company report, Spectrum Mining Corporation, 36 p.

Le Couteur, P.C., 2009. Petrographic Report on Four samples from the Wicheeda Property; unpublished company report, Spectrum Mining Corporation, 28 p.

Lovang, G., and Meyer, W., 1987. Report on Trenching, Stream Silt Concentrate and Soil Sampling on the George Group, Cariboo Mining Division. British Columbia Ministry of Energy, Mines, and Petroleum Resources, Assessment Report 16246, 18 p.

Luck, P., and Simandl, G.J., 2014. Portable X-ray fluorescence in stream sediment chemistry and indicator mineral surveys, Lonnie carbonatite complex, Canada. In: Geological Fieldwork 2013, British Columbia Ministry of Energy and Mines, British Columbia Geological Survey Paper 2014-1, this volume.

Mackay, D.A.R., and Simandl, G.J., 2014. Portable x-ray fluorescence to optimize stream sediment chemistry and indicator mineral surveys, case 1: Carbonatite-hosted Nb deposits, Aley carbonatite, British Columbia, Canada. In: Geological Fieldwork 2013, British Columbia Ministry of Energy and Mines, British Columbia Geological Survey Paper 2014-1, this volume.

Mäder, U.K., and Greenwood, H.J., 1988. Carbonatites and Related Rocks of the Prince and George Claims, Northern Rocky Mountains (93J, 93I): Geological Fieldwork 1987. British Columbia Ministry of Energy, Mines and Petroleum Resources, British Columbia Geological Survey Paper 1988-1, pp. 375-380.

Massey, J.W.H., McIntyre, D.G., Dejardins, P.J., and Cooney, R.T., 2005. Digital geology map of British Columbia. British Columbia Ministry of Energy, Mines and Petroleum Resources, British Columbia Geological Survey Open File 2005-2, DVD.

Millonig, L.J., Gerdes, A., and Groat, L.A., 2012. U-Th-Pb geochronology of meta-carbonatites and meta-alkaline rocks in the southern Canadian Cordillera: A geodynamic perspective. Lithos, 152, 202-217.

Pell, J., 1994. Carbonatites, nepheline syenites, kimberlites and related rocks in British Columbia. British Columbia Ministry of Energy, Mines and Petroleum Resources, British Columbia Geological Survey Bulletin 88, 136 p.

Simandl, G.J., Fajber, R., Paradis, S., and Simandl, L.J., 2013. Exploration for sedimentary phosphate (±REE) deposits using handheld XRF – An orientation survey. Geochemistry: Exploration, Environment, Analysis. http://dx.doi.org/10.1144/geochem2012-180. Available online.

Tantalum-Niobium International Study Center, 2013. Niobium - Raw Materials and Processing. <http://tanb.org/niobium> Accessed July 17, 2013.

Tse, P.K., 2011. China's Rare-Earth Industry. United States Geological Survey, Open-File Report 2011-1042, 11 p.

Woolley, A.R., and Kjarsgaard, B.A., 2008. Paragenetic Types of Carbonatite as Indicated by the Diversity and Relative Abundances of Associated Silicate Rocks: Evidence from a Global Database. The Canadian Mineralogist, 46, 741-752.

Fluorite and its potential as an indicator mineral for carbonatite-related rare earth element deposits

S.A. Makin[1], G.J. Simandl[2, a], and D. Marshall[1]

[1] Simon Fraser University, Department of Earth Sciences, Burnaby, BC, V5A 1S6
[2] British Columbia Geological Survey, Ministry of Energy and Mines, Victoria, BC, V8W 9N3
[a] corresponding author: George.Simandl@gov.bc.ca

Recommended citation: Makin, S.A., Simandl, G.J., and Marshall, D., 2014. Fluorite and its potential as an indicator mineral for carbonatite-related rare earth element deposits. In: Geological Fieldwork 2013, British Columbia Ministry of Energy and Mines, British Columbia Geological Survey Paper 2014-1, pp. 207-212.

Abstract

Fluorite has potential as a proximal indicator mineral for the exploration of specialty metals, particularly rare earth elements and Nb in carbonatite-related deposits. Plots of Tb/La - Tb/Ca were generated using all available published data (worldwide) to compare REE concentrations in fluorite from carbonatite, peralkaline-alkaline, Mississippi Valley Type (MVT), and vein (sedimentary, igneous, and metamorphic hosted) deposits. Y-Yb plots distinguish between fluorites from carbonatite and MVT deposits. Fluorite from carbonatite-related and MVT deposits form compositional fields with minor overlap. Ongoing investigations include: microchemical analyses of fluorites from key Canadian and foreign deposits, diagram refinement by contouring, the production of probability plots, and experimentation with discrimination diagrams incorporating normalized REE slope calculations with the presence or absence of Ce and Eu anomalies.

Keywords: Fluorite, REE, exploration, discrimination diagrams, specialty metals

---

1. Introduction

A major objective of the Specialty Metal component of the TGI-4 is to develop and improve technologies and methods that can be applied during the exploration for buried REE and Nb ± Ta deposits. Specialty metals are found in a variety of geological settings including carbonatites and peralkaline intrusions (Simandl, 2012; Simandl et al., 2012). Although fluorite is commonly associated with these specialty metals deposits, it is also present in MVT deposits, Climax-type molybdenum deposits, and fluorite ± barite veins hosted by sedimentary, igneous, and metamorphic rocks. Fluorite can accept trace elements including REEs that substitute for Ca^{2+} in its crystal structure and fluorite crystals may contain inclusions of REE-bearing fluorocarbonates or other REE-bearing minerals. As a consequence, and due to its distinctive physical properties (colour, fluorescence, high density, low hardness, and cleavage), fluorite is a prospective proximal indicator mineral, particularly for carbonatite-related Rare Earth Element (REE) deposits. Herein we present Tb/La - Tb/Ca and Logarithmic Y - Yb plots based on a current, worldwide compilation of REE abundances reported in literature, demonstrating that these diagrams can discriminate between fluorite from carbonatites and MVT deposits.

2. Fluorite

Fluorite occurs in a variety of colours ranging from transparent and colourless to nearly opaque and black, but is commonly purple, green, blue, or yellow, and can exhibit colour zoning, (Trinkler et al. 2005, Staebler et al. 2006). Fluorite is typically fluorescent, and less commonly phosphorescent, thermoluminescent, and triboluminescent. Colour in fluorite can be caused by a variety of factors including impurities, structural defects, and REE substitutions for Ca, whereas fluoresence is generally attributed to REE substitutions of divalent and trivalent cations for Ca, (Verbeek, 2006). Studies on crystals from the Bingham deposit (New Mexico) identified sector zoning in single crystals and demonstrated that trace element incorporation in fluorite is surface specific (Bosce and Rakovan, 2001).

Other distinguishing characteristics of fluorite are its crystal habit, hardness, and cleavage. Fluorite crystallizes as a cubic, face-centred lattice. Fluorine anions form square stacks forming eight-fold coordination sites for calcium. Ca cations are at the corners and centers of the cubic lattice (Nesse, 2000). Fluorite commonly forms cubes or octahedrons, less commonly dodecahedrons and, rarely, tetrahexahedrons, trapezohedrons, trisoctahedrons, hexoctahedrons, and botyroidal forms. In thin section, fluorite is isotropic and rarely displays weak, anomalous anisotropism. Twinning is typical in fluorite, following spinel-law twins that can form penetration and contact twins (Staebler et al., 2006). Fluorite generally occurs as broken fragments due to its perfect {111} cleavage in four directions (Nesse, 2000). Fluorite's softness combined with its tendency to cleave makes it an excellent proximal indicator of mineral deposits. Additionally, the density of fluorite can be as high as 3.6 g/cm^3 when enriched in REEs (Staebler et al., 2006) approaching those of common specialty metal indicator minerals such as REE-bearing hydrated carbonates and fluorocarbonates (3.5 - 5.0 g/cm^3) pyrochlore (4.2 - 6.4 g/cm^3) columbite (5.3 - 7.3 g/cm^3), and other indirect indicators such as barite (4.5 g/cm^3), celestite (3.9 - 4.0 g/cm^3), and apatite (3.1 - 3.2 g/cm^3).

Fluorite is primarily used as a flux in steelmaking, iron and steel casting, and other metallurgic processes such as primary aluminum production. Fluorite is also used in producing hydrofluoric acid, glass, enamels, cement, welding rod coatings, herbicides, Teflon, Freon, and other chlorofluorocarbons (Simandl 2009a; b; Staebler et al., 2006).

Information about fluorite occurrences in British Columbia are compiled in Pell (1992) and summarized by Simandl (2009b). Fluorite occurs as a gangue mineral in a number of REE deposits including carbonatites (e.g., Eldor, QC), peralkaline intrusions (e.g., Nechalacho, NWT; Strange Lake, QC and Labrador), REE occurrences of uncertain origin (e.g. Rock Canyon Creek, BC), carbonate-hosted zinc and lead-bearing hydrothermal deposits including MVTs (e.g., Cave in Rock, Illinois), epithermal precious metal deposits (Epinger and Closs, 1990), Climax-type molybdenum deposits (e.g. Climax, Colorado; Ludington and Plumlee, 2009), other greisens-granite-pegmatite-hosted metal-bearing deposits, and fluorite ± barite veins.

3. Historic fluorite discrimination diagrams

The REE chemistry of fluorite has been previously used to generate discrimination diagrams for deposit types. Schneider et al. (1975) and Möller et al. (1976) created logarithmic abundance ratio diagrams of REE and calcium in fluorite involving genetic terminology. These papers used atomic ratios of Tb/La and Tb/Ca to establish reference lines between genetic fields for “pegmatitic”, “hydrothermal”, and “sedimentary” fluorite. These boundaries were used by many authors (e.g. Ekambaram et al., 1986; Koç and Reçber, 2001; Sánchez et al., 2010; Schönenberger et al., 2007; Schwinn and Markl, 2005; Subías and Fernández-Nieto, 1995) to assign origin to specific deposits or fluorite districts. Gagnon et al. (2003) questioned universal validity of these diagrams. Tümenbayar (1996) developed a discrimination diagram based on logarithmic concentrations of Y versus Yb measured in ppm to classify Mongolian fluorite deposits into four categories. This diagram defined fields for epithermal, hydrothermal, pegmatitic, and magmatic fluorite deposits. Koç et al. (2003) modified the fields established by Tümenbayar (1996); however, the basis for this modification is not clear. Herein we use Tb/La - Tb/Ca and Y - Yb diagrams to plot all available fluorite data that can be assigned to carbonatite, peralkaline-alkaline, Mississippi Valley Type (MVT), and vein (sedimentary- igneous- and metamorphic-hosted) deposits.

4. Compilation diagrams

The database to construct Figures 1 to 3 was compiled from publications covering an array of deposit types worldwide. It contains more than 1000 entries of REE concentrations in fluorite. The deposit type for each entry was determined from the geological information in its source document; only entries clearly identified as carbonatite, peralkaline-alkaline, MVT, or vein type were used to construct the discrimination diagrams. Most of the data represent analyses by inductively coupled plasma mass spectroscopy (ICP-MS) or neutron activation, although some laser ablation ICP-MS results are included.

Vein-type mineralization was subdivided according to its host rock (sedimentary, igneous, or metamorphic). Carbonatite data were also divided in Figure 2 to represent fluorite in carbonatite-related fluorite deposits and fluorite from carbonatites explored for REE or Nb. The compiled data were superimposed on the modified Tb/La - Tb/Ca diagram of Möller et al. (1976). Positions of the original Möller et al. (1976) reference lines dividing the diagram into “pegmatitic”, “hydrothermal”, and “sedimentary” fields were recalculated to ppm values for ease of use by the mineral exploration community and are shown on all Tb/La - Tb/Ca plots for reference.

5. Results

Carbonatite-related fluorite data define a field that is aligned along, but lies mainly below, the pegmatite-hydrothermal reference line (Fig. 1a). The field of fluorite from MVT deposits plots on both sides of the hydrothermal-sedimentary reference line and the highest density of samples straddles this boundary (Fig. 1b). Peralkaline-alkaline related fluorite data are scattered, but with the exception of one sample, all are above the hydrothermal-sedimentary reference line (Fig. 1c). Samples from fluorite-bearing veins hosted by sedimentary deposits plot entirely below the pegmatite-hydrothermal reference line (Fig. 1d). Data from fluorite veins hosted by igneous rocks (Fig. 1e) overlap those hosted by sedimentary rock, but extend farther below the hydrothermal-sedimentary reference line. Fluorite veins hosted by metamorphic rocks (Fig. 1f) define a field that overlaps the hydrothermal and sedimentary fields, with the main concentration of samples elongated and parallel to the hydrothermal-sedimentary reference line. Figures 2 and 3 depict distinct fields for fluorite from carbonatite and MVT deposits for Tb/La - Tb/Ca and Y - Yb diagrams respectively.

6. Discussion

Distinct compositional fields were produced representing REE signatures in fluorite for carbonatite and MVT deposits (Figs. 2, 3).

Fluorite from peralkaline-alkaline settings define a broad field that lies above the sedimentary-hydrothermal reference line (Fig. 1c); and comparison between Figs. 1a and 1c demonstrate a compositional overlap between fluorites from carbonatite and peralkaline-alkaline settings.

Data from fluorite-bearing veins (Figs. 1d-f) scatter across the central parts of the Tb/La - Tb/Ca diagrams, but do not extend as far into the low Tb/La and high Tb/Ca areas as the carbonatite and peralkaline-alkaline data (Figs. 1a, c). Similarly the vein data do not extend as far into the high Tb/La and low Tb/Ca parts of the diagram as the MVT fluorite compositions. The extensive compositional overlap between fluorite-bearing veins cutting sedimentary, igneous and metamorphic rocks (Figs. 1d-f) indicates that chemistry of the local host rock is not the main factor controlling REE concentration in fluorite.

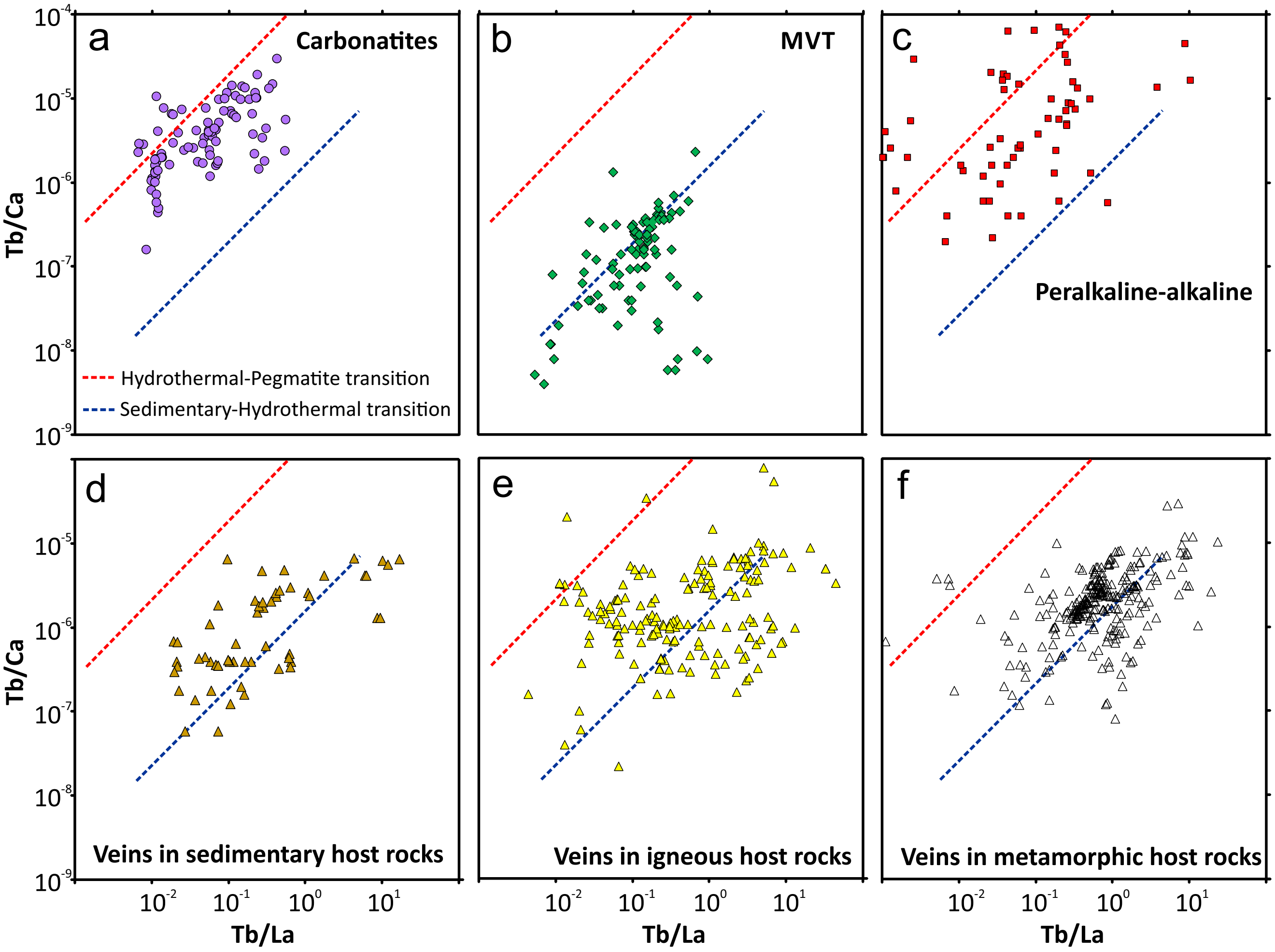

Fig. 1. Tb/La-Tb/Ca plots for fluorite (modified from Möller et al., 1976) with ratios calculated directly from Tb, La, and Ca concentrations in ppm. **a)** Carbonatite-related fluorite (from: Alvin et al., 2003; Bühn et al., 2003; Palmer and Williams-Jones, 1994; Santos et al., 1996; Xu et al., 2012). **b)** Mississippi Valley Type (MVT) fluorite (from: Bau et al., 2003; Hill et al., 2000; Levresse et al., 2006; Naldrett et al., 1987; Schneider et al., 1975; Souissi et al., 2010). **c)** peralkaline-alkaline rock-related fluorite (from: Gagnon et al., 2003; Hill et al., 2000; Koç et al., 2003; Minuzzi et al., 2008; Pekov et al., 2009; Schönenberger et al., 2008). **d)** Sedimentary rock-hosted fluorite-bearing veins (from: Hill et al., 2000; Koç and Reçber, 2001; Schwinn and Markl, 2005). **e)** Igneous rock-hosted fluorite-bearing veins (from: Ackerman, 2005; Castorina et al., 2008; Czaja et al., 2012; Dill et al., 2011; Hill et al., 2000; Levresse et al., 2006; Lüders et al., 2008; Monecke et al., 2002; Pinto-Coelho et al., 1999; Sallet et al., 2005; Schwinn and Markl, 2005). **f)** Metamorphic rock-hosted fluorite-bearing veins (from: Castorina et al., 2008; Cheilletz et al., 2010; Ekambaram et al., 1985; Lüders et al., 2008; Monecke et al., 2000; Schwinn and Markl, 2005). The red and blue dashed lines are the recalculated boundaries between the hydrothermal and pegmatite, and sedimentary and hydrothermal fields as defined by Möller et al. (1976).

A review of the relationships between the temperature of homogenization and composition of fluids relative to results of LA-ICPMS data on fluorite from the same samples might determine if the distribution of the data on the Tb/La - Tb/Ca diagrams reflects a trend of increasing fluorite crystallization temperatures moving from the lower right (high Tb/La and low Tb/Ca) to the upper left (low Tb/La and high Tb/Ca). Fluid-rock interaction is important at elevated temperatures as there is a general trend of increased solubility of REEs with increasing temperature (Wood, 1990; Williams-Jones et al., 2012). The increasing solubility is related to REE speciation, with F complexes predominant relative to Cl complexes in experimental studies up to 250°C. Sulfate, carbonate, and phosphate complexes may also be important (Williams-Jones et al. 2012), but have not been investigated experimentally. Another important geochemical factor influencing REE transport and deposition is pH with decreasing acidity (and chlorinity) driving REEs out of solution (Willams-Jones et al., 2012).

The Y - Yb diagram (Fig. 3), represents the most straightforward method for the exploration industry to distinguish between fluorite grains from carbonatite and MVT settings in stream sediments and till. Consideration of additional elements, besides REEs, will probably be required

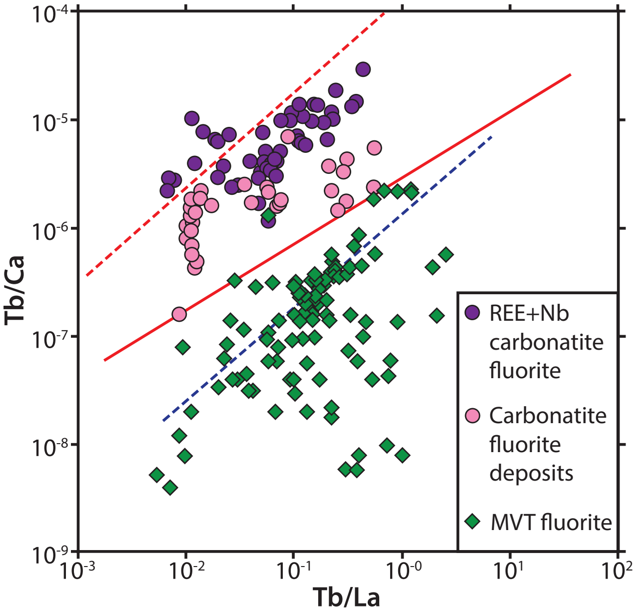

Fig. 2. Tb/La-Tb/Ca diagram showing compositional data for fluorite from carbonatite-related and MVT deposits. The solid red line defines the boundary between MVT-related fluorite and carbonatite-related fluorite. The carbonatite data are bicolored, representing fluorite found in carbonatite-related fluorite deposits and fluorite from carbonatites explored for REE or Nb. Information sources and reference lines as in Figures 1a and 1b.

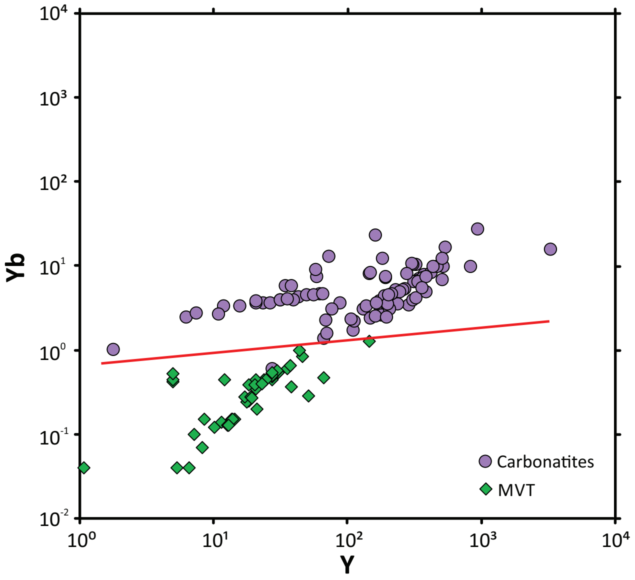

Fig. 3. Y-Yb plot for fluorite from carbonatite and MVT deposits. The carbonatite-related fluorites define a trend with a shallow positive slope and have higher concentrations of Yb than fluorites from MVT deposits with the exception of one sample. The solid red line defines the boundary between MVT-related fluorite and carbonatite-related fluorite. Information sources and reference lines as in Figures 1a and 1b.

to produce simple, user-friendly, fluorite-based, discrimination diagrams for indicator mineral studies.

7. Conclusion

Fluorite is a potential proximal indicator mineral for carbonatite-related specialty metal mineralization. Tb/La - Tb/Ca and Y - Yb diagrams may be used to distinguish between fluorite from carbonatite-related and MVT deposits; however, significant overlap exists between compositional fields of fluorites from sedimentary, igneous, and metamorphic rock hosted vein deposits. This indicates that REE concentration in fluorite is largely independent of the composition of the host rock. There is also significant overlap between compositions of fluorites from carbonatites, peralkaline-alkaline intrusions, and veins. Further refinements of these preliminary diagrams through data contouring and the production of probability plots are required. Effort is underway to analyze fluorite from key Canadian and foreign deposits using EMP and LA-ICPMS, and to create a complementary set of discrimination diagrams incorporating slopes of chondrite-normalized plots and Ce and Eu anomalies. Consideration of additional elements, besides REEs, will be investigated to produce user-friendly, fluorite-based, discrimination diagrams for indicator mineral studies.

Acknowledgments

This project received funding and support from the Targeted Geoscience Initiative 4 (2010–2015), a Natural Resources Canada program carried out under the auspices of the Geological Survey of Canada. Simon Fraser University provided research funding via a Bridging Grant and student support via funding from the Earth Sciences Department. Reviews by Pearce Luck from the British Columbia Geological Survey improved the clarity of this manuscript. His contribution is greatly appreciated.

References cited

Ackerman, L., 2005. Magmatic vs. hydrothermal origin of fluorites from Vlastějovice, Bohemian Massif. Journal of the Czech Geological Society, 50, 35-41.

Alvin, M. P., Dunphy, J. M., Groves, D. I., 2004. Nature and genesis of a carbonatite-associated fluorite deposit at Speewah, East Kimberley region, Western Australia. Mineralogy and Petrology, 80, 127-153.

Bau, M., Romer, R.L., Lüders, V., Dulski, P., 2003. Tracing element sources of hydrothermal mineral deposits: REE and Y distribution and Sr-Nd-Pb isotopes in fluorite from MVT deposits in the Pennine Orefield, England. Mineralium Deposita, 38, 992-1008.

Bühn, B., Schneider, J., Dulski, P., Rankin, A. H., 2003. Fluid-rock interaction during progressive migration of carbonatitic fluids, derived from small-scale trace element and Sr, Pb isotope distribution in hydrothermal fluorite. Geochimica et Cosmochimica Acta, 67, 4577-4595.

Bosce, S. and Rakovan J. 2002. Surface-structure-controlled sectoral zoning of the rare earth elements in fluorite from Long Lake, New York, and Bingham, New Mexico, U.S.A. Geochimica et Cosmochimica Acta, 66 (6): 997–1009.

Castorina, F., Masi, U., Padalino, G., Palomba, M., 2008. Trace-element and Sr-Nd isotopic evidence for the origin of the Sardinian fluorite mineralization (Italy). Applied Geochemistry, 23, 2906-2921.

Cheilletz, A., Gasquet, D., Filali, F., Archibald, D.A., Nespolo, M., 2010. A late Triassic 40Ar/39Ar age for the El Hammam high-REE fluorite deposit (Morocco): mineralization related to the Central Atlantic Magmatic Province?. Mineralium Deposita, 45, 323-329.

Czaja, M., Bodyl-Gajowska, S., Lisiecki, R., Meijerink, A., Mazurak, Z., 2012. The luminescence properties of rare-earth ions in natural fluorite. Physics and Chemistry of Minerals, 39, 639-648.

Dill, H. G., Hansen, B. T., Weber, B., 2011. REE contents, REE minerals and Sm/Nd isotopes of granite- and unconformity-related fluorite mineralization at the western edge of the Bohemian Massif: With special reference to the Naddburg-Wölsendorf District, SE Germany. Ore Geology Reviews, 40, 132-148.

Ekambaram, V., Brookins, D.G., Rosenberg, P.E., Emanuel, K.M., 1986. Rare-earth element geochemistry of fluorite carbonate deposits in western Montana, U.S.A.. Chemical Geology, 54, 319-331.

Eppinger, R.G., Closs, G.L., 1990. Variation of trace elements and rare earth elements in fluorite, a possible tool for exploration. Economic Geology, 85, 1896-1907.

Gagnon, J.E., Samson, I.M., Fryer, B.J., Williams-Jones, A.E., 2003. Compositional heterogeneity in fluorite and the genesis of fluorite deposits: Insights from LA-ICP-MS analysis. The Canadian Mineralogist, 41, 365-382.

Hill, G.T., Campbell, A.R., Kyle, P.R., 1999. Geochemistry of southwestern New Mexico fluorite occurrences implications for precious metals exploration in fluorite-bearing systems. Journal of Geochemical Exploration, 68, 1-20.

Koç, Ş., Özmen, Ö., Dogan, A. U., 2003. Geochemistry of fluorite mineralization in Kaman, Kirsehir, Turkey. Journal Geological Society of India, 62, 305-317.

Koç, Ş., Reçber, A., 2001. Fluid inclusion studies and geochemistry of rare earth elements of hydrothermal fluorites from Pöhrenk, Kirşehir, Central Turkey. Acta Geologica Sinica, 75, 59-65.

Levresse, G., Tritlla, J., Villareal, J., Gonzalez-Partida, E., 2006. The “El Pilote” fluorite skarn: A crucial deposit in the understanding and interpretation of the origin and mobilization of F from northern Mexico deposits. Journal of Geochemical Exploration, 89, 205-209.

Lillie, R. (2006). The great southern Illinois fluorspar deposits. In: Fluorite - the collector's choice. Fisher, J., Jarnot, M. Neumeier, G., Pasto, A., Staebler, G. and Wilson, T. (Eds.):. Lithographie, LLC, Connecticut, U.S.A. pp. 56-63.

Lüders, V., Romer, R.L., Gilg, H. A., Bodnar, R.J., Pettke, T., Misantoni, D., 2009. A geochemical study of the Sweet Home Mine, Colorado Mineral Belt, U.S.A: hydrothermal fluid evolution above a hypothesized granite cupola. Lehmann, B., Mineralium Deposita, 44, 425-434.

Ludington, S., Plumlee, G.S., 2009. Climax-type porphyry molybdenum deposits. Open-File Report 2009-1215. U.S. Department of the Interior, U.S. Geological Survey. 4-16.

Marchand, L., Joseph, D., Touray, J. C., 1976. Criteres d’analyse géochimique des gisements de fluorine bases sur l’étude de la distribution des lanthanides – application au gite de Maine (71-Cordesse, France). Mineralium Deposita, 11, 357-379.

Méary, A., Touray, J. C., Galland, D., Jebrak, M., 1985. Interprétation de l’anomalie en europium des flourines hydrothermales – Données de la resonance paramagnétique électronique: Application au gite de fluorine de Montroc (Tarn, France). Chemical Geology, 48, 115-124.

Minuzzi, O.R.R., Bastos N., Arthur C., Formoso, M.L.L., Andrade, S., Janasi, V.A., Flores, J.A., 2008. Rare earth element and yttrium geochemistry applied to the genetic study of cryolite ore at the Pitinga Mine (Amazon, Brazil). Annals of the Brazilian Academy of Sciences 80, 719-733.

Möller, P., Parekh, P.P., Schneider, H.-J., 1976. The Application of Tb/Ca-Tb/La abundance ratios to problems of fluorspar genesis. Mineralium Deposita, 11, 111-116.

Monecke, T., Kempe, U., Monecke, J., Sala, M., Wolf, D., 2002. Tetrad effect in rare earth element distribution patterns: A method of quantification with application to rock and mineral samples from granite-related rare metal deposits. Geochimica et Cosmochimica Acta, 66, 1185-1196.

Monecke, T., Monecke, J., Mönch, W., Kempe, U., 2000. Mathematical analysis of rare earth element patterns of fluorites from the Ehrenfriedersdorf tin deposit, Germany: evidence for a hydrothermal mixing process of lanthanides from two different sources. Mineralogy and Petrology, 70, 235-256.

Naldrett, D. L., Lachaine, Andre, Naldrett, S. N., 1987. Rare-earth elements, thermal history, and the colour of natural fluorites. Canadian Journal of Earth Sciences, 24, 2082-2088.

Nesse, W.D., 2000. Introduction to Mineralogy. Oxford University Press, Inc., New York, New York, 466 p.

Palmer, D.A.S., Williams-Jones, A.E., 1996. Genesis of the carbonatite-hosted fluorite deposit at Amba Dongar, India: Evidence from fluid inclusions, stable isotopes, and whole rock-mineral geochemistry. Economic Geology, 91, 934-950.

Pekov, I.V., Chukanov, N.V., Kononkova, N.N., Yakubovich, O.V., Massa, W., Voloshin, A.V., 2009. Tveitite-(Y) and REE-enriched fluorite from amazonite pegmatites of the Western Keivy, Kola Peninsula, Russia: Genetic crystal chemistry of natural Ca, REE-fluorides. Geology of Ore Deposits, 51, 595-607.

Pell, J., 1992. Fluorospar and fluorine in British Columbia. Province of British Columbia. Bulletin – Ministry of Energy Mines and Petroleum Resources. 1-82. Open File.

Pinto-Coelho, C., Botelho, N.F., Roger, G., 1999. Rare-earth elements mobility during hydrothermal alteration: the example of the Serra Branca granite, central Brazil. Geomaterials, Paris, 328, 663-670.

Sallet, R., Moritz, R., Fontignie, D., 2005. The use of vein fluorite as probe for paleofluid REE and Sr-Nd isotope geochemistry: The Santa Catarina Fluorite District, Southern Brazil. Chemical Geology, 223, 227-248.

Sánchez, V., Cardellach, E., Corbella, M., Vindel, E., Martín-Crespo, T., Boyce, A.J., 2010. Variability in fluid sources in the fluorite deposits from Asturias (N Spain): Further evidences from REE, radiogenic (Sr, Sm, Nd) and stable (S, C, O) isotope data. Ore Geology Reviews, 37, 87-100.

Santos, R., Ventura, D., Marcel A., De Oliveira, C.G., 1996. Rare earth elements geochemistry of fluorite from the Mato Preto Carbonatite Complex, Southern Brazil. Revista Brasileira de Geociências, 26, 81-86.

Schneider, H.-J., Möller, P., Parekh, P.P., 1975. Rare earth elements distribution in fluorites and carbonated sediments of the East-Alpine mid-Triassic sequences in the Nördliche Kalkalpen. Mineralium Deposita, 10, 330-344.

Schönenberger, J., Köhler, J., Markl, G., 2008. REE systematics of fluorides, calcite, and siderite in peralkaline plutonic rocks from the Gardar Province, South Greenland. R.L. Rudnick (Eds.), Chemical Geology, 247, 16-35.

Schwinn, G., Markl, G., 2005. REE systematics in hydrothermal fluorite. Chemical Geology, 216, 225-248.

Simandl, G.J., 2012. Geology and economic significance of current and future rare earth element sources. Proceedings of the 51st conference of metallurgists. J.R. Goode, G. Moldoveanu, M.S. Rayat (Eds.), Rare Earths 2012, Canadian Institute of Mining, Metallurgy and Petroleum, Niagara, Ontario, pp. 15-30.

Simandl, G.J., Prussin, E.A. and Brown, N., 2012. Specialty metals in Canada. BC Ministry of Energy and Mines, British Columbia Geological Survey; 7-48. Open File.

Simandl, G.J., 2009a. World fluorspar resources, market and deposit examples from British Columbia, Canada. BC Ministry of Energy and Mines, British Columbia Geological Survey, 4-16. Information Circular 2009.

Simandl G.J., 2009b. Fluorspar market and selected fluorite-bearing deposits, British Columbia, Canada, BC Ministry of Energy and Mines, British Columbia Geological Survey Geofile 2009-03, poster.

Souissi, F., Souissi, R., Dandurand, J.-L., 2010. The Mississippi Valley-type fluorite ore at Jebel|Stah (Zaghouan district, north-eastern Tunisia): Contribution of REE and Sr isotope geochemistries to the genetic model. Ore Geology Reviews, 37, 15-30.

Staebler, G., Deville, J., Verbeek, E., Richards, R.P., and Cesbron, F. (2006). Fluorite: From ancient treasures to modern labs and collections. In: Fluorite - the collector's choice. Fisher, J., Jarnot, M. Neumeier, G., Pasto, A., Staebler, G. and Wilson, T. (Eds.). Lithographie, LLC, Connecticut, U.S.A. pp. 4-12.

Subías, I., Fernández-Nieto, C., 1995. Hydrothermal events in the Valle de Tena (Spanish Western Pyrenees) as evidenced by fluid inclusions and trace-element distribution from fluorite deposits. Chemical Geology, 124, 267-282.

Trinkler, M., Monecke, T., Thomas, R., 2005. Constraints on the genesis of yellow fluorite in hydrothermal barite-fluorite veins of the Erzgebirge, Eastern Germany: Evidence from optical absorption spectroscopy, rare-earth element data, and fluid-inclusion investigations. The Canadian Mineralogist, 43, 883-898.

Tümenbayar, B. 1996. REE in different types of fluorites. 30th International Geological Congress, Bejing, China, 2, 685.

Verbeek, E. (2006). Fluorite Luminescence. In: Fluorite - the collector's choice. Fisher, J., Jarnot, M. Neumeier, G., Pasto, A., Staebler, G. and Wilson, T. (Eds.), Lithographie, LLC, Connecticut, U.S.A. pp. 13-19.

Willaims-Jones, A.E., Migdisov, A.A., Samson, I.M. 2012. Hydrothermal mobilization of the rare earth elements – a tale of “ceria” and “yttria”. Elements, 8, 355-360.

Wood, S.A. 1990. The aqueous geochemistry of the rare-earth elements and yttrium: 2. Theoretical predictions of speciation in hydrothermal solutions to 350 °C at saturation water vapour pressure. Chemical Geology, 88, 99-125.

Xu, C., Taylor, R.N., Li, W., Kynicky, Ji., Chakhmouradian, A.R., Song, W., 2012. Comparison of fluorite geochemistry from REE deposits in the Panxi region and Bayan Obo, China. Journal of Asian Earth Sciences, 57, 76-89.

Yuan, S., Peng J., Hu, R., Bi, X., Qi, L., Li, Z., Li, X., Shuang, Y., 2008. Characteristics of rare-earth elements (REE), strontium and neodymium isotopes in hydrothermal fluorites from the Bailashui tin deposit in the Furong ore field, southern Hunan Province, China. Chinese Journal of Geochemistry, 27, 342-350.

The nature and origin of the carbonatite-hosted Wicheeda rare earth element deposit, British Columbia

Trofanenko, J.[1], Williams-Jones, A.E.[1, a], and Simandl, G.J.[2, 3]

[1] McGill University, Department of Earth and Planetary Sciences, Montreal, QC, H3A 0E8
[2] British Columbia Geological Survey, Ministry of Energy and Mines, Victoria, BC, V8W 9N3
[3] University of Victoria, School of Earth and Ocean Sciences, Victoria, BC, V8P 5C2
[a] corresponding author: anthony.williams-jones@mcgill.ca

Recommended citation: Trofanenko, J., Williams-Jones, A.E., and Simandl, G.J., 2014. The nature and origin of the carbonatite-hosted Wicheeda Lake rare earth element deposit. In: Geological Fieldwork 2013, British Columbia Ministry of Energy and Mines, British Columbia Geological Survey Paper 2014-1, pp. 213-225.

Abstract
The Wicheeda rare earth element (REE) deposit is an example of high-grade REE mineralization in the British Columbia alkaline province. The deposit is hosted by a 145 m thick, steeply dipping lens-shaped carbonatite that intruded metasedimentary rocks of the Kechika Group, and is exposed over an area of ~ 20,000 m^2. The metasedimentary rocks comprise steeply dipping limestone and siltstone that were regionally metamorphosed to greenschist facies. These rocks were subjected to alkali metasomatism, which produced potassic fenite (K-feldspar- and biotite-rich) adjacent to the carbonatite and sodic fenite (sodic amphibole- and albite-rich) at a greater distance from it. Most of the REE mineralization is hosted by pervasively altered carbonatite, consisting of coarse-grained cream-coloured dolomite crystals rimmed by hematite, together with disseminated fine-grained biotite, pyrite, and trace apatite. The intrusion was affected by multi-stage dolomitization and fracture-associated dissolution of dolomite followed by precipitation of REE-bearing minerals (e.g., bastnäsite-(Ce) and monazite-(Ce)) along fractures and in vugs. Monazite-(Ce) occurs as fine-grained aggregates and rarely as lath-shaped inclusions in bastnäsite-(Ce), suggesting that it preceded bastnäsite-(Ce). The deposit is light-REE (LREE) enriched with a La/Lu ratio of 4314 in the dolomite carbonatite compared to 1249 in the potassic fenite and 46 in the sodic fenite. Total rare earth oxide concentrations in the deposit range from 1.1 to 11 wt.%. Cerium and lanthanum concentrations reach 5.3 and 4.1 wt.%, respectively. We propose a preliminary model in which a halogen- (mainly chlorine) and alkali-bearing hydrothermal fluid exsolved from the carbonatite magma, altered the adjacent sedimentary rocks to potassic fenite, and mobilized the REEs as chloride complexes. Distal to the intrusion, heating of formational waters by the carbonatite altered the sedimentary rocks to sodic fenite. The magmatic hydrothermal fluid partially dissolved the carbonatite, leading to deposition of bastnäsite-(Ce) and monazite-(Ce) in veins and vugs in response to an increase in pH. The Wicheeda carbonatite demonstrates the potential for economic carbonatite-hosted hydrothermal REE deposits in British Columbia.

Keywords: Wicheeda Lake, rare earth element deposit, carbonatite, fenitization, bastnäsite-(Ce), monazite-(Ce), hydrothermal concentration, REE-chloride complexes, fluid mixing

---

1. Introduction

The British Columbia alkaline province represents a potentially important but largely unexplored rare metal metallogenic province in the foreland fold and thrust belt of the Canadian Cordillera (Fig. 1 inset) that owes its origin to a change from convergent to extensional tectonics at ~ 390 Ma (Pell, 1994). This change in tectonics caused rifting that provided access for mantle-derived magmas to the crust, and led to the emplacement of a number carbonatite bodies between ~ 360 and 330 Ma (Pell, 1994; Millonig et al., 2012), including the Wicheeda intrusion, which hosts a high-grade REE deposit. The REE potential of the Wicheeda carbonatite, approximately 100 km northeast of Prince George in north-central British Columbia (Fig. 1), was first recognized by Mäder and Greenwood (1987), who described it as a 250 m diameter plug characterized by ankerite phenocrysts, unconfirmed REE-fluorocarbonates, and “baked sediments” including limestone interbedded with silty to shaley limestone, and shale of the Kechika Group (Cambrian to Early Ordovician; Betmanis, 1987). Subsequent exploration of the carbonatite by Spectrum Mining Corporation revealed a LREE-enriched deposit from drill intersections of carbonatite containing total rare earth concentrations (ΣREE) up to 3.4 wt.% REE (predominantly LREE), 0.4 wt.% niobium, and 0.2 wt.% molybdenum over 48.6 m (Lane 2009, 2010).

This study documents the nature of the Wicheeda carbonatite and its host rocks, provides a detailed description of the REE mineralization, and makes a preliminary interpretation of the genesis of this mineralization, based on detailed mapping of outcrops, diamond drill core logging, optical and EDS-assisted scanning electron microscopy, and bulk rock geochemical analyses. The principal findings of the study are: the carbonatite comprises a dolomitic core and a thin outer calcitic facies; bastnäsite-(Ce) and subordinate monazite-(Ce) are the main REE minerals; and the REE mineralization was the product of magmatic hydrothermal fluids, which also fenitized the surrounding metasedimentary rocks.

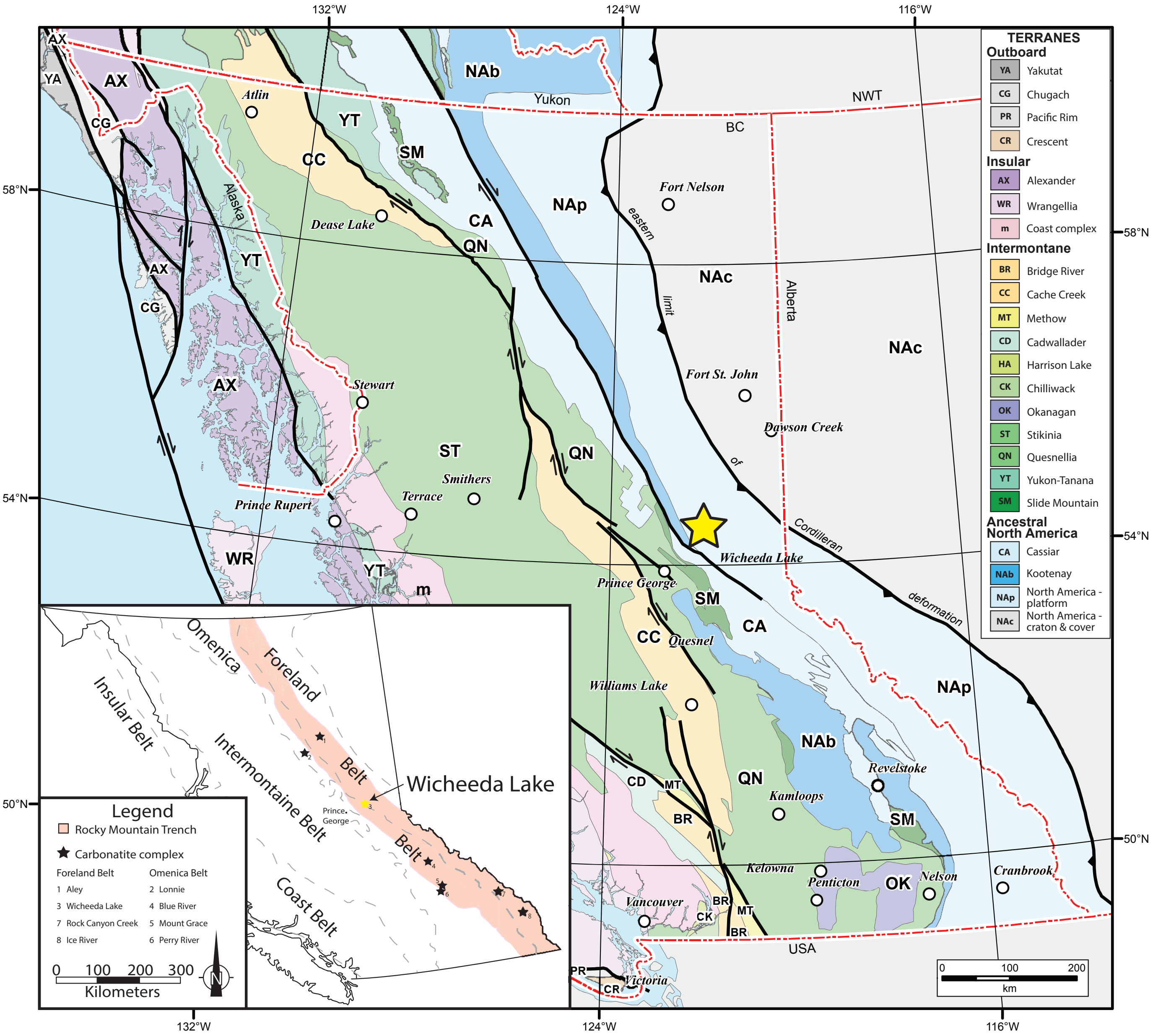

Fig. 1. Terrane assemblages and major tectonic features of Western Canada, with the Wicheeda Lake carbonatite highlighted by the yellow star. Inset: Distribution of major tectonic belts (dashed lines) and the Wicheeda carbonatite. The British Columbia alkaline Province is outlined in pink. From Colpron and Nelson (2011). Inset from Pell (1994).

2. Deposit geology

The Wicheeda complex is a dolomite and calcite carbonatite intrusion which, based on sparse outcrop and drill hole data, appears to be semi-circular in plan view (Fig. 2). On its western flank, the carbonatite is in fault contact with unaltered Kechika Group metasedimentary rocks. East of the fault, the carbonatite is surrounded by Kechika Group argillaceous limestone (Betmanis, 1987), which has been altered to potassic and sodic fenite (Fig. 2). Two outcrops of carbonatite and one of fine-grained felsic igneous rock lie to the east of the main carbonatite intrusion (Fig. 2).

The following descriptions are based on field mapping and petrographic examination using a combination of transmitted and reflected light microscopy, energy-dispersive X-ray spectroscopy (EDS)-assisted scanning electron microscopy, and cathodoluminescence.

2.1. Carbonatite

Dolomitic carbonatite occurs in the central part of the main intrusion and as an isolated outcrop ~ 150 m northeast of the main intrusion (Fig. 2). On the northeast margin of the complex, dolomite carbonatite passes gradationally into a fine-grained calcite carbonatite. Calcite carbonatite is also exposed

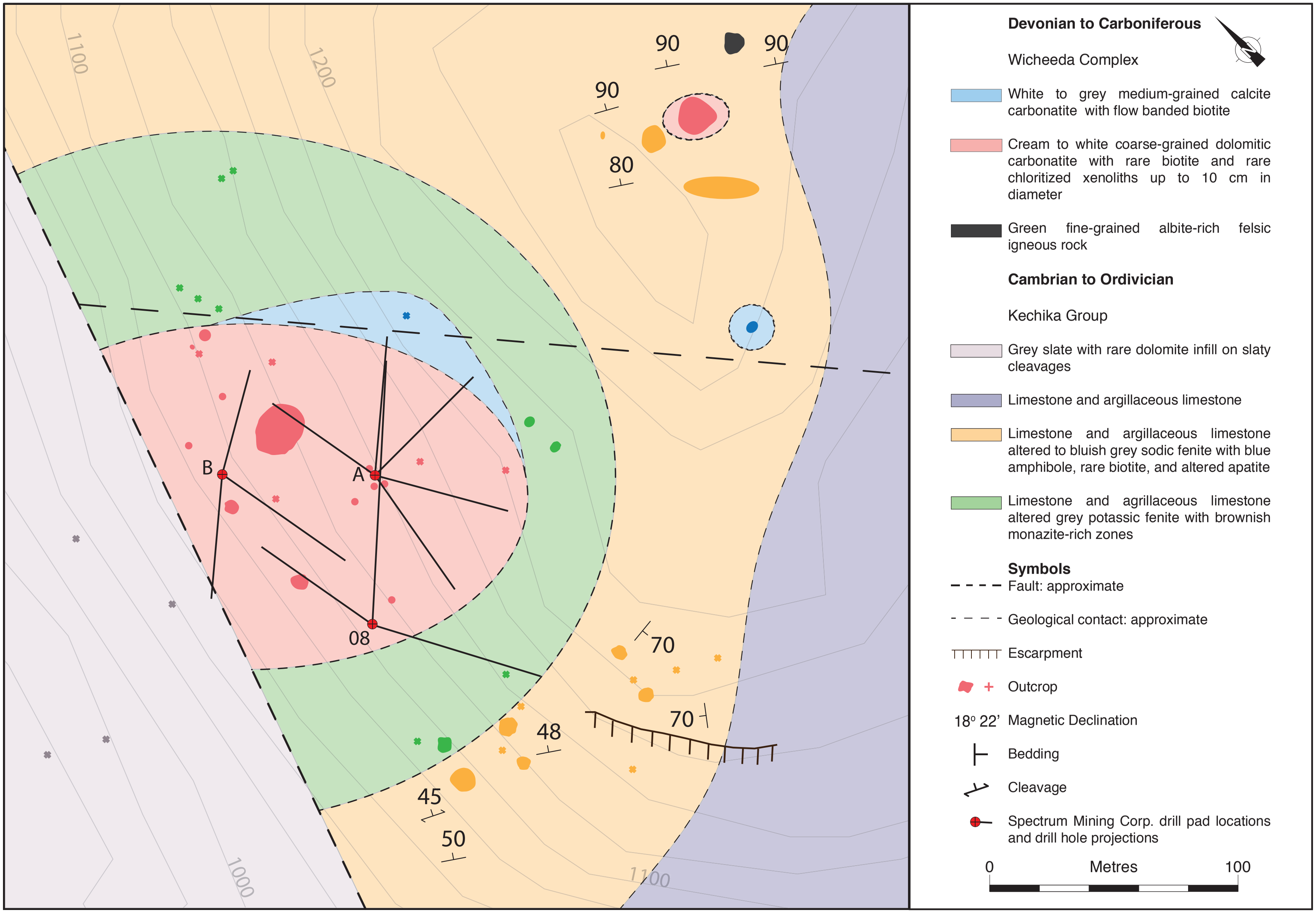

Fig. 2. Geological map of the Wicheeda carbonatite (at 54.315N, 122.051W). The location and geometry of the intrusion in relation to faults is based on fieldwork conducted in the summer of 2013.

in a single outcrop east of the main intrusion (Fig. 2).

In most outcrops, the dolomitic carbonatite is heavily oxidized dark orange or brown; where fresh, it is white to cream (Fig. 3a). It consists mainly of large euhedral dolomite crystals (70-80 vol.%) up to 2 cm in diameter accompanied by vein and vug-filling K-feldspar (5-15 vol%), dark micas (5-15 vol. %), pyrite (5 vol.%), hematite (2-5 vol.%), calcite (5 vol.%), and REE-fluorocarbonates (3-5 vol.%) including bastnäsite-(Ce) ($CeCO_3F$), parisite-(Ce) ($CaCe_2(CO_3)_3F_2$, synchysite-(Ce) ($CaCe(CO_3)_2F$), burbankite-(Ce) ($(Na,Ca)_3(Sr,Ba,Ce)_3(CO_3)_5$; 1 vol.%), and euhedral monazite-(Ce) ($CePO_4$; 1-3 vol.%). Three varieties of dolomite have been recognized. The first two comprise a relatively clear, coarse-grained, inclusion-poor variety (Dol I) and a dusty, micro-fluid inclusion-rich variety (Dol II; Figs. 3b, c). The third variety is a strongly zoned, cavity infill dolomite (Dol III; Fig. 3d). Biotite (< 2 mm flakes) and pyrite (rare euhedral cubes, < 3 mm) are disseminated in the dolomite carbonatite. Hematite (2-5 vol.%) occurs as weakly formed selvages to cleavages and veins. Calcite crosscuts the dolomite as veinlets up to 5 mm wide. Accessory rutile and molybdenite are observed as inclusions and clusters of grains in cobble- to boulder-sized chloritized xenoliths and are found within 10 metres of the contact with the fenitized sedimentary rocks. Bastnäsite-(Ce) occurs as a vug-filling phase with fan-like intergrowths of parisite-(Ce) and synchysite-(Ce) (Figs. 3b, e), which nucleates along fractured dolomite grains. Monazite-(Ce) is found as small, isolated, lath-like crystals or aggregates of crystals in vugs or veins (Fig. 3c) and rarely as fine-grained inclusions in bastnäsite-(Ce). Burbankite-(Ce) occurs in veinlets and very fine-grained inclusions in bastnäsite-(Ce). Niobian rutile ($(Ti,Nb)O_2$) (1 vol.%) forms subhedral grains included in biotite and K-feldspar.

The calcite carbonatite comprises medium-grained, equigranular, fluid inclusion-rich calcite (85-90 vol.%; Fig. 4a) with minor biotite (5-15 vol.%), albite (5-10 vol.%), aegirine (2-3 vol.%), pyrochlore (1 vol.%), cubic pyrite (1-2 vol.%), and trace apatite. Flow banding is evident locally from alternating millimetre-thick layers containing 10 to 15 vol.% of biotite crystals up to 200 µm in diameter and thicker (2 – 5 mm) calcite-rich layers (Fig. 4a). The albite is very fine-grained, with crystals generally < 100 µm long.. Commonly, the crystals contain inclusions of small rounded calcite up to 4 µm in diameter (Fig. 4b). The aegirine forms small euhedral crystals up to 100 µm long and is encountered most commonly in calcite carbonatite near the contact with the dolomite carbonatite. Trace pyrochlore occurs as brownish euhedral grains up to 200 µm in diameter (Fig. 4c). Pyrite cubes, typically > 100 µm in diameter (1-2 vol.%) and zoisite locally occur in cavities (Fig. 4c). The isolated calcite carbonatite to the east is very similar to that in the northeastern part of the main intrusion.

2.2. Kechika Group metasedimentary rocks

The Kechika Group metasedimentary rocks exposed west of the NE-SW trending fault comprise weakly foliated grey slates with a well-developed cleavage and fractures infilled by dolomite. The rocks surrounding the study area to the north, east, and south (east of the NE-SW trending fault), are thickly bedded, steeply dipping limestone and argillaceous limestone (Fig. 2; Betmanis, 1987). In the study area they have been altered to fenite. Bedding is preserved in the fenite; the strike ranges from 320 to 350° and the dip from 45 to 90° (Fig. 2).

2.3. Fenite

Adjacent to the main carbonatite intrusion, except on its western, fault-bounded side, the Kechika metasedimentary rocks have been altered to potassic fenite for distances varying from 40 m to more than 75 m from the intrusion (Fig. 2). Beyond this, to the north, east, and south, the potassic fenites pass gradationally into sodic fenites that persist to the limits of the outcrop in the study area (Fig. 2). Northeast of the carbonatite, the contact between the potassic and sodic fenite is unconstrained because of a lack of outcrop.

The potassic fenite outcrops poorly and the following descriptions are based mainly on drill core. It varies in colour from pale beige (strongly altered) to pale grey (least altered) (Fig. 5a) and is composed mainly of fine-grained anhedral albite (20-30 vol.%) that has been extensively altered to K-feldspar (35-45 vol.%). The K-feldspar is generally found as small anhedral grains (up to 50 µm in diameter) containing rare albite inclusions (Fig. 5b). Calcite (15 vol.%) is interstitial to K-feldspar and albite, and is rimmed by dolomite (10 vol.%). Rutile (2-5 vol.%) occurs locally as large grain aggregates (Fig. 5b). Apatite (2-5 vol.%) forms anhedral fragmented grains up to 100 µm in diameter (Fig. 5c) and contains albite inclusions up to 10 µm in length. It is rarely altered to britholite-(Ce) (($(Ce,Ca,Th,La,Nd)_5(SiO_4,PO_4)_3(OH,F)$), and contains elevated REE based on its blue to violet luminescence (e.g., Kempe and Gôtze, 1988). Monazite-(Ce) (2-3 vol.%) typically occurs as aggregates of small euhedral grains up to 20 µm in diameter. It is concentrated near the contacts between dolomite and K-feldspar crystals, and is frequently observed as a cavity-filling phase within the dolomite (Fig. 5c). Burbankite-(Ce) is found most commonly in thin veinlets in the potassic fenite and at the contact with the sodic fenite.

The sodic fenite consists mainly of albite (25-35 vol.%), calcite (25-35 vol.%), and riebeckite (15-20 vol. %). Sedimentary layering locally survived fenitization, and is preserved as alternating albite- and calcite-rich laminations (Fig. 6a). Albitic laminations consist of fine-grained subhedral albite laths up to 0.1 mm in length and subordinate, very fine-grained anhedral calcite. The albite is accompanied by fine-grained pyrite (oxidized in surface exposures). The calcite laminations are coarser-grained, with individual crystals ranging up to 0.8 mm in diameter. Bluish-green riebeckite is present as corroded subhedral prisms up to 100 µm in length and rarely as acicular grains. Brown biotite (15-25 vol.%) occurs as fine-grained disseminated flakes, and dark, euhedral apatite grains up to 1 mm in diameter are present throughout the albite + calcite matrix and in veinlets with calcite (Fig. 6b). Commonly, chlorite rims the biotite grains in the veinlets (Fig. 6c). Fractures in the

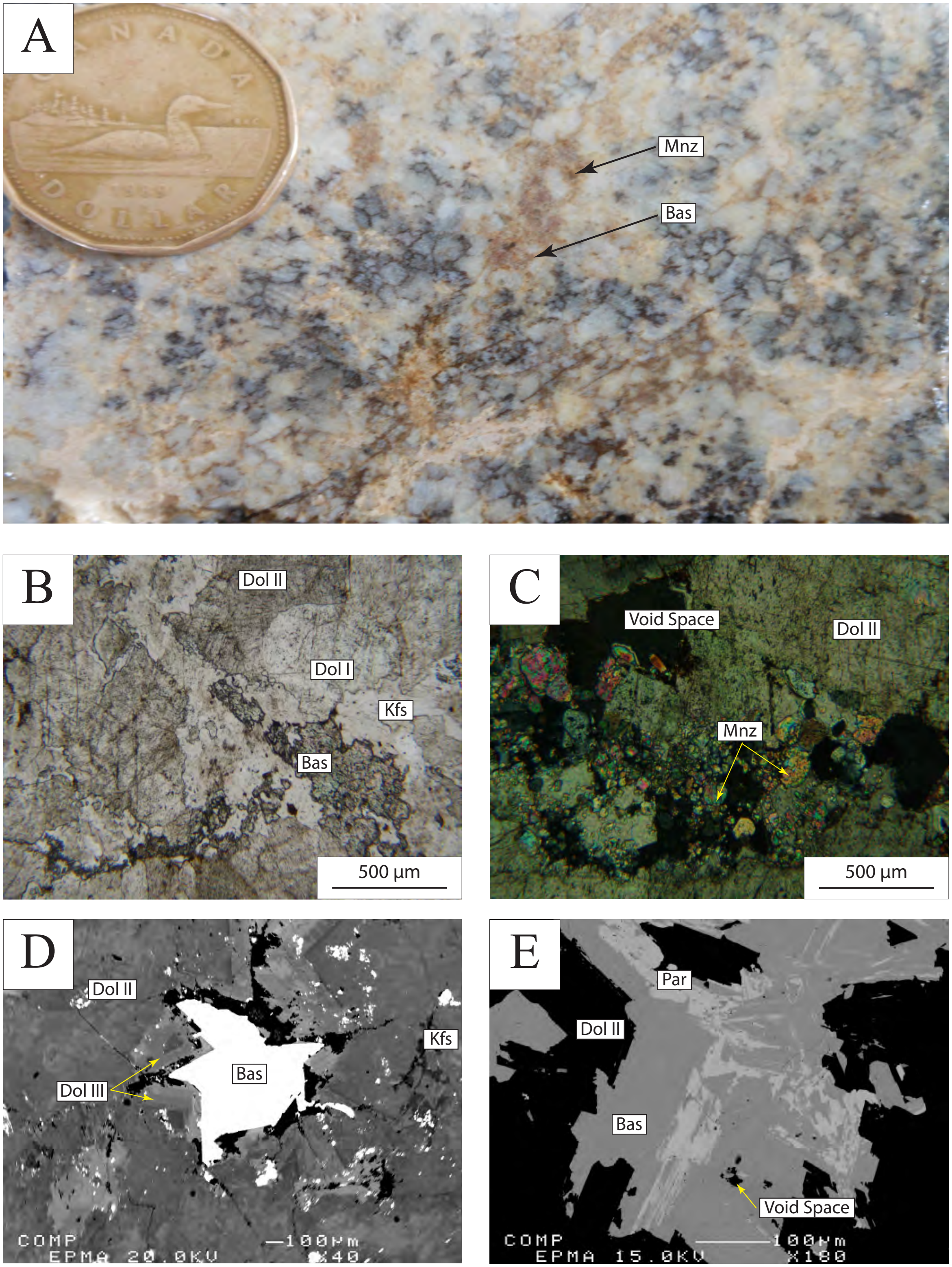

Fig. 3. **a)** Dolomite carbonatite showing brecciated dolomite with hematite (dark red) crackle texture overprinted by beige dolomite and fracture-filled brownish monazite-(Ce) (Mnz) and bastnäsite-(Ce) (Bas). **b)** Dolomite carbonatite in plane polarized light with clear Dol I and dusty Dol II dolomite and fractures infilled by K-feldspar (Kfs) and coarse bastnäsite-(Ce). **c)** Dolomite carbonatite under cross polars showing dusty dolomite Dol II and a fracture filled by K-feldspar and fine-grained monazite-(Ce). **d)** Backscatter electron image of dolomite carbonatite showing dusty dolomite with poorly defined grain boundaries Dol II and a strongly-zoned dolomite Dol III in a cavity infilled by bastnäsite-(Ce). **e)** Backscatter electron image showing a cavity in dolomite carbonatite infilled by syntaxial intergrowths of bastnäsite-(Ce) and parisite-(Ce) (Par).

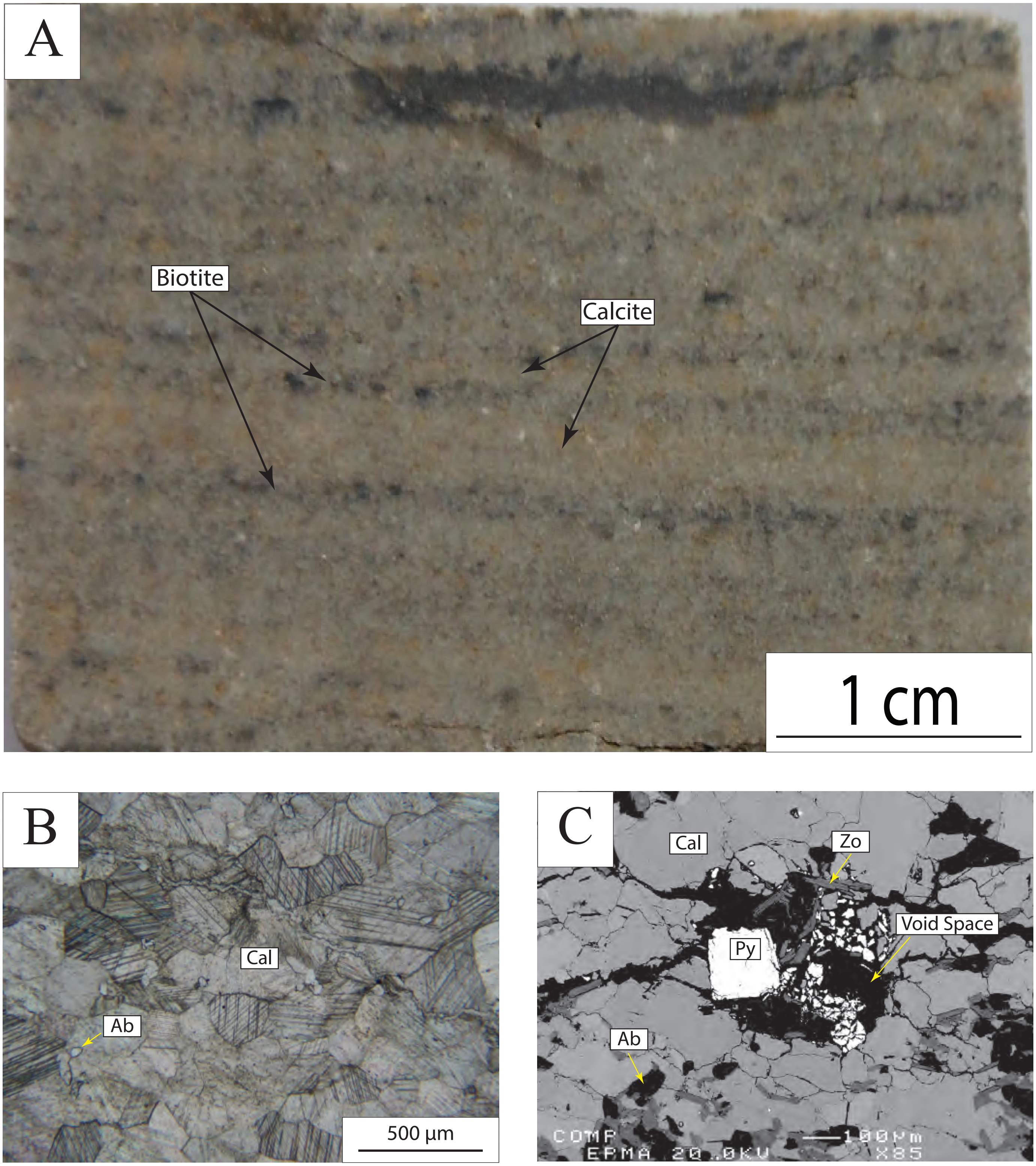

Fig. 4. Calcite carbonatite. **a)** Photograph of calcite carbonatite with alternating dark biotite-rich and white to pale grey calcite layers. **b)** Plane-polarized light image of fine-grained equigranular calcite (Cal) in calcite carbonatite accompanied by very small rare grains of albite (Ab). **c)** Backscattered electron image showing fractured calcite carbonatite containing a vug partially filled by pyrite (py), zoisite (Zo) and albite; albite is also disseminated in the matrix of the carbonatite.

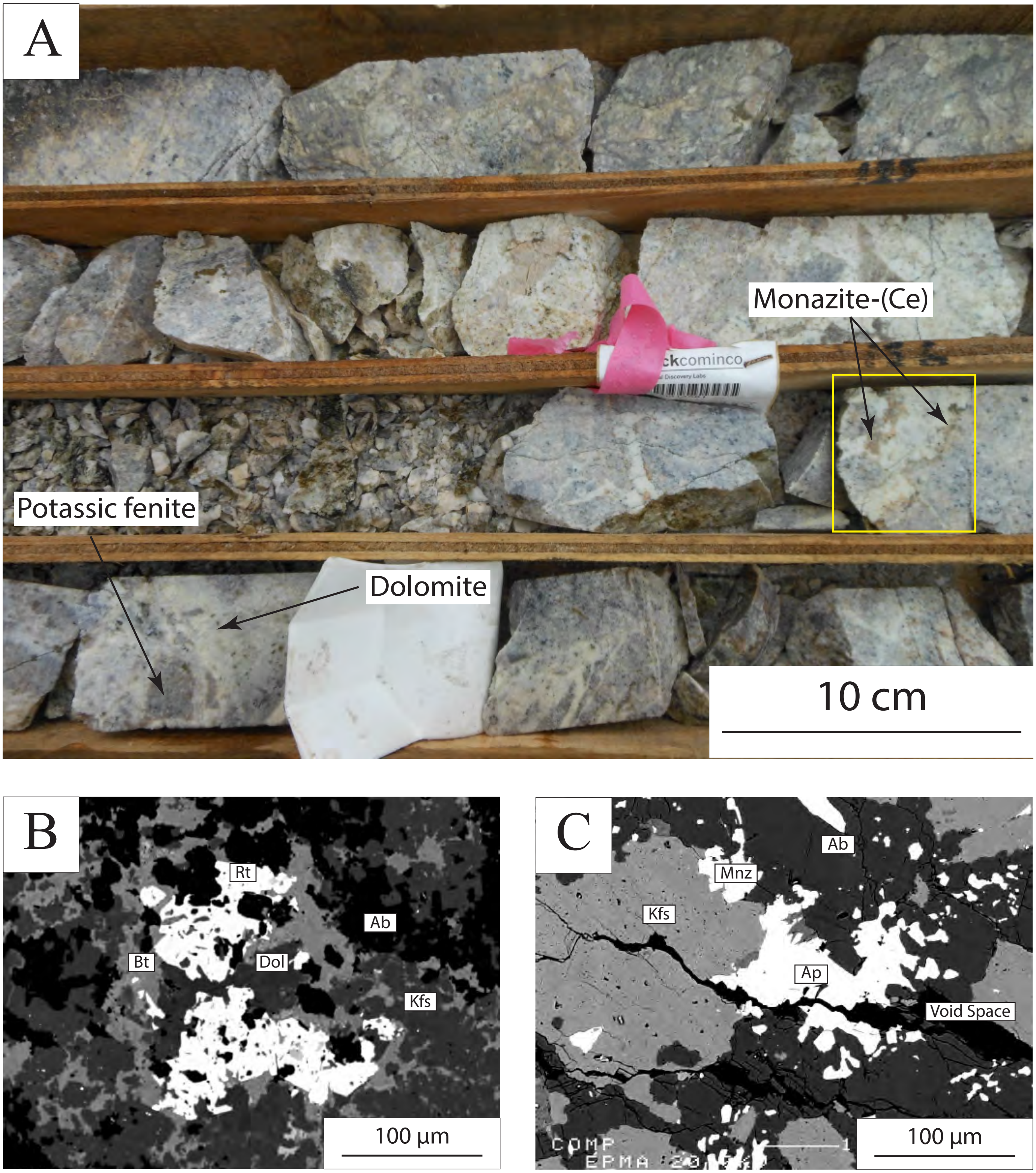

Fig. 5. Potassic fenite. **a)** Intensely altered potassic fenite from drill hole WI-09-08 (~ 135 m depth) showing beige clots of monazite-(Ce) at the contact between the fenite and dolomite-filled fractures. **b)** Backscattered electron image of potassic fenite showing albite variably replaced by K-feldspar, biotite, rutile (Rt) and dolomite (Dol). **c)** Backscattered electron image of potassic fenite with apatite and monazite-(Ce) replacing albite and K-feldspar.

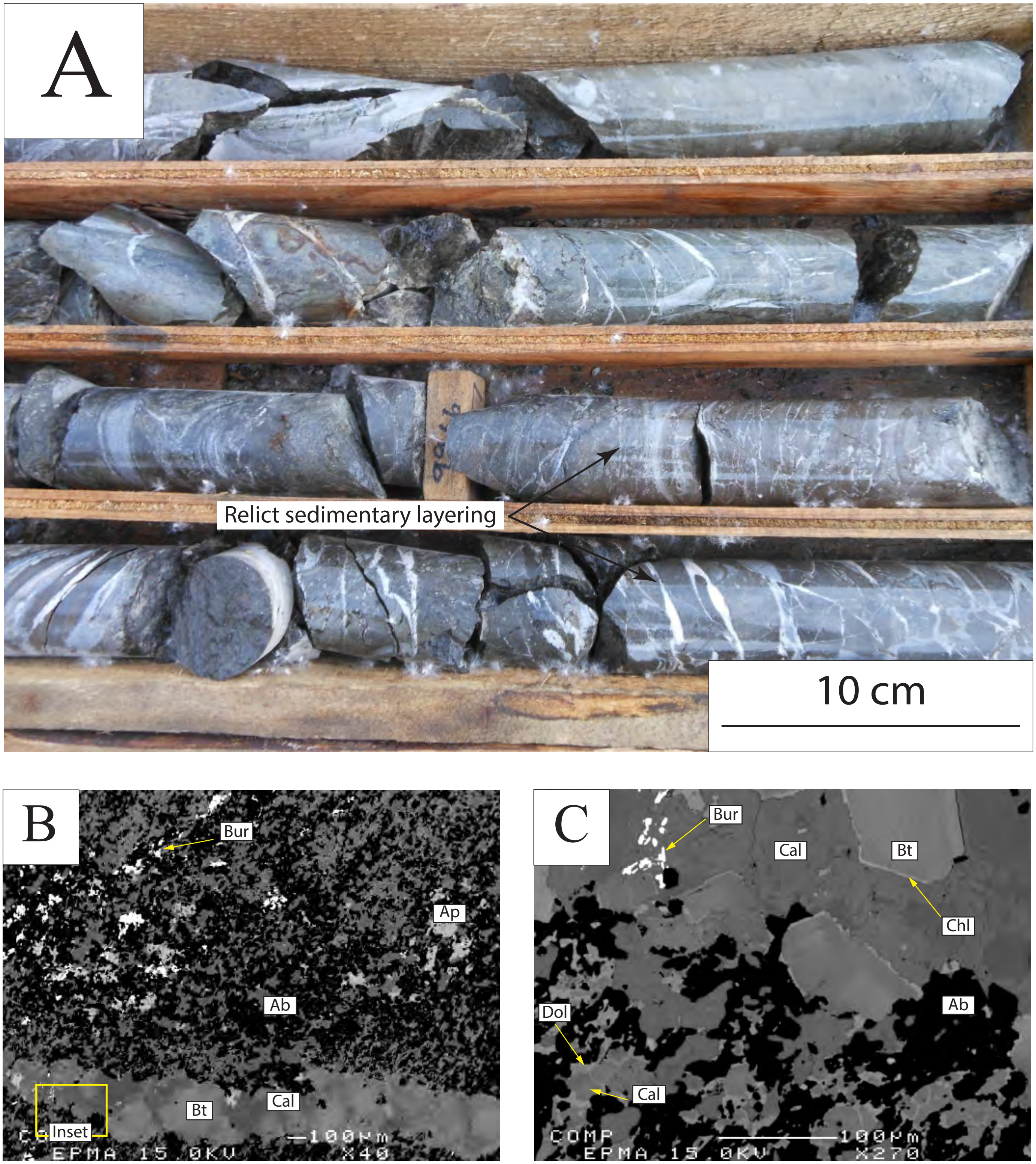

Fig. 6. Sodic fenite. **a)** Fractured sodic fenite from drill hole 08-WI-01 (180 m depth) showing relict sedimentary layering of the Kechika Group rocks, evident as alternating pale blue and pale green-grey bands. **b)** Backscattered electron image of sodic fenite with mottled albite and calcite and a crosscutting veinlet of calcite (Cal), biotite (Bt), and burbankite-(Ce) (Bur). **c)** Inset of b) showing a calcite+biotite vein with biotite rimmed by chlorite (Chl).

sodic fenite are frequently filled with dolomite (10 vol.%), siderite (5 vol.%), and locally burbankite-(Ce) (1 vol.%; Fig. 6b) near its contact with the potassic fenite. A lack of alignment of the secondary minerals described above suggests that sodic fenitization post-dated regional metamorphism.

3. Bulk Rock Geochemistry

Fourteen samples of the Wicheeda Lake carbonatite and associated fenite were analysed by ALS Laboratories in Vancouver for their bulk and trace element compositions. All samples were ground using a steel mill. The major element chemistry was determined using lithium metaborate fusion followed by Inductively Coupled Plasma Emission Spectrometry (ICPES). Loss on ignition (LOI) was determined after fusion. Total carbon and sulphur contents were determined using the LECO combustion method. The other trace elements were analyzed by Inductively Coupled Plasma Mass Spectrometry (ICPMS). The results are summarized in Table 1 and illustrated in Figs. 7- 9.

3.1. Carbonatites

Eight samples were analyzed from the dolomitic core of the main intrusion (Table 1). The main non-volatile components are CaO (25.8 wt.%), MgO (13.28 wt.%) and Fe_2O_3 (8.28 wt.%). ΣREE concentrations average 4.5 wt.% and range from 1.1 to 11.2 wt.%. There are also minor concentrations of P_2O_5 (0.89 wt.%), SrO (0.13 wt.%), BaO (0.81 wt.%), S (0.34 wt.%) and F (0.5 wt.%). The concentration of Nb averages 88 ppm and ranges from 4 ppm to 219 ppm. Concentrations of TiO_2 are below the detection limit for all of the samples.

One sample of the calcite carbonatite was analyzed (Table 1). It contains more CaO (44.9 wt.%), less MgO (2.24 wt.%), and less Fe_2O_3 (4.22 wt.%) than the dolomite carbonatite. The contents of SrO (1.59 wt%) and P_2O_5 (2.46 wt.%) are very much higher, and the BaO content (0.32 wt.%) lower than the dolomite carbonatite. The calcite carbonatite contains an order of magnitude lower ΣREE (0.4 wt.%) than the dolomite carbonatite and virtually no fluorine, but is very enriched in Nb (2500 ppm).

The carbonatites were classified using the carbonatite classification diagram of Gittins and Harmer (1997). Based on its content of Ca, Mg, Fe, and Mn, the marginal carbonatite sample classifies as a calcio-carbonatite. The eight samples collected from the core of the intrusion classify as magnesio-carbonatite, although one of these samples plots on the border of the magnesio-carbonatite and ferruginous calcio-carbonatite fields (Fig. 7).

3.2. Fenites

The potassic fenite contains an average of 27.2 wt.% SiO_2, 7.2 wt.% Al_2O_3, 8.7 wt% Fe_2O_3, 9.0 wt.% MgO, 2.92 wt.% K_2O and 0.5 wt.% Na_2O (Table 1). It has a high content of ΣREE (0.51 wt.%), Nb (1140 ppm) and P_2O_5 (0.76 wt.%) relative to the sodic fenite, but the lowest BaO (0.07 wt.%) and SrO (0.1 wt.%) contents of any of the rocks in the study area. It also contains 0.52 wt.% S and has an F content below the detection limit.

The single sodic fenite sample (Table 1) contains more SiO_2 (37 wt.%), and Na_2O (5.5 wt.%) than the potassic fenite, less Fe_2O_3 (6.2 wt.%), and has a relatively low K_2O content (0.82 wt.%). It also contains more SrO (0.48 wt.%) and BaO (0.16 wt.%) than the potassic fenite, but a lower content of P_2O_5 (0.42 wt.%) and a very much lower content of S (0.02 wt.%). The ΣREE (0.09 wt.%) and Nb (29 ppm) contents are likewise very low and the F content below the detection limit.

The differences in the Na_2O and K_2O contents of the potassic and sodic fenites confirm the classification of the two fenite types (Fig. 8), which was inferred initially from the differences in their mineralogy. In combination with differences in the contents of SiO_2, Al_2O_3, Fe_2O_3 and Nb, this also suggests that the fluids responsible for the two types of fenite likely had different sources (see below).

4. REE Distribution

Chondrite-normalized REE profiles for the Wicheeda carbonatites and fenites are LREE-enriched and lack a europium anomaly (Fig. 9). The profiles of the carbonatites, and the potassic and sodic fenite are similar, although the REE content of the dolomite carbonatite is significantly higher than those of the other rocks types (Fig. 9). The dolomite carbonatite is highly enriched in LREE (La/Lu = 4314), whereas the calcite carbonatite has a much lower degree of LREE enrichment (La/Lu = 204) and is less enriched in the REE than all except one of the fenite samples. The potassic fenite samples have REE contents comparable to or slightly greater than the calcite carbonatite. They are strongly enriched in the HREE relative to the calcite carbonatite (Fig. 9) with La/Lu values of 1209 and 1288; the Yb and Lu contents of the most REE-enriched fenite are comparable to those of the most REE-enriched dolomite carbonatite. The sodic fenite sample is the least LREE enriched of all the samples analyzed and has a La/Lu ratios of 46.

4.1. Element correlations

As discussed above, the REE mineralization at Wicheeda is largely restricted to the dolomite carbonatite. A correlation coefficient matrix was generated for the dolomite carbonatite to evaluate relationships of cerium (as a representative of the light REE) with elements in host rocks that may have influenced its concentration (Table 2). The coefficients for Ce-F, Ce-Ba, and Ce-P are 0.96, 0.39, and -0.30, respectively. The high correlation between Ce and F is consistent with the observation that fluorocarbonates such as bastnäsite-(Ce) ($CeCO_3F$) are an important host for the REE and that there are negligible proportions of other fluorine-bearing minerals, such as fluorite or fluorapatite. By contrast, although the correlation between Ce and Ba can be explained, in part, by the occurrence of burbankite $(Na,Ca)_3(Sr, Ba, Ce)_3(CO_3)_5$, its low value suggests the presence of other barium-bearing minerals or elevated concentrations of Ba in carbonate minerals or K-feldspar. Preliminary microscopic examination (optical and

Table 1. Bulk rock compositions of dolomite and calcite carbonatites, and sodic and potassic fenites, Wicheeda Lake. bdl - below detection limit. ΣREE – sum of rare earth elements and yttrium.

	Detection Limit	Dolomite Carbonatite								Calcite Carbonatite	Potassic Fenite		Sodic Fenite
%		WI-11-02	WI-11-03	WI-11-07	WI-11-09	WI-11-11	WI-11-12	WI-13-49	WI-13-62	WI-13-50	WI-13-57	WI-13-63	WI-13-55
SiO_2	0.01	4.45	4.22	3.45	2	1.05	5.42	3.55	1.48	6.33	20	34.4	37
Al_2O_3	0.01	1.41	1.16	0.96	0.53	0.28	1.56	0.31	0.28	1.78	5.86	8.49	6.46
Fe_2O_3	0.01	8.23	8.08	6.31	6.91	9.5	6.54	10.65	10	4.22	7.74	9.62	6.2
CaO	0.01	26.2	23.8	23.3	21	27.6	27.1	27.9	29.7	44.9	20.8	14.15	22.4
MgO	0.01	13.55	13.1	13.05	13.8	12.3	14.25	12.8	13.4	2.24	8.55	9.36	3.22
Na_2O	0.01	0.37	0.69	0.66	0.26	0.14	0.88	0.18	0.04	0.44	0.37	0.62	5.45
K_2O	0.01	0.47	0.1	bdl	0.04	bdl	0.04	0.02	0.13	0.7	4.44	1.42	0.82
Cr_2O_3	0.01	bdl	bdl	bdl	bdl	bdl	bdl	bdl	bdl	bdl	bdl	bdl	bdl
TiO_2	0.01	bdl	bdl	bdl	bdl	bdl	bdl	bdl	bdl	0.22	0.2	0.48	0.27
MnO	0.01	1.24	1.07	0.82	0.36	1.69	0.87	1.91	1.9	0.83	1.36	0.57	0.51
P_2O_5	0.01	1.38	0.21	1.39	0.04	1.7	1.44	0.87	0.01	2.46	1.34	0.18	0.42
SrO	0.01	0.06	0.17	0.2	0.06	0.13	0.05	0.11	0.09	1.59	0.13	0.06	0.48
BaO	0.01	0.17	0.61	0.81	bdl	0.04	bdl	0.03	0.03	0.32	0.07	bdl	0.16
LOI	0.01	38.8	36.8	37.6	35.2	39.5	39.2	40.1	42.3	32.4	27.7	18.75	17.5
Total		96.33	90.02	88.56	80.22	93.93	97.36	98.43	99.37	98.43	98.56	98.14	100.89
C	0.01	10.35	10.95	10.7	10.55	11.3	11	12.2	12.9	9.64	8.26	5.21	4.91
S	0.01	0.04	0.88	0.26	1.39	0.08	0.03	0.03	0.03	0.61	0.05	0.98	0.02
F	0.01	0.09	0.7	0.61	1.45	0.02	0.07	bdl	bdl	bdl	bdl	bdl	bdl
ppm													
Nb	0.2	153	62.2	27.2	191.5	33.7	4	13.6	219	2500	559	1720	29.3
Th	0.05	301	898	1000	1000	422	252	454	217	54.7	175.5	82.8	33.6
U	0.05	2.78	2.35	0.98	2.02	0.5	0.34	0.53	2.72	27.7	7.73	24	0.4
Zr	2	bdl	bdl	bdl	bdl	bdl	bdl	bdl	bdl	108	bdl	3	211
La	0.5	11000	22700	28300	40500	11100	6980	5720	3650	1105	2110	1165	229
Ce	0.5	14500	27900	37000	53200	15300	8620	9000	5030	2040	3030	1685	402
Pr	0.03	1100	2100	2800	4300	1100	844	820	419	177.5	261	147.5	37.1
Nd	0.1	3340	6340	8710	11900	3670	2460	2520	1225	522	796	441	115.5
Sm	0.03	311	450	682	900	334	265	281	127	55.4	107.5	55.1	15.95
Eu	0.03	88.4	86.1	143.5	178	86	71.9	58.6	30.2	14.85	32.6	15.05	4.22
Gd	0.05	162	175.5	280	390	164.5	145.5	121.5	58.7	27.7	70.6	30.9	10.7
Tb	0.01	16.6	13.65	21.4	27.2	15.35	13.55	9.3	4.64	3.21	7.9	3.52	1.44
Dy	0.05	62.5	43	66.6	84.4	53.9	50.5	24.7	12.65	14.05	28.9	13.15	7.64
Ho	0.01	7.2	4.79	7.06	9.08	6.08	6.26	2.45	1.18	2.34	3.45	1.56	1.45
Er	0.03	11.15	6.79	9.12	12.05	9.26	10.4	3.76	1.62	5.73	5.42	2.52	3.93
Tm	0.01	0.9	0.54	0.72	0.9	0.79	0.93	0.29	0.11	0.65	0.4	0.2	0.52
Yb	0.03	3.79	2.73	3.64	4.1	3.79	4.19	1.51	0.63	4.19	1.63	1.03	3.53
Lu	0.01	0.41	0.34	0.47	0.53	0.47	0.49	0.24	0.09	0.56	0.17	0.1	0.52
Y	0.5	130	102	143	190	117	136	53.9	24.4	62.5	66.5	31.2	38.5
ΣREE		30734	59925	78168	111696	31961	19609	18617	10585	4036	6522	3593	872

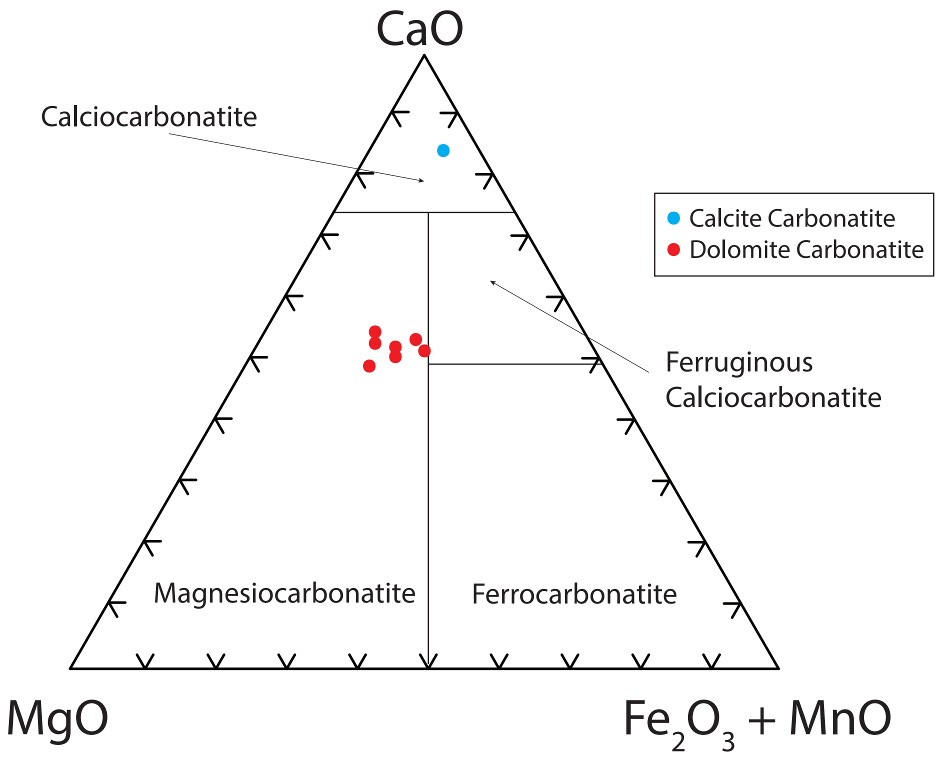

Fig. 7. Compositions of the carbonatite rocks of the Wicheeda area on the classification diagram of Gittins and Harmer (1997).

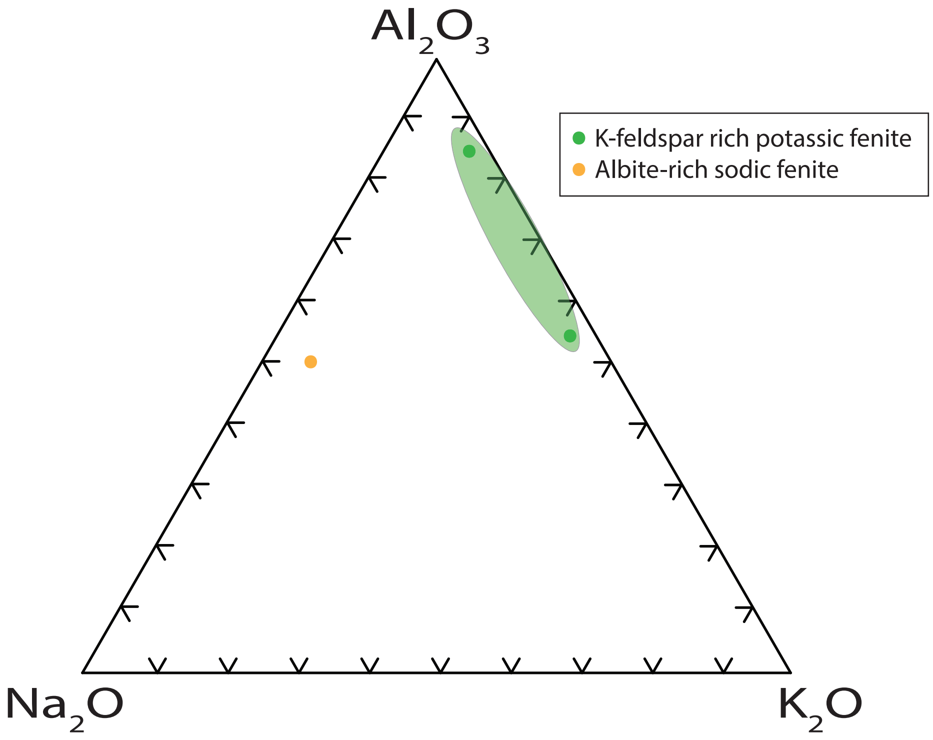

Fig. 8. Al_2O_3-Na_2O-K_2O classification diagram for Kechika Group rocks altered to albite- (orange) and K-feldspar-rich (green) fenites or sodic and potassic fenites, respectively.

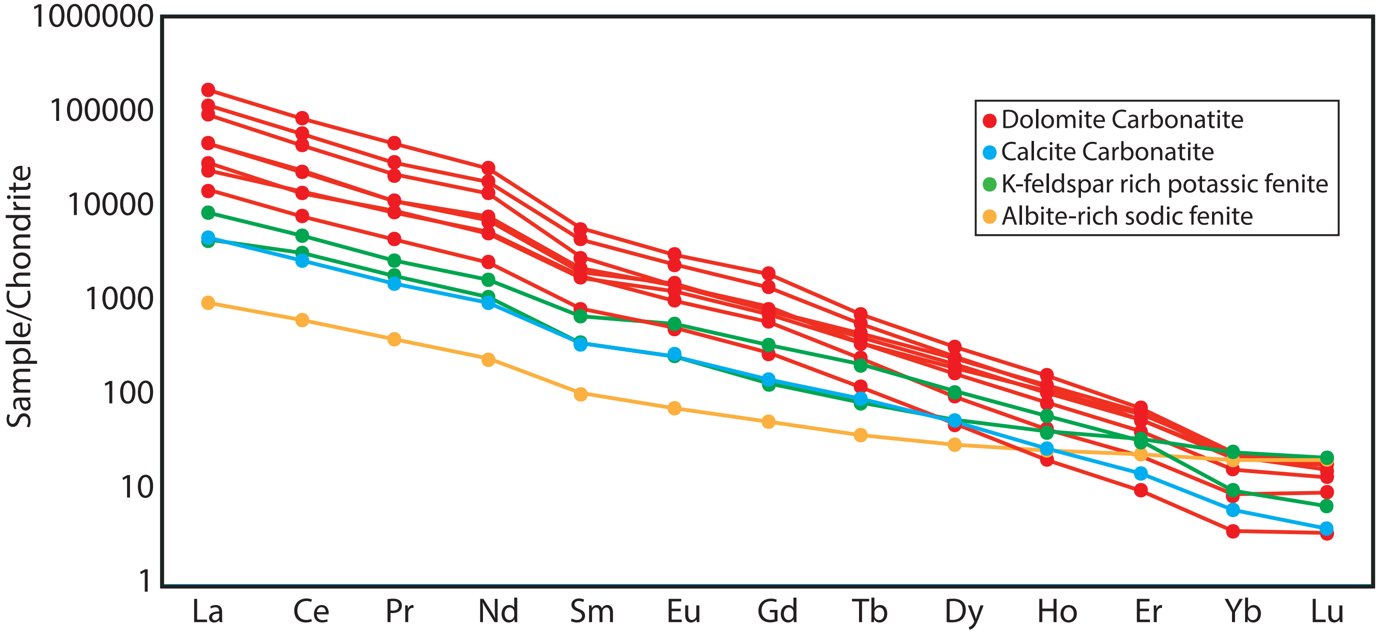

Fig. 9. Chondrite-normalized REE profiles of Wicheeda carbonatites and fenites. The chondrite values were taken from McDonough and Sun (1995).

Table 2. Correlation matrix of selected elements and oxides for dolomite carbonatite samples from the main intrusion. Data from bulk rock geochemistry.

	Ba	Ce	F	K_2O	Lu	Nb	Sm	P_2O_5	Sr	Y	Yb
Ba	1										
Ce	0.39	1									
F	0.28	0.96	1								
K_2O	-0.06	-0.22	-0.21	1							
Lu	0.14	0.58	0.47	-0.11	1						
Nb	-0.29	0.19	0.30	0.46	-0.32	1					
Sm	0.36	0.99	0.93	-0.27	0.64	0.10	1				
P_2O_5	0.06	-0.30	-0.50	0.08	0.48	-0.65	-0.20	1			
Sr	0.84	0.24	0.09	-0.38	-0.04	-0.43	0.21	0.09	1		
Y	0.16	0.75	0.67	-0.01	0.95	-0.06	0.79	0.24	-0.11	1	
Yb	0.12	0.48	0.38	0.05	0.98	-0.26	0.54	0.52	-0.12	0.93	1

EDS-assisted scanning electron microscopy), however, has not revealed the presence of other Ba-bearing minerals, e.g., barite, and K-feldspar, and K-feldspar has not yet been analyzed for its Ba content. The relatively poor Ce-Ba correlation remains unexplained.

As inclusions of monazite-(Ce) were observed in the dolomite carbonatite, we expected a weak positive correlation of Ce with P. Instead, the correlation is negative. We tentatively conclude that the signal of monazite-(Ce) was swamped by apatite (another phosphate mineral, which is found in minor proportions in the carbonatite) and that the apatite contains relatively little REE (this latter conclusion remains to be tested).

5. Discussion

Outcrop and drill core observations indicate that both the dolomite and calcite carbonatites and the host Kechika Group metasedimentary rocks were strongly altered by hydrothermal fluids. The host rocks were altered to potassic fenite surrounding the carbonatite (40 – 75 m away) and sodic fenite to the extent of the outcrop in the mapped area; the distribution of the sodic fenite is poorly constrained.

The sodic fenite, which is represented mainly by albitization, is interpreted to be the product of alteration by formational waters heated by the carbonatite. This is supported by the observation that fluids, which are initially in equilibrium with two alkali feldspars (likely the case for formational waters in contact with siltstone), will move into the stability field of albite on being heated (Lagache and Weisbrod, 1977). Using the same line of reasoning, we interpret the potassic fenite (mainly K-feldspar) to be the product of saline aqueous fluids released by the carbonatite magma (e.g., Williams-Jones and Palmer, 2002). As these fluids would have followed a cooling path after their exsolution, their physicochemical conditions would have evolved to the field of K-feldspar stability (Lagache and Weisbrod, 1977). Although, we do not know if these fluids were initially in equilibrium with two feldspars (the dolomite carbonatite contains primary K-feldspar but not albite) this is not important. The key observation is that whether or not they were initially in equilibrium with K-feldspar, they would have evolved towards its field of stability (the petrographic evidence suggests that they initiated in equilibrium with K-feldspar).

The rare earth mineralization is dominated by REE-fluorocarbonates accompanied by burbankite, cebaite-(Ce), and monazite-(Ce) in veinlets and vugs and as disseminations in the carbonatite and burbankite in veinlets in the potassic fenite and immediately adjacent sodic fenite. This shows that the mineralization is predominantly hydrothermal in origin. We propose a preliminary model in which the carbonatite magma exsolved a fluid, which fenitized the host metasediments near the intrusion to potassic fenite and heated formational water distal to the intrusion, altering the metasedimentary rocks to sodic fenite. The REE were concentrated by magmatic hydrothermal fluids, which partially dissolved the carbonatite, altering Dol I to Dol II, and led to deposition of compositionally zoned dolomite (Dol III) and later bastnäsite-(Ce) and monazite-(Ce) in veins and vugs in response to cooling and an increase in pH. As REE-fluoride mineral solubility is very low, except under extremely acidic conditions, it is proposed that REE-chloride complexes preferentially transported the REEs (Williams-Jones et al., 2012). There is the possibility that the REEs were transported as sulphate complexes (Migdisov and Williams-Jones, 2008), although this seems less likely given that sulphate minerals are rare to absent in the deposit. Like REE fluoride, REE-phosphate solubility is low, precluding the transport of elements like cerium as phosphate complexes. Instead, we consider that fluoride and phosphate acted as depositional ligands, promoting the concentration of the REE as fluorocarbonate minerals and monazite-(Ce).

6. Conclusions

The Wicheeda carbonatite is a high grade LREE deposit that was subjected to extensive alteration by magmatic fluids, and its intrusion was accompanied by pervasive fenitization of the wall rock to proximal potassic fenite and distal sodic fenite. Potassic fenitization was the product of cooling magmatic hydrothermal fluids and sodic fenitization the product of formational waters heated by the intrusion. The REE were concentrated by magmatic hydrothermal fluids, which deposited them dominantly as fluorocarbonate minerals in veinlets and vugs in the carbonatite, and to a much lesser extent as monazite-(Ce) in the potassic fenites, due to a combination of cooling and pH increase. Niobium is enriched in the calcite carbonatite in the form of pyrochlore, and is found rarely as hydrothermal niobian rutile in the dolomite carbonatite. In summary, the REE and associated HFSE mineralization in the Wicheeda deposit is exclusively hydrothermal in origin.

Acknowledgments

The authors are grateful to courtesies extended by Chris Graf. We also thank Spectrum Mining Corporation for permitting access to the property and facilities for logging the core, and Bob Lane (Plateau Minerals Corp.) for sharing his knowledge of the geology of the Wicheeda deposit. Duncan Mackay provided valuable assistance in the field and observations of the mineralization. The project received funding and support from Targeted Geoscience Initiative 4 (2010-2015), a Natural Resources Canada program carried out under the auspices of the Geological Survey of Canada. The authors would also like to thank Pearce Luck and Lawrence Aspler (British Columbia Geological Survey) for their reviews, which helped improve the manuscript.

References cited

Betmanis, A.I. 1987. Report on geological, geochemical and magnetometer surveys on the prince and George groups, cariboo mining division, British Columbia Ministry of Energy, Mines and Petroleum Resources, Assessment Report 15944.

Colpron, M., and Nelson, J.L. 2011. A digital atlas of terranes for the northern Cordillera. British Columbia Ministry of Energy and Mines, British Columbia Geological Survey, GeoFile 2011-11, scale 1:10 000 000.

Gittins, J., and Harmer, R.E. 1997. What is ferrocarbonatite? A revised classification. Journal of African Earth Sciences, 25, 159-168.

Lagache, M., and Weisbrod, A. 1977. The system: two alkali feldspars –KCl-NaCl-H_2O at moderate to high temperatures and low pressure. Contributions to Mineralogy and Petrology, 62, 77-101.

Lane, B. 2009. Diamond drilling report on the Wicheeda property. Allnorth Consultants: prepared for Spectrum Mining Corp.

Lane, B. 2010. Diamond drilling report on the Wicheeda property. Unpublished Report, Allnorth Consultants: prepared for Spectrum Mining Corp. 1-18.

Mäder, U.K., and Greenwood, H.J. 1987. Carbonatites and related rocks of the prince and George claims, northern rocky mountains (93J,93I). In: Geological Fieldwork 1987, British Columbia Ministry of Energy, Mines and Petroleum Resources, British Columbia Geological Survey Paper 1988-1, 375-380.

Migdisov, A.A., and Williams-Jones, A.E. 2008. A spectrophotometric study of Nd(III), Sm(III), and Er(III) complexation in sulfate-bearing solutions at elevated temperatures. Geochimica and Cosmochimica Acta, 72, 5291-5303.

Millonig, L.J., Gerdes, A., and Groat, L.A. 2012. U-Th-Pb geochronology of meta-carbonatites and meta-alkaline rocks in the southern Canadian Cordillera: A geodynamic perspective. Lithos, 152, 202-217.

McDonough, W.F., and Sun, S.-s, 1995. The composition of the Earth. Chemical Geology, 120, 223-253.

Pell, J., 1994. Carbonatites, nepheline syenites, kimberlites and related rocks in British Columbia. British Columbia Ministry of Energy, Mines and Petroleum Resources, British Columbia Geological Survey, Bulletin 88, 11-14.

Williams-Jones, A.E., and Palmer, D.A.S. 2008. The evolution of aqueous-carbonic fluids in the Amba Dongar carbonatite, India: implications for fenitisation. Chemical Geology 185, 283-301.

Williams-Jones, A.E., Migdisov, A.A., and Samson, I.M., 2012. Hydrothermal mobilization of the rare earth elements – a Tale of “Ceria” and “Yttria”. Elements, 8, 355-360.